Method Development and Application of Mass Spectrometry Imaging to Study Symbiotic Relationships Between Bacteria and Host Organisms

By

Erin Gemperline

A dissertation submitted in partial fulfillment of

the requirements for the degree of

Doctor of Philosophy

(Chemistry)

at the

University of Wisconsin-Madison

2016

Date of final oral examination: 04-01-2016

This dissertation is approved by the following members of the Final Oral Committee:

Lingjun Li, Professor, Pharmacy and Chemistry
Tim Bugni, Professor, Pharmacy and Chemistry
Cameron Currie, Professor, Bacteriology
Sandro Mecozzi, Professor, Chemistry
Michael Sussman, Professor, Biochemistry

To David, my husband and partner

&

To my loving parents

Acknowledgements

I would first like to acknowledge my advisor Lingjun Li, without whom this work would not be possible. Beyond the initial concepts underlying this work, she has given me the freedom and support to become an independent scientist. Dr. Li has incredibly supportive of my academic and professional goals. I feel extremely lucky to have had the opportunity to work for such a wonderful mentor who truly cares about her students on a professional and personal level. It has been an honor to work with Dr. Li and I will forever be thankful for this opportunity.

I would like to thank my committee members, Dr. Jean-Michel Ané, Dr. Tim Bugni, Dr. Cameron Currie, and Dr. Sandro Mecozzi, for their time and feedback regarding the thesis background oral, original research proposal, and this dissertation. Your support has been instrumental to my development as a scientist. I would also like to give a special thanks to Dr. Ané and Dr. Currie who are not only my committee members, but also my research collaborators. Our exciting work together has made me even more passionate about bioanalytical research.

Throughout my graduate career I was supported financially by several institutions for which I am incredibly grateful for including the NSF-GRFP (DGE-1256259), the GSFLC travel award, the Vilas conference presentation fund, the University of Wisconsin-Madison graduate school, and the Wisconsin Alumni Research Foundation.

I would like to acknowledge my first research advisors, Dr. Kevin Morris from Carthage College and Richard Blessing and Tom Cullen from Abbott Laboratories, who were incredibly patient and supportive during my undergraduate research. Their teaching and encouragement had a great impact toward setting me on my scientific career path. I am so grateful that they

were willing to take a chance on an undergraduate researcher with very little experience and it is because of them that I grew to be a confident researcher and developed an interest in pursuing analytical research as a career.

I would like to thank several student colleagues who have contributed to my projects and my graduate career. Dr. Vivian Ye taught me many lab techniques and introduced me to mass spectrometry imaging in my first year in the Li lab. Dr. Nicole Woodards, Dr. Robby Cunningham, and Dr. Rob Sturm were also great mentors in the lab during my first years of graduate school. Caitlin Keller and Kellen DeLaney have been wonderful to work with and have worked very hard to contribute to and take over my collaborative projects with other researchers on campus. Heidi Horn has been an incredibly passionate and fun collaborator to work with and I am grateful for the true partnership we had while working on this collaborative project. Dr. Tyler Greer and Dr. Chris Lietz have provided support, training, and expertise on many different problems and questions I encountered throughout my graduate research. Ling Hao, Qing Yu, Zhidan Liang, Shan Jiang, Jingxin Wang, Bingming Chen, Tony Chen, Jillian Johnson, and Amanda Buchberger have helped me talk through ideas and problems and have greatly contributed to creating a welcoming lab environment.

I would like to thank Dr. Cameron Scarlett and Molly Pellitteri-Hahn of the Analytical Instrumentation Center for maintaining and troubleshooting instruments in the School of Pharmacy. Their expertise, assistance, and discussions have been critical during my graduate career. They have been incredibly supportive and helpful with any questions I brought to them relating to instrumentation, my research projects, and much more.

Finally I would like to thanks my family and friends who have given me unconditional love and support through the ups and downs of the past 5 years of graduate school. I owe a huge

thank you to my friends in Madison, Carol, Kurt, Richard, Nick, Rich, Dan, Chelsea, Mandy, Matt and the rest of Dave's genetics classmates who have physically been there to commiserate and celebrate many events over the past 5 years. My parents, Pam and Neil Zimmerman, and my siblings, Lauren & Stu Bischel, Jacob & Maria Zimmerman, and Derek Zimmerman have always shown me unending love and support, and that was no different during graduate school. I would like to thank my grandparents Dotty & Larry Ketchum and Eileen & Elsmer Zimmerman who are/ would be very proud of my academic achievements. Last and most importantly, I would like to thank my husband, David Gemperline, who has weathered graduate school alongside me. He has fully supported me and believed in me when I didn't believe in myself. He has made me more confident, more ambitious, and helped me take myself a little less seriously. I am so grateful for the love and encouragement from all my family and friends.

Table of Contents

Method Development and Application of Mass Spectrometry for the Study of Symbiotic Relationships between Bacteria and Host Organisms

Erin Gemperline
Under the supervision of Professor Lingjun Li
University of Wisconsin- Madison

Abstract

Metabolic profiling can help shed light on cellular mechanisms; however a major technical challenge is to study endogenous metabolomic pathways without perturbing them. Most of the techniques currently in use for metabolomics studies in biological systems rely on tissue extracts which destroy the samples and result in the loss of information about analyte distribution within the tissue. Mass spectrometry imaging (MSI) has evolved as a promising technology to map a wide range of biomolecules in an anatomical context. In this dissertation, a multi-dimensional mass spectrometry-based platform was developed and applied to study interactions between bacteria and host organisms. Specifically, this work aimed to study the symbiotic relationship between soil bacteria and legume plants for agricultural and environmental sustainability applications, as well as the symbiosis between bacteria and leaf cutter ants and humans and our gut microbiota for the discovery of potentially novel antibiotics and antifungals. High-resolution, accurate-mass (HRAM) matrix-assisted laser desorption/ ionization (MALDI)-MSI was used to compare differentially treated biological samples, and liquid chromatography (LC)- electrospray ionization (ESI)- tandem mass spectrometry (MS/MS) coupled with database searching was used as a complementary mass spectrometry technique to identify interesting metabolites chosen from the MSI experiments. This work not only improves upon MSI by exploring novel sample preparation methods, but also presents a useful platform that integrates MALDI-MSI with ESI-MS in exploring the underlying chemistry of several biological symbiotic systems.

Chapter 1

Introduction and Research Summary

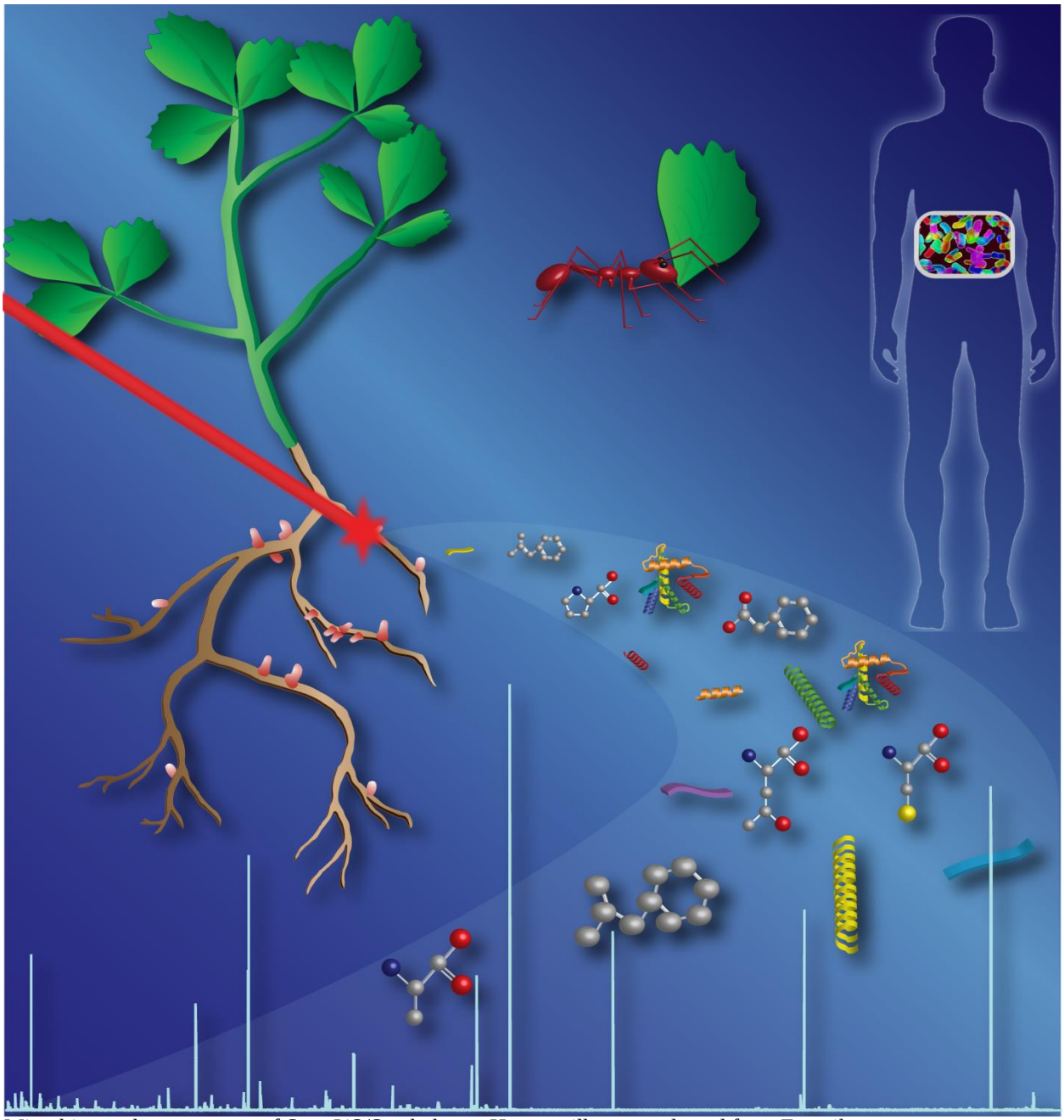

Microbiome photo courtesy of SatorI13/Stockphoto. Human silhouette adapted from Freepik.com.

Introduction and Research Summary

Mass spectrometry imaging (MSI) has evolved as a promising technology to map a wide range of biomolecules in an anatomical context.[1-8] This work focuses on improving a mass spectrometry imaging (MSI)-based platform that combines matrix-assisted laser desorption/ionization (MALDI)-MSI with conventional liquid chromatography (LC)-electrospray ionization (ESI)- tandem mass spectrometry (MS/MS). This multi-dimensional mass spectrometry (MS) platform combines the advantages provided by both MALDI and ESI approaches: attaining spatial information of select compounds and fragmentation information for structural elucidation. In addition to extensive method development, this work also demonstrates applications of the multi-dimensional MSI-based approach to study interactions between bacteria and host organisms (Chapters 3-7). Chapter 1 serves as a general introduction of the work described in this thesis and summarizes the major findings of each project. Additional information about the use of mass spectrometry for plant-omics, mass spectrometry imaging in the clinical setting, and detailed MSI protocols can be found in Appendices IV, V, and VI respectively.[9-12] Chapter 2 provides an overview of key elements associated with MSI, and highlights the applications of MSI in the study of endogenous metabolites/ small molecules in a variety of biological systems.[13]

A major limitation to the detection of metabolites by MALDI-MSI is interference of matrix-derived peaks.[14] Chapter 3 details my extensive method development in the matrix application process for improved MALDI-MSI of small molecules.[15] A comprehensive comparison of the two most widely used MALDI matrices, DHB (2,5-dihydroxybenzoic acid) and CHCA (α-cyano-4-hydroxycinnamic acid), applied via airbrush, automatic sprayer, or sublimation was performed. Each of the three matrix application techniques were first optimized

individually and then the final, optimized methods were compared between techniques. The optimized method yielding the highest number of analytes detected and the highest quality of image was adapted and applied to studies presented in Chapters 4-7.

Chapter 4 describes our characterization of metabolites in roots and root nodules of the model legume, *Medicago truncatula*, which possess symbiotic interactions with nitrogen-fixing bacteria known as Rhizobia.[8, 16-17] Understanding the metabolites involved in the biological nitrogen fixation process could have a significant impact on agricultural productivity and sustainability. Most of the techniques currently in use for studying plant metabolomics rely on plant extracts which destroy the knowledge of analyte distribution within the tissue.[18-21] I used the MALDI-MSI sample preparation methods optimized in Chapter 3 to determine the spatial distribution of various metabolites within the legume root nodule. I also used liquid chromatography (LC)-MS in conjunction with MALDI-MSI for a more comprehensive study, and used LC-MS/MS to identify the metabolites that were detected. By comparing metabolic profiles of wild-type nodules that were capable of nitrogen fixation and those mutants exhibiting deficiency in this process, I was able to obtain chemical information about these key metabolites and map their spatial distribution patterns. These results could be especially relevant to the identification of key molecular players involved in the nitrogen fixation pathway which will aid in dissecting the role played by those metabolites within the plant.

Continuing from the metabolomics work presented in the previous chapter, Chapter 5 focuses on the detection and identification of endogenous peptides in *Medicago truncatula*. In the past decade, MSI has rapidly expanded into the field of plant metabolomics;[8, 12, 22-25] however, plant peptidomics is a relatively under-explored area in mass spectrometry, and especially mass spectrometry imaging, with only a handful of reported studies. We adapted the

method developed in Chapter 3 to the detection of peptides and protein fragments instead of metabolites. However, endogenous signaling peptides are very complex and typically present at low abundances and are inherently difficult to detect, let alone produce ion images via MALDI-MSI.[26] We used a combination of MALDI-MSI and LC-ESI-MS/MS to compare wild-type plants to CLAVATA3/ Embryo –surrounding region- related (CLE) over-expresser mutants and mutants lacking nodule-specific, cysteine-rich (NCR) peptides. We imaged the spatial distribution of a variety of endogenous peptides and protein fragments and used LC-MS/MS to putatively identify the detected analytes.

Chapter 6 discusses my work on developing an innovative protocol for performing MSI-based metabolomics on the surface of organisms that enables detection of natural products, potentially new anti-microbial compounds, directly from leaf cutter ants. Fungus-growing ants, a tribe of ants that include leaf-cutter ants, have a long-standing mutualism with *Pseudonocardia*, a genus of bacteria that lives on the ants' exoskeleton. This bacterium protects the ants and their food source from harmful pathogens.[27-29] When the ants are exposed to ecologically relevant pathogens, *Pseudonocardia* naturally produce compounds with antimicrobial properties. We exposed ants with their symbiotic bacteria to three different types of pathogens and detected compounds that are expressed in response to pathogen exposure. These compounds that are only produced in response to pathogen infection could be novel candidates for new antifungal or antibacterial compounds with the goal of potentially being able to treat antibiotic-resistant diseases. We wanted to target compounds that are specifically localized to the *Pseudonocardia* on the surface of the ants' exoskeleton which traditional MALDI-MSI is not capable of doing. I therefore developed a novel MALDI-MSI method to

specifically image the *Pseudonocardia* on the surface of the ant *in vivo* and compared the metabolic profiles to that of *Pseudonocardia* exposed to pathogens *in vitro*.

Our natural product discovery work with the ant system led us to further develop methods for novel antibiotic discovery. Chapter 7 details our work on perturbing the gut microbiota and detecting changes in the secondary metabolites that the microbes produce in response to infection. Mice were colonized with the human microbiota and compared to mice raise without gut microbia (germ-free). These mice were infected with *Salmonella enterica* and an LC-MS method was used to compare the metabolites produced by the human gut microbia in order to fight off infections. MALDI-MSI was used to visualize these compounds on tissue. This study yielded many candidates for novel antibiotics and after narrowing down the list of targets by analyzing more biological replicates, these drug candidates will be isolated and validated for development as potentially novel pharmaceuticals in the future.

Chapter 8 goes into detail of a targeted metabolomics study in comparison to the preceding chapters that focus on discovery metabolomics.[30] In this chapter, I developed a reliable and sensitive assay to determine the concentration of a drug, CPP, in mouse plasma and brain tissue. CPP ((RS)-3-(2-carboxypiperazin-4-yl)-propyl-1-phosphonic acid) is a competitive antagonist of the N-methyl-D-aspartate (NMDA) receptor and is routinely used with rodent models to investigate the role of NMDA receptors in brain function.[31] Determining tissue-specific drug concentrations that correspond to specific behavioral endpoints will guide the design and interpretation of studies utilizing CPP for companion experiments performed *in vivo* and *in vitro*. I developed a multiple reaction monitoring (MRM) method using a Q-trap mass spectrometer for the absolute quantification of CPP in plasma and brain after animals were dosed with relevant amounts of CPP via intravenous (IV) and intraperitoneal (IP) injections.

Chapter 9 presents conclusions and future directions of my work on improving MSI-based methods through extensive method development and applications of this platform that integrates MALDI-MSI with ESI-LC-MS in exploring the underlying chemistry of several biological symbiotic models. Chapter 10 was written for the Wisconsin Initiative for Science Literacy and carefully and thoughtfully explains MALDI-MSI, metabolomics, and the details of my work from Chapter 4 to an audience with a more general knowledge and background.

References

1. Seeley, E. H.; Oppenheimer, S. R.; Mi, D.; Chaurand, P.; Caprioli, R. M., Enhancement of Protein Sensitivity for Maldi Imaging Mass Spectrometry after Chemical Treatment of Tissue Sections. *J Am Soc Mass Spectrom* **2008,** *19* (8), 1069-1077.

2. Deutskens, F.; Yang, J. H.; Caprioli, R. M., High Spatial Resolution Imaging Mass Spectrometry and Classical Histology on a Single Tissue Section. *J Mass Spectrom* **2011,** *46* (6), 568-571.

3. Chaurand, P.; Cornett, D. S.; Angel, P. M.; Caprioli, R. M., From Whole-Body Sections Down to Cellular Level, Multiscale Imaging of Phospholipids by Maldi Mass Spectrometry. *Mol Cell Proteomics* **2011,** *10* (2).

4. Chaurand, P.; Caprioli, R. M., Direct Profiling and Imaging of Peptides and Proteins from Mammalian Cells and Tissue Sections by Mass Spectrometry. *Electrophoresis* **2002,** *23* (18), 3125-3135.

5. Yang, J. Y.; Phelan, V. V.; Simkovsky, R.; Watrous, J. D.; Trial, R. M.; Fleming, T. C.; Wenter, R.; Moore, B. S.; Golden, S. S.; Pogliano, K.; Dorrestein, P. C., Primer on Agar-Based Microbial Imaging Mass Spectrometry. *Journal of bacteriology* **2012,** *194* (22), 6023-6028.

6. Watrous, J. D.; Dorrestein, P. C., Imaging Mass Spectrometry in Microbiology. *Nat Rev Microbiol* **2011,** *9* (9), 683-694.

7. Moree, W. J.; Yang, J. Y.; Zhao, X.; Liu, W. T.; Aparicio, M.; Atencio, L.; Ballesteros, J.; Sanchez, J.; Gavilan, R. G.; Gutierrez, M.; Dorrestein, P. C., Imaging Mass Spectrometry of a Coral Microbe Interaction with Fungi. *Journal of chemical ecology* **2013,** *39* (7), 1045-1054.

8. Gemperline, E.; Jayaraman, D.; Maeda, J.; Ane, J. M.; Li, L. J., Multifaceted Investigation of Metabolites During Nitrogen Fixation in Medicago Via High Resolution Maldi-Ms Imaging and Esi-Ms. *Journal of the American Society for Mass Spectrometry* **2015,** *26* (1), 149-158.

9. Gemperline, E.; Keller, C.; Li, L., Mass Spectrometry in Plant-Omics. *Analytical chemistry* **2016**.

10. Ye, H.; Gemperline, E.; Li, L., A Vision for Better Health: Mass Spectrometry Imaging for Clinical Diagnostics. *Clinica chimica acta; international journal of clinical chemistry* **2013,** *420*, 11-22.

11. Gemperline, E.; Li, L., Maldi-Ms-Assisted Molecular Imaging of Metabolites in Legume Plants. *Methods Mol Biol* **2015,** *1203*, 29-40.

12. Gemperline, E.; Li, L., Maldi-Mass Spectrometric Imaging for the Investigation of Metabolites in Medicago Truncatula Root Nodules. *Journal of visualized experiments : JoVE* **2014,** (85).

13. Gemperline, E.; Li, L., Maldi-Mass Spectrometric Imaging of Endogenous Metabolites in Biological Systems. *eLS* **2014,** (August), 1-9.

14. Northen, T. R.; Yanes, O.; Northen, M. T.; Marrinucci, D.; Uritboonthai, W.; Apon, J.; Golledge, S. L.; Nordstrom, A.; Siuzdak, G., Clathrate Nanostructures for Mass Spectrometry. *Nature* **2007,** *449* (7165), 1033-U1033.

15. Gemperline, E.; Rawson, S.; Li, L., Optimization and Comparison of Multiple Maldi Matrix Application Methods for Small Molecule Mass Spectrometric Imaging. *Anal Chem* **2014,** *86* (20), 10030-10035.

16. Hoffman, B. M.; Lukoyanov, D.; Yang, Z. Y.; Dean, D. R.; Seefeldt, L. C., Mechanism of Nitrogen Fixation by Nitrogenase: The Next Stage. *Chemical reviews* **2014,** *114* (8), 4041–4062.

17. Dunn, M. F., Key Roles of Microsymbiont Amino Acid Metabolism in Rhizobia-Legume Interactions. *Critical reviews in microbiology* **2014**.

18. Desbrosses, G. G.; Kopka, J.; Udvardi, M. K., Lotus Japonicus Metabolic Profiling. Development of Gas Chromatography-Mass Spectrometry Resources for the Study of Plant-Microbe Interactions. *Plant physiology* **2005,** *137* (4), 1302-1318.

19. Farag, M. A.; Huhman, D. V.; Dixon, R. A.; Sumner, L. W., Metabolomics Reveals Novel Pathways and Differential Mechanistic and Elicitor-Specific Responses in Phenylpropanoid and Isoflavonoid Biosynthesis in Medicago Truncatula Cell Cultures. *Plant Physiology* **2008,** *146* (2), 387-402.

20. Harada, K.; Fukusaki, E., Profiling of Primary Metabolite by Means of Capillary Electrophoresis-Mass Spectrometry and Its Application for Plant Science. *Plant Biotechnology* **2009,** *26* (1), 47–52.

21. Kueger, S.; Steinhauser, D.; Willmitzer, L.; Giavalisco, P., High-Resolution Plant Metabolomics: From Mass Spectral Features to Metabolites and from Whole-Cell Analysis to Subcellular Metabolite Distributions. *Plant Journal* **2012,** *70* (1), 39–50.

22. Lee, Y. J.; Perdian, D. C.; Song, Z. H.; Yeung, E. S.; Nikolau, B. J., Use of Mass Spectrometry for Imaging Metabolites in Plants. *Plant J* **2012,** *70* (1), 81-95.

23. Kaspar, S.; Peukert, M.; Svatos, A.; Matros, A.; Mock, H. P., Maldi-Imaging Mass Spectrometry - an Emerging Technique in Plant Biology. *Proteomics* **2011,** *11* (9), 1840-1850.

24. Ye, H.; Gemperline, E.; Venkateshwaran, M.; Chen, R.; Delaux, P. M.; Howes-Podoll, M.; Ane, J. M.; Li, L., Maldi Mass Spectrometry-Assisted Molecular Imaging of Metabolites During Nitrogen Fixation in the *Medicago Truncatula-Sinorhizobium Meliloti* Symbiosis. *Plant J* **2013,** *75* (1), 130–145.

25. Bjarnholt, N.; Li, B.; D'Alvise, J.; Janfelt, C., Mass Spectrometry Imaging of Plant Metabolites - Principles and Possibilities. *Natural product reports* **2014,** *31* (6), 818-837.

26. Batut, J.; Mergaert, P.; Masson-Boivin, C., Peptide Signalling in the Rhizobium-Legume Symbiosis. *Current opinion in microbiology* **2011,** *14* (2), 181-187.

27. Poulsen, M.; Cafaro, M. J.; Erhardt, D. P.; Little, A. E. F.; Gerardo, N. M.; Tebbets, B.; Klein, B. S.; Currie, C. R., Variation in Pseudonocardia Antibiotic Defence Helps Govern Parasite-Induced Morbidity in Acromyrmex Leaf-Cutting Ants. *Env Microbiol Rep* **2010,** *2* (4), 534-540.

28. Currie, C. R.; Scott, J. A.; Summerbell, R. C.; Malloch, D., Fungus-Growing Ants Use Antibiotic-Producing Bacteria to Control Garden Parasites. *Nature* **1999,** *398* (6729), 701-704.

29. Currie, C. R.; Bot, A. N. M.; Boomsma, J. J., Experimental Evidence of a Tripartite Mutualism: Bacteria Protect Ant Fungus Gardens from Specialized Parasites. *Oikos* **2003,** *101* (1), 91-102.

30. Gemperline, E.; Laha, K.; Scarlett, C. O.; Pearce, R. A.; Li, L., Measurement of Nmda Receptor Antagonist, Cpp, in Mouse Plasma and Brain Tissue Following Systematic Administration Using Ion-Pair Lcms/Ms. *Analytical methods : advancing methods and applications* **2014,** *6* (16), 6389-6396.

31. Harris, E. W.; Ganong, A. H.; Monaghan, D. T.; Watkins, J. C.; Cotman, C. W., Action of 3-((+/-)-2-Carboxypiperazin-4-Yl)-Propyl-1-Phosphonic Acid (Cpp): A New and Highly Potent Antagonist of N-Methyl-D-Aspartate Receptors in the Hippocampus. *Brain research* **1986,** *382* (1), 174-177.

Chapter 2

MALDI- Mass Spectrometric Imaging of Endogenous Metabolites in Biological Systems

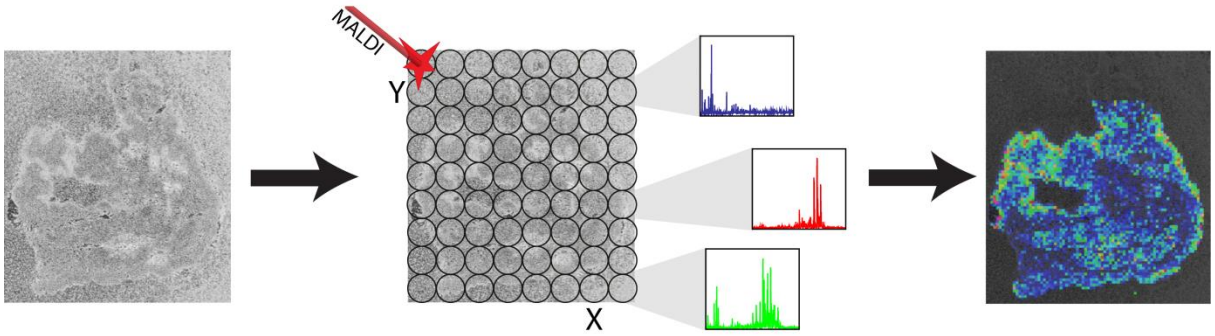

Adapted from **Gemperline, E.**; Li, L. "MALDI-Mass Spectrometric Imaging of Endogenous Metabolites in Biological Systems" *eLS.* (2014) DOI: 10.1002/9780470015902.a0023207

Abstract

Matrix-assisted laser desorption/ionization (MALDI)-mass spectrometric imaging (MSI) is a powerful, relatively new technology that allows for the detection of molecules directly from biological systems and also provides the spatial distribution for these analytes within the tissue sample. MSI has gained considerable popularity for the study of endogenous metabolites as metabolites are the end product of various biochemical processes, and represent a biological snapshot of an organism's biochemistry at a given time. Although the underlying concept is simple, factors such as choice of ionization method, sample preparation, instrumentation and data analysis must be taken into account and tailored for successful applications of MSI, especially for the study of small molecules. MALDI-MSI has been successfully applied to the study of endogenous metabolites in animal, plant, bacteria, and fungal tissues and has provided new insights into biological functions and pathways, interspecies interactions, and novel natural products.

Introduction

Metabolomics is a growing field with many important biological applications including biomarker discovery, deciphering metabolic pathways in plants and other biological systems, and toxicology profiling.[1-7] Metabolites typically possess molecular weights below 1000 Da and are often classified as small molecule analytes. A metabolic profile provides a snapshot of an organism's metabolism and underlying biochemistry at a given time. Although metabolomic data can aid in the assignment of gene and enzyme function, the relation between metabolites and proteins/genes is not always straightforward. Conventional tissue extraction methods have been used for the global analysis of metabolites, but provide minimal spatial information. Matrix-assisted laser desorption/ionization (MALDI)-mass spectrometric imaging (MSI) is a powerful, relatively new technology that can be used to determine the spatial distribution of endogenous or exogenous molecules present in biological tissues. MSI uses a computer-controlled x-y stage, which holds the sample, and allows for the laser to raster across the sample and mass spectra to be collected at every pre-defined raster point. After completing the 2D raster, an ion image can be created using software to select a single mass from the spectrum and the software will display the relative abundance of that ion as a coloured map of signal intensity at each raster point. A general scheme for MSI is shown in **Figure 1**. Advantages of MALDI-MSI include the ability to detect a broad mass range of compounds, such as metabolites, lipids, peptides, proteins, etc., the ability to detect multiple analytes in a single experiment without the need for labels or prior knowledge of the analytes, and the preservation of biologically relevant spatial information. Using MALDI-MSI to study each different class of biomolecules comes with unique challenges. Some unique challenges associated with the study of small molecules

using MALDI-MSI include matrix interference and potential analyte delocalization. Technological advances have reduced these challenges and MALDI-MSI is becoming a popular tool for the study of metabolites in many different biological systems.

MALDI-MSI: Basic Principles and Workflow

Ionization

Creating ions is critical to mass spectrometric analysis as the mass spectrometer only detects charged particles. With MALDI-MS, analytes are co-crystallized with matrix, typically an organic acid. When the laser irradiates the sample, the matrix is ablated, forming a gas plume in which matrix and analyte ions are generated. MALDI is referred to as a soft ionization technique and produces primarily singly-charged ions. The two types of lasers commonly used in MALDI instruments are nitrogen lasers and neodymium-doped yttrium aluminum garnet (Nd:YAG) lasers. The spatial resolution of MS images is determined by the size of the laser beam diameter and the size of the matrix crystals.

Sample Preparation

Proper methods and techniques used to prepare samples for MSI are crucial for ensuring reproducible and reliable data. First, tissues of interest are harvested from the specimen and immediately frozen. One common procedure after harvesting tissue is to snap-freeze the sample in dry ice or liquid nitrogen and store it at -80ºC until use.[8] A second method involves loosely wrapping the tissue in aluminum foil and gently placing it into liquid nitrogen, ice-cold ethanol or isopropanol bath for 30-60 seconds.[9] The second method is a gentler approach because of the longer freezing process, which avoids tissue cracking and fragmentation. Next, the tissue can be sectioned, typically 10-20 μm thick slices,[10] using a cryostat. It can be helpful to first embed the

sample in supporting media such as gelatin[4] or sucrose[11] which allows for easy handling and precise sectioning of tissue samples without introducing interferences to mass spectrometer. Next, the tissue sections can be thaw-mounted onto a stainless steel conductive plate, indium-tin-oxide (ITO)-coated conductive glass slides, or regular glass slides, depending on instrumentation.[9] An advantage of using glass slides is that optical images can be taken of the samples. These images can be obtained with powerful microscopes or a simple scanner and co-registered with the ion images generated with MSI. For clinical samples, the glass slides can be used for histological analysis prior to MSI which allows for additional information gained from one sample. The final step before MSI analysis is choosing and applying the matrix.

Matrix Application

Matrix selection and application is a crucial step in preparing samples for MALDI-MSI. The two most common matrices used for MSI are CHCA (α-cyano-4-hydroxycinnamic acid) and DHB (2,5-dihydroxy benzoic acid).[9, 12-13] New matrices are constantly being explored, including ionic matrices, made by mixing conventional matrices with organic bases,[14-15] DAN (1,5-diaminonapthalene), DMAN (1,8-bis(dimethylamino)napthalene), DHPT (2,3,4,5-tetra(3',4'-dihydroxylphenyl)thiophene), TiO_2 nanoparticles, etc.[16-20] The matrix influences the ionization efficiency, interference, and signal intensity for MSI experiments due to chemical properties such as homogenous deposition/ crystallization and vacuum stability. Choosing a matrix is especially important when studying small molecules because conventional matrices produce their own matrix ions in the low mass range (0-500 Da) which are also detected by the mass spectrometer and could potentially mask analytes of interest. Some of the more novel matrices reduce this problem.

Matrix application is another area under continuous development. Potential limitations caused by this step include diffusion of metabolites within the tissue and heterogeneous size of crystal formation. Matrix application methods can be divided into two categories: solvent-based and solvent-free. For solvent-based application methods, several types of matrix application apparatuses are available that deposit matrix either as homogeneous layers (spray coating) or discrete spots (microspotting). Spray devices such as the manual airbrush, automatic TM Sprayer from HTX Imaging, and automatic ImagePrep from Bruker Daltonics are all capable of applying a uniform layer; the airbrush requires more skill on the part of the user to achieve homogenous coverage and crystal size. Solvent-free matrix application methods include sublimation or dry coating.[21-22] Solvent free matrix application methods are used more often for studying metabolites as too much solvent deposited on the tissue has the tendency of delocalizing small molecules. With new solvent-based spraying systems, like the TM-Sprayer, the nozzle of the device is heated for increased evaporation of solvents, making it a viable option for studying metabolites without causing analyte delocalization.

Instrumentation

Time-of-flight (TOF) and TOF/TOF analyzers are the most common type of mass spectrometers used in MALDI-MSI applications. In TOF analyzers, ions are accelerated and the *m/z* is determined by the time the ions take to travel through the TOF tube.[23] This design allows for the analysis of a wide mass range of molecules and fast analysis time.

Compared to the relatively low mass resolving power offered by TOF/TOF mass analyzer, the Orbitrap Fourier transform mass spectrometer is gaining popularity in MSI applications. The Orbitrap provides superior mass resolution and accuracy which is extremely

important for identifying metabolites as identifications are primarily based on accurate mass matching. In an Orbitrap mass spectrometer, *m/z* values are determined by measuring the axial oscillation frequency of ions in an electrostatic field moving back and forth along a spindle-like electrode, where the mass of the ion is related to the frequency.[24] Disadvantages of the commercially available MALDI-Orbitrap compared to TOF instruments are the larger laser beam size, which limits the spatial resolution of the images to approximately 75 μm, slower analysis time, and limited mass range. Analysis time depends on the raster step size and image area; however, MSI experiments that take hours to perform on a TOF instrument could take up to several days to perform on an Orbitrap instrument. Recently the Spengler group has developed a custom MALDI imaging ion source with the ability to perform MSI with a spatial resolution of 5 μm.[25] Theoretically, TOF instruments have an unlimited mass range whereas Orbitrap instruments are limited to approximately *m/z* 4000 since higher *m/z* compounds are difficult to retain during the orbital rotation.

In Fourier transform ion cyclotron resonance (FT-ICR) mass analyzers ions are excited and induce a charge which generates a signal called free induction decay (FID). The useful signal is extracted from the FID by performing a Fourier transform, thus generating a mass spectrum. FT-ICR mass analyzers are often reported to have mass errors of less than 1 ppm.[26] Like the Orbitrap, MALDI-FT-ICR instruments also suffer from long analysis times, but one advantage of the FT-ICR is that it has a higher upper mass limit when compared to the Orbitrap studies. TOF instruments can still be used for untargeted metabolomics studies, but may require additional, complementary analyses with high mass accuracy electrospray ionization mass spectrometers (ESI-MS).

Data Analysis

Vendor specific MSI analysis software (e.g., FlexImaging from Bruker Daltonics, ImageQuest from Thermo Fisher Scientific and TissueView from Applied Biosystems/MDS) are commonly used to extract distribution maps, or images, for selected analytes from the collected data. Open source software, such as BioMap (http://www.maldi-msi.org), is also capable of producing the ion images.

Data processing is oftentimes the bottleneck for MSI experiments, as typically manual extraction of ion images is extremely time-consuming for large-scale analyses, such as untargeted studies. A readily available (free for use at http://www4.ncsu.edu/~dcmuddim/msireader.html) MSI data processing software has been developed, called MSiReader,[27] which can automatically generate a list of *m/z's* of interest by defining a region of interest and a reference region and excluding the *m/z* values in the reference region from those in the region of interest. A list of *m/z*'s, either automatically created or manually generated, can then be imported and images will be extracted for every m/z in the list. Software such as MSiReader drastically decreases data processing time in comparison to manual data processing, allowing for higher throughput and faster overall analysis.

Assigning identifications to metabolites is not a straightforward task when performing untargeted metabolomics studies. Typically, the first step of identifying metabolites in a complex sample is to obtain their accurate mass, within 5 ppm error, using high resolution instrumentation. These accurate masses can be searched against online databases such as METLIN, HMDB, KEGG, PubChem, ChemSpider, MassBank, MMCD, LIPID MAPS, and more. Since these online databases contain different metabolites, and no database is complete, a new tool called MetaboSearch (free for use at http://omics.georgetown.edu/metabosearch.html)

has been developed that will search four common databases, HMDB, MMCD, METLIN, and LIPID MAPS, automatically rather than searching each database individually, by hand.[28] Database searching will often result in multiple potential identifications for a given mass. To further narrow down identification assignments, tandem mass spectra can be collected for each metabolite of interest which will provide characteristic fragmentation peaks for the compound. Recently tandem mass spectra have been compiled into some of these databases so that experimental spectra can be manually compared to reference spectra. MetFrag (free for use at http://msbi.ipb-halle.de/MetFrag/) is a useful tool for computer assisted identification of metabolite mass spectra that can be used to manually compare experimental tandem mass data to computer predicted tandem mass spectra for metabolites of interest.[29] MetFusion (free for use at http://msbi.ipb-halle.de/MetFusion/) combines information from MassBank and MetFrag for more accurate predictions.[30] Even with the aid of fragmentation prediction software and reference tandem mass spectra in online databases, confident identifications of metabolites are still difficult as many metabolites share common fragments. This is an area where more work and progress is greatly needed.

Quantitative MALDI-MSI has been difficult to achieve. Recently, software tools have been developed to address this issue, such as Quantinetix from ImaBiotech. Källback *et al.* have developed software for quantitation via isotopic labeling and normalization of analytes[31] and Shariatgorji *et al*. have developed in-house software for MSI quantitation based on signal intensities.[32]

Applications

Animal Tissue MSI

MALDI-MSI has been used to study molecular distributions in human and animal tissues since it was first demonstrated by Caprioli *et al.* in 1997.[33] The majority of MSI studies performed on animal and human tissues examine larger molecules, such as peptides and proteins, or exogenous small molecules, such as drugs and their metabolites. Many proof-of-principle studies have been done for the analysis of small molecules on animal tissue sections, but studies have also been done that used MALDI-MSI to reveal insight into biological processes. Goto-Inoue *et al.* used MALDI-MSI to detect changes in metabolite distribution during testicular maturation in mice.[34] In this study, distributions of metabolites, including lipids, in different layers of the seminiferous tubules were compared in 2 week and 8 week-old mice. Layer-specific molecules including 13 phosphatidylcholine compounds, sphingomyeline, glutathione, 7 seminolipids, 2 phosphatidyleinositols, sulfatide, and UDP-HexNAc showed different localizations in the 2 week vs. 8 week-old mice. These results, shown in **Figure 2**, provided insight into the cellular mechanisms associated with testicular maturation and reproductive function. Scott *et al.* applied MALDI-MSI to detect and characterize potential biomarkers of radiation-induced tissue damage in mouse gastrointestinal tract and lung tissue.[35] This work showed unique spatial distributions of lipid species when damaged tissue was compared to healthy tissue which could be potential indicators correlating to radiation dose and onset of diseases caused by radiation.

Plant Tissue MSI

Currently the majority of MSI experiments use animal tissue sections or small tumor biopsies, but more recently, the use of MALDI-MSI has expanded into the field of plant metabolomics. A recent review provides a comprehensive list of studies using MALDI-MSI (and other MSI ionization sources) to study metabolites in various plant tissues in the past 8 years.[36] Araujo *et al.* used MALDI-MSI to analyze lignin in Eucalyptus for use in production of bioethanol.[37] The ratio of lignin subunits determines the properties of the lignin; therefore the researchers aimed to detect and relatively quantitate lignin subunits in this work. They were able to detect and identify 22 lignin monomers using this method. Most of these studies are proof-of-principle studies, but several have used MSI to obtain further insight into biological processes. Ye *et al.* used this technique to detect differences in metabolite distributions in root and nodule tissues in *Medicago truncatula*.[4] This study also compared mutant strains of plant and symbiotic bacteria and identified metabolites, such as heme and formononetin MalGlc, which were present in functional, nitrogen-fixing nodules and absent from non-functional nodules. The results are shown in **Figure 3**. The information gained from using this technique could provide valuable insight into the biological nitrogen fixation process in legume plants.

Bacteria and Fungi MSI

Within the past 5-6 years MSI of microbial colonies from liquid and agar media has been performed. In a proof-of-principle study, Gonzalez *et al.* used MALDI-MSI to study the metabolic exchange patterns between a diverse array of microbes.[38] Metabolites excreted from single-species colonies have been a rich source of therapeutics; therefore, the authors were interested in studying the secreted and colony-associated metabolites when multiple bacterial

colonies came into contact with each other. These researchers examined cultured, environmental samples and showed the ability of MSI to detect differences in metabolic factors associated with different members of the microbial community within the sample, shown in **Figure 4**. Traxler *et al.* also used MSI to study metabolites produced when bacterial species interact with each other.[39] This study revealed that 629 compounds were produced, most of them with unknown identifications. The results of the study indicate that interspecies interactions can lead to unexpected biosynthetic shifts in secondary metabolite production pathways. In addition to studying the interactions between bacterial species, MALDI-MSI has been used to study interactions between bacteria and fungi. Moree *et al.* studied the molecular interactions between fungi and a coral microbe with the goal of improving functional understanding of microbial metabolites and potentially discovering anti-infective agent natural products.[22] The authors used MSI to visualize compounds with anti-fungal properties localized to the colony or secreted; these results are shown in **Figure 5**. The origin and directionality of secreted metabolites were more clearly detected using this method and a number of metabolites were detected that were produced by the bacteria when in contact with the fungi. At the interaction site between the bacteria and fungi, some metabolites were barely detected indicating that they were consumed, inhibited, or suppressed. Secondary metabolites, often referred to as natural products, have also been detected from fungal fruiting bodies with MALDI-MSI. Bhandari *et al.* used MALDI-MSI to study fruiting bodies and pellets of two different model species of fungi that are well-known for efficient production of secondary metabolites with biological activities.[40] This study is more of a proof-of-principle study, highlighting the in-house modified MALDI source capable of spatial resolutions as low as 5 μm. Using this specialized MALDI instrument, the researchers performed MSI and detected known secondary metabolites, elucidating the spatial distribution of

the compounds and comparing the secondary metabolite production between submerged fungal cultures and fruiting bodies.

Conclusions and Future Directions

Over the past decade, MSI has obtained increasing attention from biologists and become more routinely employed to map various classes of biomolecules from biological specimen. Using this technique, chemical and biological hypotheses can be generated based on spatial mapping of biomolecules. MSI has been increasingly employed in the study of human and animal tissues and has been extended into the study of plants. Very recently MSI has also been used to study intercellular communication via metabolomics approach in bacteria and fungi. Many MSI metabolomics studies demonstrate their utility by proof-of-principle experiments, but this technique allows for discovery and untargeted experiments that could provide new insight into biological pathways and eventually enable correlation with proteomics, transcriptomics and genomics data. With the new technical advances in the field of mass spectrometry, MSI has the potential to expand into many new areas of research and be employed as a powerful tool for a myriad of biological applications.

Acknowledgements

Preparation of this manuscript was supported in part by the National Science Foundation (NSF CHE- 0957784) and National Institutes of Health through grant 1R01DK071801. E.G. acknowledges an NSF Graduate Research Fellowship (DGE-1256259). L.L. acknowledges an H. I. Romnes Faculty Fellowship.

References

1. Heuberger, A. L.; Broeckling, C. D.; Kirkpatrick, K. R.; Prenni, J. E., Application of Nontargeted Metabolite Profiling to Discover Novel Markers of Quality Traits in an Advanced Population of Malting Barley. *Plant Biotechnol J* **2014,** *12* (2), 147-160.

2. Pendyala, G.; Want, E. J.; Webb, W.; Siuzdak, G.; Fox, H. S., Biomarkers for Neuroaids: The Widening Scope of Metabolomics. *J Neuroimmune Pharm* **2007,** *2* (1), 72-80.

3. Spegel, P.; Sharoyko, V. V.; Goehring, I.; Danielsson, A. P.; Malmgren, S.; Nagorny, C. L.; Andersson, L. E.; Koeck, T.; Sharp, G. W.; Straub, S. G.; Wollheim, C. B.; Mulder, H., Time-Resolved Metabolomics Analysis of Beta-Cells Implicates the Pentose Phosphate Pathway in the Control of Insulin Release. *The Biochemical journal* **2013,** *450* (3), 595-605.

4. Ye, H.; Gemperline, E.; Venkateshwaran, M.; Chen, R. B.; Delaux, P. M.; Howes-Podoll, M.; Ane, J. M.; Li, L. J., Maldi Mass Spectrometry-Assisted Molecular Imaging of Metabolites During Nitrogen Fixation in the Medicago Truncatula-Sinorhizobium Meliloti Symbiosis. *Plant J* **2013,** *75* (1), 130-145.

5. West, P. R.; Weir, A. M.; Smith, A. M.; Donley, E. L. R.; Cezar, G. G., Predicting Human Developmental Toxicity of Pharmaceuticals Using Human Embryonic Stem Cells and Metabolomics. *Toxicol Appl Pharm* **2010,** *247* (1), 18-27.

6. Wei, R., Metabolomics and Its Practical Value in Pharmaceutical Industry. *Curr Drug Metab* **2011,** *12* (4), 345-358.

7. Kobayashi, T.; Nishiumi, S.; Ikeda, A.; Yoshie, T.; Sakai, A.; Matsubara, A.; Izumi, Y.; Tsumura, H.; Tsuda, M.; Nishisaki, H.; Hayashi, N.; Kawano, S.; Fujiwara, Y.; Minami, H.; Takenawa, T.; Azuma, T.; Yoshida, M., A Novel Serum Metabolomics-Based Diagnostic Approach to Pancreatic Cancer. *Cancer Epidem Biomar* **2013,** *22* (4), 571-579.

8. Jehl, B.; Bauer, R.; Dorge, A.; Rick, R., The Use of Propane-Isopentane Mixtures for Rapid Freezing of Biological Specimens. *Journal of Microscopy-Oxford* **1981,** *123* (Sep), 307-309.

9. Schwartz, S. A.; Reyzer, M. L.; Caprioli, R. M., Direct Tissue Analysis Using Matrix-Assisted Laser Desorption/Ionization Mass Spectrometry: Practical Aspects of Sample Preparation. *J Mass Spectrom* **2003,** *38* (7), 699-708.

10. Crossman, L.; McHugh, N. A.; Hsieh, Y. S.; Korfmacher, W. A.; Chen, J. W., Investigation of the Profiling Depth in Matrix-Assisted Laser Desorption/Ionization Imaging Mass Spectrometry. *Rapid Commun Mass Sp* **2006,** *20* (2), 284-290.

11. Verhaert, P. D. E. M.; Pinkse, M. W. H.; Strupat, K.; Conaway, M. C. P., Imaging of Similar Mass Neuropeptides in Neuronal Tissue by Enhanced Resolution Maldi Ms with an Ion Trap-Orbitrap$^{(Tm)}$ Hybrid Instrument. *Methods Mol Biol* **2010,** *656*, 433-449.

12. Chen, R.; Hui, L.; Sturm, R. M.; Li, L., Three Dimensional Mapping of Neuropeptides and Lipids in Crustacean Brain by Mass Spectral Imaging. *J Am Soc Mass Spectr* **2009,** *20* (6), 1068-1077.

13. DeKeyser, S. S., Kutz-Naber, K.K., Schmidt, J.J., Barrett-Wilt, G.A.and Li, L., Mass Spectral Imaging of Neuropeptides in Crustacean Nervous Tissue by Maldi Tof/Tof. *J Proteome Res* **2007,** *6*, 1782-1791.

14. Fitzgerald, J. J. D.; Kunnath, P.; Walker, A. V., Matrix-Enhanced Secondary Ion Mass Spectrometry (Me-Sims) Using Room Temperature Ionic Liquid Matrices. *Anal Chem* **2010,** *82* (11), 4413-4419.

15. Lemaire, R.; Tabet, J. C.; Ducoroy, P.; Hendra, J. B.; Salzet, M.; Fournier, I., Solid Ionic Matrixes for Direct Tissue Analysis and Maldi Imaging. *Anal Chem* **2006,** *78* (3), 809-819.

16. Thomas, A.; Charbonneau, J. L.; Fournaise, E.; Chaurand, P., Sublimation of New Matrix Candidates for High Spatial Resolution Imaging Mass Spectrometry of Lipids: Enhanced Information in Both Positive and Negative Polarities after 1,5-Diaminonapthalene Deposition. *Anal Chem* **2012,** *84* (4), 2048-2054.

17. Ye, H.; Gemperline, E.; Li, L. J., A Vision for Better Health: Mass Spectrometry Imaging for Clinical Diagnostics. *Clin Chim Acta* **2013,** *420*, 11-22.

18. Shroff, R.; Rulisek, L.; Doubsky, J.; Svatos, A., Acid-Base-Driven Matrix-Assisted Mass Spectrometry for Targeted Metabolomics. *Proc Natl Acad Sci U S A* **2009,** *106* (25), 10092-10096.

19. Chen, S.; Chen, L.; Wang, J.; Hou, J.; He, Q.; Liu, J.; Xiong, S.; Yang, G.; Nie, Z., 2,3,4,5-Tetrakis(3',4'-Dihydroxylphenyl)Thiophene: A New Matrix for the Selective Analysis of Low Molecular Weight Amines and Direct Determination of Creatinine in Urine by Maldi-Tof Ms. *Anal Chem* **2012,** *84* (23), 10291-10297.

20. Shrivas, K.; Hayasaka, T.; Sugiura, Y.; Setou, M., Method for Simultaneous Imaging of Endogenous Low Molecular Weight Metabolites in Mouse Brain Using Tio2 Nanoparticles in Nanoparticle-Assisted Laser Desorption/Ionization-Imaging Mass Spectrometry. *Anal Chem* **2011,** *83* (19), 7283-7289.

21. Hankin, J. A.; Barkley, R. M.; Murphy, R. C., Sublimation as a Method of Matrix Application for Mass Spectrometric Imaging. *Journal of the American Society for Mass Spectrometry* **2007,** *18* (9), 1646-1652.

22. Moree, W. J.; Yang, J. Y.; Zhao, X.; Liu, W. T.; Aparicio, M.; Atencio, L.; Ballesteros, J.; Sanchez, J.; Gavilan, R. G.; Gutierrez, M.; Dorrestein, P. C., Imaging Mass Spectrometry of a Coral Microbe Interaction with Fungi. *Journal of chemical ecology* **2013,** *39* (7), 1045-1054.

23. Cohen, M. Z., A Historical Overview of the Phenomenologic Movement. *Image J Nurs Sch* **1987,** *19* (1), 31-34.

24. Makarov, A., Electrostatic Axially Harmonic Orbital Trapping: A High-Performance Technique of Mass Analysis. *Anal Chem* **2000,** *72* (6), 1156-1162.

25. Guenther, S.; Rompp, A.; Kummer, W.; Spengler, B., Ap-Maldi Imaging of Neuropeptides in Mouse Pituitary Gland with 5 Mu M Spatial Resolution and High Mass Accuracy. *Int J Mass Spectrom* **2011,** *305* (2-3), 228-237.

26. Debois, D.; Ongena, M.; Cawoy, H.; De Pauw, E., Maldi-Fticr Ms Imaging as a Powerful Tool to Identify Paenibacillus Antibiotics Involved in the Inhibition of Plant Pathogens. *Journal of the American Society for Mass Spectrometry* **2013,** *24* (8), 1202-1213.

27. Robichaud, G.; Garrard, K. P.; Barry, J. A.; Muddiman, D. C., Msireader: An Open-Source Interface to View and Analyze High Resolving Power Ms Imaging Files on Matlab Platform. *Journal of the American Society for Mass Spectrometry* **2013,** *24* (5), 718-721.

28. Zhou, B.; Wang, J. L.; Ressom, H. W., Metabosearch: Tool for Mass-Based Metabolite Identification Using Multiple Databases. *Plos One* **2012,** *7* (6).

29. Wolf, S.; Schmidt, S.; Muller-Hannemann, M.; Neumann, S., In Silico Fragmentation for Computer Assisted Identification of Metabolite Mass Spectra. *Bmc Bioinformatics* **2010,** *11*.

30. Gerlich, M.; Neumann, S., Metfusion: Integration of Compound Identification Strategies. *J Mass Spectrom* **2013,** *48* (3), 291-298.

31. Kallback, P.; Shariatgorji, M.; Nilsson, A.; Andren, P. E., Novel Mass Spectrometry Imaging Software Assisting Labeled Normalization and Quantitation of Drugs and Neuropeptides Directly in Tissue Sections. *J Proteomics* **2012,** *75* (16), 4941-4951.

32. Shariatgorji, M.; Nilsson, A.; Goodwin, R.; Zhang, X.; Schintu, N.; Svenningsson, P.; Andren, P. E., Maldi-Ms Imaging and Quantitation of Primary Amine Neurotransmitters Dopamine, Gaba and Glutamate Directly in Brain Tissue Sections. In *2013 American Society for Mass Spectrometry Annual Conference*, Minneapolis, MN, 2013.

33. Caprioli, R. M.; Farmer, T. B.; Gile, J., Molecular Imaging of Biological Samples: Localization of Peptides and Proteins Using Maldi-Tof Ms. *Anal Chem* **1997,** *69* (23), 4751-4760.

34. Goto-Inoue, N.; Hayasaka, T.; Zaima, N.; Setou, M., Imaging Mass Spectrometry Reveals Changes of Metabolites Distribution in Mouse Testis During Testicular Maturation. *Surface and Interface Analysis* **2011,** *44*, 749-754.

35. Scott, A. J.; Jones, J. W.; Orschell, C. M.; MacVittie, T. J.; Kane, M. A.; Ernst, R. K., Mass Spectrometry Imaging Enriches Biomarker Discovery Approaches with Candidate Mapping. *Health physics* **2014,** *106* (1), 120-128.

36. Bjarnholt, N.; Li, B.; D'Alvise, J.; Janfelt, C., Mass Spectrometry Imaging of Plant Metabolites - Principles and Possibilities. *Natural product reports* **2014**.

37. Araujo, P.; Ferreira, M. S.; de Oliveira, D. N.; Pereira, L.; Sawaya, A. C.; Catharino, R. R.; Mazzafera, P., Mass Spectrometry Imaging: An Expeditious and Powerful Technique for Fast in Situ Lignin Assessment in Eucalyptus. *Anal Chem* **2014,** *86* (7), 3415-3419.

38. Gonzalez, D. J.; Xu, Y.; Yang, Y. L.; Esquenazi, E.; Liu, W. T.; Edlund, A.; Duong, T.; Du, L.; Molnar, I.; Gerwick, W. H.; Jensen, P. R.; Fischbach, M.; Liaw, C. C.; Straight, P.; Nizet, V.; Dorrestein, P. C., Observing the Invisible through Imaging Mass Spectrometry, a Window into the Metabolic Exchange Patterns of Microbes. *J Proteomics* **2012,** *75* (16), 5069-5076.

39. Traxler, M. F.; Watrous, J. D.; Alexandrov, T.; Dorrestein, P. C.; Kolter, R., Interspecies Interactions Stimulate Diversification of the Streptomyces Coelicolor Secreted Metabolome. *mBio* **2013,** *4* (4).

40. Bhandari, D. R.; Shen, T.; Rompp, A.; Zorn, H.; Spengler, B., Analysis of Cyathane-Type Diterpenoids from Cyathus Striatus and Hericium Erinaceus by High-Resolution Maldi Ms Imaging. *Analytical and bioanalytical chemistry* **2014,** *406* (3), 695-704.

Figures

Figure 1.

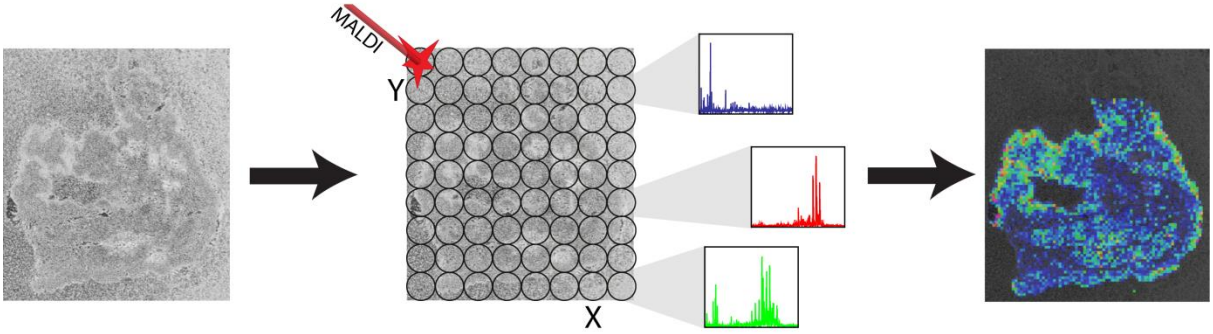

Figure 1. MALDI-MSI Workflow. Samples are prepared by sectioning tissue samples and mounting them on a glass slide or MALDI target plate followed by application of matrix. MSI uses a computer-controlled x-y stage, which holds the sample, and allows for the laser to raster across the sample and mass spectra to be collected at every pre-defined raster point. After completing the 2D raster, an ion image can be created using software to select a single mass from the spectrum and the software will display the relative abundance of that ion as a heat map of signal intensity at each raster point.

Figure 2.

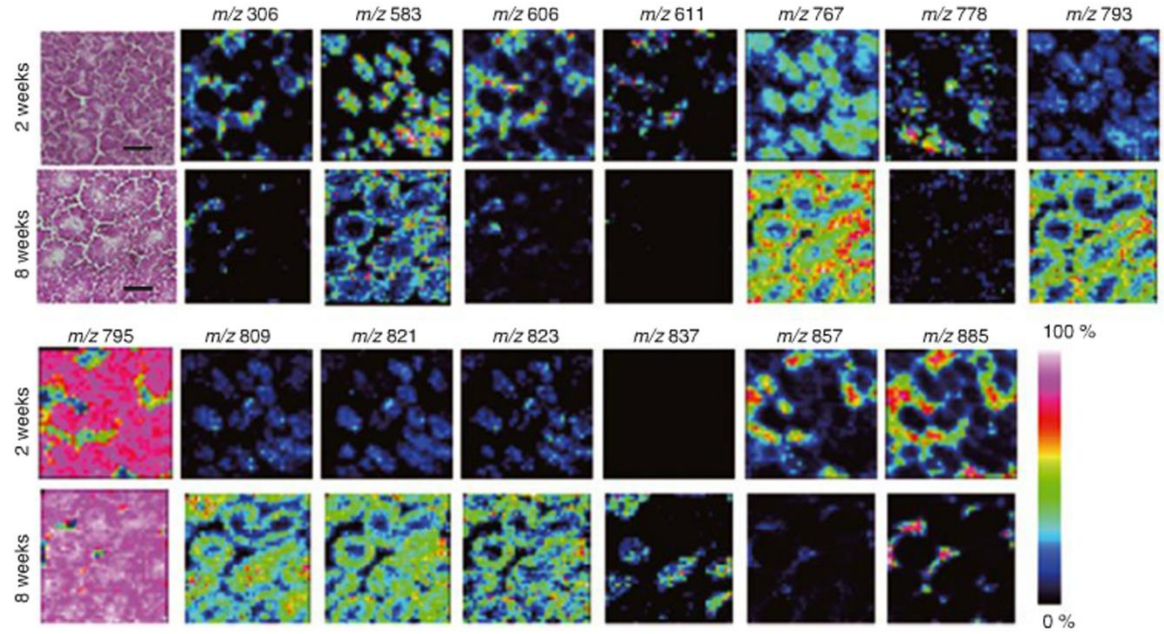

Figure 2. The result of MSI analyses of testis in negative-ion mode. Hematoxylin and eosin staining results and ion images of 14 representative peaks. Scale bar is 100 μm. Reprinted with permission from Ref. 34. Copyright 2011 John Wiley & Sons, Ltd.

Figure 3.

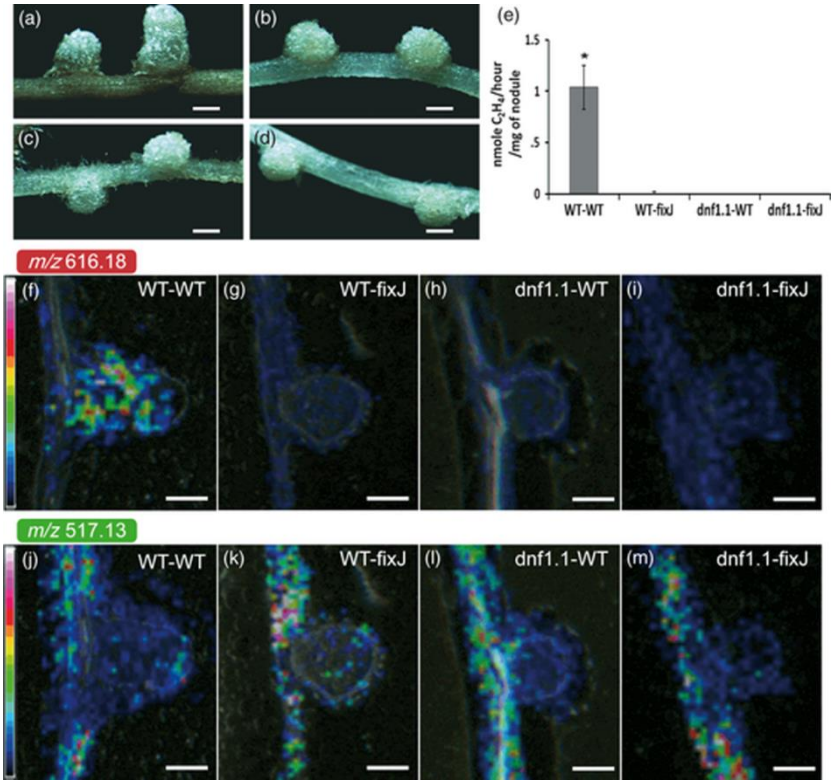

Figure 3. Comparison of the metabolite distribution in nitrogen fixing and non-fixing *Medicago truncatula* (Medicago) nodules. (a) Nodules on a wild-type (WT) Medicago plant inoculated with the WT strain of rhizobia (WT/WT). (b) Nodules on a WT plant inoculated with the *fixJ* mutant of rhizobia (WT/*fixJ*). (c) Nodules on a Medicago *dnf1–1* mutant inoculated with the WT strain of rhizobia (*dnf1*/WT). (d) Nodules on a Medicago *dnf1–1* mutant inoculated with the *fixJ* mutant of rhizobia (*dnf1*/*fixJ*). (e) Nitrogen fixation activity. Each bar corresponds to the mean value of acetylene reduction for eight plants assayed 3 weeks after inoculation. Error bars indicate standard error (SE). (f–i)Distribution of the heme moiety at *m*/*z* 616.18 in the four different nodule types: WT/WT (f), WT/*fixJ* (g), *dnf1*/WT (h) and *dnf1*/*fixJ* (i). The heme moiety was detected only in fixing nodules in (f). (j–m) Distribution of the metabolite formononetin MalGlc at *m*/*z* 517.13 on WT/WT (j), WT/*fixJ* (k), *dnf1*/WT (l) and *dnf1*/*fixJ* (m), showing great similarity in contrast to (f)–(i). Scale bars = 1 mm. Reprinted with permission from Ref. 4. Copyright 2013 John Wiley & Sons, Ltd.

Figure 4.

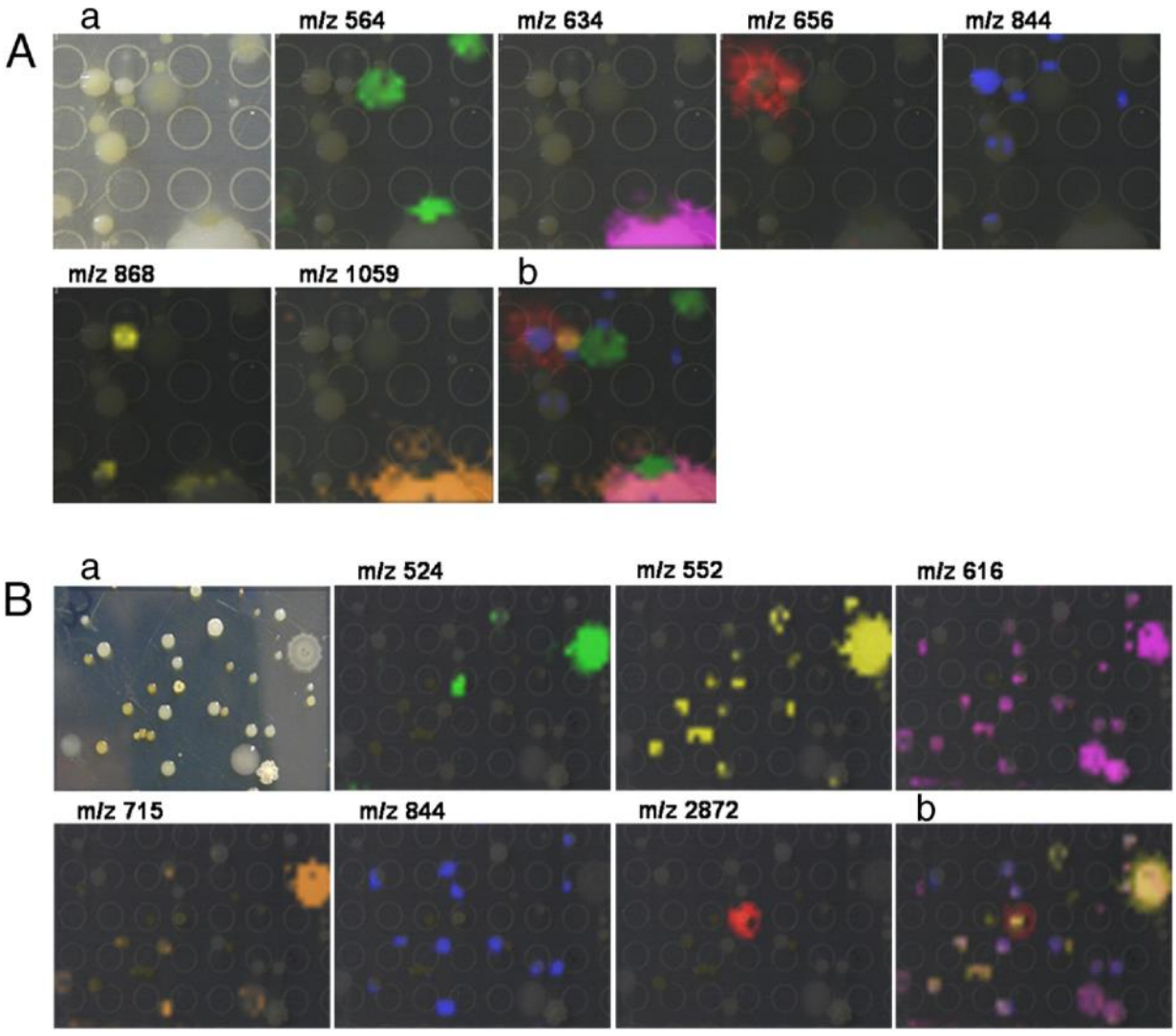

Figure 4. MSI of multiple complex samples. A. Los Angeles garden soil. B. La Jolla Shores beach marine sediment. (a) Respective photographs of microbial communities. (b) Overlay of multiple ions observed within the microbial community. Reprinted with permission from Ref. 38. Copyright 2012 Elsevier.

Figure 5.

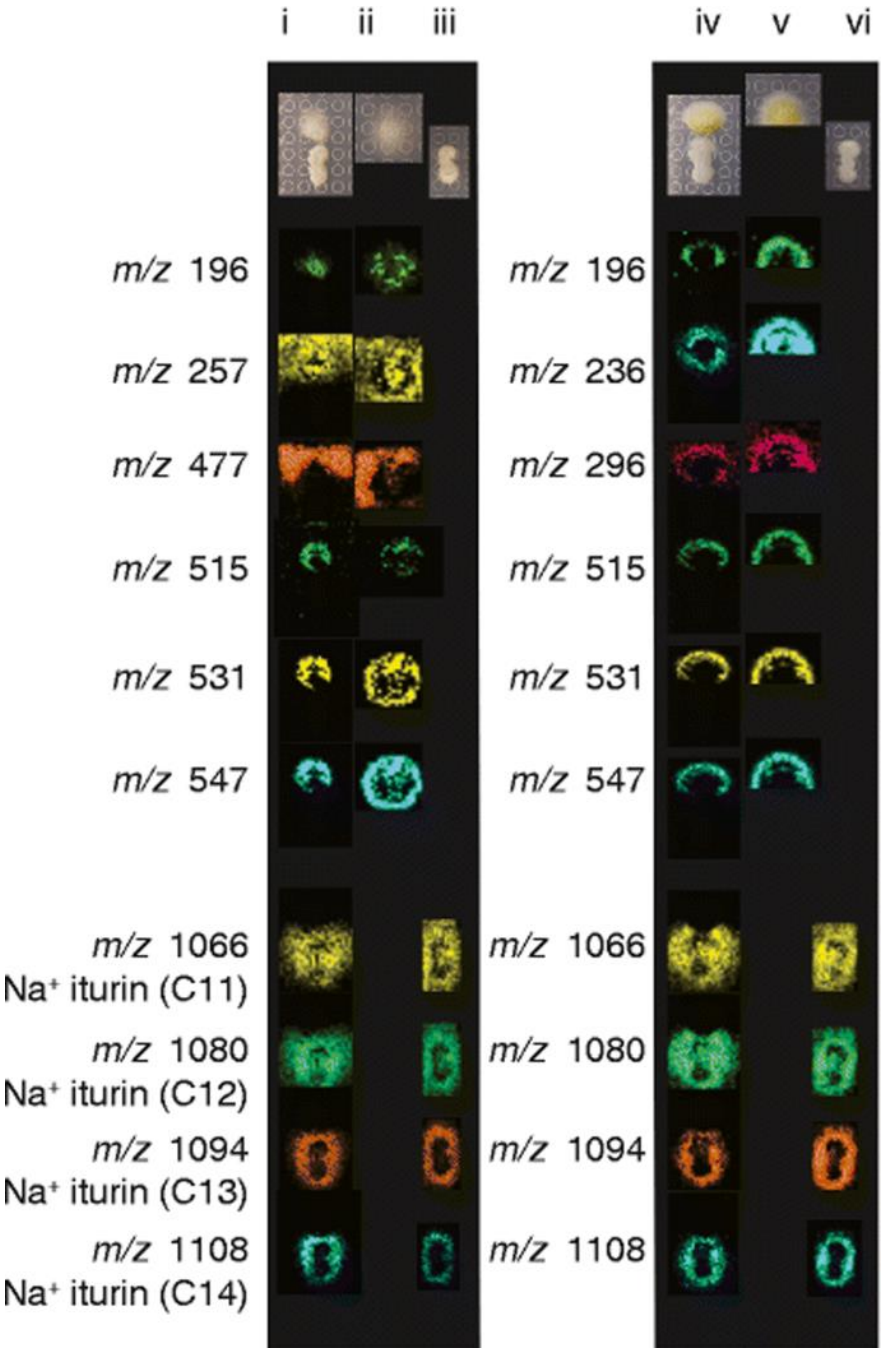

Figure 5. MALDI-MSI of the interaction between GA40 (bacteria) and *A. fumigatus* fungi (left) compared to interaction of GA40 *vs. A. niger* fungi (right) including the controls (i) GA40 on the bottom and *A. fumigatus* on the top (ii) *A. fumigatus* control (iii) GA40 control (iv) GA40 on the bottom and *A. niger* on the top (v) *A. niger* control (half of a colony was imaged) (vi) GA40 control. Reprinted with permission from Ref. 22. Copyright 2013 Springer.

Chapter 3

Optimization and Comparison of Multiple MALDI Matrix Application Methods for Small Molecule Mass Spectrometric Imaging

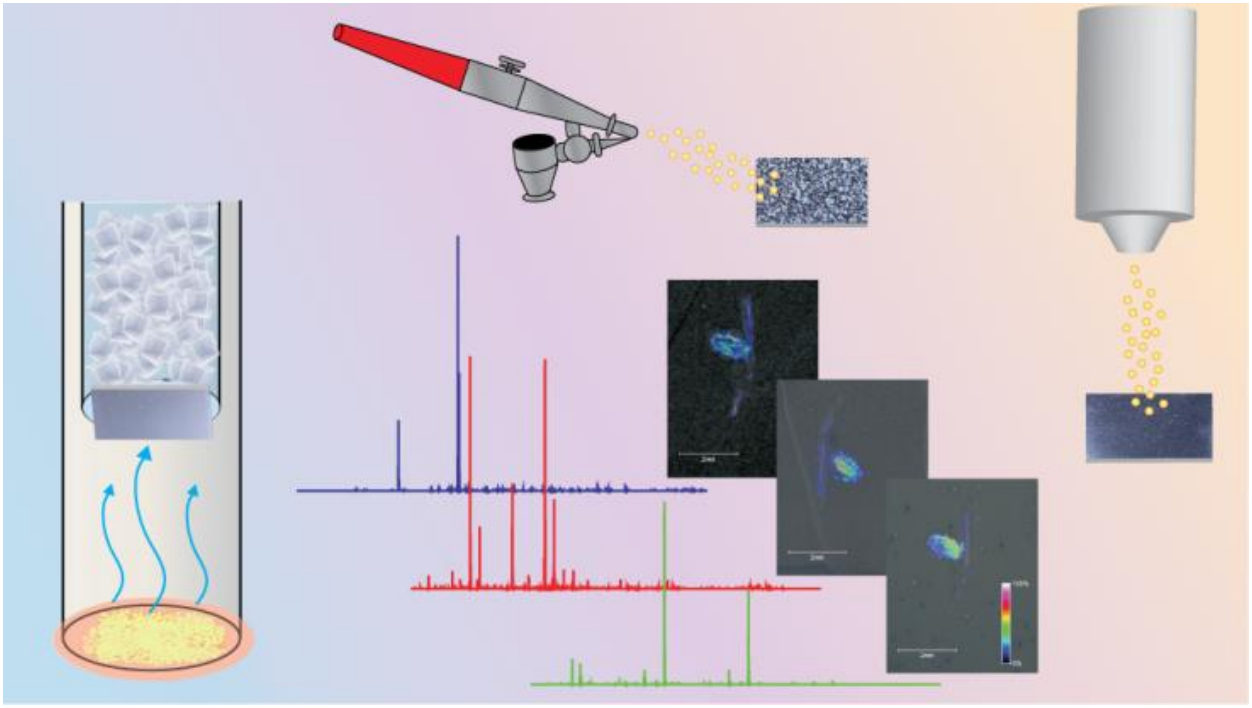

Adapted from **Gemperline, E.**; Rawson, S.; Li, L. "Optimization and Comparison of Multiple MALDI Matrix Application Methods for Small Molecule Mass Spectrometric Imaging" *Analytical Chemistry*. 86(20):10030-10035. (2014) doi:10.1021/ac5028534

Abstract

The matrix application technique is critical to the success of a matrix-assisted laser desorption/ionization (MALDI) experiment. This work presents a systematic study aiming to evaluate three different matrix application techniques for MALDI mass spectrometric imaging (MSI) of endogenous metabolites from legume plant, *Medicago truncatula*, root nodules. Airbrush, automatic sprayer, and sublimation matrix application methods were optimized individually for detection of metabolites in the positive ionization mode exploiting the two most widely-used MALDI matrices, 2,5-dihydroxybenzoic acid (DHB) and α-cyano-4-hydroxycinnamic acid (CHCA). Analytical reproducibility and analyte diffusion were examined and compared side-by-side for each method. When using DHB, the optimized method developed for the automatic matrix sprayer system resulted in approximately double the number of metabolites detected when compared to sublimation and airbrush. The automatic sprayer method also showed more reproducible results and less analyte diffusion than the airbrush method. Sublimation matrix deposition yielded high spatial resolution and reproducibility, but fewer analytes in the higher *m/z* range (500-1000 *m/z*). When the samples were placed in a humidity chamber after sublimation, there was enhanced detection of higher mass metabolites, but increased analyte diffusion in the lower mass range. When using CHCA, the optimized automatic sprayer method and humidified sublimation method resulted in double the number of metabolites detected compared to standard airbrushing.

Introduction

Metabolomics is a growing field with many important biological applications including biomarker discovery, deciphering metabolic pathways in plants and other biological systems, and toxicology profiling.[1-7] Studying the metabolome of a cell/organism can provide insights into its actual biochemical state.[8] Most techniques currently used for metabolomics require tissue extracts, but knowing the location of a biomolecule within a specific tissue can reveal key insights into its role and function within the organism.[9-11] MALDI-MSI has become a powerful tool to visualize the distribution of a wide range of molecules within biological tissues.[12-20]

MALDI requires deposition of an organic, crystalline compound, known as matrix, on the tissue of interest to assist analyte desorption and ionization.[16] The matrix application technique plays a crucial role in the quality of mass spectral images, especially when obtaining high spatial resolution images.[21-23] Among other instrumental parameters, such as raster step size, laser beam diameter, etc., spatial resolution and reproducibility of results are also limited by the matrix crystal size and application consistency.[23-24] In this work, three matrix application methods were systematically optimized and compared: airbrush, automatic sprayer, and sublimation. Airbrush matrix application has been widely used in MALDI imaging[6, 15, 17, 25-26] and is relatively fast and simple. The major limitation of airbrush matrix application is that the velocity of the spray is controlled manually and cannot be strictly monitored. This causes the quality of the spray to be extremely user dependent, and is often not reproducible. Variations in the spray velocity and duration cause inconsistent application and applying too much solvent to the tissue can cause analyte diffusion, especially when working with small molecules.[22] Automatic sprayer systems, such as the TM-Sprayer from HTX Technologies, have been developed to remove the variability seen with manual airbrush application by robotically controlling the temperature, solvent flow

rate, velocity of the matrix spraying nozzle during each pass, and number of passes. Using an automatic sprayer system, the matrix density and crystal size can be much more uniform, making the experimental results more reproducible; however, this method is more time-consuming than matrix application performed with an airbrush. Sublimation is a solvent-free matrix application technique that is becoming more and more popular for mass spectral imaging of metabolites and small molecules.[27] Sublimation reduces analyte diffusion because there is no solvent sprayed directly onto the tissue that can delocalize small molecules. The drawback of this method is that the lack of solvent causes some compounds to go undetected;[28] however, placing the sample in a humidity chamber, post-sublimation, may extract these higher mass compounds.

In this work we optimized and compared the utilization of three matrix application techniques, exploiting the two most widely-used MALDI matrices, 2,5-dihydroxybenzoic acid (DHB) and α-cyano-4-hydroxycinnamic acid (CHCA), using the metabolome of *Medicago truncatula* root and nodule tissue as a model. Previously, metabolites of various chemical species, including amino acids, sugars, organic acids, lipids, flavonoids and their conjugates, were characterized and mapped on *M. truncatula* roots and nodules using the conventional matrix, DHB, applied manually with an airbrush.[6] Improving the matrix application technique for high spatial resolution imaging of small molecules holds promise for better mechanistic understanding of biological pathways and processes in *M. truncatula* and the methodology developed for small molecule MSI can be transferred to many other important biological systems and applications. Previous publications compare and optimize one matrix application method for many different matrices,[21, 29-30] compare dry coating vs. spray matrix application methods,[31-33] or compare two different spray methods.[22, 34] Herein we present a detailed optimization process for three different matrix application techniques with a focus on studying endogenous small

molecules. We report an automatic sprayer method that can achieve sublimation-like imaging results and a sublimation procedure that can detect more higher-mass metabolites than traditional sublimation.

Materials and Methods

M. truncatula plants were grown and prepared for MSI (see supplemental information for details). Matrix deposition was carried out using three different techniques: airbrush (Paasche Airbrush Company, Chicago, IL, USA) coupled with 75 ml steel container, TM-Sprayer system (HTX Technologies, LLC, Carrboro, NC, USA), and sublimation apparatus (Chemglass Life Science, Vineland, NJ, USA). The concentration of matrix applied with an airbrush was 150 mg/ml DHB (in 0.1% formic acid and 50% methanol) or 10 mg/ml CHCA (in 0.1% formic acid and 70% methanol) and the airbrush was held 35 cm from the plate. Ten or more coatings were applied; the spray duration was 15s with 30s dry time between each coating. For sublimation matrix deposition, 300 mg of dry DHB or CHCA was weighed out into the reservoir of the sublimation apparatus. Two previously reported methods and adaptations of these previously reported methods were performed and compared for optimized reproducibility, metabolite detection, and signal intensity. For matrix application with the automatic sprayer 40 mg/ml DHB (in 0.1% formic acid and 50% methanol) or 10 mg/ml CHCA (in 0.1% formic acid and 70% methanol) was used as matrix. The temperature, nozzle velocity, solvent flow rate, and number of passes were systematically changed and optimized. Methods previously reported by HTX Imaging Technologies and novel methods were investigated and compared for optimized reproducibility, metabolite detection, and signal intensity. MSI was carried out using an Ultraflextreme MALDI- TOF/TOF and metabolites were identified based on accurate mass

matching and MS/MS fragmentation in our previously published work[6] (see supplemental information for details). **SI Table 1** lists the identified metabolites shown in subsequent figures and **SI Figures 1-5** show MS/MS spectra of the metabolites detected in the Medicago root nodules compared to metabolite standards in order to confirm the metabolite identifications.

Results and Discussion

Airbrush Matrix Application

Previous work used the well-established airbrush application as described above to map metabolites in root nodules and neuropeptides in crustacean tissue with MALDI-MSI.[6, 15, 35] The quality of the matrix application varies greatly depending on the skill and preference of the user.

Sublimation Matrix Application

For DHB, two previously reported methods[21, 27] and two adaptations of these previously reported methods were performed and compared for optimized reproducibility, metabolite detection, and signal intensity. A summary of the parameters used for each of the four methods is listed in **SI Table 2**. Method 1, reported by Hankin *et al.*, started at room temperature (RT) and gradually increased to 110 °C. The procedure reported by Thomas *et al.* (Method 2) required a temperature of 140 °C, but a drop in temperature was observed as the sublimation apparatus was placed into the heating mantle. Therefore, in the method adapted from this procedure (Method 3), the temperature was initially set to 190 °C so the temperature would drop to 140 °C when the sublimation apparatus was placed in the heating mantle. Method 4 adds an additional step to Method 1, similar to the procedure proposed by Goodwin *et al.*, in which the samples were exposed to a saturated moist atmosphere after sublimation.[31] After the matrix sublimation was complete, the glass slide was placed in a humidity chamber with deionized

water for approximately 45 min, and allowed to dry at room temperature before MSI. It was observed that the methods that gradually raised the temperature from RT gave more even coverage of matrix and performed more consistently between runs. In this comparison, analyte signal was distinguished from matrix signal using the MS images as guides. MS images were extracted by manually clicking on each peak in the spectrum. Peaks corresponding to images where no signal was seen in the matrix only area and signal was present on the *M. truncatula* tissue were considered metabolites. Significantly more metabolite peaks were observed using gradual heating with the humidity chamber step (Method 4), in comparison with gradual heating and no humidity (Method 1), especially in the higher mass region (above *m/z* 500). **SI Figure 6** shows several representative MS images comparing gradual heating sublimation methods without and with humidity (Methods 1 and 4 respectively), illustrating that gradual heating without humidity produced less analyte diffusion than gradual heating with humidity in the lower mass range, while gradual heating with humidity enhanced metabolite detection in the higher mass range. SI Figure 6 also compares the MS spectra from these methods, showing the increased detection of higher *m/z* metabolites when the humidity step was employed.

For CHCA, five gradual heating methods were examined that involved beginning at RT and gradually increasing the temperature to 120, 140, 150, 152, or 160 °C over the course of 10 min. Heating to 152 °C provided homogenous coverage and good signal intensity; 160 °C generated too thick of a layer of CHCA and 150 °C was slightly too thin of a layer to give consistent results. A sixth method was examined in which the sublimation chamber was gradually heated to 152 °C over 10 minutes, followed by 45 minutes in the humidity chamber as described above. A summary of the parameters used for each of the four methods is listed in **SI**

Table 3. Unlike the results described above, adding the humidity chamber step did not increase the metabolite detection and only served to diffuse analytes in the lower mass region.

Automatic Sprayer Matrix Application

For DHB, five automatic sprayer matrix application methods were developed for the automatic TM-Sprayer system. The parameters used for each of the five methods are summarized in **SI Table 4**; 3 mm line spacing and a nozzle temperature of 80 °C was used for all methods. The first method (Method 1) was recommended by the manufacturer of the automatic sprayer system method for detecting metabolites. The solvent flow rate and spray nozzle velocity were changed in the different methods to produce a drier spray. As the solvent flow rate decreases, the spray becomes drier because less solvent is being sprayed onto the sample. Increasing the velocity of the spray nozzle also produces a drier spray because the nozzle is spraying matrix over the sample for a shorter period of time. Method 4, listed in the table, is the driest, most sublimation-like spray because it has the highest nozzle velocity and the lowest solvent flow rate. Changing the number of passes allows for adjustment of the matrix density to provide suitable MS signal. All methods performed with the automatic sprayer system provide excellent reproducibility and consistency in crystal size and coverage. The number of metabolites detected and the extent of analyte diffusion, visualized with MSI, was compared between all five methods; representative MS images comparing 3 of the sprayer methods are shown in **SI Figure 7**. The “driest method” (Method 4) allowed for the detection of nearly double the number of metabolites when compared to the other four methods examined. The use of Method 4 allowed for detection of metabolites over the entire mass range suggesting that the method was dry enough to detect metabolites in the low mass region without causing them to

diffuse and dilute, but had enough solvent to extract higher mass metabolites from the tissue for detection.

For CHCA, six automatic sprayer matrix application methods were developed for the automatic TM-Sprayer system. The parameters used for each of the six methods are summarized in **SI Table 5**; a nozzle temperature of 80 °C was used for all methods. All automatic sprayer methods performed equivalently with regards to metabolite detection and little analyte diffusion; therefore, the optimized method is the method suggested by the manufacturer because it requires the least amount of time for application. Using 10 mg/ml CHCA may require extra cleaning of the sprayer apparatus depending on the quality of the syringe pump used in the setup; we recommend using 5 mg/ml CHCA and doubling the number of passes to achieve equivalent results without the chance of clogging the sprayer.

Comparison of Optimized Airbrush, Sublimation, and Automatic Sprayer Methods

The optimized sublimation and automatic sprayer methods were directly compared to the standard, well-used airbrush matrix application method by performing MSI on serial sections of *M. truncatula* root nodule tissue, for both DHB and CHCA. When applying matrix with these three very different techniques and performing MSI of samples coated using the different application methods in a single run, the overall signal and metabolite detection decreased significantly when compared to results from performing MSI of the techniques individually. One reason for this could be due to the varying crystal size in a single experiment, which causes limited detection in TOF/TOF mass analyzers. Even with the decreased metabolite detection, it is still clear that the optimized automatic sprayer method facilitates the detection of the highest number of metabolites. **Figure 1** shows optical images comparing matrix coverage and crystal

size for the airbrush, optimized automatic sprayer, and optimized sublimation matrix application methods respectively for a) DHB and b) CHCA. Sublimation produces one even layer of matrix; the automatic sprayer produces very small, uniform crystals, while the airbrush produces larger crystals of varying sizes. **Figure 2** compares MS profiling spectra for pure matrix using the airbrush (blue), optimized automatic sprayer (red), and optimized sublimation (green) matrix application methods for a) DHB and b) CHCA. For both matrices, the matrix signal is highest in the airbrush spectrum and there are more matrix ion peaks than the other two methods, which could cause interference with some of the metabolites of interest. All three matrix application techniques produce slightly different matrix ion peak patterns; the automatic sprayer and sublimation techniques could be complementary ways to detect low molecular weight metabolites that are masked by high intensity matrix peaks. **Figure 3** and **Figure 4** show comparisons of representative MS images of *M. truncatula* root nodules using the airbrush, automatic sprayer, and sublimation methods optimized for DHB and CHCA respectively. Compared to the airbrush method, the sublimation and automatic sprayer methods show less analyte diffusion and a greater number of metabolites detected. For DHB the sublimation method shows some analyte diffusion in the lower mass range due to the humidity chamber step, but there are also some metabolites detected in the higher mass range that would not have been detected without the humidity chamber step.

Conclusions

Monitoring metabolite distribution is extremely important for the overall understanding of molecular pathways in many biological systems and fields of study. This work presents a comprehensive evaluation of three major MALDI matrix application techniques with the two

most widely-used matrices (DHB and CHCA) for MS imaging of small molecules. The use of the optimized automatic sprayer methods significantly increases the number of metabolites detected within a defined mass range, especially when using DHB. The ability of the automatic sprayer to enhance metabolite detection while maintaining the spatial distribution of small molecules within a biological tissue sample, when compared to airbrush and sublimation matrix application methods, was demonstrated by acquiring positive ion images from serial tissue sections of *M. truncatula*. The optimized automatic sprayer method and sublimation methods reduce analyte diffusion that is typically seen with traditional airbrush matrix application methods.

The combined use of solvent-free (sublimation) and solvent-based (automatic sprayer) matrix application techniques can provide complementary matrix peak profile results, providing the possibility to detect metabolites that were masked by interfering matrix ion peaks in one matrix application method but not masked in the other. There were very few metabolites that were only detected with the sublimation or airbrush methods, therefore, the optimized automatic sprayer method is recommended for detection of the greatest number of metabolites during a single experiment.

Strict optimization of matrix application technique seems to be more critical when working with DHB. The procedure for applying DHB with the automatic sprayer or via sublimation was extremely critical to the quality of the MS images, whereas similar results were obtained using CHCA regardless of the procedure used to apply the matrix.

Using the optimized sprayer methods to apply DHB and CHCA respectively on serial sections of plant root nodule tissue provided complementary detection of endogenous

metabolites. Over 100 compounds were detected using each matrix with approximately 60% of the detected metabolites uniquely detected using either DHB or CHCA and approximately 40% overlap between methods.

Future work using alternative matrices in both positive and negative ionization modes to test the ability of the optimized automatic sprayer method compared to the optimized sublimation method would further characterize the advantages of using one method over the other, or a combination of both automatic sprayer and sublimation matrix application techniques.

Acknowledgements

The authors would like to acknowledge Dr. Jean-Michel Ané in the Department of Agronomy at UW-Madison for providing *Medicago truncatula* samples. The authors would like to acknowledge Dr. John Markley, the National Magnetic Resonance Facility at Madison (NMRFAM) which is supported by NIH grant P41GM103399 (NIGMS), and the Biological Magnetic Resonance Data Bank (BMRB) which is funded by RO1 GM109046 for the use of the heme standard. This work was supported by funding from a National Science Foundation (NSF) Graduate Research Fellowship (DGE-1256259) to E.G. and by funding from the University of Wisconsin Graduate School and the Wisconsin Alumni Research Foundation (WARF) and Romnes Faculty Research Fellowship program to L.L.

References

1. Wei, R., Metabolomics and Its Practical Value in Pharmaceutical Industry. *Curr Drug Metab* **2011,** *12* (4), 345-358.

2. Kobayashi, T.; Nishiumi, S.; Ikeda, A.; Yoshie, T.; Sakai, A.; Matsubara, A.; Izumi, Y.; Tsumura, H.; Tsuda, M.; Nishisaki, H.; Hayashi, N.; Kawano, S.; Fujiwara, Y.; Minami, H.; Takenawa, T.; Azuma, T.; Yoshida, M., A Novel Serum Metabolomics-Based Diagnostic Approach to Pancreatic Cancer. *Cancer Epidem Biomar* **2013,** *22* (4), 571-579.

3. West, P. R.; Weir, A. M.; Smith, A. M.; Donley, E. L. R.; Cezar, G. G., Predicting Human Developmental Toxicity of Pharmaceuticals Using Human Embryonic Stem Cells and Metabolomics. *Toxicol Appl Pharm* **2010,** *247* (1), 18-27.

4. Spegel, P.; Sharoyko, V. V.; Goehring, I.; Danielsson, A. P.; Malmgren, S.; Nagorny, C. L.; Andersson, L. E.; Koeck, T.; Sharp, G. W.; Straub, S. G.; Wollheim, C. B.; Mulder, H., Time-Resolved Metabolomics Analysis of Beta-Cells Implicates the Pentose Phosphate Pathway in the Control of Insulin Release. *The Biochemical journal* **2013,** *450* (3), 595-605.

5. Pendyala, G.; Want, E. J.; Webb, W.; Siuzdak, G.; Fox, H. S., Biomarkers for Neuroaids: The Widening Scope of Metabolomics. *J Neuroimmune Pharm* **2007,** *2* (1), 72-80.

6. Ye, H.; Gemperline, E.; Venkateshwaran, M.; Chen, R.; Delaux, P. M.; Howes-Podoll, M.; Ane, J. M.; Li, L., Maldi Mass Spectrometry-Assisted Molecular Imaging of Metabolites During Nitrogen Fixation in the Medicago Truncatula-Sinorhizobium Meliloti Symbiosis. *The Plant journal : for cell and molecular biology* **2013,** *75* (1), 130-145.

7. Gemperline, E.; Li, L., Maldi-Mass Spectrometric Imaging for the Investigation of Metabolites in Medicago Truncatula Root Nodules. *Journal of Visualized Experiments* **2014,** (85), e51434.

8. Amaya, K. R.; Sweedler, J. V.; Clayton, D. F., Small Molecule Analysis and Imaging of Fatty Acids in the Zebra Finch Song System Using Time-of-Flight-Secondary Ion Mass Spectrometry. *J Neurochem* **2011,** *118* (4), 499-511.

9. McDonnell, L. A.; Heeren, R. M. A., Imaging Mass Spectrometry. *Mass Spectrom Rev* **2007,** *26* (4), 606-643.

10. Goto-Inoue, N.; Hayasaka, T.; Zaima, N.; Setou, M., Imaging Mass Spectrometry Reveals Changes of Metabolites Distribution in Mouse Testis During Testicular Maturation. *Surf Interface Anal* **2012,** *44* (6), 749-754.

11. Yang, H. J.; Sugiura, Y.; Ishizaki, I.; Sanada, N.; Ikegami, K.; Zaima, N.; Shrivas, K.; Setou, M., Imaging of Lipids in Cultured Mammalian Neurons by Matrix Assisted Laser/Desorption Ionization and Secondary Ion Mass Spectrometry. *Surf Interface Anal* **2010,** *42* (10-11), 1606-1611.

12. Lee, Y. J.; Perdian, D. C.; Song, Z. H.; Yeung, E. S.; Nikolau, B. J., Use of Mass Spectrometry for Imaging Metabolites in Plants. *Plant J.* **2012,** *70* (1), 81-95.

13. Stoeckli, M.; Chaurand, P.; Hallahan, D. E.; Caprioli, R. M., Imaging Mass Spectrometry: A New Technology for the Analysis of Protein Expression in Mammalian Tissues. *Nat Med* **2001,** *7* (4), 493-496.

14. Kaspar, S.; Peukert, M.; Svatoš, A.; Matros, A.; Mock, H. P., Maldi-Imaging Mass Spectrometry - an Emerging Technique in Plant Biology. *Proteomics* **2011,** *11* (9), 1840-1850.

15. DeKeyser, S. S.; Kutz-Naber, K. K.; Schmidt, J. J.; Barrett-Wilt, G. A.; Li, L., Imaging Mass Spectrometry of Neuropeptides in Decapod Crustacean Neuronal Tissues. *Journal of proteome research* **2007,** *6* (5), 1782-1791.

16. Caprioli, R. M.; Farmer, T. B.; Gile, J., Molecular Imaging of Biological Samples: Localization of Peptides and Proteins Using Maldi-Tof Ms. *Anal Chem* **1997,** *69* (23), 4751-4760.

17. Lietz, C. B.; Gemperline, E.; Li, L., Qualitative and Quantitative Mass Spectrometry Imaging of Drugs and Metabolites. *Advanced drug delivery reviews* **2013**.

18. Hamm, G.; Carre, V.; Poutaraud, A.; Maunit, B.; Frache, G.; Merdinoglu, D.; Muller, J. F., Determination and Imaging of Metabolites from Vitis Vinifera Leaves by Laser Desorption/Ionisation Time-of-Flight Mass Spectrometry. *Rapid Commun Mass Sp* **2010,** *24* (3), 335-342.

19. Lazova, R.; Seeley, E. H.; Keenan, M.; Gueorguieva, R.; Caprioli, R. M., Imaging Mass Spectrometry-a New and Promising Method to Differentiate Spitz Nevi from Spitzoid Malignant Melanomas. *Am J Dermatopath* **2012,** *34* (1), 82-90.

20. Liu, Q.; Xiao, Y. S.; Pagan-Miranda, C.; Chiu, Y. M.; He, L., Metabolite Imaging Using Matrix-Enhanced Surface-Assisted Laser Desorption/Ionization Mass Spectrometry (Me-Saldi-Ms). *Journal of the American Society for Mass Spectrometry* **2009,** *20* (1), 80-88.

21. Thomas, A.; Charbonneau, J. L.; Fournaise, E.; Chaurand, P., Sublimation of New Matrix Candidates for High Spatial Resolution Imaging Mass Spectrometry of Lipids: Enhanced Information in Both Positive and Negative Polarities after 1,5-Diaminonapthalene Deposition. *Anal Chem* **2012,** *84* (4), 2048-2054.

22. Baluya, D. L.; Garrett, T. J.; Yost, R. A., Automated Maldi Matrix Deposition Method with Inkjet Printing for Imaging Mass Spectrometry. *Anal Chem* **2007,** *79* (17), 6862-6867.

23. Goodwin, R. J. A., Sample Preparation for Mass Spectrometry Imaging: Small Mistakes Can Lead to Big Consequences. *J Proteomics* **2012,** *75* (16), 4893-4911.

24. Balluff, B.; Schone, C.; Hofler, H.; Walch, A., Maldi Imaging Mass Spectrometry for Direct Tissue Analysis: Technological Advancements and Recent Applications. *Histochem Cell Biol* **2011,** *136* (3), 227-244.

25. Shimma, S.; Sugiura, Y.; Hayasaka, T.; Hoshikawa, Y.; Noda, T.; Setou, M., Maldi-Based Imaging Mass Spectrometry Revealed Abnormal Distribution of Phospholipids in Colon Cancer Liver Metastasis. *J Chromatogr B* **2007,** *855* (1), 98-103.

26. Ye, H.; Gemperline, E.; Li, L., A Vision for Better Health: Mass Spectrometry Imaging for Clinical Diagnostics. *Clinica chimica acta; international journal of clinical chemistry* **2013,** *420*, 11-22.

27. Hankin, J. A.; Barkley, R. M.; Murphy, R. C., Sublimation as a Method of Matrix Application for Mass Spectrometric Imaging. *Journal of the American Society for Mass Spectrometry* **2007,** *18* (9), 1646-1652.

28. Rubakhin, S. S.; Jurchen, J. C.; Monroe, E. B.; Sweedler, J. V., Imaging Mass Spectrometry: Fundamentals and Applications to Drug Discovery. *Drug Discov Today* **2005,** *10* (12), 823-837.

29. Peukert, M.; Matros, A.; Lattanzio, G.; Kaspar, S.; Abadia, J.; Mock, H. P., Spatially Resolved Analysis of Small Molecules by Matrix-Assisted Laser Desorption/Ionization Mass Spectrometric Imaging (Maldi-Msi). *The New phytologist* **2012,** *193* (3), 806-815.

30. Shanta, S. R.; Kim, T. Y.; Hong, J. H.; Lee, J. H.; Shin, C. Y.; Kim, K. H.; Kim, Y. H.; Kim, S. K.; Kim, K. P., A New Combination Maldi Matrix for Small Molecule Analysis: Application to Imaging Mass Spectrometry for Drugs and Metabolites. *The Analyst* **2012,** *137* (24), 5757-5762.

31. Goodwin, R. J.; Macintyre, L.; Watson, D. G.; Scullion, S. P.; Pitt, A. R., A Solvent-Free Matrix Application Method for Matrix-Assisted Laser Desorption/Ionization Imaging of Small Molecules. *Rapid communications in mass spectrometry : RCM* **2010,** *24* (11), 1682-1686.

32. Trimpin, S.; Herath, T. N.; Inutan, E. D.; Wager-Miller, J.; Kowalski, P.; Claude, E.; Walker, J. M.; Mackie, K., Automated Solvent-Free Matrix Deposition for Tissue Imaging by Mass Spectrometry. *Anal Chem* **2010,** *82* (1), 359-367.

33. Goodwin, R. J. A.; Mackay, C. L.; Nilsson, A.; Harrison, D. J.; Farde, L.; Andren, P. E.; Iverson, S. L., Qualitative and Quantitative Maldi Imaging of Positron Emission Tomography Ligands Raclopride (a D2 Dopamine Antagonist) and Sch 23390 (a D1 Dopamine Antagonist) in Rat Brain Tissue Sections Using a Solvent-Free Dry Matrix Application. *Anal. Chem.* **2011,** *83*, 9694-9701.

34. Chen, Y.; Allegood, J.; Liu, Y.; Wang, E.; Cachon-Gonzalez, B.; Cox, T. M.; Merrill, A. H., Jr.; Sullards, M. C., Imaging Maldi Mass Spectrometry Using an Oscillating Capillary Nebulizer Matrix Coating System and Its Application to Analysis of Lipids in Brain from a Mouse Model of Tay-Sachs/Sandhoff Disease. *Anal Chem* **2008,** *80* (8), 2780-2788.

35. Chen, R.; Cape, S. S.; Sturm, R. M.; Li, L., Mass Spectrometric Imaging of Neuropeptides in Decapod Crustacean Neuronal Tissues. *Methods Mol Biol* **2010,** *656*, 451-463.

Figures

Figure 1.

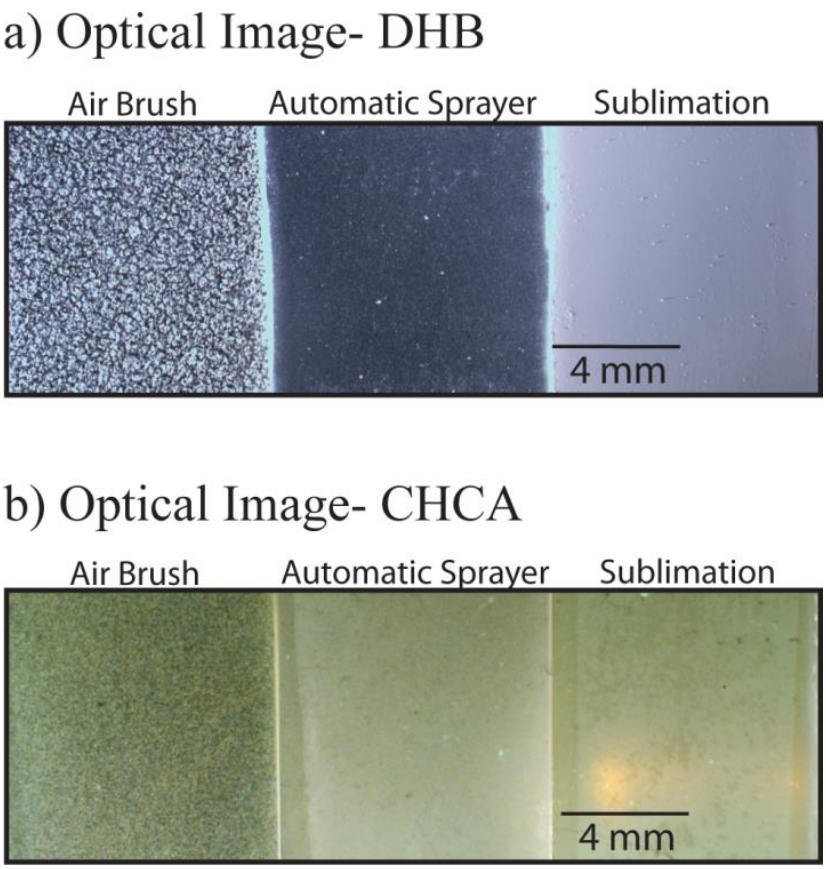

Figure 1. Comparison of MALDI-MSI of *Medicago truncatula* root nodules using the previously reported airbrush method, automatic sprayer Method 4, and sublimation Method 4. (a) Optical images comparing matrix coverage and crystal size for the airbrush (left), optimized automatic sprayer (middle), and optimized sublimation (right) matrix application methods using DHB for the matrix. (b) Optical images comparing matrix coverage and crystal size for the airbrush (left), optimized automatic sprayer (middle), and optimized sublimation (right) matrix application methods using CHCA for the matrix.

Figure 2.

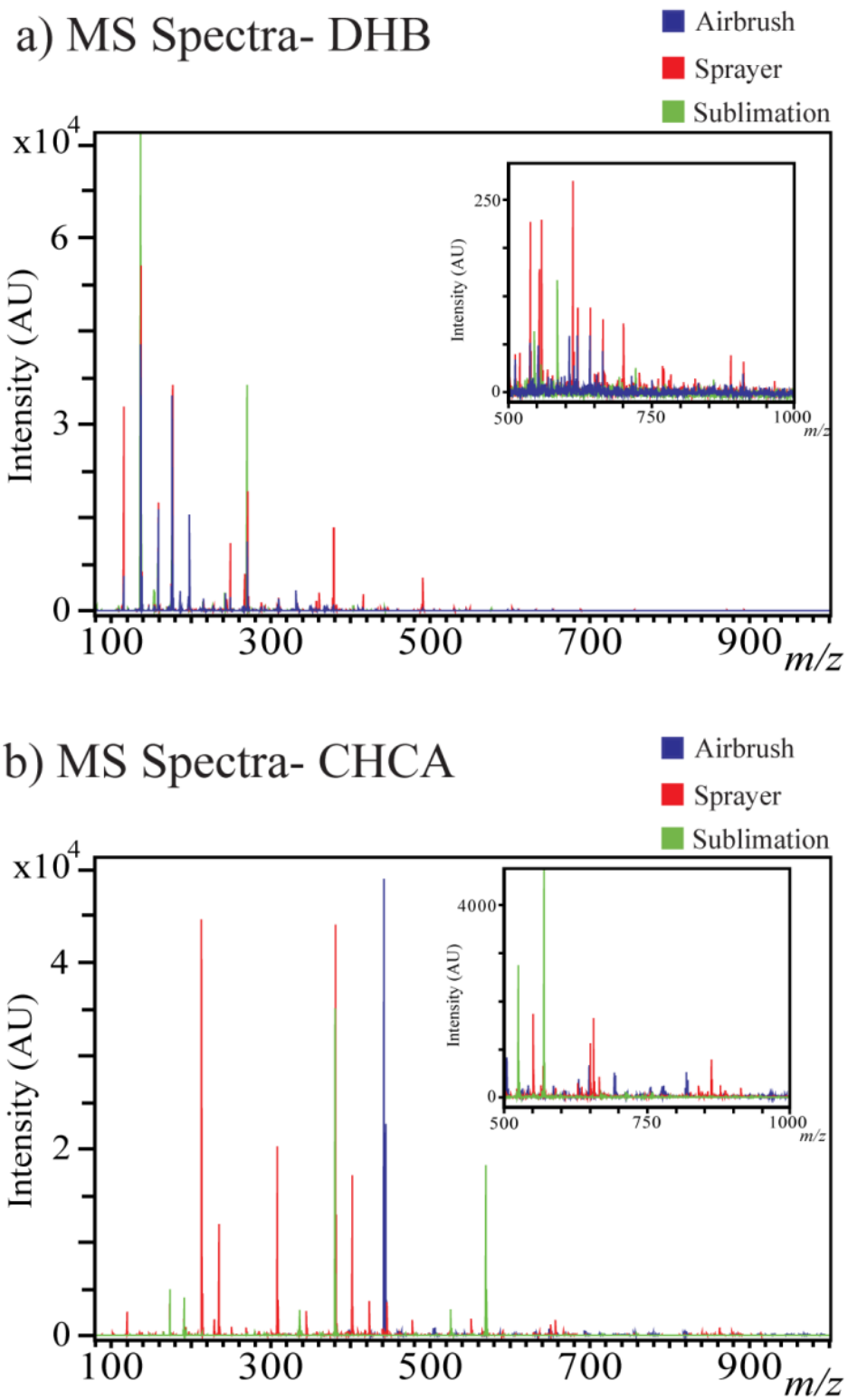

Figure 2. MS profiles of pure a) DHB and b) CHCA matrix peaks (with no sample) when applied to a glass slide with the airbrush (blue), optimized automatic sprayer (red), and the optimized sublimation (green) matrix application methods. Inlays show the MS spectra zoomed in to the higher *m/z* range (*m/z* 500-1000).

Figure 3.

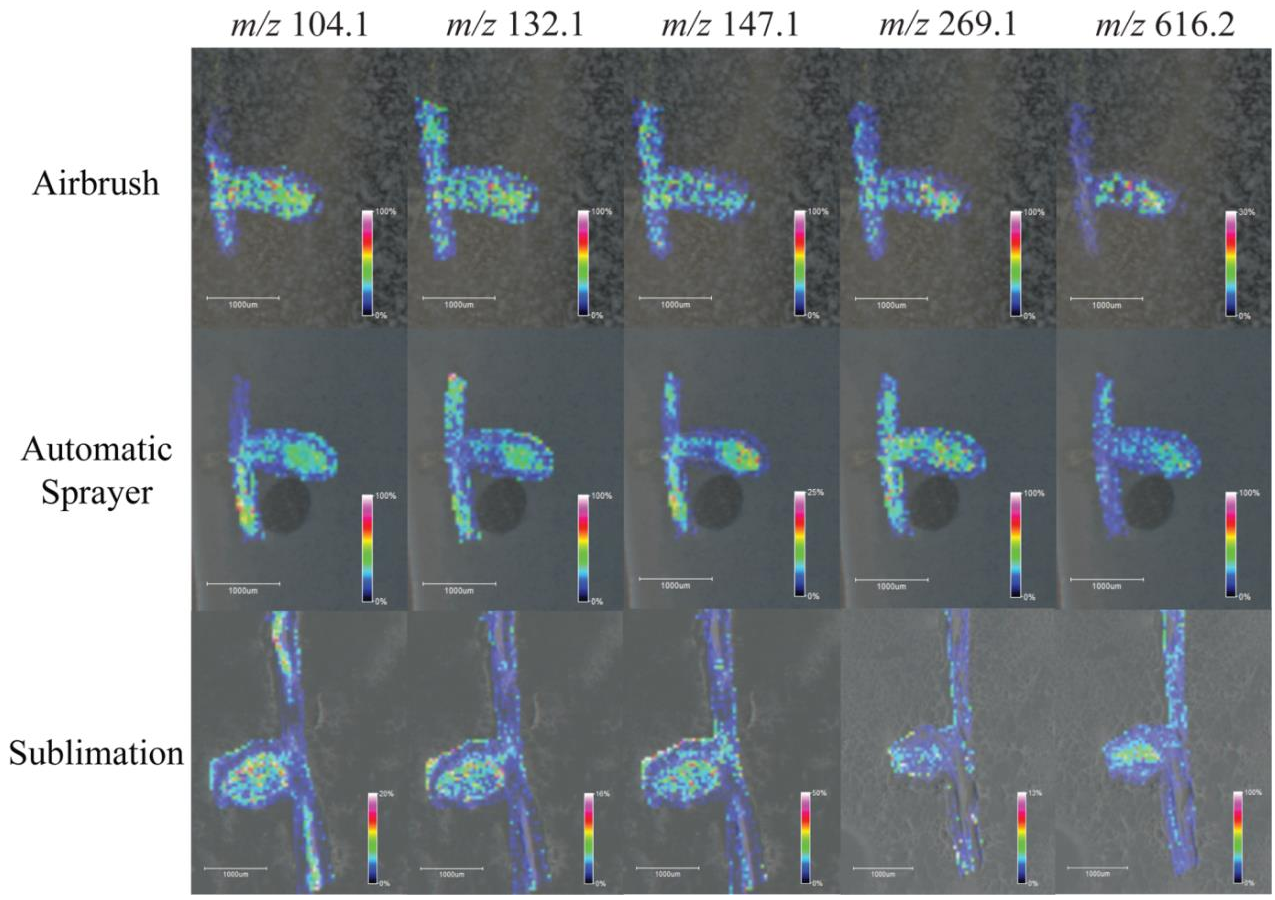

Figure 3. Images generated of *m/z* 104.1 (choline), *m/z* 132.1 (leucine), *m/z* 147.1 (glutamine), *m/z* 269.1 (unknown), and *m/z* 616.2 (heme, [M+]) by applying DHB with the airbrush (top), optimized automatic sprayer method (middle), and optimized sublimation method (bottom) to serial sections of *Medicago truncatula* root nodules.

Figure 4.

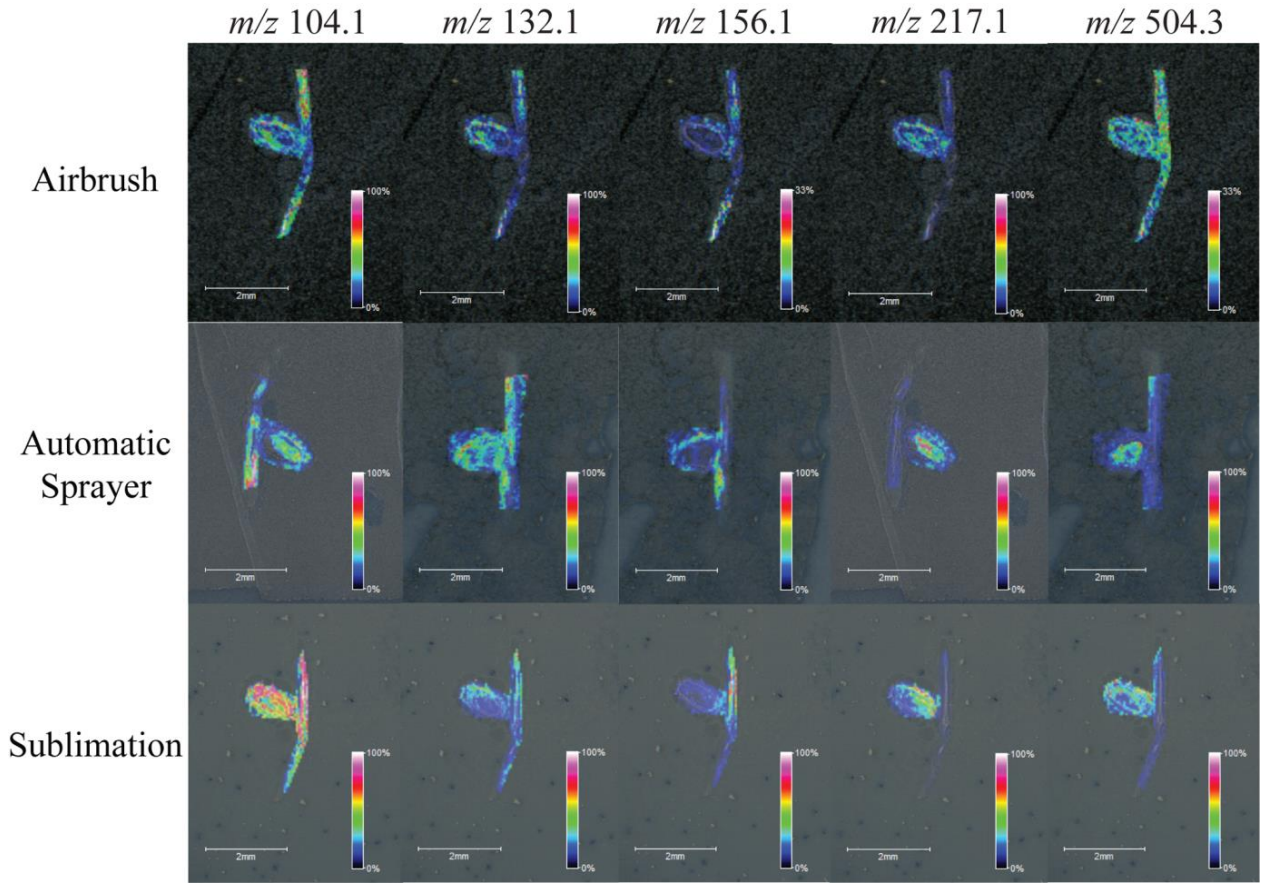

Figure 4. Images generated of *m/z* 104.1 (choline), *m/*z 132.1 (leucine), *m/*z 156.1 (histidine), *m/*z 217.1 (unknown), and *m/*z 504.3 (unknown) by applying CHCA with the airbrush (top), optimized automatic sprayer method (middle), and optimized sublimation method (bottom) to serial sections of *Medicago truncatula* root nodules.

Supporting Information

Table of Contents

Experimental Procedures (SI)

Chemicals and Reagents.

DHB was purchased from Acros Organics (Morris Plains, NJ, USA). CHCA was purchased from Sigma Aldrich (St. Louis, MO, USA). Liquid chromatography- MS grade solvents were purchased from Fisher Scientific (Fair Lawn, NJ, USA). Choline, leucine, glutamine and histidine standards were purchased from Sigma Aldrich (St. Louis, MO, USA). The heme standard was

Plant Materials and Rhizobial Strains

Medicago truncatula WT Jemalong A17 was used in this study. *Sinorhizobium meliloti* strain Rm1021 was used for inoculation.

Plant Growth and Inoculation with Rhizobia

Medicago seeds were acid scarified, surface sterilized and germinated as previously described.[36] One-day-old seedlings were placed on plates containing modified Fahraeus medium overlaid with sterile germination paper, and grown for 7 days in a growth chamber. The roots were inoculated with *S. meliloti* WT and incubated in the growth chamber for 2 weeks for nodule development. Nodules selected from each sample for metabolite imaging were approximately 14 days old.

Tissue Sampling, Sectioning

M. truncatula root nodules were cut from the plant leaving 3-4 mm of root attached to the nodule, embedded in gelatin (100 mg/ml in deionized water). Immediately after dissection, the embedded tissue was flash frozen in a dry ice/ethanol bath and stored at -80°C until use. Root nodules were sectioned at 16 µm thickness using a Thermo 550 cryostat (Thermo Scientific, Bremen, Germany) and thaw-mounted onto an indium tin oxide (ITO)-coated glass slide (Delta Technologies, LTD, Loveland, CO, USA).

MALDI-Mass Spectrometry.

MSI of nodulated *M. truncatula* roots were performed on an UltrafleXtreme MALDI-TOF/TOF (Bruker Daltonics, Billerica, MA, USA) analyzer equipped with a 2 kHz, FlatTop smartbeam-II™ Nd:YAG laser (spot diameter down to 20 µm). The laser was operating in reflectron positive ion mode at 1 kHz using the "minimum" laser focus setting. To produce ion images, spectra were generated by averaging 500 laser shots over the mass range *m/z* 80-1000 and collected at 50 µm intervals in both the *x* and *y* dimensions across the surface of the sample. The mass spectra were externally calibrated using matrix peaks or external standards applied directly to the glass slide. Image files were processed and MS images of the metabolites were generated using the flexImaging software package (Bruker Daltonics, Billerica, MA, USA).

Metabolite Identification with MSI.

During MSI experiments, *M. truncatula* root nodule tissue sections were imaged as well as areas of pure matrix applied with one of the three matrix application techniques. Peaks in the mass spectra were selected individually to extract the ion images. Images that appeared only in the root nodule tissue, showed localization to the tissue, and were not present in the pure matrix areas, were considered metabolites. Metabolites were identified by performing MSI with a high-resolution MALDI-Orbitrap or Q-Exactive mass spectrometer to obtain accurate masses within 5 ppm. Accurate masses were searched against databases such as METLIN, PubChem, ChemSpider, and MetFrag. The accurate mass matching results were supported by performing MS/MS experiments and matching the characteristic fragmentation patterns of each metabolite to literature, standards, or fragmentation prediction software.

SI Table 1. Identified Metabolites in *M. truncatula*

Name of Metabolite	Theoretical $[M+H]^+$ or *[M+]	Orbitrap Measured $[M+H]^+$	Measurement Error (ppm)	TOF/TOF Measured $[M+H]^+$
choline*	104.1070	104.1073	2.9	104.1
leucine	132.1019	132.1018	1.1	132.1
glutamine	147.0764	147.0762	1.4	147.1
histidine	156.0768	156.0766	1.5	156.1
heme*	616.1768	616.1751	2.8	616.2

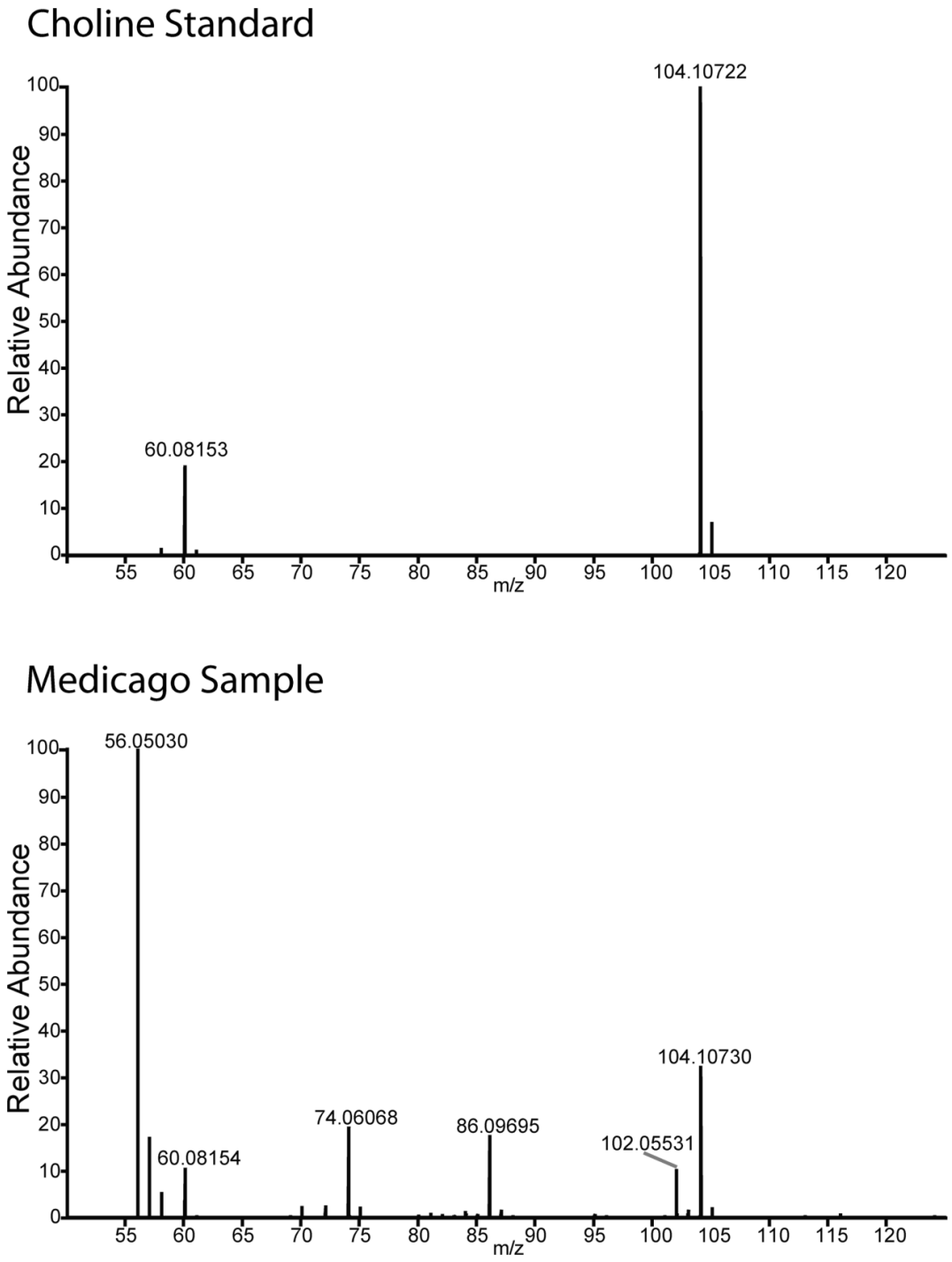

SI Figure 1. MS/MS spectra of m/z 104.1 measured from the Medicago root nodule sample compared to the MS/MS spectra of a purchased choline standard, using a Q-Exactive mass spectrometer, confirming choline as the identification of m/z 104.1.

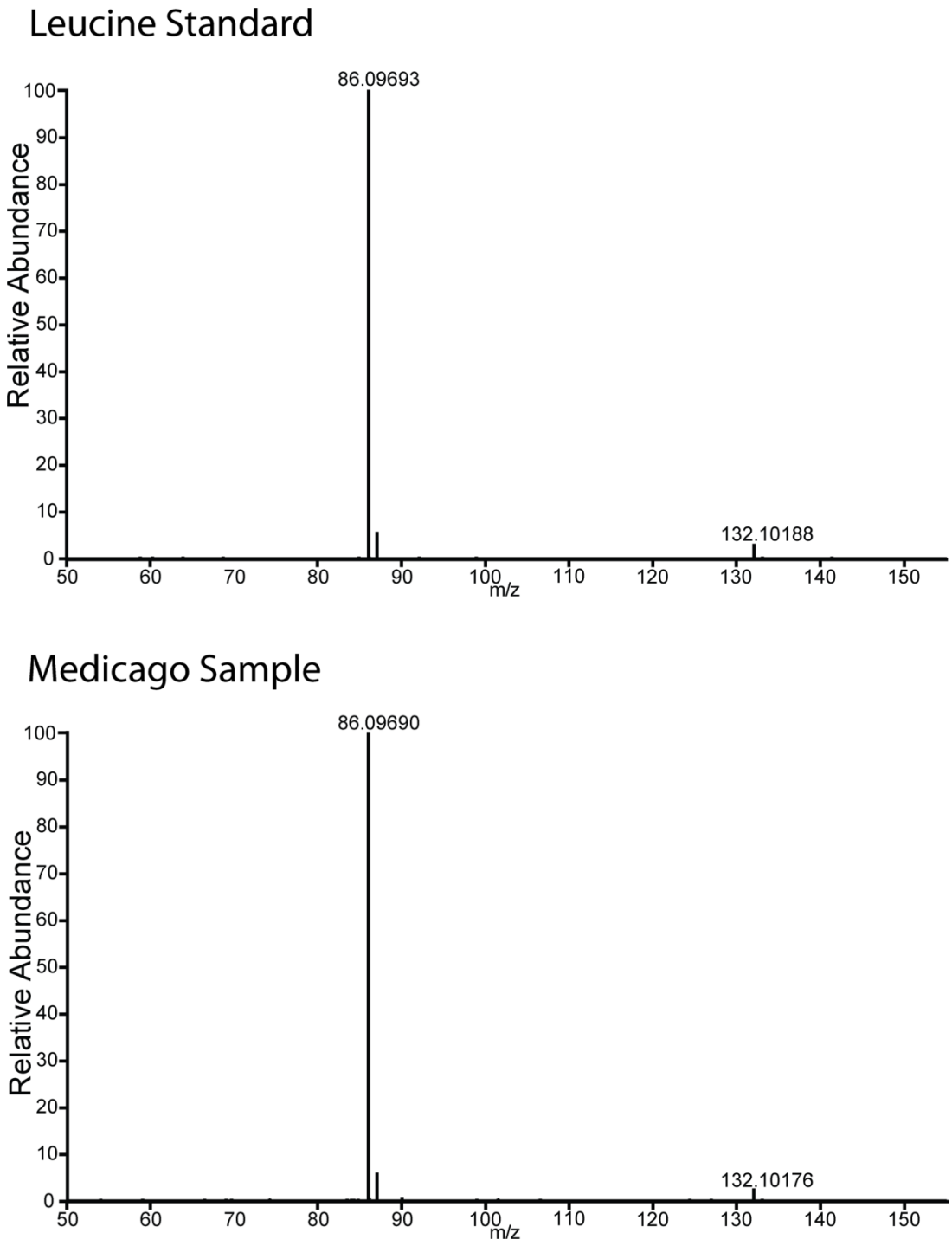

SI Figure 2. MS/MS spectra of m/z 132.1 measured from the Medicago root nodule sample compared to the MS/MS spectra of a purchased leucine standard, using a Q-Exactive mass spectrometer, confirming leucine as the identification of m/z 132.1.

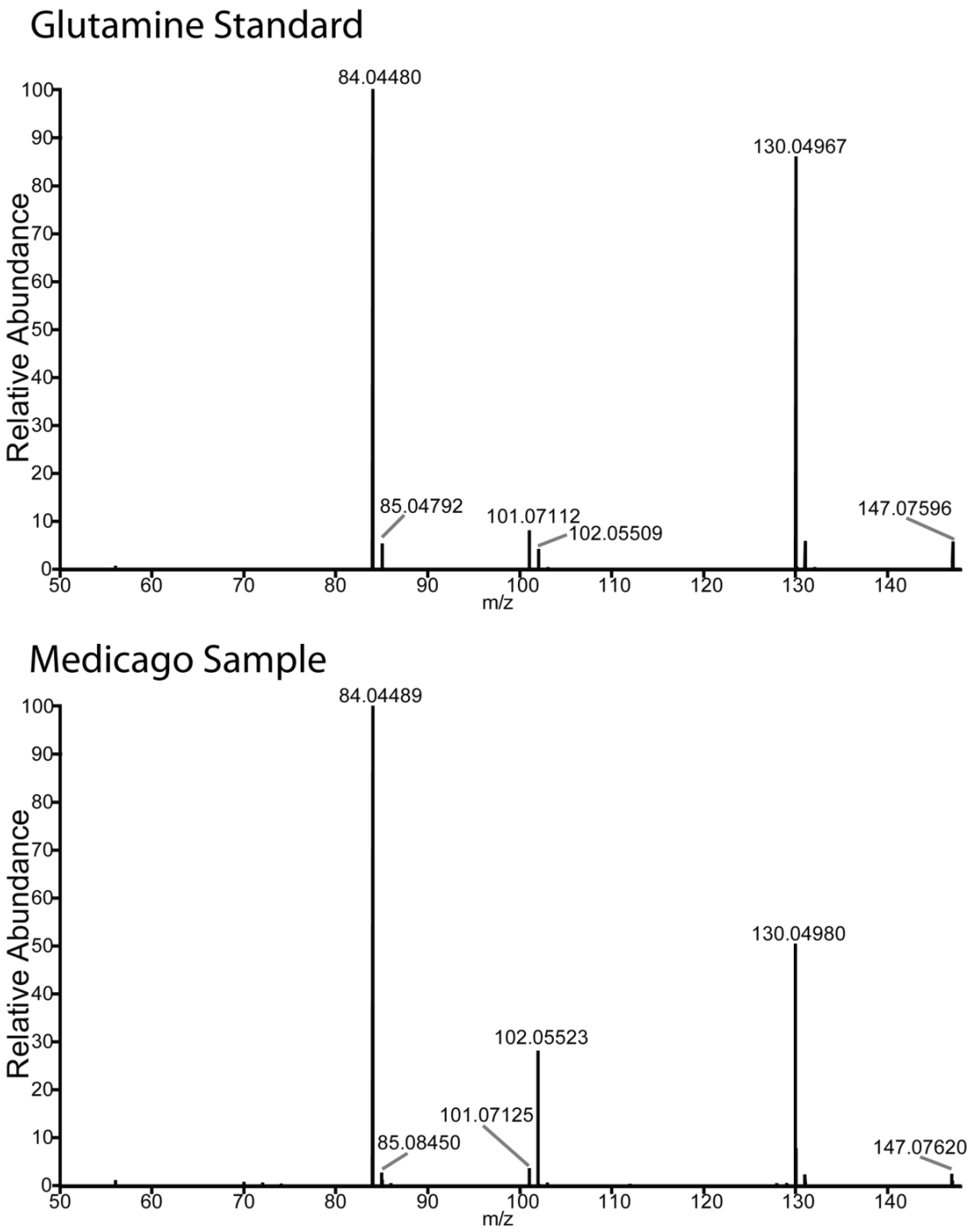

SI Figure 3. MS/MS spectra of m/z 147.1 measured from the Medicago root nodule sample compared to the MS/MS spectra of a purchased glutamine standard, using a Q-Exactive mass spectrometer, confirming glutamine as the identification of m/z 147.1.

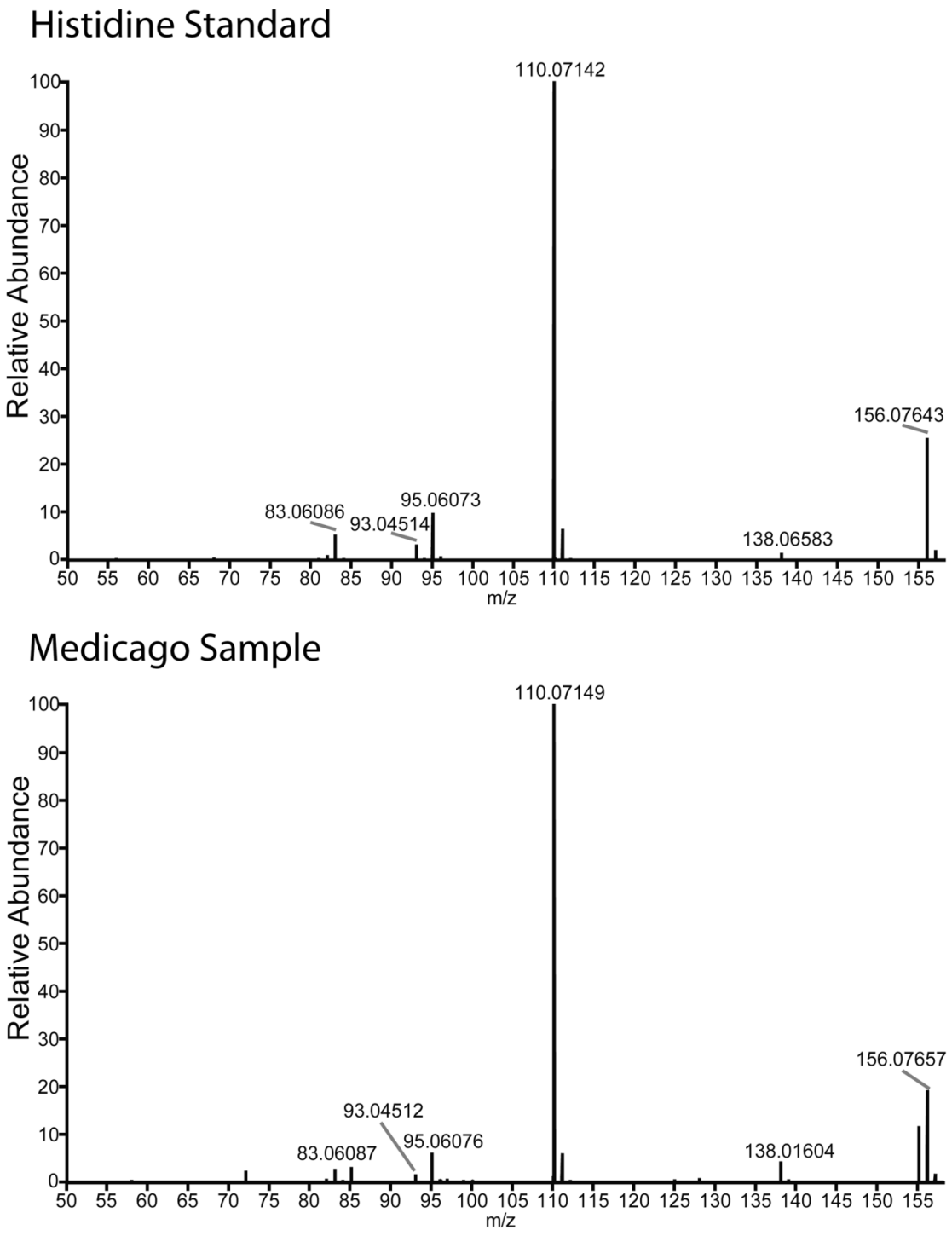

SI Figure 4. MS/MS spectra of m/z 156.1 measured from the Medicago root nodule sample compared to the MS/MS spectra of a purchased histidine standard, using a Q-Exactive mass spectrometer, confirming histidine as the identification of m/z 156.1.

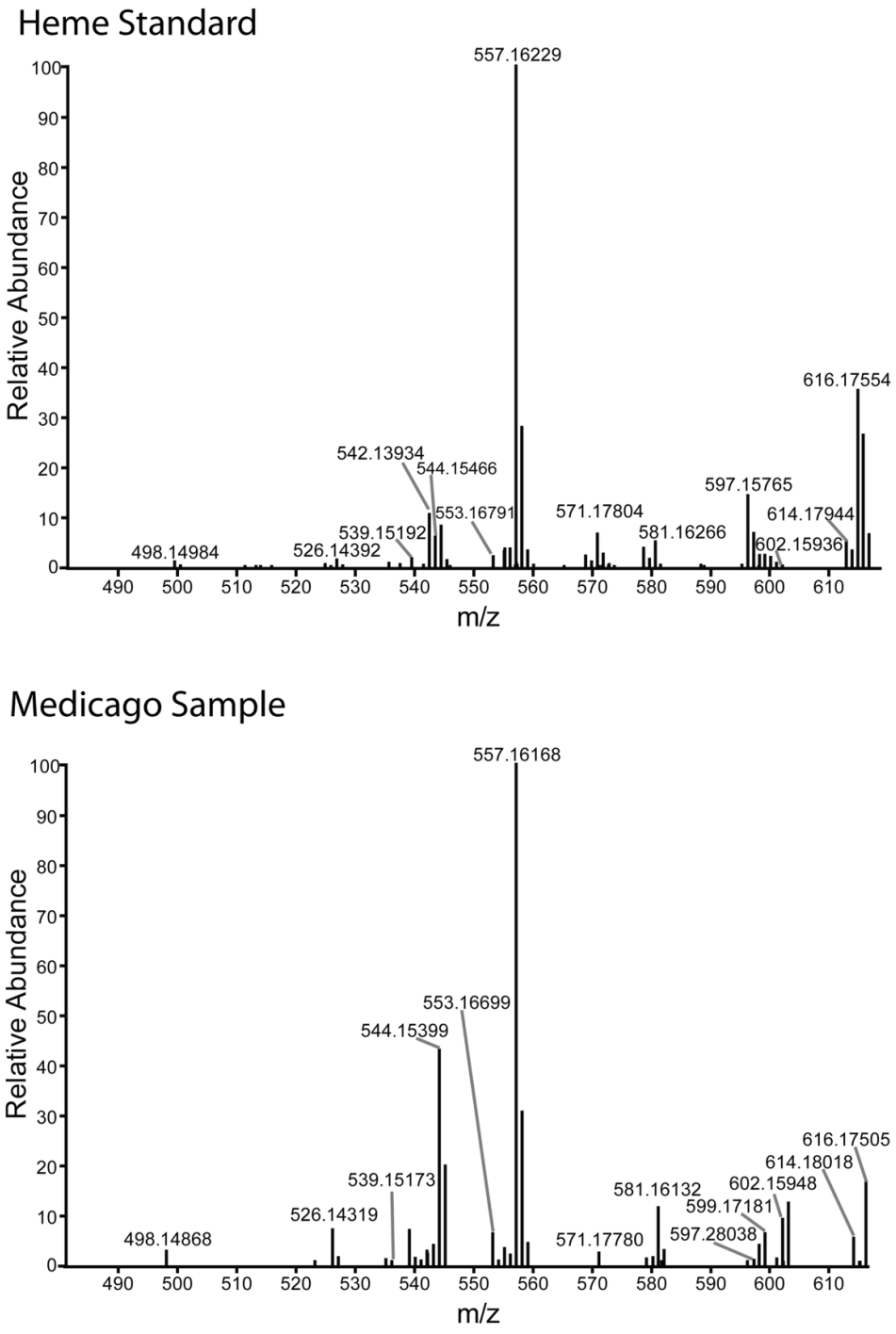

SI Figure 5. MS/MS spectra of m/z 616.2 measured from the Medicago root nodule sample compared to the MS/MS spectra of a purchased heme standard, using a MALDI-Orbitrap mass spectrometer, confirming heme as the identification of m/z 616.2.

SI Table 2. Conditions Used in the Four DHB Matrix Sublimation Procedures

	Sublimation Time (min)	Humidity Time (min)	Start Temp. (°C)	End Temp. (°C)
Method 1	10	0	24	120
Method 2	4.25	0	140	140
Method 3	4.25	0	190	140
Method 4	10	45	24	120

SI Table 3. Conditions Used in the Six CHCA Matrix Sublimation Procedures

	Sublimation Time (min)	Humidity Time (min)	Start Temp. (°C)	End Temp. (°C)
Method 1	10	0	24	120
Method 2	10	0	24	140
Method 3	10	0	24	160
Method 4	10	0	24	150
Method 5	10	0	24	152
Method 6	10	45	24	152

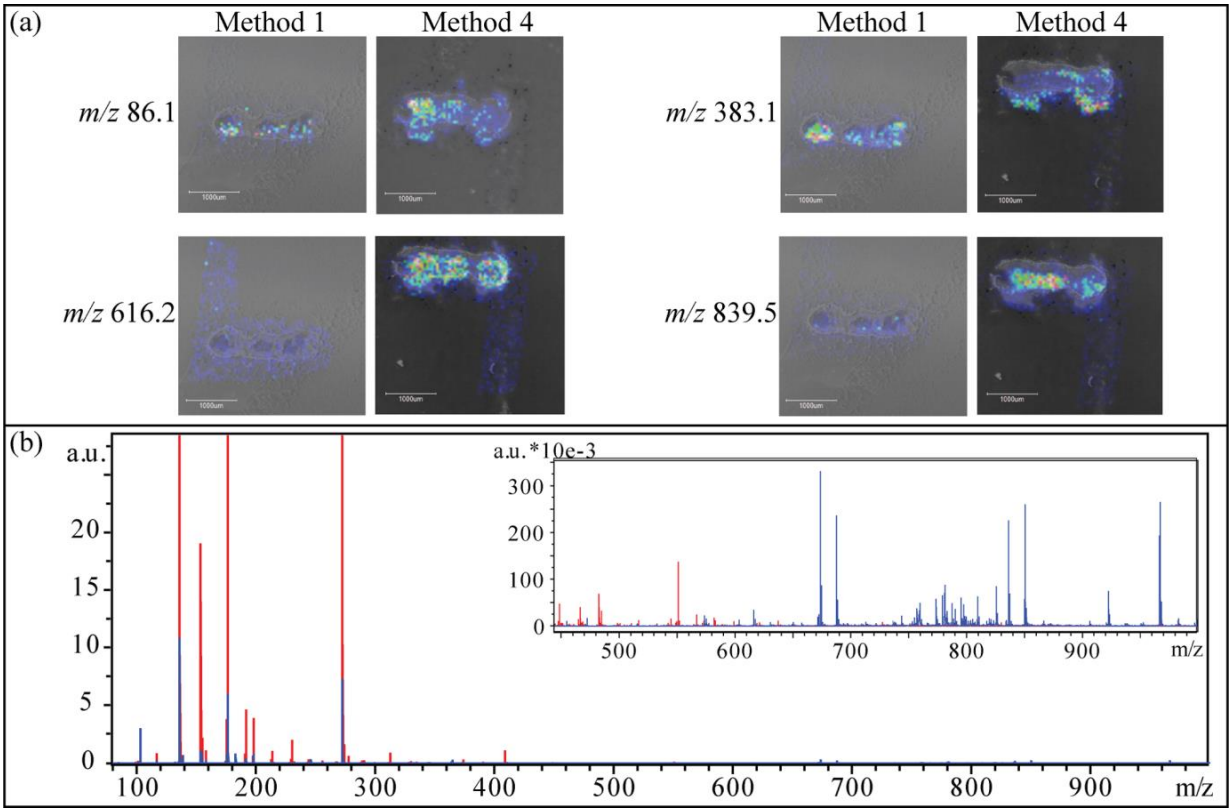

SI Figure 6. Comparison of MALDI-MSI of *Medicago truncatula* root nodules using DHB sublimation Methods 1 and 4. (a) Images generated of *m/z* 86.1 (piperidine- putative ID), *m/z* 383.1 (unknown), *m/z* 616.2 (heme, [M+]) and *m/z* 839.5 (phosphatidylinositol lipid- putative ID) using Method 1 (left) and Method 4 (right). (b) MS spectra comparing sublimation without (red) and with (blue) the humidity chamber step. Inlays show the MS spectra zoomed in to the higher *m/z* range where Method 4 enables detection of more putative metabolite peaks.

SI Table 4. Parameters Used in the Five DHB Automatic Sprayer Procedures

	Velocity (mm/min)	Flow Rate (mL/min)	# of Passes	Line Spacing (mm)	Matrix Density (mg/mm^2)
Method 1	950	0.200	8	3	0.0225
Method 2	1200	0.200	4	3	0.0089
Method 3	1200	0.150	8	3	0.0133
Method 4	1250	0.050	24	3	0.0128
Method 5	1200	0.200	8	3	0.0178

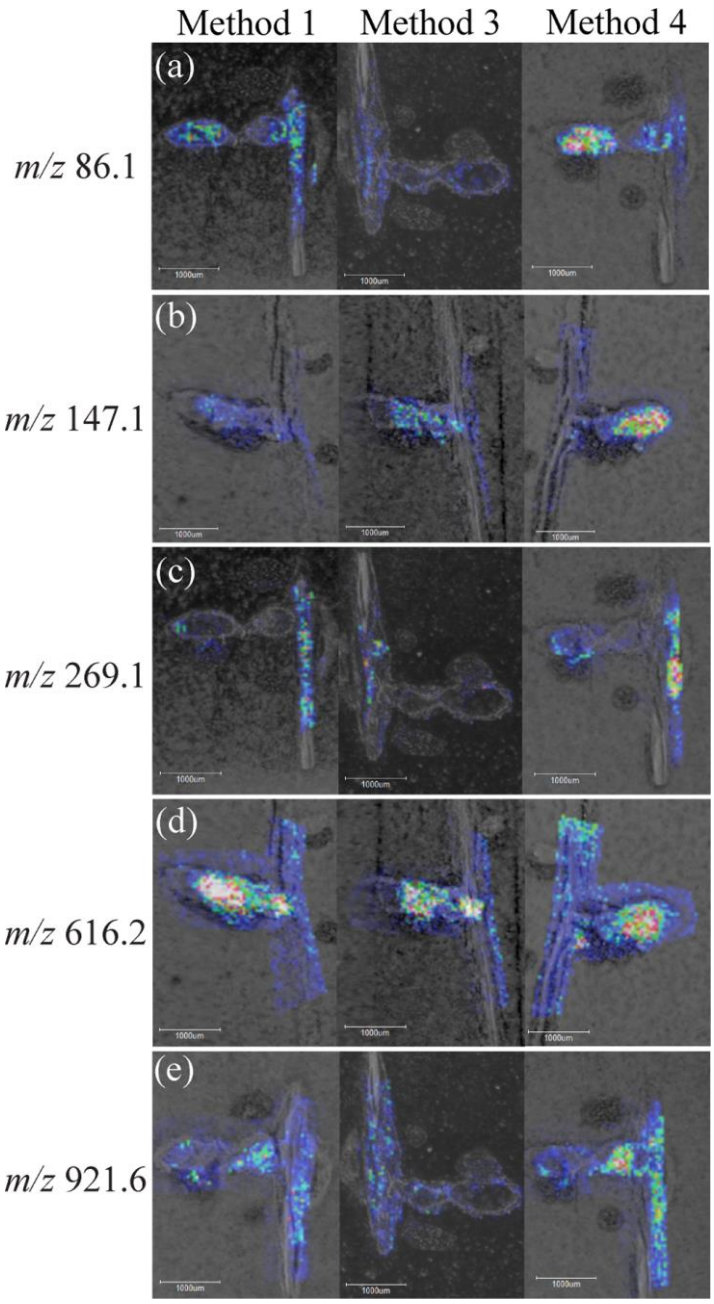

SI Figure 7. Comparison of MALDI-MSI of *Medicago truncatula* root nodules using DHB automatic sprayer methods 1, 3, and 4. Images generated of (a) *m/z* 86.1 (piperidine), (b) *m/z* 147.1 (lysine), (c) *m/z* 269.1 (formononetin), (d) *m/z* 616.2 (heme [M+]), and (e) *m/z* 921.6 (unknown) using Method 1 (left), Method 3 (middle), and Method 4 (right).

SI Table 5. Parameters Used in the Five CHCA Automatic Sprayer Procedures

	Velocity (mm/min)	Flow Rate (mL/min)	# of Passes	Line Spacing (mm)	Matrix Density (mg/mm^2)
Method 1	1200	0.240	2	1.5	0.0027
Method 2	1200	0.240	4	3	0.0027
Method 3	1250	0.050	20	3	0.0027
Method 4	1250	0.100	10	3	0.0027
Method 5	1250	0.100	4	3	0.0011
Method 6	1250	0.100	4	1.5	0.0021

References

36. Catoira, R.; Galera, C.; de Billy, F.; Penmetsa, R.; Journet, E.; Maillet, F.; Rosenberg, C.; Cook, D.; Gough, C.; Denarie, J., Four Genes of Medicago Truncatula Controlling Components of a Nod Factor Transduction Pathway. *The Plant Cell* **2000**, 12 (9), 1647–1665.

TECHNICAL NOTE

#34 Dry Matrix Spray Application for MALDI Imaging of Metabolites in Root Nodule Tissue in *Medicago truncatula* Yielding Sublimation-like Results.

Application

Sublimation is typically the matrix application method of choice for MALDI MS imaging of small molecules such as metabolites. Sublimation yields very fine crystals amenable to high-spatial-resolution-MSI and reduces analyte diffusion that can be seen in solvent-based matrix application methods. 2,5-dihydroxybenzoic acid (DHB) is a matrix suitable for imaging metabolites. DHB can easily be dissolved in 50:50 Water:Methanol (0.1% Trifluoroacetic Acid) solution. The data presented here were obtained as part of a MALDI MS imaging experiment whose purpose was to compare the metabolites detect in the root nodules of the Medicago truncatula when using sublimation vs. dry spray.

Intended Use Of This Technical Note

The goal of this document is to illustrate possible uses of the TM-Sprayer for Research Purpose Only. HTX Technologies, its partners, and the users that have accepted to share their data do not make any guarantees as to the performance of the illustrated workflow, and each lab should insure that replicating these experiments respects applicable health and safety regulations.

Imaging Workflow

Root nodules were dissected out of the plant, embedded in gelatin (100 mg/ml in deionized water), and frozen on dry ice. Cryosections (16 microns) of snap frozen root nodule tissue were thaw-mounted on ITO coated slides.

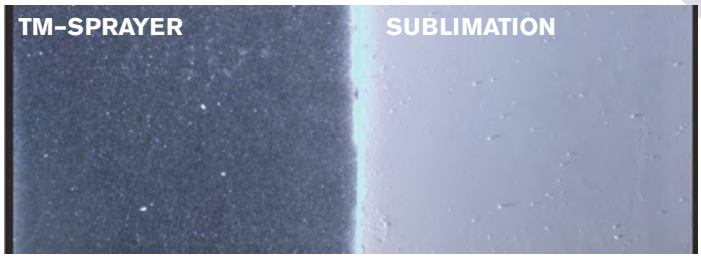

Figure 1. Optical image of matrix crystals comparing crystal size and coverage when matrix is applied with the TM-Sprayer vs. sublimation. The dry spray method on the TM-Sprayer produces extremely fine crystals and sublimation produces a continuous layer of matrix.

Tissue sections were then sprayed with DHB matrix (40 mg/ml, Methanol 50%, TFA 0.1%) using the HTX TM-Sprayer and the following conditions:

Flow Rate	50 µL/min
Spray Nozzle Velocity	1,250 mm/min
Spray Nozzle Temperature	80°C
Track Spacing	3 mm
Number of Passes	24, criss-cross and offset
Time per path	4 minutes, 30 seconds
Nitrogen Pressure	10 psi

Spectra were collected across the entire tissue area using the ultrafleXtreme MALDI-TOF/TOF (Bruker Daltonics, Billerica, MA, USA) analyzer equipped with a 2 kHz, FlatTop smartbeam-II™ Nd:YAG laser in reflectron positive mode over a mass range of m/z 80 to 1000. A total of 500 laser shots were accumulated and averaged from each laser spot, using the "minimum" laser spot diameter setting and a raster width of 50 µm. Calibration was performed externally using DHB cluster peaks or external calibrants in the mass range of m/z 100 to 750.

Experimental Summary

Tissue type	Root Nodule
Preservation	Cryogenic Storage
Tissue cut	16 µm thickness
MALDI Plate	ITO Coated Glass Slides
Matrix deposition	DHB 40mg/ml, 0.1% TFA in 50:50 MeOH/H_20
MALDI Laser	FlatTop smartbeam-II™ Nd:YAG laser
Acquisition mode	Reflector mode

Instrumentation and Supplies

Microtome	Microm HM525
MALDI plate	ITO coated slides
Matrix	Acros Organics
Matrix Sprayer	HTX TM-Sprayer™
MALDI MS	BRUKER ultrafleXtreme™
Imaging software	BRUKER flexImaging

Results and MALDI MS Images

MALDI MS images were compared to images obtained from samples that used sublimation as the matrix application method.

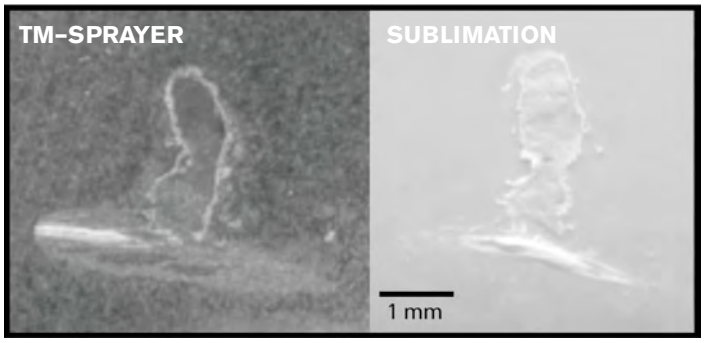

Figure 2. Reference Optical Image of *Medicago truncatula* root nodule with matrix applied via TM-Sprayer and sublimation

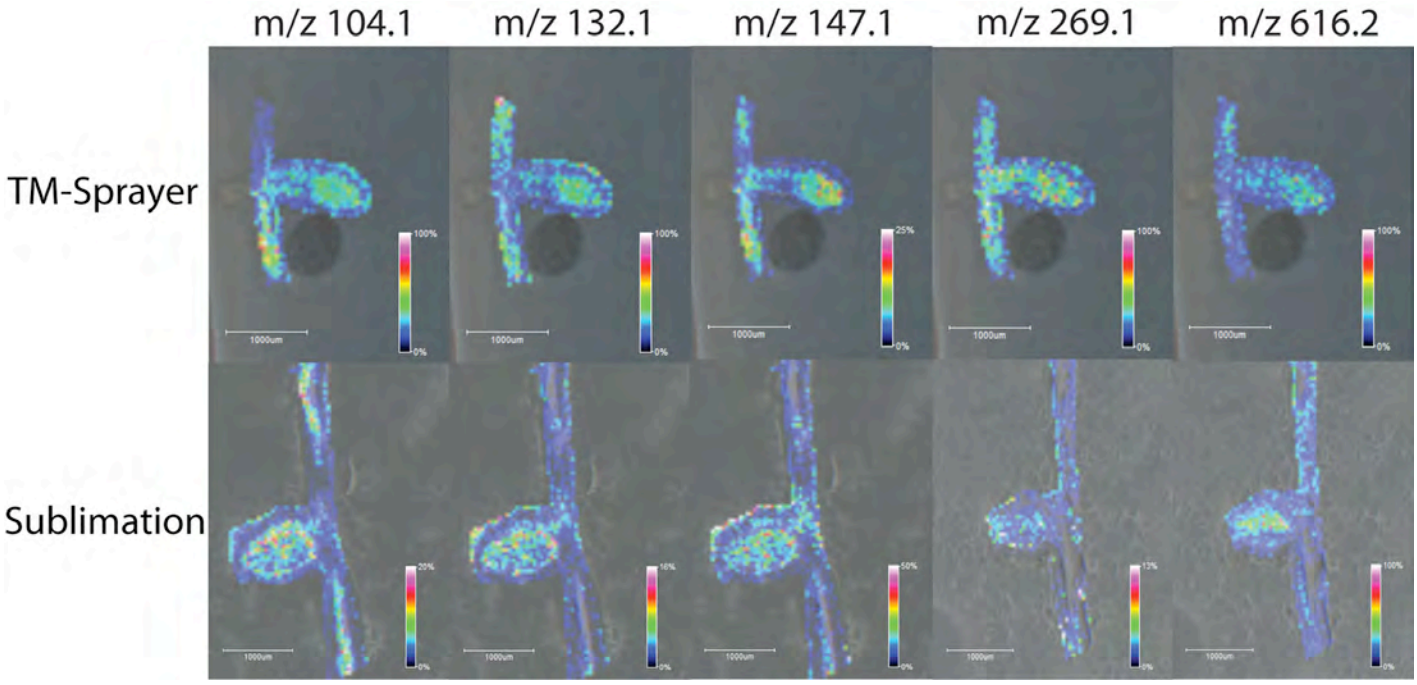

Figure 3. Representative ion images of m/z 104.1, 132.1, 147.1, 269.1, and 616.2 comparing metabolite distribution when matrix is applied with the TM-Sprayer vs. sublimation. The TM-Sprayer produces ion distributions comparable to sublimation. Scale bar = 1 mm

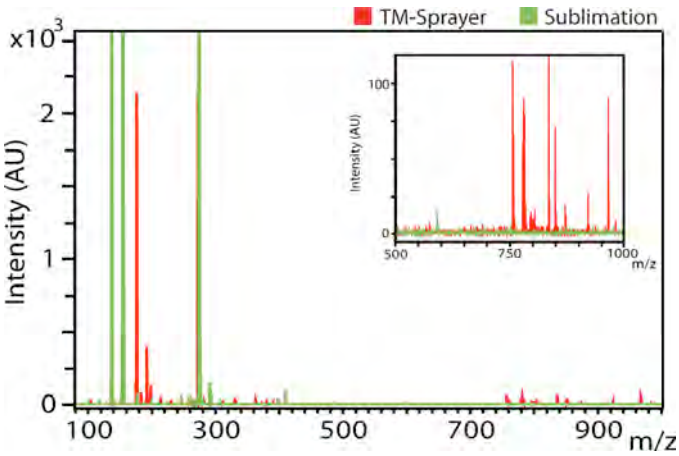

Figure 4. Mass spectra of Medicago samples showing metabolite ions when matrix is applied via TM-Sprayer or sublimation. Metabolites with m/z 80-1000 were imaged. The inlay zooms in on the higher mass region, m/z 500-1000, where sublimation does not generate a high number of metabolite peaks.

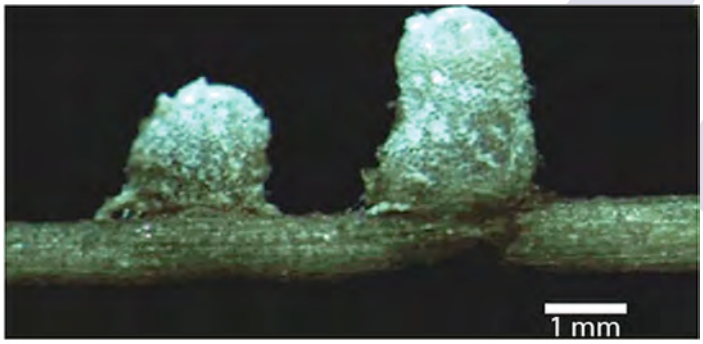

Figure 5. *Medicago truncatula* root nodules before dissection. (Image courtesy of Dr. Jean-Michel Ané in the Department of Agronomy at the University of Wisconsin- Madison)

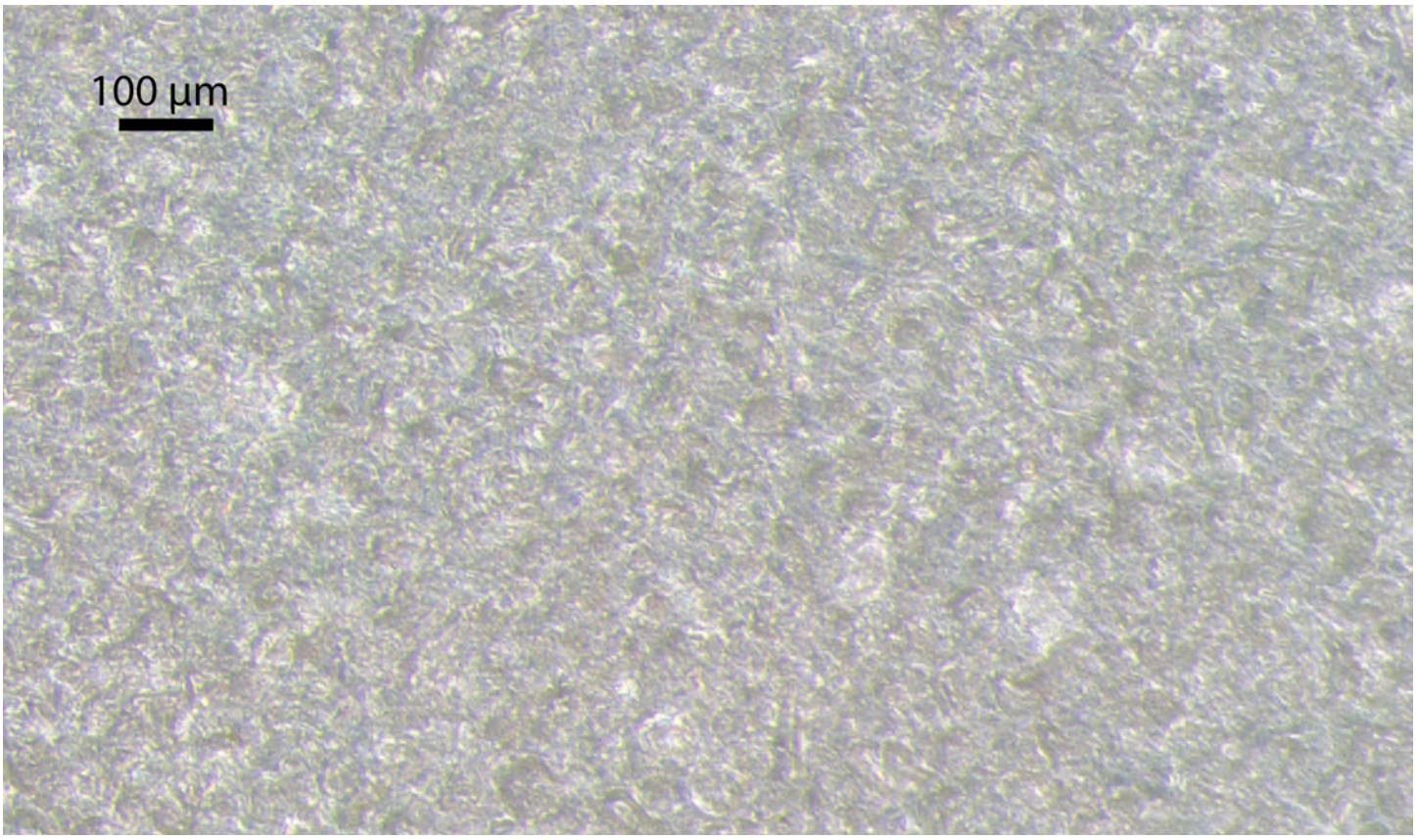

Figure 6. High resolution optical image of DHB matrix crystal size and coverage when applied with the TM-Sprayer

Acknowledgements

The tissue images and MS data presented in this note were provided by Erin Gemperline and Dr. Lingjun Li, Department of Chemistry and School of Pharmacy, University of Wisconsin- Madison, Madison, WI, USA

TM-Sprayer™ Tissue MALDI Sample Preparation System

The HTX TM-Sprayer™ System is an automated MALDI matrix deposition system offering high reproducibility and superior data quality for Mass Spectrometry Imaging

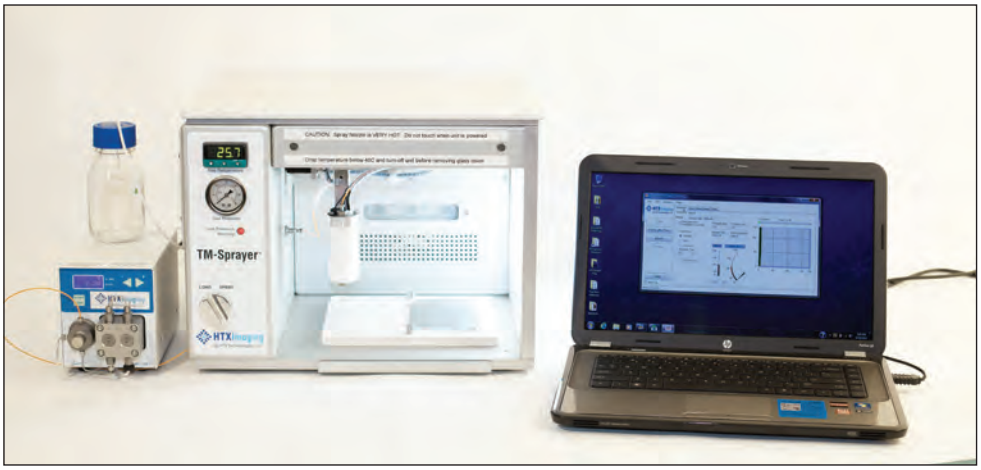

The HTX TM-Sprayer™ is an easy-to-use, versatile spraying system that provides an automated process for Sample Preparation in Mass Spectrometry Imaging.

The patented spray technology of the TM-Sprayer™ guarantees a very fine, uniform and consistent matrix coating crucial for high-resolution imaging and relative quantification of analytes.

The new HTX Technologies' spray nozzle, featured in the next generation TM-Sprayer, creates a fine solvent mist that can be deposited in a precise and adjustable pattern over all or part of any MALDI plate.

Spray characteristics (wet or dry) are easily adjustable via the intuitive operator interface. Users can create and save methods for reproducible operation.

Key Characteristics

- Patented technology providing very small matrix droplets (<10 microns)
- High flow rate and fast sample prep (10 to 20 minutes per plate)
- Highly consistent matrix deposition across entire sample area (+/- 3% by weight)
- Unique use of temperature and nitrogen flow to control evaporation rate and matrix crystal formation
- Validated protocols for most matrices (e.g.: SA, CHCA, DHB)
- Validated protocols for Trypsin digestion
- Continuous matrix coverage as needed for high-resolution imaging
- Rugged operation and easy clean-up

TM-Sprayer™ Specifications

Deposition: Spray deposition in linear or serpentine modes with variables offsets

Spray Nozzle Flow: 50 to 1000µl/min

Sheath Gas: Ambient to 130°C (+/- 2°C), software selected

Gas Supply: Sheath gas flow 5-15.5 liter/min

Spray Nozzle Position: Spray nozzle mounted on Cartesian stage

Electrical: 24V Power Supply

Dimensions/Weight: 17 x 15 x 13in (43 x 38 x 33cm), 38lbs (17Kg)

TM-Sprayer™ is available worldwide exclusively from HTX Technologies, LLC. To request further information contact:

Alain Creissen
Imaging Product Manager, HTX Technologies
acreissen@htximaging.com

HTX Technologies offers innovative sample preparation systems for advanced analytical platforms. Our integrated workflow solutions include user training, instruments, software, consumables and method development services.

HTXImaging
by HTX Technologies, LLC

PO Box 16007 Chapel Hill, NC 27516, USA
Tel +1-919-928-5688 ◆ Fax +1-919-928-5153
info@htximaging.com ◆ www.htximaging.com

Chapter 4

Multifaceted Investigation of Metabolites During Nitrogen Fixation in Medicago via High Resolution MALDI-MS Imaging and ESI-MS

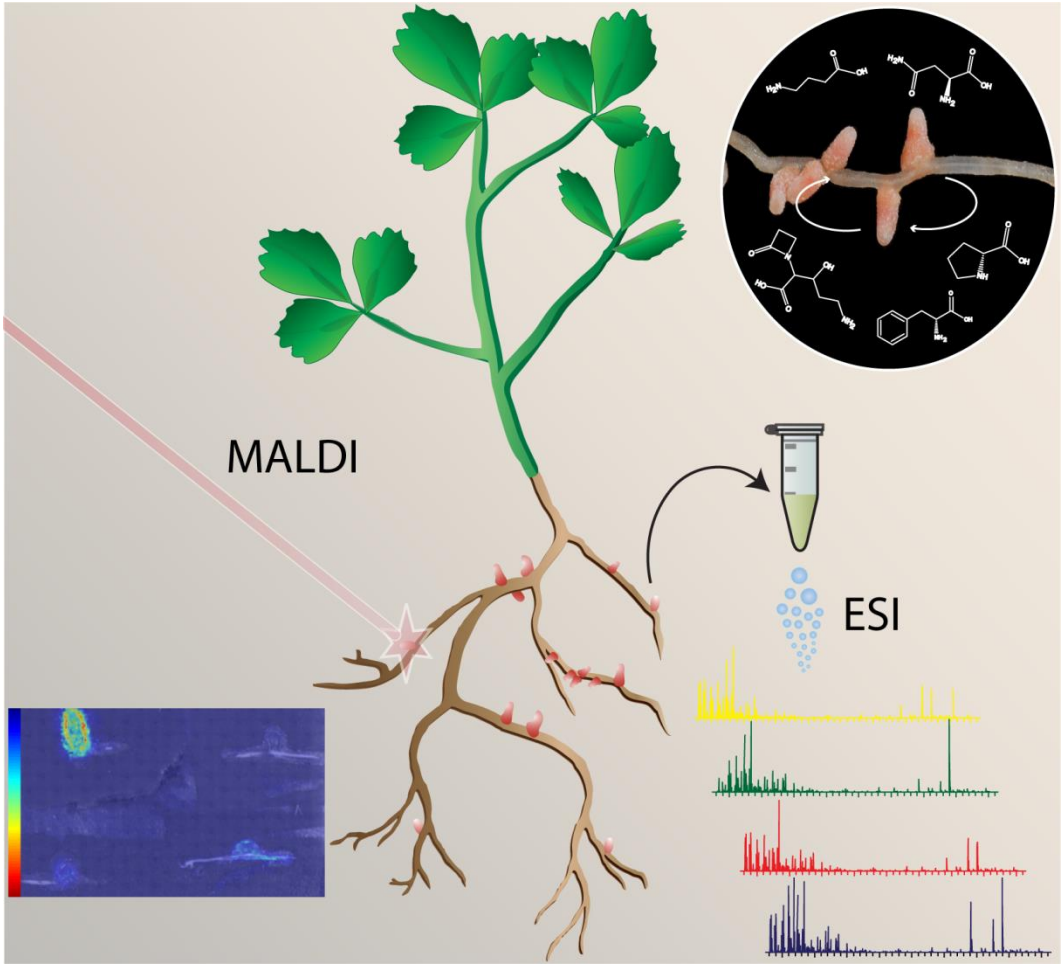

Adapted from **Gemperline, E.**; Jayaraman, D.; Maeda, J.; Ané, J.; Li, L. "Multifaceted Investigation of Metabolites During Nitrogen Fixation in the *Medicago truncatula-Sinorhizobium meliloti* Symbiosis Via High Resolution MALDI-MS Imaging and ESI-MS" *Journal of the American Society for Mass Spectrometry*.26(1):149-158 (2015) doi: 10.1007/s13361-014-1010-0

Abstract

Legumes have developed the unique ability to establish a symbiotic relationship with soil bacteria known as rhizobia. This interaction results in the formation of root nodules in which rhizobia thrive and reduce atmospheric dinitrogen into plant-usable ammonium through biological nitrogen fixation (BNF). Due to the availability of genetic information for both of the symbiotic partners, the *Medicago truncatula–Sinorhizobium meliloti* association is an excellent model for examining the BNF process. Although metabolites are important in this symbiotic association, few studies have investigated the array of metabolites that influence this process. Of these studies, most target only a few specific metabolites, the roles of which are either well known or are part of a well-characterized metabolic pathway. Here, we used a multifaceted mass spectrometric (MS) approach to detect and identify the key metabolites that are present during BNF using the *Medicago truncatula–Sinorhizobium meliloti* association as the model system. High mass accuracy and high resolution matrix-assisted laser desorption/ionization (MALDI) and electrospray ionization (ESI) Orbitrap instruments were used in this study and provide complementary results for more in-depth characterization of the nitrogen-fixation process. We used well-characterized plant and bacterial mutants to highlight differences between the metabolites that are present in functional vs. non-functional nodules. Our study highlights the benefits of using a combination of mass spectrometric techniques to detect differences in metabolite composition and the distributions of these metabolites in plant biology.

Introduction

The importance of nitrogen in sustaining life across kingdoms cannot be overstated, as nitrogen is a principal component of many essential biomolecules.[1-2] Despite its abundance, accounting for approximately 78% of earth's atmosphere in the form of dinitrogen (N_2), most organisms, including plants, are unable to metabolize nitrogen.[1-2] The process of converting N_2 into the ammoniacal form (NH_3) is referred to as N_2 fixation and can be accomplished via any of the following processes: (i) biogeochemical processes, (ii) an industrial process called the Haber–Bosch process, and (iii) biological processes, through a select group of microorganisms, termed diazotrophs.[1] The contribution of the biogeochemical process is negligible, with the latter two abovementioned processes accounting for the majority of N_2 fixation.[1] The industrial production of nitrogenous fertilizers by the Haber–Bosch process can fulfill the crop nitrogen requirement but with heavy economic and environmental costs.[3] In fact, this process accounts for 50% of the fossil fuel utilization in agriculture and 1-3% of the annual global fossil fuel usage.[2] Furthermore, the cost of nitrogenous fertilizers has increased significantly due to increasing fossil fuel costs. In addition to the increased cost of production, nitrogen fertilizers have also significant environmental and ecological effects. To state a few, nitrous oxide, which is a decomposition product of nitrogenous fertilizer, is much more active than carbon dioxide as a greenhouse gas.[2] In addition, leaching loss, which accounts for 30–50% of the applied nitrogenous fertilizers, leads to the eutrophication of waterways.[2, 4] Therefore, to sustainably feed the burgeoning population, there is an urgent need to optimize alternative nitrogen sources.[2] A select group of microorganisms possesses an enzyme, nitrogenase, which enables them to fix atmospheric N_2 into the ammoniacal form.[5] This process is termed biological nitrogen fixation

(BNF), and the amount of nitrogen fixed on land is comparable to that of the Haber–Bosch process.[1] In fact, biological nitrogen fixation was the only major source of nitrogen fixation before the advent of chemical fertilizers and can be performed by either free-living microorganisms or those that live in symbiotic association with other organisms.[1, 5] Symbiotic nitrogen fixation accounts for the bulk of BNF[5] and is principally performed by a group of bacteria collectively called rhizobia in association with the *Leguminosae* family of plants (legumes). This family of plants fixes approximately 40–60 million tons of nitrogen per year and plays a pivotal role in food and energy security.[2, 6] *Medicago truncatula* (Medicago), which is a model legume, has been subject to intense study in the past two decades, not only to determine the molecular, genetic, and biochemical aspects of BNF, but also to understand general legume biology.[7-12]

Medicago forms a symbiotic association with the bacterium *Sinorhizobium meliloti*. The process is initiated by the exchange of metabolites.[13] Plants secrete isoflavonoids, the perception of which leads to the secretion of the lipochitooligosaccharide Nod factors by rhizobia. A communication channel is thus established between the host plant and the rhizobia, leading to a series of events culminating in the formation of specialized structures called nodules on the roots of the host plant.[14] These nodules provide an ecological niche inside which the bacterial nitrogenase enzyme is protected from free oxygen and the bacteria differentiate into specialized forms, called bacteroids, which fix atmospheric nitrogen.[15] Critical to the success of this interaction is the nutrient exchange between the host plant and the bacteria, which requires the plant metabolism not only to supply carbon, nitrogen, and other nutrients to the bacteroids, but also to utilize the metabolites that are released by the bacteroids.[6, 15-16] Despite the importance of metabolites in this symbiotic association, little work has been done to investigate the array of

metabolites influencing this association. Most available studies target a few specific metabolites, the roles of which are either well known or are a part of a well-characterized metabolic pathway.[17] Although recent refinements in various chromatographic and mass spectrometric platforms have led to large-scale, non-targeted metabolic studies in the legume–rhizobium symbiosis, these studies were performed using either homogenized metabolite extracts or Medicago cell suspension cultures and fail to provide the spatial distribution of metabolites.[17-23] In the past decade, mass spectrometric imaging (MSI) has rapidly expanded into the field of plant metabolomics as it provides important spatial information about many different molecular species of interest in a single experiment.[24-28] In order to better understand the spatial distribution of metabolites during this symbiosis, we previously used matrix-assisted laser desorption/ionization (MALDI)-TOF MSI on Medicago root nodules, identifying amino acids, sugars, organic acids, lipids, flavonoids and their conjugates and demonstrating their distribution in root and nodule tissues.[27]

Although it does not provide spatial information, electrospray ionization (ESI)–liquid chromatography (LC)-MS provides complementary results to MALDI-MS due to the different ionization mechanisms of these two techniques. These complementary techniques therefore offer a more complete description of the metabolome that would be critical for a mechanistic understanding of the metabolic exchange that defines nitrogen fixation. Here, we use high resolution MALDI-MSI and ESI-LC-MS for a more in-depth study of the Medicago root and nodule metabolomes during nitrogen fixation. In this study, wild-type (wt) plants and rhizobia that are capable of BNF were compared to well-characterized plant and bacterial mutants that are defective in nitrogen fixation in order to detect metabolic differences that are relevant to nitrogen

fixation, generating valuable information for understanding the underlying mechanisms of the BNF process.

Materials and Methods

Plant Growth and Inoculation with Rhizobia

Medicago seeds were germinated as previously described,[29] after which one-day-old seedlings were grown in a growth-chamber on modified Fåhræus medium that was overlaid with germination paper. After 7 days, the roots were inoculated with a rhizobial suspension at OD_{600} = 0.01 and grown for 2 weeks. After 14 days, nodules from each sample were selected for metabolite imaging. The plants that were used in this study were *Medicago truncatula* Jemalong A17 (wt) and the mutant *dnf1-1*. The bacteria that were used for the inoculation were *Sinorhizobium meliloti* Rm1021(wt) and the mutant VO2683 *(fixJ2*.3:Tn5-233).[30] The four plant-rhizobia sample combination types that were used in this study are referred to as wt-wt, wt-*fixJ*, *dnf1*-wt, and *dnf1-fixJ*.

Tissue Extraction

Root nodules with approximately 1-2 mm of root on each side were detached from the plant, placed into a pre-chilled mortar, flash-frozen with liquid nitrogen and ground to powder. The powder was transferred to a pre-chilled 1.5-mL Eppendorf tube. The metabolites were extracted with 2:2:1 methanol:chloroform:water (v/v). The solution was vortexed briefly and sonicated for 10 min followed by incubation at -20 ^{o}C for 15 min. The solution was then centrifuged at 20,000 ×g for 10 min to pellet the plant material. The resulting aqueous supernatant was collected and dried in a SpeedVac. The lower organic layer was removed from

the plant particulate matter and dried in a SpeedVac. This process was used for all four of the sample types. The samples were stored at -80 ^{o}C until analysis.

Sample Preparation for MALDI

Root nodules with approximately 1-2 mm of root on each side were detached from the plant. The individual nodules were embedded in gelatin (100 mg/mL in double-distilled water) and gently frozen on dry ice. The frozen tissue was then sectioned into 16-µm slices using a cryostat at -20 ^{o}C. The sections were thaw-mounted onto a standard glass microscope slide. Matrix (40 mg/mL DHB in 50:50 water:methanol) was applied using a TM Sprayer (HTX Technologies, LLC, Carrboro, NC, USA). DHB was purchased from Sigma-Aldrich (St. Louis, MO, USA).

MALDI-Orbitrap MSI and MS/MS

A MALDI-Orbitrap mass spectrometer (Thermo Scientific, Waltham, MA, USA) that was equipped with an N2 laser (spot diameter of 75 µm) was used in positive ion mode for imaging and MS/MS. Three technical replicates of three biological replicates were imaged using a mass range of *m/z* 100-900, a mass resolution of 60,000, and a mass error of $\leq$ 5 ppm. The tissue region to be imaged and the raster step size were controlled using the LTQ Tune software (Thermo Scientific, Waltham, MA, USA). The instrument methods were created using Xcalibur (Thermo Scientific, Waltham, MA, USA). To generate images, the spectra were collected at 75-µm intervals in both the x and y dimensions across the surface of the sample. A list of the detected peaks was automatically created using MSiReader[31] by selecting the wt-wt sample as the "region of interest" and subtracting the peaks from the matrix to create a list of detected *m/z* values. Ion images were automatically generated from this list using MSiReader. The *m/z*

values that produced ion images in only the wt-wt samples and none of the mutant samples were compiled into a list of "metabolites of interest". Each metabolite of interest was then manually confirmed as a unique metabolite peak (not an isotope, matrix peak, or artifact) via the manual interpretation of the averaged mass spectrum using ImageQuest (Thermo Scientific, Waltham, MA, USA). MS/MS collision-induced-dissociation (CID) fragments were collected by isolating each *m/z* of interest and manually adjusting the collision energy for each compound (from 19-42 eV).

Q-Exactive for ESI-MS

To acquire LC-ESI-MS and MS/MS data, four biological replicates of Medicago root nodule extracts were resuspended in either water (for the aqueous samples) or methanol (for the organic samples) to a final concentration of 5 mg/mL. The samples were separated on a Kinetix C18 column (2.1-mm internal diameter × 150-mm length, 1.7-μm particle size; Phenomenex, Torrance, CA, USA), equipped with a corresponding guard column, and heated to 35 °C. The mobile phases were (A) water with 0.1% formic acid and (B) acetonitrile with 0.1% formic acid. The aqueous samples were separated within 90 min under the following conditions: 0-10 min, isocratic hold at 1% B; 10-20 min, linear gradient from 1-3% B; 20-68 min, linear gradient from 3-50% B; 68-84 min, linear gradient from 50-95% B; and finally re-equilibration of the system at 1% B for 5 min. The organic samples were separated within 90 min under the following conditions: 0-20 min, linear gradient from 1-50 % B; 20-84 min, linear gradient from 50-99% B; and finally re-equilibration of the system at 1% B for 5 min. The flow rate was 0.3 mL/min and the injection volume was 5 μL. The samples were kept at 10 °C during the analysis. MS and MS/MS data were acquired on a Q-Exactive instrument (Thermo Scientific, Waltham, MA,

USA) that was equipped with an ESI source operated in positive ion mode. The MS scan range was from *m/z* 75–1000. The MS/MS scan range was adjusted depending on the parent mass and high-energy collision dissociation (HCD). The MS/MS data were collected for the targeted metabolites at collision energies of 25, 30, 35, and 40 eV. SIEVE (Thermo Scientific, Waltham, MA, USA) was used to determine the "metabolites of interest". A small molecule component extraction experiment was carried out using SIEVE; the wt-wt samples were used as references and were compared to the 3 mutant samples using 3-5 technical replicates of 4 biological replicates of each sample type. The features were extracted from the data after alignment and framing. The *m/z* values that had at least 2-fold higher intensity in the wt-wt samples compared to any of the three mutant samples in at least 2 of the biological replicates, a CV <20%, and a p-value < 0.05 were considered "metabolites of interest". An inclusion list was generated of the "metabolites of interest" and those *m/z* values were subjected to MS/MS.

Metabolite Identifications

The "metabolites of interest" were identified by searching the accurate mass obtained on the Orbitrap instruments and the MS/MS data using MetFrag.[32] The top 15-20 MS/MS peaks and their intensities were imported into MetFrag, and the neutral exact mass of the parent ion was calculated. The masses were searched within 5 ppm using KEGG, PubChem, and ChemSpider databases. Several adducts were searched for each parent mass, including: [M+H], [M+], [M+Na], and [M+K]. The compounds with MS/MS data that convincingly matched the *in silico* fragmentation, i.e. most or all of the experimental fragment peaks matched theoretical fragments within 10 ppm and no other metabolites in the database matched the experimental fragments, were identified.

Results and Discussion

MALDI-Orbitrap MS Imaging

This study utilized wild-type (wt) plants and bacteria and the well-characterized plant mutant (*dnf1*)[33-34] and bacterial mutant (*fixJ*),[27] which are deficient in nitrogen fixation. By comparing the wt-wt samples that are capable of performing nitrogen fixation to the combinations of mutant samples, wt-*fixJ*, *dnf1*-wt, and *dnf1*-*fixJ*, which are all incapable of nitrogen fixation, the metabolites that might be relevant to nitrogen fixation were identified. To detect and identify the metabolites that might be relevant to biological nitrogen fixation, MALDI-MSI was performed on Medicago sections from all four of the sample types. Once the data were collected, ion images were generated using MSiReader as described above. The images were manually confirmed as belonging to metabolite peaks, and a list of "metabolites of interest" was generated from the *m/z* values that produced ion distributions in the wt-wt (functional) nodules but not in any of the three mutant (non-functional) nodules. The representative metabolites that showed distinct distribution patterns in the wt-wt samples and not in the mutant samples are shown in **Figure 1**. Figure 1a shows a photograph of each of the four sample types that were used in this study. **Figure 1b** shows the optical image of the four sample types immediately prior to MSI acquisition. **Figure 1c** shows ten representative ion images of metabolites that were found only in the wt-wt samples. These representative metabolites show different spatial distributions throughout the root and nodule portions of the sample, providing further information about these metabolites and their role in nitrogen fixation. **Table S1** in the supplemental information provides a complete list of the "metabolites of interest" that were determined by MALDI-MSI. The MALDI-Orbitrap provides significant advantages for

untargeted metabolomics studies compared to more common instrumentation with modest mass spectral resolution, such as MALDI-ToF-ToF instruments, because accurate mass measurements can be acquired, which are essential for metabolomics. Many studies using MALDI-ToF-ToF instruments require accurate masses to be acquired using other instrumentation, typically ESI instruments. This criterion not only increases the number of experiments that need to be performed, but also provides no guarantee that the molecular species of interest that are detected by MALDI will also ionize with ESI. The high resolving power of MALDI-Orbitrap also permits the detection of metabolites that are separated by as little as 0.003 Da. The use of the high mass accuracy and high resolution MALDI-Orbitrap allows for better detection and more complete coverage of the metabolome, which can lead to greater insight into biological processes.

ESI-Q-Exactive MS

To complement the MALDI-MS data, the root nodule extracts of each of the four sample types were also analyzed by LC-ESI-MS using a Q-Exactive instrument. SIEVE software was used to align and frame the replicates of the four sample types, and a list of "metabolites of interest" was compiled for further targeted MS/MS studies using the parameters that were described in the Materials and Methods section. Representative data from SIEVE that were used to select the "metabolites of interest" are provided in **Figure 2**. The panels on the left show XIC (extracted ion chromatogram) peaks, demonstrating that the metabolite has an at least 2-fold greater intensity in the wt-wt samples (blue) compared to any of the mutant samples (red, green, and yellow). The panels on the right display the information on the left in bar graph form, in which each bar represents a different replicate. **Table S2** in the supplemental information

provides a complete list of the "metabolites of interest" that were determined by ESI-MS. The ESI experiments produced fewer "metabolites of interest" compared to the MALDI experiments. It is likely that the statistical method of determining the "metabolites of interest" using SIEVE was much more stringent compared to manually generating a list of "metabolites of interest" using the MALDI data, resulting in fewer metabolite hits. In addition, MALDI tends to ionize a higher number of compounds to begin with for several reasons. First, MALDI produces in-source fragmentation which could fragment delicate molecules into multiple fragments that are then detected. Second, ESI typically ionizes more polar compounds, where MALDI can ionize a wider range of compounds, potentially resulting in higher detection of "metabolites of interest". Complementary data were obtained using both MALDI and ESI instrumentation; 90 "metabolites of interest" were detected with MALDI, and 21 "metabolites of interest" were detected with ESI. Of the combined 111 metabolites that were detected using both methods, only 7 "metabolites of interest" were detected using both MALDI and ESI.

Metabolite Identifications

Assigning confident molecular identifications for *m/z* values is typically the bottleneck for untargeted metabolomics studies. Searching the accurate mass alone using the many metabolomics databases that are available online often results in tens to hundreds of possible identifications. MS/MS experiments were conducted on the selected "metabolites of interest" from both the MALDI and ESI studies, although acceptable MS/MS data could not be collected for all of the metabolites that were detected by MALDI-MSI. MetFrag was used to search the accurate mass and MS/MS data. **Figure 3** presents representative results from MetFrag and the complete MS/MS MetFrag search results for all identified compounds can be found in the

supplemental information. The peaks correspond to experimental MS/MS data. The precursor ion is shown in blue. Green indicates experimental peaks that matched to *in silico* fragmentation peaks, and red indicates experimental peaks that did not match to *in silico* fragmentation peaks for the selected metabolite. The spectra in Figure 3 indicate good correlation with the *in silico* fragmentation data. Red peaks could be a result of noise/ background ions or other molecular species/isomers with the same or very similar *m/z* values that were also selected in the fragmentation window. A list of 34 annotated "metabolites of interest" is shown in **Table 1**. Accurate mass and comparison to theoretical fragmentation allows for annotation of identified peaks. For unambiguous metabolite identification, experimental data should be compared with metabolite standards.

The detected peaks may be higher in the wt-wt samples compared to the samples containing plant or bacterial mutants because the fully functional nodules in the wt-wt samples may require a greater activity of the identified metabolites for efficient nitrogen fixation and/or the export of fixed nitrogen to the plants, in contrast to the wt-*fixJ*, *dnf1*-wt, and *dnf1-fixJ* combinations in which non-functional or non-fixing nodules were formed. The identified metabolites belonged to different classes, including organic acids and amino acids. The possible role of some of these metabolites in legume nodulation has either been established or hypothesized, while for most others, the roles have yet to be ascertained. For instance, asparagine has been implicated in nitrogen cycling between various plant organs, and the fixed nitrogen in indeterminate nodules is exported as asparagine for use by plants through the xylem sap of the plant. Similarly, glutamine is also a nitrogen (amide) exporter from indeterminate nodules for use by the plant.[35-37] In addition glutamine, glutamate, and arginine may act as signals indicating the plant's nitrogen status, which in turn is hypothesized to regulate nodule

growth and activity.[38-40] Nitrogen fixation is an energy-expending process, and it is estimated that the plants expend approximately 5–12 grams of carbon for every gram of nitrogen that is fixed. Therefore, this process is tightly regulated, and it is hypothesized that the above-mentioned amino acids act as internal sensors for the plant nitrogen status.[41-43]

Proline betaine (the N-methylated form of proline) belongs to a select group of organic osmolytes called compatible solutes, the accumulation of which enables cells to increase the intracellular osmotic pressure, which in turn protects some macromolecular structures during osmotic stress.[44] In addition to being an osmoprotectant, proline betaine also acts as an energy source, in particular as a carbon and nitrogen source for *Sinorhizobium meliloti* in low-osmolarity environments.[45] The ability of *Sinorhizobium meliloti* to utilize proline betaine as an energy source enables this species to colonize legume roots efficiently and offers a competitive advantage against other soil bacteria that compete for plant carbon sources for colonization. Furthermore, betaines induce nodulation (*nod*) genes in *Sinorhizobium meliloti*. Taken together, proline and/or its N-methylated form may act as an important energy source for bacteria during early stages of symbiotic interaction and also prior to bacteroid differentiation in the infection process.[46]

A heme moiety is a critical component of leghemoglobins, which are essential for maintaining microaerobic conditions in the nodule environment. The enzyme nitrogenase contains Fe and Mo protein components, which are incompatible with free oxygen, indicating that nitrogenase can function efficiently only under microaerobic conditions.[47] Leghemoglobin monitors the oxygen level in the cytosol of infected cells and maintains this level at optimum concentrations for the functioning of nitrogenase and also for bacterial respiration.

MSI is a relatively new technique in the field of plant sciences. The combination of the high resolution MALDI and ESI Orbitrap instrumentation provides novel advantages over previous studies of biological processes in plant models. Most previously published MALDI-MSI studies of plant metabolites were done with TOF instruments with potential interference from matrix peaks in the low mass region. Thus, these prior studies often required additional experiments on high mass accuracy instruments, typically ESI instruments, in order to identify detected compounds, with no guarantee that metabolites detected with MALDI would also be detected with ESI. Many plant metabolomics studies employ only LC-MS for analysis; employing both LC-MS and MALDI-MSI in our study allows for different types of metabolites to be detected and identified in addition to obtaining spatial information.

Conclusions and Future Directions

We demonstrated the benefits of using MALDI and ESI for the complementary detection of metabolites, permitting a more in-depth characterization of the Medicago metabolome and nitrogen-fixation process. High-resolution Orbitrap instruments provide the accurate mass measurements that are necessary for metabolite identification. More than 100 “metabolites of interest” were detected using a combination of these MS approaches, only approximately one-third of which were identified based on accurate mass matching and MS/MS fragmentation. The knowledge gained via the comparison of nitrogen-fixing and non-nitrogen-fixing nodules can provide insight into the roles of metabolites in symbiotic nitrogen fixation. Future studies can

use the information gained in this study to elucidate the metabolic pathways that are responsible for nitrogen fixation.

Acknowledgements

This work was supported by funding from the University of Wisconsin Graduate School and the Wisconsin Alumni Research Foundation (WARF), a Romnes Faculty Research Fellowship program to L.L. and a National Science Foundation (NSF) grant to JMA (NSF#0701846). E.G. acknowledges an NSF Graduate Research Fellowship (DGE-1256259). The MALDI-Orbitrap and Q-Exactive instruments were purchased through an NIH shared instrument grant (NCRR S10RR029531).

References

1. Hoffman, B. M.; Lukoyanov, D.; Yang, Z. Y.; Dean, D. R.; Seefeldt, L. C., Mechanism of Nitrogen Fixation by Nitrogenase: The Next Stage. *Chemical reviews* **2014,** *114* (8), 4041–4062.

2. Ferguson, B. J.; Indrasumunar, A.; Hayashi, S.; Lin, M. H.; Lin, Y. H.; Reid, D. E.; Gresshoff, P. M., Molecular Analysis of Legume Nodule Development and Autoregulation. *Journal of integrative plant biology* **2010,** *52* (1), 61–76.

3. Lau, W.; Fischbach, M. A.; Osbourn, A.; Sattely, E. S., Key Applications of Plant Metabolic Engineering. *PLoS biology* **2014,** *12* (6), e1001879.

4. Graham, P. H.; Vance, C. P., Legumes: Importance and Constraints to Greater Use. *Plant Physiology* **2003,** *131* (3), 872–877.

5. Dunn, M. F., Key Roles of Microsymbiont Amino Acid Metabolism in Rhizobia-Legume Interactions. *Critical reviews in microbiology* **2014**.

6. Udvardi, M.; Poole, P. S., Transport and Metabolism in Legume-Rhizobia Symbioses. *Annual review of plant biology* **2013,** *64*, 781–805.

7. Cook, D., *Medicago Truncatula* - a Model in the Making! Commentary. *Current Opinion in Plant Biology* **1999,** *2* (4), 301-304.

8. Benloch, R.; Navarro, C.; Beltran, J. P.; Canas, L. A., Floral Development of the Model Legume *Medicago Truncatula*: Ontogeny Studies as a Tool to Better Characterize Homeotic Mutations. *Sexual Plant Reproduction* **2003,** *15* (5), 231–241.

9. Gallardo, K.; Le Signor, C.; Vandekerckhove, J.; Thompson, R. D.; Burstin, J., Proteomics of *Medicago Truncatula* Seed Development Establishes the Time Frame of Diverse Metabolic Processes Related to Reserve Accumulation. *Plant Physiology* **2003,** *133* (2), 664–682.

10. Wang, H. L.; Chen, J. H.; Wen, J. Q.; Tadege, M.; Li, G. M.; Liu, Y.; Mysore, K. S.; Ratet, P.; Chen, R. J., Control of Compound Leaf Development by Floricaula/Leafy Ortholog Single Leaflet1 in *Medicago Truncatula*. *Plant Physiology* **2008,** *146* (4), 1759–1772.

11. Branca, A.; Paape, T. D.; Zhou, P.; Briskine, R.; Farmer, A. D.; Mudge, J.; Bharti, A. K.; Woodward, J. E.; May, G. D.; Gentzbittel, L.; Ben, C.; Denny, R.; Sadowsky, M. J.; Ronfort, J.; Bataillon, T.; Young, N. D.; Tiffin, P., Whole-Genome Nucleotide Diversity, Recombination, and Linkage Disequilibrium in the Model Legume *Medicago Truncatula*. *Proceedings of the National Academy of Sciences of the United States of America* **2011,** *108* (42), E864–E870.

12. Samac, D. A.; Penuela, S.; Schnurr, J. A.; Hunt, E. N.; Foster-Hartnett, D.; Vandenbosch, K. A.; Gantt, J. S., Expression of Coordinately Regulated Defence Response Genes and Analysis of Their Role in Disease Resistance in *Medicago Truncatula*. *Molecular Plant Pathology* **2011,** *12* (8), 786–798.

13. Rasmussen, S.; Parsons, A. J.; Jones, C. S., Metabolomics of Forage Plants: A Review. *Annals of botany* **2012,** *110* (6), 1281–1290.

14. Venkateshwaran, M.; Volkening, J. D.; Sussman, M. R.; Ané, J. M., Symbiosis and the Social Network of Higher Plants. *Curr Opin Plant Biol* **2013,** *16* (1), 118–127.

15. White, J.; Prell, J.; James, E. K.; Poole, P., Nutrient Sharing between Symbionts. *Plant Physiology* **2007,** *144* (2), 604–614.

16. Draper, J.; Rasmussen, S.; Zubair, H., Metabolite Analysis and Metabolomics in the Study of Biotrophic Interactions between Plant and Microbes. First ed.; Blackwell Publishing: Annual Plant Reviews, 2011; Vol. 43, pp 25–59.

17. Desbrosses, G. G.; Kopka, J.; Udvardi, M. K., *Lotus Japonicus* Metabolic Profiling. Development of Gas Chromatography-Mass Spectrometry Resources for the Study of Plant-Microbe Interactions. *Plant Physiol* **2005,** *137* (4), 1302–1318.

18. Colebatch, G.; Desbrosses, G.; Ott, T.; Krusell, L.; Montanari, O.; Kloska, S.; Kopka, J.; Udvardi, M. K., Global Changes in Transcription Orchestrate Metabolic Differentiation During Symbiotic Nitrogen Fixation in *Lotus Japonicus*. *Plant J* **2004,** *39* (4), 487–512.

19. Suzuki, H.; Reddy, M. S. S.; Naoumkina, M.; Aziz, N.; May, G. D.; Huhman, D. V.; Sumner, L. W.; Blount, J. W.; Mendes, P.; Dixon, R. A., Methyl Jasmonate and Yeast Elicitor Induce Differential Transcriptional and Metabolic Re-Programming in Cell Suspension Cultures of the Model Legume *Medicago Truncatula*. *Planta* **2005,** *220* (5), 696–707.

20. Farag, M. A.; Huhman, D. V.; Lei, Z. T.; Sumner, L. W., Metabolic Profiling and Systematic Identification of Flavonoids and Isoflavonoids in Roots and Cell Suspension Cultures of *Medicago Truncatula* Using Hplc-Uv-Esi-Ms and Gc-Ms. *Phytochemistry* **2007,** *68* (3), 342–354.

21. Farag, M. A.; Huhman, D. V.; Dixon, R. A.; Sumner, L. W., Metabolomics Reveals Novel Pathways and Differential Mechanistic and Elicitor-Specific Responses in Phenylpropanoid and Isoflavonoid Biosynthesis in Medicago Truncatula Cell Cultures. *Plant Physiology* **2008,** *146* (2), 387-402.

22. Harada, K.; Fukusaki, E., Profiling of Primary Metabolite by Means of Capillary Electrophoresis-Mass Spectrometry and Its Application for Plant Science. *Plant Biotechnology* **2009,** *26* (1), 47–52.

23. Kueger, S.; Steinhauser, D.; Willmitzer, L.; Giavalisco, P., High-Resolution Plant Metabolomics: From Mass Spectral Features to Metabolites and from Whole-Cell Analysis to Subcellular Metabolite Distributions. *Plant Journal* **2012,** *70* (1), 39–50.

24. Lee, Y. J.; Perdian, D. C.; Song, Z. H.; Yeung, E. S.; Nikolau, B. J., Use of Mass Spectrometry for Imaging Metabolites in Plants. *Plant Journal* **2012,** *70* (1), 81-95.

25. Kaspar, S.; Peukert, M.; Svatos, A.; Matros, A.; Mock, H. P., Maldi-Imaging Mass Spectrometry - an Emerging Technique in Plant Biology. *Proteomics* **2011,** *11* (9), 1840-1850.

26. Gemperline, E.; Li, L., Maldi-Mass Spectrometric Imaging for the Investigation of Metabolites in Medicago Truncatula Root Nodules. *Journal of visualized experiments : JoVE* **2014,** (85).

27. Ye, H.; Gemperline, E.; Venkateshwaran, M.; Chen, R.; Delaux, P. M.; Howes-Podoll, M.; Ane, J. M.; Li, L., Maldi Mass Spectrometry-Assisted Molecular Imaging of Metabolites During Nitrogen Fixation in the *Medicago Truncatula-Sinorhizobium Meliloti* Symbiosis. *Plant J* **2013,** *75* (1), 130–145.

28. Bjarnholt, N.; Li, B.; D'Alvise, J.; Janfelt, C., Mass Spectrometry Imaging of Plant Metabolites - Principles and Possibilities. *Natural product reports* **2014,** *31* (6), 818-837.

29. Catoira, R.; Galera, C.; de Billy, F.; Penmetsa, R.; Journet, E.; Maillet, F.; Rosenberg, C.; Cook, D.; Gough, C.; Denarie, J., Four Genes of *Medicago Truncatula* Controlling Components of a Nod Factor Transduction Pathway. *The Plant Cell* **2000,** *12* (9), 1647–1665.

30. Oke, V.; Long, S. R., Bacteroid Formation in the Rhizobium-Legume Symbiosis. *Current opinion in microbiology* **1999,** *2* (6), 641–646.

31. Robichaud, G.; Garrard, K. P.; Barry, J. A.; Muddiman, D. C., Msireader: An Open-Source Interface to View and Analyze High Resolving Power Ms Imaging Files on Matlab Platform. *Journal of the American Society for Mass Spectrometry* **2013,** *24* (5), 718-721.

32. Wolf, S.; Schmidt, S.; Muller-Hannemann, M.; Neumann, S., In Silico Fragmentation for Computer Assisted Identification of Metabolite Mass Spectra. *Bmc Bioinformatics* **2010,** *11*.

33. Mitra, R. M.; Long, S. R., Plant and Bacterial Symbiotic Mutants Define Three Transcriptionally Distinct Stages in the Development of the *Medicago Truncatula*/*Sinorhizobium Meliloti* Symbiosis. *Plant Physiology* **2004,** *134* (2), 595–604.

34. Wang, D.; Griffitts, J.; Starker, C.; Fedorova, E.; Limpens, E.; Ivanov, S.; Bisseling, T.; Long, S. R., A Nodule-Specific Protein Secretory Pathway Required for Nitrogen-Fixing Symbiosis. *Science* **2010,** *327* (5969), 1126–1129.

35. Sprent, J. I.; James, E. K., Legume Evolution: Where Do Nodules and Mycorrhizas Fit In? *Plant Physiology* **2007,** *144* (2), 575-581.

36. Sprent, J., Legume Nodulation: A Global Perspective. Wiley-Blackwell: 2009.

37. Sulieman, S.; Tran, L. S. P., Asparagine: An Amide of Particular Distinction in the Regulation of Symbiotic Nitrogen Fixation of Legumes. *Crit Rev Biotechnol* **2013,** *33* (3), 309-327.

38. Schulze, J., Source-Sink Manipulations Suggest an N-Feedback Mechanism for the Drop in N-2 Fixation During Pod-Filling in Pea and Broad Bean. *Journal of Plant Physiology* **2003,** *160* (5), 531-537.

39. Fischinger, S. A.; Drevon, J. J.; Claassen, N.; Schulze, J., Nitrogen from Senescing Lower Leaves of Common Bean Is Re-Translocated to Nodules and Might Be Involved in a N-Feedback Regulation of Nitrogen Fixation. *Journal of Plant Physiology* **2006,** *163* (10), 987-995.

40. Sulieman, S.; Fischinger, S. A.; Gresshoff, P. M.; Schulze, J., Asparagine as a Major Factor in the N-Feedback Regulation of N-2 Fixation in *Medicago Truncatula*. *Physiologia Plantarum* **2010,** *140* (1), 21-31.

41. Parsons, R.; Stanforth, A.; Raven, J. A.; Sprent, J. I., Nodule Growth and Activity May Be Regulated by a Feedback Mechanism Involving Phloem Nitrogen. *Plant Cell and Environment* **1993,** *16* (2), 125-136.

42. Touraine, B., Nitrate Uptake by Roots- Transporters and Root Development. In *Nitrogen Acquisition and Assimilation in Higher Plants*, Amancio S; I, S., Eds. Kluwer: The Netherlands, 2004; pp 1-34.

43. Schubert S, The Apoplast of Indeterminatelegume Nodules: Compartment for Transport of Amino Acids, Amides and Sugars? In *The Apoplast of Higher Plants: Compartment of Storage, Trasnport and Reactions.*, Sattelmacher B; WJ, H., Eds. Springer: The Netherlands, 2007; pp 445-454.

44. Boscari, A.; Van de Sype, G.; Le Rudulier, D.; Mandon, K., Overexpression of Bets, a *Sinorhizobium Meliloti* High-Affinity Betaine Transporter, in Bacteroids from *Medicago Sativa* Nodules Sustains Nitrogen Fixation During Early Salt Stress Adaptation. *Molecular Plant-Microbe Interactions* **2006,** *19* (8), 896-903.

45. Alloing, G.; Travers, I.; Sagot, B.; Le Rudulier, D.; Dupont, L., Proline Betaine Uptake in *Sinorhizobium Meliloti*: Characterization of Prb, an Opp-Like Abc Transporter Regulated by Both Proline Betaine and Salinity Stress. *Journal of Bacteriology* **2006,** *188* (17), 6308-6317.

46. Luyten, E.; Vanderleyden, J., Survey of Genes Identified in *Sinorhizobium Meliloti* Spp., Necessary for the Development of an Efficient Symbiosis. *European Journal of Soil Biology* **2000,** *36* (1), 1-26.

47. Appleby, C. A., Leghemoglobin and Rhizobium Respiration. *Annual Review of Plant Physiology and Plant Molecular Biology* **1984,** *35*, 443-478.

Tables

Table 1. Annotations of "Metabolites of Interest" Detected in Medicago Root Nodules

Metabolite	Measured *m/z*	Theoretical *m/z*	Δ ppm
Aminobutryic acid	104.0708	104.0706	1.9
Methyl-piperidin-iumone [M+]	114.0915	114.0913	1.4
Proline	116.0706	116.0706	0.0
Aminopentene-diol*	118.0863	118.0863	0.0
Isoleucinol	118.1228	118.1226	1.3
Asparagine*	133.0607	133.0608	0.8
Glutamic Acid	148.0603	148.0604	0.9
Asparagine [M+Na]*	155.0425	155.0427	1.3
3-thiophen-1-yl propanoic acid	158.0397	158.0396	0.7
Ethyl-aminocyclopentane carboxylic acid	158.1173	158.1176	1.6
Phenylalanine	166.0859	166.0863	2.1
Asparagine [M+K]*	171.0165	171.0167	1.2
Arginine	175.1187	175.1190	1.4
Tyrosine	182.0810	182.0812	1.0
Methyl-alpha-galactopyranoside	195.0862	195.0863	0.6
Ethyl-aminocyclopentane carboxylic acid [M+K]	196.0731	196.0734	1.7
Proclavaminic acid*	203.1024	203.1026	1.0
Methyl-alpha-galactopyranoside [M+Na]*	217.0678	217.0682	1.8
Proclavaminic acid [M+Na]	225.0840	225.0846	2.4
Proclavaminic acid [M+K]	241.0577	241.0585	3.3
Dihydroxybenzoic acid succinimido ester	252.0500	252.0503	1.2
5-amino-2-(aminomethyl)-6-butoxyoxane-3,4-diol [M+Na]	257.1462	257.1472	3.9
9H-fluoren-9-yl-di(propan-2-yl)phosphane	283.1618	283.1610	2.9
N-(4-guanidinobutyl)-3-methyldecanamide	299.2802	299.2805	1.1
SAM (S-adenosyl-L-methionine)	399.1441	399.1445	1.1
2-hydroxy-5-[[2-phenyl-2-[4-(phenylcarbamoylamino) phenyl]sulfanylacetyl]amino]benzoic acid	514.1423	514.1431	1.5
2-[hydroxy-[(2R)-3-hydroxy-2-[(9E,12E)-octadeca-9,12- dien oyl]oxypropoxy]phosphoryl]oxyethyl-trimethylazanium [M+]	520.3395	520.3398	0.5
Oleoyl lysophosphatidylcholine	522.3552	522.3554	0.5
18-[(4Z)-4-[(2-hydroxy-5-nitrophenyl)hydrazinylidene]-3-oxocyclohexa-1,5-dien-1-yl]octadecanoic acid [M+]	541.3125	541.3146	3.9
3-[[[[(2R,3S,4R,5R)-5-(6-aminopurin-9-yl)-3,4-dihydroxy oxolan-2-yl]methoxy-hydroxyphosphoryl]oxy-hydroxy phosphoryl]oxy-hydroxyphosphoryl]oxypropanoic acid	580.0223	580.0242	3.1
[[(2R,3S,5R)-5-[4-amino-5-(4-aminobutyldisulfanyl)-2-oxopyrimidin-1-yl]-3-hydroxyoxolan-2-yl]methoxy-hydroxyphosphoryl] phosphono hydrogen phosphate [M+]	602.0052	602.0067	2.4
(Z)-4-oxo-2-[(Z)-1-oxooctadec-9-enyl]-12-henicosenoic acid	603.5340	603.5347	1.1
1,3-dilinolenin	613.4814	613.4827	2.0
Heme	617.1844	617.1846	0.4

Ions are [M+H] unless otherwise specified. * Found in both MALDI and ESI

Figures

Figure 1

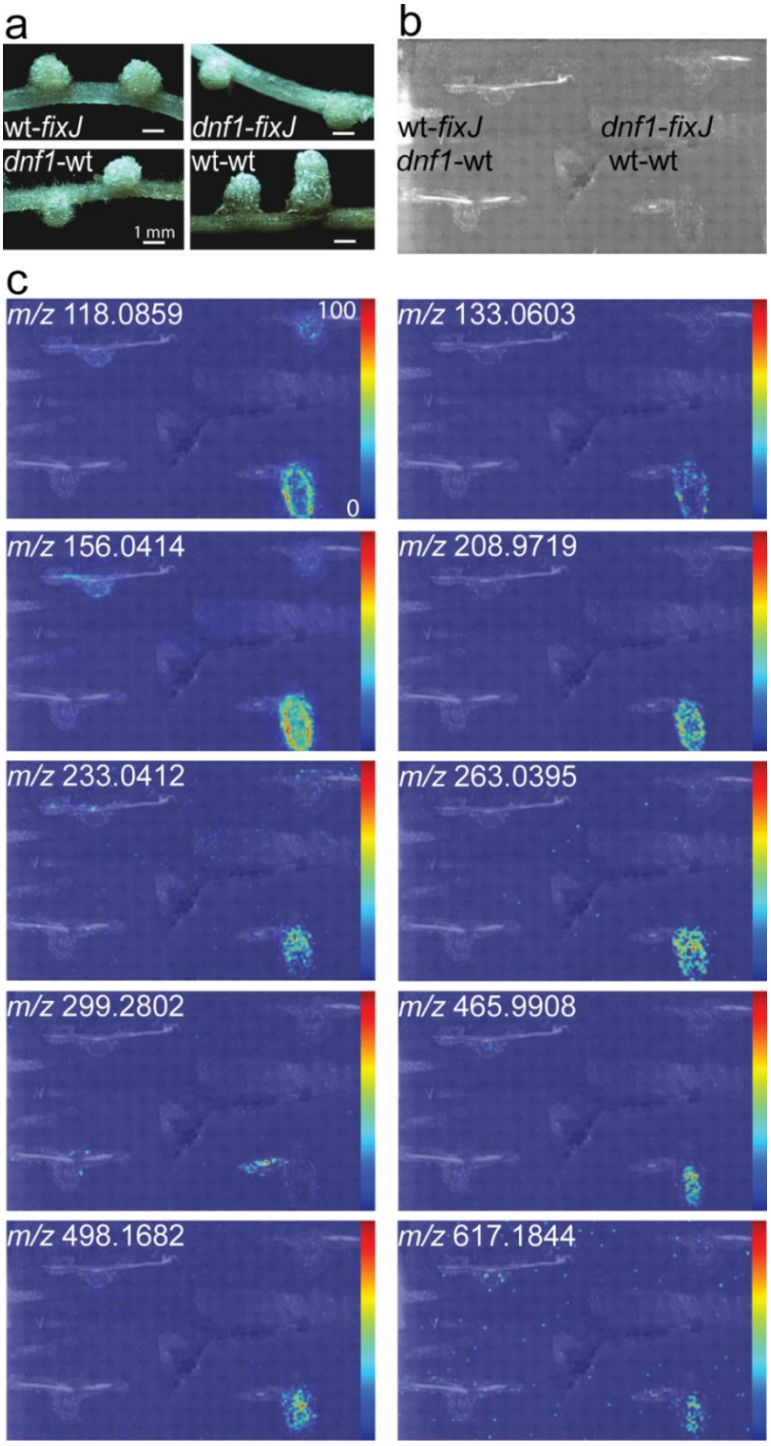

Figure 1. MALDI-MSI of metabolites in Medicago. a) A photograph of all four of the sample types that were used in this study: wt-*fixJ*, *dnf1-fixJ*, *dnf1*-wt, and wt-wt. b) Thaw-mounted Medicago sections on a glass slide that was covered with DHB matrix prior to MALDI-MSI. c) Representative ion images of metabolites with distinct spatial distributions that were found only in the wt-wt samples. Scale bar = 1 mm**.**

Figure 2

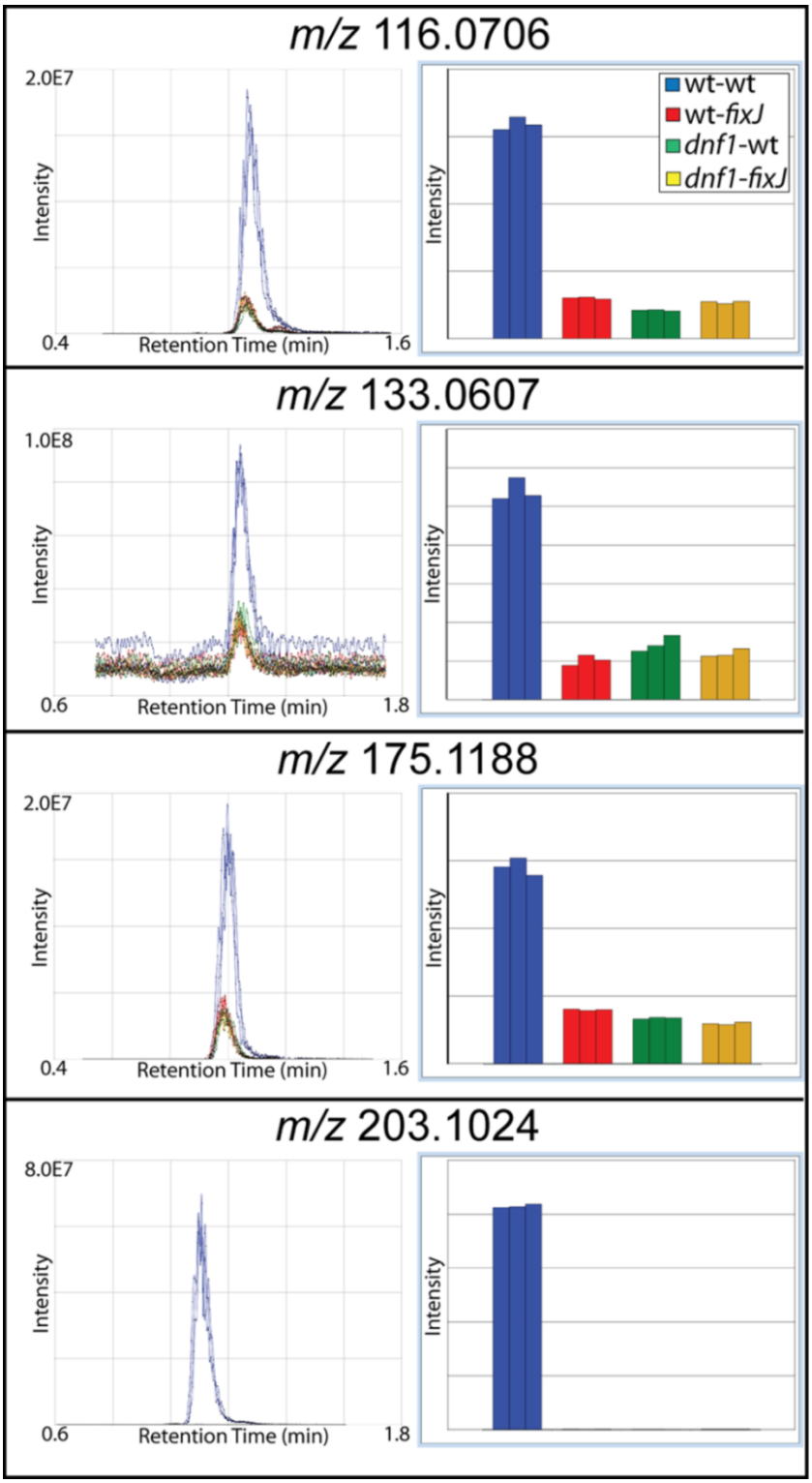

Figure 2. ESI-MS of metabolites in Medicago. Representative data from SIEVE, which was used to select the "metabolites of interest". Blue indicates wt-wt samples; red indicates wt-*fixJ* samples; green indicates *dnf1*-wt samples; and yellow indicates *dnf1-fixJ* samples. The panels on the left show XIC peaks, demonstrating that the metabolite has at least 2-fold greater intensity in the wt-wt samples compared to any of the mutant samples. The panels on the right visualize the information on the left in bar graph form.

Figure 3

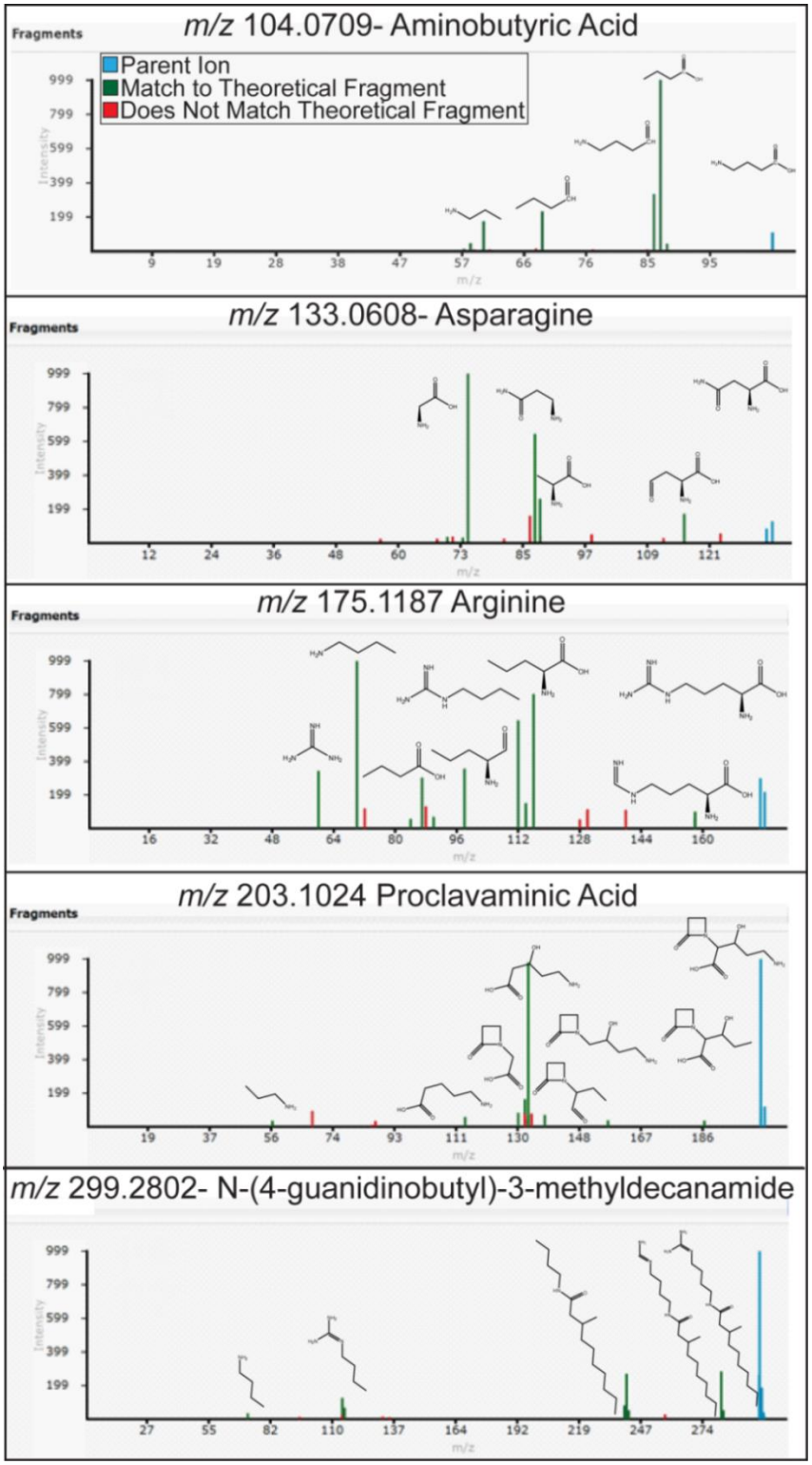

Figure 3. MS/MS data confirmed with MetFrag. Representative MS/MS spectra of the identified "metabolites of interest" and the molecular structures of the matched fragments. Blue indicates the parent ion; green indicates MS/MS peaks that matched the *in silico* fragmentation in MetFrag; and red indicates the experimental peaks that did not match the *in silico* fragmentation.

Supporting Information

Table S1. Metabolites of Interest (*m/z*) Determined from MALDI-MSI

114.1273	**196.0729**	261.2167	423.9813	**522.3552**	582.4121
118.0859	198.0710	263.0395	445.2702	524.0563	583.9925
119.0895	**203.1022**	273.1203	464.9456	526.3250	589.5172
133.0603	208.9719	279.0136	465.9908	536.1234	591.5336
140.0651	210.9760	**283.1618**	480.9190	540.3047	**602.0052**
155.0422	214.9474	290.0849	481.2299	**541.3125**	**603.5340**
156.0414	**217.0676**	291.0831	483.2461	543.3995	608.4283
156.0447	217.1903	297.1777	485.2628	544.3360	**613.4814**
156.0477	221.1853	299.1359	487.9736	556.2784	**617.1844**
158.0397	**225.0840**	**299.2802**	498.1682	557.1617	617.5497
158.1173	233.0412	323.1934	502.9020	559.3965	617.9789
171.0162	**241.0577**	339.2886	503.9474	560.3098	747.3759
180.0992	**252.0500**	352.9188	504.3430	564.0486	749.5071
191.1748	254.1019	**399.1441**	**514.1423**	566.4372	765.4819
192.9980	**257.1462**	408.0072	**520.3395**	**580.0223**	774.4442

Bold indicates metabolites that have been identified and are listed in Table 1

Table S2. Metabolites of Interest (*m/z*) Determined from ESI-MS

104.0708	**118.1228**	**148.0603**	**171.0165**	**195.0862**	415.2114
114.0915	120.0807	149.1242	**175.1188**	**203.1024**	
116.0706	**133.0607**	**155.0425**	**182.0808**	**217.0678**	
118.0863	134.1176	**166.0859**	192.9986	387.1927	

Bold indicates metabolites that have been identified and are listed in Table 1

MS/MS Spectra Matched with the MetFrag Database for *in silico* Metabolite Identifications

Aminobutyric Acid, *m/z* 104.0706

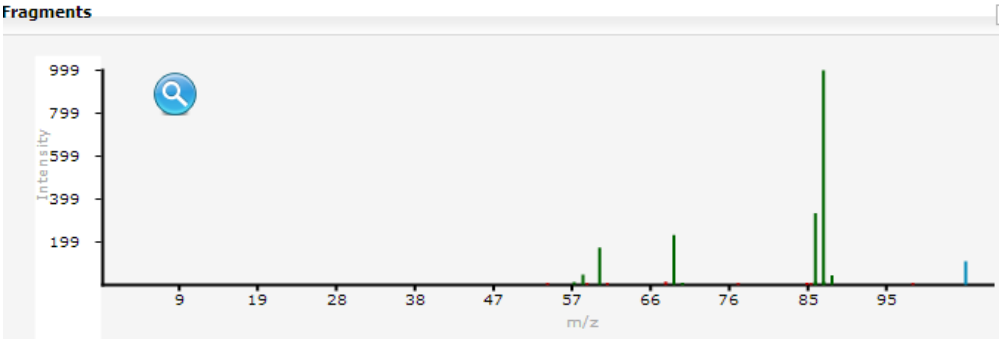

Methyl-piperidin-iumone, *m/z* 114.0913

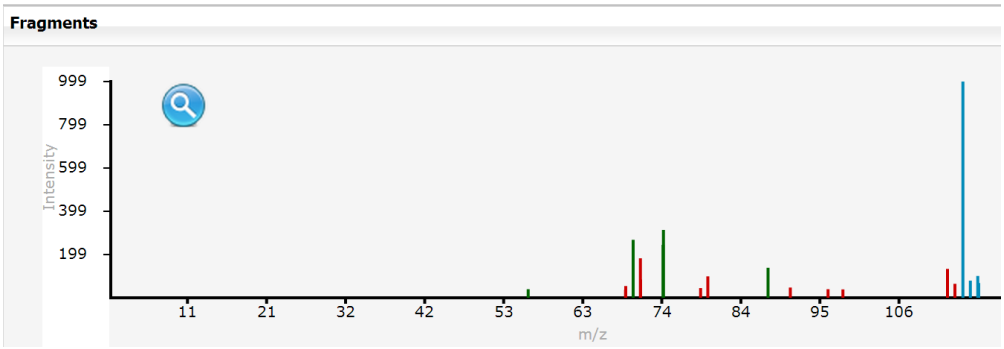

Proline, *m/z* 116.0706

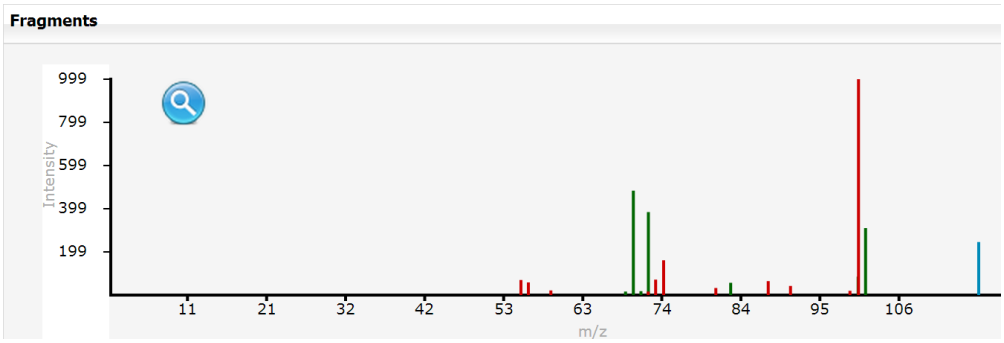

Aminopentene-diol, *m/z* 118.0863

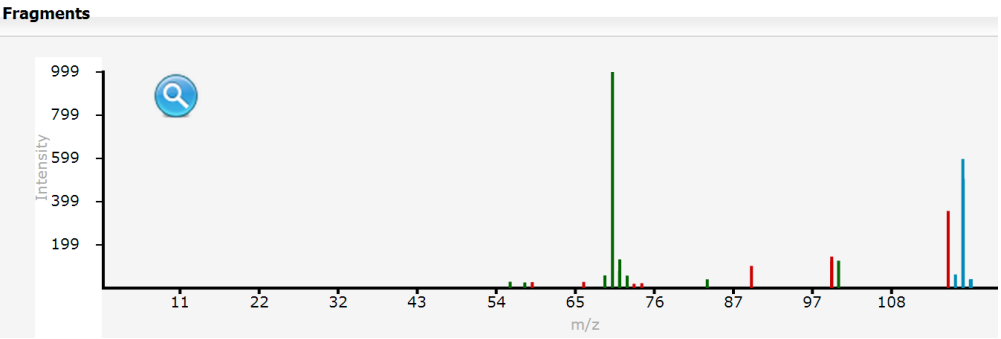

Isoleucinol, *m/z* 118.1226

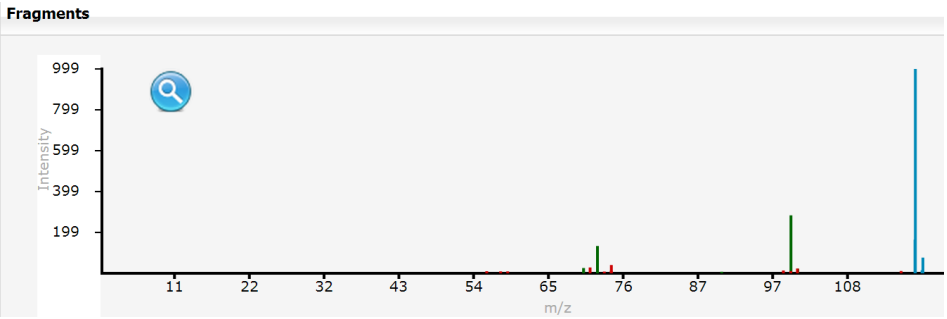

Asparagine, [M+H] *m/z* 133.0608, [M+Na] *m/z* 155.0427, [M+K] *m/z* 171.0167

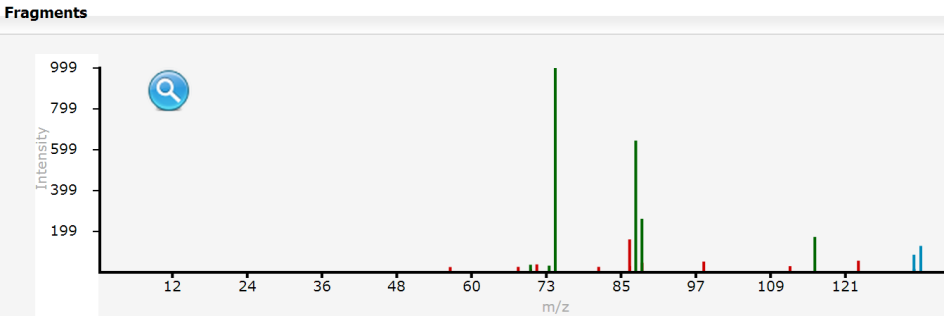

Glutamic Acid, *m/z* 148.0604

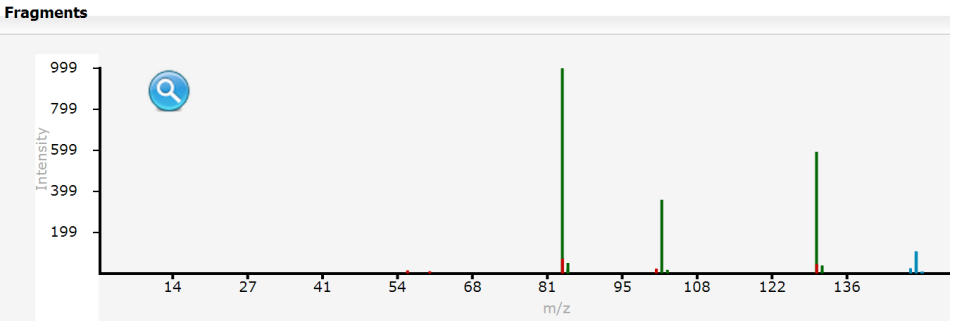

3-thiophen-1-yl propanoic acid, *m/z* 158.0396

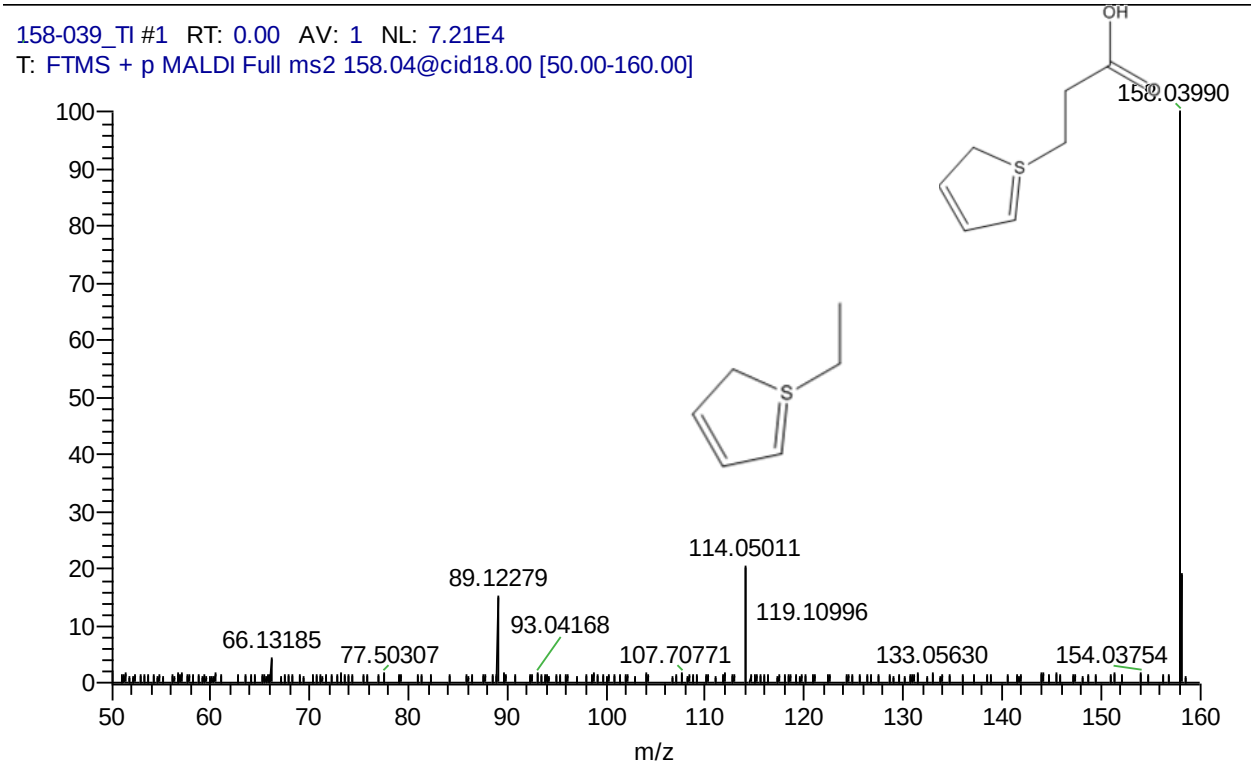

Ethyl-aminocyclopentane carboxylic acid, [M+H] *m/z* 158.1173, [M+K] *m/z* 196.0734

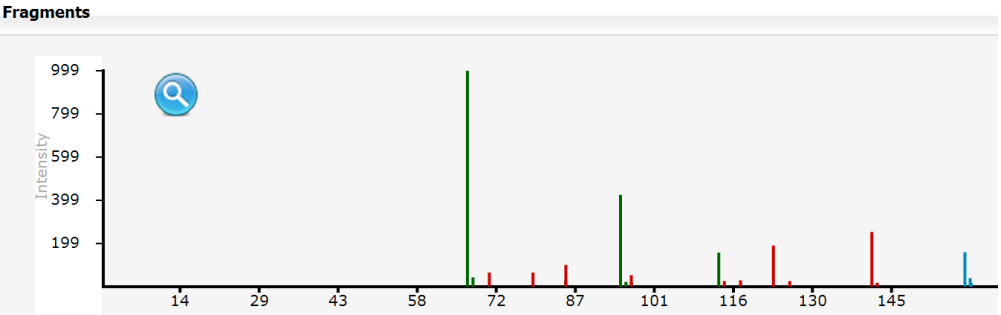

Phenylalanine, *m/z* 166.0863

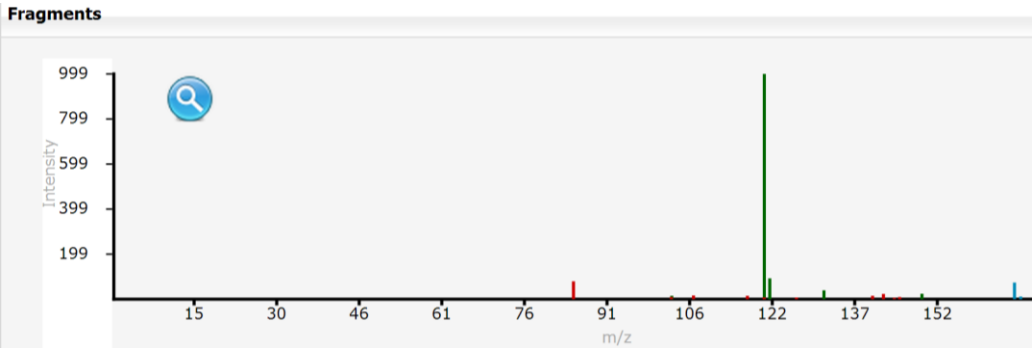

Arginine, *m/z* 175.1190

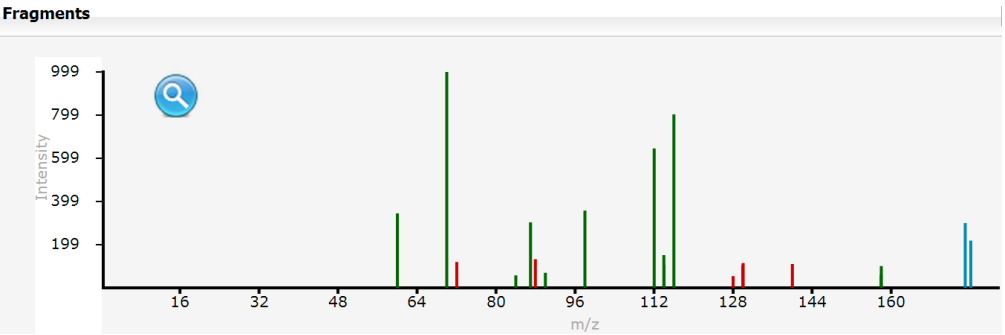

Tyrosine, *m/z* 182.0812

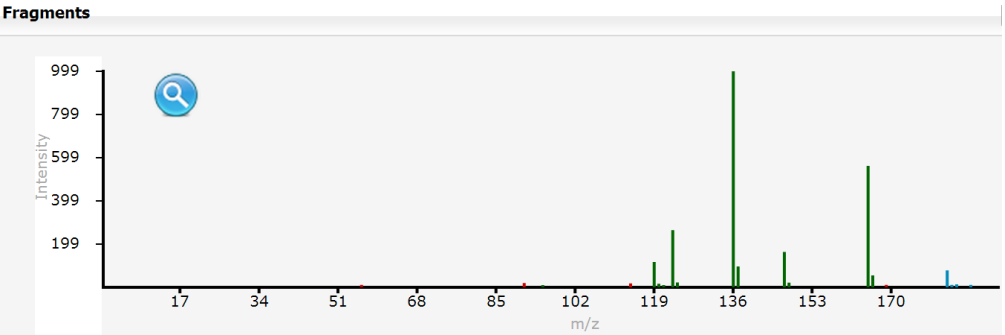

Methyl-alpha-D-galactopyranoside, [M+H] *m/z* 195.0863, [M+Na] *m/z* 217.0682

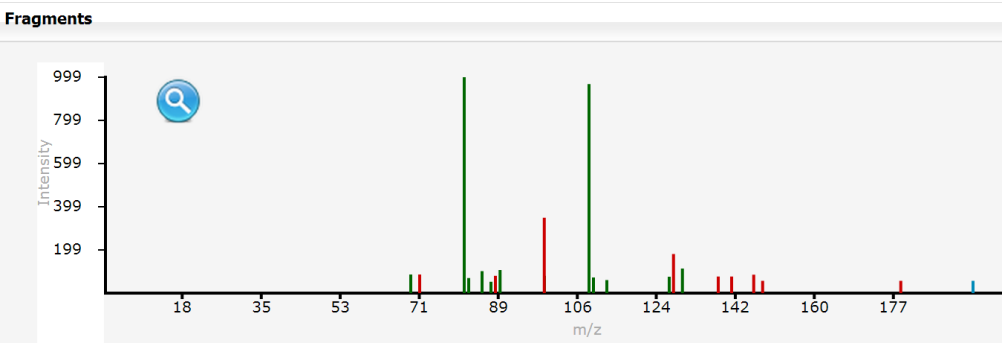

Proclavaminic Acid, [M+H] *m/z* 203.1026, [M+Na] *m/z* 225.0846, [M+K] *m/z* 241.0585

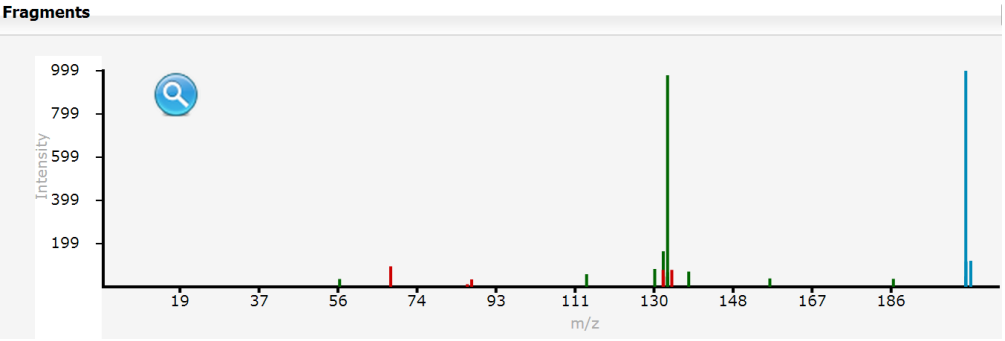

Dihydroxybenzoic acid succinimido ester, *m/z* 252.0503

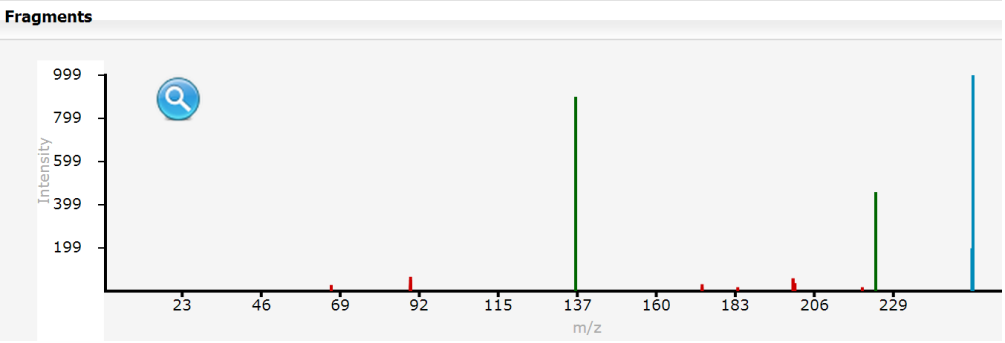

5-amino-2-aminomethyl-6-butoxyoxane-3,4-diol , [M+Na] *m/z* 257.1472

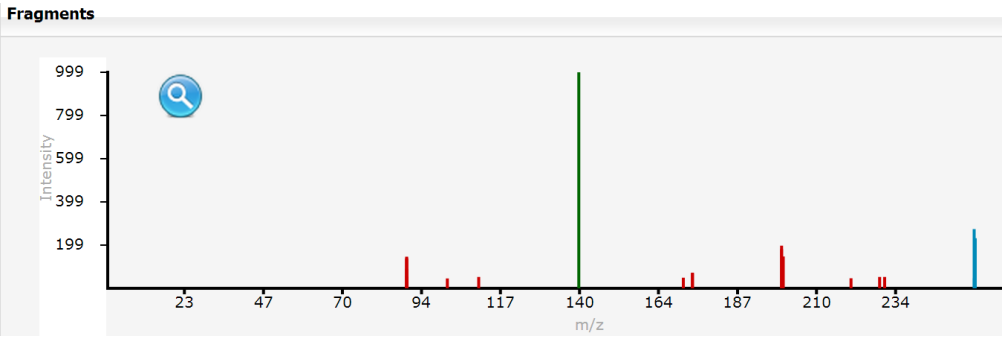

N-(4-guanidinobutyl)-3-methyldecanamide, *m/z* 299.2805

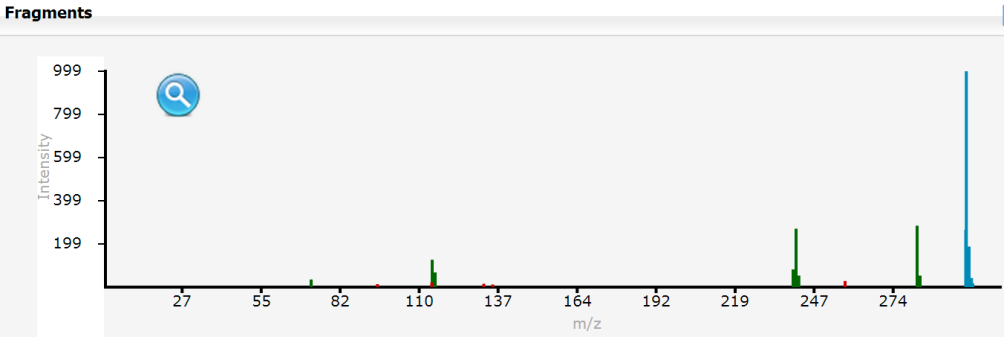

9H-fluoren-9-yl-di(propan-2-yl)phosphane, *m/z* 283.1610

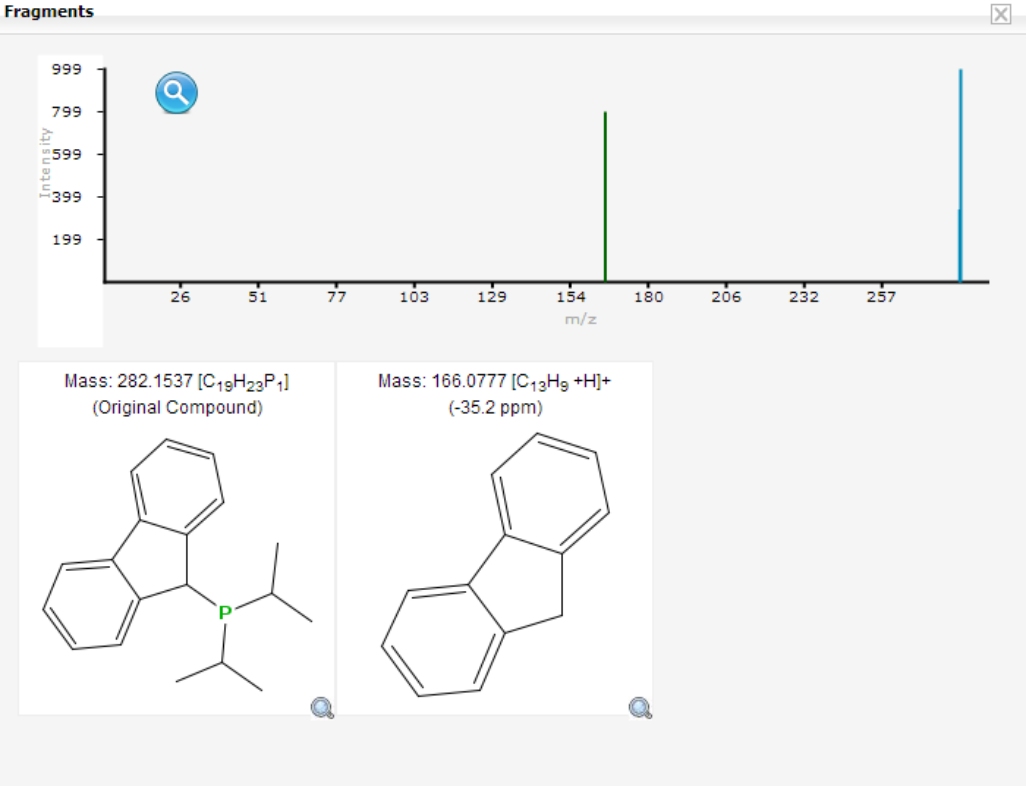

SAM (S-adenosyl-L-methionine), *m/z* 399.1445

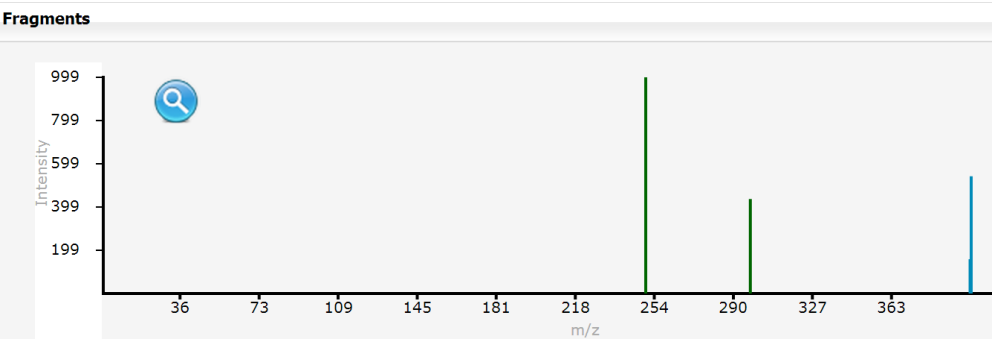

2-hydroxy-5-[[2-phenyl-2-[[4-(phenylcarbamoylamino)phenyl]thio]acetyl]amino]benzoic acid, *m/z* 514.1431

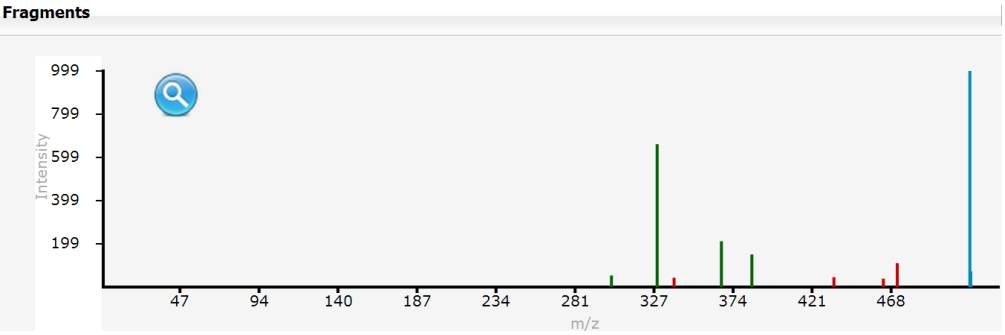

2-[hydroxy-[(2R)-3-hydroxy-2-[(9E,12E)-octadeca-9,12-dienoyl]oxypropoxy]phosphoryl]oxyethyl-trimethylazanium, [M+] *m/z* 520.3398

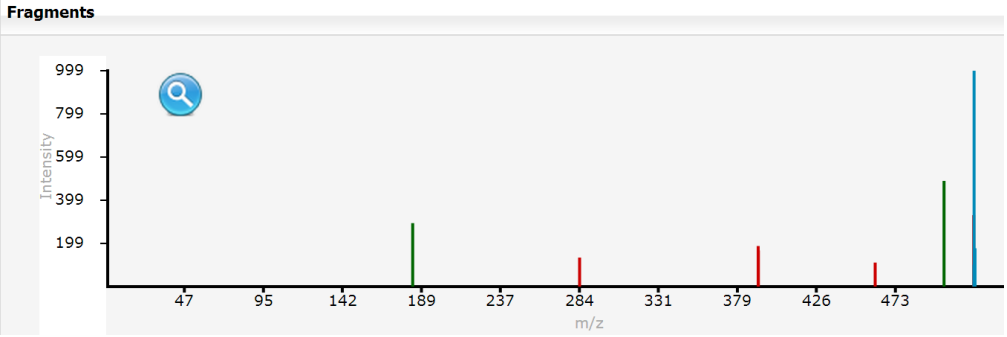

Oleoyl lysophosphatidylcholine, *m/z* 522.3554

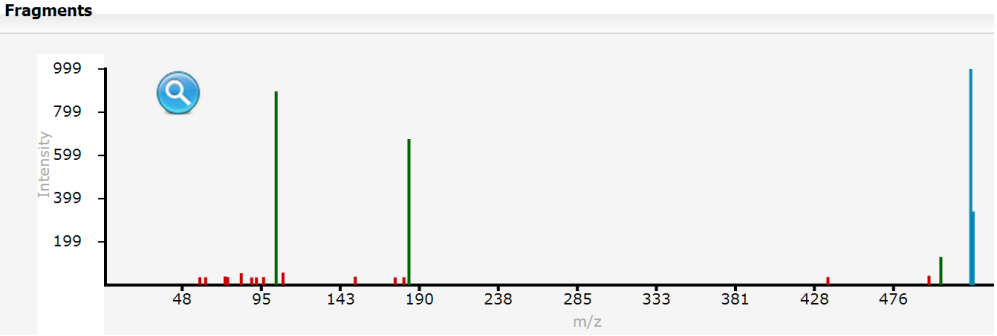

18-[(4Z)-4-[(2-hydroxy-5-nitrophenyl)hydrazinylidene]-3-oxocyclohexa-1,5-dien-1-yl]octadecanoic acid, [M+] *m/z* 541.3146

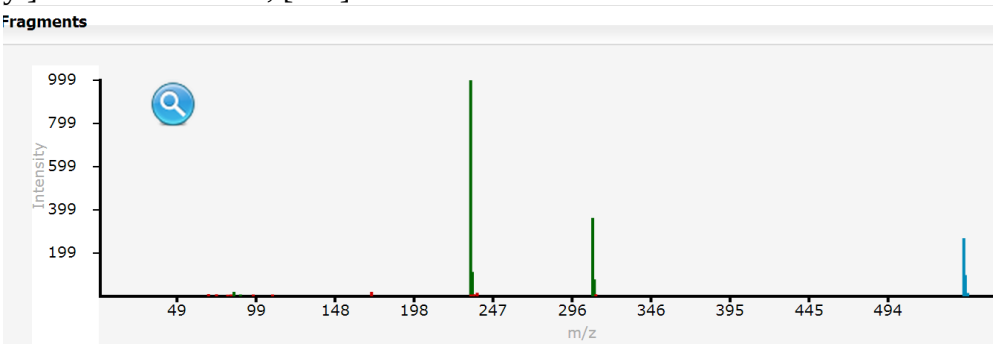

3-[[[[(2R,3S,4R,5R)-5-(6-aminopurin-9-yl)-3,4-dihydroxyoxolan-2-yl]methoxy-hydroxyphosphoryl]oxy-hydroxyphosphoryl]oxy-hydroxyphosphoryl]oxypropanoic acid, *m/z* 580.0242

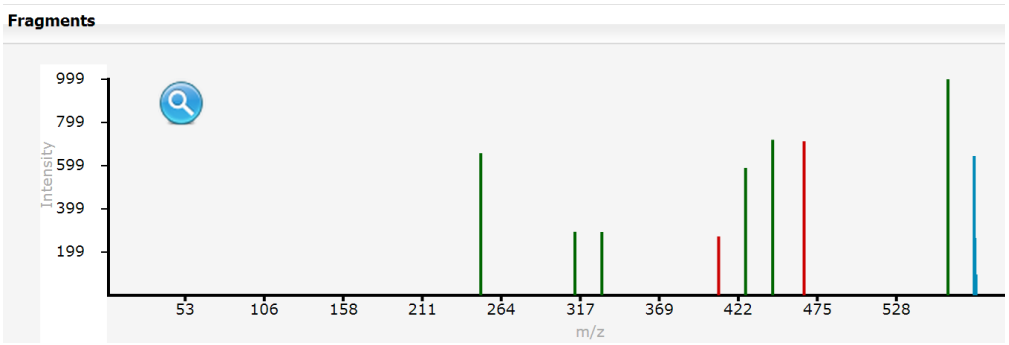

[[(2R,3S,5R)-5-[4-amino-5-(4-aminobutyldisulfanyl)-2-oxopyrimidin-1-yl]-3-hydroxyoxolan-2-yl]methoxy-hydroxyphosphoryl] phosphono hydrogen phosphate, [M+] *m/z* 602.0067

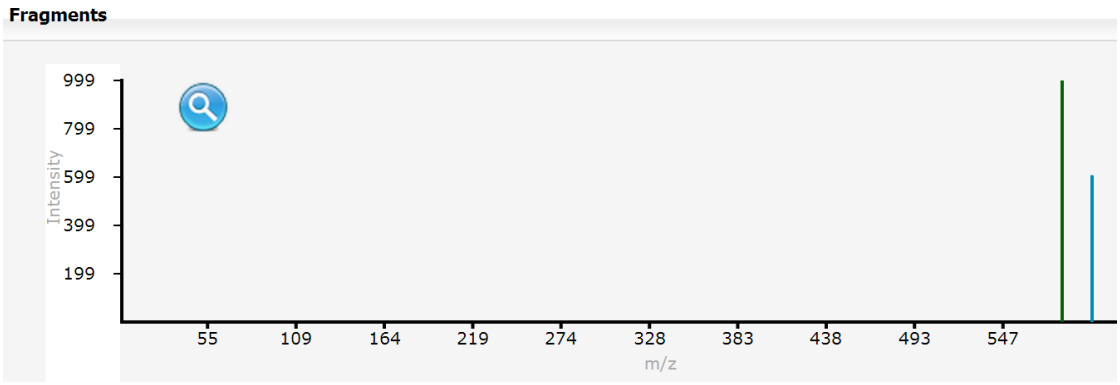

(Z)-4-oxo-2-[(Z)-1-oxooctadec-9-enyl]-12-henicosenoic acid, *m/z* 603.5347

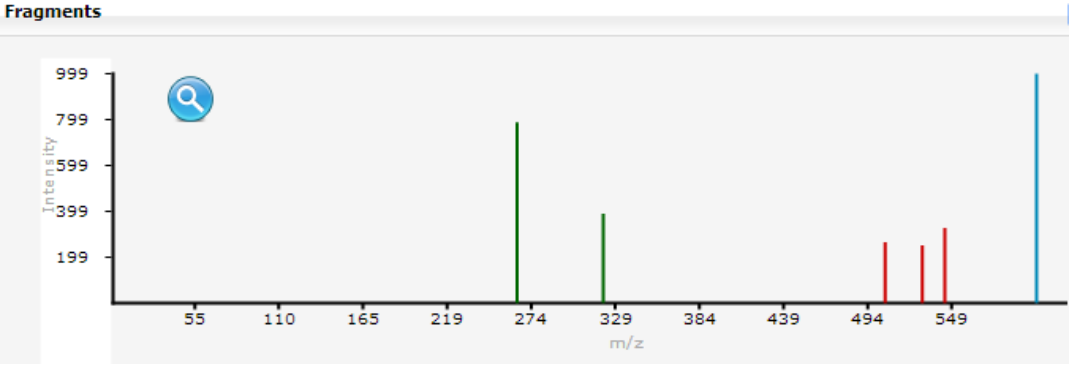

1,3-dilinolenin, *m/z* 613.4827

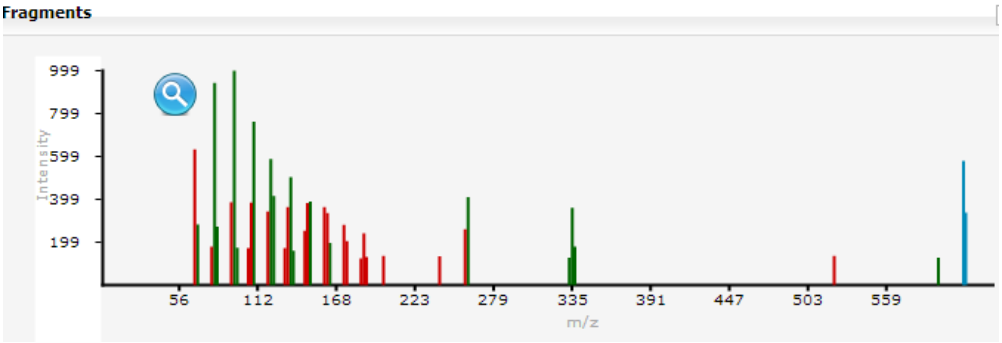

Heme, *m/z* 617.1846

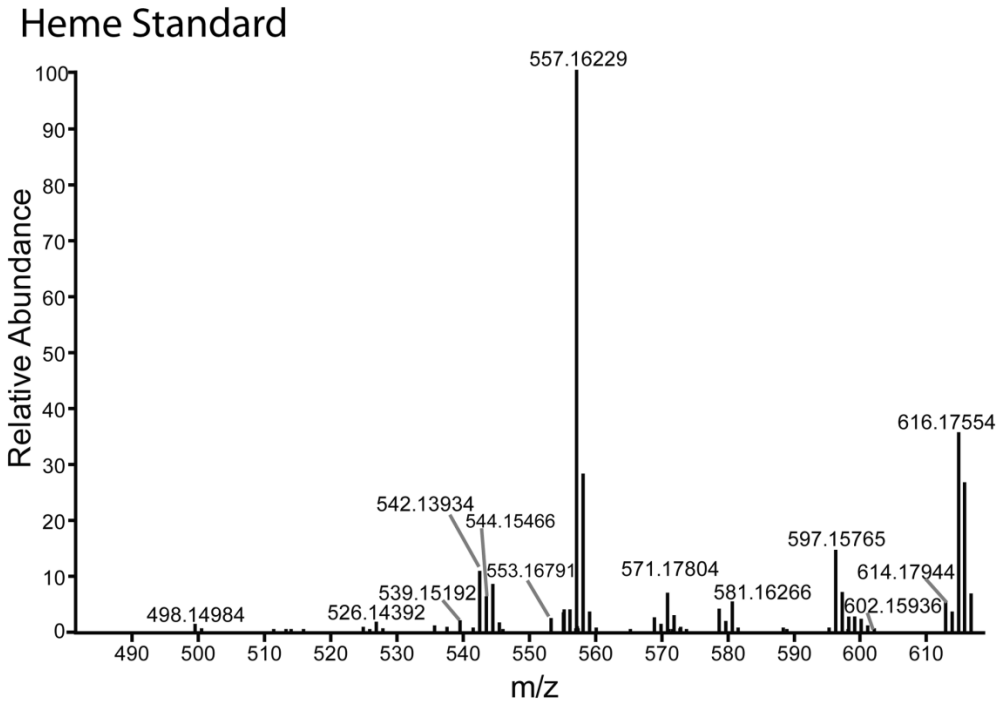

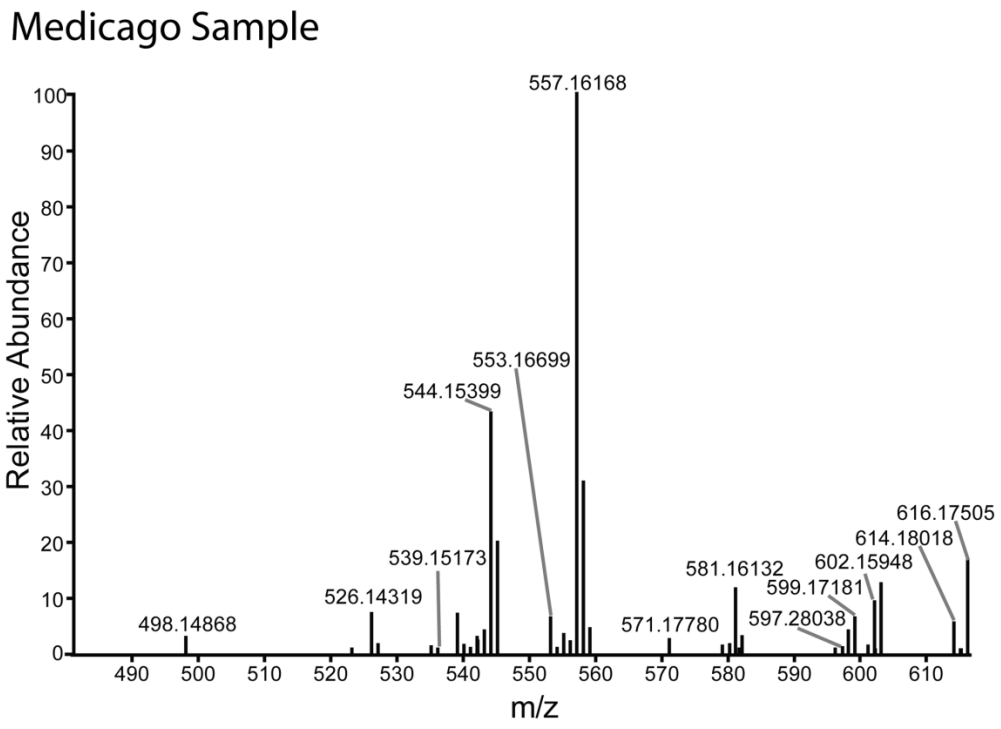

TECHNICAL NOTE

#28 Optimization of DHB Matrix Spray for MALDI Imaging of Metabolites in Root Nodule Tissue of the *Medicago truncatula – Sinorhizobium meliloti* Symbiosis

Application

2,5-dihydroxybenzoic acid (DHB) is a matrix suitable for imaging metabolites. DHB can easily be dissolved in 50:50 Water:Methanol (0.1% Trifluoroacetic Acid) solution. When imaging metabolites DHB can be sprayed directly onto tissue sections with no pre-treatment, but may show interfering peaks in the low mass region of the mass spectra. The data presented here were obtained as part of a MALDI MS imaging experiment whose purpose was to detect metabolites present in the root nodules of the *Medicago truncatula – Sinorhizobium meliloti* symbiosis during nitrogen fixation.

Intended Use Of This Technical Note

The information provided in this document was not peer reviewed and is intended to illustrate possible uses of the TM-Sprayer. HTX Technologies, the manufacturers referenced in this note and the users that have accepted to share their data do not make any guarantees as to the performance of the illustrated workflow.

Imaging Workflow

Root nodules were dissected out of the plant, embedded in gelatin (100 mg/ml in deionized water), and frozen on dry ice. Cryosections (14 microns) of snap frozen root nodule tissue was mounted on ITO-coated glass slides.

Tissue sections were then sprayed with DHB matrix (40mg/ml, Methanol 50%, TFA 0.1%) using the HTX TM-Sprayer and the following conditions:

Flow Rate	50 µl/min
Spray Nozzle Velocity	1250 mm/min
Spray Nozzle Temperature	80°C
Track Spacing	3 mm
Number of Passes	24, criss-cross and offset
Nitrogen Pressure	10 psi

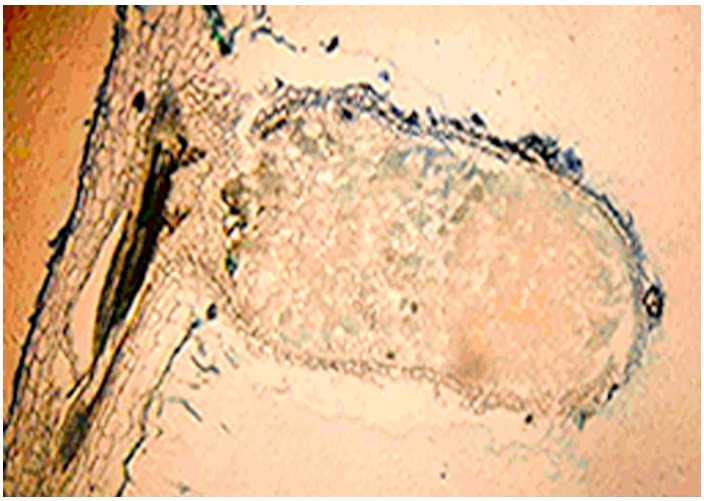

Figure 1. Methylene blue stained *Medicago truncatula* root nodule (Image courtesy of Dr. Jean-Michel Ané lab in the Department of Agronomy at UW-Madison.)

Spectra were collected across the entire tissue area using the ultrafleXtreme MALDI-TOF/TOF (Bruker Daltonics, Billerica, MA, USA) analyzer equipped with a 2 kHz, FlatTop smartbeam-II™ Nd:YAG laser in reflectron positive mode over a mass range of m/z 80 to 1000. A total of 500 laser shots were accumulated and averaged from each laser spot, using the "minimum" laser spot diameter setting and a raster width of 50µm. Calibration was performed externally using DHB cluster peaks in the mass range of m/z 100 to 750.

Experimental Summary

Tissue type	Root nodule
Preservation	Cryogenic storage
Tissue cut	14 µm thickness
MALDI Plate	Glass slide adapter
Matrix deposition	DHB 40mg/ml, 0.1% TFA in 50:50 MeOH/H_20
MALDI Laser	FlatTop smartbeam-II™ Nd:YAG laser
Acquisition mode	Reflectron positive

Instrumentation and Supplies

Microtome	Thermo Microm HM525
MALDI plate	ITO coated slides
Matrix	Acros Organics
Matrix Sprayer	HTX TM-Sprayer™
MALDI MS	BRUKER ultrafleXtreme™
Imaging software	BRUKER flexImaging

Acknowledgements

The tissue images and MS data presented in this note were provided by Erin Gemperline (Department of Chemistry) and Dr. Lingjun Li (Department of Chemistry and School of Pharmacy), University of Wisconsin-Madison, Madison, WI, USA

Results and MALDI MS Images

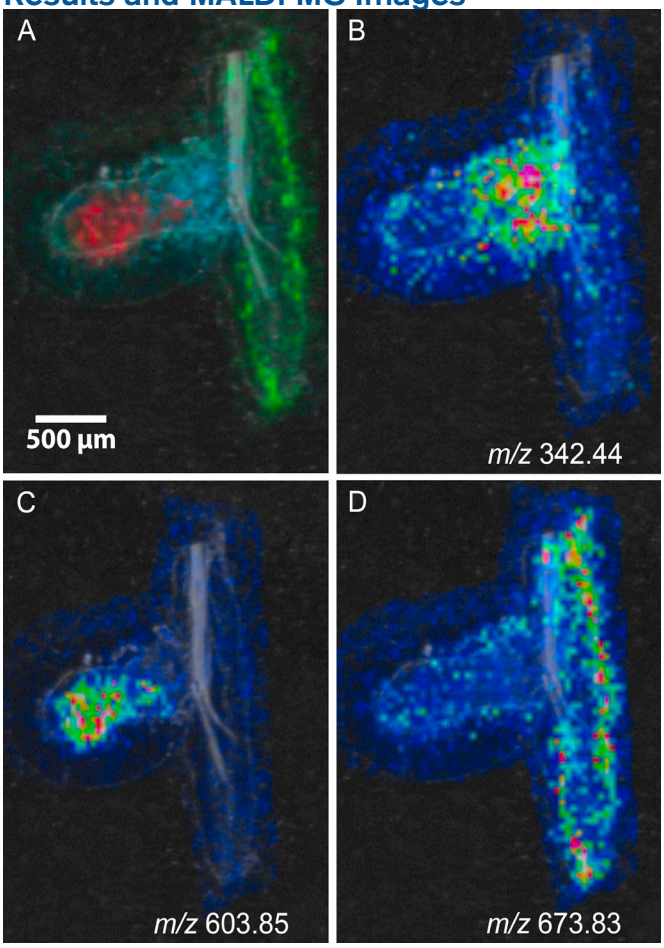

Figure 2. A) Overlaid images of m/z 342.44, 603.85, and 673.83 which show spatial differentiation in different parts of the root nodule. B) Distribution of m/z 342.44 localized to the nitrogen fixation zone region. C) Distribution of m/z 603.85 localized to the outer nodule region. D) Distribution of m/z 673.83 localized to the root region.

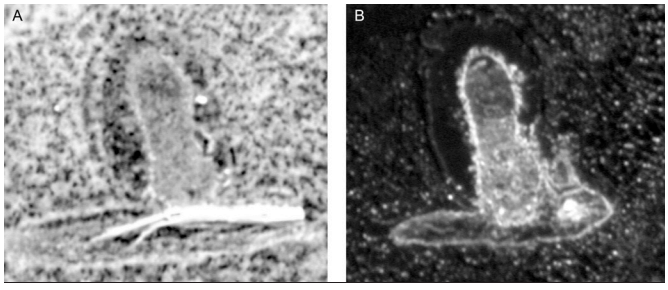

Figure 3. Reference Optical Image

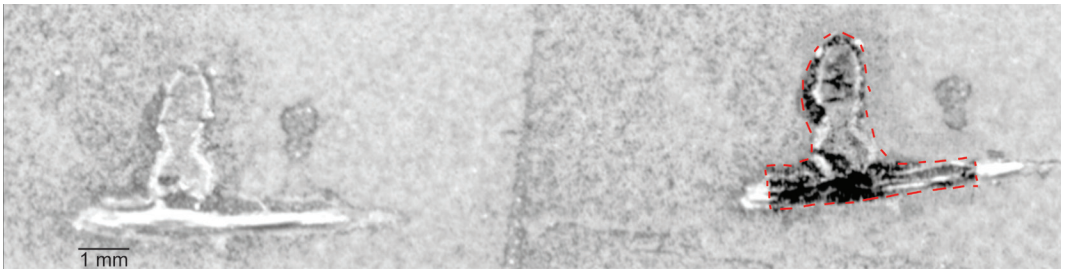

Figure 4. Optical image of serial tissue sections before (left) and after (right) MALDI- MSI. The area of tissue that was imaged is outlined in red on the right.

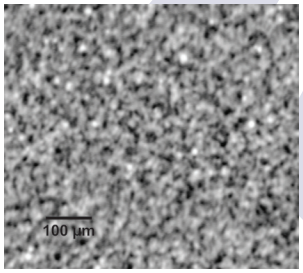

Figure 5. Zoomed in imaged of matrix crystals showing crystal size and coverage.

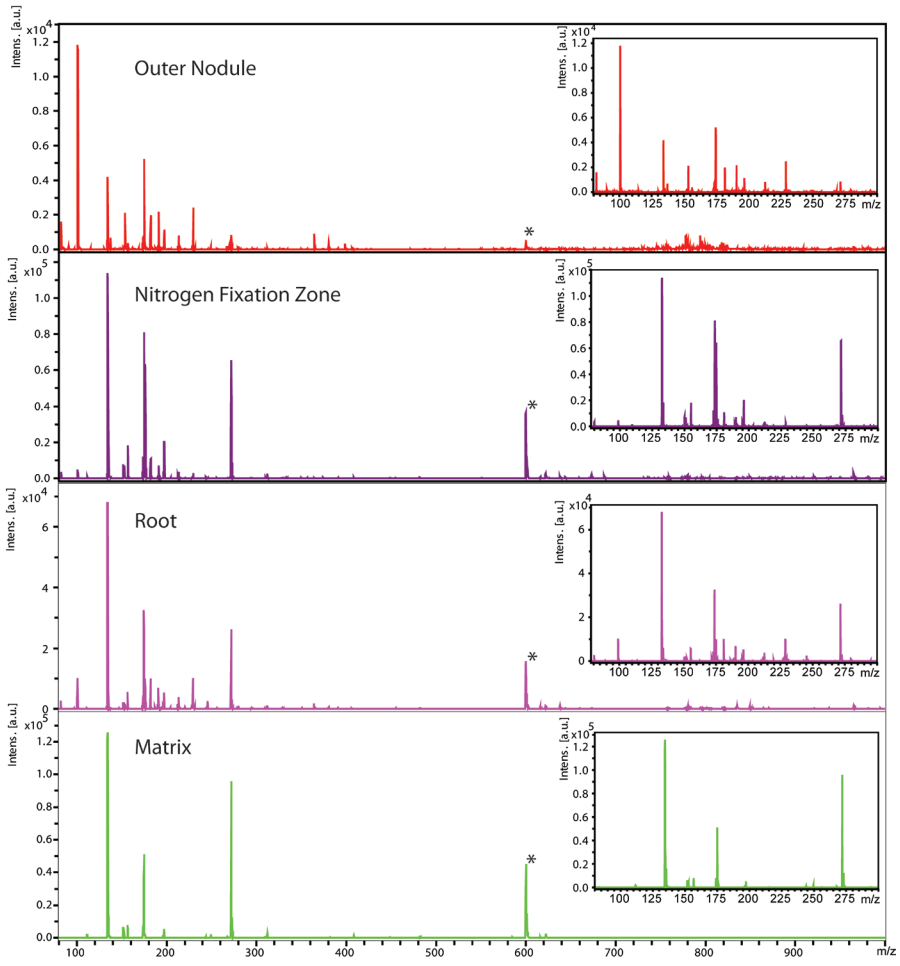

Figure 6. Mass spectra for the three distinct regions of the root nodule tissue: outer nodule, nitrogen fixation zone, and root. Metabolites with m/z 80-1000 were imaged. The inlay zooms in on the region m/z 80-300 which has the greatest abundance of different metabolites. The calculated [M+H]+ for FMRFamide is 599.3, which was added to the matrix as an internal calibrant.

Figure 7. *Medicago truncatula*- intact plant before dissection (Image courtesy of Dr. Jean-Michel Ané in the Department of Agronomy at UW-Madison.)

TM-Sprayer™ Tissue MALDI Sample Preparation System

The HTX TM-Sprayer™ System is an automated MALDI matrix deposition system offering high reproducibility and superior data quality for Mass Spectrometry Imaging

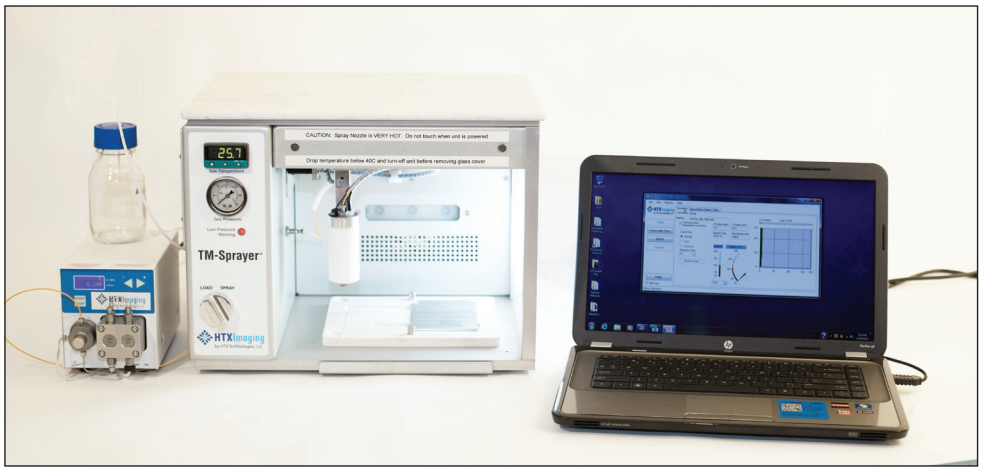

The HTX TM-Sprayer™ is an easy-to-use, versatile spraying system that provides an automated process for Sample Preparation in Mass Spectrometry Imaging.

The patented spray technology of the TM-Sprayer™ guarantees a very fine, uniform and consistent matrix coating crucial for high-resolution imaging and relative quantification of analytes.

The new HTX Technologies' spray nozzle, featured in the next generation TM-Sprayer, creates a fine solvent mist that can be deposited in a precise and adjustable pattern over all or part of any MALDI plate.

Spray characteristics (wet or dry) are easily adjustable via the intuitive operator interface. Users can create and save methods for reproducible operation.

Key Characteristics

- Patented technology providing very small matrix droplets (<10 microns)
- High flow rate and fast sample prep (10 to 20 minutes per plate)
- Highly consistent matrix deposition across entire sample area (+/- 3% by weight)
- Unique use of temperature and nitrogen flow to control evaporation rate and matrix crystal formation
- Validated protocols for most matrices (e.g.: SA, CHCA, DHB)
- Validated protocols for Trypsin digestion
- Continuous matrix coverage as needed for high-resolution imaging
- Rugged operation and easy clean-up

TM-Sprayer™ Specifications

Deposition: Spray deposition in linear or serpentine modes with variables offsets

Spray Nozzle Flow: 50 to 1000µl/min

Sheath Gas: Ambient to 150°C (+/- 2°C), software selected

Gas Supply: Sheath gas flow 5-15.5 liter/min

Spray Nozzle Position: Spray nozzle mounted on Cartesian stage

Electrical: 36V Power Supply

Dimensions/Weight: 17 x 15 x 13in (43 x 38 x 33cm), 38lbs (17Kg)

TM-Sprayer™ is available worldwide exclusively from HTX Technologies, LLC. To request further information contact:

Alain Creissen
Imaging Product Manager, HTX Technologies
acreissen@htximaging.com

HTX Technologies offers innovative sample preparation systems for advanced analytical platforms. Our integrated workflow solutions include user training, instruments, software, consumables and method development services.

HTXImaging
by HTX Technologies, LLC

PO Box 1036, Carrboro, NC 27510, USA
Tel +1-919-928-5688 ◆ Fax +1-919-928-5153
info@htximaging.com ◆ www.htximaging.com

Chapter 5

Examination of Endogenous Peptides in *Medicago truncatula* using Mass Spectrometry Imaging

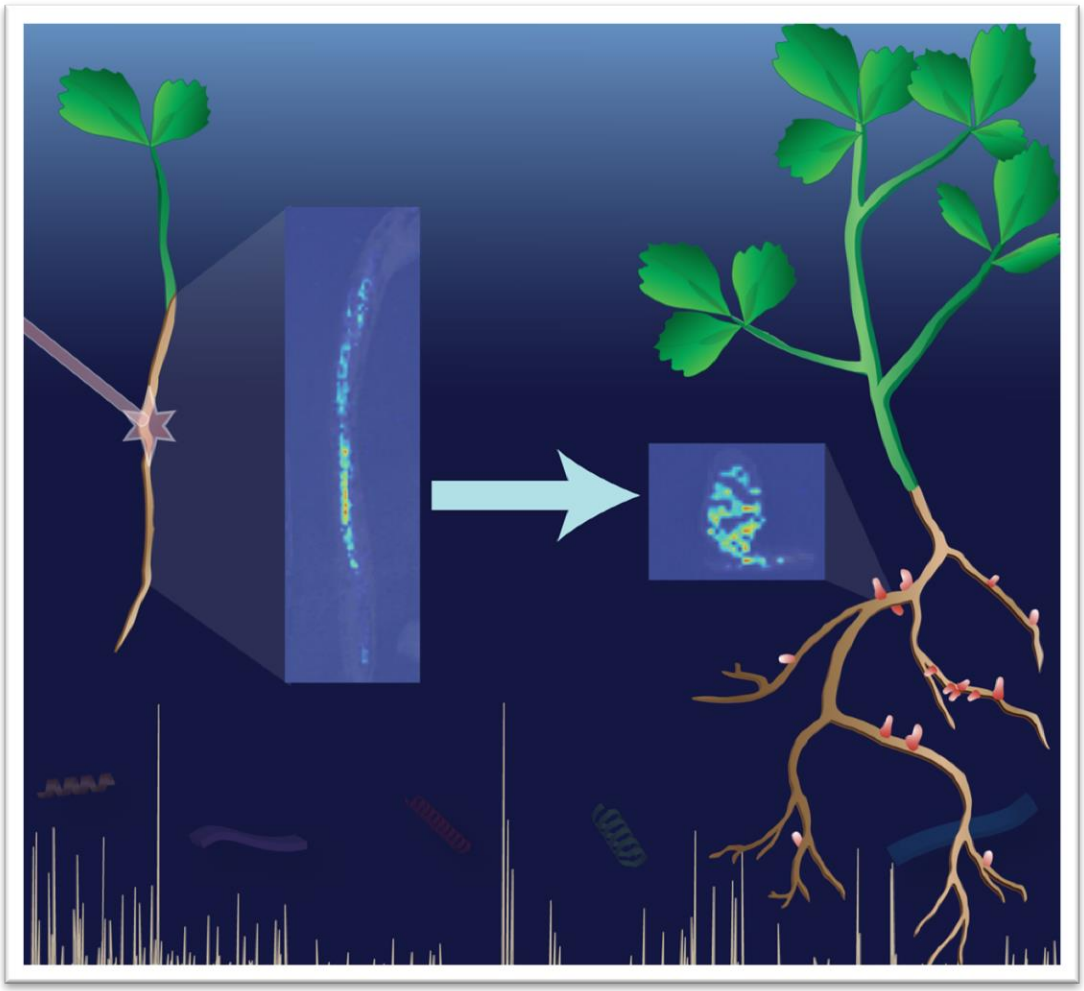

Adapted from **Gemperline, E.**; Keller, C.; Maeda, J.; Jayaraman, D.; Sussman, M.; Ané, J.; Li, L. "Examination of Endogenous Peptides in *Medicago truncatula* using Mass Spectrometry Imaging" *In Preparation*

Abstract

Plant sciences is a rapidly developing area of study due to the urgent need to address many of the most important questions facing humanity today with regard to agriculture, medicine, biofuels, environmental decontamination, ecological sustainability, etc. Endogenous plant peptides can act as signaling molecules and have been shown to affect cell division, development, nodulation, reproduction, symbiotic associations and defense reactions. However, plant peptidomics is a relatively new and underdeveloped field; therefore there is a growing need to investigate the role endogenous peptides play in an organism on a molecular level. Mass spectrometric imaging (MSI) shows great promise for biological analyses because it allows for the detection of thousands of analytes in a single experiment, and also displays information about the spatial distribution of the detected analytes. Despite the prediction of a large number of plant peptides, their detection and imaging with spatial localization and chemical specificity is currently lacking. Here we present a pilot study analyzing the endogenous peptides and proteins in *Medicago truncatula* (Medicago) using matrix-assisted laser desorption/ionization (MALDI)-MSI. One-week-old Medicago seedling roots and mature Medicago roots and root nodules were analyzed. In addition to studying the Medicago peptidome and proteome at different ages, wild-type (wt) plants were compared to well-characterized Medicago mutants that are known to lack certain classes of peptides (*dnf1-1*) or over-express certain classes of peptides (*35S*:*MtCLE13*). Hundreds of endogenous peptides and protein fragments were imaged and showed interesting spatial distribution differences between different ages of plants and between the wt and various mutants.

Introduction

Plant science is an extremely important and rapidly developing area of study. Basic research into plant science is central to addressing many of the most important questions facing humanity today with regard to agriculture, environmental contamination, ecological sustainability, biofuels, medicine, etc. For instance, growing robust crops with increased yield affects more than just the agriculture industry; crop plants also play a role in environmental sustainability and contamination. Furthermore, research into biofuels for sustainable energy often involves non-food crop plants.[1-4] Additionally, many plants have the natural ability to withstand attacks from pests and pathogens in their environment; this ability is being studied in the medical and agricultural communities to combat rampant drug- and pesticide-resistance.[5-8] Studying plant processes on a molecular level can provide further insights into the inner workings of plant cells, cell-cell communication, and even plant-environment interactions.

The field of plant proteomics is rapidly growing and focuses on the study of proteins and enzymes expressed within various plant tissues. Traditional plant proteomic methods, using gel electrophoresis, suffer from several limitations including difficulty in analyzing highly basic or acidic proteins, bias towards more abundant proteins, and limited dynamic range, making low abundance proteins hard to detect.[9-10] Mass spectrometry offers higher sensitivity, selectivity, and structural determination capabilities, making it an advantageous technique for a wide range of applications in plant proteomics.[11]

Branching off of proteomics, plant peptidomics, or studying endogenous peptides produced by a plant, is a relatively new and underdeveloped field; therefore there is a growing need to investigate the role endogenous peptides play in a plant on a molecular level.[12-16] As

signaling molecules, plant peptides have been shown to affect cell division, development, nodulation, reproduction, symbiotic associations and defense reactions.[16-20] Secreted peptides can act at low nanomolar concentrations, and the mature plant peptides are usually processed from larger polypeptides that undergo extensive proteolysis and posttranslational modifications (PTMs);[19] therefore, the discovery and identification of bioactive signaling peptides represents a significant analytical challenge.

Mass spectrometric imaging (MSI) shows great promise for biological analyses because it allows for molecular analysis of tissue while retaining information about the spatial distribution of different analytes including proteins, peptides, lipids, and small molecules.[21] During an MSI experiment, an array of mass spectra are collected from a tissue slice in a predefined raster pattern, resulting in a two-dimensional distribution map for each mass measured. One of the advantages of MSI is that it lends itself to discovery experiments as it allows for the analysis of thousands of analytes in a single experiment, and provides spatial information along with the mass analysis.

In the past decade, MSI has rapidly expanded into the field of plant metabolomics.[21-27] However, as previously mentioned, plant peptidomics is a relatively under-explored area in mass spectrometry, and especially mass spectrometry imaging. One of the very few reports on plant peptide imaging focuses on imaging cyclotides in petunias.[28] Additionally, while mass spectrometry analysis is the gold standard for proteomic analysis in general, very few reports use MALDI-MSI for plant proteomics. A known allergenic protein in peaches was shown to be localized to the skin of the peach using MSI,[29] a lipid-transfer protein was imaged in tomato seeds,[30] and two reviews show MALDI-MSI of proteins in soybean cotyledons or barley grains

as a proof-of –principle,[24, 31] but no further applications of MSI to plant proteomics have been reported so far.

Here we present a pilot study into the endogenous peptides and proteins in the model legume, *Medicago truncatula* (Medicago) using MALDI-MSI. MALDI-MSI was used to analyze one-week-old Medicago seedling roots and mature Medicago roots and root nodules. MSI was performed using both of the most common MALDI matrices, 2,5-dihydroxybenzoic acid (DHB) and α-cyano-4-hydroxycinnamic acid (CHCA) in the mass range from *m/z* 900-4000.[32] In addition to studying the Medicago peptidome and proteome at different ages, wild-type (wt) plants were also compared to well-characterized Medicago mutants that are known to lack certain classes of peptides (*dnf1-1*) or over-express certain classes of peptides (*35S*:*MtCLE13*). In addition to the MALDI-MSI experiments, parallel ESI-MS experiments were conducted in order to obtain accurate mass and high quality tandem mass information for the *m/z* values detected via MSI. *De novo* sequencing was performed on the peptides detected with ESI using PEAKS software.[33] Hundreds of endogenous peptides and protein fragments were imaged and showed interesting spatial distribution differences between different ages of plants and between the wt and various mutants.

Materials and Methods

Plant Growth and Inoculation with Rhizobia

Medicago truncatula seeds of wild-type (Jenalong A17), *dnf1-1*, and *35S:CLE13* were scarified with pure sulfuric acid and sterilized with 8% (w/v) calcium hypochlorite solution.

Freshly germinated one-day-old seedlings were transferred to square plates containing nitrogen-free modified Fahraeus medium,[34] after which one-day-old seedlings were grown in a growth-chamber on modified Fåhræus medium that was overlaid with germination paper. For nodule sampling, ten seedlings were placed per plate and the root part of the plate was covered by aluminum foil. The plates were placed vertically on a shelf at room temperature under fluorescent light. After five days of growth, the roots were inoculated with *S. meliloti* Rm1021 (wild-type)[35] using a rhizobial suspension with an OD_{600} of 0.1, and continued to grow for three weeks for nodule development. At three weeks old, nodules were separated from the roots and ground to fine powder in liquid nitrogen. For seedling sampling, one hundred of one-day-old seedlings were transferred to a plate including nitrogen-free modified Fahraeus medium. After seven days, entire seedlings were collected, immediately frozen and ground with liquid nitrogen.

Sample Preparation for MALDI

For the mature plants, root nodules with approximately 2-3 mm of surrounding root were detached from the plant. The individual nodules were embedded in gelatin (100 mg/mL in double-distilled water) and gently frozen on dry ice. For the seedlings, 2-3 cm long portions of the root were cut from the seedling, embedded in gelatin (100 mg/mL in double-distilled water) and gently frozen on dry ice. The frozen tissue was then sectioned into 16-µm slices using a cryostat at -20 ^{o}C. The sections were thaw-mounted onto standard glass microscope slides. Matrix (40 mg/mL DHB in 50:50 water:methanol or 10 mg/mL CHCA in 50:50 water:acetonitrile) was applied using a TM Sprayer (HTX Technologies, LLC, Carrboro, NC, USA). The TM Sprayer method for DHB was as follows: 80 °C, 0.1 mL/min flow rate, 24

passes- rotate and offset, 3 mm spacing, velocity of 1250 mm/min. The TM Sprayer method for CHCA was as follows: 90 °C, 0.2 mL/min flow rate, 8 passes- rotate and offset, 3 mm spacing, velocity of 1100 mm/min. DHB and CHCA were purchased from Sigma-Aldrich (St. Louis, MO, USA).

MALDI-Orbitrap MSI and MS/MS

A high-resolution, accurate mass (≤ 5ppm error) MALDI- LTQ Orbitrap hybrid mass spectrometer (Thermo Scientific, Waltham, MA, USA) equipped with a N_2 laser (spot diameter of 75 µm) was used in positive ion mode for MSI and MS/MS of both mature nodules and one-week-old seedlings. Multiple technical replicates of three or more biological replicates were imaged using a mass range of *m/z* 900-4000, a mass resolution of 60,000. The tissue region to be imaged and the raster step size were controlled using the LTQ Tune software (Thermo Scientific, Waltham, MA, USA). The instrument methods were created using Xcalibur (Thermo Scientific, Waltham, MA, USA). To generate images, the spectra were collected at 75-µm intervals in both the x and y dimensions across the surface of the sample. Peptide images were extracted automatically using MSiReader.[36] Briefly, a list of the detected peaks was automatically created using MSiReader by selecting the plant tissue as the "region of interest" and subtracting the peaks from the matrix to create a list of detected *m/z* values. Ion images were automatically generated from this list using the "generate an image for each peak in a list" function in MSiReader. Each extracted image was then manually confirmed as a true image (not an isotope or matrix peak). MS/MS collision-induced-dissociation (CID) and high-energy collisional dissociation (HCD) fragments were collected using the MALDI-Orbitrap by isolating each *m/z* of interest and manually adjusting the collision energy for each compound (from 19-42 eV).

Tissue Extraction

Approximately 50-100 root nodules with 2-3 mm of surrounding root were detached from mature Medicago plants or approximately 50 one-week-old Medicago seedlings were removed from the growth media and placed into a pre-chilled mortar, flash-frozen with liquid nitrogen and ground to powder. The powder was transferred to a pre-chilled 13-mL PTFE-coated centrifuge tube. The endogenous peptides were extracted with 3:1:4 methanol:chloroform:water (v/v). The solution was vortexed briefly and centrifuged for 10 min at 4 °C and 4700 rpm. The resulting aqueous supernatant was collected and dried in a SpeedVac. An additional 4 parts methanol was added to the remaining solution, followed by briefly vortexing, and centrifuging for 5 min at 4 °C and 4700 rpm. The organic layer was removed from the protein pellet and both fractions were dried in a SpeedVac. The samples were stored at -80 ^{o}C until analysis.

Q-Exactive for ESI-MS

To acquire LC-ESI-MS/MS data, Medicago root nodule or seedling extracts were initially subjected to SCX fractionation on a Waters Alliance HPLC using a PolySulfoethyl A column (2.1-mm internal diameter × 200-mm length, 5-μm particle size with 300 Å pore size; PolyLC Inc.,Columbia, MD). The mobile phases were (A) 10 mM ammonium formate in 75% water/ 25% acetonitrile at pH≈6.8 and (B) 500 mM ammonium formate in 75% water/ 25% acetonitrile at pH=3. The samples were separated within 80 min under the following conditions: 0-15 min, 0% B; 15-45 min, 0-50% B; 45-55 min, 50-100% B; 55-65 min, 100% B; 65-65.5 min, 100-0% B; and finally re-equilibration at 0% B for 14.5 min. The column temperature was 30 °C, the flow rate was 0.2 mL/min, and the injection volume was 100 μL. Fractions were collected every 6 minutes between 10-70 min of the gradient. The fractions were combined and dried down 3

times with pure water to remove excess salts. Following SCX fractionation, the samples were resuspended in either water (for the aqueous fractions) or acetonitrile (for the organic and protein fractions) to a final concentration of 0.34 μg/μL (a total of 1.2 μg loaded onto the column). The samples were then separated on a NanoAcquity UPLC (Waters Corporation, Milford, MA) using a self-packed column (75 μm internal diameter × 160-mm length, 1.7-μm particle size with 130 Å pore size). The mobile phases were (A) water with 0.1% formic acid and (B) acetonitrile with 0.1% formic acid. The samples were separated within 108 min under the following conditions: 0-2 min, 0-4% B; 2-70 min, 4-30% B; 70-71 min, 30-75 %B; 71-81 min, 75% B; 81-82 min, 75-95% B; 82-92 min, 75-95% B; 92-93 min, 95-0% B, and finally re-equilibration at 0% B for 15 min. The flow rate was 0.3 mL/min and the injection volume was 3.5 μL. The samples were kept at 4 °C during the analysis. MS/MS data were acquired on a Q-Exactive Orbitrap instrument (Thermo Scientific, Waltham, MA, USA) that was equipped with an ESI source operated in positive ion mode. A top-15 data-dependent analysis (DDA) method was used with the full MS scan range from *m/z* 300–2000, a normalized collision energy of 30, a dynamic exclusion of 30 sec, an MS1 resolution of 35,000, and an MS2 resolution of 17,500.

Results and Discussion

MALDI-Orbitrap MS Imaging

This study utilized wild-type (wt) Medicago and the well-characterized Medicago mutants *dnf1-1* and *35S*:*MtCLE13*.[37-38] A complete summary of the putative peptide *m/z* values detected can be found in the supplemental information. These tables detail a list of *m/z* values

detected in each replicate, a comparison of the peptides detected using CHCA compared to DHB, and a comparison of the peptides detected in the seedling roots compared to the mature roots and nodules.

CHCA and DHB were chosen as complementary matrices for MALDI-MSI. There was a surprisingly small percentage of peptide masses detected using both DHB and CHCA as shown in the Venn diagrams in **Figure 1**. A greater number of peptides were detected using CHCA as the matrix in comparison to DHB. Sinapic acid (SA), a matrix more often used to analyze higher molecular weight, species such as peptides and proteins, was also used but did not show improved signal or detectability compared to CHCA. Once the data were collected, ion images were generated using MSiReader as described above. Representative images of putative peptides detected with CHCA and/ or DHB matrices in the mature Medicago roots and root nodules are shown in **Figure 2**. These representative images show different spatial distributions throughout the root and nodule portions of the sample, which could provide further insight into the function of these putative peptides/ proteins within the plant.

Putative peptides in Medicago roots were also compared at different stages of plant development. **Figure 3** presents representative putative peptide images that showed distinct distribution patterns in the Medicago seedlings and the mature roots and root nodules. Some of the detected species show similar distribution patterns when we compare the seedlings to the mature plants (**Figure 4a**); however, other putative peptides seem to shift their localization from the root to the root nodules as they develop into older plants (**Figure 4b-c**). This implies that these putative peptides/ proteins may play a role in nodule development or other nodule related

processes. **Figure 4** shows Venn diagrams comparing the numbers of putative peptides detected in the seedlings compared to the mature plants.

In addition to comparing wild-type (wt) Medicago roots/ root nodules at two different stages of development, wt plants were also compared to two different mutants. In the first mutant line, 35S:MtCLE13, the CLAVATA3/endosperm-surrounding region (CLE) family of peptides is over expressed; therefore, this mutant was thought to be a good model for MSI method development to diminish the challenge of trying to detect low concentration peptides. **Figure 5** displays putative peptides that were detected in the 35S:MtCLE13 plants, but not in the wt plants. It is thought that these putative peptides could belong to the CLE peptide family, but are in too low of concentration to be detected via MALDI-MSI in the wt plants. We also compared the wt plants to *dnf1-1* mutants which develop stunted, non-functional nodules. **Figure 6** shows putative peptides that were detected in the wt plants but were absent from the *dnf1-1* plants. This suggests that these putative peptides may play a role in nodule development or function.

Peptide/ Protein Identification

Accurate mass matching can be used to identify peptides and proteins, although the more widely-accepted approach is to match MS/MS data to sequenced genomes or by *de novo* sequencing, with software packages like PEAKS.[33] **Table 1** details a list of *m/z* values detected via MALDI-MSI and LC-MS/MS that were able to be *de novo* sequenced using PEAKS. The LC-MS/MS spectra were *de novo* sequenced using PEAKS. Since MALDI-MSI typically generates +1 charged ions and LC-MS typically generates +2 or +3 charged peptide ions, the molecular weight of each peptide detected was calculated from the acquired *m/z* in order to

compare data across ionization methods. Using the molecular weights, the PEAKS *de novo* sequencing data generated from LC-MS/MS experiments was searched for peptide masses detected via MALDI-MSI. Since these calculations were made and multiple ionization sources were used, a mass error of < 10 ppm was allowed for confident peptide identification via *de novo* sequencing. The annotated MS/MS spectra used for *de novo* sequencing can be found in the supplemental information.

In addition to *de novo* sequencing, PEAKS also allows for MS/MS matching to sequenced genomes. PEAKS was used to generate a mass list from the LC-MS/MS data of unique peptide masses that matched proteins from the genome data within a 0.1% false discovery rate. A .fasta file of the complete *Medicago truncatula* proteome was generated using PubMed and used for peptide identification. Using this method, 10 imaged peptides were identified. Example images and corresponding LC-MS/MS spectra for these unique peptides are shown in **Figure 7** (all additional unique peptides with corresponding LC-MS/MS spectra are show in the supplemental information). A complete list of the imaged unique peptides is shown in **Table 2**.

Conclusions and Future Directions

Overall we demonstrated the benefits of using MALDI and ESI for the complementary detection and identification of endogenous peptides and protein fragments in plants. Using both CHCA and DHB as MALDI matrices for MSI greatly increased the coverage of peptides/ protein fragments that were detected. We noticed interesting changes in the numbers of peptides detected between seedlings and mature plants. In addition to the difference in overall peptides,

we also observed changes in the spatial distributions of peptides detected in both the seedlings and mature plants. Due to the low concentrations of endogenous peptides in wt plant tissues, peptide enrichment strategies might be a valuable next step for targeting and detecting specific classes of peptides in a biologically relevant manner. Other sample preparation strategies, such as applying a protease inhibitor to the tissue slices immediately after sectioning, could allow for the detection of more endogenous peptides rather than protein fragments. Additional biological studies examining the peptides/ protein fragments detected in this study could reveal more insights into the functions of these peptides within the plant at different stages of development.

Acknowledgements

The author would like to thank Caitlin Keller for her extensive work acquiring and analyzing the data from this project and continuing the collaboration in the future. The author would also like to thank Junko Maeda and Dhileepkumar Jayaraman for growing the Medicago plants. This work was supported by funding from the University of Wisconsin Graduate School and the Wisconsin Alumni Research Foundation (WARF), a Romnes Faculty Research Fellowship program to L.L. and a National Science Foundation (NSF) grant to JMA (NSF#0701846). E.G. acknowledges an NSF Graduate Research Fellowship (DGE-1256259). The MALDI-Orbitrap and Q-Exactive instruments were purchased through an NIH shared instrument grant (NCRR S10RR029531).

References

1. Quinn, L. D.; Gordon, D. R.; Glaser, A.; Lieurance, D.; Flory, S. L., Bioenergy Feedstocks at Low Risk for Invasion in the USA: A "White List" Approach. *Bioenergy Research* **2015,** *8*, 471-481.

2. Tadege, M.; Chen, F.; Murray, J.; Wen, J.; Ratet, P.; Udvardi, M. K.; Dixon, R. A.; Mysore, K. S., Control of Vegetative to Reproductive Phase Transition Improves Biomass Yield and Simultaneously Reduces Lignin Content in Medicago Truncatula. *BioEnergy Research* **2015,** *8* (2), 857-867.

3. Kumar, S.; Kumaria, S.; Tandon, P., Efficient in Vitro Plant Regeneration Protocol from Leaf Explant of Jatropha Curcas L - a Promising Biofuel Plant. *J Plant Biochem Biot* **2010,** *19* (2), 275-277.

4. Hung, K. H.; Chiang, T. Y.; Chiu, C. T.; Hsu, T. W.; Ho, C. W., Isolation and Characterization of Microsatellite Loci from a Potential Biofuel Plant Miscanthus Sinensis (Poaceae). *Conserv Genet* **2009,** *10* (5), 1377-1380.

5. Dewick, P. M., *Medicinal Natural Products: A Biosynthetic Approach*. 3 ed.; Wiley: Chichester, 2009.

6. Russo, P.; Frustaci, A.; Del Bufalo, A.; Fini, M.; Cesario, A., Multitarget Drugs of Plants Origin Acting on Alzheimer's Disease. *Current medicinal chemistry* **2013,** *20* (13), 1686-1693.

7. Kano, S., Artemisinin-Based Combination Therapies and Their Introduction in Japan. *Kansenshogaku Zasshi* **2014,** *88* (3 Suppl 9-10), 18-25.

8. Kittakoop, P.; Mahidol, C.; Ruchirawat, S., Alkaloids as Important Scaffolds in Therapeutic Drugs for the Treatments of Cancer, Tuberculosis, and Smoking Cessation. *Curr Top Med Chem* **2014,** *14* (2), 239-252.

9. Roe, M. R.; Griffin, T. J., Gel-Free Mass Spectrometry-Based High Throughput Proteomics: Tools for Studying Biological Response of Proteins and Proteomes. *Proteomics* **2006,** *6* (17), 4678-4687.

10. Zhang, Y. Y.; Fonslow, B. R.; Shan, B.; Baek, M. C.; Yates, J. R., Protein Analysis by Shotgun/Bottom-up Proteomics. *Chemical Reviews* **2013,** *113* (4), 2343-2394.

11. Jorrin-Novo, J. V.; Pascual, J.; Sanchez-Lucas, R.; Romero-Rodriguez, M. C.; Rodriguez-Ortega, M. J.; Lenz, C.; Valledor, L., Fourteen Years of Plant Proteomics Reflected in Proteomics: Moving from Model Species and 2de-Based Approaches to Orphan Species and Gel-Free Platforms. *Proteomics* **2015,** *15* (5-6), 1089-1112.

12. Clynen, E.; Baggerman, G.; Veelaert, D.; Cerstiaens, A.; Van der Horst, D.; Harthoorn, L.; Derua, R.; Waelkens, E.; De Loof, A.; Schoofs, L., Peptidomics of the Pars Intercerebralis-

Corpus Cardiacum Complex of the Migratory Locust, Locusta Migratoria. *Eur J Biochem* **2001,** *268* (7), 1929-1939.

13. Verhaert, P.; Uttenweiler-Joseph, S.; de Vries, M.; Loboda, A.; Ens, W.; Standing, K. G., Matrix-Assisted Laser Desorption/Ionization Quadrupole Time-of-Flight Mass Spectrometry: An Elegant Tool for Peptidomics. *Proteomics* **2001,** *1* (1), 118-131.

14. Buchberger, A.; Yu, Q.; Li, L., Advances in Mass Spectrometric Tools for Probing Neuropeptides. *Annu Rev Anal Chem (Palo Alto Calif)* **2015**.

15. Dallas, D. C.; Guerrero, A.; Parker, E. A.; Robinson, R. C.; Gan, J. N.; German, J. B.; Barile, D.; Lebrilla, C. B., Current Peptidomics: Applications, Purification, Identification, Quantification, and Functional Analysis. *Proteomics* **2015,** *15* (5-6), 1026-1038.

16. Matsubayashi, Y.; Sakagami, Y., Peptide Hormones in Plants. In *Annual Review of Plant Biology*, Annual Reviews: Palo Alto, 2006; Vol. 57, pp 649-674.

17. Lindsey, K., Plant Peptide Hormones: The Long and the Short of It. *Curr Biol* **2001,** *11* (18), R741-R743.

18. Kondo, T.; Sawa, S.; Kinoshita, A.; Mizuno, S.; Kakimoto, T.; Fukuda, H.; Sakagami, Y., A Plant Peptide Encoded by Clv3 Identified by in Situ Maldi-Tof Ms Analysis. *Science* **2006,** *313* (5788), 845-848.

19. Farrokhi, N.; Whitelegge, J. P.; Brusslan, J. A., Plant Peptides and Peptidomics. *Plant Biotechnology Journal* **2008,** *6* (2), 105-134.

20. Yamaguchi, Y.; Huffaker, A., Endogenous Peptide Elicitors in Higher Plants. *Current Opinion in Plant Biology* **2011,** *14* (4), 351-357.

21. Balluff, B.; Schone, C.; Hofler, H.; Walch, A., Maldi Imaging Mass Spectrometry for Direct Tissue Analysis: Technological Advancements and Recent Applications. *Histochemistry and cell biology* **2011,** *136* (3), 227-244.

22. Gemperline, E.; Jayaraman, D.; Maeda, J.; Ane, J. M.; Li, L., Multifaceted Investigation of Metabolites During Nitrogen Fixation in Medicago Via High Resolution Maldi-Ms Imaging and Esi-Ms. *J Am Soc Mass Spectrom* **2015,** *26* (1), 149-158.

23. Lee, Y. J.; Perdian, D. C.; Song, Z. H.; Yeung, E. S.; Nikolau, B. J., Use of Mass Spectrometry for Imaging Metabolites in Plants. *Plant Journal* **2012,** *70* (1), 81-95.

24. Kaspar, S.; Peukert, M.; Svatoš, A.; Matros, A.; Mock, H. P., Maldi-Imaging Mass Spectrometry - an Emerging Technique in Plant Biology. *Proteomics* **2011,** *11* (9), 1840-1850.

25. Gemperline, E.; Li, L., Maldi-Mass Spectrometric Imaging for the Investigation of Metabolites in Medicago Truncatula Root Nodules. *Journal of visualized experiments : JoVE* **2014,** (85).

26. Ye, H.; Gemperline, E.; Venkateshwaran, M.; Chen, R.; Delaux, P. M.; Howes-Podoll, M.; Ane, J. M.; Li, L., Maldi Mass Spectrometry-Assisted Molecular Imaging of Metabolites During Nitrogen Fixation in the *Medicago Truncatula-Sinorhizobium Meliloti* Symbiosis. *Plant J* **2013,** *75* (1), 130–145.

27. Bjarnholt, N.; Li, B.; D'Alvise, J.; Janfelt, C., Mass Spectrometry Imaging of Plant Metabolites - Principles and Possibilities. *Natural product reports* **2014,** *31* (6), 818–837.

28. Poth, A. G.; Mylne, J. S.; Grassl, J.; Lyons, R. E.; Millar, A. H.; Colgrave, M. L.; Craik, D. J., Cyclotides Associate with Leaf Vasculature and Are the Products of a Novel Precursor in Petunia (Solanaceae). *J Biol Chem* **2012,** *287* (32), 27033-27046.

29. Cavatorta, V.; Sforza, S.; Mastrobuoni, G.; Pieraccini, G.; Francese, S.; Moneti, G.; Dossena, A.; Pastorello, E. A.; Marchelli, R., Unambiguous Characterization and Tissue Localization of Pru P 3 Peach Allergen by Electrospray Mass Spectrometry and Maldi Imaging. *J Mass Spectrom* **2009,** *44* (6), 891-897.

30. Bencivenni, M.; Faccini, A.; Zecchi, R.; Boscaro, F.; Moneti, G.; Dossena, A.; Sforza, S., Electrospray Ms and Maldi Imaging Show That Non-Specific Lipid-Transfer Proteins (Ltps) in Tomato Are Present as Several Isoforms and Are Concentrated in Seeds. *J Mass Spectrom* **2014,** *49* (12), 1264-1271.

31. Grassl, J.; Taylor, N. L.; Millar, A. H., Matrix-Assisted Laser Desorption/Ionisation Mass Spectrometry Imaging and Its Development for Plant Protein Imaging. *Plant methods* **2011,** *7* (1), 21.

32. Chen, R.; Cape, S. S.; Sturm, R. M.; Li, L., Mass Spectrometric Imaging of Neuropeptides in Decapod Crustacean Neuronal Tissues. *Methods Mol Biol* **2010,** *656*, 451-463.

33. Ma, B.; Zhang, K.; Hendrie, C.; Liang, C.; Li, M.; Doherty-Kirby, A.; Lajoie, G., Peaks: Powerful Software for Peptide De Novo Sequencing by Tandem Mass Spectrometry. *Rapid communications in mass spectrometry : RCM* **2003,** *17* (20), 2337-2342.

34. Catoira, R.; Galera, C.; de Billy, F.; Penmetsa, R.; Journet, E.; Maillet, F.; Rosenberg, C.; Cook, D.; Gough, C.; Denarie, J., Four Genes of *Medicago Truncatula* Controlling Components of a Nod Factor Transduction Pathway. *The Plant Cell* **2000,** *12* (9), 1647–1665.

35. Oke, V.; Long, S. R., Bacteroid Formation in the Rhizobium-Legume Symbiosis. *Current opinion in microbiology* **1999,** *2* (6), 641–646.

36. Robichaud, G.; Garrard, K. P.; Barry, J. A.; Muddiman, D. C., Msireader: An Open-Source Interface to View and Analyze High Resolving Power Ms Imaging Files on Matlab Platform. *Journal of the American Society for Mass Spectrometry* **2013,** *24* (5), 718-721.

37. Mitra, R. M.; Long, S. R., Plant and Bacterial Symbiotic Mutants Define Three Transcriptionally Distinct Stages in the Development of the *Medicago Truncatula*/*Sinorhizobium Meliloti* Symbiosis. *Plant Physiology* **2004,** *134* (2), 595–604.

38. Wang, D.; Griffitts, J.; Starker, C.; Fedorova, E.; Limpens, E.; Ivanov, S.; Bisseling, T.; Long, S. R., A Nodule-Specific Protein Secretory Pathway Required for Nitrogen-Fixing Symbiosis. *Science* **2010,** *327* (5969), 1126–1129.

Tables

Table 1. List of *m/z* values that were *de novo* sequenced using PEAKS

De Novo Sequenced Peptides (molecular weight)			
MALDI Measured	**LC-MS Measured**	**Δ ppm**	**Peptide Sequence**
908.4234	908.4240	0.66	FGGSTVEVN
962.4813	962.4743	7.31	TVNEEKLM
990.5163	990.5134	2.89	PSPPLRGEP
			EPPPHVTSK
1006.5114	1006.5195	8.09	TVGKGAHAGPP
1008.4694	1008.4624	6.98	DDARPPQGGP
1021.5575	1021.5556	1.85	AVGKDYRLT
1068.5733	1068.5791	5.42	CKVWPLPGK
			CKVWPPLGK
1094.5280	1094.5244	3.28	PQTEAPAVGAP
1106.5081	1106.4993	7.92	YNDQDTPVR
1106.5255	1106.5356	9.10	TDSSAPGGFLR
1112.5974	1112.5938	3.21	STGGVAAPRAVQ
			TSGVQAPRGPK
1159.6191	1159.6084	9.20	TEAATATPAVTK
1170.6070	1170.6133	5.38	VLDPGDSDLLK
			LVDPGDSDLLK
			GPDDSDLVLLK
			DPGDSDLVLLK
			DPGSDDLVLLK
1175.5925	1175.5935	0.88	TGAEGKVHSYK
1179.6039	1179.6135	8.10	KAPPPVADDTK
1186.5763	1186.5830	5.68	TVGNGPVEASGLS
1192.5108	1192.5107	0.09	HGGTEDPVTSGH
1300.6790	1300.6775	1.12	QSSHSPVLVKGF
1300.6790	1300.6697	7.12	TVGAVDAVTLMPQ
1308.6282	1308.6211	5.45	SYFANAQPQQR
1342.6713	1342.6663	3.72	QSVKMTNAHSLQ
1376.7577	1376.7598	1.55	VSLALVCSPVPHR
1728.9683	1728.9597	4.95	KPLNVELGFKAVAAGLC

Table 2. List of *m/z* values of unique peptides for which MS images were acquired

[M+H]	Protein Group	Protein ID	Protein Accession	Peptide	Protein Description
965.51694	47	92	gi|657381377	C.TVIDAPGHR.D	GTP-binding elongation factor Tu family protein
	47	93	gi|657381378	C.TVIDAPGHR.D	GTP-binding elongation factor Tu family protein
	47	94	gi|357496973	C.TVIDAPGHR.D	Elongation factor 1-alpha
1132.53084	215	973	gi|657377737	K.ANENKPVMTE	wound-inducible basic family protein
1160.61634	43	137	gi|657399288	A.ETAATATPAVTK.S	NADPH-protochlorophyllide oxidoreductase
1162.59554	31	174	gi|357474991	M.A(+42.01)ASGEEKKIST.S	Low-temperature inducible
	31	175	gi|355508836	M.A(+42.01)ASGEEKKIST.S	nodulin-like protein
	31	176	gi|388522163	M.A(+42.01)ASGEEKKIST.S	unknown
1171.62114	71	564	gi|388504426	S.IVDPGDSDIIK.T	unknown
	71	565	gi|217073834	S.IVDPGDSDIIK.T	unknown
	71	566	gi|657371310	S.IVDPGDSDIIK.T	ribosomal protein L7Ae/L30e?S12e?Gadd45 family protein
	71	567	gi|355496648	S.IVDPGDSDIIK.T	ribosomal protein L7Ae/L30e?S12e?Gadd45 family protein
	71	568	gi|357502689	S.IVDPGDSDIIK.T	60S ribosomal protein L30
	71	569	gi|388496542	S.IVDPGDSDIIK.T	unknown
1180.62144	148	341	gi|388522541	K.AVAPPPVADDTK.A	unknown
	148	342	gi|657373135	K.AVAPPPVADDTK.A	carboxy-terminal region remorin
	148	352	gi|388492578	K.AVAPPPVADDTK.A	unknown
1293.67314	149	496	gi|388507838	T.GVIFEPFEEVK.K	unknown
	149	497	gi|357468557	T.GVIFEPFEEVK.K	Ferritin-3
	149	498	gi|355505618	T.GVIFEPFEEVK.K	Ferritin
	149	524	gi|217073043	T.GVIFEPFEEVK.K	unknown
	149	526	gi|657385619	T.GVLFEPFEEVK.K	ferritin
	149	527	gi|388491178	T.GVLFEPFEEVK.K	unknown
	149	528	gi|355518020	T.GVLFEPFEEVK.K	ferritin
	149	529	gi|217073544	T.GVLFEPFEEVK.K	unknown
	149	530	gi|357492793	T.GVLFEPFEEVK.K	Ferritin-2
	149	535	gi|355498374	T.GVIFEPFEEVK.K	ferritin
	149	536	gi|388499902	T.GVIFEPFEEVK.K	unknown
	149	537	gi|217073522	T.GVIFEPFEEVK.K	unknown
	149	538	gi|357506141	T.GVIFEPFEEVK.K	Ferritin-1
1337.67014	61	103	gi|657379753	G.TPQEATHPDTLK.A	tonoplast intrinsic protein
	61	104	gi|32363409	G.TPQEATHPDTLK.A	Probable aquaporin TIP-type
	61	105	gi|9716259	G.TPQEATHPDTLK.A	aquaporin
1483.75454	13	32	gi|357471525	A.AFRVSPQPGVPAEE.A	ribulose biphosphate carboxylase large chain
	13	33	gi|355507102	A.AFRVSPQPGVPAEE.A	ribulose biphosphate carboxylase large chain domain protein
	13	34	gi|543174105	A.AFRVSPQPGVPAEE.A	ribulose- 1,5-biphosphate carboxylase/ oxygenase large subunit (chloroplast)
	13	35	gi|404332436	A.AFRVSPQPGVPAEE.A	ribulose- 1,5-biphosphate carboxylase/ oxygenase large subunit
	13	36	gi|153012229	A.AFRVSPQPGVPAEE.A	ribulose- 1,5-biphosphate carboxylase/ oxygenase large subunit (chloroplast)
	13	37	gi|404332513	A.AFRVSPQPGVPAEE.A	ribulose- 1,5-biphosphate carboxylase/ oxygenase large subunit
	13	38	gi|355501595	A.AFRVSPQPGVPAEE.A	ribulose biphosphate carboxylase large chain domain protein
	13	39	gi|357512583	A.AFRVSPQPGVPAEE.A	ribulose biphosphate carboxylase large chain
	13	40	gi|404332359	A.AFRVSPQPGVPAEE.A	ribulose- 1,5-biphosphate carboxylase/ oxygenase large subunit
	13	41	gi|357502811	A.AFRVSPQPGVPAEE.A	ribulose biphosphate carboxylase large chain
	13	42	gi|124360830	A.AFRVSPQPGVPAEE.A	ribulose biphosphate carboxylase large chain
	13	43	gi|355496709	A.AFRVSPQPGVPAEE.A	ribulose biphosphate carboxylase large chain domain protein
1976.02434	11	29	gi|355501329	N.NKNNPNLFNNLVYTPLT.I	basic 7S globulin-like protein
	11	30	gi|87240526	N.NKNNPNLFNNLVYTPLT.I	Peptidase A1, pepsin
	11	31	gi|357512051	N.NKNNPNLFNNLVYTPLT.I	Basic 7S globulin

Figures

Figure 1

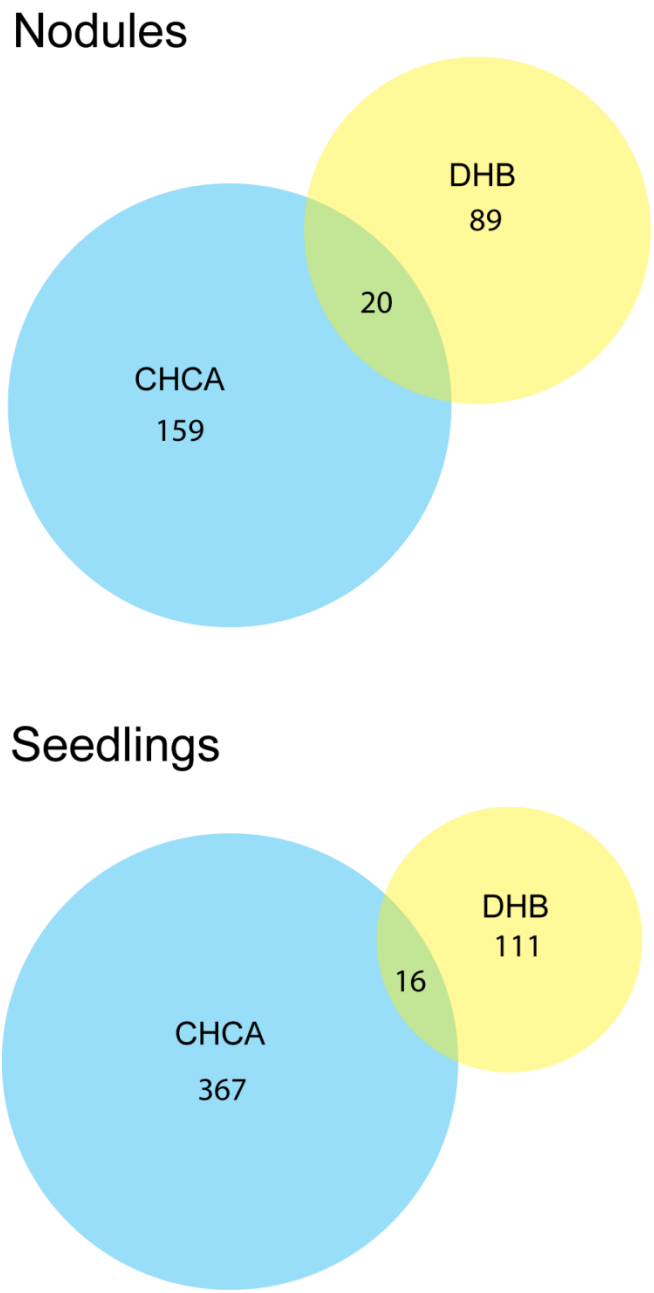

Figure 1. Comparison of the numbers of endogenous peptides detected using either CHCA or DHB as MALDI matrices in both mature Medicago roots/ root nodules and seedling roots.

Figure 2

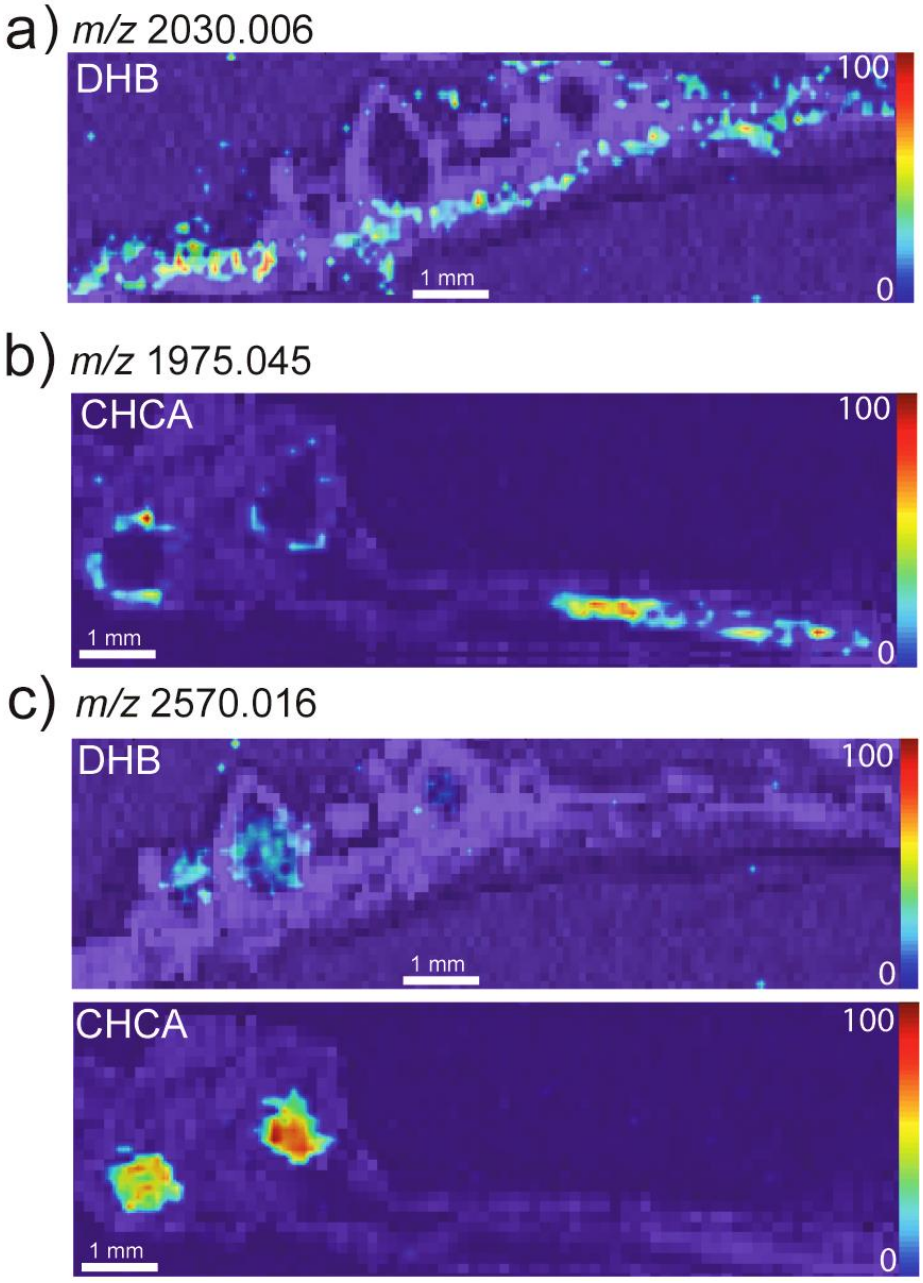

Figure 2. Representative images of putative peptides detected with CHCA and/ or DHB matrices in the mature Medicago roots and root nodules showing different spatial distributions throughout the root and nodule portions of the plant. a) *m/z* 2030.006 was only detected using DHB as the matrix and is localized to the plant root. b) *m/z* 1975.045 was only detected using CHCA as the matrix and is localized to the plant root and outer portion of the nodules. c) *m/z* 2570.016 was detected using both DHB and CHCA as the matrix and is localized to the nodules. Intensity scale = high (red) to low (blue).

Figure 3

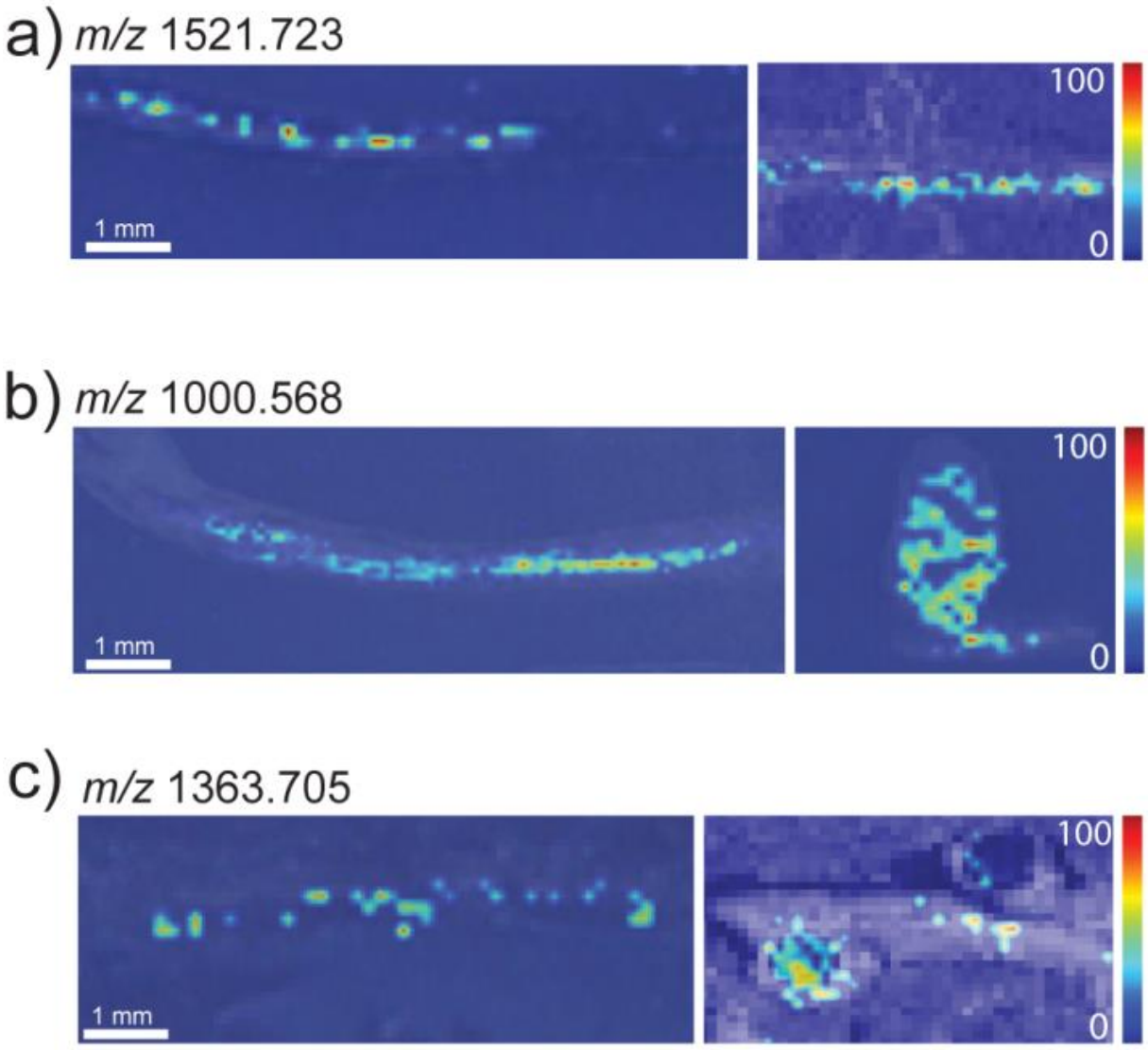

Figure 3. Representative putative peptide images showing distinct distribution patterns in the Medicago seedlings and the mature roots and root nodules. a) *m/z* 1521.723 shows a similar distribution pattern in both the seedlings to the mature plants. b) *m/z* 1000.568 and c) *m/z* 1363.705 represent two of the detected peptides that show a shift in their localization from the root to the root nodules as they develop into older plants.

Figure 4

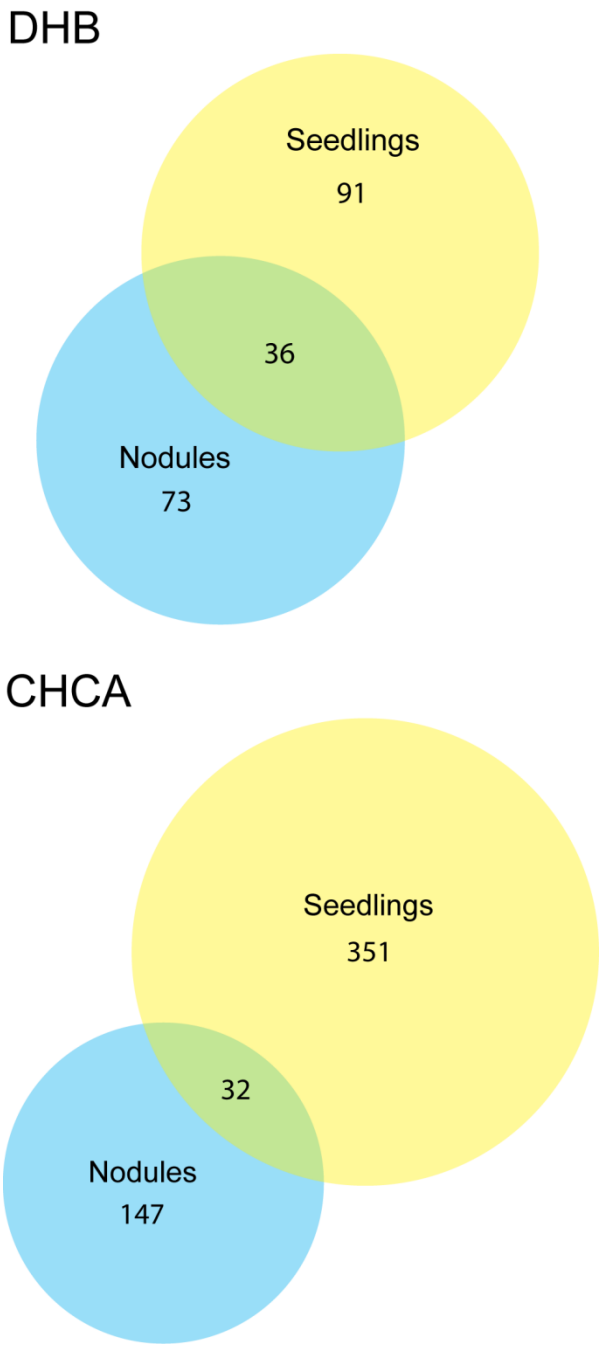

Figure 4. Comparison of the endogenous peptides detected in Medicago roots at different stages of development. The diagrams show the numbers of peptides present uniquely in the young seedlings compared to the mature plants, as well as the number of detected peptides that are present at both stages of development. The results are shown for the peptides detected using both the DHB and CHCA matrices.

Figure 5

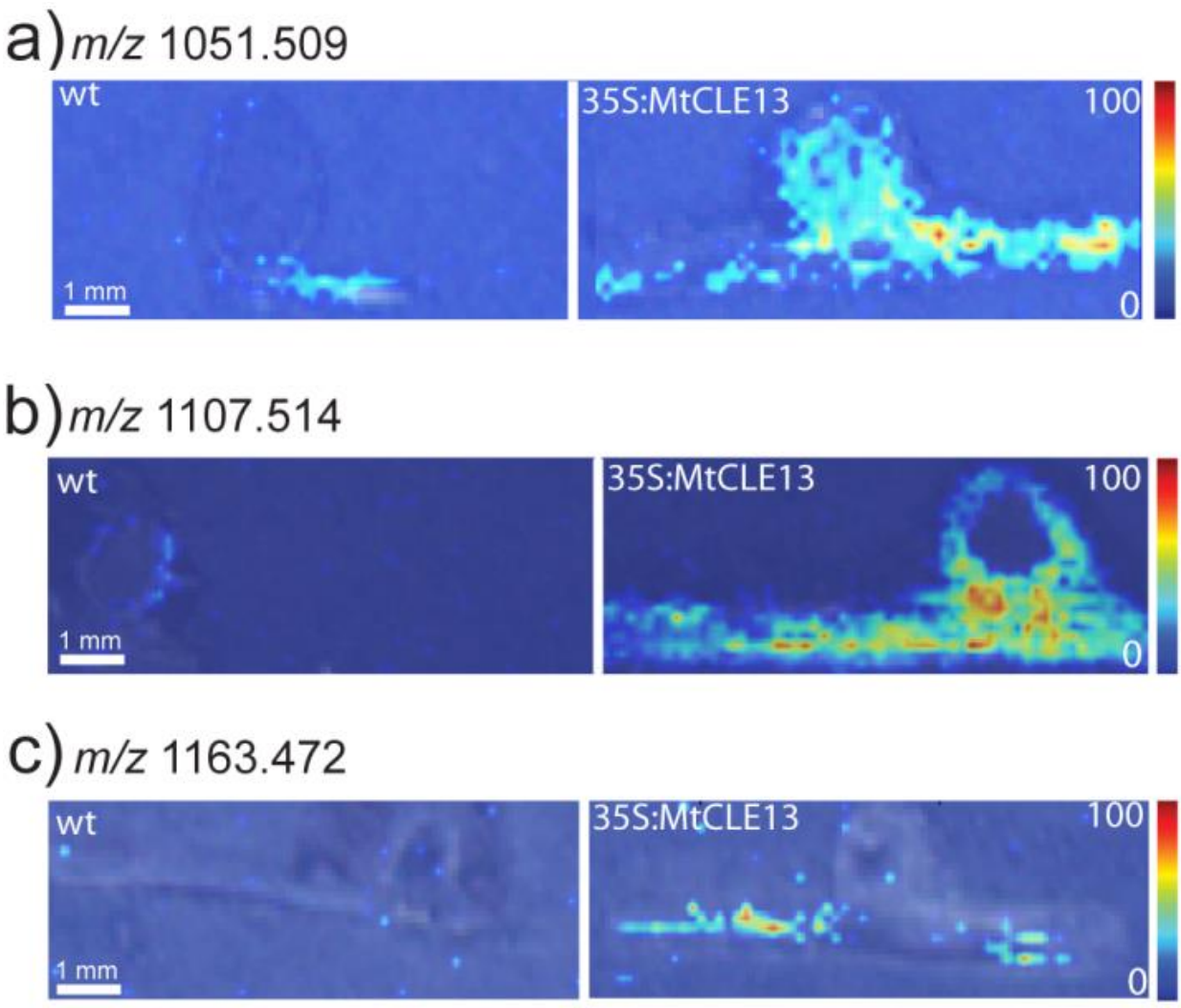

Figure 5. Putative peptides that were detected in the 35S:MtCLE13 plants (demonstrating over-expression of CLAVATA3/endosperm-surrounding region (CLE) peptides), but are present in much lower concentrations in the wt plants. a) *m/z* 1051.509 is located in both the plant root and nodule. b) *m/z* 1107.514 is distributed to the plant root and outer nodule. c) *m/z* 1163.472 is localized to the plant root.

Figure 6

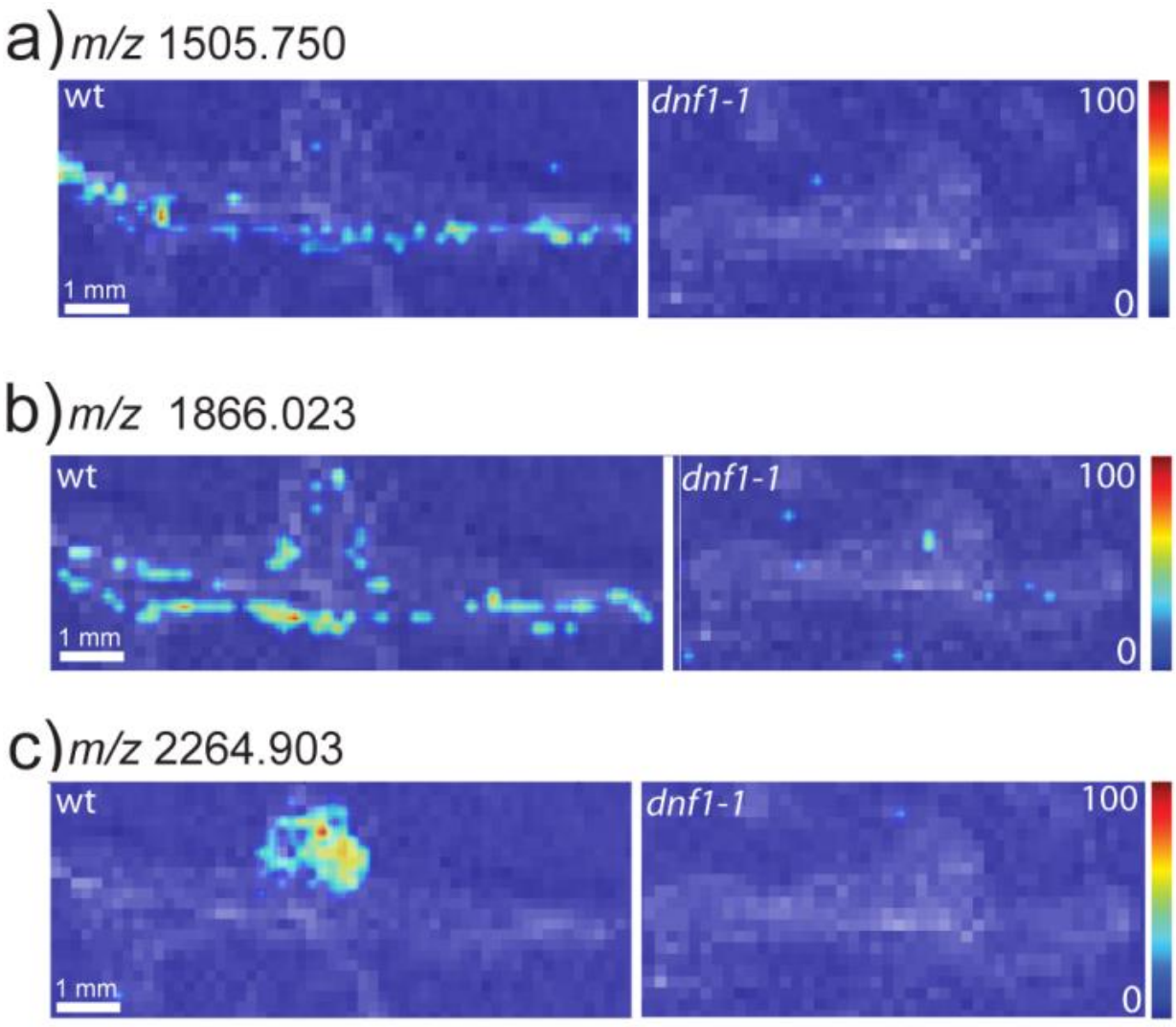

Figure 6. Putative peptides that were detected in the wt plants but were absent from the *dnf1-1* plants. *dnf1-1* mutants develop stunted, non-functional nodules, suggesting that these putative peptides may play a role in nodule development or function. a) *m/z* 1505.750 is localized to the root. b) *m/z* 1866.023 is distributed to the plant root and outer nodule. c) *m/z* 2264.903 is localized to the plant nodule.

Figure 7

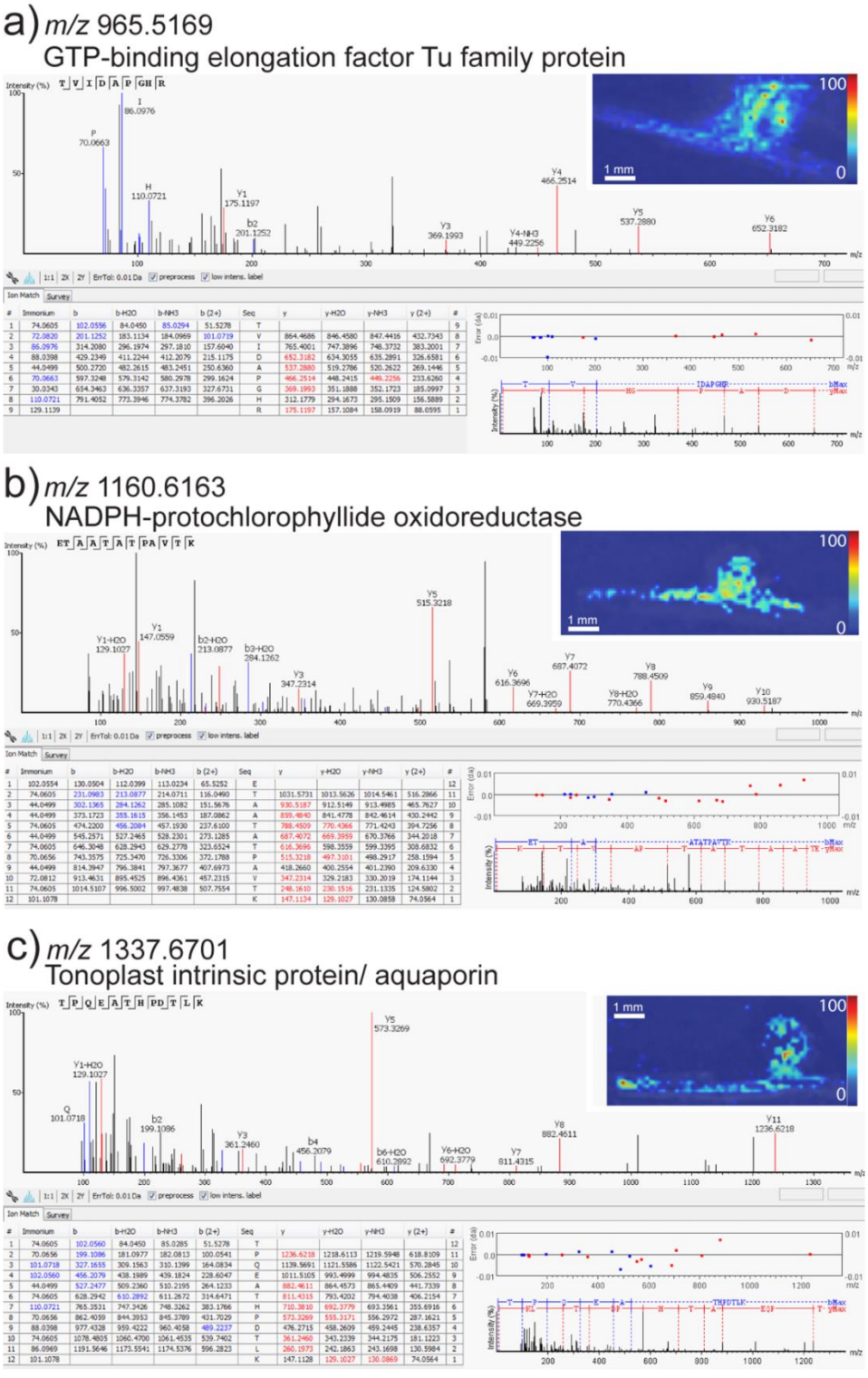

Figure 7. Example images and corresponding LC-MS/MS spectra unique peptides of known Medicago proteins. The MS/MS with annotated *de novo* sequencing, the predicted protein, and the corresponding MS image are shown.

Supporting Information

DHB Nod Summary

09-30-15_DHB_CLE
09-30-15_DHB_wt
11-21-14_DHB_wt1
11-21-14_DHB_wt2
122815_DHB_CLE1
122815_DHB_wt1
122815_DHB_CLE2
122815_DHB_wt2
030615_DHB_dnf1
030615_DHB_wt1
030615_DHB_dnf2
030615_DHB_wt2
012615_DHB_wt1
012615_DHB_wt2
012615_DHB_wt3

m/z	**Description**
905.45371	wt root
909.42962	CLE nod
909.43346	CLE root, wt nod
909.43396	CLE root, wt nod
911.44556	CLE all
911.44811	CLE root, wt nod
911.44866	CLE root, wt nod
915.25511	root
915.25522	root
919.43210	wt root
921.44493	root
921.44556	all over
921.44576	all over
921.44603	CLE all, wt root
921.44712	strong wt
921.44724	wt all
931.22969	root
931.22989	root
935.42472	root
937.41976	all over
937.41979	root
937.42226	all over
937.42233	all over
938.42603	CLE root, wt all
944.37325	wt nod
947.49772	CLE root
947.49785	CLE nod, wt root
947.49961	all over
947.49983	all over
949.51435	wt root
949.51819	wt
951.40134	CLE root
951.49516	root
951.49520	root
959.57074	CLE root
959.57345	wt nod
959.57379	wt nod
960.34865	wt nod
961.24220	CLE root
963.47309	CLE root
963.48679	CLE all, wt root
963.49143	root
965.50828	all over
965.50845	all over
965.50847	all over
965.50864	all over
965.51231	all over
965.51242	all over
967.47052	CLE root
967.47066	CLE root
967.51683	strong wt
967.51728	all over
975.54434	CLE all, wt nod
975.54750	CLE root, wt nod
975.54779	CLE root, wt nod
978.35717	CLE nod
978.35779	nod, stronger CLE
979.49012	wt all
981.48233	all over
981.48255	CLE all, wt root
981.48268	all over
981.48311	all over
981.48512	all over
981.48529	all over
981.52092	all over
981.52464	CLE root, wt nod
991.52401	CLE root
991.52448	CLE nod, wt root
991.52755	all over
991.52780	all over
992.53075	all over
993.50336	CLE nod, wt root
993.50346	root
995.48486	nod, stronger wt
997.49955	all over, stronger CLE
1000.57049	CLE root, wt nod
1000.57078	CLE root, wt nod
1007.49851	CLE root
1007.50023	CLE root, wt nod

1007.50039	root
1009.47738	CLE root
1011.47117	outer nod
1011.47969	root
1011.48034	root
1012.47610	root
1017.31983	all over
1019.43846	CLE all
1023.28087	CLE root, wt nod
1025.55187	CLE root, wt nod
1025.55202	CLE root, wt nod
1027.45149	CLE root
1027.45158	root
1027.45377	CLE root
1027.45385	CLE root
1033.41633	wt nod
1051.50890	root
1051.50901	root
1051.50902	CLE all, wt root
1051.50903	CLE all, wt root
1067.48276	CLE all
1069.58125	CLE root, wt nod
1091.53768	all over
1091.53886	root and outer nod
1091.53967	all over
1091.54018	all over
1091.54019	CLE all, wt root
1091.54091	all over
1091.54190	all over
1091.54256	all over
1107.51126	nod
1107.51236	all over
1107.51372	CLE all
1107.51399	CLE all
1107.51406	CLE nod, wt all
1107.51440	nod
1107.51782	all over
1107.51804	all over
1113.60531	CLE root, wt nod
1127.56554	CLE All, wt nod
1127.56585	all over
1143.53872	CLE All, wt nod
1143.53893	CLE All, wt nod
1145.47039	CLE all
1145.47546	CLE All, wt nod
1145.47562	CLE All, wt nod
1146.60289	nod
1157.63142	CLE root, wt nod
1160.62974	CLE root, wt nod
1160.62980	CLE All, wt nod
1163.47245	CLE root
1176.60309	CLE root, wt nod
1176.60311	CLE root, wt nod
1177.54318	root
1177.54343	root
1193.51432	CLE root
1193.51783	CLE root, wt all
1193.51807	CLE root, wt all
1227.39381	CLE root
1261.75706	CLE nod
1285.70201	CLE root
1287.69612	root
1299.71079	CLE all
1299.71100	CLE nod
1299.71483	CLE root, wt nod
1299.71484	CLE root, wt all
1321.69308	CLE nod
1321.69318	CLE root
1321.69928	all over
1321.69958	all over
1331.53774	CLE root
1337.66675	CLE all
1337.67169	CLE All, wt nod
1337.67187	CLE All, wt nod
1363.70483	nod
1379.68436	wt nod
1407.58590	CLE root
1505.75036	wt root
1521.72035	wt root
1521.72103	wt root
1537.10356	nod
1538.11900	CLE root, wt nod
1540.12927	nod
1542.14704	nod
1542.14806	nod
1545.16533	nod
1564.12947	nod
1564.13051	nod
1566.14338	nod
1572.19452	nod
1586.21014	nod
1678.65341	wt nod
1866.02347	wt all
1866.02589	wt all
1953.05613	all over
1953.05638	all over
1953.05770	wt all, dnf root
1953.05880	wt all, dnf root
1976.04051	root
1976.04459	wt all
1991.01132	all over
1991.01534	all over
1992.01645	wt nod

2012.99663	wt root
2030.00632	wt root
2068.08281	all over
2068.08420	all over
2068.08728	wt nod
2107.08548	all over
2107.08605	all over
2107.08735	wt all, dnf root
2107.08855	wt nod, dnf root
2233.78493	wt nod
2233.81475	wt nod
2249.75860	wt nod

2249.76902	wt nod
2249.78026	wt nod
2264.90327	wt nod
2532.04850	wt nod
2532.04897	wt nod
2532.04980	wt nod
2532.06232	nod
2532.06496	nod
2554.03065	wt nod
2554.03217	wt nod
2555.03374	wt nod
2570.00283	wt nod
2570.00499	wt nod
2571.02264	nod

2592.98809	wt nod
2646.09037	wt nod
2646.09048	wt nod
2646.09154	wt nod
2646.10747	nod
2668.07304	wt nod
2669.07720	wt nod
2684.04706	wt nod
2964.37627	wt root
3292.52259	wt root
3468.47224	wt outer nod
3589.12967	wt nod

DHB Seedling Summary

11-07-14_DHB_wt_6h
11-07-14_DHB_wt_48h
11-11-15_DHB_wt
11-11-15_DHB_CLE
12-13-15_DHB_CLE1
12-13-15_DHB_wt1
12-13-15_DHB_CLE2
12-13-15_DHB_wt2
12-13-15_DHB_CLE3
12-13-15_DHB_wt3
12-13-15_DHB_CLE4

m/z	**Description**
900.71596	CLE
902.92682	CLE
902.92801	both
902.93171	CLE
905.44420	both
905.44685	both
905.44933	mid vein
905.44990	
908.65253	both
908.65319	mid vein
908.65338	both
909.42667	both
909.42674	both- mid vein
909.42804	both mid vein
909.43010	
909.43032	
909.43035	both
909.43065	mid vein
909.43144	both- mid vein
909.43148	both- mid vein
909.53073	
909.53183	
911.44272	both
911.44344	both- mid vein
911.44447	both mid vein
911.44683	
911.44739	mid vein
911.44753	both
911.44804	both- mid vein
911.65525	CLE
912.45114	both- mid vein
913.67114	CLE
917.60231	both- mid vein
917.60232	both
917.70354	CLE
919.42626	Both
919.42653	both
919.42933	
919.43118	
919.43118	mid vein
921.43758	both
921.44182	both
921.44480	
921.44616	
935.40113	both
935.40132	both
935.40351	
935.40508	wt
935.40602	mid vein
935.40675	
935.40703	CLE
937.34169	mid vein
937.41727	both
937.41734	both
937.41860	both
937.41955	
937.42107	both
937.42154	
937.42209	mid vein
937.42263	CLE
937.58683	
944.93378	both
944.93396	both
947.49972	
949.38562	mid vein
949.51509	mid vein
951.43845	both
951.95937	
953.56241	wt
955.57852	wt
958.51474	wt
958.51625	wt
959.57099	
959.57184	
959.57187	both- mid vein
959.57246	
960.90795	CLE
960.90820	CLE
960.91291	
960.91374	CLE
960.91378	CLE
963.48847	wt
963.48928	wt
963.49439	
965.50486	both
965.50487	both
965.50750	
965.50980	mid vein
965.51102	
967.51138	wt
972.53249	CLE
972.53684	mid vein
972.53710	both
972.53786	both- mid vein
975.54152	both
975.54382	both
975.54543	
975.54551	both
975.54554	
975.54629	mid vein
975.54630	
975.54652	both- mid vein
975.54693	both- mid vein
979.46530	both
979.46679	both
979.47055	
979.47059	
981.47919	both
981.48218	

981.48416	
981.48432	mid vein
982.48275	both
982.89930	both
982.89952	both
982.90121	both
982.90441	
982.90461	both
984.48887	mid vein
984.59077	CLE mid vein
984.59346	mid vein
984.59425	both- mid vein
984.59426	both- mid vein
991.52420	
992.41762	
995.45879	both
995.45908	both
995.46391	
995.47864	
995.50154	
997.47501	both
997.47530	both
997.48012	
998.48323	
1000.56208	CLE
1000.56454	CLE mid vein
1000.56564	both
1000.56788	both- mid vein
1000.56797	mid vein
1000.56810	both- mid vein
1002.22815	wt
1007.51930	wt
1012.46307	
1013.50337	CLE
1013.50855	mid vein
1014.40043	
1019.43479	wt
1019.44027	CLE
1019.44078	
1019.44170	
1022.56524	both
1022.56543	wt
1022.57055	
1030.36759	both
1030.36801	both- outer
1030.37092	
1030.37326	
1030.37334	both
1030.37426	
1049.49103	wt
1051.45690	CLE mid vein
1051.45938	CLE
1051.46475	mid vein
1051.50501	wt
1051.50540	wt
1051.50686	wt
1051.50827	
1051.50952	wt
1051.51058	
1051.51089	
1061.44992	wt
1061.45278	
1065.46380	both
1065.46832	wt
1065.46960	
1067.47908	both
1067.47963	both
1067.48169	wt
1067.48277	
1067.48348	wt
1067.48379	
1067.48499	
1068.61066	wt
1069.48942	wt
1081.50041	wt
1081.50143	
1089.46581	wt
1091.54198	
1091.54379	
1095.53593	
1098.94989	CLE
1106.56726	wt
1107.51563	
1107.51600	
1107.51618	
1107.53347	
1108.56474	both
1108.56604	both
1108.57152	
1111.49579	wt
1113.48474	both- strong CLE
1113.48556	CLE mid vein
1113.49057	
1113.49085	CLE
1113.49127	
1114.49466	CLE
1119.58418	both
1127.46978	wt
1127.47026	wt
1129.48665	both
1129.48683	both
1137.59446	
1137.59528	
1138.63868	both- mid vein
1138.64050	both
1138.64251	both
1138.64439	both- mid vein
1138.64448	mid vein
1138.64485	both
1143.53408	mid vein
1149.62609	both mid vein
1149.62635	both- mid vein
1149.62801	both
1149.63090	both
1149.63136	
1149.63237	both
1149.63250	mid vein
1149.63311	both- mid vein
1151.64611	
1151.64676	
1160.62150	both- mid vein
1160.62275	both mid vein
1160.62514	both
1160.62672	mid vein
1160.62701	both- mid vein

1160.62713	both- mid vein
1171.61381	both
1171.61494	both- mid vein
1171.61541	both- mid vein
1176.59406	CLE
1176.60003	both- mid vein
1176.60041	mid vein
1176.60118	both- mid vein
1177.54419	
1187.58140	both mid vein
1187.58235	both- mid vein
1187.58420	both mid vein
1187.58659	both
1187.58806	mid vein
1187.58854	both
1187.58902	both
1193.51875	
1199.48477	both
1199.48708	both
1199.48871	
1199.49085	
1199.49178	
1209.50869	wt
1209.56698	both mid vein
1209.56918	both
1209.57006	mid vein
1209.57063	both- mid vein
1209.57106	both- mid vein
1213.47108	both
1225.54008	both mid vein
1225.54140	both
1225.54413	mid vein
1225.54437	both- mid vein
1225.54525	both- mid vein
1233.71999	both- mid vein
1233.72003	both mid vein
1233.72259	both mid vein
1233.72531	
1233.72566	both
1233.72575	
1233.72604	mid vein
1233.72625	both- mid vein
1233.72685	both- mid vein
1247.73508	both mid vein
1247.73534	both- mid vein
1247.73839	both
1247.74025	both
1247.74099	
1247.74122	
1247.74186	both- mid vein
1247.74227	both- mid vein
1247.74261	mid vein
1261.75094	both mid vein
1261.75100	both- mid vein
1261.75296	both
1261.75583	
1261.75605	both
1261.75624	
1261.75661	
1261.75766	mid vein
1261.75767	both
1261.75837	
1261.75837	both- mid vein
1263.77110	
1264.77501	
1269.72323	both
1271.67493	both mid vein
1271.67570	both- mid vein
1271.67928	both
1271.68111	both
1271.68224	both- mid vein
1271.68255	mid vein
1271.68346	both- mid vein
1275.54364	CLE
1275.77202	
1275.77224	both
1275.77323	both- mid vein
1283.73309	both mid vein
1283.73386	both- mid vein
1283.73561	both
1283.73865	both
1283.73919	
1283.73998	both- mid vein
1283.74036	mid vein
1283.74051	both- mid vein
1285.69102	both- mid vein
1285.69196	both mid vein
1285.69655	both
1285.69813	mid vein
1285.69917	both- mid vein
1291.53900	both
1291.53934	both
1293.66449	both- mid vein
1299.70684	both mid vein
1299.70684	both- mid vein
1299.70898	both
1299.71141	both
1299.71187	
1299.71251	
1299.71367	both- mid vein
1299.71371	mid vein
1299.71429	both
1299.71510	
1301.68690	CLE
1301.69529	mid vein
1305.71854	both
1305.71941	
1305.72197	both- mid vein
1305.72256	both- mid vein
1307.68204	both- mid vein
1309.63617	both
1309.63835	mid vein
1313.72510	both
1313.72733	both- mid vein
1313.72806	both- mid vein
1321.68913	both- mid vein
1321.68932	both mid vein
1321.69160	both
1321.69436	both
1321.69576	both- mid vein
1321.69623	mid vein
1321.69659	both- mid vein
1323.65582	both
1323.65906	both- mid vein
1331.52653	CLE
1331.53376	mid vein

1337.66222	both mid vein
1337.66245	both- mid vein
1337.66497	both
1337.66768	both
1337.66917	mid vein
1337.66928	both- mid vein
1337.66994	both
1339.65109	

1341.71402	both- mid vein
1341.71739	both
1341.72208	mid vein
1341.72265	both- mid vein
1341.72273	both- mid vein
1341.72280	both
1359.65056	both mid vein
1359.65066	mid vein

1359.65164	both- mid vein
1363.70578	both
1379.67803	both
1379.67978	mid vein
1483.77094	mid vein
1521.72595	mid vein
2275.59516	

CHCA Nod Summary

093015_CHCA_CLE
093015_CHCA_wt
013015_CHCA-wt
122815_CHCA1_CLE
122815_CHCA1_wt
122815_CHCA2_CLE
122815_CHCA2_wt

m/z	**Description**
905.27949	all over
907.99887	CLE root
907.99982	wt root
908.99663	both
908.99689	all over
908.99779	CLE
909.43146	CLE
909.43175	CLE
911.44726	CLE
911.94651	CLE mid vein
912.45050	CLE root
915.01653	CLE root/ outer nod
921.44698	wt
922.26332	CLE root
930.99076	CLE root
931.22900	CLE mid vein
935.28942	all over
935.29014	all over
939.60615	CLE root
941.27895	CLE root
946.96358	CLE mid vein
952.97447	CLE root
959.57414	CLE root
965.30010	all over
965.30101	all over
965.51004	wt
965.51037	wt
968.94759	CLE mid vein
970.63812	CLE root
977.96697	CLE root
982.17266	CLE nod
983.54802	nod
983.54867	nod
984.59034	nod/ nod root
984.59357	CLE all, wt root
984.59423	CLE all, wt root
984.59621	all over
985.56315	wt nod
985.56335	wt nod
986.55181	CLE
986.55431	CLE
987.57958	wt nod
993.94137	CLE mid vein
998.14924	CLE nod
1000.56811	CLE
1000.56978	nod/ nod root
1000.57052	all over
1000.57056	nod
1007.31022	both root
1009.91724	CLE mid vein
1013.59499	wt nod
1014.12594	CLE nod
1014.58617	CLE
1037.32191	all over
1063.02843	CLE root/ outer nod
1064.56084	wt nod
1064.56097	wt nod
1072.64620	CLE root
1072.92354	CLE root
1085.00788	CLE root
1088.89524	CLE root
1091.54165	both
1091.54226	Stronger wt
1097.34344	all over
1097.34449	all over
1107.00161	CLE root
1120.02593	CLE root/ outer nod
1122.97240	CLE mid vein
1135.99861	CLE root
1142.01714	CLE root/ outer nod
1146.47916	CLE root
1157.98871	CLE mid vein
1160.62653	CLE all, wt root
1160.62701	CLE all, wt root
1160.62899	all over
1160.62934	all over
1173.96195	CLE mid vein
1176.60063	CLE
1176.60708	CLE
1180.61188	CLE
1196.58370	CLE
1239.63600	wt nod
1321.69539	CLE
1321.69633	CLE
1337.66939	CLE
1343.67995	wt root, CLE root/ nod
1343.68076	wt nod root/ CLE stronger
1346.70312	CLE root
1500.97561	root
1504.10552	root
1505.46938	root
1510.12290	root
1516.13978	root
1535.48063	root
1538.11989	root
1540.50628	root
1547.48055	root
1565.48932	root
1571.47699	root
1589.48917	root
1607.50088	root
1613.48829	root
1625.51279	all over
1643.52412	all over

1655.49955	root
1658.06968	root
1667.52190	root
1674.04080	root
1685.53389	root
1696.02562	root
1697.51185	root
1722.61277	nod root
1753.16568	nod
1757.55553	all over
1799.56556	root
1817.55496	root
1829.57796	root/ outer nod
1859.56384	root
1866.65460	nod root
1871.58747	root
1889.59765	root
1925.69357	nod root
1931.60701	root
1965.19358	nod
1967.63113	root
1975.04534	mid vein/ outer nod
1979.60721	root
1991.01723	mid vein/ outer nod
1997.02685	mid vein/ outer nod
1997.61893	root
2003.62574	root
2021.62440	root
2039.62955	root
2063.63686	root
2069.73374	nod root
2087.74661	nod root
2103.71967	nod root
2105.63868	root
2153.68091	root
2183.67133	root
2195.69154	root
2225.68554	root
2233.80347	nod root
2233.80485	wt root
2249.77725	nod root
2249.78068	nod
2249.78728	nod
2250.78109	wt root
2267.69640	root
2327.73404	root
2345.73253	root
2363.73556	root
2405.74720	root
2429.74668	root
2447.75827	root
2459.77876	root
2465.33535	root
2471.75558	root
2481.32286	root/ outer nod
2487.31755	root
2513.76515	root
2533.07623	nod
2554.06783	nod
2570.02774	nod
2591.81145	root
2592.01209	nod
2614.99436	nod
2630.96571	nod
2646.11694	nod
2669.11038	nod
2676.82166	root
2684.07213	nod
2706.05571	nod
2723.86012	root
2772.86961	root
2795.87000	root
2813.87751	root
2855.89230	root
2934.91883	root
2939.94784	nod root
3018.94420	root
3102.00139	nod root
3118.97878	nod root
3119.98279	root
3137.98022	root
3180.99323	root
3221.99832	root
3223.00307	root
3253.03224	root
3264.04920	nod root
3280.02740	not root
3300.03199	root
3342.04044	root
3384.05734	root
3426.09839	nod root
3442.07760	nod root
3469.07411	root
3588.15265	nod root
3605.13414	nod root/ outer nod
3631.12717	root
3668.15346	root
3673.13875	root
3708.15508	root
3750.18024	root
3792.17407	root
3835.19107	root
3876.19934	root
3913.24900	root
3919.20994	root

CHCA Seedling Summary

120815_CHCA_CLE1
120815_CHCA_wt1
120815_CHCA_CLE2
120815_CHCA_wt2
121315_CHCA_CLE1
121315_CHCA_wt1
121315_CHCA_CLE2
121315_CHCA_CLE3
121315_CHCA_wt3
121315_CHCA_CLE4
121315_CHCA_wt4

m/z	**Description**
900.03985	
900.03989	
900.04102	
900.04279	
900.04469	
900.04474	
900.04497	
900.04523	
900.71890	
901.20380	
901.20404	
903.22058	
903.22084	
906.28645	
906.97544	
906.98021	
906.98037	
906.98046	
906.98049	
908.08555	
908.08557	
908.08577	
908.09039	
908.09042	
908.09067	
908.65364	CLE
908.94437	
908.94950	
908.95426	
908.99100	
908.99537	
908.99568	
908.99598	
908.99600	
908.99608	
908.99618	
908.99704	
909.08903	wt
911.94349	
912.98468	
912.98494	
912.98959	
912.98993	
913.10992	wt
913.99107	
915.00996	
915.01003	
915.01415	
915.01494	
915.01507	
915.01520	
915.01528	
915.01588	
915.02008	
916.98915	
916.98937	
917.00573	
919.15439	CLE
920.24957	
921.02272	
922.26190	
922.26352	
924.05836	
924.05838	
924.05947	
924.06340	
924.06340	
924.06360	
924.06364	
926.97770	CLE
926.97773	
929.08299	wt
930.97264	
930.97281	
930.98405	
930.98651	
930.98759	
930.98823	
930.98922	
930.98943	
930.98950	
930.98994	
930.99004	
930.99411	
931.99351	
932.96131	
932.96167	
932.96183	
932.98409	
933.05300	
933.05324	
933.96355	
933.96862	
933.96891	
936.22142	
936.30123	
936.95730	
936.99583	
936.99740	
938.23397	
938.23723	
938.23747	
938.23794	
938.23894	
938.24243	
940.12036	wt mid vein
941.15479	
941.15861	
941.15875	CLE
942.94524	

942.95066	
942.95068	
942.95079	CLE
946.01558	
946.05923	
946.18733	CLE
946.94502	
946.95618	
952.97019	
955.02680	
955.02704	
956.09467	wt mid vein
956.56304	wt mid vein
957.08750	wt
958.91890	
958.92447	CLE
958.92464	CLE
958.97641	
958.97753	
959.98162	CLE
960.21588	
960.21595	
960.21779	
961.98842	
961.98850	
961.98878	
961.99390	
961.99396	
961.99417	
961.99420	
963.13522	CLE
963.13915	CLE
963.49507	wt
963.49668	wt
963.49678	wt
965.50936	
965.50944	
965.50965	
965.51159	
965.51191	
965.51477	
965.51485	
965.51506	
965.51507	
966.26935	
966.27430	
968.06992	
968.07026	
968.62075	
968.62307	
970.57854	wt
972.53491	mid vein
972.53622	CLE mid vein
972.53682	
972.53730	
972.54065	mid vein
973.06393	wt
974.95080	
974.95250	
976.18865	
976.19398	
976.19429	
977.95968	
977.96393	
977.96483	
977.96529	
977.96533	
977.96542	
977.96547	
977.96643	
979.10481	
979.11022	
979.11034	CLE
979.96687	CLE
980.11424	CLE
984.37065	mid vein
984.59113	mid vein
984.59265	mid vein
984.59308	mid vein
984.59393	
984.59467	
984.59472	
984.59616	mid vein
984.59631	mid vein
984.59633	mid vein
984.59692	
984.59714	mid vein
986.55155	
988.08911	
991.04654	
991.04681	
991.52691	wt
991.52700	
992.98239	
993.92303	
993.93481	
993.93499	
993.94063	
993.94077	
995.30910	wt mid vein
998.15058	CLE
998.15072	
999.93389	
999.93393	
999.93417	
999.93987	
1000.56742	mid vein
1000.56746	mid vein
1000.56783	
1000.56790	mid vein
1000.56841	
1000.56853	
1000.56944	
1000.57003	mid vein
1000.57321	
1000.57329	mid vein
1000.57330	mid vein
1002.37947	mid vein
1002.38049	mid vein
1002.38200	CLE mid vein
1003.05899	
1003.05914	
1004.16998	CLE
1004.17520	
1006.02347	
1006.02907	

1006.02957	
1007.30936	wt
1008.08221	wt
1008.33030	mid vein
1009.89224	
1009.89233	
1009.89252	
1009.89826	
1009.89831	
1013.02721	
1013.02750	
1014.10034	
1014.12443	
1014.12467	CLE
1014.12655	CLE
1014.40520	CLE mid vein
1015.13163	CLE
1015.40345	mid vein
1015.40404	mid vein
1015.90831	
1015.90834	
1015.90856	
1015.91412	
1015.91439	
1015.91444	
1018.04031	
1019.02870	
1019.02877	
1019.03102	
1019.03451	
1019.03483	
1020.14159	
1020.14187	
1020.14385	CLE
1020.14396	
1020.14740	
1020.14775	
1020.20498	
1020.20569	CLE
1021.02857	
1021.92287	
1021.92862	
1021.92898	
1022.09984	
1022.10161	
1022.10180	
1022.10224	
1022.20518	
1024.30354	CLE mid vein
1024.30427	CLE mid vein
1025.05864	
1025.09569	wt
1026.06320	
1027.99775	
1027.99952	
1028.14607	
1028.93149	
1028.93747	
1028.93768	
1029.00594	
1030.07304	
1030.07330	
1030.07335	
1030.37394	mid vein
1030.37409	mid vein
1030.37485	mid vein
1031.07707	
1031.07971	
1031.38047	mid vein
1031.88041	
1031.88624	
1031.88654	
1031.88661	
1032.37850	mid vein
1034.01257	
1034.01825	
1034.01859	
1034.94884	
1034.94899	
1034.95334	
1034.95488	
1034.95492	
1034.95512	
1034.95567	
1035.01773	**wt**
1035.01801	
1036.11321	
1036.11506	
1036.11935	CLE
1036.11940	
1036.11949	
1037.12172	
1037.89841	
1037.89846	
1037.89981	
1037.90449	
1038.07415	
1038.07516	
1038.07637	
1039.07699	
1039.08027	
1040.02996	wt
1040.96831	
1040.97035	
1041.04403	
1041.04411	CLE
1041.04435	
1041.06990	
1041.97454	CLE
1044.90646	
1044.90647	
1044.90837	
1044.91250	
1044.91255	
1044.91276	
1044.91282	
1046.04471	wt
1047.05059	
1047.05361	
1049.04808	
1049.98429	
1049.99019	
1049.99046	
1049.99049	
1049.99067	
1050.92316	

1050.92349	
1050.92708	
1050.92931	
1050.92936	
1050.92944	
1050.92956	
1050.92966	
1050.92994	
1050.99343	
1051.92764	
1051.98554	wt
1052.35580	mid vein
1052.35592	mid vein
1052.35658	mid vein
1052.35979	mid vein
1052.36021	CLE mid vein
1053.87032	
1055.05356	
1056.00074	
1056.00567	wt
1056.00598	
1056.00606	
1056.01173	
1056.01216	
1056.01223	
1056.93997	
1056.94161	
1056.94457	
1056.94635	
1056.94646	
1056.94726	
1056.95266	
1059.07183	
1063.01494	
1063.01521	
1063.02116	
1063.02392	
1065.96061	
1065.96065	
1065.96083	
1065.96687	
1065.96711	

1066.07575	
1066.07578	
1066.89756	
1066.90113	
1066.90147	
1066.90722	
1066.90740	
1066.90766	
1066.90779	
1068.33009	mid vein
1068.33055	mid vein
1068.33225	mid vein
1068.33273	mid vein
1068.33341	CLE mid vein
1069.03068	
1069.03143	
1069.03230	
1069.03699	
1071.97483	
1071.98104	
1071.98134	
1071.98155	
1072.64742	
1072.91667	
1072.91691	
1072.91847	
1072.91938	
1072.92299	
1072.92326	
1072.92330	
1075.04423	wt
1075.05071	
1082.05222	
1082.05253	
1084.05557	
1084.06156	
1085.00001	
1085.00623	
1085.00655	
1085.00657	
1085.00677	
1087.94929	

1088.89150	
1088.89177	
1088.89209	**CLE**
1088.89396	
1089.07627	
1091.01936	
1091.01941	
1091.02010	
1091.02589	
1091.02590	
1091.02613	
1091.02618	
1096.97188	
1097.12320	
1097.12347	
1098.02979	
1098.03009	
1098.03030	
1098.03209	
1100.97748	
1100.97749	
1100.97774	
1100.98403	
1100.98404	
1100.98430	
1101.98556	
1104.04769	
1104.04792	
1105.05066	
1105.05381	
1106.99171	
1106.99822	
1106.99838	
1106.99851	
1106.99866	
1106.99873	
1107.00537	
1109.37443	
1109.37470	
1110.05923	
1110.06583	
1110.06583	

1110.06590	
1110.06600	
1110.06620	
1110.63922	
1112.94262	
1112.94267	CLE
1113.09695	
1113.09696	
1113.09718	
1118.70198	
1120.01760	
1120.02146	
1120.02433	
1120.02435	
1120.02464	
1120.02466	
1120.02492	
1122.96864	
1122.96870	
1122.96891	
1123.01863	
1123.02540	
1126.03165	
1126.03833	
1126.03841	
1126.03869	
1126.03877	
1126.03881	**CLE**
1126.04035	
1126.04501	
1126.04551	
1127.03866	
1129.06389	
1129.07039	
1129.07070	
1129.07082	
1129.07089	
1131.97885	
1131.97901	
1132.59567	wt
1132.59894	wt
1135.98949	

1135.99408	
1135.99634	
1135.99651	
1135.99661	
1135.99734	
1135.99770	
1138.00174	
1142.00851	
1142.01051	
1142.01231	
1142.01552	
1142.01566	
1142.01567	
1142.01581	
1142.01607	
1143.01489	
1144.65271	
1144.65460	
1146.13330	wt mid vein
1146.61134	wt
1146.61137	wt
1147.95043	
1147.95060	
1147.95083	
1147.95779	
1147.95792	
1148.02477	
1148.11904	
1157.98540	
1157.98591	
1160.62501	mid vein
1160.62501	mid vein
1160.62647	
1160.62650	mid vein
1160.62722	
1160.62727	
1160.62796	
1160.63207	mid vein
1160.63224	mid vein
1160.63226	mid vein
1160.63233	mid vein
1161.41526	CLE mid vein

1161.41755	CLE
1164.60186	
1164.60202	
1166.05120	
1168.11470	wt
1176.60036	
1176.60093	
1176.60129	
1176.60202	
1176.60655	mid vein
1176.60656	mid vein
1176.60661	mid vein
1177.60606	mid vein
1179.95239	
1179.95267	
1182.02984	
1182.03017	
1182.95977	
1182.95985	
1182.96742	
1182.96748	
1182.97451	
1184.03540	
1184.09031	wt
1190.13899	CLE
1190.13918	
1200.06594	
1203.13418	wt
1203.13435	wt
1204.00189	wt
1204.00939	
1204.00965	
1204.94131	
1204.94163	
1204.94890	
1204.94895	
1204.94923	
1205.94523	
1205.95318	
1206.11131	CLE
1209.07573	
1209.17907	CLE

1209.17910	
1217.04776	
1217.04824	
1219.10501	wt
1219.10578	wt
1219.97424	
1219.98840	CLE
1220.91521	
1220.91523	
1220.91549	
1220.92295	
1220.92297	
1220.92322	
1220.92324	
1225.05921	
1225.15615	CLE
1225.15627	
1225.15646	
1226.93252	
1226.93257	
1226.93287	
1226.94042	
1226.94042	
1226.94069	
1235.08262	wt
1236.88836	
1238.08881	
1239.02702	
1239.02735	
1239.95862	
1239.96654	
1239.96684	
1241.12244	
1241.13018	
1241.13030	
1241.13051	
1242.90832	
1242.90859	
1245.04601	
1245.04640	
1245.98435	
1246.05075	

1252.06270	
1252.06304	
1254.99724	
1254.99747	
1255.92999	
1255.93803	
1255.93807	
1255.93829	
1255.93835	
1256.00518	
1256.93905	
1256.93929	
1256.99809	
1256.99835	
1260.07050	
1260.95495	
1261.00665	
1261.01457	
1261.01484	
1261.01487	
1261.01503	
1261.07379	
1261.94592	
1261.95390	
1261.95411	
1261.95428	
1262.02167	
1262.02194	
1262.03019	
1262.95388	
1267.03286	wt
1267.03312	
1267.97073	
1267.97260	
1274.03916	
1274.03939	
1276.98206	
1276.99008	
1276.99037	
1276.99051	
1277.92204	
1277.92349	

1277.93034	
1277.93062	
1280.06108	
1280.06446	
1283.00225	wt
1283.00228	
1283.01066	CLE
1283.94380	
1283.94426	
1286.07182	
1290.01827	
1290.01861	
1293.07921	
1293.08154	
1296.03439	
1296.03466	
1296.08725	
1296.08749	
1299.92188	
1300.10658	
1300.34632	
1302.04820	wt
1302.04855	CLE
1303.28258	
1303.28284	
1304.42943	
1308.66110	wt mid vein
1309.05429	
1309.05583	
1309.06036	
1309.06071	
1311.32718	wt
1311.33579	
1311.33604	
1312.00039	
1312.00375	
1312.06292	
1313.01477	
1315.07179	
1315.07529	
1315.07556	
1315.07636	

1317.76302	
1318.02578	
1319.25607	
1319.39184	
1319.39216	
1319.39498	
1319.40064	
1320.39755	
1321.08624	
1321.09050	
1321.69568	mid vein
1321.69572	
1321.69664	
1321.69702	
1321.69782	
1321.70287	mid vein
1321.70329	mid vein
1321.70329	mid vein
1321.70334	mid vein
1325.03129	
1325.03160	
1327.70481	
1328.03385	
1328.03503	
1331.04676	
1331.04772	
1331.05512	
1331.05540	
1333.73872	
1333.74062	
1335.36219	
1335.36802	
1335.36821	
1335.36834	
1335.36840	
1335.36841	
1335.37677	
1337.05689	
1337.06325	
1337.06685	
1337.37048	wt
1337.67552	mid vein

1338.30359	
1338.68368	mid vein
1343.01401	CLE
1343.01403	
1343.67502	mid vein
1343.67773	
1343.67852	
1343.67900	
1343.67905	
1343.68401	mid vein
1343.68402	mid vein
1343.68415	mid vein
1343.68416	mid vein
1347.01191	
1347.02083	
1348.42277	outer root
1353.03905	
1354.27737	
1354.27742	
1358.98735	
1358.98735	
1358.98752	
1359.65380	
1361.79104	
1361.79417	
1374.95858	
1374.95884	
1375.44986	outer nod
1377.76400	
1377.76723	
1405.81610	
1405.81750	
1415.96358	
1415.97339	
1415.97344	
1415.97346	
1421.78997	
1421.79193	
1428.05705	
1429.06667	
1431.93862	
1431.94072	

1431.94858	
1431.94862	
1431.94871	
1431.94872	
1434.07990	
1435.07547	
1437.96527	
1444.03055	
1444.03081	
1447.91487	
1449.84203	
1449.84495	
1450.05034	
1450.05063	
1456.06609	wt
1463.08077	
1463.08110	
1465.81614	
1465.81698	
1466.02407	
1466.02434	
1467.03167	
1468.03011	
1472.03322	
1472.03349	**wt**
1472.04348	
1472.04373	
1479.05588	
1479.05616	
1481.99385	
1482.00410	CLE
1485.06963	
1485.06992	
1488.00405	
1488.00408	
1488.00423	
1488.01440	
1488.01440	
1488.01461	
1493.86847	
1493.86969	
1501.04467	

1501.04499	
1503.99294	
1504.10395	
1504.11430	
1505.75828	wt mid vein
1507.06057	
1509.84256	
1509.84354	
1517.00335	
1517.01135	
1517.01143	
1520.08502	
1520.08529	
1522.73267	mid vein
1536.06117	
1536.06149	
1538.89839	
1538.90057	
1539.05650	
1543.75413	mid vein
1543.75574	mid vein
1552.02529	
1552.02556	
1552.03650	
1552.03654	
1553.86945	
1553.86950	
1582.92555	
1583.92878	
1597.89617	
1597.90026	
1620.03526	wt
1620.04731	
1625.94859	
1625.95312	
1626.05021	wt
1641.92215	
1641.92418	
1642.03237	wt
1642.03245	
1642.03248	
1642.03268	
1642.03294	
1655.05485	
1655.05507	
1657.99680	
1658.00906	**wt**
1658.00919	
1659.00439	
1669.97407	
1671.02883	
1671.02888	
1671.98584	
1685.94850	
1685.95433	
1690.07950	
1706.04577	
1714.00034	
1714.00704	
1729.97471	
1729.97768	
1759.02966	
1759.03161	
1774.00079	
1774.00550	
1802.05270	
1802.05529	
1818.02594	
1818.02761	
1831.06400	wt
1846.07790	
1846.07996	
1847.04791	
1862.05197	
1862.05896	
1890.10343	
1890.10597	
1906.07825	
1906.08225	
1934.12954	
1934.13323	
1950.10330	
1950.10614	
1978.15741	CLE
1994.13652	

Annotated MS/MS spectra used for *de novo* sequencing.

MW 908.4238

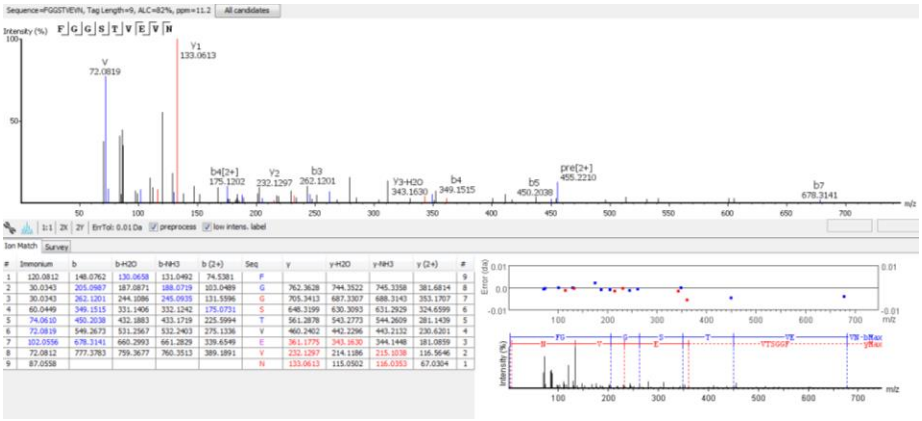

MW 962.4813

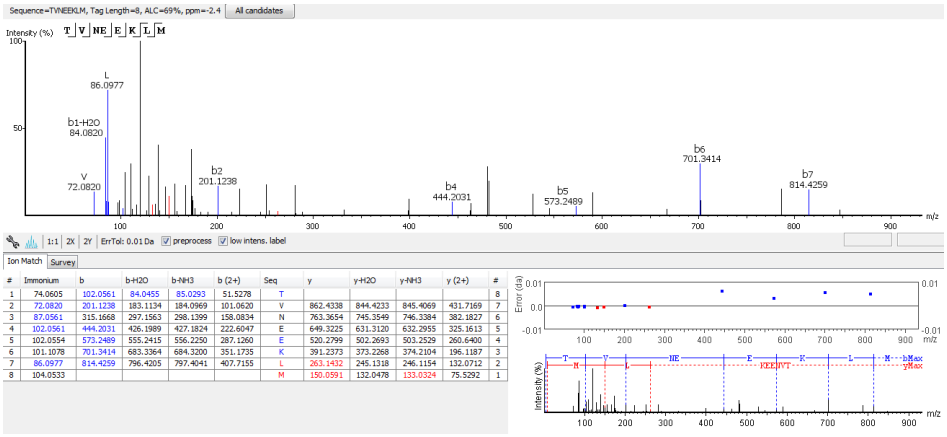

MW 990.5163

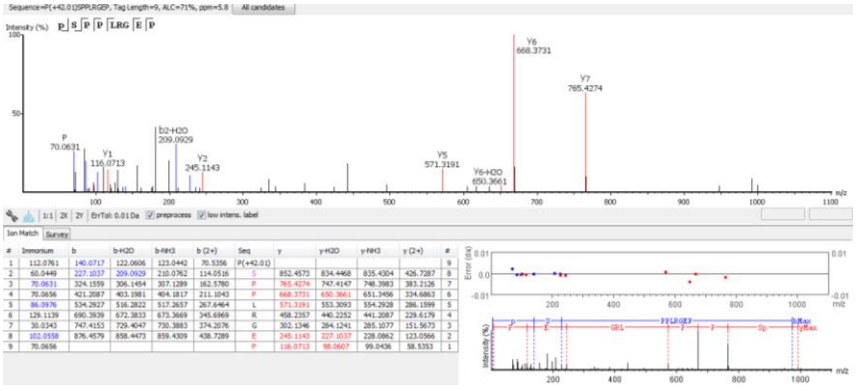

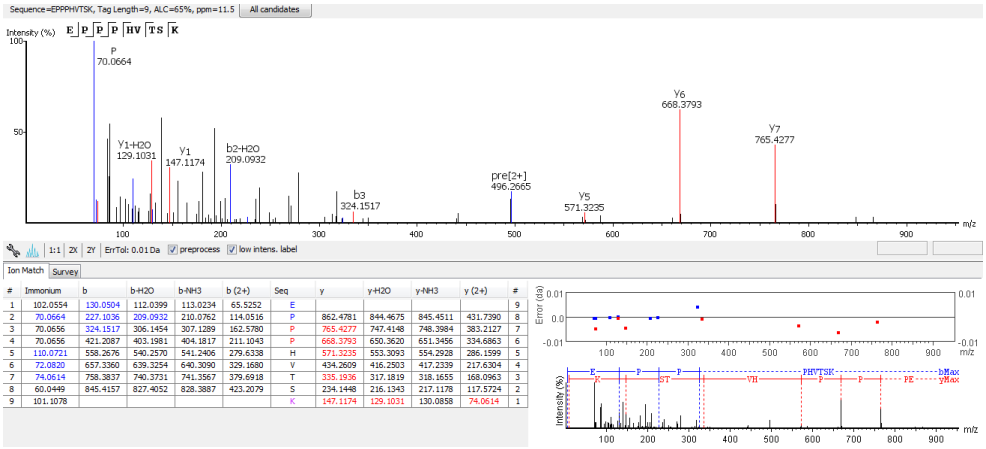

#	Immonium	b	b-H2O	b-NH3	b (2+)	Seq	y	y-H2O	y-NH3	y (2+)	#
1	102.0554	130.0504	112.0399	113.0234	65.5252	E					9
2	70.0664	227.1036	209.0932	210.0762	114.0516	P	862.4781	844.4675	845.4511	431.7390	8
3	70.0656	324.1517	306.1454	307.1289	162.5780	P	765.4277	747.4148	748.3984	383.2127	7
4	70.0656	421.2087	403.1981	404.1817	211.1043	P	668.3793	650.3620	651.3456	334.6863	6
5	110.0721	558.2676	540.2570	541.2406	279.6338	H	571.3235	553.3093	554.2928	286.1599	5
6	72.0820	657.3360	639.3254	640.3090	329.1680	V	434.2609	416.2503	417.2339	217.6304	4
7	74.0614	758.3837	740.3731	741.3567	379.6918	T	335.1936	317.1819	318.1655	168.0963	3
8	60.0449	845.4157	827.4052	828.3887	423.2079	S	234.1448	216.1343	217.1178	117.5724	2
9	101.1078					K	147.1174	129.1031	130.0858	74.0614	1

MW 1006.5114

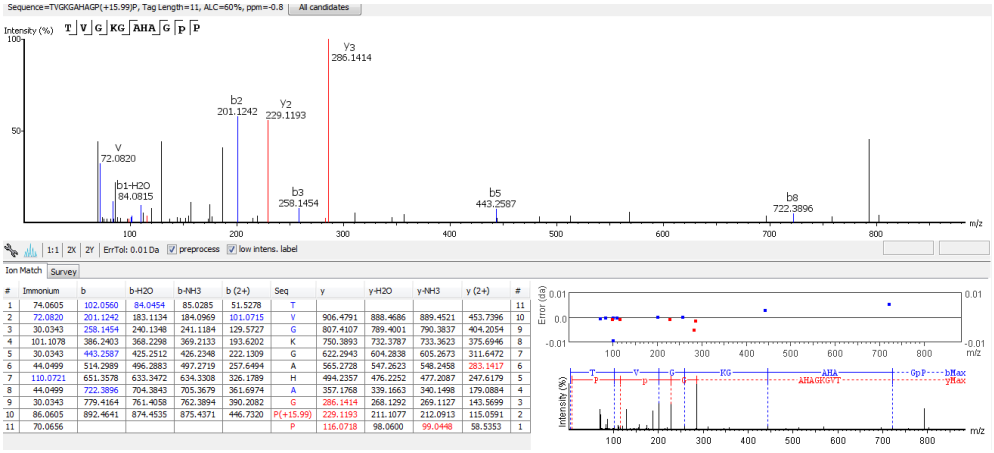

#	Immonium	b	b-H2O	b-NH3	b (2+)	Seq	y	y-H2O	y-NH3	y (2+)	#
1	74.0605	102.0560	84.0454	85.0285	51.5278	T					11
2	72.0820	201.1242	183.1134	184.0969	101.0715	V	906.4791	888.4686	889.4521	453.7396	10
3	30.0343	258.1454	240.1348	241.1184	129.5727	G	807.4107	789.4001	790.3837	404.2054	9
4	101.1078	386.2403	368.2298	369.2133	193.6202	K	750.3893	732.3787	733.3623	375.6946	8
5	30.0343	443.2587	425.2512	426.2348	222.1309	G	622.2943	604.2838	605.2673	311.6472	7
6	44.0499	514.2989	496.2883	497.2719	257.6494	A	565.2728	547.2623	548.2458	283.1417	6
7	110.0721	651.3578	633.3472	634.3308	326.1789	H	494.2357	476.2252	477.2087	247.6179	5
8	44.0499	722.3896	704.3843	705.3679	361.6974	A	357.1768	339.1663	340.1498	179.0884	4
9	30.0343	779.4164	761.4058	762.3894	390.2082	G	286.1414	268.1292	269.1127	143.5699	3
10	86.0605	892.4641	874.4535	875.4371	446.7320	P(+15.99)	229.1193	211.1077	212.0913	115.0591	2
11	70.0656					P	116.0718	98.0600	99.0448	58.5353	1

MW 1008.4694

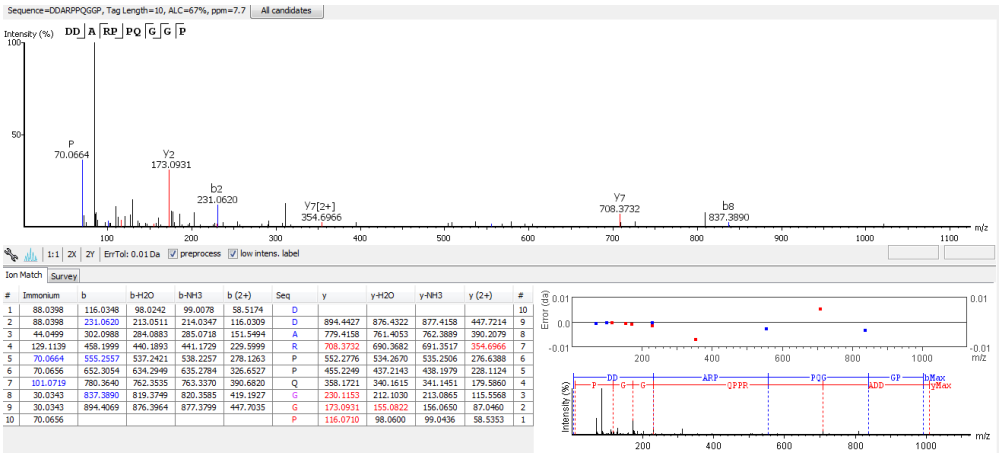

#	Immonium	b	b-H2O	b-NH3	b (2+)	Seq	y	y-H2O	y-NH3	y (2+)	#
1	88.0398	116.0348	98.0242	99.0078	58.5174	D					10
2	88.0398	231.0620	213.0511	214.0347	116.0309	D	894.4427	876.4322	877.4158	447.7214	9
3	44.0499	302.0988	284.0883	285.0718	151.5494	A	779.4158	761.4053	762.3889	390.2079	8
4	129.1139	458.1999	440.1893	441.1729	229.5999	R	708.3732	690.3682	691.3517	354.6966	7
5	70.0664	555.2557	537.2421	538.2257	278.1263	P	552.2776	534.2670	535.2506	276.6388	6
6	70.0656	652.3054	634.2949	635.2784	326.6527	P	455.2249	437.2143	438.1979	228.1124	5
7	101.0719	780.3640	762.3535	763.3370	390.6820	Q	358.1721	340.1615	341.1451	179.5860	4
8	30.0343	837.3890	819.3749	820.3585	419.1927	G	230.1153	212.1030	213.0865	115.5568	3
9	30.0343	894.4069	876.3964	877.3799	447.7035	G	173.0931	155.0822	156.0650	87.0460	2
10	70.0656					P	116.0710	98.0600	99.0436	58.5353	1

MW 1021.5575

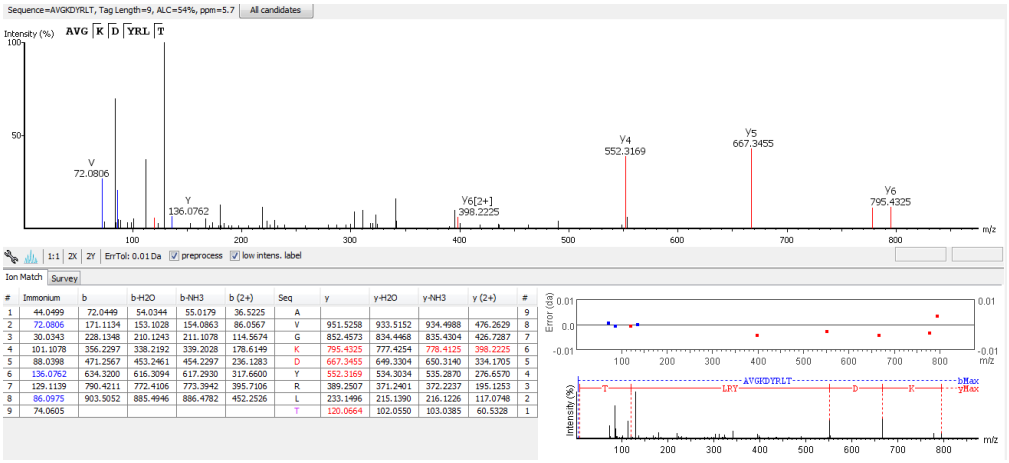

#	Immonium	b	b-H2O	b-NH3	b (2+)	Seq	y	y-H2O	y-NH3	y (2+)	#
1	44.0499	72.0449	54.0344	55.0179	36.5225	A					9
2	72.0806	171.1134	153.1028	154.0863	86.0567	V	951.5258	933.5152	934.4988	476.2629	8
3	30.0343	228.1348	210.1243	211.1078	114.5674	G	852.4573	834.4468	835.4304	426.7287	7
4	101.1078	356.2297	338.2192	339.2028	178.6149	K	795.4325	777.4254	778.4125	398.2225	6
5	88.0398	471.2567	453.2461	454.2297	236.1283	D	667.3455	649.3304	650.3140	334.1705	5
6	136.0762	634.3200	616.3094	617.2930	317.6600	Y	552.3169	534.3034	535.2870	276.6570	4
7	129.1139	790.4211	772.4106	773.3942	395.7106	R	389.2507	371.2401	372.2237	195.1253	3
8	86.0975	903.5052	885.4946	886.4782	452.2526	L	233.1496	215.1390	216.1226	117.0748	2
9	74.0605					T	120.0664	102.0550	103.0385	60.5328	1

MW 1068.5733

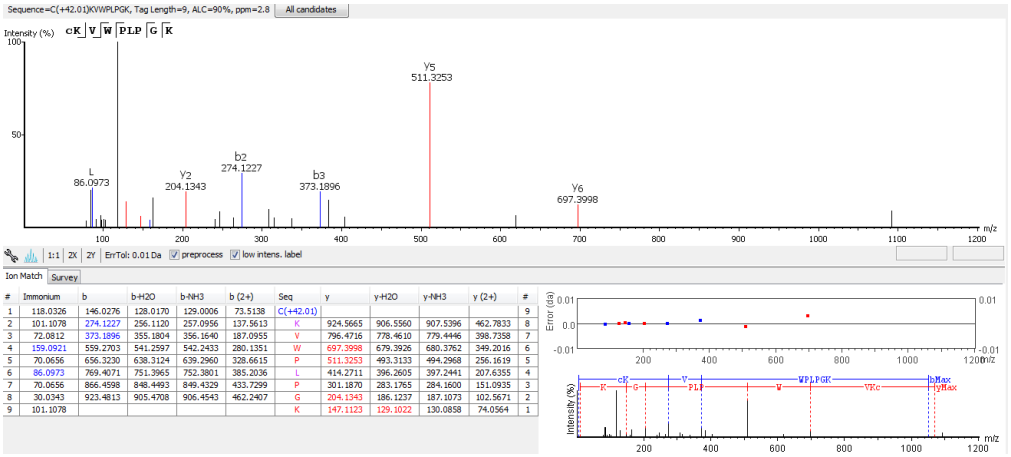

#	Immonium	b	b-H2O	b-NH3	b (2+)	Seq	y	y-H2O	y-NH3	y (2+)	#
1	118.0326	146.0276	128.0170	129.0006	73.5138	C(+42.01)					9
2	101.1078	274.1227	256.1120	257.0956	137.5613	K	924.5665	906.5560	907.5396	462.7833	8
3	72.0812	373.1896	355.1804	356.1640	187.0955	V	796.4716	778.4610	779.4446	398.7358	7
4	159.0921	559.2703	541.2597	542.2433	280.1351	W	697.3998	679.3926	680.3762	349.2016	6
5	70.0656	656.3230	638.3124	639.2960	328.6615	P	511.3253	493.3133	494.2968	256.1619	5
6	86.0973	769.4071	751.3965	752.3801	385.2036	L	414.2711	396.2605	397.2441	207.6355	4
7	70.0656	866.4598	848.4493	849.4329	433.7299	P	301.1870	283.1765	284.1600	151.0935	3
8	30.0343	923.4813	905.4708	906.4543	462.2407	G	204.1343	186.1237	187.1073	102.5671	2
9	101.1078					K	147.1123	129.1022	130.0858	74.0564	1

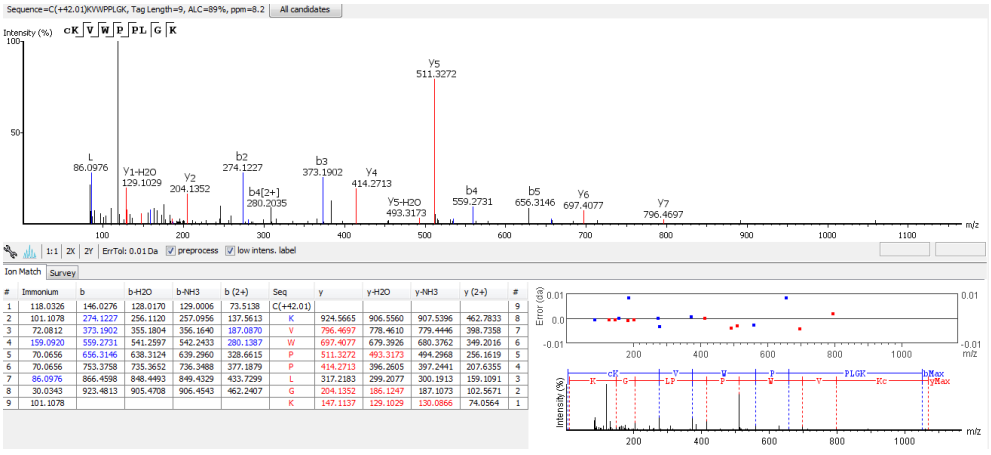

#	Immonium	b	b-H2O	b-NH3	b (2+)	Seq	y	y-H2O	y-NH3	y (2+)	#
1	118.0326	146.0276	128.0170	129.0006	73.5138	C(+42.01)					9
2	101.1078	274.1227	256.1120	257.0956	137.5613	K	924.5665	906.5560	907.5396	462.7833	8
3	72.0812	373.1902	355.1804	356.1640	187.0870	V	796.4697	778.4610	779.4446	398.7358	7
4	159.0920	559.2731	541.2597	542.2433	280.1387	W	697.4077	679.3926	680.3762	349.2016	6
5	70.0656	656.3146	638.3124	639.2960	328.6615	P	511.3272	493.3173	494.2968	256.1619	5
6	70.0656	753.3758	735.3652	736.3488	377.1879	P	414.2713	396.2605	397.2441	207.6355	4
7	86.0976	866.4598	848.4493	849.4329	433.7299	L	317.2183	299.2077	300.1913	159.1091	3
8	30.0343	923.4813	905.4708	906.4543	462.2407	G	204.1352	186.1247	187.1073	102.5671	2
9	101.1078					K	147.1137	129.1029	130.0866	74.0564	1

MW 1094.5280

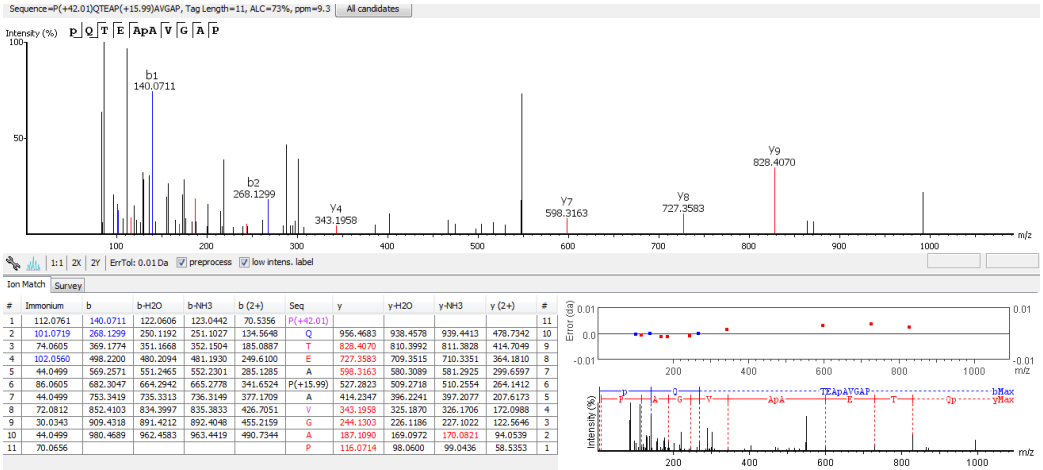

#	Immonium	b	b-H2O	b-NH3	b (2+)	Seq	y	y-H2O	y-NH3	y (2+)	#
1	112.0761	140.0711	122.0606	123.0442	70.5356	P(+42.01)					11
2	101.0719	268.1299	250.1192	251.1027	134.5648	Q	956.4683	938.4578	939.4413	478.7342	10
3	74.0605	369.1774	351.1668	352.1504	185.0887	T	828.4070	810.3992	811.3828	414.7049	9
4	102.0560	498.2200	480.2094	481.1930	249.6100	E	727.3583	709.3515	710.3351	364.1810	8
5	44.0499	569.2571	551.2465	552.2301	285.1285	A	598.3163	580.3089	581.2925	299.6597	7
6	86.0605	682.3047	664.2942	665.2778	341.6524	P(+15.99)	527.2823	509.2718	510.2554	264.1412	6
7	44.0499	753.3419	735.3313	736.3149	377.1709	A	414.2347	396.2241	397.2077	207.6173	5
8	72.0812	852.4103	834.3997	835.3833	426.7051	V	343.1958	325.1870	326.1706	172.0988	4
9	30.0343	909.4318	891.4212	892.4048	455.2159	G	244.1303	226.1186	227.1022	122.5646	3
10	44.0499	980.4689	962.4583	963.4419	490.7344	A	187.1090	169.0972	170.0821	94.0539	2
11	70.0656					P	116.0714	98.0600	99.0436	58.5353	1

MW 1106.5081

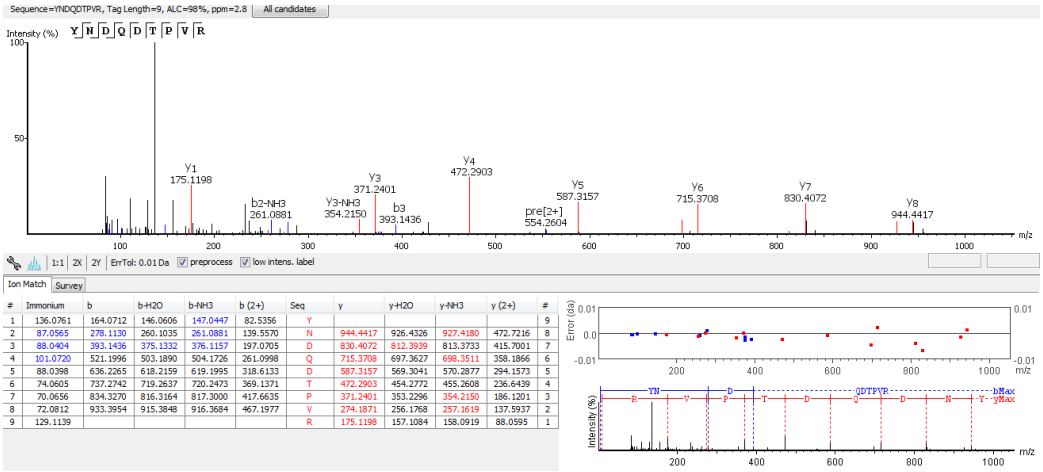

#	Immonium	b	b-H2O	b-NH3	b (2+)	Seq	y	y-H2O	y-NH3	y (2+)	#
1	136.0761	164.0712	146.0606	147.0447	82.5356	Y					9
2	87.0565	278.1130	260.1035	261.0881	139.5570	N	944.4417	926.4326	927.4180	472.7216	8
3	88.0404	393.1436	375.1332	376.1157	197.0705	D	830.4072	812.3939	813.3733	415.7001	7
4	101.0720	521.1996	503.1890	504.1726	261.0998	Q	715.3708	697.3627	698.3511	358.1866	6
5	88.0398	636.2265	618.2159	619.1995	318.6133	D	587.3157	569.3041	570.2877	294.1573	5
6	74.0605	737.2742	719.2637	720.2473	369.1371	T	472.2903	454.2772	455.2608	236.6439	4
7	70.0656	834.3270	816.3164	817.3000	417.6635	P	371.2401	353.2296	354.2150	186.1201	3
8	72.0812	933.3954	915.3848	916.3684	467.1977	V	274.1871	256.1768	257.1619	137.5937	2
9	129.1139					R	175.1198	157.1084	158.0919	88.0595	1

MW 1106.5255

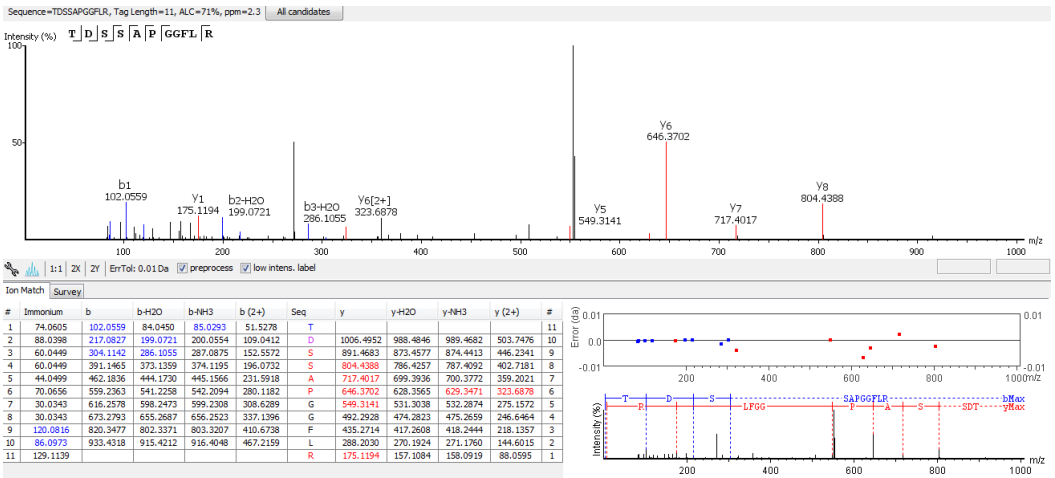

#	Immonium	b	b-H2O	b-NH3	b (2+)	Seq	y	y-H2O	y-NH3	y (2+)	#
1	74.0605	102.0559	84.0450	85.0293	51.5278	T					11
2	88.0398	217.0827	199.0721	200.0554	109.0412	D	1006.4952	988.4846	989.4682	503.7476	10
3	60.0449	304.1142	286.1055	287.0875	152.5572	S	891.4683	873.4577	874.4413	446.2341	9
4	60.0449	391.1465	373.1359	374.1195	196.0732	S	804.4388	786.4257	787.4092	402.7181	8
5	44.0499	462.1836	444.1730	445.1566	231.5918	A	717.4017	699.3936	700.3772	359.2021	7
6	70.0656	559.2363	541.2258	542.2094	280.1182	P	646.3702	628.3565	629.3471	323.6878	6
7	30.0343	616.2578	598.2473	599.2308	308.6289	G	549.3141	531.3038	532.2874	275.1572	5
8	30.0343	673.2793	655.2687	656.2523	337.1396	G	492.2928	474.2823	475.2659	246.6464	4
9	120.0816	820.3477	802.3371	803.3207	410.6738	F	435.2714	417.2608	418.2444	218.1357	3
10	86.0973	933.4318	915.4212	916.4048	467.2159	L	288.2030	270.1924	271.1760	144.6015	2
11	129.1139					R	175.1194	157.1084	158.0919	88.0595	1

MW 1112.5974

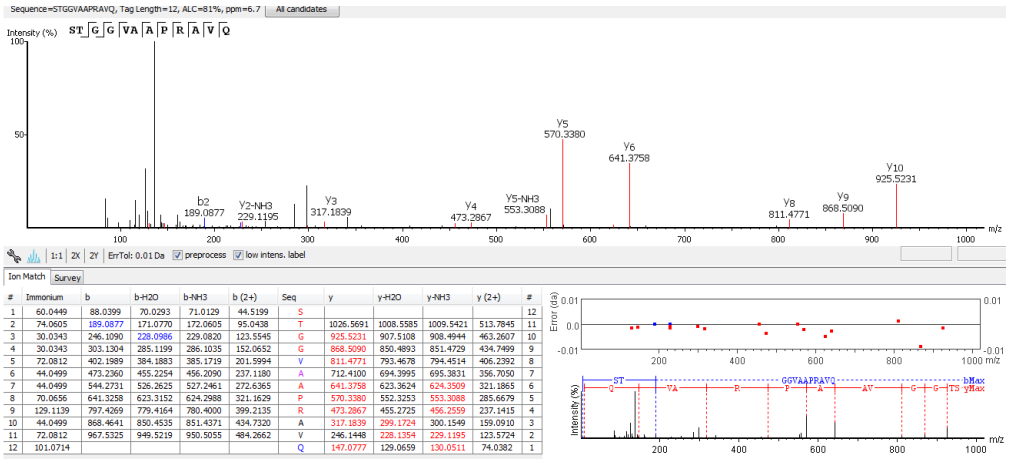

#	Immonium	b	b-H2O	b-NH3	b (2+)	Seq	y	y-H2O	y-NH3	y (2+)	#
1	60.0449	88.0399	70.0293	71.0129	44.5199	S					12
2	74.0605	189.0877	171.0770	172.0605	95.0438	T	1026.5691	1008.5585	1009.5421	513.7845	11
3	30.0343	246.1090	228.0986	229.0820	123.5545	G	925.5231	907.5108	908.4944	463.2607	10
4	30.0343	303.1304	285.1199	286.1035	152.0652	G	868.5090	850.4893	851.4729	434.7499	9
5	72.0812	402.1989	384.1883	385.1719	201.5994	V	811.4771	793.4678	794.4514	406.2392	8
6	44.0499	473.2360	455.2254	456.2090	237.1180	A	712.4100	694.3995	695.3831	356.7050	7
7	44.0499	544.2731	526.2625	527.2461	272.6365	A	641.3758	623.3624	624.3509	321.1865	6
8	70.0656	641.3258	623.3152	624.2988	321.1629	P	570.3380	552.3253	553.3088	285.6679	5
9	129.1139	797.4269	779.4164	780.4000	399.2135	R	473.2867	455.2725	456.2559	237.1415	4
10	44.0499	868.4641	850.4535	851.4371	434.7320	A	317.1839	299.1724	300.1549	159.0910	3
11	72.0812	967.5325	949.5219	950.5055	484.2662	V	246.1448	228.1354	229.1195	123.5724	2
12	101.0714					Q	147.0777	129.0659	130.0511	74.0382	1

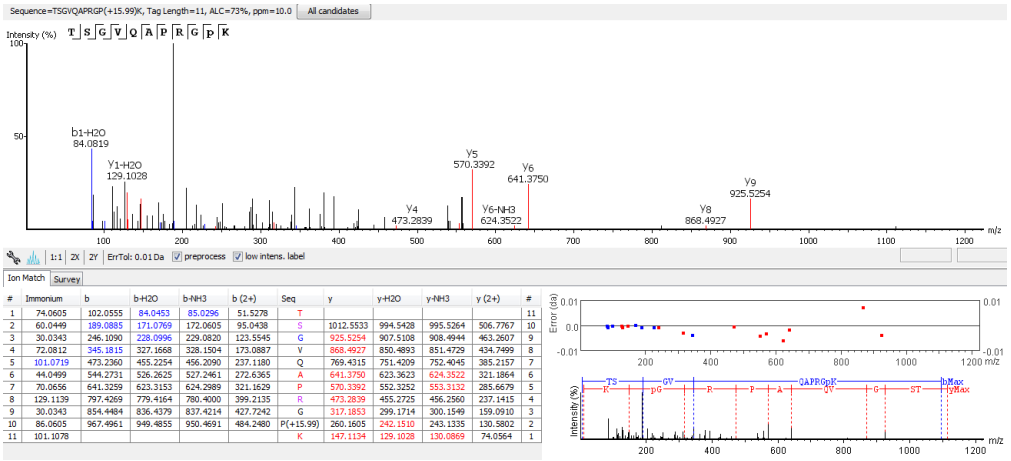

#	Immonium	b	b-H2O	b-NH3	b (2+)	Seq	y	y-H2O	y-NH3	y (2+)	#
1	74.0605	102.0555	84.0453	85.0296	51.5278	T					11
2	60.0449	189.0885	171.0769	172.0605	95.0438	S	1012.5533	994.5428	995.5264	506.7767	10
3	30.0343	246.1090	228.0996	229.0820	123.5545	G	925.5254	907.5108	908.4944	463.2607	9
4	72.0812	345.1815	327.1668	328.1504	173.0887	V	868.4927	850.4893	851.4729	434.7499	8
5	101.0719	473.2360	455.2254	456.2090	237.1180	Q	769.4315	751.4209	752.4045	385.2157	7
6	44.0499	544.2731	526.2625	527.2461	272.6365	A	641.3750	623.3623	624.3522	321.1864	6
7	70.0656	641.3259	623.3153	624.2989	321.1629	P	570.3392	552.3252	553.3132	285.6679	5
8	129.1139	797.4269	779.4164	780.4000	399.2135	R	473.2839	455.2725	456.2560	237.1415	4
9	30.0343	854.4484	836.4379	837.4214	427.7242	G	317.1853	299.1714	300.1549	159.0910	3
10	86.0605	967.4961	949.4855	950.4691	484.2480	P(+15.99)	260.1605	242.1510	243.1335	130.5802	2
11	101.1078					K	147.1134	129.1028	130.0869	74.0564	1

MW 1159.6191

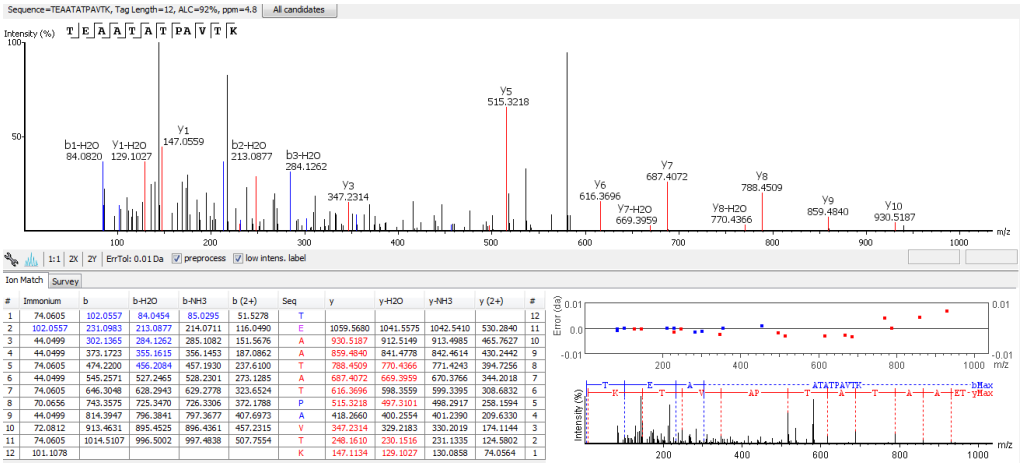

#	Immonium	b	b-H2O	b-NH3	b (2+)	Seq	y	y-H2O	y-NH3	y (2+)	#
1	74.0605	102.0557	84.0454	85.0295	51.5278	T					12
2	102.0557	231.0983	213.0877	214.0711	116.0490	E	1059.5680	1041.5575	1042.5410	530.2840	11
3	44.0499	302.1365	284.1262	285.1082	151.5676	A	930.5187	912.5149	913.4985	465.7627	10
4	44.0499	373.1723	355.1615	356.1453	187.0862	A	859.4840	841.4778	842.4614	430.2442	9
5	74.0605	474.2200	456.2094	457.1930	237.6100	T	788.4509	770.4366	771.4243	394.7256	8
6	44.0499	545.2571	527.2465	528.2301	273.1285	A	687.4072	669.3959	670.3766	344.2018	7
7	74.0605	646.3048	628.2943	629.2778	323.6524	T	616.3696	598.3559	599.3395	308.6832	6
8	70.0656	743.3575	725.3470	726.3306	372.1788	P	515.3218	497.3101	498.2917	258.1594	5
9	44.0499	814.3947	796.3841	797.3677	407.6973	A	418.2660	400.2554	401.2390	209.6330	4
10	72.0812	913.4631	895.4525	896.4361	457.2315	V	347.2314	329.2183	330.2019	174.1144	3
11	74.0605	1014.5107	996.5002	997.4838	507.7554	T	248.1610	230.1516	231.1335	124.5802	2
12	101.1078					K	147.1134	129.1027	130.0858	74.0564	1

MW 1170.6070

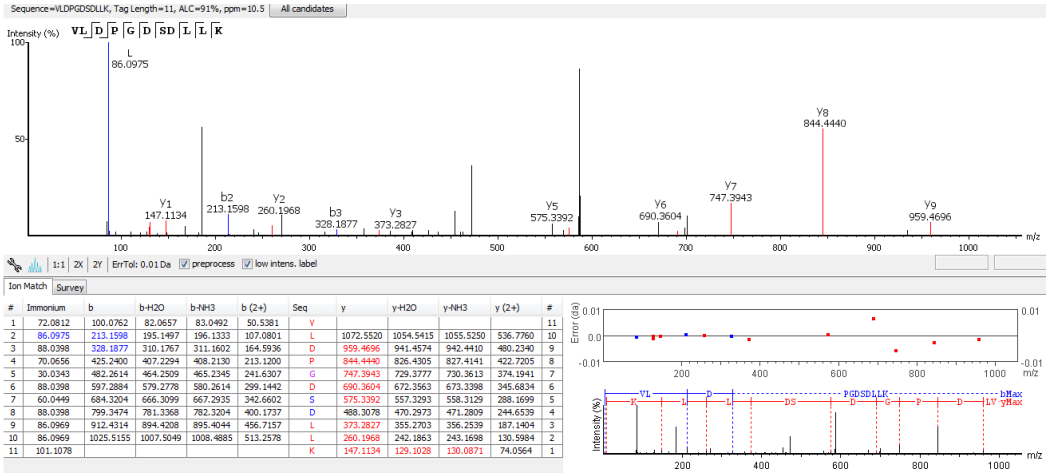

#	Immonium	b	b-H2O	b-NH3	b (2+)	Seq	y	y-H2O	y-NH3	y (2+)	#
1	72.0812	100.0762	82.0657	83.0492	50.5381	V					11
2	86.0975	213.1598	195.1497	196.1333	107.0801	L	1072.5520	1054.5415	1055.5250	536.7760	10
3	88.0398	328.1877	310.1767	311.1602	164.5936	D	959.4696	941.4574	942.4410	480.2340	9
4	70.0656	425.2400	407.2294	408.2130	213.1200	P	844.4440	826.4305	827.4141	422.7205	8
5	30.0343	482.2614	464.2509	465.2345	241.6307	G	747.3943	729.3777	730.3613	374.1941	7
6	88.0398	597.2884	579.2778	580.2614	299.1442	D	690.3604	672.3563	673.3398	345.6834	6
7	60.0449	684.3204	666.3099	667.2935	342.6602	S	575.3392	557.3293	558.3129	288.1699	5
8	88.0398	799.3474	781.3368	782.3204	400.1737	D	488.3078	470.2973	471.2809	244.6539	4
9	86.0969	912.4314	894.4208	895.4044	456.7157	L	373.2827	355.2703	356.2539	187.1404	3
10	86.0969	1025.5155	1007.5049	1008.4885	513.2578	L	260.1968	242.1863	243.1698	130.5984	2
11	101.1078					K	147.1134	129.1028	130.0871	74.0564	1

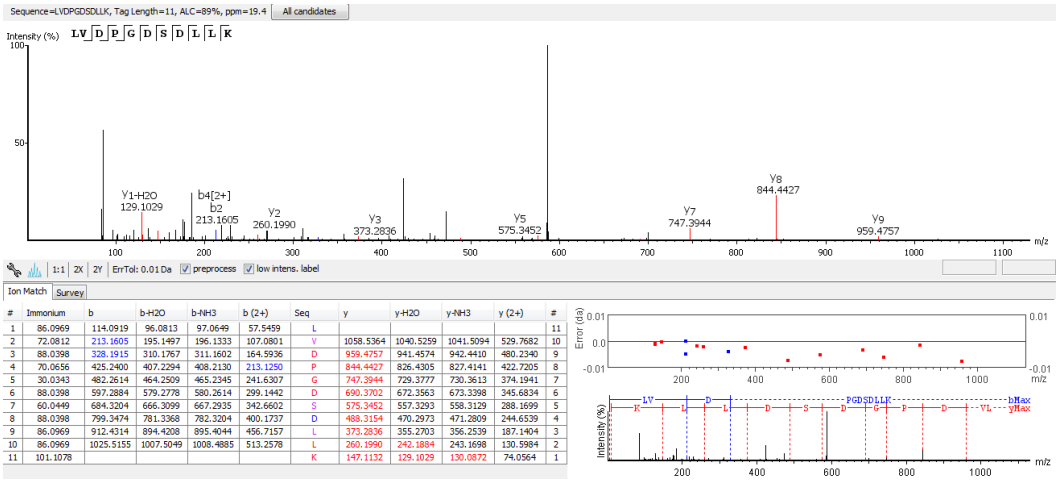

#	Immonium	b	b-H2O	b-NH3	b (2+)	Seq	y	y-H2O	y-NH3	y (2+)	#
1	86.0969	114.0919	96.0813	97.0649	57.5459	L					11
2	72.0812	213.1605	195.1497	196.1333	107.0801	V	1058.5364	1040.5259	1041.5094	529.7682	10
3	88.0398	328.1915	310.1767	311.1602	164.5936	D	959.4757	941.4574	942.4410	480.2340	9
4	70.0656	425.2400	407.2294	408.2130	213.1250	P	844.4427	826.4305	827.4141	422.7205	8
5	30.0343	482.2614	464.2509	465.2345	241.6307	G	747.3944	729.3777	730.3613	374.1941	7
6	88.0398	597.2884	579.2778	580.2614	299.1442	D	690.3702	672.3563	673.3398	345.6834	6
7	60.0449	684.3204	666.3099	667.2935	342.6602	S	575.3452	557.3293	558.3129	288.1699	5
8	88.0398	799.3474	781.3368	782.3204	400.1737	D	488.3154	470.2973	471.2809	244.6539	4
9	86.0969	912.4314	894.4208	895.4044	456.7157	L	373.2836	355.2703	356.2539	187.1404	3
10	86.0969	1025.5155	1007.5049	1008.4885	513.2578	L	260.1990	242.1884	243.1698	130.5984	2
11	101.1078					K	147.1132	129.1029	130.0872	74.0564	1

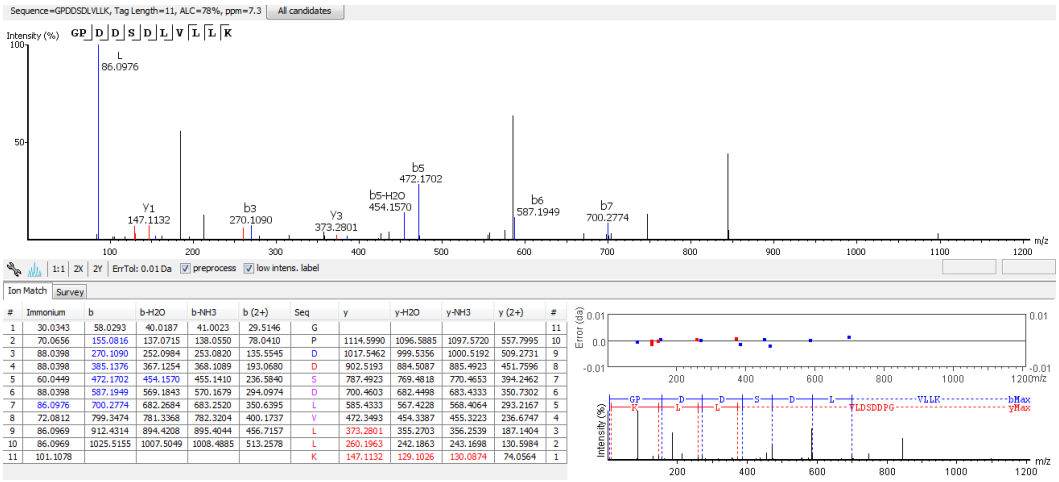

#	Immonium	b	b-H2O	b-NH3	b (2+)	Seq	y	y-H2O	y-NH3	y (2+)	#
1	30.0343	58.0293	40.0187	41.0023	29.5146	G					11
2	70.0656	155.0816	137.0715	138.0550	78.0410	P	1114.5990	1096.5885	1097.5720	557.7995	10
3	88.0398	270.1090	252.0984	253.0820	135.5545	D	1017.5462	999.5356	1000.5192	509.2731	9
4	88.0398	385.1376	367.1254	368.1089	193.0680	D	902.5193	884.5087	885.4923	451.7596	8
5	60.0449	472.1702	454.1570	455.1410	236.5840	S	787.4923	769.4818	770.4653	394.2462	7
6	88.0398	587.1949	569.1843	570.1679	294.0974	D	700.4603	682.4498	683.4333	350.7302	6
7	86.0976	700.2774	682.2684	683.2520	350.6395	L	585.4333	567.4228	568.4064	293.2167	5
8	72.0812	799.3474	781.3368	782.3204	400.1737	V	472.3493	454.3387	455.3223	236.6747	4
9	86.0969	912.4314	894.4208	895.4044	456.7157	L	373.2801	355.2703	356.2539	187.1404	3
10	86.0969	1025.5155	1007.5049	1008.4885	513.2578	L	260.1963	242.1863	243.1698	130.5984	2
11	101.1078					K	147.1132	129.1026	130.0874	74.0564	1

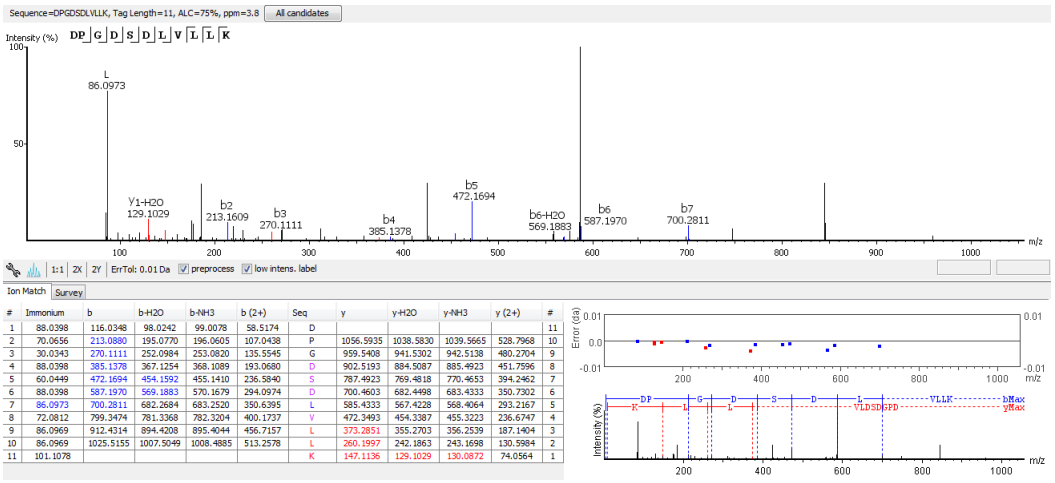

#	Immonium	b	b-H2O	b-NH3	b (2+)	Seq	y	y-H2O	y-NH3	y (2+)	#
1	88.0398	116.0348	98.0242	99.0078	58.5174	D					11
2	70.0656	213.0880	195.0770	196.0605	107.0438	P	1056.5935	1038.5830	1039.5665	528.7968	10
3	30.0343	270.1111	252.0984	253.0820	135.5545	G	959.5408	941.5302	942.5138	480.2704	9
4	88.0398	385.1378	367.1254	368.1089	193.0680	D	902.5193	884.5087	885.4923	451.7596	8
5	60.0449	472.1694	454.1592	455.1410	236.5840	S	787.4923	769.4818	770.4653	394.2462	7
6	88.0398	587.1970	569.1883	570.1679	294.0974	D	700.4603	682.4498	683.4333	350.7302	6
7	86.0973	700.2811	682.2684	683.2520	350.6395	L	585.4333	567.4228	568.4064	293.2167	5
8	72.0812	799.3474	781.3368	782.3204	400.1737	V	472.3493	454.3387	455.3223	236.6747	4
9	86.0969	912.4314	894.4208	895.4044	456.7157	L	373.2851	355.2703	356.2539	187.1404	3
10	86.0969	1025.5155	1007.5049	1008.4885	513.2578	L	260.1997	242.1863	243.1698	130.5984	2
11	101.1078					K	147.1136	129.1029	130.0872	74.0564	1

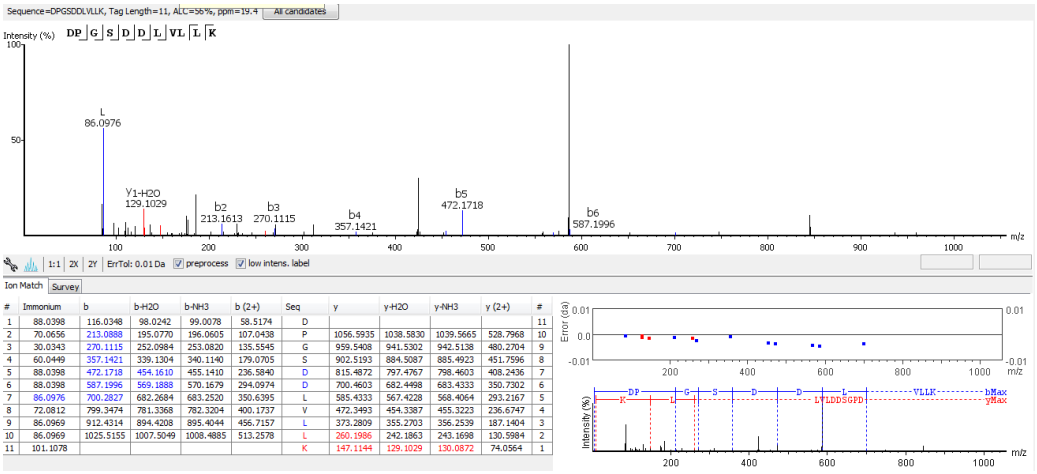

#	Immonium	b	b-H2O	b-NH3	b (2+)	Seq	y	y-H2O	y-NH3	y (2+)	#
1	88.0398	116.0348	98.0242	99.0078	58.5174	D					11
2	70.0656	213.0888	195.0770	196.0605	107.0438	P	1056.5935	1038.5830	1039.5665	528.7968	10
3	30.0343	270.1115	252.0984	253.0820	135.5545	G	959.5408	941.5302	942.5138	480.2704	9
4	60.0449	357.1421	339.1304	340.1140	179.0705	S	902.5193	884.5087	885.4923	451.7596	8
5	88.0398	472.1718	454.1610	455.1410	236.5840	D	815.4872	797.4767	798.4603	408.2436	7
6	88.0398	587.1996	569.1888	570.1679	294.0974	D	700.4603	682.4498	683.4333	350.7302	6
7	86.0976	700.2827	682.2684	683.2520	350.6395	L	585.4333	567.4228	568.4064	293.2167	5
8	72.0812	799.3474	781.3368	782.3204	400.1737	V	472.3493	454.3387	455.3223	236.6747	4
9	86.0969	912.4314	894.4208	895.4044	456.7157	L	373.2809	355.2703	356.2539	187.1404	3
10	86.0969	1025.5155	1007.5049	1008.4885	513.2578	L	260.1986	242.1863	243.1698	130.5984	2
11	101.1078					K	147.1144	129.1029	130.0872	74.0564	1

MW 1175.5925

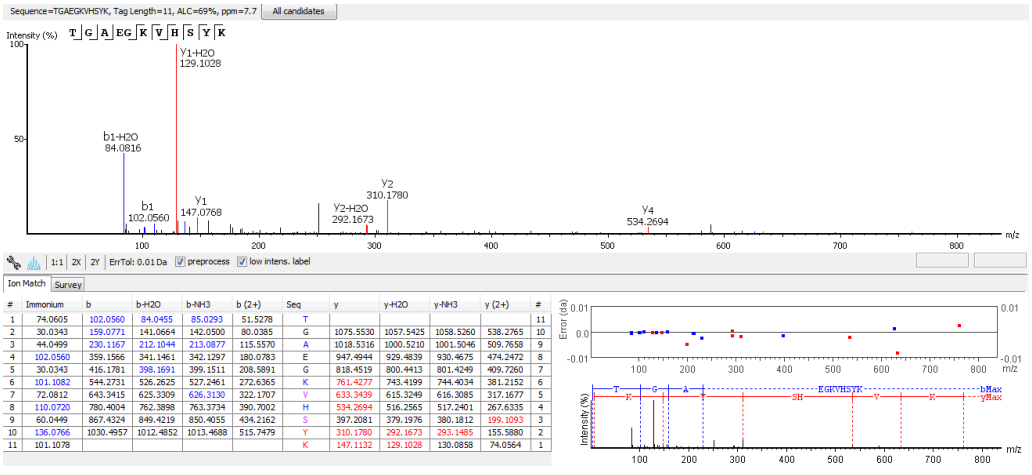

#	Immonium	b	b-H2O	b-NH3	b (2+)	Seq	y	y-H2O	y-NH3	y (2+)	#
1	74.0605	102.0560	84.0455	85.0293	51.5278	T					11
2	30.0343	159.0771	141.0664	142.0500	80.0385	G	1075.5530	1057.5425	1058.5260	538.2765	10
3	44.0499	230.1167	212.1044	213.0877	115.5570	A	1018.5316	1000.5210	1001.5046	509.7658	9
4	102.0560	359.1566	341.1461	342.1297	180.0783	E	947.4944	929.4839	930.4675	474.2472	8
5	30.0343	416.1781	398.1691	399.1511	208.5891	G	818.4519	800.4413	801.4249	409.7260	7
6	101.1082	544.2731	526.2625	527.2461	272.6365	K	761.4277	743.4199	744.4034	381.2152	6
7	72.0812	643.3415	625.3309	626.3130	322.1707	V	633.3439	615.3249	616.3085	317.1677	5
8	110.0720	780.4004	762.3898	763.3734	390.7002	H	534.2694	516.2565	517.2401	267.6335	4
9	60.0449	867.4324	849.4219	850.4055	434.2162	S	397.2081	379.1976	380.1812	199.1093	3
10	136.0766	1030.4957	1012.4852	1013.4688	515.7479	Y	310.1780	292.1673	293.1485	155.5880	2
11	101.1078					K	147.1132	129.1028	130.0858	74.0564	1

MW 1179.6039

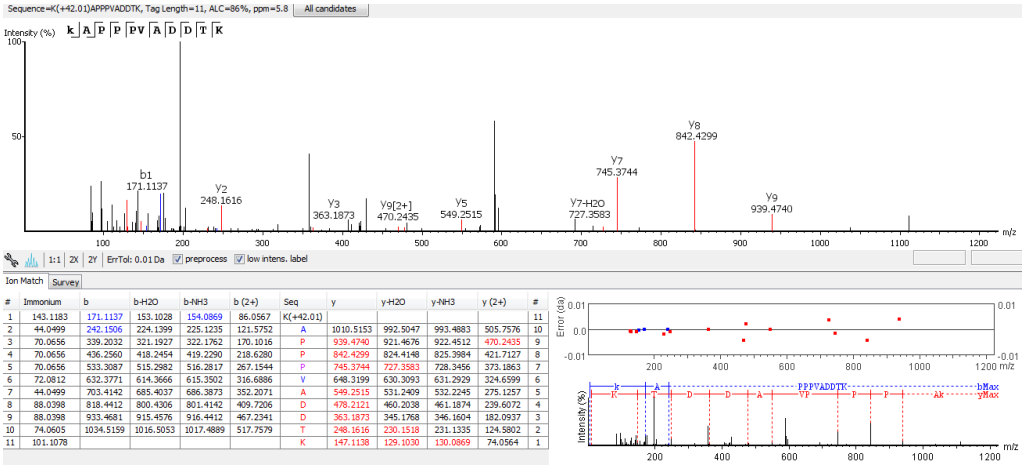

#	Immonium	b	b-H2O	b-NH3	b (2+)	Seq	y	y-H2O	y-NH3	y (2+)	#
1	143.1183	171.1137	153.1028	154.0869	86.0567	K(+42.01)					11
2	44.0499	242.1506	224.1399	225.1235	121.5752	A	1010.5153	992.5047	993.4883	505.7576	10
3	70.0656	339.2032	321.1927	322.1762	170.1016	P	939.4740	921.4676	922.4512	470.2435	9
4	70.0656	436.2560	418.2454	419.2290	218.6280	P	842.4299	824.4148	825.3984	421.7127	8
5	70.0656	533.3087	515.2982	516.2817	267.1544	P	745.3744	727.3583	728.3456	373.1863	7
6	72.0812	632.3771	614.3666	615.3502	316.6886	V	648.3199	630.3093	631.2929	324.6599	6
7	44.0499	703.4142	685.4037	686.3873	352.2071	A	549.2515	531.2409	532.2245	275.1257	5
8	88.0398	818.4412	800.4306	801.4142	409.7206	D	478.2121	460.2038	461.1874	239.6072	4
9	88.0398	933.4681	915.4576	916.4412	467.2341	D	363.1873	345.1768	346.1604	182.0937	3
10	74.0605	1034.5159	1016.5053	1017.4889	517.7579	T	248.1616	230.1518	231.1335	124.5802	2
11	101.1078					K	147.1138	129.1030	130.0869	74.0564	1

MW 1186.5763

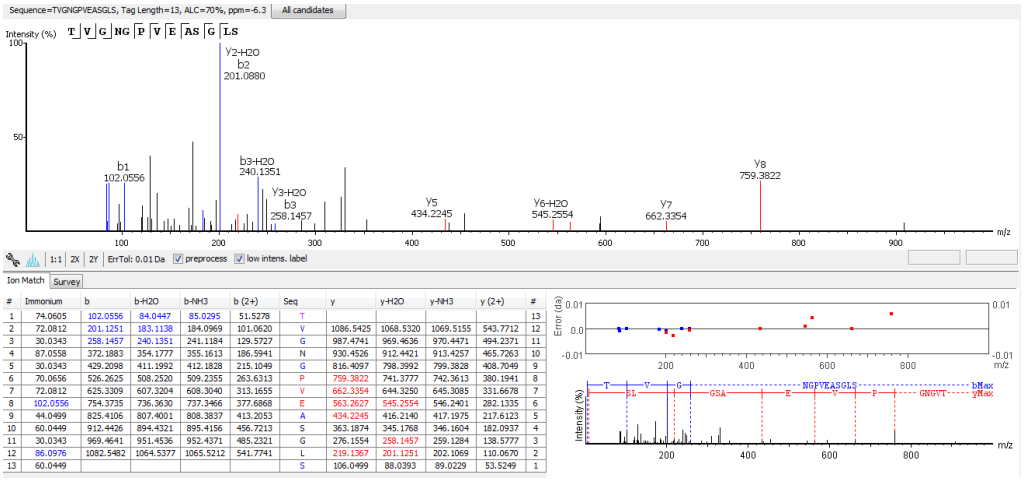

#	Immonium	b	b-H2O	b-NH3	b (2+)	Seq	y	y-H2O	y-NH3	y (2+)	#
1	74.0605	102.0556	84.0447	85.0295	51.5278	T					13
2	72.0812	201.1251	183.1138	184.0969	101.0620	V	1086.5425	1068.5320	1069.5155	543.7712	12
3	30.0343	258.1457	240.1351	241.1184	129.5727	G	987.4741	969.4636	970.4471	494.2371	11
4	87.0558	372.1883	354.1777	355.1613	186.5941	N	930.4526	912.4421	913.4257	465.7263	10
5	30.0343	429.2098	411.1992	412.1828	215.1049	G	816.4097	798.3992	799.3828	408.7049	9
6	70.0656	526.2625	508.2520	509.2355	263.6313	P	759.3822	741.3777	742.3613	380.1941	8
7	72.0812	625.3309	607.3204	608.3040	313.1655	V	662.3354	644.3250	645.3085	331.6678	7
8	102.0556	754.3735	736.3630	737.3466	377.6868	E	563.2627	545.2554	546.2401	282.1335	6
9	44.0499	825.4106	807.4001	808.3837	413.2053	A	434.2245	416.2140	417.1975	217.6123	5
10	60.0449	912.4426	894.4321	895.4156	456.7213	S	363.1874	345.1768	346.1604	182.0937	4
11	30.0343	969.4641	951.4536	952.4371	485.2321	G	276.1554	258.1457	259.1284	138.5777	3
12	86.0976	1082.5482	1064.5377	1065.5212	541.7741	L	219.1367	201.1251	202.1069	110.0670	2
13	60.0449					S	106.0499	88.0393	89.0229	53.5249	1

MW 1192.5108

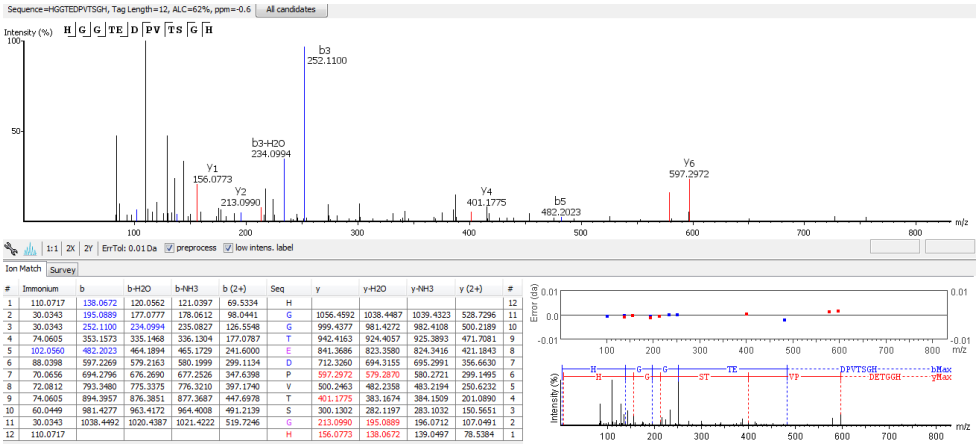

#	Immonium	b	b-H2O	b-NH3	b (2+)	Seq	y	y-H2O	y-NH3	y (2+)	#
1	110.0717	138.0672	120.0562	121.0397	69.5334	H					12
2	30.0343	195.0889	177.0777	178.0612	98.0441	G	1056.4592	1038.4487	1039.4323	528.7296	11
3	30.0343	252.1100	234.0994	235.0827	126.5548	G	999.4377	981.4272	982.4108	500.2189	10
4	74.0605	353.1573	335.1468	336.1304	177.0787	T	942.4163	924.4057	925.3893	471.7081	9
5	102.0560	482.2023	464.1894	465.1729	241.6000	E	841.3686	823.3580	824.3416	421.1843	8
6	88.0398	597.2269	579.2163	580.1999	299.1134	D	712.3260	694.3155	695.2991	356.6630	7
7	70.0656	694.2796	676.2690	677.2526	347.6398	P	597.2972	579.2870	580.2721	299.1495	6
8	72.0812	793.3480	775.3375	776.3210	397.1740	V	500.2463	482.2358	483.2194	250.6232	5
9	74.0605	894.3957	876.3851	877.3687	447.6978	T	401.1775	383.1674	384.1509	201.0890	4
10	60.0449	981.4277	963.4172	964.4008	491.2139	S	300.1302	282.1197	283.1032	150.5651	3
11	30.0343	1038.4492	1020.4387	1021.4222	519.7246	G	213.0990	195.0889	196.0712	107.0491	2
12	110.0717					H	156.0773	138.0672	139.0497	78.5384	1

MW 1300.6790

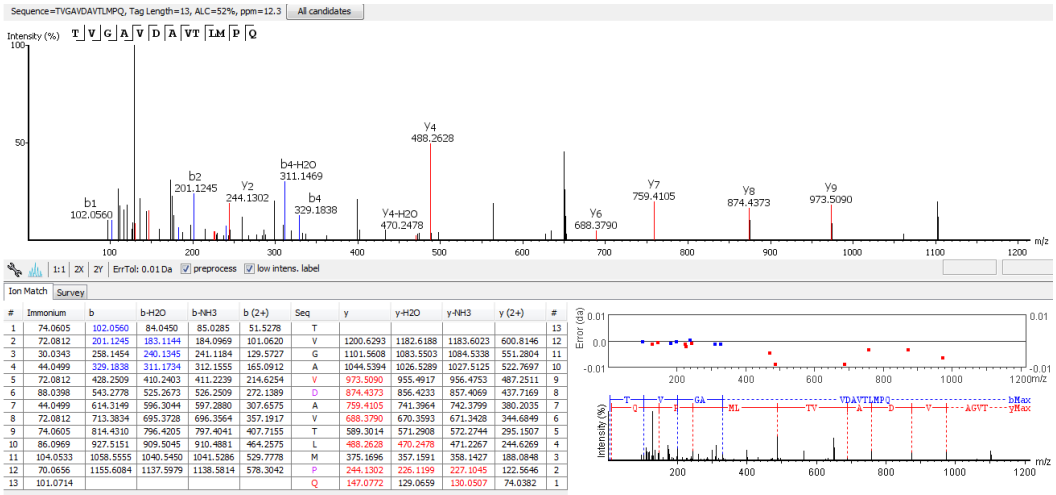

#	Immonium	b	b-H2O	b-NH3	b (2+)	Seq	y	y-H2O	y-NH3	y (2+)	#
1	74.0605	102.0560	84.0450	85.0285	51.5278	T					13
2	72.0812	201.1245	183.1144	184.0969	101.0620	V	1200.6293	1182.6188	1183.6023	600.8146	12
3	30.0343	258.1454	240.1345	241.1184	129.5727	G	1101.5608	1083.5503	1084.5338	551.2804	11
4	44.0499	329.1838	311.1734	312.1555	165.0912	A	1044.5394	1026.5289	1027.5125	522.7697	10
5	72.0812	428.2509	410.2403	411.2239	214.6254	V	973.5090	955.4917	956.4753	487.2511	9
6	88.0398	543.2778	525.2673	526.2509	272.1389	D	874.4373	856.4233	857.4069	437.7169	8
7	44.0499	614.3149	596.3044	597.2880	307.6575	A	759.4105	741.3964	742.3799	380.2035	7
8	72.0812	713.3834	695.3728	696.3564	357.1917	V	688.3790	670.3593	671.3428	344.6849	6
9	74.0605	814.4310	796.4205	797.4041	407.7155	T	589.3014	571.2908	572.2744	295.1507	5
10	86.0969	927.5151	909.5045	910.4881	464.2575	L	488.2628	470.2478	471.2267	244.6269	4
11	104.0533	1058.5555	1040.5450	1041.5286	529.7778	M	375.1696	357.1591	358.1427	188.0848	3
12	70.0656	1155.6084	1137.5979	1138.5814	578.3042	P	244.1302	226.1199	227.1045	122.5646	2
13	101.0714					Q	147.0772	129.0659	130.0507	74.0382	1

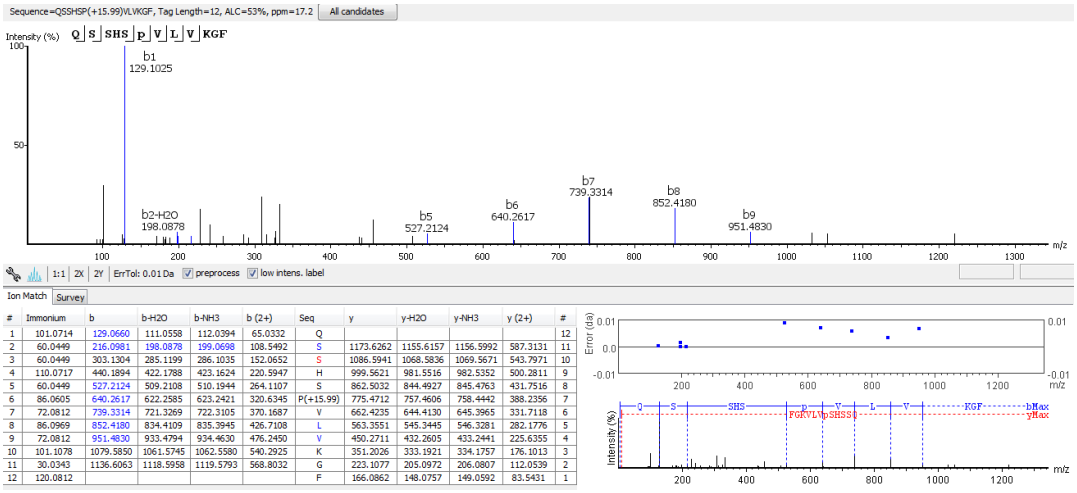

#	Immonium	b	b-H2O	b-NH3	b (2+)	Seq	y	y-H2O	y-NH3	y (2+)	#
1	101.0714	129.0660	111.0558	112.0394	65.0332	Q					12
2	60.0449	216.0981	198.0878	199.0698	108.5492	S	1173.6262	1155.6157	1156.5992	587.3131	11
3	60.0449	303.1304	285.1199	286.1035	152.0652	S	1086.5941	1068.5836	1069.5671	543.7971	10
4	110.0717	440.1894	422.1788	423.1624	220.5947	H	999.5621	981.5516	982.5352	500.2811	9
5	60.0449	527.2124	509.2108	510.1944	264.1107	S	862.5032	844.4927	845.4763	431.7516	8
6	86.0605	640.2617	622.2585	623.2421	320.6345	P(+15.99)	775.4712	757.4606	758.4442	388.2356	7
7	72.0812	739.3314	721.3269	722.3105	370.1687	V	662.4235	644.4130	645.3965	331.7118	6
8	86.0969	852.4180	834.4109	835.3945	426.7108	L	563.3551	545.3445	546.3281	282.1776	5
9	72.0812	951.4830	933.4794	934.4630	476.2450	V	450.2711	432.2605	433.2441	225.6355	4
10	101.1078	1079.5850	1061.5745	1062.5580	540.2925	K	351.2026	333.1921	334.1757	176.1013	3
11	30.0343	1136.6063	1118.5958	1119.5793	568.8032	G	223.1077	205.0972	206.0807	112.0539	2
12	120.0812					F	166.0862	148.0757	149.0592	83.5431	1

MW 1308.6282

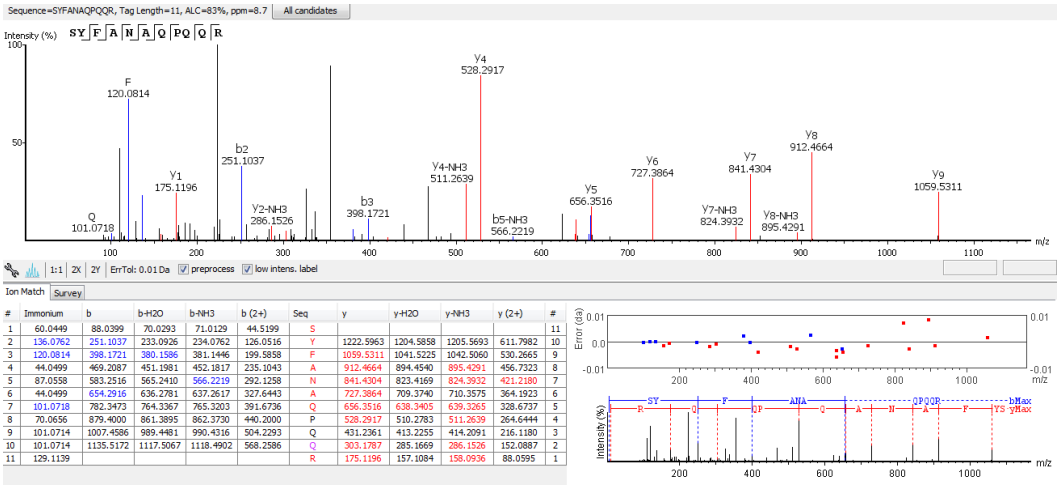

#	Immonium	b	b-H2O	b-NH3	b (2+)	Seq	y	y-H2O	y-NH3	y (2+)	#
1	60.0449	88.0399	70.0293	71.0129	44.5199	S					11
2	136.0762	251.1037	233.0926	234.0762	126.0516	Y	1222.5963	1204.5858	1205.5693	611.7982	10
3	120.0814	398.1721	380.1586	381.1446	199.5858	F	1059.5311	1041.5225	1042.5060	530.2665	9
4	44.0499	469.2087	451.1981	452.1817	235.1043	A	912.4664	894.4560	895.4291	456.7323	8
5	87.0558	583.2516	565.2410	566.2219	292.1258	N	841.4304	823.4169	824.3932	421.2180	7
6	44.0499	654.2916	636.2781	637.2617	327.6443	A	727.3864	709.3740	710.3575	364.1923	6
7	101.0718	782.3473	764.3367	765.3203	391.6736	Q	656.3516	638.3405	639.3265	328.6737	5
8	70.0656	879.4000	861.3895	862.3730	440.2000	P	528.2917	510.2783	511.2639	264.6444	4
9	101.0714	1007.4586	989.4481	990.4316	504.2293	Q	431.2361	413.2255	414.2091	216.1180	3
10	101.0714	1135.5172	1117.5067	1118.4902	568.2586	Q	303.1787	285.1669	286.1526	152.0887	2
11	129.1139					R	175.1196	157.1084	158.0936	88.0595	1

MW 1342.6713

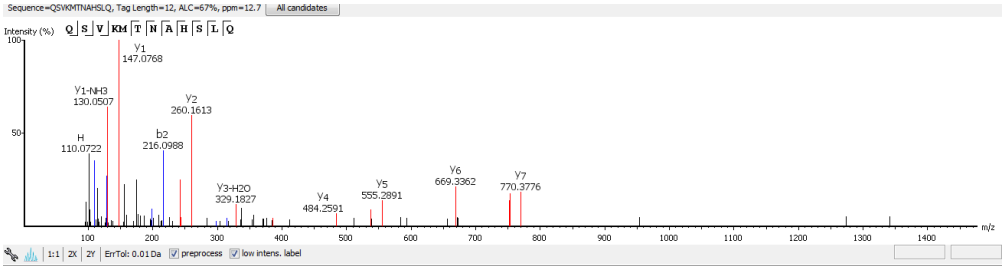

#	Immonium	b	b-H2O	b-NH3	b (2+)	Seq	y	y-H2O	y-NH3	y (2+)	#
1	101.0714	129.0666	111.0558	112.0394	65.0332	Q					12
2	60.0449	216.0988	198.0883	199.0726	108.5492	S	1215.6150	1197.6045	1198.5880	608.3075	11
3	72.0812	315.1673	297.1563	298.1469	158.0834	V	1128.5830	1110.5725	1111.5560	564.7915	10
4	101.1078	443.2618	425.2512	426.2348	222.1309	K	1029.5146	1011.5040	1012.4876	515.2573	9
5	104.0533	574.3023	556.2917	557.2753	287.6512	M	901.4196	883.4091	884.3926	451.2098	8
6	74.0605	675.3500	657.3394	658.3230	338.1750	T	770.3776	752.3656	753.3552	385.6945	7
7	87.0558	789.3929	771.3823	772.3659	395.1964	N	669.3362	651.3209	652.3044	335.1657	6
8	44.0499	860.4300	842.4194	843.4030	430.7150	A	555.2891	537.2772	538.2615	278.1443	5
9	110.0722	997.4889	979.4783	980.4619	499.2444	H	484.2591	466.2408	467.2244	242.6257	4
10	60.0449	1084.5210	1066.5105	1067.4940	542.7605	S	347.1925	329.1827	330.1655	174.0963	3
11	86.0969	1197.6050	1179.5945	1180.5780	599.3025	L	260.1613	242.1502	243.1423	130.5802	2
12	101.0714					Q	147.0768	129.0666	130.0507	74.0382	1

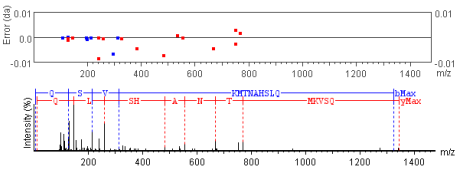

MW 1376.7577

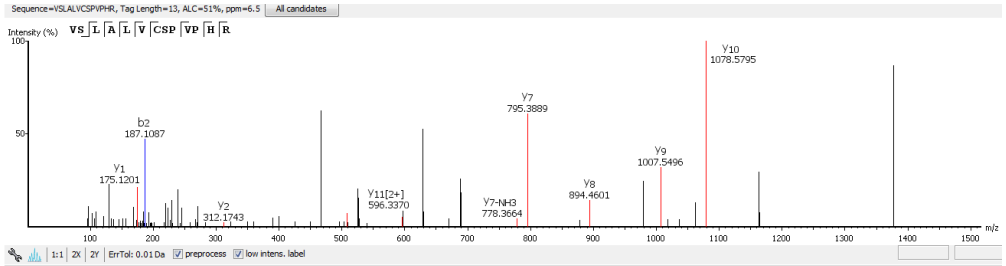

#	Immonium	b	b-H2O	b-NH3	b (2+)	Seq	y	y-H2O	y-NH3	y (2+)	#
1	72.0812	100.0762	82.0657	83.0492	50.5381	V					13
2	60.0449	187.1087	169.0977	170.0813	94.0541	S	1278.6986	1260.6881	1261.6716	639.8493	12
3	86.0969	300.1923	282.1818	283.1653	150.5962	L	1191.6666	1173.6561	1174.6396	596.3370	11
4	44.0499	371.2294	353.2189	354.2025	186.1147	A	1078.5795	1060.5720	1061.5555	539.7913	10
5	86.0969	484.3135	466.3029	467.2865	242.6567	L	1007.5496	989.5349	990.5185	504.2727	9
6	72.0812	583.3819	565.3713	566.3549	292.1909	V	894.4601	876.4509	877.4344	447.7307	8
7	76.0220	686.3911	668.3806	669.3641	343.6956	C	795.3889	777.3824	778.3664	398.1965	7
8	60.0449	773.4231	755.4125	756.3961	387.2115	S	692.3838	674.3732	675.3568	346.6919	6
9	70.0656	870.4759	852.4653	853.4489	435.7379	P	605.3517	587.3412	588.3248	303.1759	5
10	72.0812	969.5443	951.5338	952.5173	485.2722	V	508.3026	490.2885	491.2720	254.6495	4
11	70.0656	1066.5970	1048.5865	1049.5701	533.7985	P	409.2306	391.2200	392.2036	205.1153	3
12	110.0717	1203.6560	1185.6455	1186.6290	602.3280	H	312.1743	294.1673	295.1509	156.5889	2
13	129.1139					R	175.1201	157.1084	158.0919	88.0595	1

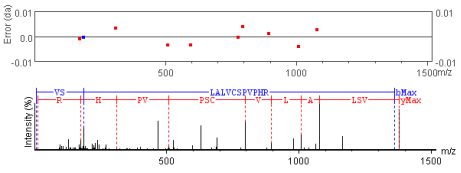

MW 1728.9683

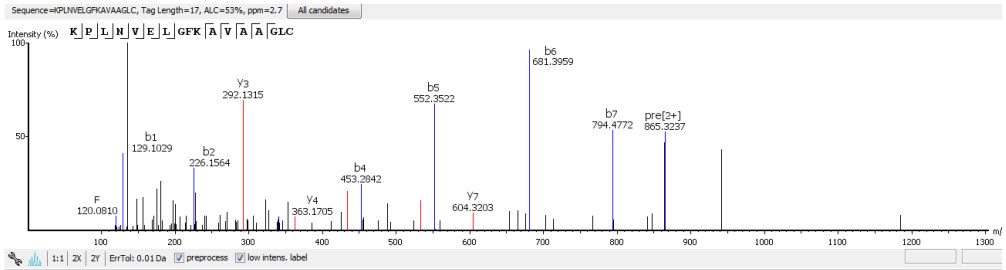

#	Immonium	b	b-H2O	b-NH3	b (2+)	Seq	y	y-H2O	y-NH3	y (2+)	#
1	101.1078	129.1029	111.0922	112.0758	65.0514	K					17
2	70.0656	226.1564	208.1450	209.1285	113.5778	P	1601.8719	1583.8615	1584.8450	801.4360	16
3	86.0969	339.2389	321.2290	322.2126	170.1198	L	1504.8191	1486.8086	1487.7921	752.9095	15
4	87.0558	453.2842	435.2720	436.2556	227.1413	N	1391.7351	1373.7246	1374.7081	696.3676	14
5	72.0812	552.3522	534.3404	535.3240	276.6755	V	1277.6921	1259.6816	1260.6652	639.3461	13
6	102.0554	681.3959	663.3829	664.3665	341.1967	E	1178.6238	1160.6133	1161.5968	589.8119	12
7	86.0969	794.4772	776.4670	777.4506	397.7388	L	1049.5812	1031.5707	1032.5542	525.2906	11
8	30.0343	851.4990	833.4885	834.4720	426.2495	G	936.4971	918.4865	919.4701	468.7485	10
9	120.0810	998.5674	980.5569	981.5405	499.7837	F	879.4756	861.4651	862.4487	440.2378	9
10	101.1078	1126.6624	1108.6519	1109.6354	563.8312	K	732.4072	714.3967	715.3802	366.7036	8
11	44.0499	1197.6995	1179.6890	1180.6725	599.3497	A	604.3203	586.3017	587.2853	302.6561	7
12	72.0812	1296.7679	1278.7574	1279.7410	648.8840	V	533.2792	515.2646	516.2482	267.1376	6
13	44.0499	1367.8051	1349.7946	1350.7781	684.4025	A	434.2051	416.1962	417.1798	217.6034	5
14	44.0499	1438.8422	1420.8317	1421.8152	719.9211	A	363.1705	345.1591	346.1427	182.0848	4
15	30.0343	1495.8636	1477.8531	1478.8367	748.4318	G	292.1315	274.1220	275.1056	146.5663	3
16	86.0969	1608.9476	1590.9371	1591.9207	804.9738	L	235.1111	217.1005	218.0841	118.0555	2

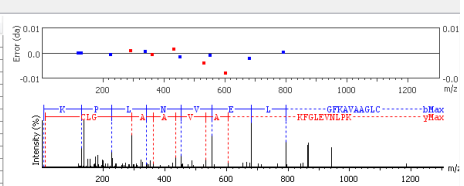

Annotated MS/MS spectra of unique peptides

m/z 1132.53084, Wound-inducible Basic Family Protein

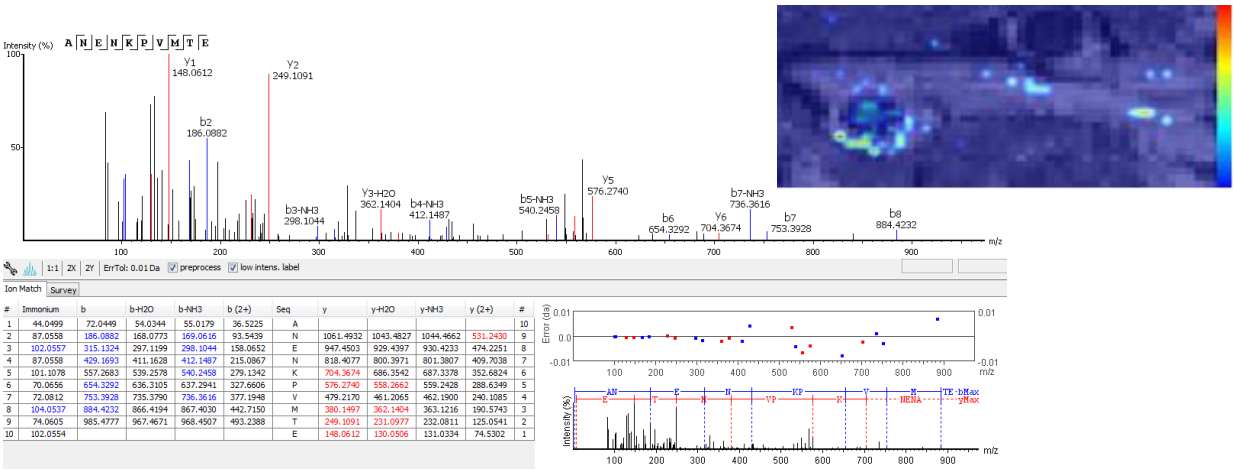

#	Immonium	b	b-H2O	b-NH3	b (2+)	Seq	y	y-H2O	y-NH3	y (2+)	#
1	44.0499	72.0449	54.0344	55.0179	36.5225	A					10
2	87.0558	186.0882	168.0773	169.0616	93.5439	N	1061.4932	1043.4827	1044.4662	531.2430	9
3	102.0557	315.1324	297.1199	298.1044	158.0652	E	947.4503	929.4397	930.4233	474.2251	8
4	87.0558	429.1693	411.1628	412.1487	215.0867	N	818.4077	800.3971	801.3807	409.7038	7
5	101.1078	557.2683	539.2578	540.2458	279.1342	K	704.3674	686.3542	687.3378	352.6824	6
6	70.0656	654.3292	636.3105	637.2941	327.6606	P	576.2740	558.2662	559.2428	288.6349	5
7	72.0812	753.3928	735.3790	736.3616	377.1948	V	479.2170	461.2065	462.1900	240.1085	4
8	104.0537	884.4232	866.4194	867.4030	442.7150	M	380.1497	362.1404	363.1216	190.5743	3
9	74.0605	985.4777	967.4671	968.4507	493.2388	T	249.1091	231.0977	232.0811	125.0541	2
10	102.0554					E	148.0612	130.0506	131.0344	74.5302	1

m/z 1162.59554, Low-temperature Inducible/ Nodulin-like Protein

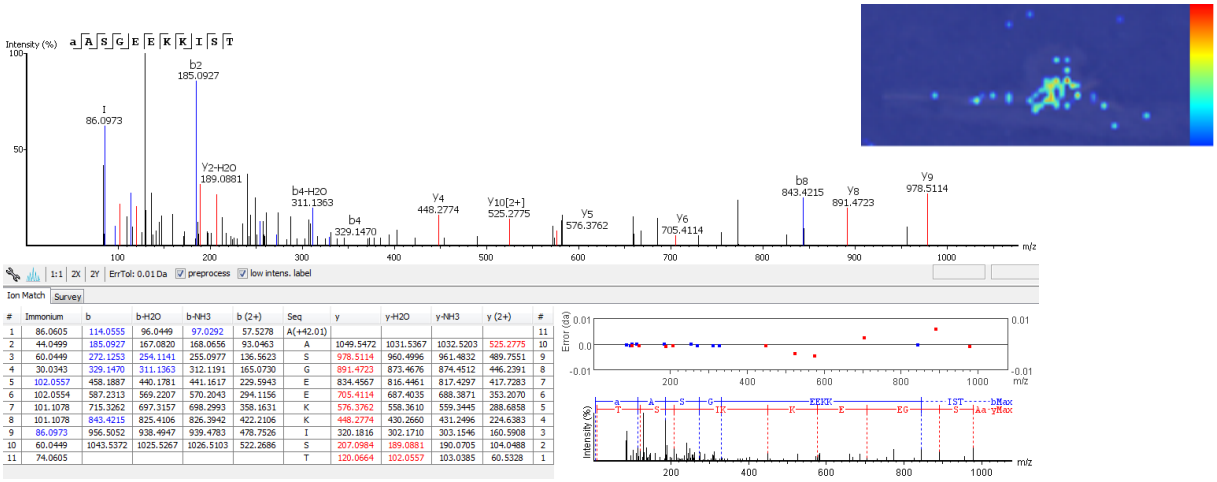

#	Immonium	b	b-H2O	b-NH3	b (2+)	Seq	y	y-H2O	y-NH3	y (2+)	#
1	86.0605	114.0555	96.0449	97.0292	57.5278	A(+42.01)					11
2	44.0499	185.0927	167.0820	168.0656	93.0463	A	1049.5472	1031.5367	1032.5203	525.2775	10
3	60.0449	272.1253	254.1141	255.0977	136.5623	S	978.5114	960.4996	961.4832	489.7551	9
4	30.0343	329.1470	311.1363	312.1191	165.0730	G	891.4723	873.4676	874.4512	446.2391	8
5	102.0557	458.1887	440.1781	441.1617	229.5943	E	834.4567	816.4461	817.4297	417.7283	7
6	102.0554	587.2313	569.2207	570.2043	294.1156	E	705.4114	687.4035	688.3871	353.2070	6
7	101.1078	715.3262	697.3157	698.2993	358.1631	K	576.3762	558.3610	559.3445	288.6858	5
8	101.1078	843.4215	825.4106	826.3942	422.2106	K	448.2774	430.2660	431.2496	224.6383	4
9	86.0973	956.5052	938.4947	939.4783	478.7526	I	320.1816	302.1710	303.1546	160.5908	3
10	60.0449	1043.5372	1025.5267	1026.5103	522.2686	S	207.0984	189.0881	190.0705	104.0488	2
11	74.0605					T	120.0664	102.0557	103.0385	60.5328	1

m/z 1171.62114, 60S Ribosomal Protein L30

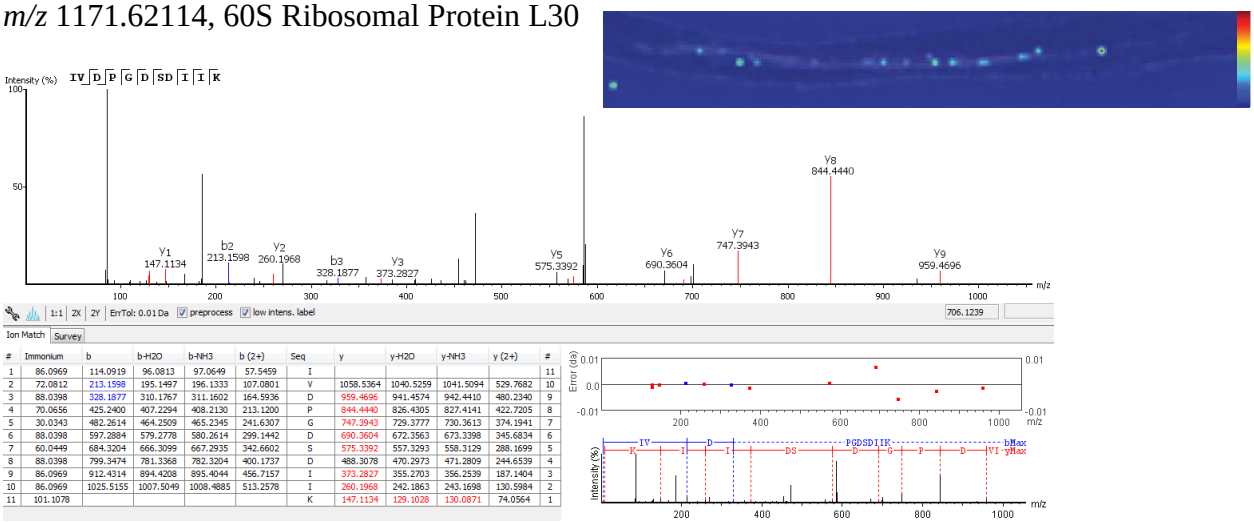

#	Immonium	b	b-H2O	b-NH3	b (2+)	Seq	y	y-H2O	y-NH3	y (2+)	#
1	86.0969	114.0919	96.0813	97.0649	57.5459	I					11
2	72.0812	213.1598	195.1497	196.1333	107.0801	V	1058.5364	1040.5259	1041.5094	529.7682	10
3	88.0398	328.1877	310.1767	311.1602	164.5936	D	959.4696	941.4574	942.4410	480.2340	9
4	70.0656	425.2400	407.2294	408.2130	213.1200	P	844.4440	826.4305	827.4141	422.7205	8
5	30.0343	482.2614	464.2509	465.2345	241.6307	G	747.3943	729.3777	730.3613	374.1941	7
6	88.0398	597.2884	579.2778	580.2614	299.1442	D	690.3604	672.3563	673.3398	345.6834	6
7	60.0449	684.3204	666.3099	667.2935	342.6602	S	575.3392	557.3293	558.3129	288.1699	5
8	88.0398	799.3474	781.3368	782.3204	400.1737	D	488.3078	470.2973	471.2809	244.6539	4
9	86.0969	912.4314	894.4208	895.4044	456.7157	I	373.2827	355.2703	356.2539	187.1404	3
10	86.0969	1025.5155	1007.5049	1008.4885	513.2578	I	260.1968	242.1863	243.1698	130.5984	2
11	101.1078					K	147.1134	129.1028	130.0871	74.0564	1

m/z 1180.62144, Carboxy-terminal Region Remorin

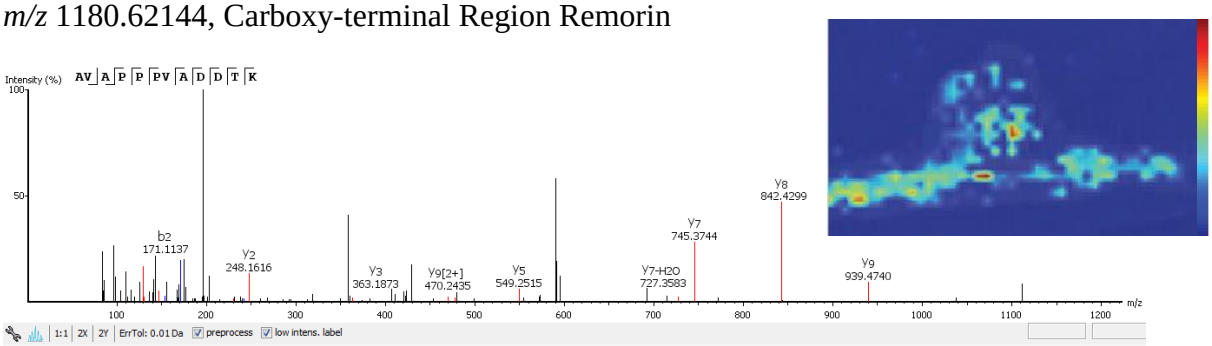

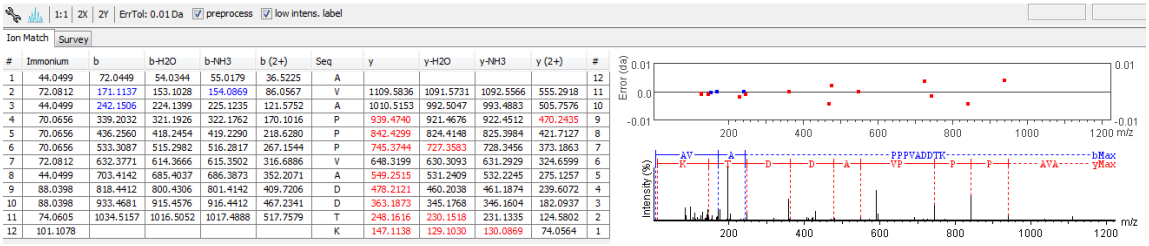

#	Immonium	b	b-H2O	b-NH3	b (2+)	Seq	y	y-H2O	y-NH3	y (2+)	#
1	44.0499	72.0449	54.0344	55.0179	36.5225	A					12
2	72.0812	171.1137	153.1028	154.0869	86.0567	V	1109.5836	1091.5731	1092.5566	555.2918	11
3	44.0499	242.1506	224.1399	225.1235	121.5752	A	1010.5153	992.5047	993.4883	505.7576	10
4	70.0656	339.2032	321.1926	322.1762	170.1016	P	939.4740	921.4676	922.4512	470.2435	9
5	70.0656	436.2560	418.2454	419.2290	218.6280	P	842.4299	824.4148	825.3984	421.7127	8
6	70.0656	533.3087	515.2982	516.2817	267.1544	P	745.3744	727.3583	728.3456	373.1863	7
7	72.0812	632.3771	614.3666	615.3502	316.6886	V	648.3199	630.3093	631.2929	324.6599	6
8	44.0499	703.4142	685.4037	686.3873	352.2071	A	549.2515	531.2409	532.2245	275.1257	5
9	88.0398	818.4412	800.4306	801.4142	409.7206	D	478.2121	460.2038	461.1874	239.6072	4
10	88.0398	933.4681	915.4576	916.4412	467.2341	D	363.1873	345.1768	346.1604	182.0937	3
11	74.0605	1034.5157	1016.5052	1017.4888	517.7579	T	248.1616	230.1518	231.1335	124.5802	2
12	101.1078					K	147.1138	129.1030	130.0869	74.0564	1

m/z 1293.67314, Ferritin

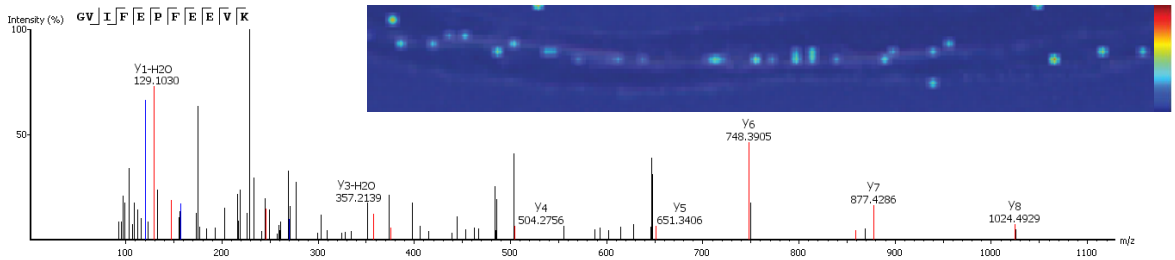

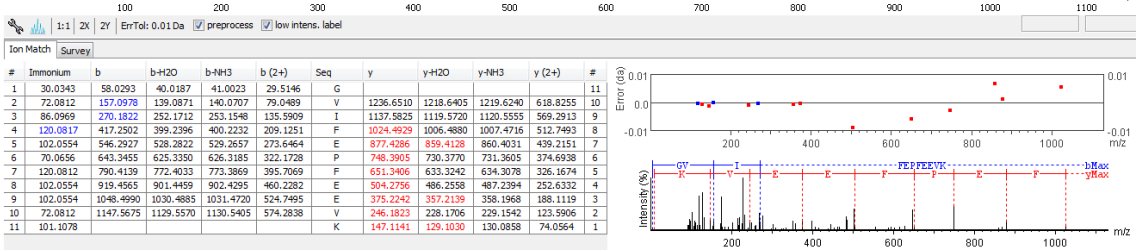

#	Immonium	b	b-H2O	b-NH3	b (2+)	Seq	y	y-H2O	y-NH3	y (2+)	#
1	30.0343	58.0293	40.0187	41.0023	29.5146	G					11
2	72.0812	157.0978	139.0871	140.0707	79.0489	V	1236.6510	1218.6405	1219.6240	618.8255	10
3	86.0969	270.1822	252.1712	253.1548	135.5909	I	1137.5825	1119.5720	1120.5555	569.2913	9
4	120.0817	417.2502	399.2396	400.2232	209.1251	F	1024.4929	1006.4880	1007.4716	512.7493	8
5	102.0554	546.2927	528.2822	529.2657	273.6464	E	877.4286	859.4128	860.4031	439.2151	7
6	70.0656	643.3455	625.3350	626.3185	322.1728	P	748.3905	730.3770	731.3605	374.6938	6
7	120.0812	790.4139	772.4033	773.3869	395.7069	F	651.3406	633.3242	634.3078	326.1674	5
8	102.0554	919.4565	901.4459	902.4295	460.2282	E	504.2756	486.2558	487.2394	252.6332	4
9	102.0554	1048.4990	1030.4885	1031.4720	524.7495	E	375.2242	357.2139	358.1968	188.1119	3
10	72.0812	1147.5675	1129.5570	1130.5405	574.2838	V	246.1823	228.1706	229.1542	123.5906	2
11	101.1078					K	147.1141	129.1030	130.0858	74.0564	1

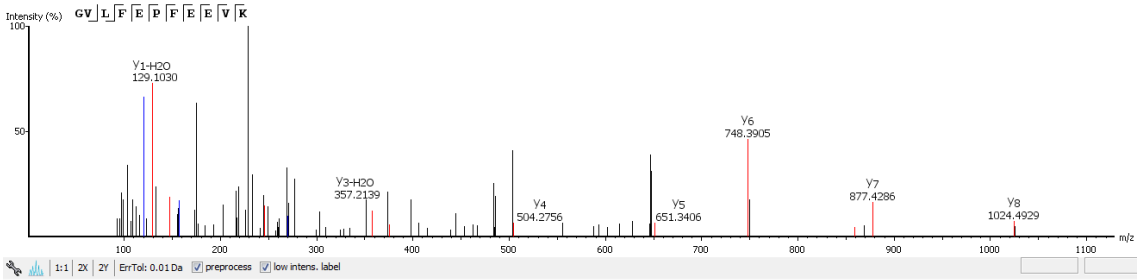

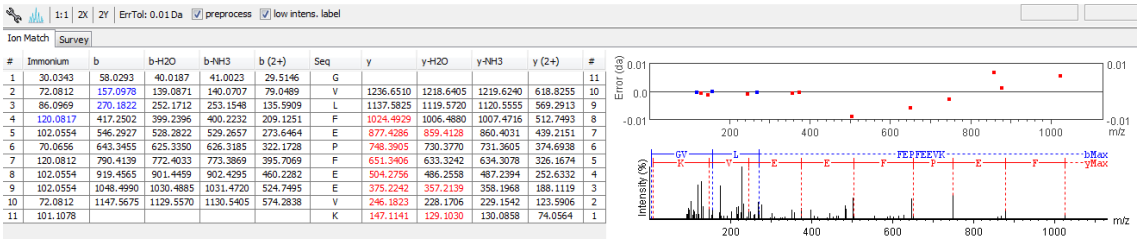

#	Immonium	b	b-H2O	b-NH3	b (2+)	Seq	y	y-H2O	y-NH3	y (2+)	#
1	30.0343	58.0293	40.0187	41.0023	29.5146	G					11
2	72.0812	157.0978	139.0871	140.0707	79.0489	V	1236.6510	1218.6405	1219.6240	618.8255	10
3	86.0969	270.1822	252.1712	253.1548	135.5909	L	1137.5825	1119.5720	1120.5555	569.2913	9
4	120.0817	417.2502	399.2396	400.2232	209.1251	F	1024.4929	1006.4880	1007.4716	512.7493	8
5	102.0554	546.2927	528.2822	529.2657	273.6464	E	877.4286	859.4128	860.4031	439.2151	7
6	70.0656	643.3455	625.3350	626.3185	322.1728	P	748.3905	730.3770	731.3605	374.6938	6
7	120.0812	790.4139	772.4033	773.3869	395.7069	F	651.3406	633.3242	634.3078	326.1674	5
8	102.0554	919.4565	901.4459	902.4295	460.2282	E	504.2756	486.2558	487.2394	252.6332	4
9	102.0554	1048.4885	1030.4885	1031.4720	524.7495	E	375.2242	357.2139	358.1968	188.1119	3
10	72.0812	1147.5570	1129.5570	1130.5405	574.2838	V	246.1823	228.1706	229.1542	123.5906	2
11	101.1078					K	147.1141	129.1030	130.0858	74.0564	1

m/z 1483.75454, Ribulose Biphosphate Carboxylase/ Oxygenase Large Chain Domain Protein

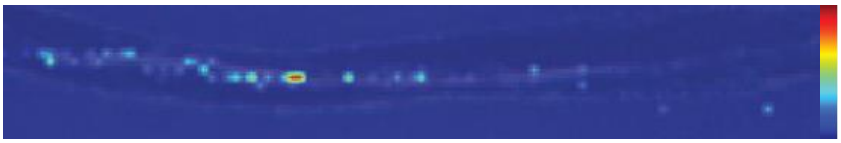

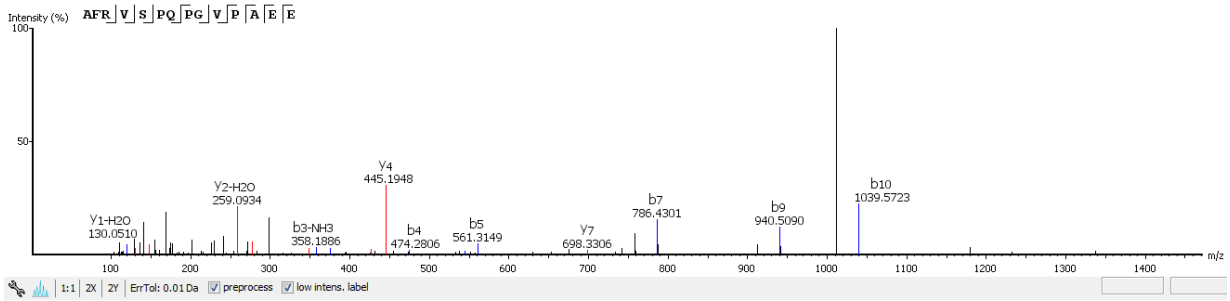

#	Immonium	b	b-H2O	b-NH3	b (2+)	Seq	y	y-H2O	y-NH3	y (2+)	#
1	44.0499	72.0449	54.0344	55.0179	36.5225	A					14
2	120.0817	219.1133	201.1028	202.0863	110.0567	F	1412.7168	1394.7063	1395.6898	706.8584	13
3	129.1139	375.2163	357.2039	358.1886	188.1072	R	1265.6484	1247.6379	1248.6215	633.3242	12
4	72.0812	474.2806	456.2723	457.2559	237.6414	V	1109.5472	1091.5367	1092.5203	555.2736	11
5	60.0449	561.3149	543.3043	544.2924	281.1574	S	1010.4789	992.4683	993.4519	505.7394	10
6	70.0656	658.3676	640.3571	641.3406	329.6838	P	923.4468	905.4363	906.4199	462.2234	9
7	101.0714	786.4301	768.4156	769.3992	393.7131	Q	826.3940	808.3835	809.3671	413.6970	8
8	70.0656	883.4789	865.4684	866.4520	442.2395	P	698.3306	680.3250	681.3085	349.6678	7
9	30.0343	940.5090	922.4899	923.4734	470.7502	G	601.2827	583.2722	584.2557	301.1414	6
10	72.0812	1039.5723	1021.5583	1022.5419	520.2844	V	544.2613	526.2507	527.2343	272.6306	5
11	70.0656	1136.6216	1118.6111	1119.5946	568.8108	P	445.1948	427.1822	428.1659	223.0964	4
12	44.0499	1207.6587	1189.6482	1190.6317	604.3293	A	348.1422	330.1295	331.1131	174.5701	3
13	102.0554	1336.7013	1318.6908	1319.6743	668.8506	E	277.1042	259.0934	260.0760	139.0515	2
14	102.0554					E	148.0611	130.0510	131.0334	74.5302	1

m/z 1976.02434, Basic 7S Globulin/ Peptidase A1, Pepsin

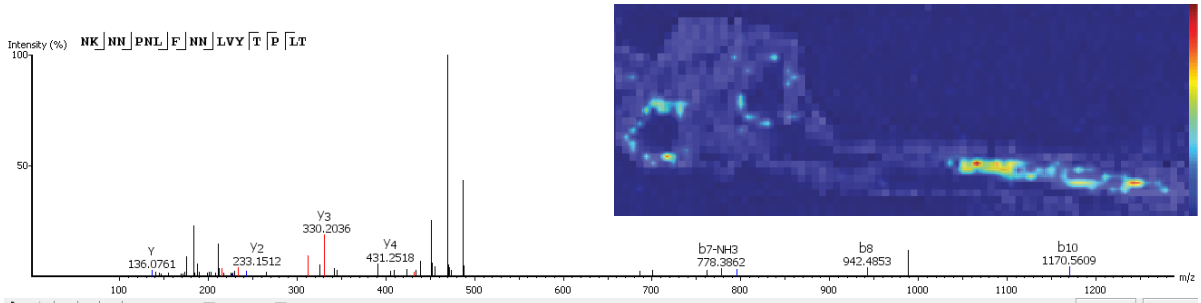

#	Immonium	b	b-H2O	b-NH3	b (2+)	Seq	y	y-H2O	y-NH3	y (2+)	#
1	87.0558	115.0508	97.0402	98.0238	58.0254	N					17
2	101.1078	243.1475	225.1351	226.1198	122.0729	K	1861.9806	1843.9701	1844.9536	931.4903	16
3	87.0558	357.1886	339.1781	340.1617	179.0943	N	1733.8857	1715.8752	1716.8588	867.4429	15
4	87.0558	471.2360	453.2210	454.2046	236.1158	N	1619.8428	1601.8323	1602.8158	810.4214	14
5	70.0656	568.2843	550.2737	551.2573	284.6422	P	1505.7998	1487.7893	1488.7728	753.3999	13
6	87.0558	682.3273	664.3167	665.3003	341.6636	N	1408.7471	1390.7366	1391.7201	704.8735	12
7	86.0969	795.4114	777.4008	778.3862	398.2057	L	1294.7041	1276.6936	1277.6771	647.8521	11
8	120.0812	942.4853	924.4692	925.4528	471.7399	F	1181.6201	1163.6096	1164.5931	591.3101	10
9	87.0558	1056.5227	1038.5122	1039.4957	528.7614	N	1034.5516	1016.5411	1017.5247	517.7758	9
10	87.0558	1170.5609	1152.5551	1153.5386	585.7828	N	920.5087	902.4982	903.4818	460.7544	8
11	86.0969	1283.6497	1265.6392	1266.6227	642.3248	L	806.4658	788.4553	789.4388	403.7329	7
12	72.0812	1382.7180	1364.7075	1365.6910	691.8590	V	693.3817	675.3712	676.3547	347.1909	6
13	136.0761	1545.7814	1527.7709	1528.7544	773.3907	Y	594.3134	576.3028	577.2864	297.6567	5
14	74.0605	1646.8291	1628.8186	1629.8021	823.9146	T	431.2518	413.2394	414.2230	216.1250	4
15	70.0656	1743.8818	1725.8713	1726.8549	872.4409	P	330.2036	312.1946	313.1754	165.6012	3
16	86.0969	1856.9658	1838.9553	1839.9388	928.9829	L	233.1512	215.1407	216.1226	117.0748	2
17	74.0605					T	120.0655	102.0550	103.0385	60.5328	1

Chapter 6

Mass Spectrometry Imaging Reveals a Diversity of Chemical Response to Pathogen Exposure in the Coevolved Fungus-Growing Ant/ *Pseudonocardia* Symbiotic System

Photograph © Alex Wild

Adapted from **Gemperline, E.**; Horn, H.; Currie, C.; Li, L. "Novel MALDI-Mass Spectrometry Imaging Method for the Analysis of Bacteria on the Exoskeleton of Fungus-Growing Ants" *In Preparation* and **Gemperline, E.**; Horn, H.; Chevrette, M.; Mevers, E.; Clardy, J.; Li, L.; Currie, C. "Diversity of Chemical Response to Pathogen Exposure Reveals Insights into the Co-evolved Fungus-Growing Ant/*Pseudonocardia* Symbiotic System" *In Preparation*

Abstract

Fungus-growing ants have a long-standing mutualism with *Pseudonocardia*, a bacterium that lives on the ants' exoskeleton and protects their fungal garden food source from harmful pathogens, including *Escovopsis*, a pathogen that has evolved to specifically target the ants' fungal garden. Typically, these microbial interactions would be studied using cultures and co-cultures on agar plates; however these *in vitro* bioassays may not accurately represent the metabolome of the ant/*Pseudonocardia*/*Escovopsis* interaction *in vivo*. We present a novel mass spectrometry imaging (MSI) method to detect compounds produced by *Pseudonocardia* on the surface of the ants' exoskeletons (specifically the propleural plate) in response to pathogen exposure. When the ants are exposed to pathogens, *Pseudonocardia* naturally produce compounds with anti-microbial properties. We compared these *in vivo* imaging results to *in vitro* bioassays and found that microbes express a different suite of small molecules in their coevolved systems compared to those molecules induced when grown under culture conditions. This study aimed to compare the metabolic profiles of *Pseudonocardia* grown in culture (*in vitro*) to *Pseudonocardia* on the exoskeleton of fungus-growing ants (*in vivo*) in response to multispecies interactions, with applications toward an improved method for novel natural product discovery.

Significance Statement

The study reported here shows a valuable, innovative protocol for the induction of secondary metabolites, potentially novel anti-microbial drug candidates, from the ant/*Pseudonocardia* symbiosis. We have compared the metabolic profiles of microbial culture bioassays to that of the same species *in vivo* for the first time using mass spectrometry imaging.

Introduction

Species interactions, while complex and diverse, drive the evolution and diversity of life. Microbes, arguably the most ubiquitous organisms, form varied species associations that are facilitated by chemical communication, which is poorly characterized to date.[1] Due to the difficult nature of observing microbial communication, most chemical interactions—mediated by small molecules—have been studied in pairwise interactions when microbes are removed from their relevant ecological and evolutionary environments.[2-3] While informative, this approach may not observe the full diversity of small molecules that are mediating microbial interactions. Here we use a well-defined host-microbe mutualism in the fungus-growing ant system to explore differences in chemical profiles of a mutualistic bacterium when grown in culture and when the bacterium resides in its coevolved system. Understanding these chemical interactions *in vitro* and *in vivo* will provide insight into complex microbial interactions that are shaping their evolutionary trajectories and guide future discovery of novel natural products.

Fungus-growing ants (Tribe Attini) participate in a multi-partite symbiosis whose associations span from mutualistic to pathogenic. This tribe of ants maintains an obligate mutualism with a Basidiomycete fungus which they cultivate and consume as their sole food source.[4-6] The fungus garden, a monoculture, is susceptible to a fungal pathogen in the genus *Escovopsis* which may entirely consume the cultivar.[7] In order to protect their food source, the ants evolved an additional microbial mutualism: a bacterium in the genus *Pseudonocardia*

resides on the exoskeleton of the ants and provides antimicrobial protection against fungal pathogens.[8-10] Removal of *Pseudonocardia* from ants causes their fungal cultivar to be more susceptible to *Escovopsis* infection,[8] and bioassays between *Pseudonocardia* and *Escovopsis* show that *Pseudonocardia* actively inhibits the growth of *Escovopsis*.[10-11] Although several small molecules produced by *Pseudonocardia* have been characterized *in vitro*,[12-13] no studies to date have examined if these same molecules detected *in vitro* are also produced *in vivo.* Developing an approach to study secondary metabolites *in vivo* could reveal functionally and ecologically relevant chemical interactions between microbial species as well as unlock a vast array of novel natural products.

In this study, mass spectrometry imaging (MSI) was used to examine species interactions between *Pseudonocardia* and three ecologically relevant pathogens: *Escovopsis sp. 1, Escovopsis sp. 2,* and *Trichoderma viridae, in vitro* and *in vivo.* Both strains of *Escovopsis* were isolated from fungus-growing ant systems and *T. viridae* is a common soil pathogen. MSI has rapidly developed into a powerful analytical technique for understanding the spatial distributions of molecules within biological samples. MALDI-MSI is typically performed on thin slices of tissue, however many microbial MSI studies use bacterial cultures or co-cultures on agar plates.[14-17] MSI of bacterial colonies in culture traditionally uses a small sieve to apply a coat of dry matrix to the sample before MSI, which often yields poor signal and inconsistent MSI results. We have developed an improved method of applying matrix to the bacterial cultures that resulted in improved signal, analyte detection, and reproducibility. The use of co-cultures,

two different cell types or organisms grown together in culture, is a simple way to study interactions between microbial species *in vitro*, but these systems may not produce the same secondary metabolites as they would in their native ecological niche. Thus, in addition to the improved method for MSI of bacterial colonies *in vitro*, we present here a novel MSI method for detecting metabolic profiles produced by *Pseudonocardia* on the surface of the ants' propleural plate *in vivo* (**Figure 2**). The novel method, described in detail in the materials and methods section, enabled accurate *in vivo* MSI of *Pseudonocardia* on the ant exoskeleton. This study aimed to compare the metabolic profiles of *Pseudonocardia* grown in culture (*in vitro*) to *Pseudonocardia* on the exoskeleton (specifically the propleural plate) of fungus-growing ants (*in vivo*) in response to multispecies interactions.

Results

In vitro MALDI-MSI

Two strains of *Pseudonocardia* were isolated from two different species of *Acromyrmex* leaf-cutter ants, subsequently called *Pseudonocardia sp. octospinosus* and *Pseudonocardia sp. echinatior*. Bacteria and fungi were grown together in a co-culture, as previously described,[8] and MSI was performed on the zone of inhibition (the portion of the agar that separates the bacteria from the fungi where the bacteria secrete molecules that inhibit growth of the fungi).[15] The metabolites produced in response to pathogen exposure were analyzed via MALDI-MSI and

were compared to control samples of each microbe cultured in isolation. **Figure 1A** shows representative MS images of compounds produced by *Pseudonocardia* in response to each pathogen. Compared to the control, these images clearly show compounds produced by the bacterium in response to pathogen presence. Additionally, **Figure 1A** demonstrates the ability to observe select compounds that are secreted by *Pseudonocardia* only in response to particular pathogens indicative of a species-specific response.

Total numbers of *m/z* values (≥ *m/z* 300) detected in each treatment are represented in **Figure 1B.** A cutoff of *m/z* 300 and above was chosen in order to exclude many primary metabolites, as most known antimicrobial compounds have a molecular weight greater than 300 Da. The majority of treatments produced between 300-400 distinct *m/z* values. Among those *m/z*, each treatment produced several mass spectral peaks that were unique (listed in the supplemental information **Table S1**). While each strain of *Pseudonocardia* produced unique *m/z* in response to all pathogens, both expressed many more unique masses when challenged with the generalist pathogen, *T. viridae*. Additionally, *Pseudonocardia* did produce shared compounds in response to exposure to multiple pathogens regardless of the type of pathogen it was challenged with (**Figure S1**).

Total mass spectra are analyzed using a Partial Least Squares-Discriminant Analysis (PLS-DA) demonstrating a 'metabolic fingerprint' for each treatment (**Figure 1C)**. Each co-culture condition is represented by a different color point in the plot and the shaded area

represents the 95% confidence region of each fingerprint. Interestingly, each strain produced a unique community of metabolites under non-pathogen-exposure conditions. Although these two strains are genomically similar, they show distinct metabolic fingerprints. Additionally, each bacterial strain produced a distinct suite of molecules in response to each pathogen, as each treatment occupies significantly different space in the PLS-DA plot. A PLS-DA plot comparing each pathogen in isolation and in co-culture is shown in **Figure S2** and shows distinct metabolic fingerprints.

In vivo MALDI-MSI

In order to compare the compounds produced *in vitro* to those that are produced *in vivo*, we developed a novel method for MSI of *Pseudonocardia* on the surface of the ants' propleural plates, as described in the materials and methods section below and shown in **Figure 2**. A description of the method proof-of-principle is discussed in the supplemental information.

Two different colonies of leaf-cutter ants, *Acromyrmex octospinosus* and *A. echinatior*, and their corresponding *Pseudonocardia* were exposed to 4 different treatments: a no exposure treatment (control), exposure to *E. sp. 1*, exposure to *E. sp. 2*, and exposure to *T. viridae*. *Pseudonocardia* on the ants' propleural plate (**Figure 2)** were subsequently analyzed via MALDI-MSI after treatment. The same fungal and bacterial strains were used for both the *in vitro* and *in vivo* experiments. **Figure 3A** shows representative MS images of compounds produced by *Pseudonocardia* on the propleural plate. Similar to the *in vitro* bioassays, these

images clearly show compounds produced in response to exposure to any of the pathogens and some compounds that were only produced in response to a particular pathogen.

Figure 3B represents the number of *m/z* values observed for each treatment (≥ *m/z* 300). Fewer compounds in total were detected in all treatments of *A. octospinosus* compared to treatments of *A. echinatior*. Unique *m/z* values were observed in each pathogen treatment (see supplemental information **Table S2**). Interestingly, it was observed that some of the unique compounds such as *m/z* 331.168, 478.064, and 623.189, produced only in response to pathogen exposure, were produced by both strains of *Pseudonocardia*, although the majority of the unique compounds were only produced by one strain of *Pseudonocardia*. Again, similar to the *in vitro* results, *Pseudonocardia* produced certain compounds in response to pathogen exposure regardless of the type of pathogen it was challenged with (**Figure S3**).

PLS-DA of mass spectra from these *in vivo* conditions revealed a colony specific response (**Figure 3C).** Each color point in the plot represents a different ant analyzed in the experiment and the shaded area represents the 95% confidence region of each metabolic fingerprint. Metabolic fingerprints for each treatment showed little variation; however a significant difference was revealed between the two different strains of *Pseudonocardia* regardless of the treatment. This is expected given the fewer number of unique *m/z* values detected *in vivo* compared to the *in vitro*, co-culture experiments.

In vivo Target Compound Elucidation

In order to obtain putative identifications of the detected compounds of interest, online databases were searched based on accurate mass matching (within 5 ppm error) using MetaboSearch.[18] Unique *m/z* values that do not currently match compounds located in the online metabolite databases searched with MetaboSearch are indicated with an asterisk in **Table S1** and **Table S2**. Of the 48 compounds (45 unique to one *Pseudonocardia* species, 3 produced by both *Pseudonocardia* species) detected from the *in vivo* study, 32 compounds returned no hits from database searching and could be potentially novel natural products. In order to dereplicate compounds of interest, *Pseudonocardia* and fungi were grown in liquid co-culture as previously described.[19] LC-MS and MALDI-MS analyses were performed on metabolite extractions from the liquid co-cultures in order to determine the best growth conditions for expression of the target compounds identified via *in vivo* MALDI-MSI. Unsurprisingly the unique compounds detected *in vivo* were unable to be replicated in *in vitro* liquid co-cultures; therefore highly creative method development will be a necessary future step for isolation and characterization of these potentially novel anti-microbial compounds.

Comparison of Compounds Produced *in vitro* and *in vivo*

In order to compare the compounds produced *in vitro* to those that are produced *in vivo*, all bacterial and fungal strains were the same for the *in vitro* and *in vivo* studies. **Figure 4** shows representative MS images of compounds produced by *Pseudonocardia* on the ants' propleural

plates compared to compounds produced by *Pseudonocardia* in culture or co-culture. These images clearly show compounds produced in response to exposure to any of the pathogens and some compounds that were only produced in response to a particular pathogen. The majority of these example compounds were produced on the ants in response to pathogen exposure, but not produced in culture. Interestingly, some of these compounds (specifically *m/z* 622.035 and *m/z* 768.122) were detected in the control bioassay but not detected on the control ants *in vivo*. We detected 46 compounds (≥ *m/z* 300) from *Pseudonocardia sp. octospinosus* and 53 compounds from *Pseudonocardia sp. echinatior in vivo* and 179 compounds from *Pseudonocardia sp. octospinosus* and 253 compounds from *Pseudonocardia sp. echinatior in vitro* that were expressed in response to pathogen exposure and could be potential candidates for novel antimicrobial compounds.

PLS-DA of mass spectra comparing the *in vitro* and *in vivo* conditions for *Pseudonocardia sp. octospinosus* (**Figure 4B**) and *Pseudonocardia sp. echinatior* (**Figure 4C**) yielded assay-specific metabolic fingerprints. In the overall comparison, metabolic fingerprints for each *in vivo* treatment showed little variation; more variation was seen amongst treatments *in vitro*. The greatest variation in metabolic fingerprints was shown between the *in vitro* vs. *in vivo* treatments, highlighting the fact that ecological and evolutionarily relevant interactions play a large role in the metabolites produced by *Pseudonocardia*.

Discussion

From a technological standpoint, the work presented here demonstrated a method for improved MALDI-MSI of metabolites from *in vitro* bioassays. By applying the MALDI matrix with an automatic sprayer system, instead of the more traditional method of applying dry matrix powder with a sieve, we were able to acquire more reproducible images with higher signal intensity. Furthermore it was essential to use MSI for this study in order to be truly confident that the detected compounds were indeed being produced by *Pseudonocardia*; therefore, we designed a completely new method for MALDI-MSI of this system *in vivo*. This is a valuable, innovative protocol that can be adapted in the future for imaging the surface of other organisms in order to tackle difficult biological questions. This protocol was demonstrated for studying the ecology of the ant/*Pseudonocardia* symbiosis, with striking differences observed in the metabolic profiles produced by these interactions when studied *in vivo* vs. *in vitro*.

In this work we demonstrate that interactions between *Pseudonocardia* and different species of pathogens produce vastly different chemical responses. Each species of *Pseudonocardia* produced unique compounds in response to each different pathogen they were exposed to. Interestingly, in the co-culture conditions, both species of *Pseudonocardia* produced significantly more unique compounds in response to the generalist pathogen, *T. viridae,* compared to the number of compounds elicited in response to either strain of *Escovopsis*. In the *in vivo* preparation, *Pseudonocardia* produced more compounds in response to *Escovopsis*. Furthermore, for the *in vivo* study, a significant difference was observed in the metabolic profiles

between the two different strains of *Pseudonocardia*, while only subtle differences in the metabolic fingerprints were observed due to pathogen exposure.

Furthermore, we find that multi-species, coevolved associations elicit different molecular responses than pairwise interactions in culture. When studying these interactions *in vitro*, we noticed that in the co-culture conditions, both species of *Pseudonocardia* produced significantly more unique compounds in response to the generalist pathogen, *T. viridae*, compared to the number of compounds elicited in response to either strain of *Escovopsis*, as mentioned above. We initially hypothesized that *Pseudonocardia* may have developed a more specific response to the coevolved pathogen, *Escovopsis*, while a larger suite of molecules were elicited from the presence of the generalist pathogen, *T. viridae*. However, this same trend was not observed *in vivo*, where *Pseudonocardia* produced more compounds in response to *Escovopsis*. In light of the *in vivo* results, it appears that studying bacteria in their natural environment may yield novel, complementary natural products to the traditional *in vitro* studies. Additionally, significantly fewer metabolites were produced by *Pseudonocardia in vivo* compared to *in vitro*, suggesting that the mutualism plays a substantial role in determining which secondary metabolite clusters are expressed in a given scenario. Future work should consider the ecologically and evolutionary relevant interactions as we attempt to answer questions regarding the expression of cryptic secondary metabolite clusters.

We were interested in identifying potential target compounds that were detected in the *in vivo* experiments. First we searched online databases using MetaboSearch, as described above. We then attempted to use traditional methods of scaling-up the concentration of target compounds by growing liquid co-cultures, extracting secondary metabolites, purifying via LC-MS and analyzing compound structure with NMR spectroscopy. However, there were significant difficulties observing the same molecules using MALDI or electrospray ionization (ESI)-MS on liquid culture extracts. This was expected as it is well documented that different MS ionization methods yield different detectable ions and because *in vitro* methods are clearly missing key elements of the *in vivo* systems, which results in different chemical signatures. This implies that future novel products research may require a novel, *in vivo* approach for isolation and characterization of biologically relevant natural products/ candidate drug targets.

Microbial interactions are without doubt complex and their ecological chemical interactions are currently poorly characterized. The dawn of genomic research reveals great potential to produce many more secondary metabolites, now recognized as important signaling molecules, than are currently reported.[20] Conditions under which microbes express or induce metabolites have been elusive and the work here emphasizes the importance of ecological and evolutionarily relevant interactions to fully characterize the molecules involved in microbial species associations.

Materials and Methods

In vitro Bioassays

Pseudonocardia was isolated from each colony[21] and bioassays between the bacteria and pathogenic fungi (*Escovopsis sp. 1, Escovopsis sp. 2,* and *Trichoderma viridae*) were performed according to Currie *et al*.1999.[8] Each bioassay was performed in triplicate on YMEA media (4g yeast extract, 4 g dextrose, 10 g malt extract, 15g agar in 1 L distilled H_2O). *Pseudonocardia* was inoculated in the center of the petri dish and allowed to grow for 2 weeks. Each fungal pathogen was inoculated on the edge of each petri dish and grew for 1 week after which samples from the zone of inhibition were prepared for MSI.

Subcolony Preparation and Pathogen Treatment

Subcolonies of ants and fungus garden were made for each colony and each pathogen treatment in a sterile petri dish. Approximately 1 g of fungus garden was placed in a plastic weigh boat with minor worker ants included. Four major workers with *Pseudonocardia* bloom covering their entire exoskeleton were removed from the main fungus garden in order to ensure the approximate same age among all workers. Cultures of *Escovopsis sp. SES* and *Escovopsis sp. AL* and *Trichoderma viridae* were grown one week on Potato Dextrose Medium (39g Potato Dextrose Medium, 15 g agar) prior to infection. Infection of subcolonies occurred by applying fungal spores directly to the fungus garden. Control subcolonies were similarly inoculated with

a sterile inoculation loop. Subcolonies were left for 20 hours after which focal ants were removed and frozen at -20°C for further processing.

Ant Colony Maintenance

Two colonies of *Acromyrmex* leaf-cutter ants were used: colony ST040116-01 *Acromyrmex octospinosus*, Panama; colony CC031209-02 *A. echinatior*, Panama. Both colonies were kept in a temperature controlled room (27°C) at the University of Wisconsin-Madison prior to this experiment.

Sample Preparation for MALDI-MSI

Bacterial colonies and their neighboring zone of inhibition were cut from the agar plate using a razor blade and carefully transferred to a glass slide using a spatula. The colony and agar was dehydrated in a desiccator overnight before matrix application. For the *in vivo* ant imaging, grooves were cut into glass slides and double-sided tape was applied to the back of the slide where the grooves cut all the way through the slide. The double-sided tape allows for a flexible backing in which ants of different sizes can still be positioned so that their propleural plate is parallel to the top of the slide, which is important for obtaining sub-5 ppm accurate mass measurements. Treated and control ants were removed from their subcolonies and frozen at -20 °C for 1 hour. The ant thoraxes were removed and inlaid into the groove of the slide with the propleural plate facing outward and even with the top of the slide. An additional thin strip

of double sided tape was applied below the propleural plate to stabilize and secure the thorax into place.

For both agar and ant MSI, matrix (40 mg/mL DHB in 50:50 water:methanol) was applied to the dried agar or ants using a TM Sprayer (HTX Technologies, LLC, Carrboro, NC, USA). DHB was purchased from Sigma-Aldrich (St. Louis, MO, USA). The TM Sprayer method for applying DHB to the ants and dried agar was as follows: 80 °C, 0.2 mL/min flow rate, 8 passes-rotate and offset, 3 mm spacing, 30 sec dry time between passes, velocity of 950 mm/min.

MALDI-Orbitrap MSI

A MALDI-Orbitrap LTQ mass spectrometer (Thermo Scientific, Waltham, MA, USA) equipped with a N_2 laser (spot diameter of 75 μm) was used in positive ion mode for MS imaging. Three biological replicates of each treatment type were imaged at a spatial resolution of 100 μm for the bioassays using a mass range of *m/z* 100-1700, a mass resolution of 60,000 and a mass error of ≤ 5 ppm. For *in vivo* MSI, three rounds of imaging were conducted over the course of several months in which three ants of each treatment type were imaged at a spatial resolution of 75 μm using the same instrumental settings listed above. The region to be imaged and the raster step size were controlled using the LTQ software (Thermo Scientific) and the instrument methods were created using Xcalibur (Thermo Scientific). Ants/ co-cultures were imaged in groups of three according to their treatment type. Three groups of three ants for each sample type and control were imaged (nine total biological replicates). Three biological

replicates were imaged for each co-culture treatment and control as the co-culture samples showed very little variability between samples.

MALDI-MSI Data Processing and Analysis

Raw data files acquired from MALDI-MSI were uploaded to MSiReader.[22] MSiReader was used to create a list of compounds of interest by selecting the propleural plate as the "interrogated zone" and subtracting the matrix peaks chosen as the "reference zone". A list of *m/z* values was generated in this way for nine control ants and nine ants for each treatment type and the lists were combined into one list; duplicated masses (within 5 ppm mass error) and isotopic peaks were removed. Note that *m/z* values for ion adducts were not verified and removed from the mass list. This process was used for both ant species and three biological replicates of all co-culture controls and treatments. Ion images were automatically generated with MSiReader for every sample/ treatment using the combined mass lists. All images were normalized to the TIC. Mass lists were manually cross-checked between all treatment and sample types to determine if each compound was unique to a specific treatment or shared between treatments. Compounds were determined to be valid target compounds if they were present in at least five of the nine biological replicates for the *in vivo* assays and at least two of the three biological replicates for the *in vitro* assays. Unique compounds (potential target compounds) were defined as compounds present in pathogen treated samples and not in the control samples.

Statistical Analysis

Mass intensity lists were compiled using ImageQuest software (Thermo Scientific) and then analyzed using MetaboAnalyst.[23-24] Masses under *m/z* 300.000 were removed before analysis. Mass peak lists were analyzed with a mass tolerance of 0.003 *m/z* and retention time tolerance set to 1 sec. Data were filtered using standard deviation to eliminate non-informative variables and then normalized by sum and auto-scaled. PLS-DA was performed on the normalized data.

Sample Preparation and MALDI-Orbitrap MS Analysis of Liquid Culture Extracts

A MALDI-Orbitrap LTQ mass spectrometer (Thermo Scientific, Waltham, MA, USA) equipped with a N_2 laser was used in positive ion mode for MS analysis of liquid co-culture extractions. Dry samples were resuspended in combinations of methanol, water, and dichloromethane (DCM) according to their solubility profiles. Samples were combined with either α-cyano-4-hydroxycinnamic acid (CHCA, 10 mg/mL in 50% acetonitrile) or DHB (150 mg/mL in 50% methanol) MALDI matrices in a 50:50 ratio and 1 μL spots were spotted onto the stainless-steel MALDI target plate. A mass range of *m/z* 300-1700 and a mass resolution of 60,000 were used for data collection. The laser energy was controlled using the LTQ software (Thermo Scientific) and the instrument methods were created using Xcalibur (Thermo Scientific).

Acknowledgements

The authors would like to thank Tracy Drier in the UW-Madison Chemistry Glass Shop for creating the custom glass slides for the *in vivo* MALDI-MSI; without them this work would not have been possible. The authors would like to thank Sam Marquardt for his help in maintaining the ant colonies and sample preparation. Support for this research was provided by the University of Wisconsin–Madison (UW-Madison), Office of the Vice Chancellor for Research and Graduate Education with funding from the Wisconsin Alumni Research Foundation (WARF). LL acknowledges an H. I. Romnes Faculty Research Fellowship and a Vilas Distinguished Achievement Professorship with funding provided by the WARF and UW-Madison School of Pharmacy. CC acknowledges NIH U19TW009872-01. E.G. acknowledges an NSF Graduate Research Fellowship (DGE-1256259). The MALDI-Orbitrap was purchased through an NIH shared instrument grant (NCRR S10RR029531).

References

1. Romero, D.; Traxler, M. F.; Lopez, D.; Kolter, R., Antibiotics as Signal Molecules. *Chemical reviews* **2011,** *111* (9), 5492-5505.

2. Seyedsayamdost, M. R.; Cleto, S.; Carr, G.; Vlamakis, H.; Joao Vieira, M.; Kolter, R.; Clardy, J., Mixing and Matching Siderophore Clusters: Structure and Biosynthesis of Serratiochelins from Serratia Sp. V4. *Journal of the American Chemical Society* **2012,** *134* (33), 13550-13553.

3. Traxler, M. F.; Watrous, J. D.; Alexandrov, T.; Dorrestein, P. C.; Kolter, R., Interspecies Interactions Stimulate Diversification of the Streptomyces Coelicolor Secreted Metabolome. *mBio* **2013,** *4* (4).

4. Weber, N. A., Fungus-Growing Ants. *Science* **1966,** *153* (3736), 587-604.

5. Hölldobler, B.; Wilson, E. O., *The Ants*. Belknap Press of Harvard University Press: Cambridge, MA, 1990.

6. Chapela, I. H.; Rehner, S. A.; Schultz, T. R.; Mueller, U. G., Evolutionary History of the Symbiosis between Fungus-Growing Ants and Their Fungi. *Science* **1994,** *266* (5191), 1691-1694.

7. Currie, C. R.; Mueller, U. G.; Malloch, D., The Agricultural Pathology of Ant Fungus Gardens. *Proceedings of the National Academy of Sciences of the United States of America* **1999,** *96* (14), 7998-8002.

8. Currie, C. R.; Scott, J. A.; Summerbell, R. C.; Malloch, D., Fungus-Growing Ants Use Antibiotic-Producing Bacteria to Control Garden Parasites. *Nature* **1999,** *398* (6729), 701-704.

9. Currie, C. R.; Bot, A. N. M.; Boomsma, J. J., Experimental Evidence of a Tripartite Mutualism: Bacteria Protect Ant Fungus Gardens from Specialized Parasites. *Oikos* **2003,** *101* (1), 91-102.

10. Poulsen, M.; Cafaro, M. J.; Erhardt, D. P.; Little, A. E. F.; Gerardo, N. M.; Tebbets, B.; Klein, B. S.; Currie, C. R., Variation in Pseudonocardia Antibiotic Defence Helps Govern Parasite-Induced Morbidity in Acromyrmex Leaf-Cutting Ants. *Env Microbiol Rep* **2010,** *2* (4), 534-540.

11. Cafaro, M. J.; Poulsen, M.; Little, A. E. F.; Price, S. L.; Gerardo, N. M.; Wong, B.; Stuart, A. E.; Larget, B.; Abbot, P.; Currie, C. R., Specificity in the Symbiotic Association between Fungus-Growing Ants and Protective Pseudonocardia Bacteria. *P Roy Soc B-Biol Sci* **2011,** *278* (1713), 1814-1822.

12. Oh, D. C.; Poulsen, M.; Currie, C. R.; Clardy, J., Dentigerumycin: A Bacterial Mediator of an Ant-Fungus Symbiosis. *Nat Chem Biol* **2009,** *5* (6), 391-393.

13. Carr, G.; Derbyshire, E. R.; Caldera, E.; Currie, C. R.; Clardy, J., Antibiotic and Antimalarial Quinones from Fungus-Growing Ant-Associated Pseudonocardia Sp. *J Nat Prod* **2012,** *75* (10), 1806-1809.

14. Bouslimani, A.; Sanchez, L. M.; Garg, N.; Dorrestein, P. C., Mass Spectrometry of Natural Products: Current, Emerging and Future Technologies. *Nat Prod Rep* **2014,** *31* (6), 718-729.

15. Yang, J. Y.; Phelan, V. V.; Simkovsky, R.; Watrous, J. D.; Trial, R. M.; Fleming, T. C.; Wenter, R.; Moore, B. S.; Golden, S. S.; Pogliano, K.; Dorrestein, P. C., Primer on Agar-Based Microbial Imaging Mass Spectrometry. *Journal of bacteriology* **2012,** *194* (22), 6023-6028.

16. Moree, W. J.; Yang, J. Y.; Zhao, X.; Liu, W. T.; Aparicio, M.; Atencio, L.; Ballesteros, J.; Sanchez, J.; Gavilan, R. G.; Gutierrez, M.; Dorrestein, P. C., Imaging Mass Spectrometry of a Coral Microbe Interaction with Fungi. *Journal of chemical ecology* **2013,** *39* (7), 1045-1054.

17. Gemperline, E. L., L, Maldi-Mass Spectrometric Imaging of Endogenous Metabolites in Biological Systems. *eLS* **2014,** *2014* (August), 1-9.

18. Zhou, B.; Wang, J. L.; Ressom, H. W., Metabosearch: Tool for Mass-Based Metabolite Identification Using Multiple Databases. *Plos One* **2012,** *7* (6).

19. Ramadhar, T. R.; Beemelmanns, C.; Currie, C. R.; Clardy, J., Bacterial Symbionts in Agricultural Systems Provide a Strategic Source for Antibiotic Discovery. *The Journal of antibiotics* **2014,** *67* (1), 53-58.

20. Bentley, S. D.; Chater, K. F.; Cerdeno-Tarraga, A. M.; Challis, G. L.; Thomson, N. R.; James, K. D.; Harris, D. E.; Quail, M. A.; Kieser, H.; Harper, D.; Bateman, A.; Brown, S.; Chandra, G.; Chen, C. W.; Collins, M.; Cronin, A.; Fraser, A.; Goble, A.; Hidalgo, J.; Hornsby, T.; Howarth, S.; Huang, C. H.; Kieser, T.; Larke, L.; Murphy, L.; Oliver, K.; O'Neil, S.; Rabbinowitsch, E.; Rajandream, M. A.; Rutherford, K.; Rutter, S.; Seeger, K.; Saunders, D.; Sharp, S.; Squares, R.; Squares, S.; Taylor, K.; Warren, T.; Wietzorrek, A.; Woodward, J.; Barrell, B. G.; Parkhill, J.; Hopwood, D. A., Complete Genome Sequence of the Model Actinomycete Streptomyces Coelicolor A3(2). *Nature* **2002,** *417* (6885), 141-147.

21. Cafaro, M. J.; Currie, C. R., Phylogenetic Analysis of Mutualistic Filamentous Bacteria Associated with Fungus-Growing Ants. *Canadian journal of microbiology* **2005,** *51* (6), 441-446.

22. Robichaud, G.; Garrard, K. P.; Barry, J. A.; Muddiman, D. C., Msireader: An Open-Source Interface to View and Analyze High Resolving Power Ms Imaging Files on Matlab Platform. *Journal of the American Society for Mass Spectrometry* **2013,** *24* (5), 718–721.

23. Xia, J.; Sinelnikov, I. V.; Han, B.; Wishart, D. S., Metaboanalyst 3.0--Making Metabolomics More Meaningful. *Nucleic acids research* **2015,** *43* (W1), W251-257.

24. Xia, J.; Psychogios, N.; Young, N.; Wishart, D. S., Metaboanalyst: A Web Server for Metabolomic Data Analysis and Interpretation. *Nucleic acids research* **2009,** *37* (Web Server issue), W652-660.

Figures

Figure 1

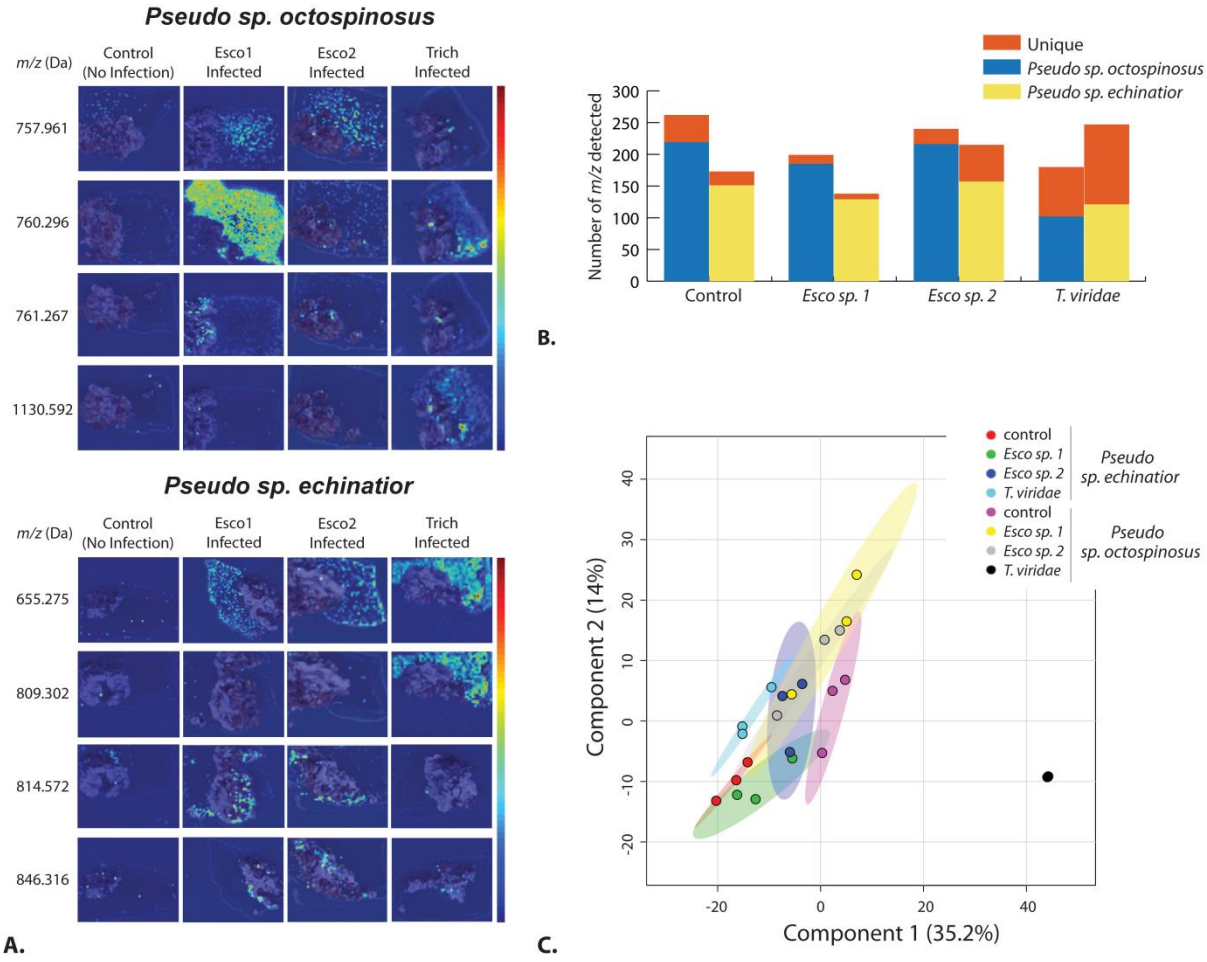

Figure 1. A) Representative MS images of *Pseudonocardia* co-cultures. B) Total numbers of *m/z* detected (≥ *m/z* 300) through MSI for each strain of *Pseudonocardia in vitro* under no exposure, control treatment as well as pathogen treatments. C) Partial Least Squares-Discriminant Analysis (PLS-DA) plot of mass intensity spectra for each treatment group *in vitro* (≥ *m/z* 300). Control treatments represent *Pseudonocardia* grown in culture with no pathogen exposure. Individual points represent one replicate. Shaded areas represent the 95% confidence area for each treatment.

Figure 2

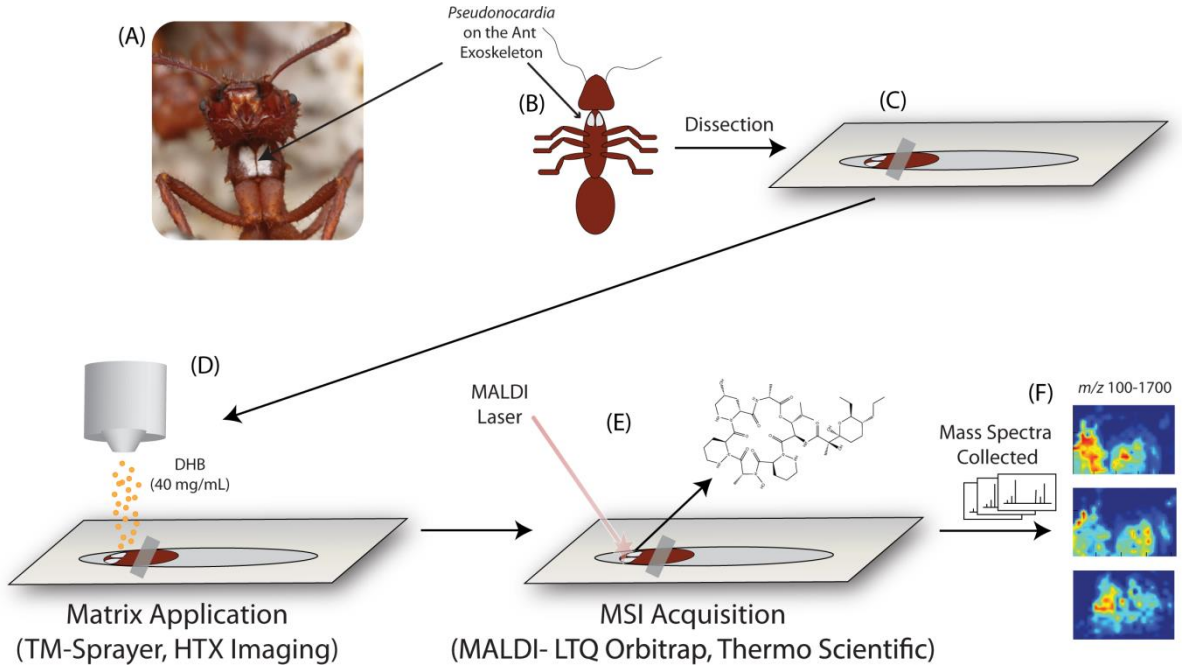

Figure 2. Workflow for mass spectrometry imaging of *Pseudonocardia* on the surface of the ant propleural plate. A) and B) show a photograph and a cartoon, respectively, of *Pseudonocardia*, on the ant exoskeleton. C) Grooves were cut into glass slides and double-sided tape was applied to the back of the slide, allowing for a flexible backing in which ants of different sizes can still be positioned so that their propleural plate is parallel to the top of the slide. The ant thoraxes were removed and positioned into the groove of the slide with the propleural plate facing outward and even with the top of the slide. An additional thin strip of double sided tape was applied below the propleural plate to stabilize and secure the thorax into place. D) Matrix was applied to the slide using an automatic sprayer. E) A laser was fired at the sample to ionize compounds of interest and introduce them into the mass spectrometer. F) An array of mass spectra was acquired using a MALDI-LTQ Orbitrap and compiled into MS images.

Figure 3

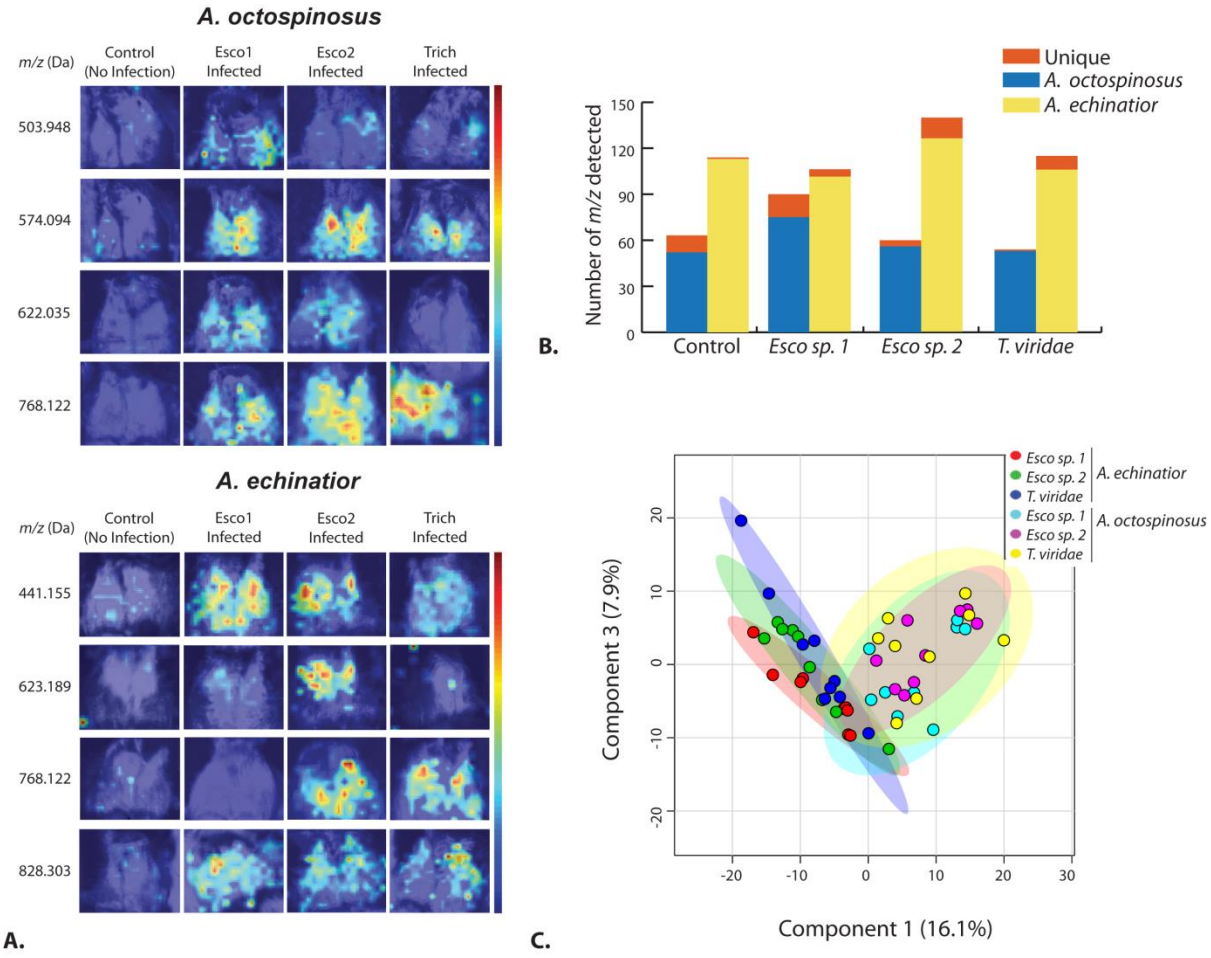

Figure 3. A) Representative MS images of *Pseudonocardia* on the surface of the ant propleural plate. B) Total numbers of *m/z* detected (≥ *m/z* 300) through MSI for each strain of *Pseudonocardia in vivo* under no exposure control treatment as well as pathogen treatments. C) Partial Least Squares-Discriminant Analysis (PLS-DA) plot of mass intensity spectra for each treatment group *in vivo* (≥ *m/z* 300). Control treatments represent *Pseudonocardia* grown on the ant propleural plate with no pathogen exposure. Individual points represent one replicate. Shaded areas represent the 95% confidence area for each treatment.

Figure 4

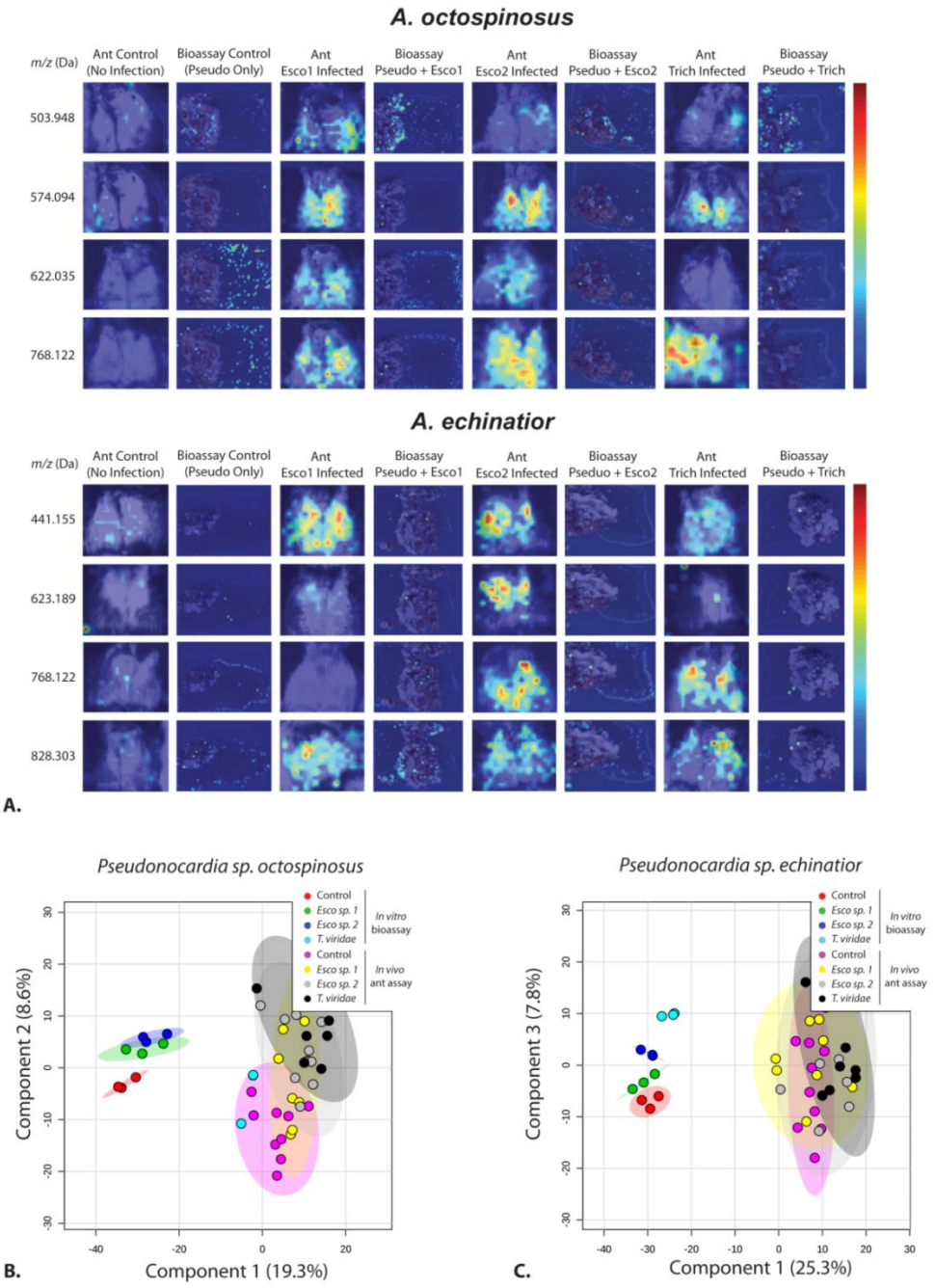

Figure 4. A) Representative MS images comparing *Pseudonocardia in vitro* and *in vivo*. Partial Least Squares-Discriminant Analysis (PLS-DA) plot of mass intensity spectra for each treatment group *in vitro* and *in vivo* (≥ *m/z* 300) for B) *Pseudonocardia sp. octospinosus* and C) *Pseudonocardia sp. echinatior*. Control treatments represent *Pseudonocardia* with no pathogen exposure. Individual points represent one replicate. Shaded areas represent the 95% confidence area for each treatment.

Supplemental Information

In vivo MSI Method Proof-of-Principle

As proof of principle and to determine the best method of placing the ants on the slide, ants were raised without *Pseudonocardia* bacteria and ProteoMass MALDI-MS calibration mix (Sigma-Aldrich) was spiked onto the propleural plate. Three methods of placing the ants on the slide were tested: 1) remove just the propleural plate and place it in the groove of the slide; 2) dissect out the upper portion of the thorax that contains the propleural plate and place it in the groove; and 3) dissect out the entire thorax and place it in the groove with additional tape over the bottom portion of the thorax to secure into place. Images were obtained for six calibration standards in the mass range of 200-1700 *m/z*. Method 1 showed an error of 3.1-5.4 ppm, method 2 showed 4.2-6.4 ppm error, and method 3 showed 0.6-2.7 ppm error.

Table S1. Unique *m/z* values observed in each pathogen treatment *in vitro*

Pseudonocardia sp. octospinosus							
Control		***Escovopsis sp. 1***	***Escovopsis sp. 2***	***Trichoderma viridae***			
321.219*	666.434	322.054*	403.024*	303.134*	407.145*	636.273*	972.393*
329.084*	672.419*	329.015*	465.121*	306.121	417.221*	637.075*	973.567*
356.200*	675.105*	343.187*	525.121*	313.058*	433.155	652.247*	977.59*
364.096	704.389*	360.188*	526.912*	314.084*	530.344*	654.268*	988.366*
376.124*	745.019*	360.361*	527.177	314.091	556.099*	657.283*	991.56*
399.970*	751.027*	500.046*	542.97*	318.129*	557.108*	657.291*	1130.592*
402.021*	759.065*	635.111	568.041*	319.069*	559.378*	658.296*	
402.051*	767.000*	641.342*	570.144*	324.214*	565.053*	664.377*	
408.019*	767.984*	649.047*	580.949*	325.199*	575.502	666.637*	
429.240	768.122	650.032*	581.319	326.123*	586.406*	671.271*	
438.145*	884.486*	657.084*	599.94*	329.167	596.095*	687.264*	
450.976*	891.704	950.951*	637.476*	330.938*	598.109*	688.112*	
535.298*	1035.509*	1018.4*	671.028*	332.075	598.297*	693.231	
541.023*	1193.567*	1019.408*	675.092*	334.14*	599.119	696.096*	
548.31*	1247.372*		679.065*	344.134*	599.968*	699.265	
558.063*	1353.399*		695.460	356.167	600.120*	706.63*	
563.005*	1500.481*		696.022*	357.152*	601.135*	718.336*	
565.29*	1515.449*		697.477	363.147	601.489*	719.083*	
566.438*	1516.452*		699.105*	368.203	604.024*	726.068*	
580.045*			708.982*	369.189*	614.272*	740.317*	
582.412*			744.283*	378.152*	615.297*	756.293*	
599.990*			744.302	396.338*	619.121*	764.275	
614.91*			757.961*	399.145	621.101*	804.552	
622.035			953.531*	406.159*	630.265*	892.127*	
Pseudonocardia sp. echinatior							
Control	***Escovopsis sp. 1***	**Escovopsis sp. 2**		***Trichoderma viridae***			
306.048	303.185*	305.304*	691.068*	306.121	425.148*	579.131*	687.264*
329.084*	330.938*	306.080	693.010*	312.035*	425.980	580.949*	688.021*
374.024*	369.155*	314.091	693.117	324.214*	435.108	581.955*	688.269
399.97*	556.998*	320.171*	693.334*	328.008*	442.132*	582.961*	690.070*
420.061	633.075	336.074*	695.038*	328.115*	445.093*	583.254	693.231
466.951*	649.047*	347.094*	696.022*	329.167	447.110*	583.965*	694.026*
541.023*	650.032*	348.071	703.191*	330.046*	447.130	595.104*	694.236*
566.438*	657.084*	350.086*	705.321*	345.045	448.027*	599.940*	697.053*
580.045*	905.054*	365.105*	708.982*	345.142*	449.129*	619.092*	699.081*
582.412*		386.048*	711.434*	346.019*	462.102	634.057*	699.105*
596.020		402.196*	713.449*	347.175*	472.000*	634.091*	703.039*
622.035		403.024*	714.033*	352.027*	490.038*	635.066*	705.185*
635.18*		404.171*	718.003*	353.164*	492.067*	643.109*	706.189*
636.083*		440.109*	744.283*	354.057*	505.037*	646.475*	712.054*
688.394*		443.045*	745.314*	365.164*	506.011*	650.066*	719.021*
707.062*		481.094*	756.493*	366.112	508.049*	654.268*	719.036*
708.047*		540.04*	758.509*	368.001*	510.078*	656.075*	719.083*
745.019*		551.309	761.286*	368.203	514.048*	657.047*	740.317*
768.122		554.169*	761.309*	369.189*	521.011*	657.283*	759.292*
876.731*		568.041*	772.525	370.031*	524.058*	659.075*	761.267
884.486*		570.144*	777.281	370.052	527.020*	659.097*	764.275
941.274*		574.129	786.542	376.039	530.045*	669.256*	780.250*
		574.430*	800.557*	378.994*	530.344*	669.292	790.919*
		587.314*	814.572	381.158*	542.069	670.263*	804.552
		609.072*	1157.36*	383.002*	542.994*	670.294*	809.302*
		610.443*	1499.474*	383.975*	546.018	671.271*	843.292*
		658.066*		398.975*	549.975*	672.047*	867.238*
		671.028*		406.159*	558.295	672.275*	1035.509*
		672.011*		407.986	558.968*	674.096*	1191.344*
		675.092*		412.100*	564.030*	681.058*	1353.399*
		679.065*		419.135	565.950*	681.079*	
		687.176*		425.012*	576.248*	683.108*	

*Denotes *m/z* values that are not found in online metabolite databases (searched with MetaboSearch with a mass tolerance of ± 5 ppm) and could be potentially novel compounds

Figure S1

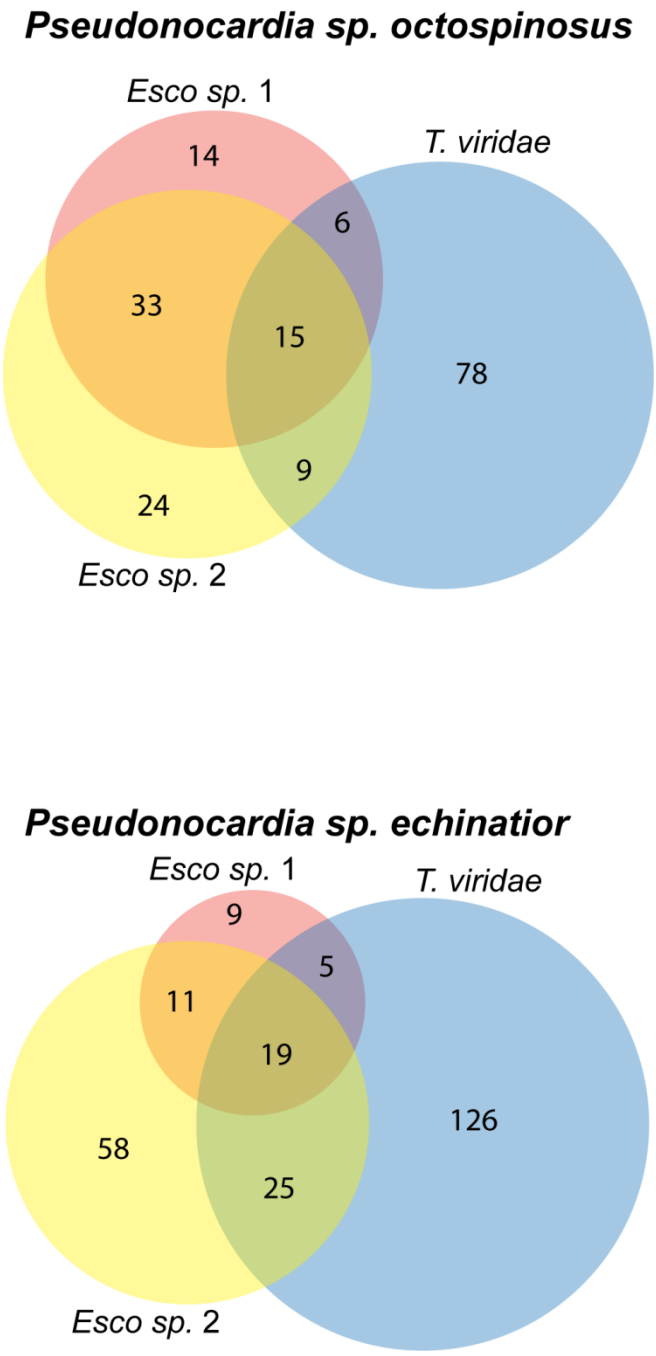

Figure S1. Venn diagrams showing the number of compounds detected from *Pseudonocardia* in response to each different pathogen exposure *in vitro*. Compounds were detected that are unique to a specific pathogen exposure, while others seem to be elicited regardless of the type of pathogen *Pseudonocardia* was exposed to.

Figure S2

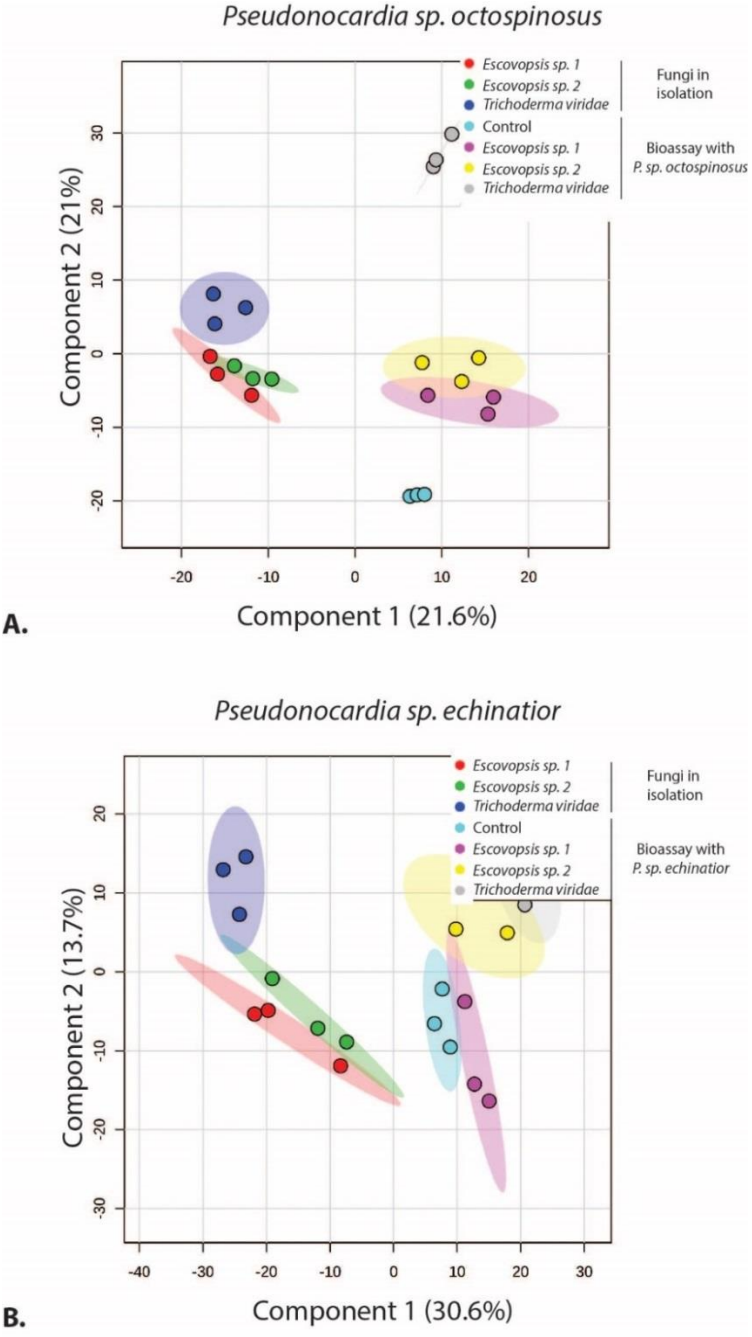

Figure S2. Partial Least Squares-Discriminant Analysis (PLS-DA) plot of mass intensity spectra for each pathogen monoculture and co-culture treatment group (≥ *m/z* 300) for A) *Pseudonocardia sp. octospinosus* and B) *Pseudonocardia sp. echinatior*. Control treatments represent *Pseudonocardia* grown in culture with no pathogen exposure. Individual points represent one replicate. Shaded areas represent the 95% confidence area for each treatment.

Table S2. Unique *m/z* values observed in each pathogen treatment *in vivo*

Pseudonocardia sp. octospinosus				***Pseudonocardia sp. echinatior***			
Control	***Escovopsis sp. 1***	***Escovopsis sp. 2***	***T. viridae***	**Control**	***Escovopsis sp. 1***	***Escovopsis sp. 2***	***T. viridae***
315.202	360.188*	361.143	331.168*	471.234	409.246*	311.182*	348.071
331.151	382.107*	444.091*			569.453*	331.168*	350.086*
338.145	399.192*	604.024*			618.113*	347.175*	478.064
376.183	439.101	744.082			704.250*	355.171	496.339
498.176	456.201				737.311*	366.112	607.409*
561.391	478.064					383.110*	617.981*
565.290	490.084*					385.120*	772.525
623.189*	503.948*					399.199*	773.139*
719.299	507.176*					412.100*	786.542
775.267	561.222*					414.097	
783.147	619.121*					453.245	
848.041	620.009*					494.224*	
	643.109*					623.189*	
	655.152					824.122*	
	755.367*						

*Denotes *m/z* values that are not found in online metabolite databases (searched with MetaboSearch with a mass tolerance of ± 5 ppm) and could be potentially novel compounds

Figure S3

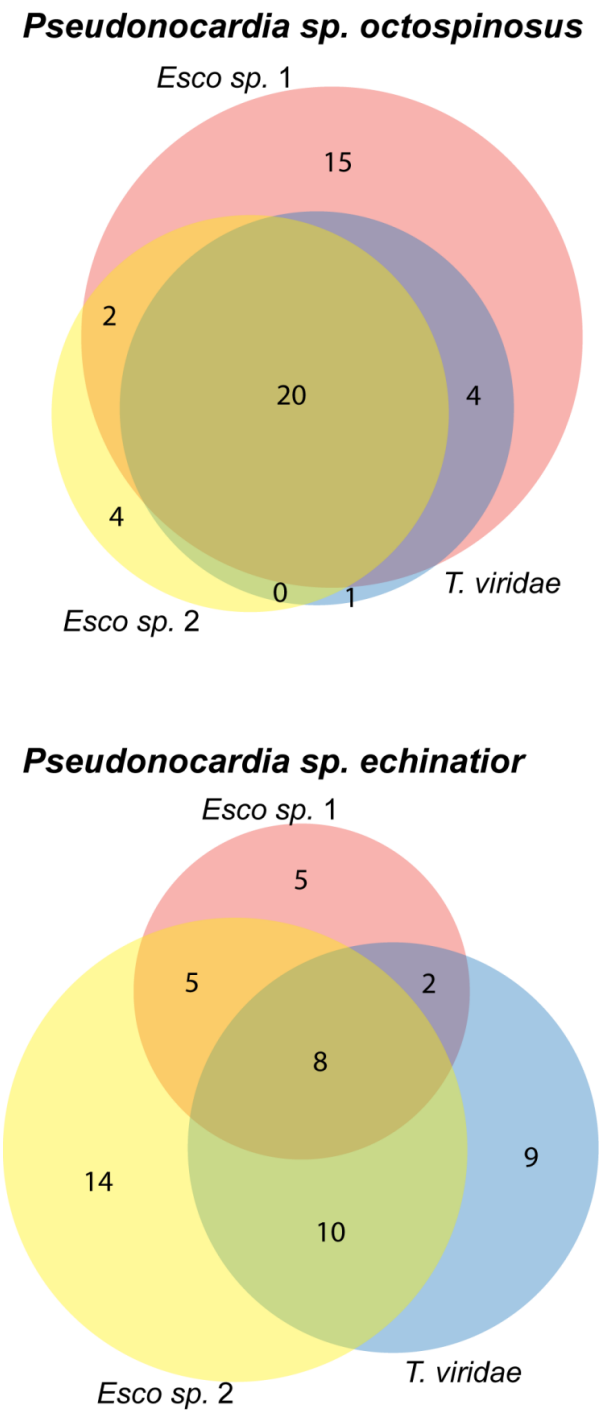

Figure S3. Venn diagrams showing the number of compounds detected from *Pseudonocardia* in response to each different pathogen exposure *in vivo*. Compounds were detected that are unique to a specific pathogen exposure, while others seem to be elicited regardless of the type of pathogen *Pseudonocardia* was exposed to.

TECHNICAL NOTE

#36 Homogenous Spray Application of DHB on Dried Agar for MALDI Imaging of Microbial Cultures

Application

MALDI imaging of microbial colonies on agar media is a growing application for mass spectrometry; however, matrix deposition on agar is often complicated. Typically, matrix is applied to wet agar using a fine sieve to dust matrix powder over the top of the slide, which often yields low to medium signal intensity and poor reproducibility. Here we present a more reproducible method of applying 2,5-dihydroxybenzoic acid (DHB) to dried agar slices for MALDI imaging of metabolites from bacterial colonies.

Intended Use Of This Technical Note

The goal of this document is to illustrate possible uses of the TM-Sprayer for Research Purpose Only. HTX Technologies, its partners, and the users that have accepted to share their data do not make any guarantees as to the performance of the illustrated workflow, and each lab should insure that replicating these experiments respects applicable health and safety regulations.

Imaging Workflow

Part of the bacterial colony and the surrounding agar were sliced out of the petri dish using a razor blade and carefully laid on a glass slide using a metal spatula, ensuring there were no bubbles underneath the agar. The slides were dried down in a desiccator at room temperature overnight. Note that drying time will vary depending on the size of the agar slice and the effectiveness of the desiccator.

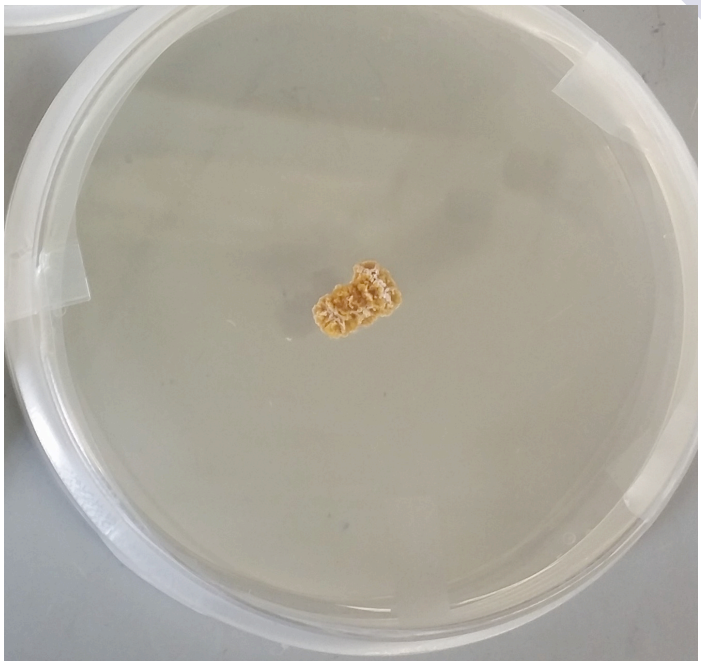

Figure 1. Bacterial colony grown on agar media

Tissue sections were then sprayed with DHB matrix (40 mg/ml, Methanol 50%, TFA 0.1%) using the HTX TM-Sprayer and the following conditions:

Flow Rate	100 µL/min
Spray Nozzle Velocity	950 mm/min
Spray Nozzle Temperature	80°C
Track Spacing	3 mm
Number of Passes	10, criss-cross and offset
Time per path	1.5–1.6 min
Nitrogen Pressure	10 psi

Spectra were collected across the entire agar/colony area using a MALDI- LTQ Orbitrap (Thermo Scientific, Waltham, MA, USA) analyzer equipped with a nitrogen laser in positive mode over a mass range of *m/z* 100 to 2000. The raster width was set to 100 µm for imaging.

Experimental Summary

Tissue type	Agar/ bacterial colony
Preservation	Dried in desiccator
Tissue cut	Intact
MALDI Plate	Standard glass slides
Matrix deposition	DHB 40mg/ml, 0.1% FA in 50:50 MeOH/H_20
MALDI Laser	60 Hz Nitrogen Laser
Acquisition mode	Positive

Instrumentation and Supplies

MALDI plate	Standard glass slides
Matrix	Acros Organics
Matrix Sprayer	HTX TM-Sprayer™
MALDI MS	Thermo MALDI- LTQ Orbitrap™
Imaging software	Thermo ImageQuest™; MSiReader[1]

Results and MALDI MS Images

MALDI MS images of compounds detected in the agar and the bacterial colony when matrix was applied using the method above were compared to images acquired when the matrix was applied via dry coating with a sieve.

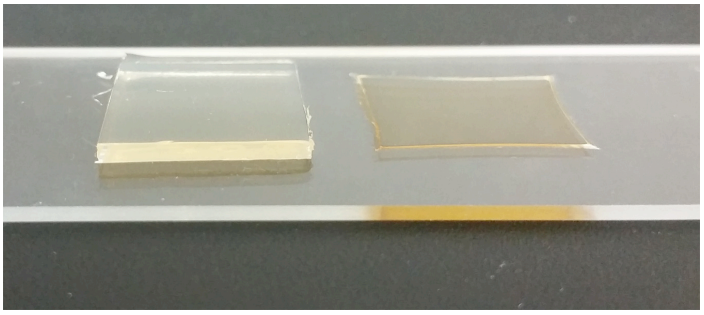

Figure 2. Agar before (left) and after (right) drying

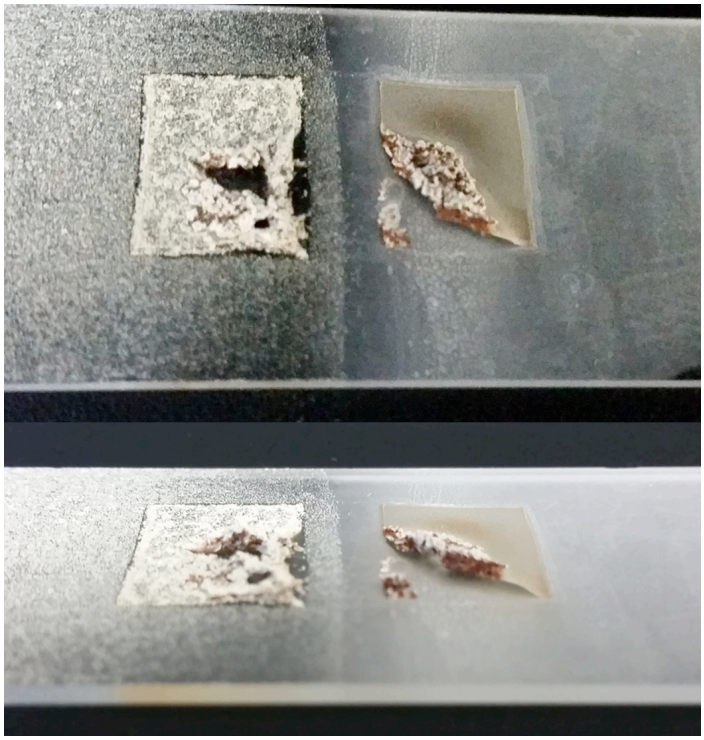

Figure 3. Agar that has been drying too long. It has begun to crack and flake away from the glass slide.

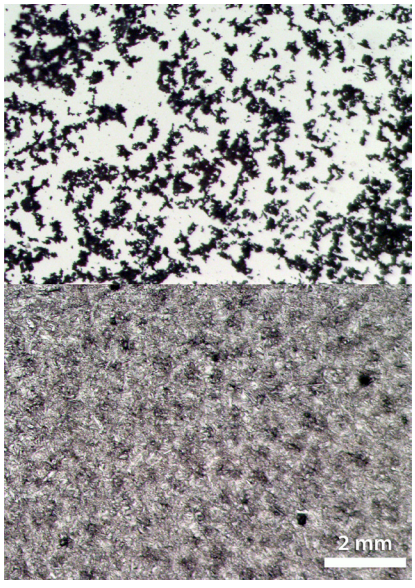

Figure 4. High resolution image of DHB matrix crystal size and coverage on a glass slide when applied with the TM-Sprayer (left) compared to application via sieve (right). Scale bar = 2 mm

References

1) Robichaud, G., Garrard, K. P., Barry, J. A., Muddiman, D. C.: MSiReader: an open-source interface to view and analyze high resolving power MS imaging files on Matlab platform. J Am Soc Mass Spectrom 24(5), 718–721 (2013)

Acknowledgements

The agar images and MS data presented in this note were provided by Erin Gemperline and Dr. Lingjun Li, Department of Chemistry and School of Pharmacy, University of Wisconsin- Madison, Madison, WI, USA

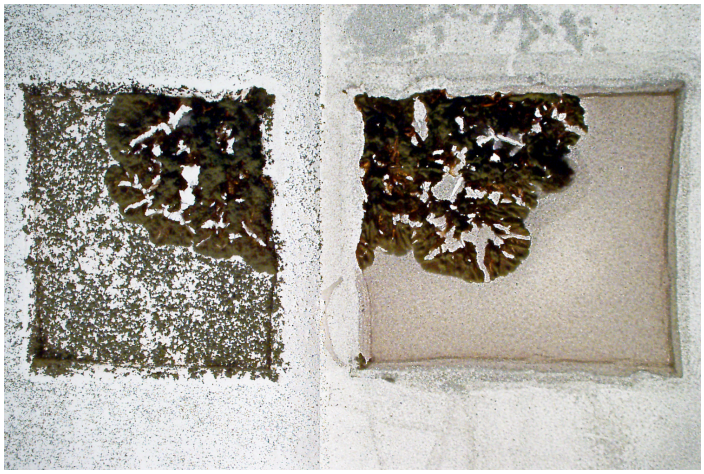

Figure 5. Agar and bacterial colony on glass slide with matrix applied via dry sieve (left) and TM-Sprayer (right).

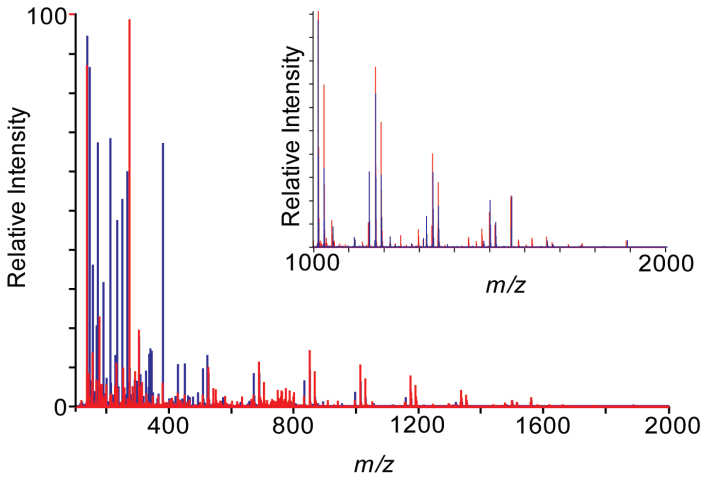

Figure 6. Mass spectra of bacterial colony samples when matrix is applied via TM-Sprayer (red) or sieve (blue). Metabolites with *m/z*100-2000 were acquired. The inlay zooms in on the higher mass region, *m/z* 1000-2000, where dry sieving does not generate as many peaks as the TM Sprayer.

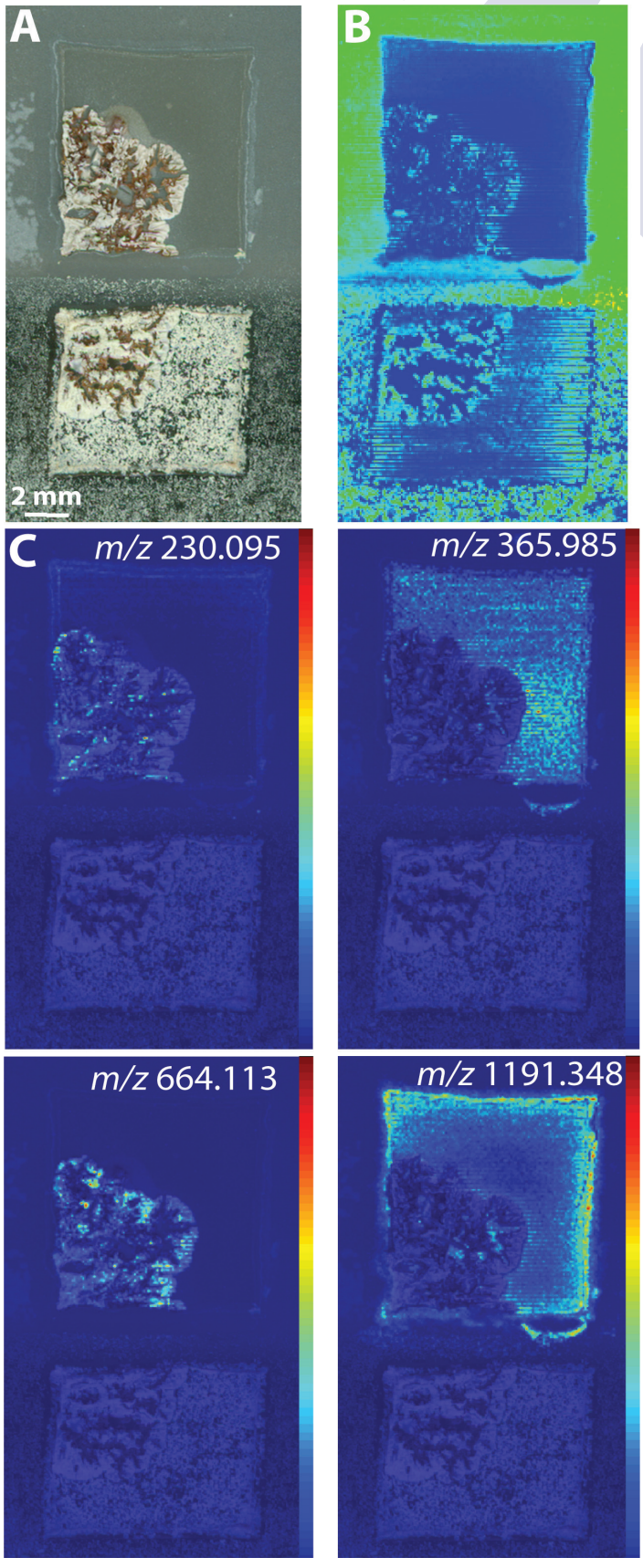

Figure 7. A) Optical image of the bacterial colony on agar with DHB applied via TM-Sprayer (top) or sieve (bottom). B) TIC image comparing the DHB coverage of the two application methods. C) Representative ion images of m/z 230.095, 365.985, 664.113, and 1191.348 comparing metabolite distribution when matrix is applied with the TM-Sprayer vs. sieve. Scale bar = 2 mm, Intensity scale = low abundance (blue) to high abundance (red).

TM-Sprayer™ Tissue MALDI Sample Preparation System

The HTX TM-Sprayer™ System is an automated MALDI matrix deposition system offering high reproducibility and superior data quality for Mass Spectrometry Imaging

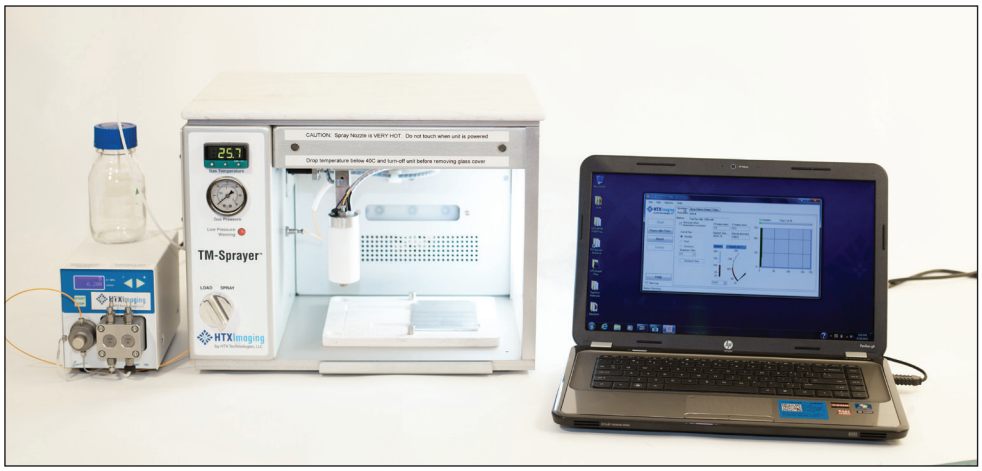

The HTX TM-Sprayer™ is an easy-to-use, versatile spraying system that provides an automated process for Sample Preparation in Mass Spectrometry Imaging.

The patented spray technology of the TM-Sprayer™ guarantees a very fine, uniform and consistent matrix coating crucial for high-resolution imaging and relative quantification of analytes.

The new HTX Technologies' spray nozzle, featured in the next generation TM-Sprayer, creates a fine solvent mist that can be deposited in a precise and adjustable pattern over all or part of any MALDI plate.

Spray characteristics (wet or dry) are easily adjustable via the intuitive operator interface. Users can create and save methods for reproducible operation.

Key Characteristics

- Patented technology providing very small matrix droplets (<10 microns)
- High flow rate and fast sample prep (10 to 20 minutes per plate)
- Highly consistent matrix deposition across entire sample area (+/- 3% by weight)
- Unique use of temperature and nitrogen flow to control evaporation rate and matrix crystal formation
- Validated protocols for most matrices (e.g.: SA, CHCA, DHB)
- Validated protocols for Trypsin digestion
- Continuous matrix coverage as needed for high-resolution imaging
- Rugged operation and easy clean-up

TM-Sprayer™ Specifications

Deposition: Spray deposition in linear or serpentine modes with variables offsets

Spray Nozzle Flow: 50 to 1000µl/min

Sheath Gas: Ambient to 130°C (+/- 2°C), software selected

Gas Supply: Sheath gas flow 5-15.5 liter/min

Spray Nozzle Position: Spray nozzle mounted on Cartesian stage

Electrical: 24V Power Supply

Dimensions/Weight: 17 x 15 x 13in (43 x 38 x 33cm), 38lbs (17Kg)

TM-Sprayer™ is available worldwide exclusively from HTX Technologies, LLC. To request further information contact:

Alain Creissen
Imaging Product Manager, HTX Technologies
acreissen@htximaging.com

HTX Technologies offers innovative sample preparation systems for advanced analytical platforms. Our integrated workflow solutions include user training, instruments, software, consumables and method development services.

HTXImaging
by HTX Technologies, LLC

PO Box 16007 Chapel Hill, NC 27516, USA
Tel +1-919-928-5688 ◆ Fax +1-919-928-5153
info@htximaging.com ◆ www.htximaging.com

Chapter 7

Mass Spectrometric Examination of the Human Microbiome as a Source of Novel Drug Candidates

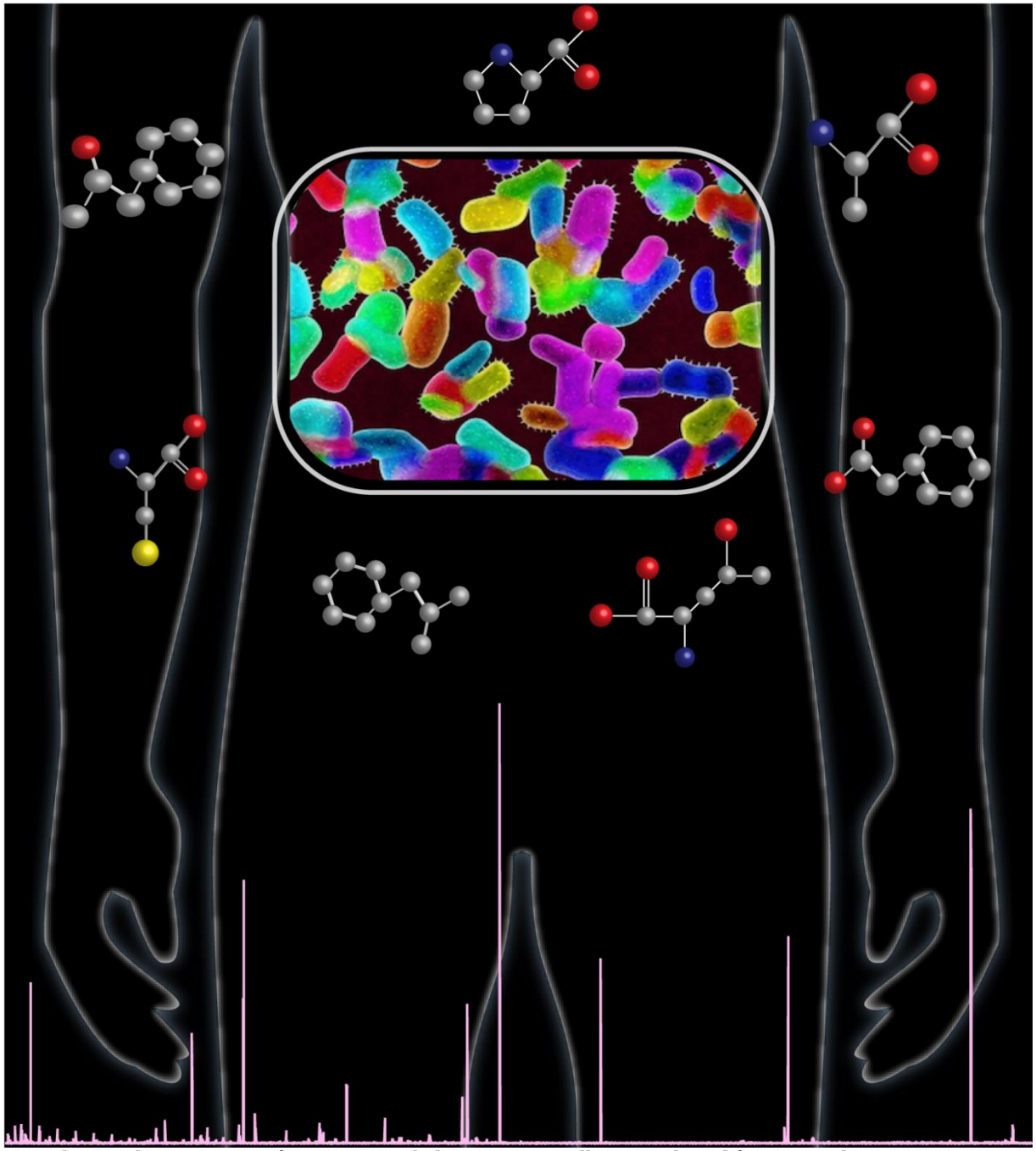

Microbiome photo courtesy of SatorI13/Stockphoto. Human silhouette adapted from Freepik.com.

Abstract

Symbiotic bacteria within the human microbiome play a key role in their host's health. Studying the human microbiome is critical to realizing the full potential of personalized medicine and understanding nearly all aspects of human biology and health. Small molecule natural products produced by bacteria within the human microbiome represent one of the most promising and untapped sources of new drug leads to treat diverse disease conditions, including antibiotic-resistant pathogens. In this study, microbe-free mice, colonized with the human colonic microbiome, were exposed to *Salmonella enterica* and a high-resolution liquid chromatography (LC)-mass spectrometry (MS) platform was used to detect small molecules produced by the human gut microbiota in response to pathogen infection, and matrix-assisted laser desorption/ionization (MALDI)- mass spectrometry imaging (MSI) was used to visualize the detected compounds on tissue. A number of small molecules were detected that are significantly upregulated in response to infection, compared to the control. Importantly, a number of the detected compounds are putative novel molecules, and thus represent exciting new drug leads.

Introduction

The discovery and development of the first antibiotic, penicillin, revolutionized the medical field,[1] and initiated the "golden-age" of antibiotics.[2] In the antibiotic era, diverse suites of small molecules were discovered and developed primarily from natural products produced by bacteria. During this "golden age", the average lifespan of the population greatly increased, some infectious diseases were almost wiped out, and several neoplastic and viral diseases became manageable.[3] Antibiotics are often the first line of defense against most infectious agents but, unfortunately, the uncontrolled use of antibiotics has led to the rampant evolution of antibiotic resistance. Antibiotic resistant pathogens represent one of the most pressing world-wide health issues. Alarmingly, the discovery and production of novel antibiotics, including natural products, has not been able to keep up with the surge of antibiotic resistant pathogens, as more than 70% of pathogenic bacteria are resistant to most antibiotics on the market today.[3] Thus, there is a critical and urgent need to discover novel therapeutics to treat infectious diseases.

Bacteria in the human microbiome represent an especially promising source of new antimicrobials with high clinical potential.[4] The human microbiome, consisting of several hundred species of microbes,[5] has been shown to affect the host's overall health by producing small molecules that act as signals between various organs and body systems.[6] In addition to influencing the host's physiology, the microbiota directly affects human health through antibiotic and anti-virulence activity, which can help to prevent pathogen infection.[4] Thus, the small molecules produced by bacteria within the human microbiome could act as a potential source of new drug leads to treat a variety of diseases.

A key challenge to harnessing the human microbiome as a rich source of novel drug leads is to study the microbiota *in vivo*. Rather than culturing human microbes *in vitro*, our study used a

mouse model that was colonized with 90 different strains of human microbes. Mass spectrometry (MS) is a powerful analytical tool for high-throughput analysis of biological samples and rapid comparison of compounds detected between different sample types. Furthermore, mass spectrometry imaging (MSI) allows for the detection of compounds from a tissue cross-section while retaining the spatial information of where the detected compounds are located within that tissue.[7] The combination of mice colonized with the human microbiota and MSI as a tool for analysis allows for an *in vivo* study of the natural products, and potential novel drug targets, produced by the microbiota in response to infection by pathogens.

We have developed a new experimental approach to examine the metabolites produced by gut microbes in response to infection, *in vivo*. This study used liquid chromatography (LC)-MS and matrix-assisted laser desorption/ionization (MALDI)-MSI to compare different metabolites detected in infected aposymbiotic (germ-free) mice, infected humanized mice, and uninfected humanized mice. Here, we employed this approach to help identify new drug leads from the human microbiome.

Materials and Methods

Mouse Sample Preparation

Germ-free mice were reared using isolators that maintain pups in aseptic conditions. Mature male mice were colonized with the human colonic microbiome (90 strains of human microbes) through oral exposure. These strains were selected because they are important taxa within the gut microbiota and genome sequences are available for each strain. After waiting approximately 2 weeks for the colonies to establish, infection experiments were conducted by

crossing the presence/absence of human microbiome with the presence/absence of the human gut pathogen, *Salmonella enterica* (Salmonella), in the mice. The sample types for this experiment include: 1) germ-free mice exposed to Salmonella, 2) mice colonized with human gut microbia (humanized mice), 3) humanized mice exposed to Salmonella that did not show symptoms of infection, 4) humanized mice exposed to Salmonella that showed symptoms of infection. The mice were sacrificed after they were determined to be sufficiently infected, based on symptoms and expected course of the disease in literature. Cecum, small intestines, liver, and kidneys were dissected from the animal and stored at -80 °C for further sample preparation.

Analyte Extractions

The contents of the cecum and small intestines were removed and placed into pre-chilled 13-mL PTFE (polytetrafluoroethylene) tubes. The analytes were extracted with 3:1:4 methanol:chloroform:water (v/v) yielding an aqueous metabolite, organic metabolite, and protein fraction for each sample. The metabolite samples (aqueous and organic fractions) were processed via 3 kDa molecular weight cutoff (MWCO) to remove non-soluble waste material from the samples. Samples were dehydrated with a SpeedVac and stored at -80 °C until analysis.

LC-MS Acquisition

For LC-MS acquisition, samples were resuspended in either water (aqueous metabolite samples) or acetonitrile (organic samples) to a final concentration of 10 mg/mL. The samples were separated on a Cortecs C18 column (2.1-mm internal diameter × 100-mm length, 1.6-μm particle size; Waters Corporation, Milford, MA, USA), equipped with a corresponding guard column, and heated to 35 °C using a Waters Acquity UPLC. The mobile phases were (A) water with 0.1% formic acid and (B) acetonitrile with 0.1% formic acid. The aqueous metabolite

samples were separated within 35 min under the following conditions: 0-5min, isocratic hold at 1% B; 5-10 min, linear gradient from 1-3% B; 10-18 min, linear gradient from 3-40% B; 18-22 min, linear gradient from 40-80% B; column cleaning at 95% B for 5 min; and finally re-equilibration of the system at 1% B for 8 min. The organic metabolite samples were separated within 35 min under the following conditions: 0-22 min, linear gradient from 1-95 % B; column cleaning at 95% B for 5 min; and finally re-equilibration of the system at 1% B for 8 min. The flow rate was 0.3 mL/min and the injection volume was 5 μL. The samples were kept at 10 °C during the analysis.

Metabolite MS data were acquired on a Q-Exactive instrument (Thermo Scientific, Waltham, MA, USA) that was equipped with an ESI source operated in positive ion mode. The MS scan range was from *m/z* 200–1700 and the MS/MS scan range was adjusted depending on the parent mass and high-energy collision dissociation (HCD) with a collision energy of 30 eV was used.

Sample Preparation for MALDI

A section of small intestines was dissected from each mouse. The small intestine sections were embedded in gelatin (100 mg/mL in double-distilled water) and gently frozen on dry ice. The frozen tissue was then sectioned into 12-μm slices using a cryostat at -20 ^{o}C. The sections were thaw-mounted onto an indium tin oxide (ITO)-coated glass microscope slide. Matrix (40 mg/mL DHB in 50:50 water:methanol) was applied using a TM Sprayer (HTX Technologies, LLC, Carrboro, NC, USA). The TM Sprayer method for applying DHB was as follows: 80 °C, 0.05 mL/min flow rate, 24 passes- rotate and offset, 3 mm spacing, velocity of 1250 mm/min. DHB was purchased from Sigma-Aldrich (St. Louis, MO, USA).

MALDI-ToF/ToF MSI

An ultrafleXtreme MALDI- time-of-flight (ToF)/ToF mass spectrometer (Bruker Daltonics, Billerica, MA, USA) was used for MSI of the small intestines. To generate images, spectra were collected at 20 µm intervals in both the x and y dimensions across the surface of the sample. Each mass spectrum was generated by averaging 500 laser shots over the *m/z* 100-1700 mass range in positive ion mode. Mass spectra were externally calibrated using standard mixtures applied directly to the glass slide. Ion images were extracted using FlexImaging software (Bruker Daltonics). Masses were internally calibrated again after the imaging acquisition was complete using FlexAnalysis.

Data Analysis

Metabolomics data for the different sample types were compared using SIEVE (Thermo Scientific, Waltham, MA, USA). A small molecule component extraction experiment was carried out using SIEVE; a pathogen-infected sample was used as the reference sample and all replicates were compared to the controls (germ-free, infected and humanized, non-infected) using 2 technical replicates of 4 humanized, infected biological replicates. The features were extracted from the data after alignment and framing. The *m/z* values that had at least 2-fold higher intensity in the pathogen-infected sample compared to the controls were considered "metabolites of interest". To be considered a potential target compound, the specific *m/z* was elevated in both technical replicates and at least 2 of the 4 biological replicates.

Results and Discussion

Using a high resolution LC/MS platform, we have identified a number of promising small molecules produced by the human gut microbiota that are significantly upregulated in the infection treatment compared to the control. Importantly, by accurate mass matching metabolite

databases using MetaboSearch,[8] we have selected a number of these small molecules as targets for further characterization. Furthermore, we have shown that more unique small molecules were detected during infection versus uninfected. Examples of the detected compounds that showed upregulation in the humanized, infected mice compared to the controls are shown in **Figure 1**. Using SIEVE software, 134 compounds were found that showed upregulation in response to Salmonella infection compared to control. A list of all upregulated compounds is shown in **Table 1**.

MALDI-MSI was used to visualize the spatial distribution of the novel drug candidates detected by LC-MS. A ToF-ToF instrument was chosen for MSI experiments due to its superior spatial resolution capabilities compared to other available MALDI instruments. **Figure 2** shows an example MS image of one of these candidates, *m/z* 327.1. Compounds that ionize in electrospray ionization (traditionally used in LC-MS) do not always ionize with MALDI. Additionally, ToF mass spectrometers do not provide accurate mass measurements (within 5 ppm error) and calibration tends to drift throughout long imaging runs, so it is difficult to confidently identify detected compounds or compare samples between instrumentation. For these reasons, it is not surprising that we were only able to image one of our highly specific novel drug targets with confidence.

Interestingly, there were noticeable differences in the metabolites produced by the microbiome in the humanized, infected mice that showed symptoms compared to the humanized, infected mice without symptoms of infection. Example compounds that showed differential upregulation between these two sample types are shown in **Figure 3**. Understanding differences in metabolomic response to infection in mice that do not develop symptoms could have interesting implications. If this result was not caused by insufficient exposure to Salmonella, the

microbiota for the mice that do not show symptoms could be producing compounds that fight off Salmonella faster than the microbiota of the mice with symptoms.

Conclusions and Future Directions

As mentioned above, we have identified a number of promising small molecules produced by the human gut microbiota that are significantly upregulated in the infection treatment compared to the control. We detected 134 secondary metabolites via LC-MS that were produced in response to infection. Importantly, of these 134 compounds, 105 of them are putative novel molecules (based on accurate mass matching via MetaboSearch), and thus represent exciting new drug leads. These findings suggest that the community of symbiotic microbes associated with this host respond to pathogens through metabolic shifts that are complex and largely unknown, and that these shifts could be specific to the microbial threat involved.

We are currently in the process of collecting and preparing six additional biological replicates for each sample type. We anticipate that this will improve the confidence of our results and narrow down the list of candidate drug targets. In the future, reduced list of novel antibiotic candidates will be isolated and validated for development as potentially novel pharmaceuticals in collaboration with Dr. Jon Clardy's lab at Harvard Medical School. In addition to the metabolomics study, conducting LC-MS/MS proteomics experiments could provide an understanding of the changes in the microbial proteomes in response to pathogen infection. This could provide insight into the molecular pathways involved in the response.

Acknowledgements

The author would like to thank Caitlin Keller and Jenny Bratburd for their contributions to this project. Jenny prepared and collected the mice samples, while Caitlin aided in the MS sample preparation and data analysis. The author would like to thank Dr. Cameron Currie for his insight and mentorship on the project as well as the NIH funding provided to C.C. (NIH CETR Grant 144-PRJ94CP). We thank Dr. Frederico Rey for supplying the mice used in this study. This work was supported by funding from the University of Wisconsin Graduate School and the Wisconsin Alumni Research Foundation (WARF), a Romnes Faculty Research Fellowship program to L.L. E.G. acknowledges an NSF Graduate Research Fellowship (DGE-1256259). The MALDI-Orbitrap and Q-Exactive instruments were purchased through an NIH shared instrument grant (NCRR S10RR029531).

References

1. Fleming, A., On the Antibacterial Action of Cultures of a Penicillium, with Special Reference to Their Use in the Isolation of B. Influenzae. 1929. *Bulletin of the World Health Organization* **2001,** *79* (8), 780-790.

2. Katz, L.; Baltz, R. H., Natural Product Discovery: Past, Present, and Future. *Journal of industrial microbiology & biotechnology* **2016,** *43* (2-3), 155-176.

3. Berdy, J., Thoughts and Facts About Antibiotics: Where We Are Now and Where We Are Heading. *J Antibiot* **2012,** *65* (8), 385-395.

4. Antunes, L. C.; McDonald, J. A.; Schroeter, K.; Carlucci, C.; Ferreira, R. B.; Wang, M.; Yurist-Doutsch, S.; Hira, G.; Jacobson, K.; Davies, J.; Allen-Vercoe, E.; Finlay, B. B., Antivirulence Activity of the Human Gut Metabolome. *mBio* **2014,** *5* (4), e01183-01114.

5. Structure, Function and Diversity of the Healthy Human Microbiome. *Nature* **2012,** *486* (7402), 207-214.

6. Krishnan, S.; Alden, N.; Lee, K., Pathways and Functions of Gut Microbiota Metabolism Impacting Host Physiology. *Current opinion in biotechnology* **2015,** *36*, 137-145.

7. Gemperline, E.; Li, L., Maldi-Mass Spectrometric Imaging of Endogenous Metabolites in Biological Systems. *eLS* **2014**.

8. Zhou, B.; Wang, J.; Ressom, H. W., Metabosearch: Tool for Mass-Based Metabolite Identification Using Multiple Databases. *PloS one* **2012,** *7* (6), e40096.

Tables

Table 1. List of upregulated compounds (*m/z*) that are putative novel drug candidates

m/z					
268.1040	355.2532	424.3055	500.3079	575.3392	782.4000
286.2013	357.2783	425.2373	502.2872	589.2722	785.5056
288.2899	358.2815	426.2114	503.2828	592.3054	785.5921
292.1972	361.2946	427.2149	506.2932	603.3201	788.2281
293.0420	366.2249	430.2372	511.3469	603.4073	800.4145
296.1217	367.1126	433.1672	513.2698	608.3165	800.5271
296.1534	367.1954	437.2008	514.3599	622.3207	802.6181
299.1165	373.2630	437.2170	516.3399	625.3895	807.5729
308.7018	381.2247	445.3024	517.2775	625.7943	809.3679
309.1434	385.7222	446.2403	524.2680	632.3257	822.3949
310.0205	389.2585	447.2405	525.2646	633.3457	822.4000
315.2358	389.2685	451.2157	525.3082	653.3074	829.5544
317.1032	401.2589	457.2237	536.3406	653.8129	851.4150
317.2265	403.2190	467.2841	538.3208	654.3053	856.4202
319.1474	405.2608	468.2220	539.2585	655.3271	883.5317
321.2574	410.3263	469.2247	543.2533	717.4095	937.4633
324.1892	411.1877	469.2369	550.3574	729.3779	1111.5430
327.1201	411.2217	469.7385	555.2748	732.4436	1122.4862
331.2056	411.7077	477.1453	556.7767	761.4412	1215.6256
332.1284	412.1912	478.2622	562.2465	763.4595	
341.1214	412.3310	484.3134	568.2612	766.2498	
345.1309	415.2189	488.7287	573.2852	767.5841	
349.1156	422.7580	490.2576	573.3571	768.4074	**134 Total**

Figures

Figure 1

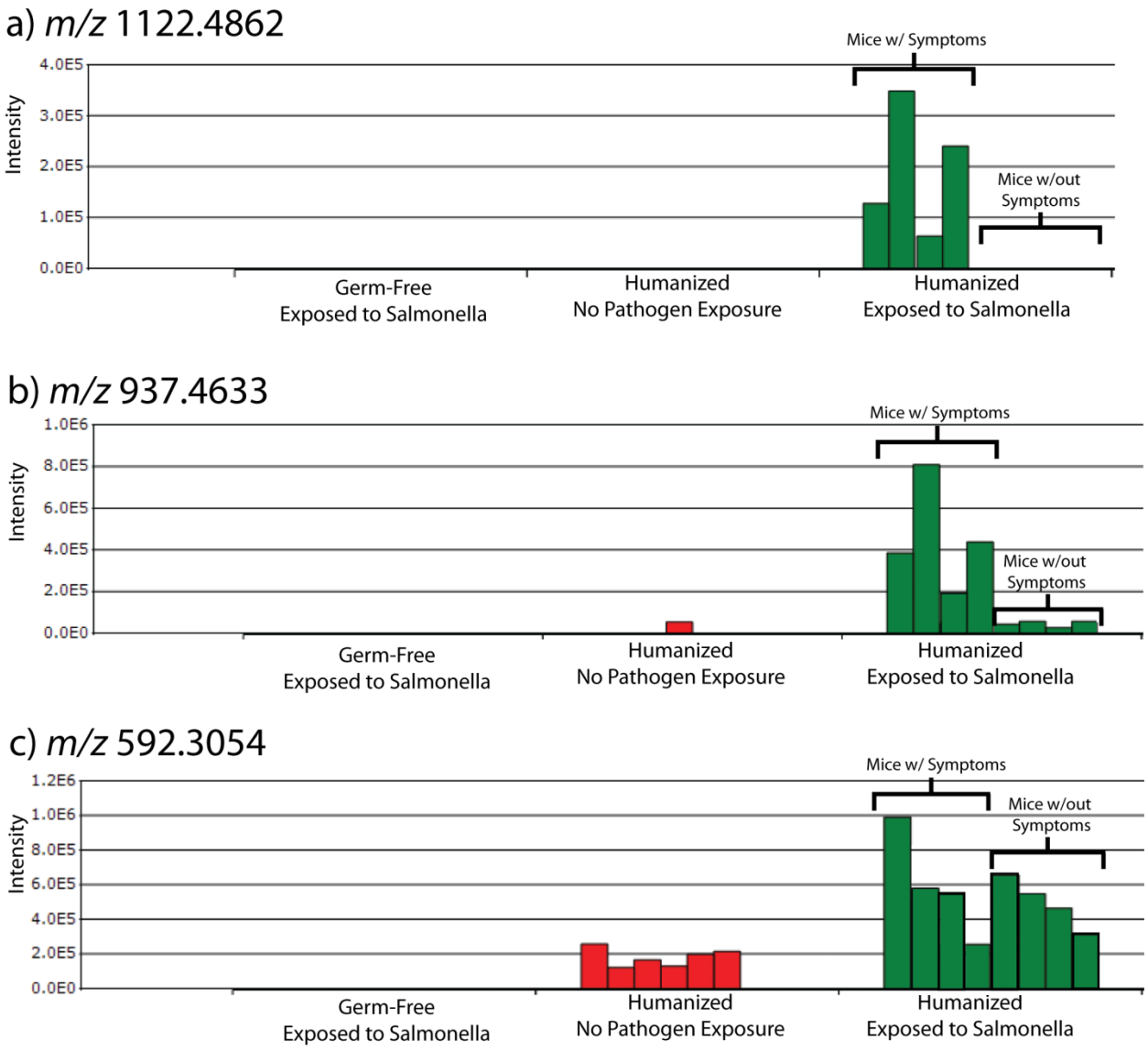

Figure 1. Examples of the detected compounds that showed upregulation in the humanized, infected mice compared to the controls. a) *m/z* 1122.4862 and b) *m/z* 937.4633 were upregulated in the humanized mice that show symptoms of infection. c) *m/z* 592.3054 was upregulated in all humanized mice that were exposed to Salmonella regardless of symptoms.

Figure 2

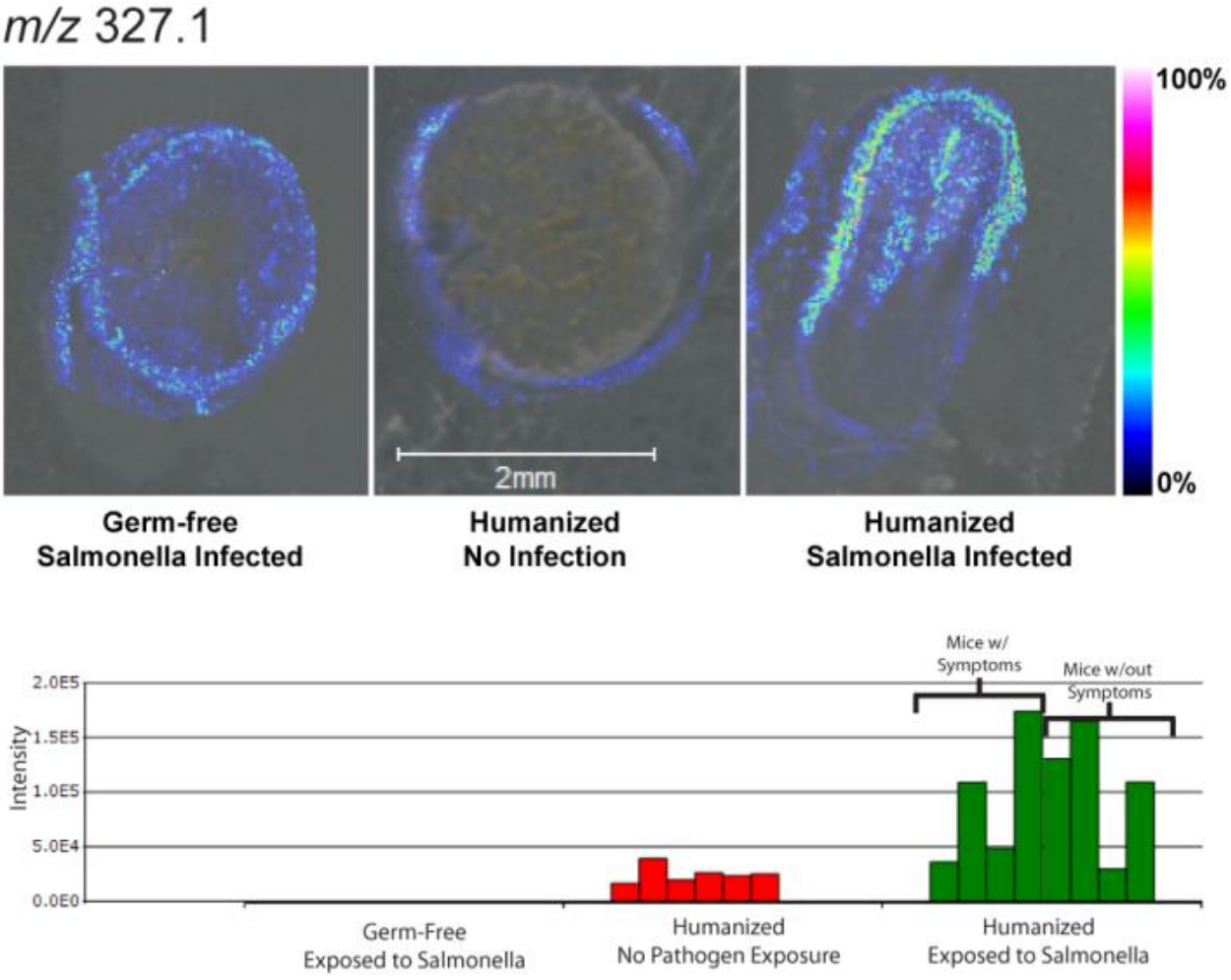

Figure 2. An example MS image of a novel drug candidate compound detected by LC-MS, *m/z* 327.1. Although MALDI-MSI is not a quantitative technique, this image suggests upregulation of *m/z* 327.1 in the humanized, infected mice. *m/z* 327.1 is primarily localized to the tissue/ mucous membrane portion of the sample which is where the gut microbia would reside.

Figure 3

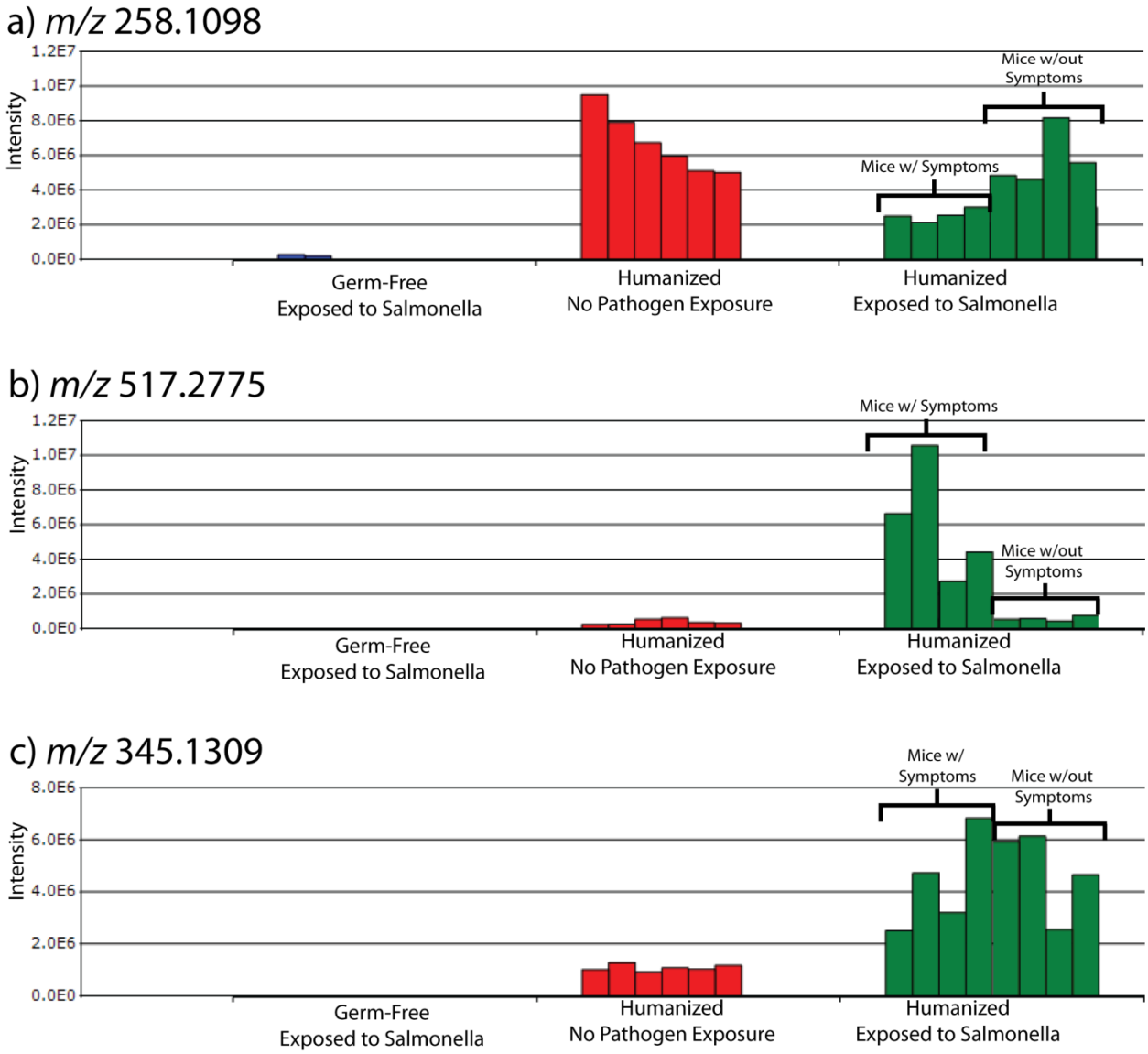

Figure 3. Example compounds that showed differential upregulation between the humanized, infected mice that showed symptoms compared to the humanized, infected mice without symptoms of Salmonella infection. a) *m/z* 258.1098 and b) *m/z* 517.2775 are examples of detected compounds in which the humanized, infected mice that did not show symptoms better corresponded to the humanized, non-infected mice rather than the humanized, infected mice with symptoms. c) *m/z* 345.1309 is an example where all humanized mice samples that were exposed to Salmonella regardless of symptoms show consistent upregulation.

Chapter 8

Measurement of NMDA Receptor Antagonist, CPP, in Mouse Plasma and Brain Tissue Following Systemic Administration Using Ion-Pair LC-MS/MS

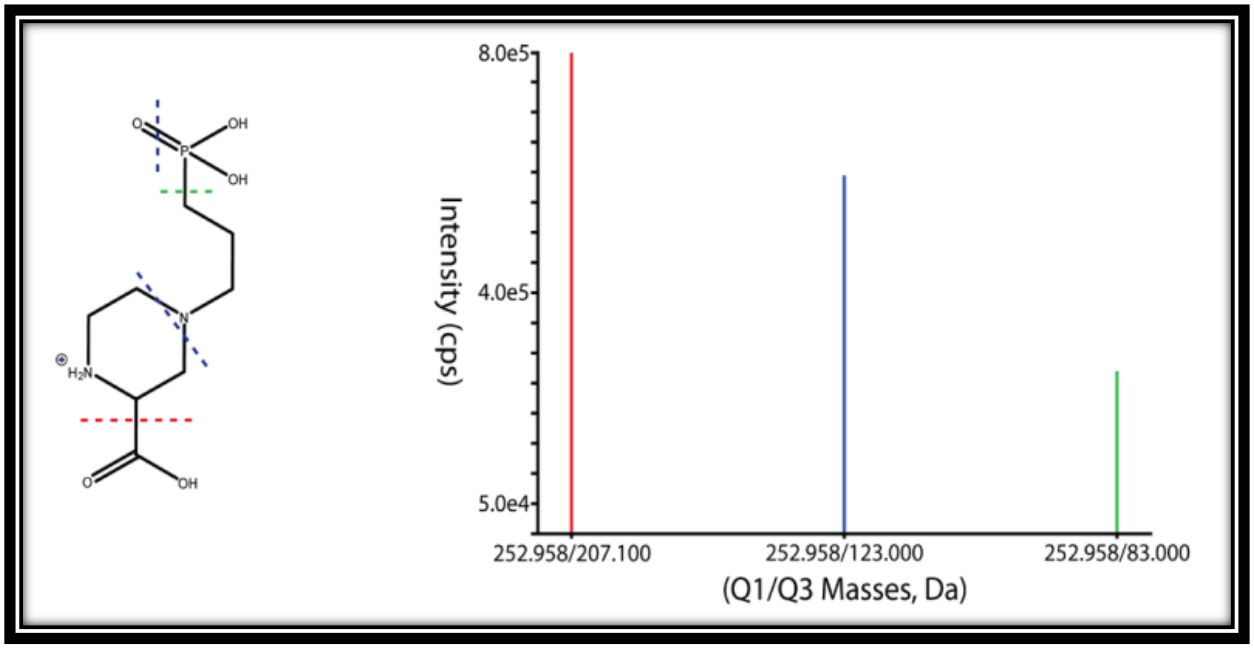

Adapted from **Gemperline, E.**; Laha, K.; Scarlett, C.; Pearce, R.; Li, L. "Measurement of NMDA Receptor Antagonist, CPP, in Mouse Plasma and Brain Tissue Following Systemic Administration Using Ion-Pair LC-MS/MS" *Analytical Methods*. 6(16):6389-6396. (2014) doi: 10.1039/C4AY01168F

Abstract

(RS)-3-(2-carboxypiperazin-4-yl)-propyl-1-phosphonic acid (CPP) is a competitive antagonist of the N-methyl-D-aspartate (NMDA) receptor and is routinely used with rodent models to investigate the role of NMDA receptors in brain function. This highly polar compound is difficult to separate from biological matrices. A reliable and sensitive assay was developed for the determination of CPP in plasma and tissue. In order to overcome the challenges relating to the physicochemical properties of CPP we employed an initial separation using solid phase extraction harnessing mixed-mode anion exchange. Then an ion-pair UPLC C18 separation was performed followed by MS/MS with a Waters Acquity UPLC interfaced to an AB Sciex QTrap 5500 mass spectrometer, which was operated in positive ion ESI mode. Multiple reaction monitoring (MRM) mode was utilized to detect the analyte and internal standard. The precursor to product ions used for quantitation for CPP and internal standard were *m/z* 252.958 → 207.100 and 334.955 → 136.033, respectively. This method was applied to a pharmacokinetic study and examined brain tissue and plasma concentrations following intravenous and intraperitoneal injections of CPP. The elimination half-life ($t_{1/2}$) of CPP was 8.8 minutes in plasma and 14.3 minutes in brain tissue, and the plasma to brain concentration ratio was about 18:1. This pharmacokinetic data will aid the interpretation of the vast number of studies using CPP to investigate NMDA receptor function in rodents and the method itself can be used to study many other highly polar analytes of interest.

Introduction

The purpose of our work was to determine the concentrations of (RS)-3-(2-carboxypiperazin-4-yl)-propyl-1-phosphonic acid (CPP), a competitive antagonist of the N-methyl-D-aspartate (NMDA) receptor, in plasma and brain tissue following systemic administration in rodent models. Determining tissue-specific drug concentrations that correspond to specific behavioural endpoints will guide the design and interpretation of studies utilizing CPP for companion experiments performed *in vivo* and *in vitro*.

The NMDA receptor is a glutamate-activated ion channel that is permeable to cations, including sodium and calcium. It contributes to excitatory synaptic transmission throughout the central nervous system, and is essential to higher cognitive functions.[1] The role of NMDA receptors in learning and memory has been extensively documented.[2-6] Many stimulus paradigms that induce long-term potentiation, a form of synaptic plasticity that is widely studied as a cellular correlate of memory, depend critically on activation of NMDA receptors to trigger downstream signaling processes.[7-11] The role of NMDA receptors goes beyond memory, as these receptors influence a vast number of cognitive processes and neurological diseases related to excitatory synaptic transmission.[12] NMDA receptor modulation has been shown to influence Alzheimer's disease,[13-15] Parkinson's disease,[16-17] general anesthesia,[18-19] depression,[20-21] and neuropathic pain.[22]

Research in all of these areas has utilized CPP as a pharmacological tool to investigate the role of NMDA receptors and the functional consequences of their impairment. CPP antagonizes the NMDA receptor by reversibly binding to the glutamate binding site.[8] CPP was synthesized as an analogue of 2-amino-5-phosphonopentanoic acid (AP5) and 2-amino-7-phosphonoheptanoic

acid (AP7),[23] which are also commonly used to block NMDA receptors *in vitro*. CPP is highly selective for NMDA receptors,[24] and is 5-fold more potent than AP5 or AP7. What makes CPP so useful experimentally is that, despite having hydrophilic properties, it crosses the blood-brain barrier.[4, 24-25] Therefore, unlike most other competitive antagonists, it is effective even when administered systemically. CPP's high potency, specificity for NMDA receptors, and penetration of the blood-brain barrier has led to its wide spread adoption. At doses that range between 0.5 mg/kg to 10 mg/kg, systemic administration of CPP in rodents has been shown to suppress seizure activity,[24, 26] interfere with addiction paradigms,[27] block stress-induced responses,[28-29] produce antidepressant-like effects,[30] disrupt neurogenesis,[31] modulate Parkinson's disease models,[32-33] increase amyloid β levels in Alzheimer's disease models,[34] impair learning and memory,[3-5, 35] and block both long-term potentiation (LTP) and long-term depression (LTD).[36-38] Although these studies have demonstrated the ability of CPP to alter a plethora of behavioral responses, the degree to which NMDA receptors in the CNS must be blocked in order to produce a given response remains unknown. The interpretation of *in vitro* studies that could provide this type of information will require detailed knowledge of the concentration of antagonist that reaches the brain following systemic administration.

Published pharmacokinetic analyses of CPP are limited. A review of the literature identified only two papers that examined CPP concentrations following systemic administration, one utilizing liquid scintillation spectrometry and the second based on HPLC-UV analysis of a CPP derivative. In exploration of CPP's clinical potential, levels of [H^3]CPP in serum and CSF were measured in pigs following intravenous injection.[25] Absolute concentrations were not measured, but the half-life of CPP (81±10 minutes) and the CSF:serum ratio (0.28±0.03) were reported. In a second study, plasma concentrations of CPP were measured 1-5 hours following

oral administration to baboons.[26] Concentrations of CPP in plasma ranged from 0.6 to 0.8 μg/ml over this timeframe following an oral dose that produced a potent anti-convulsant effect (32 mg/kg). These measurements utilized a derivatization protocol, but had a detection limit of only 80 ng/ml. A major advantage of using mass spectrometry over either previously described method is that with mass spectrometry the analyte can be identified both by its retention time and molecular weight. Using a triple quadrupole mass spectrometer, analytes can be fragmented and specific fragments can be monitored which eliminates most interference from complex biological matrices and allows for confident analyte detection and quantitation. With an interest in measuring CPP concentrations in plasma and brain tissue in rodents following systemic administration of relevant doses, the present work aimed to develop a reliable and reproducible analytical method.

Assay development was challenging because of the physicochemical properties of CPP (**Figure 1A**). Being a highly polar compound and lacking a chromophore that would allow routine UV-Vis spectrophotometric analysis, CPP required suitable methodologies to be optimized for extraction from tissue or plasma, sample preparation, and HPLC separation prior to mass spectrometry analysis. Unfortunately, CPP would not elute from HILIC columns, which makes it difficult to achieve adequate elution or separation. Additionally, CPP is poorly retained on C18 columns under standard conditions. To overcome these challenges we used an ion-pairing agent, HFBA, with a C18 column. In this study, we report a high quality method that allowed sensitive detection and accurate quantification of CPP in complex biological matrices.

Materials and Methods

Chemicals and Reagents

CPP was purchased from Tocris Bioscience (Bristol, UK). Internal standard (IS) isotopically labeled cyclic adenosine monophosphate ($^{13}C_5$ cAMP) was purchased from Toronto Research Chemicals Inc. (Toronto, Ontario, Canada). Ammonium hydroxide solution and formic acid (mass-spec grade) were purchased from Sigma Aldrich (Saint Louis, MO). Heptafluorobutyric acid (HFBA) was purchased from Thermo Scientific Pierce (Rockford, IL). HPLC grade water, methanol, and acetonitrile (AcN), and hydrochloric acid (ACS reagent grade) were purchased from Fisher Scientific (Waltham, MA).

Calibration Standards/Quality Control Samples

A 10 mg/ml stock solution of CPP in water was prepared by dissolving 10 mg CPP powder in 1 mL of water and stored in a polypropylene centrifuge tube at -20°C. A 10 µg/ml stock solution of IS was prepared in water. Working solutions (10x) of CPP and IS were made by dilution in water and used to prepare calibration standard samples. Different calibration ranges were assessed for mouse plasma and brain tissue. For plasma six non-zero CPP standards, ranging from 5 ng/ml to 1500 ng/ml, were prepared by adding 10 µl of working solution of CPP and 10 µl IS working solution (0.5 µg/ml) to aliquots (100 µl) of plasma. For brain tissue five non-zero CPP standards, ranging from 0.9 ng/g to 44 ng/g, were prepared by adding 10 µl of working solution of CPP and 10 µl IS working solution (0.5 µg/ml) to individual blank brain samples (0.34 g) in 2 ml 0.01N HCl prior to homogenization. Five replicates of all standards were prepared. Blank samples consisted of the appropriate matrix devoid of CPP or IS. Zero samples were prepared by adding 10 µl of IS to plasma or brain blanks. Calibration curves were

generated from the areas of the analyte and IS using a 1/x weighted linear regression for brain tissue samples and a 1/x weighted quadratic regression for plasma samples.

Sample Preparation

All experiments conformed to the guidelines laid out by the Guide for the Care and Use of Laboratory Animals, and were conducted with the approval of the University of Wisconsin-Madison (Madison, Wisconsin) Animal Care and Use Committee.

Trunk blood was collected in heparinized tubes following decapitation of anesthetized animals, and plasma was separated by centrifugation. Plasma samples were immediately processed after collection. Aliquots (100 μl) of plasma samples were added to 10 μl IS working solution (0.5 μg/ml) in a 1.5 ml polypropylene centrifuge tube. To this 200 μl 0.01N HCl was added, then samples were vortex-mixed and centrifuged at 14,000xg for 5 minutes at 4°C. The supernatant was added to 700 μl 1.5% NH_4OH (v/v) in order to basify the solution prior to solid phase extraction (SPE).

Brain tissue was weighed immediately following decapitation and placed on ice. Tissue was then homogenized in glass test tubes with 2 ml 0.01N HCl using a rotor-stator homogenizer. The brain homogenate was transferred to 15 ml centrifuge tubes and centrifuged at 15,000xg for 25 minutes at 4°C. The supernatant was transferred to a fresh 15 ml conical polypropylene tube. The pelleted tissue was resuspended in 2 mL 0.01N HCl and centrifuged for a second time at 15,000xg for 25 minutes at 4°C. The supernatant from the second spin was combined with the supernatant from the first spin. 3.5 mL 5% NH_4OH (v/v) was then added in order to basify the solution prior to SPE.

SPE was performed using Oasis MAX SPE cartridges from Waters (Milford, MA). The SPE cartridge was conditioned with methanol, equilibrated with water, and then the basified sample was loaded. The cartridge was washed with 5% NH_4OH and then washed with methanol. Analyte was eluted with 8% formic acid/77% methanol (v/v).

Following SPE, samples were dried down in a speed vacuum concentrator. Plasma samples were resuspended in 60 μL diluent (20 mM HFBA in 99:1 water:AcN) and brain tissue samples were resuspended in 20 μL diluent. Samples were shaken, spun down with a centrifuge for 10 s, and transferred to HPLC vials.

Instrumentation

LC-MS/MS analysis was performed with a Waters Acquity binary pump UPLC system (Milford, MA) interfaced to an AB Sciex QTrap 5500 (Framingham, MA) mass spectrometer with a Turbo V ™ source. Waters Acquity UPLC Console 1.50 software was used to control the UPLC and Analyst 1.6 software by AB Sciex was used to control the mass spectrometer.

LC-MS/MS Conditions

The mass spectrometer conditions were optimized for CPP by directly infusing a 100 ng/mL solution of neat CPP into the mass spectrometer and using the compound optimization setting in the software. Temperature, source gas, curtain gas, ion spray voltages, and collision gas parameters were optimized manually. This process was repeated for the internal standard using a stock solution of cAMP in 20 mM HFBA in 99:1 water:AcN at a concentration of 4.5 μg/ml. The precursor to product ions (Q1 → Q3) selected for the analyte, CPP, were *m/z* 252.958 → 207.100, 252.958 → 123.000, and 252.958 → 83.000, shown in **Figure 1A**. The

precursor to product ions (Q1 → Q3) selected for the internal standard, cAMP, were *m/z* 334.955 → 136.033, 334.955 → 119.050, and 334.955 → 293.925, shown in **Figure 1B**.

For the LC-MS/MS experiments, the analyte and IS were separated on a Waters Acquity UPLC BEH C18 column (100 x 2.1 mm ID, 1.7 μm) coupled with a Waters Acquity UPLC BEH C18 VanGuard pre-column with (5 x 2.1 mm ID). Mobile phase A was 20 nM HFBA in water and mobile phase B was 20 mM HFBA in acetonitrile. An aliquot of 7 μL of each sample was injected into the column. The following gradient was used to separate the analyte and IS (time/minute, % mobile phase B): (0, 1), (4, 6), (4.1, 95), (5.5, 95), (5.6, 1), (8, 1). The flow rate was set at 0.35 mL/min, the column temperature was 35 °C, and the samples were kept at 10 °C throughout the experiment.

The mass spectrometer was operated in positive ion ESI mode. Multiple reaction monitoring (MRM) mode was utilized to detect the analyte and internal standard. The precursor to product ions used for quantitation for CPP and cAMP were *m/z* 252.958 → 207.100 and 334.955 → 136.033, respectively. The MRM method contained two periods; CPP was detected in Period 1 (0.0- 2.7 min) and cAMP was detected in Period 2 (2.7-8.0 min). The operational parameters for the mass spectrometer during Period 1 are as follows: curtain gas- 35.0 psi, collision gas- high, ionspray voltage- 4500.0 V, temperature- 625.0 °C, ion source gas 1- 30.0 psi, ion source gas 2- 50.0 psi, declustering potential- 81.0 V, entrance potential- 10.0 V, Q1 resolution- unit, Q3 resolution- low, collision energy- 25 eV, collision cell exit potential- 18 V. The operational parameters for the mass spectrometer during Period 2 are as follows: curtain gas- 55.0 psi, collision gas- high, ionspray voltage- 4500.0 V, temperature- 675.0 °C, ion source gas 1- 30.0 psi, ion source gas 2- 50.0 psi, declustering potential- 86.0 V, entrance potential- 10.0 V, Q1 resolution- unit, Q3 resolution- low, collision energy- 25 eV, collision cell exit potential- 18

V. Peak area ratios of CPP and IS were calculated manually and with AB Sciex MultiQuant 2.1 software by generating calibration curves employing linear or quadratic fits with 1/x weighting. Parameters obtained from these calibration curves were used to back-calculate CPP concentration in mouse plasma.

Immediately following all LC-MS runs with HFBA, the column was flushed with 95% acetonitrile or methanol for at least 10 minutes to remove residual HFBA. The HFBA mobile phase solvents were removed from the LC system and the system was purged and primed with non-HFBA containing solvents to remove residual HFBA.

Method Validation

Linearity, Accuracy, Precision, Sensitivity

Linearity, precision, and accuracy were evaluated using the calibration curve. Linearity was evaluated by the R^2 value on the calibration curve. Accuracy is defined as the closeness between measured and true values and was assessed by the percent relative error (RE), which is calculated as [(actual amount-measured amount)/actual amount] x 100. Precision was assessed by the percent coefficient of variance (CV), which is calculated as [standard deviation of measurements / mean] x 100. Intra-day precision and accuracy were assessed by QC samples equivalent to each point on the calibration curve. The limit of detection (LOD) was tested by injecting samples of neat CPP in water and determining the concentration at which the analyte signal is five times larger than the blank sample. For the LOD study, serial dilutions of neat CPP stock solution in pure water were used. The lower limit of quantitation (LLOQ) was determined

from peak areas of the analyte and IS in plasma and defined as the lowest concentration in which the peak area of the sample is five times greater than the area of the blank.

Specificity and Matrix Effects

For this study, the most prominent transition for the analyte and IS were used for quantification; however, three daughter ions for both the analyte and IS were selected and monitored to ensure specificity of the experiment. Solvent calibrations and plasma calibration samples were prepared for evaluating the matrix effects. The matrix calibration samples were prepared by spiking 25 µL of plasma with 10 µL of 2 ng/µL CPP solution and 10 µL of 0.5 ng/µL cAMP solution. The comparable solvent calibration sample was prepared by spiking 25 µL of water with 10 µL of 2 ng/µL CPP solution and 10 µL of 0.5 ng/µL cAMP solution. Plasma and solvent calibration samples were dried down and resuspended in 50 µL of diluent. The matrix effect was calculated as [(the ratio of the peak area of the analyte in post-extraction matrix/the peak area of diluent spiked with the analyte)-1] x 100 (n=3).

It is important to note that immediately following all LC-MS runs with HFBA, the column should be flushed with 95% acetonitrile or methanol for at least 10 minutes to remove residual HFBA. The HFBA mobile phase solvents should be removed from the LC system and the system should be purged and primed with non-HFBA containing solvents. Regular cleaning of the MS instrument should remove residual HFBA.

Recovery

Percent recovery was calculated from peak areas of spiked samples and post-preparation spiked samples (n=6). Samples were prepared according to the described SPE procedure and spiked with 20 ng of analyte and 5 ng of IS pre- or post-preparation, dried down, and

resuspended in 50 μL diluent before analysis. Extraction recovery was calculated as [the ratio of peak area of the analyte extracted from the biological matrix/ the peak area of diluent spiked with the analyte] x 100. The recovery of the IS was assessed with the same method.

Stability

Due to the small sample volumes used in this experiment, the entire sample was consumed during each analysis; therefore, the autosampler stability was the most relevant to the experiment. Autosampler stability of the plasma matrix was tested by running freshly prepared samples of 1.0, 10.0, 20.0, and 30.0 ng CPP and 5.0 ng IS in plasma (n=3) immediately and after 11 hrs.

In Vivo Pharmacokinetic Study

CPP solutions for injection were made from CPP stock solution diluted in saline. Injections were given to mice of the 129/SvJ x C57BL/6J background that were between 4-8 weeks of age. Whole blood and brain tissue were collected from animals after decapitation under deep general anesthesia with isoflurane. For pharmacokinetic study bolus tail vein intravenous (i.v.) injections and intraperitoneal (i.p.) injections were examined. Injection volume was 5 ml/kg for i.v. and 10 ml/kg for i.p. Dosages of i.v. injections included 0.25, 0.5, 1.0, and 2.0 mg/kg, samples were collected 45 minutes following injection, and there were five replicates for each dose. Individual animals were used for a time point study, animals were sacrificed at 10, 15, 30, 45, 60, and 90 minutes following i.v. injection, and there were three or more replicates for each time point. Dosages of i.p. injections included 3.0 and 9.0 mg/kg, samples were collected 60

minutes following injection, and there were five replicates for each dose. Individual animals were used for a time point study, animals were sacrificed at 45, 60, 75, and 90 minutes following i.p. injection, and there were three or more replicates for each time point.

The pharmacokinetic parameters of CPP including maximum concentration (C_{max}) and time point of maximum concentration (T_{max}) were acquired for both plasma and brain tissue following i.v. and i.p injections. Elimination half-time ($t_{1/2}$) was determined by fitting the concentration-time profiles of plasma and brain tissue after i.v. injection to a one-phase exponential decay using Prism5 (GraphPad Software, Inc., La Jolla, CA). Pharmacokinetic parameters are reported as mean ± SEM.

Results and Discussion

Method Validation

Linearity, Accuracy, Precision, Sensitivity

The higher end of the plasma calibration curve range began to saturate the detector on the mass spectrometer; therefore, a quadratic fit was used with an R^2 value of 0.99. Intra-day precision and accuracy was calculated for all points on the calibration curve, shown in **Table 1**. Precision was assessed by the CV and is defined as the closeness of measurements of the same concentration. Accuracy was assessed by the RE between measured and nominal concentrations. CV and RE values were less than 15%. Due to the small sample volumes used in this experiment, the entire sample was consumed during each analysis; therefore, the inter-day precision and accuracy is not analyzed. The LOD, the concentration at which the analyte signal

is five times larger than the blank sample was determined to be 50 ag on column (5 μL injection of 10 ag/mL CPP in water). The LLOQ is 0.3 ng for plasma samples.

Specificity and Matrix Effects

Representative chromatograms obtained from blank diluent, neat CPP (20 ng), blank plasma, and plasma spiked 20 ng CPP are shown in **Figure 2**. A peak is occasionally observed in the blank plasma solutions at a retention time overlapping with that of CPP. This peak is believed to be potassiated HFBA. Protonated CPP has an exact mass of 253.094785 while potassiated HFBA has a mass of 252.949635 ($\Delta m = 0.145$ Da) and the two compounds have similar transition masses. The inherent nature of the Q-trap as a low resolution mass spectrometer does not allow for differentiation of masses that are this close together, therefore the potassiated HFBA generates a peak in the blanks samples. This effect has been accounted for in the calibration curves as the intercepts do not go through zero. The effects of the plasma matrix on ion suppression were evaluated at relevant concentration levels (20 ng CPP). A suppression of -12.27 ± 9.45% was observed for CPP in plasma and a slight enhancement of +4.60 ± 11.70% was observed for IS.

Recovery

Recovery of CPP was determined by dividing the peak area of the sample with CPP spiked in pre-preparation by the peak area of the sample with CPP spiked in post-preparation in 3 replicates each in the plasma matrix. This method was also used to analyze the recovery of the IS. Average recovery for CPP in plasma was 58.21 ± 13.40% and average recovery for IS in plasma was 88.04 ± 12.59%.

Stability

Autosampler stability (10°C) was determined for the analyte and IS in plasma at relevant concentrations. The stability is shown in the form of percentage of relative concentration of samples run after 11 hours to samples run initially (mean ± SD). The results are summarized in **Table 2**.

Pharmacokinetics

The described method was used to assay CPP concentrations in mice following systemic administration. I.V. administration of CPP at a series of doses indicated a linear relationship between the dose and concentration for both plasma and brain tissue over the concentration range examined (**Figure 3A**). I.P. administration at two doses revealed a similar relationship (**Figure 3B**). We calculated the brain to plasma concentration ratio using the 1 mg/kg dose for i.v. administration and 3 mg/kg dose for i.p. administration, yielding 0.07 ± 0.01 and 0.06 ± 0.01, respectively. A detailed concentration-time profile was performed using i.v. administration of 1 mg/kg CPP (**Figure 4**). C_{max} for plasma was 2113 ± 202 ng/ml (n=3) at T_{max} (10 minutes), which was the first time point assayed. C_{max} for brain tissue was 23.9 ± 6.0 ng/g (n=4) at T_{max} (15 minutes), also the first time point assayed. The elimination of CPP was modeled as one-phase exponential decay. The $t_{1/2}$ of CPP in plasma was 8.8 minutes and the $t_{1/2}$ of CPP in tissue was 14.3 minutes. The concentration-time profile of CPP following I.P. injection of 9 mg/kg CPP was assessed over a relevant timeframe (**Figure 5**). Following I.P. administration C_{max} for CPP in plasma was 1259 ± 177 ng/ml (n=8) at T_{max} (60 minutes), while C_{max} for CPP in brain tissue was 87 ± 32 ng/g (n=5) at T_{max} (45 minutes).

Conclusions

A reliable and sensitive ion-pair LC-MS/MS assay for the determination of CPP in mouse plasma and tissue was developed. Using this method we report a pharmacokinetic analysis of CPP, a competitive antagonist of the NMDA receptor that is routinely used to investigate the role of NMDA receptors in brain function. Importantly, this assay does not require a tritiated compound, which is not readily available, it is 100 times more sensitive than the derivatization method presented by Patel *et al.*,[26] and it is suitable for extensive pharmacokinetic studies. The pharmacokinetics of CPP presented here will inform research into the myriad of NMDA-dependent processes.

Acknowledgements

The authors would like to thank Feng Xiang for pursuing various methodologies in the early stages of development and Mark Perkins for performing animal injections during the *in vivo* pharmacokinetic study. This work was supported by National Science Foundation Graduate Research Fellowship (DGE-1256259) to E.G., National Institutes of Health National Research Service Award (1F32GM106670) to K.L., National Institutes of Health grant (GM101497) to R.P., National Institutes of Health grant (R01DK071801) to L.L., and the University of Wisconsin Graduate School, the Wisconsin Alumni Research Foundation, and Romnes Faculty Research Fellowship program to L.L.

References

1. Paoletti, P.; Bellone, C.; Zhou, Q., NMDA receptor subunit diversity: impact on receptor properties, synaptic plasticity and disease. *Nature reviews. Neuroscience* **2013,** *14* (6), 383-400.

2. Morris, R. G.; Anderson, E.; Lynch, G. S.; Baudry, M., Selective impairment of learning and blockade of long-term potentiation by an N-methyl-D-aspartate receptor antagonist, AP5. *Nature* **1986,** *319* (6056), 774-776.

3. Lyford, G. L.; Jarrard, L. E., Effects of the Competitive Nmda Antagonist Cpp on Performance of a Place and Cue Radial Maze Task. *Psychobiology* **1991,** *19* (2), 157-160.

4. Pontecorvo, M. J.; Clissold, D. B.; White, M. F.; Ferkany, J. W., N-Methyl-D-Aspartate Antagonists and Working Memory Performance - Comparison with the Effects of Scopolamine, Propranolol, Diazepam, and Phenylisopropyladenosine. *Behav Neurosci* **1991,** *105* (4), 521-535.

5. Cole, B. J.; Klewer, M.; Jones, G. H.; Stephens, D. N., Contrasting Effects of the Competitive Nmda Antagonist Cpp and the Noncompetitive Nmda Antagonist Mk-801 on Performance of an Operant Delayed Matching to Position Task in Rats. *Psychopharmacology* **1993,** *111* (4), 465-471.

6. Takahashi, E.; Niimi, K.; Itakura, C., Subthreshold pharmacological and genetic approaches to analyzing Ca(v)2.1-mediated NMDA receptor signaling in short-term memory. *Eur J Pharmacol* **2010,** *645* (1-3), 113-118.

7. Collingridge, G. L.; Kehl, S. J.; McLennan, H., Excitatory amino acids in synaptic transmission in the Schaffer collateral-commissural pathway of the rat hippocampus. *The Journal of physiology* **1983,** *334*, 33-46.

8. Harris, E. W.; Ganong, A. H.; Monaghan, D. T.; Watkins, J. C.; Cotman, C. W., Action of 3-((+/-)-2-carboxypiperazin-4-yl)-propyl-1-phosphonic acid (CPP): a new and highly potent antagonist of N-methyl-D-aspartate receptors in the hippocampus. *Brain research* **1986,** *382* (1), 174-177.

9. Walker, D. L.; Gold, P. E., Effects of the novel NMDA antagonist, NPC 12626, on long-term potentiation, learning and memory. *Brain research* **1991,** *549* (2), 213-221.

10. Kato, K.; Clifford, D. B.; Zorumski, C. F., Long-term potentiation during whole-cell recording in rat hippocampal slices. *Neuroscience* **1993,** *53* (1), 39-47.

11. Ahmed, T.; Sabanov, V.; D'Hooge, R.; Balschun, D., An N-methyl-D-aspartate-receptor dependent, late-phase long-term depression in middle-aged mice identifies no GluN2-subunit bias. *Neuroscience* **2011,** *185*, 27-38.

12. Traynelis, S. F.; Wollmuth, L. P.; McBain, C. J.; Menniti, F. S.; Vance, K. M.; Ogden, K. K.; Hansen, K. B.; Yuan, H.; Myers, S. J.; Dingledine, R., Glutamate receptor ion channels: structure, regulation, and function. *Pharmacological reviews* **2010,** *62* (3), 405-496.

13. Reisberg, B.; Doody, R.; Stoffler, A.; Schmitt, F.; Ferris, S.; Mobius, H. J.; Grp, M. S., Memantine in moderate-to-severe Alzheimer's disease. *New Engl J Med* **2003,** *348* (14), 1333-1341.

14. Tariot, P. N., Contemporary issues in the treatment of Alzheimer's disease: tangible benefits of current therapies. *The Journal of clinical psychiatry* **2006,** *67 Suppl 3*, 15-22; quiz 23.

15. Winblad, B.; Jones, R. W.; Wirth, Y.; Stoffler, A.; Mobius, H. J., Memantine in moderate to severe Alzheimer's disease: a meta-analysis of randomised clinical trials. *Dementia and geriatric cognitive disorders* **2007,** *24* (1), 20-27.

16. Hallett, P. J.; Standaert, D. G., Rationale for and use of NMDA receptor antagonists in Parkinson's disease. *Pharmacology & therapeutics* **2004,** *102* (2), 155-174.

17. Aarsland, D.; Ballard, C.; Walker, Z.; Bostrom, F.; Alves, G.; Kossakowski, K.; Leroi, I.; Pozo-Rodriguez, F.; Minthon, L.; Londos, E., Memantine in patients with Parkinson's disease dementia or dementia with Lewy bodies: a double-blind, placebo-controlled, multicentre trial. *Lancet Neurol* **2009,** *8* (7), 613-618.

18. Wakasugi, M.; Hirota, K.; Roth, S. H.; Ito, Y., The effects of general anesthetics on excitatory and inhibitory synaptic transmission in area CA1 of the rat hippocampus in vitro. *Anesthesia and analgesia* **1999,** *88* (3), 676-680.

19. Nishikawa, K.; MacIver, M. B., Excitatory synaptic transmission mediated by NMDA receptors is more sensitive to isoflurane than are non-NMDA receptor-mediated responses. *Anesthesiology* **2000,** *92* (1), 228-236.

20. Paul, I. A.; Skolnick, P., Glutamate and depression: clinical and preclinical studies. *Annals of the New York Academy of Sciences* **2003,** *1003*, 250-272.

21. Skolnick, P.; Popik, P.; Trullas, R., Glutamate-based antidepressants: 20 years on. *Trends in pharmacological sciences* **2009,** *30* (11), 563-569.

22. Petrenko, A. B.; Yamakura, T.; Baba, H.; Shimoji, K., The role of N-methyl-D-aspartate (NMDA) receptors in pain: a review. *Anesthesia and analgesia* **2003,** *97* (4), 1108-1116.

23. Davies, J.; Evans, R. H.; Herrling, P. L.; Jones, A. W.; Olverman, H. J.; Pook, P.; Watkins, J. C., CPP, a new potent and selective NMDA antagonist. Depression of central neuron responses, affinity for [3H]D-AP5 binding sites on brain membranes and anticonvulsant activity. *Brain research* **1986,** *382* (1), 169-173.

24. Lehmann, J.; Schneider, J.; McPherson, S.; Murphy, D. E.; Bernard, P.; Tsai, C.; Bennett, D. A.; Pastor, G.; Steel, D. J.; Boehm, C.; et al., CPP, a selective N-methyl-D-aspartate (NMDA)-type receptor antagonist: characterization in vitro and in vivo. *The Journal of pharmacology and experimental therapeutics* **1987,** *240* (3), 737-746.

25. Kristensen, J. D.; Hartvig, P.; Karlsten, R.; Gordh, T.; Halldin, M., CSF and plasma pharmacokinetics of the NMDA receptor antagonist CPP after intrathecal, extradural and i.v. administration in anaesthetized pigs. *British journal of anaesthesia* **1995,** *74* (2), 193-200.

26. Patel, S.; Chapman, A. G.; Graham, J. L.; Meldrum, B. S.; Frey, P., Anticonvulsant activity of the NMDA antagonists, D(-)4-(3-phosphonopropyl) piperazine-2-carboxylic acid (D-CPP) and D(-)(E)-4-(3-phosphonoprop-2-enyl) piperazine-2-carboxylic acid (D-CPPene) in a rodent and a primate model of reflex epilepsy. *Epilepsy research* **1990,** *7* (1), 3-10.

27. Carmack, S. A.; Kim, J. S.; Sage, J. R.; Thomas, A. W.; Skillicorn, K. N.; Anagnostaras, S. G., The competitive NMDA receptor antagonist CPP disrupts cocaine-induced conditioned place preference, but spares behavioral sensitization. *Behavioural brain research* **2013,** *239*, 155-163.

28. Blundell, J.; Adamec, R., The NMDA receptor antagonist CPP blocks the effects of predator stress on pCREB in brain regions involved in fearful and anxious behavior. *Brain research* **2007,** *1136* (1), 59-76.

29. Martin, K. P.; Wellman, C. L., NMDA receptor blockade alters stress-induced dendritic remodeling in medial prefrontal cortex. *Cereb Cortex* **2011,** *21* (10), 2366-2373.

30. Autry, A. E.; Adachi, M.; Nosyreva, E.; Na, E. S.; Los, M. F.; Cheng, P. F.; Kavalali, E. T.; Monteggia, L. M., NMDA receptor blockade at rest triggers rapid behavioural antidepressant responses. *Nature* **2011,** *475* (7354), 91-95.

31. Namba, T.; Ming, G. L.; Song, H.; Waga, C.; Enomoto, A.; Kaibuchi, K.; Kohsaka, S.; Uchino, S., NMDA receptor regulates migration of newly generated neurons in the adult hippocampus via Disrupted-In-Schizophrenia 1 (DISC1). *Journal of neurochemistry* **2011,** *118* (1), 34-44.

32. Lange, K. W.; Loschmann, P. A.; Sofic, E.; Burg, M.; Horowski, R.; Kalveram, K. T.; Wachtel, H.; Riederer, P., The competitive NMDA antagonist CPP protects substantia nigra neurons from MPTP-induced degeneration in primates. *Naunyn-Schmiedeberg's archives of pharmacology* **1993,** *348* (6), 586-592.

33. Akita, H.; Honda, Y.; Ogata, M.; Noda, K.; Saji, M., Activation of the NMDA receptor involved in the alleviating after-effect of repeated stimulation of the subthalamic nucleus on motor deficits in hemiparkinsonian rats. *Brain research* **2010,** *1306*, 159-167.

34. Verges, D. K.; Restivo, J. L.; Goebel, W. D.; Holtzman, D. M.; Cirrito, J. R., Opposing synaptic regulation of amyloid-beta metabolism by NMDA receptors in vivo. *The Journal of neuroscience : the official journal of the Society for Neuroscience* **2011,** *31* (31), 11328-11337.

35. Ward, L.; Mason, S. E.; Abraham, W. C., Effects of the NMDA antagonists CPP and MK-801 on radial arm maze performance in rats. *Pharmacology, biochemistry, and behavior* **1990,** *35* (4), 785-790.

36. Abraham, W. C.; Mason, S. E., Effects of the NMDA receptor/channel antagonists CPP and MK801 on hippocampal field potentials and long-term potentiation in anesthetized rats. *Brain research* **1988,** *462* (1), 40-46.

37. Hernandez, R. V.; Derrick, B. E.; Rodriguez, W. A.; Martinez, J. L., Jr., (+/-) CPP, an NMDA receptor antagonist, blocks the induction of commissural-CA3 LTP in the anesthetized rat. *Brain research* **1994,** *656* (1), 215-219.

38. Ge, Y.; Dong, Z.; Bagot, R. C.; Howland, J. G.; Phillips, A. G.; Wong, T. P.; Wang, Y. T., Hippocampal long-term depression is required for the consolidation of spatial memory. *Proceedings of the National Academy of Sciences of the United States of America* **2010,** *107* (38), 16697-16702.

Tables

Table 1. The intra-day precision (CV) and accuracy (RE) of the LC-MS/MS method used to quantitate CPP in mouse plasma

N	Nominal Amount (ng)	Measured Amount (mean ± SD, ng)	CV (%)	RE (%)
7	0.5	0.55 ± 0.02	3.32	8.38
9	2.5	2.44 ± 0.21	8.70	2.65
7	10.0	9.93 ± 0.64	6.41	0.70
9	50.0	49.52 ± 4.86	9.82	0.97
7	100.0	100.92 ± 8.14	8.07	0.91
8	150.0	149.58 ± 13.84	9.25	0.28

Table 2. Autosampler stability of CPP and IS at all concentrations used to generate the calibration curves in plasma. The stability is shown in the form of percentage of relative concentration of samples run at several time points

Matrix	Compound	Amount (ng)	Stability (%)
Plasma (11 hr)	CPP	1.0	97.33 ± 2.04
		10.0	98.65 ± 9.01
		20.0	93.43 ± 2.79
		30.0	84.98 ± 9.68
	IS	5.0	88.50 ± 2.44

Figures

Figure 1

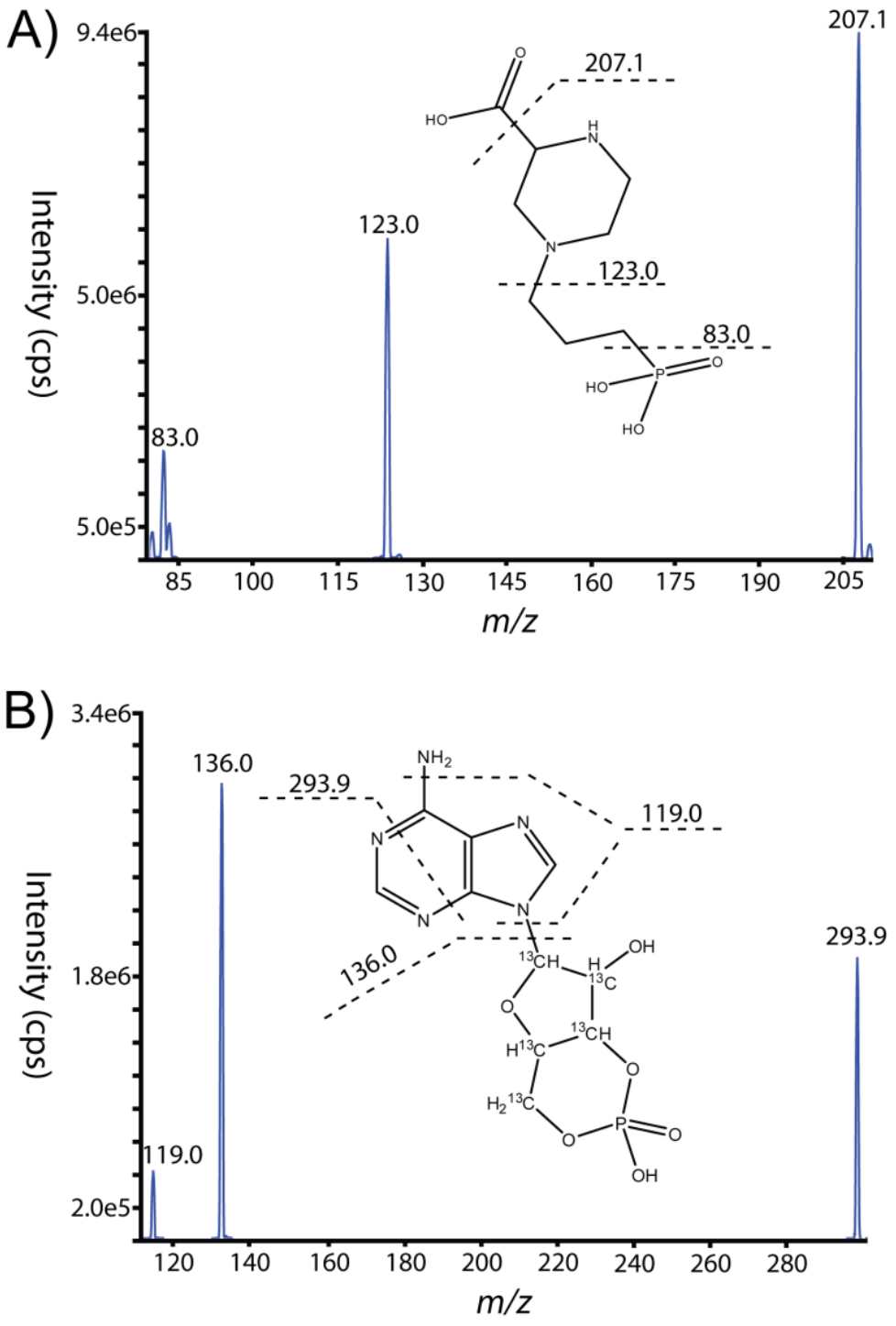

Figure 1. MS/MS spectra showing A) CPP fragment ions 207.100, 123.000, and 83.000 and B) fragment ions 136.033, 119.050, and 293.925 monitored in the MRM experiments.

Figure 2

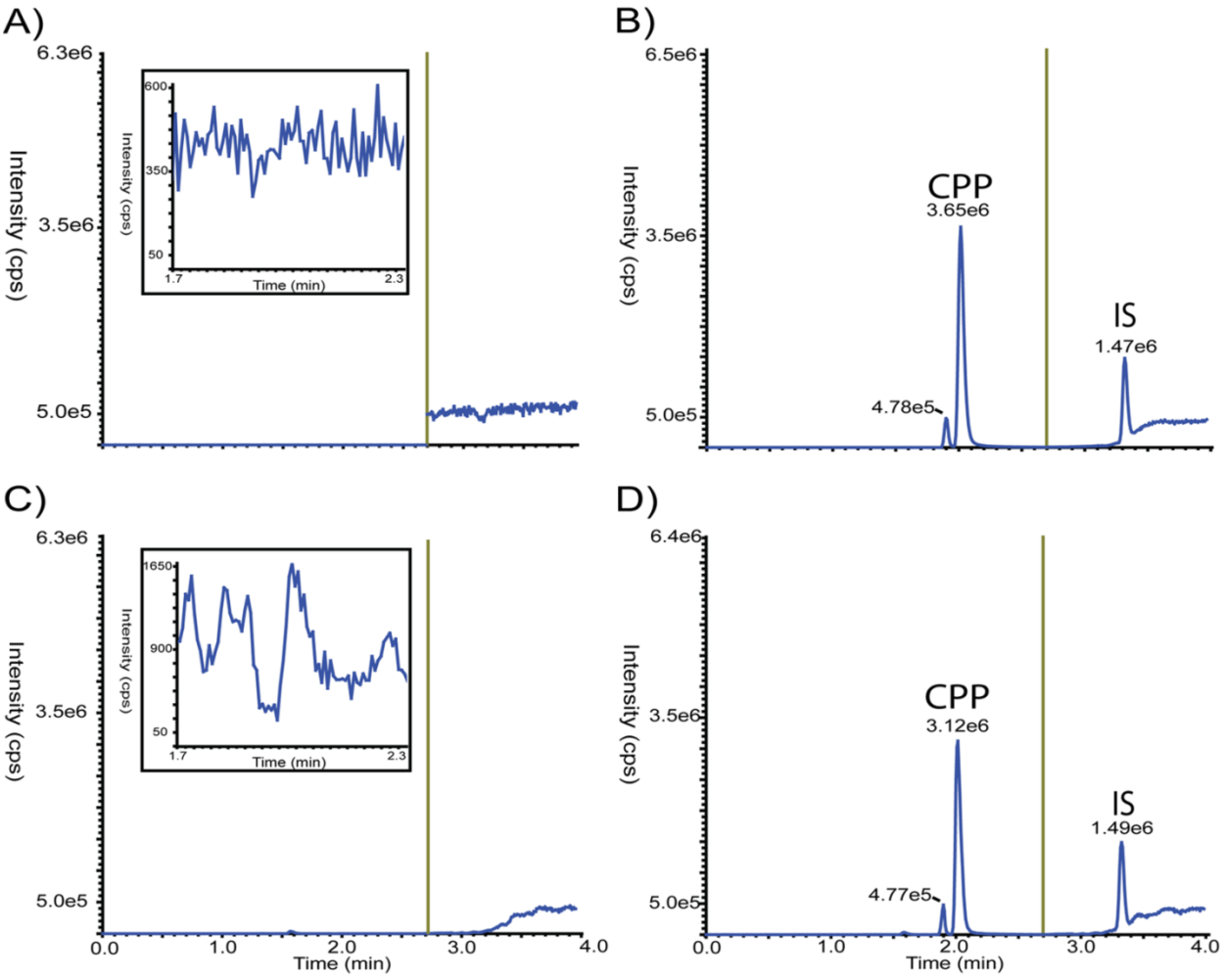

Figure 2. Representative chromatograms obtained from A) blank diluent, B) 20 ng neat CPP, C) blank plasma with inlay of zoomed in chromatogram, and D) plasma spiked with 20 ng CPP. The green line in each chromatogram separates the two periods of the MS method. Period 1 measures CPP while period 2 measures IS.

Figure 3

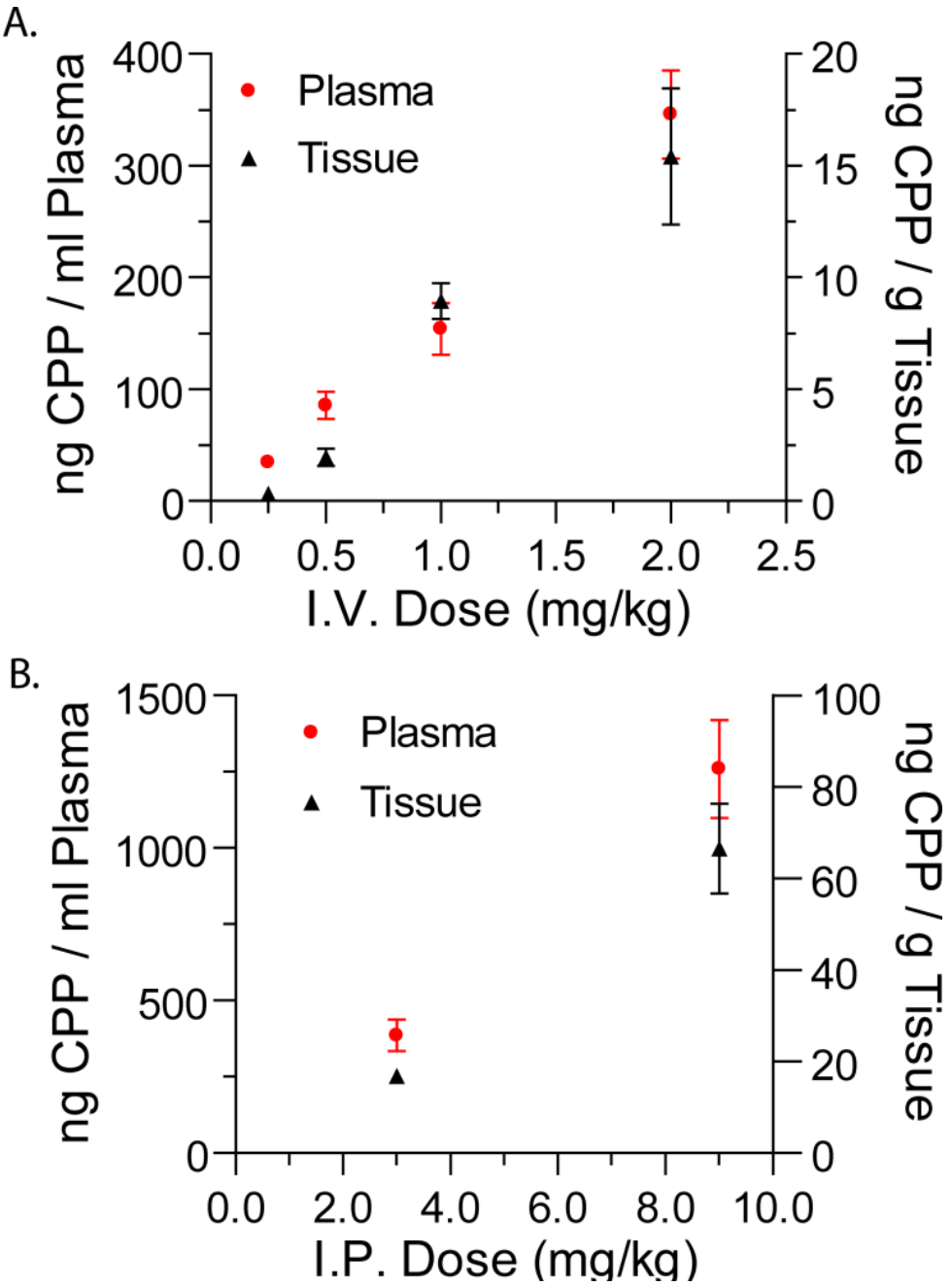

Figure 3. CPP dose-concentration relationships. A) Animals were administered CPP by i.v. injection, and were sacrificed 45 minutes later in order to sample plasma and brain tissue. B) Animals were administered CPP by i.p. injection, and were sacrificed 60 minutes later in order to sample plasma and brain tissue. The left axis presents plasma concentration and the right axis presents tissue concentration. Symbols and error bars are mean ± SEM

Figure 4

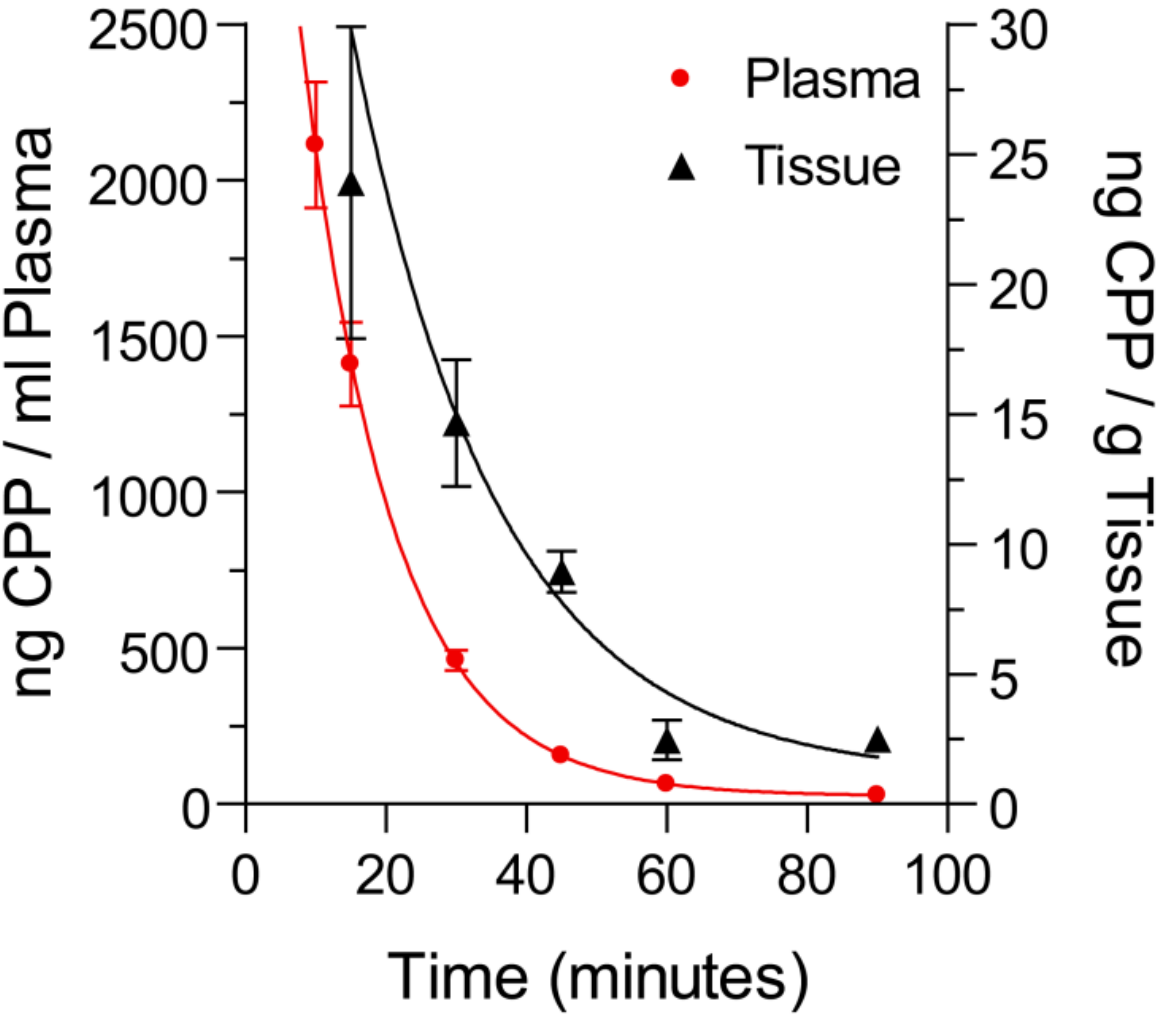

Figure 4. Concentration-time plot for plasma and brain tissue following i.v. injection of 1 mg/kg CPP. Non-linear regression was performed with an on-phase exponential decay, for plasma r^2=0.964, for brain tissue r^2=0.774. Symbols and error bars are mean ± SEM.

Figure 5

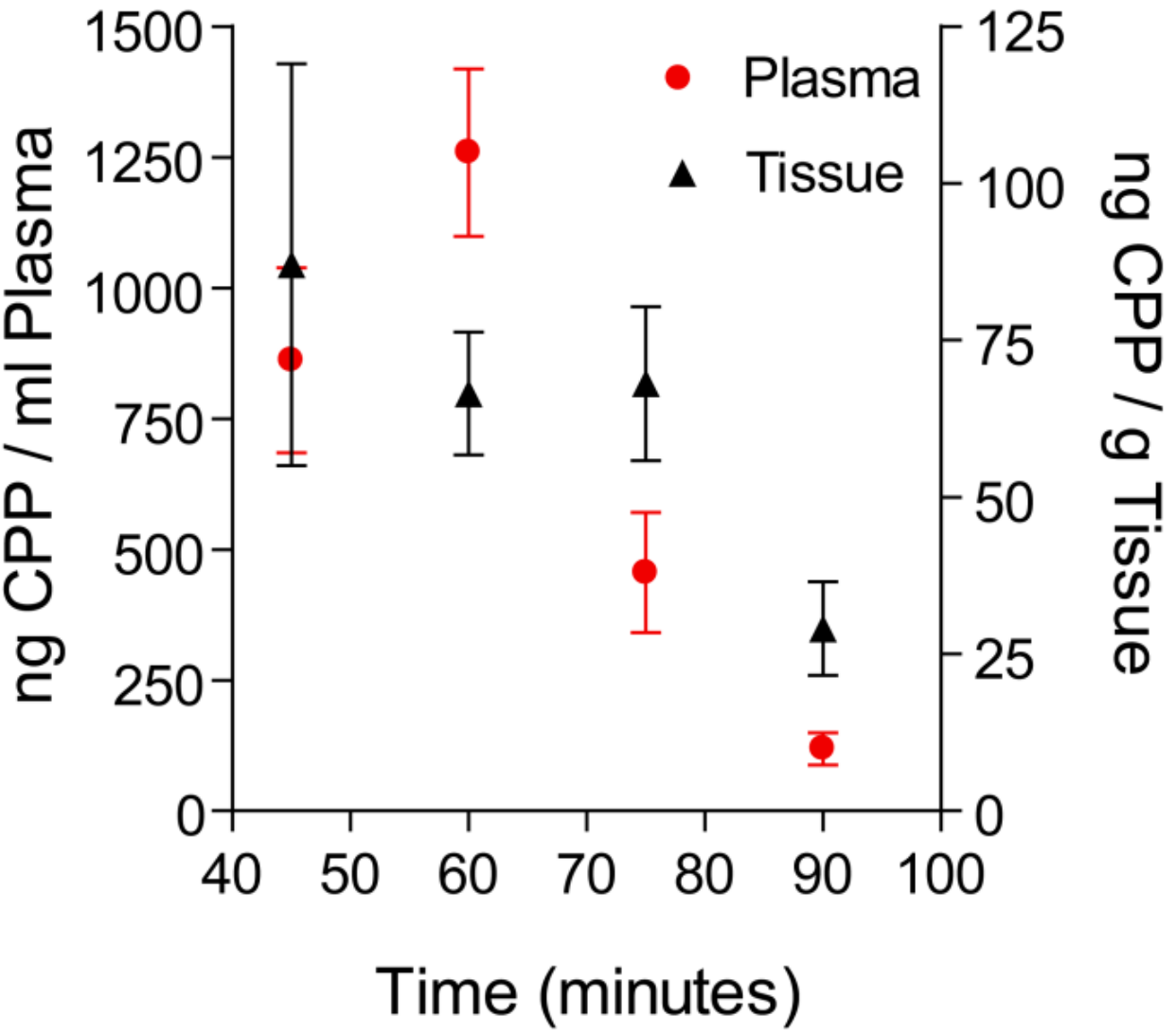

Figure 5. Concentration-time plot for plasma and brain tissue following i.p. injection of 9 mg/kg CPP. Symbols and error bars are mean ± SEM.

Chapter 9

Conclusions and Future Directions

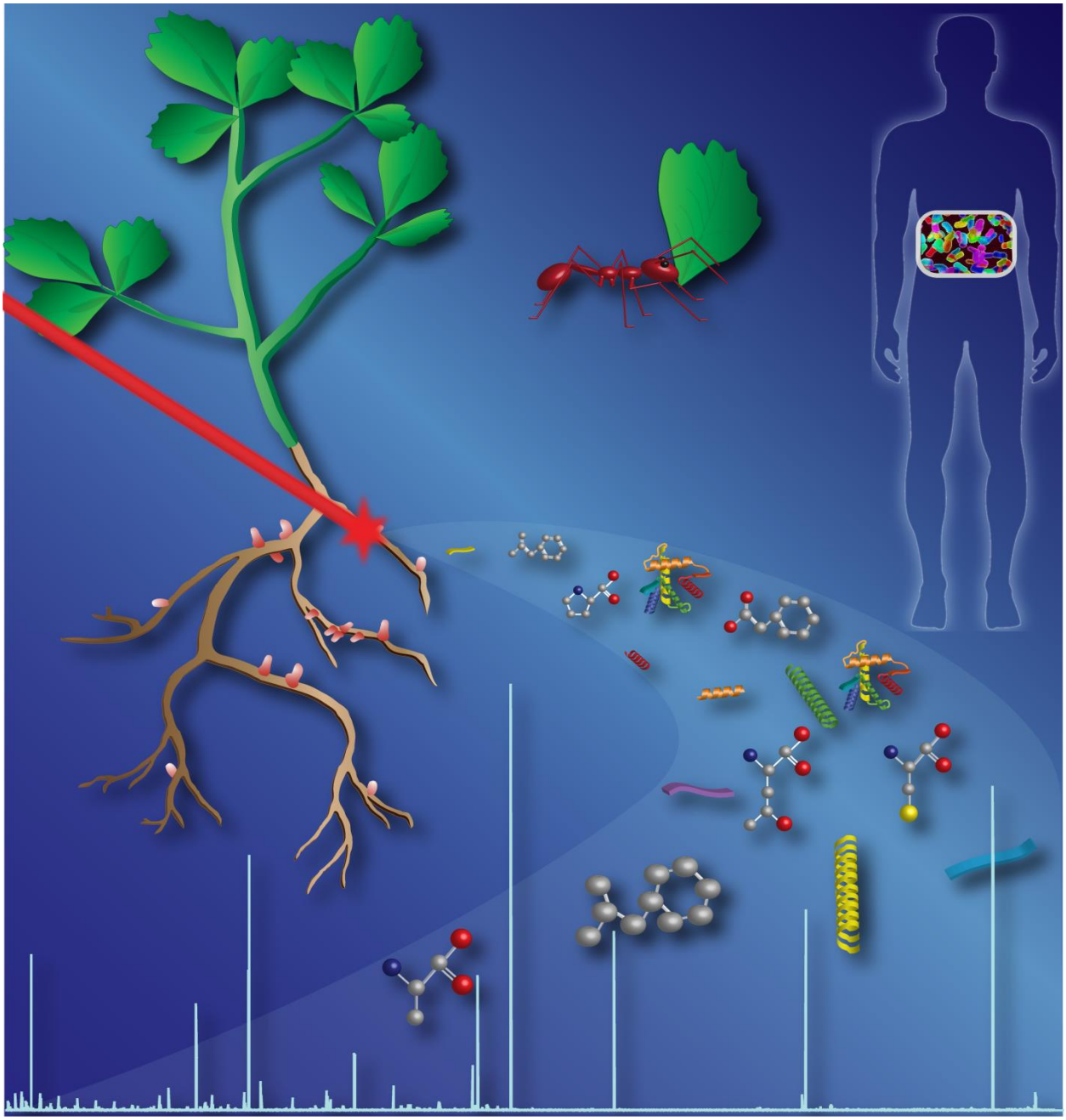

Microbiome photo courtesy of SatorI13/Stockphoto. Human silhouette adapted from Freepik.com.

Conclusions

This work not only improves upon MSI through extensive method development, but also presents a useful platform that integrates MALDI-MSI with ESI-LC-MS in exploring the underlying chemistry of several biological symbiotic systems. In Chapter 3, I was able to greatly improve MSI detection of metabolites from thin tissue slices, by focusing on the optimization of the matrix application process. Overall, using the optimized method developed for the TM Sprayer automatic matrix application system (0.05 mL/min flow rate, 1250 mm/min velocity, 24 passes, crisscross and offset, 3 mm line spacing, 80 °C) resulted in a 3-fold increase in the number of metabolites detected in comparison to the original method using an artist airbrush to apply the matrix. The TM Sprayer achieved comparable analyte localization to solvent-free, sublimation matrix application and also achieved more detectable metabolites due to the use of solvent to extract metabolites from the tissue. This method was easily and successfully used for metabolite MSI on other types of samples and tissues.

I used this method to obtain valuable information on the identity and spatial distribution of metabolites in the model legume, *Medicago truncatula*, as presented in Chapter 4. New knowledge was obtained regarding the putative roles of key metabolites involved in symbiotic nitrogen-fixation through the comparison of metabolite profiles and molecular ion images obtained from nitrogen fixing and non-fixing nodules with MALDI-MSI. MALDI-MS/MS and LC-MS/MS experiments on putative metabolites were performed to confirm the assignments of region-specific metabolites that were found only in nodules that were capable of nitrogen fixation. I detected approximately 100 metabolites that were only present in nitrogen fixation-capable nodules. Of those 104 metabolites, 34 were confidently identified as primarily amino acids and other organic acids. I then focused on MSI of endogenous peptides in *Medicago*

truncatula (Medicago) in Chapter 5. We adapted the method developed in Chapter 3 to the detection of peptides instead of metabolites in mature Medicago root nodules and Medicago seedlings. We were able to image the spatial distribution of 277 putative endogenous peptides/ protein fragments in the mature root nodules and 496 putative endogenous peptides/ protein fragments in the seedlings. We identified 10 peptides based on MS/MS information and accurate mass matching to the *Medicago truncatula* proteome. We were able to identify 22 peptides by *de novo* sequencing using PEAKS. Additional biological studies into the identified peptides/ protein fragments would greatly strengthen the significance and impact of this study.

Chapter 6 shifted to a new symbiotic system, the fungus-growing ant and the bacteria, *Pseudonocardia*. I developed a method for improved MALDI-MSI detection of metabolites *in vitro* and designed a completely new method for MALDI-MSI of this system *in vivo*. MSI of bacterial colonies grown on agar plates was pioneered by the Dorrestein group[1-5] and traditionally used a small sieve to apply a coat of dry matrix to the sample before MSI. I found that this approach yielded poor signal and inconsistent MSI results. I therefore developed a matrix application method using the TM-Sprayer to apply matrix to the bacterial colony and surrounding agar in a homogeneous and reproducible manner which greatly improved the number of metabolites that could be detected from the samples. Additionally, we challenged the *Pseudonocardia* with ecologically relevant pathogens *in vitro* and *in vivo*. We found that a greater number of compounds were detected *in vitro* and the metabolic profiles produced by the bacteria *in vitro* vs. *in vivo* were substantially different, suggesting that studying bacteria in their natural environment may yield novel, complementary natural products to the traditional *in vitro* studies. We detected 46 compounds ($\geq$ *m/z* 300) from *Pseudonocardia sp. octospinosus* and 53 compounds from *Pseudonocardia sp. echinatior in vivo* and 179 compounds from

Pseudonocardia sp. octospinosus and 253 compounds from *Pseudonocardia sp. echinatior in vitro* that were expressed in response to pathogen exposure and could be potential candidates for novel antimicrobial compounds. We briefly tried to identify some of the natural product candidates that were detected on the ants *in vivo* in collaboration with Dr. Jon Clardy's lab at Harvard Medical School; however, this approach used *in vitro* methods to scale up the candidate molecules detected during *in vivo* experiments, but these same molecules were not seen using this approach. It will take creative and highly specific method development to create a new procedure for scaling-up, isolation, and structural elucidation of these potentially novel compounds.

Our natural product discovery work with the ant system led us to further develop methods for novel antibiotic discovery in Chapter 7. We colonized mice with the human gut microbiota and exposed the microbes to Salmonella. Using a high resolution LC-MS platform, we have detected a number of promising small molecules produced by the human gut microbiota that are significantly upregulated in the infection treatment compared to the control. In the pilot study, we detected 134 compounds via LC-MS that were produced in response to infection. MALDI-MSI was also used to visualize these detected compounds within the tissue. Importantly, a number of these detected compounds are putative novel molecules (based on accurate mass matching via the database searching tool, MetaboSearch), and thus represent exciting new drug leads. Additional biological replicates are currently being acquired and prepared for LC-MS. Further replicates will likely reduce the number of target molecules and improve the confidence of these results.

Finally, I developed a multiple reaction monitoring (MRM) method using a Q-trap mass spectrometer to determine the concentration of a drug, CPP, in mouse plasma and brain tissue

that is 100 times more sensitive than previously reported methods of quantifying CPP.[6] This method required the use of an ion-pairing agent, HFBA, due to the challenging physiochemical properties of CPP itself. We analyzed the linearity, accuracy, precision, sensitivity, specificity, matrix effects, recovery, and stability of CPP using our assay. Additionally, a pharmacokinetics study of CPP in mouse plasma and brain tissue was performed. The $t_{1/2}$ of CPP in plasma was 8.8 minutes and the $t_{1/2}$ of CPP in tissue was 14.3 minutes. A time course shows the elimination profile of CPP in mouse plasma and brain tissue following an I.P. (intraperitoneal) injection of 9 mg/kg CPP. Determining tissue-specific drug concentrations that correspond to specific behavioral endpoints will guide the design and interpretation of studies utilizing CPP for companion experiments performed *in vivo* and *in vitro*. The step of adding HFBA to the LC mobile phase can aid other researchers in performing chromatography and quantification of other challenging compounds.

Future Directions

The Medicago metabolomics study in Chapter 4 could be investigated in further detail. There are several mass spectrometry experiments that could be performed, such as negative mode LC-MS and MALDI-MSI as well as MALDI-MSI using other matrices which would potentially enhance the ionization and detectability of other classes of metabolites. Additionally, in the work described in Chapter 4, we report only metabolites that were present in the wild-type (wt), nitrogen fixing nodules and not present in any of the mutant samples. Since we performed MSI on combinations of wt plants/ mutant bacteria and mutant plants/ wt bacteria, we could further dissect the role each symbiont plays in the nitrogen fixation process by determining

which metabolites are only knocked out when we have one wt symbiont and one mutant symbiont. Finally, biological investigation would greatly strengthen the findings and impact of the current study; however, it can be extremely difficult to generate genetic mutants that knock out genes in specific metabolic pathways. Several difficulties may arise when genetically disrupting large metabolic pathways including: mutants that would be lethal for *Medicago truncatula*, mutants that are in redundant genetic pathways which would result in no metabolism changes, and mutants that cause the unintended upregulation/downregulation of other metabolic pathways rather than the pathways of interest.

For the study described in Chapter 5, further refinement of matrix application parameters and methods would be beneficial to acquire better-resolved MS images of peptides with greater coverage. Peptide images were acquired using several MALDI matrices, DHB, DHA, CHCA, DAN, and SA; however, MS/MS was only acquired with DHB and CHCA. Theoretically using the other above mentioned matrices, we could identify other classes of endogenous peptides. There were few *m/z* values detected in both MALDI and ESI, where we would ideally use LC-ESI-MS/MS for fragmentation and subsequent *de novo* sequencing of the peptides for identification since MALDI fragmentation of singly charged species is notoriously poor. The peptide extraction method could be further optimized in attempts to find a method that extracts peptides better corresponding to the peptides detected with MALDI-MSI. Further peptide enrichment strategies both on tissue and for tissue extractions could be explored by optimizing a method for applying antibodies on tissue for the detection of specific endogenous peptides of interest. Additionally, applying a protease inhibitor to the tissue slices immediately after sectioning could minimize potential endogenous peptide and protein degradation and allow for the detection of more endogenous peptides rather than protein fragments. This strategy would

also require method development as it would likely require a wash step in order to remove excess protease inhibitor prior to MS analysis. Additional biological studies examining the peptides/ protein fragments detected in this study could reveal more insights into the functions of these peptides within the plant at different stages of development.

Further work is currently underway for the Ant/ *Pseudonocardia* system described in Chapter 6. Using the MALDI-MSI method developed here future work will focus on studying the complex host-symbiont dynamics of this system. We propose to use a symbiont-switching strategy to determine which symbiotic player, ant host or *Pseudonocardia,* is driving the metabolomics response to pathogen presence. Five colonies each of two different ant species, *A. octospinosus* and *A. echinatior,* were collected in Panama. Five pupae of each species were removed from their colonies and raised by workers of the opposite species, effectively switching the *Pseudonocardia* strain the developing ant acquires. These host-symbiont 'switches' were exposed to one system-specific pathogen, and the metabolic profile will be examined and compared to natural host-symbiont pairings in order to determine ant host influence on secondary metabolite induction. Samples are currently being prepared for mass spectrometry.

The human microbiome project, described in Chapter 7, in still in progress. We are currently acquiring mice as additional biological replicates to improve the confidence of our results and likely narrow the list of candidate target compounds. In the future we plan to work with Dr. Jon Clardy's lab to isolate and identify the novel antimicrobial candidate compounds that were detected in the described experiment. Additionally, we are also conducting LC-MS/MS proteomics experiments to complement the metabolomics experiments. Understanding changes in the microbial proteomes in response to pathogen infection could provide insight into the molecular pathways involved in the response. Future work could involve infecting the

mouse/ human microbiota system with other pathogens (such as *Pseudomonas aeruginosa*, MRSA, *Candida albicans*, *E. coli*, Enterobacter, *Citrobacter rodentium*, etc.) to determine if exposure to other pathogens elicits a different response from the microbiota and produces more novel drug candidates. Furthermore, with access to human clinical fecal samples, other combinations of human gut microbiota could be cultured and challenged with various pathogens to see if different combinations of gut microbes have a different response to pathogen infection and potentially produce other novel antimicrobial candidates.

In summary, the work described in this dissertation has showcased a powerful MALDI-MSI/ ESI-LC-MS/MS platform that can facilitate the mapping and identification of various types of biomolecules from tissues and extracts. I have greatly improved upon sample preparation methods for thin tissue sections and bacterial colonies on agar. Additionally, I developed a novel method for *in vivo* MSI of compounds on the surface of an organism in comparison to traditional MSI that only performs on thin sections sliced from the inside of a tissue. I not only developed these methods, but also applied them to complex biological systems and challenging questions. These methods can be easily transferred to the study of other biological systems and will hopefully aid other researchers in their work. It is anticipated that the analytical methodology developed here and experimental data we obtained in these studies can impact future research in analytical chemistry, plant biology, and pharmaceutical science.

References

1. Yang, J. Y.; Phelan, V. V.; Simkovsky, R.; Watrous, J. D.; Trial, R. M.; Fleming, T. C.; Wenter, R.; Moore, B. S.; Golden, S. S.; Pogliano, K.; Dorrestein, P. C., Primer on Agar-Based Microbial Imaging Mass Spectrometry. *J Bacteriol* **2012,** *194* (22), 6023-6028.

2. Watrous, J. D.; Dorrestein, P. C., Imaging mass spectrometry in microbiology. *Nat Rev Microbiol* **2011,** *9* (9), 683-694.

3. Traxler, M. F.; Watrous, J. D.; Alexandrov, T.; Dorrestein, P. C.; Kolter, R., Interspecies interactions stimulate diversification of the Streptomyces coelicolor secreted metabolome. *mBio* **2013,** *4* (4).

4. Moree, W. J.; Yang, J. Y.; Zhao, X.; Liu, W. T.; Aparicio, M.; Atencio, L.; Ballesteros, J.; Sanchez, J.; Gavilan, R. G.; Gutierrez, M.; Dorrestein, P. C., Imaging mass spectrometry of a coral microbe interaction with fungi. *Journal of chemical ecology* **2013,** *39* (7), 1045-1054.

5. Gonzalez, D. J.; Xu, Y.; Yang, Y. L.; Esquenazi, E.; Liu, W. T.; Edlund, A.; Duong, T.; Du, L.; Molnar, I.; Gerwick, W. H.; Jensen, P. R.; Fischbach, M.; Liaw, C. C.; Straight, P.; Nizet, V.; Dorrestein, P. C., Observing the invisible through imaging mass spectrometry, a window into the metabolic exchange patterns of microbes. *J Proteomics* **2012,** *75* (16), 5069-5076.

6. Patel, S.; Chapman, A. G.; Graham, J. L.; Meldrum, B. S.; Frey, P., Anticonvulsant activity of the NMDA antagonists, D(-)4-(3-phosphonopropyl) piperazine-2-carboxylic acid (D-CPP) and D(-)(E)-4-(3-phosphonoprop-2-enyl) piperazine-2-carboxylic acid (D-CPPene) in a rodent and a primate model of reflex epilepsy. *Epilepsy research* **1990,** *7* (1), 3-10.

Chapter 10

Summary of

“Method Development and Application of Mass Spectrometry Imaging for the Study of Symbiotic Relationships between Bacteria and Host Organisms”

for the Wisconsin Initiative for Science Literacy

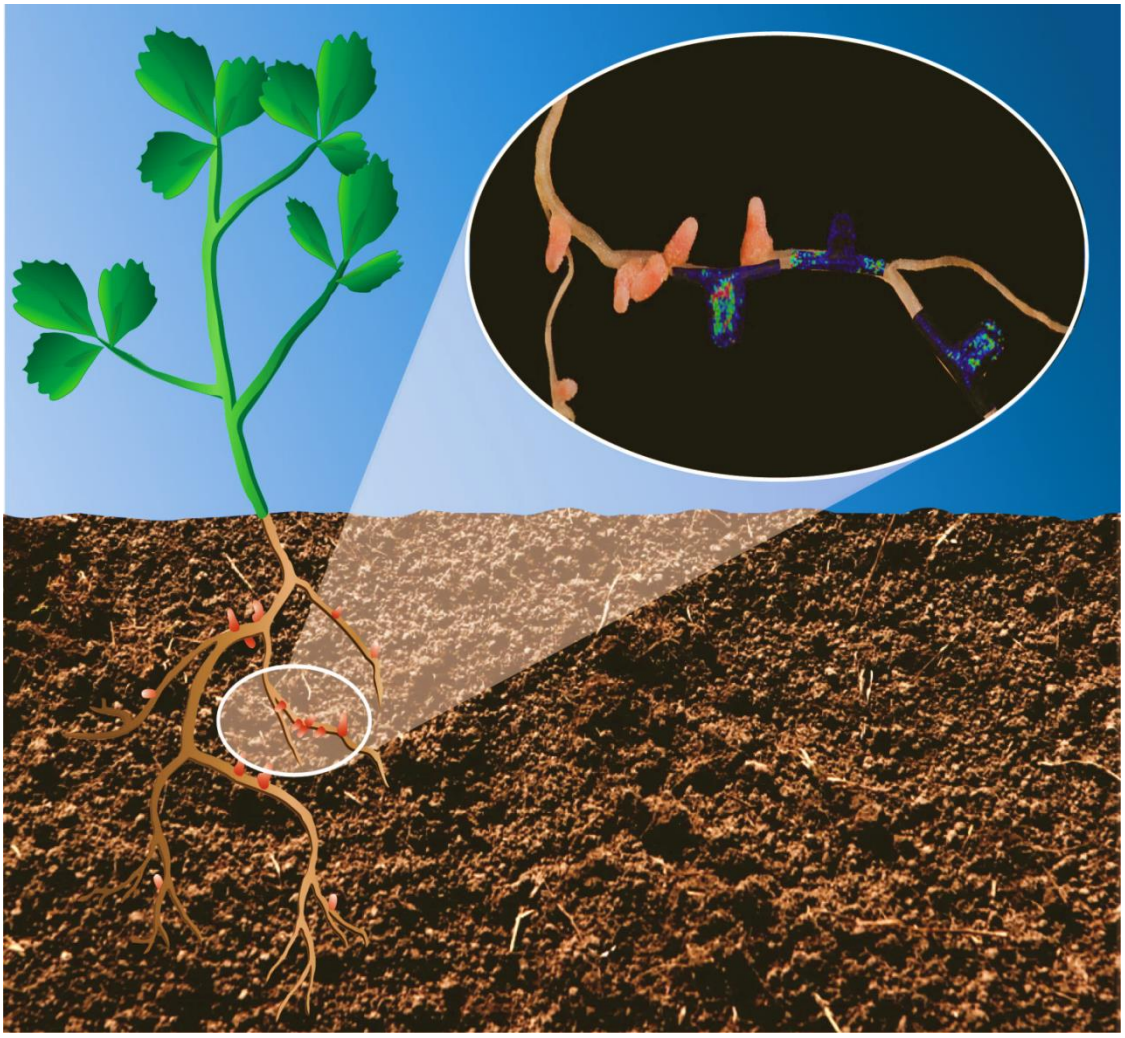

Introduction

In order to understand how biological systems work, it is important to study their underlying chemistry. Diseased organisms have different biochemistries than healthy organisms. We can find new ways to detect and treat diseases by comparing the differences in chemical activity between healthy and diseased states. There are many different classes of chemicals inside an organism that we can study, from proteins to peptides to small molecules/ metabolites. Your genes encode information to create proteins and proteins produce small molecules/ metabolites that the cells in our bodies directly use for fuel, structure, cell signaling, defense, and many other key roles. Organic acids (citric acid, amino acids, etc.), sugars (glucose, fructose, sucrose, etc.), alcohols, antioxidants, and lipids are all classified as metabolites. For my research I chose to study these different metabolites because by looking at the small molecules that are directly produced and used by the cell, you get a picture of what is going on in the cell at a given time.

How does my research relate to the study of metabolites?

My research over the last 4 ½ years has largely focused on the analysis of metabolites in plants by developing analytical techniques and methods to detect changes in metabolites between normal and mutant plants. I want to know what kinds of metabolites are in my plants and where they are located within the plants. In my research, I use a tool called a mass spectrometer to detect metabolites. The mass spectrometer allows me to measure the mass of hundreds of metabolites the plant samples and determine which ones are found in my normal plant samples and not found in the mutant plants. The type of mass spectrometry I use is a special technique

called mass spectrometry imaging. Using mass spectrometry imaging, I not only get the mass of each metabolite found in my plants, but I can also see a picture of the location of those metabolites within the plant (roots, leaves, stem, etc.).

Why plants?

In the introduction above, I used the example of wanting to know the differences between healthy and diseased states. For my research, I am actually looking at the difference in metabolites between normal and mutated legume plants. Legume plants, like soybeans, alfalfa, chickpeas, and other types of beans, are very important crops to the agriculture industry. Think back to elementary school when you learned about crop rotations. Farmers rotate what types of crops they plant in their fields because different crops suck up different nutrients from the soil. Legumes are one class of crops that can actually put nutrients back into the soil. The nutrient we are talking about is nitrogen. Legume plants have developed a symbiotic relationship (meaning the relationship is beneficial for both partners) with a bacteria that lives in soil, called rhizobia. The rhizobia take nitrogen from the air and "fix" it, or turn it into a form of nitrogen that the plant can actually use, in a process known as biological nitrogen fixation. In return, the plant provides a source of carbon for the rhizobia, which the bacteria need to survive. The bacteria are attracted to the roots of the legume plants and make their way inside the plants' roots. When bacteria enter a plant's roots, the roots form special structures, called root nodules, shown in **Figure 1**, and this is where the bacteria fix nitrogen for the plants.

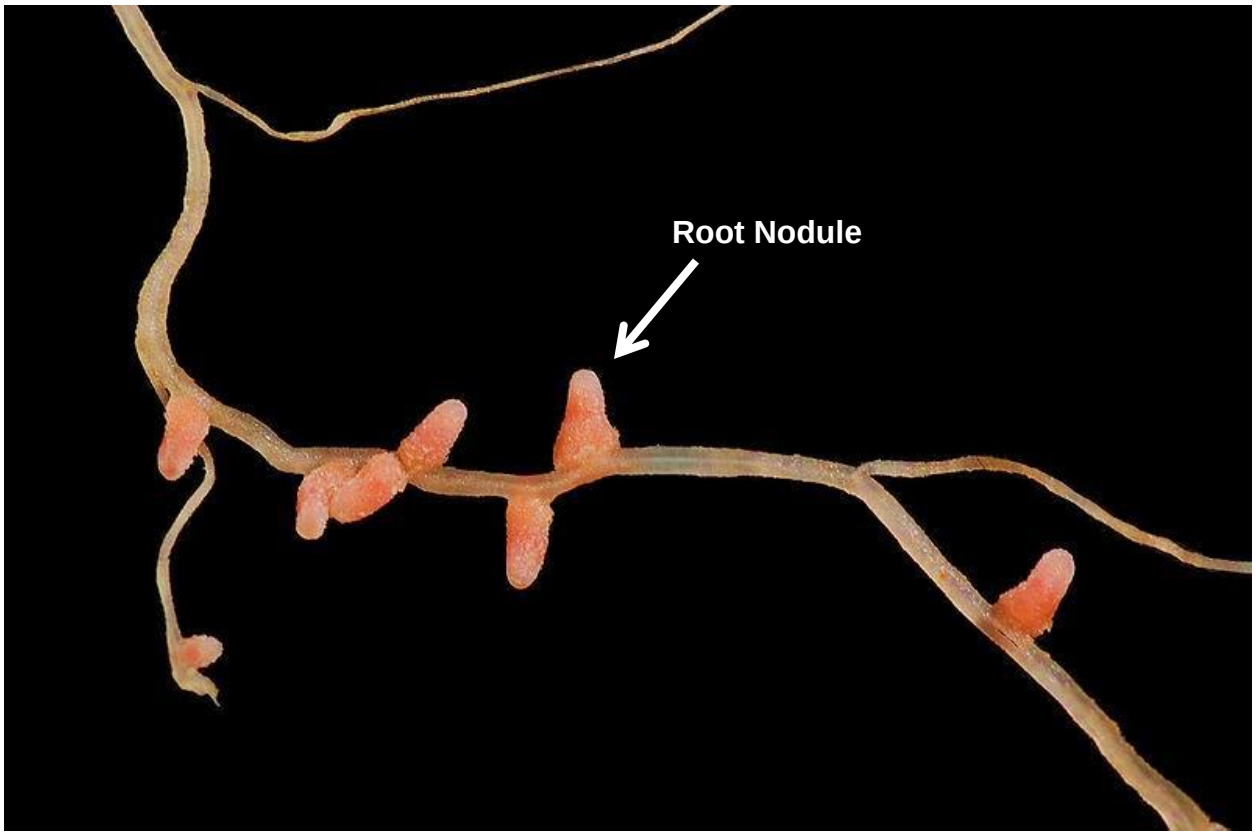

Figure 1. Photograph of legume root nodules. Photo courtesy of the Jean-Michel Ané research group in the department of agronomy at the University of Wisconsin- Madison

For my research, the normal plants are capable of fixing nitrogen while the mutant plants have a genetic mutation that makes them unable to fix nitrogen. My goal was to detect and identify the metabolites produced and exchanged between the plant and the bacteria when biological nitrogen fixation happens. To do this I compared the metabolites in the root nodules of normal plants to the metabolites in the mutant plants to figure out what the mutant plants were missing that made them unable to fix nitrogen. The goal of my research is to help biologists understand the mechanisms behind biological nitrogen fixation so scientists can make this process more efficient for the agriculture industry. The end goal is to put more nitrogen back into the soil so other plants can use this natural nitrogen instead of nitrogen fertilizers. By

increasing the supply of natural nitrogen in the soil, scientists hope crop yields will increase and the need for costly and potentially harmful nitrogen fertilizers will decrease.

What is mass spectrometry and how does it work?

Mass spectrometry is one of the most popular techniques used for analyzing metabolites because it offers speed, sensitivity to detect tiny amounts of molecules, and the ability to detect hundreds of metabolites at once. There are three basic parts of a mass spectrometer. The first part is an ionization source, which is very important because a mass spectrometer can only detect ions, which are molecules that have a positive or a negative charge. To be more precise, a mass spectrometer measures a molecules mass-to-charge ratio (represented as *m/z*). The molecules must have a positive/ negative charge in order for the mass spectrometer to measure them because mass spectrometers use electric and/or magnetic fields to move ions through the various parts of the mass spectrometer. MALDI, which stands for Matrix-Assisted Laser Desorption/ Ionization, is the main type of ionization source on the mass spectrometers I use in my research. Although the name seems long and daunting, the acronym tells you exactly what is going on in this phenomenon. **Figure 2** illustrates this process. Matrix-Assisted: First, I apply a matrix over my sample. A matrix is just a type of small, organic acid that forms crystals and can absorb ultraviolet (UV) light. Laser: Next, we shoot our matrix-coated sample with a laser. Desorption/ Ionization: The matrix absorbs the UV light from the laser and heats up, causing the matrix to vaporize, releasing a cloud of matrix ions and metabolite ions from the sample.

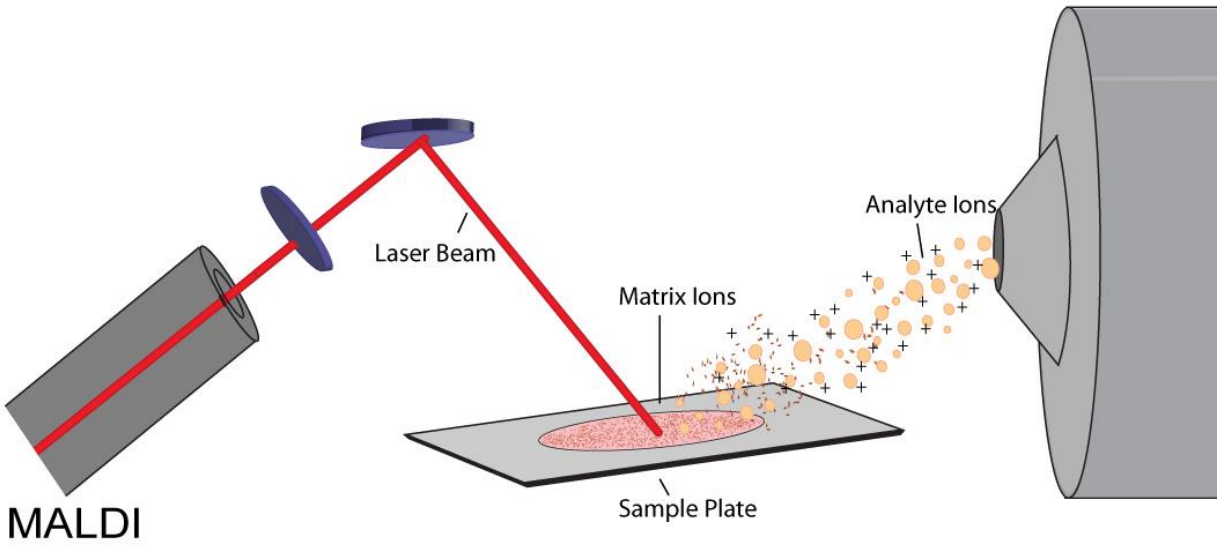

Figure 2. Cartoon showing the MALDI ionization method. A laser shoots the matrix-coated sample creating a cloud of charged matrix and analyte molecules. An applied electric/ magnetic field guides ions into the mass spectrometer. Analyte ions are the metabolite ions from the sample underneath the matrix.

Once the electric field guides ions into the mass spectrometer, the second part of the mass spectrometer, called the mass analyzer, separates the charged ions based on their mass-to-charge ratio (*m/z*). The mass of the molecule is roughly equal to the *m/z* number measured by the mass spectrometer divided by the charge of the molecule. My research focuses on small molecules and since the molecules are small in size, they can typically only fit one charge on them before other charges start to repel each other. For example, if we brought the positive ends of two magnets close to each other, they would repel each other in the same way two positive charges would repel each other if they were trying to fit too close to each other on the surface of a small molecule. Since the charge on metabolites is almost always +1, the mass-to-charge ratio essentially tells us the mass of the molecule that was detected by the mass spectrometer; for example, if the molecule had a +2 charge, the *m/z* number shown by the mass spectrometer would be equal to the mass of the compound divided by 2. Back to the mass analyzer: to separate the ions, the instrument applies an electric field that makes the charged ions accelerate

toward the end of the instrument. As they accelerate, they separate due to the differences in their masses. If you pushed a skateboard and a truck with the same amount of force, you can imagine that there would be a difference in how long it takes each to reach the finish line.

The last component of the mass spectrometer is the detector, which sits at the "finish line" and detects the masses of the ions as they reach it. A computer converts the signal from the mass spectrometer, typically an electric current, into a mass spectrum that scientists can interpret. **Figure 3** shows a mass spectrum of a plant sample. The y-axis shows the abundance of each ion and the x-axis is the mass-to-charge ratio of each ion. Each peak on the mass spectrum represents a unique molecule detected by the mass spectrometer.

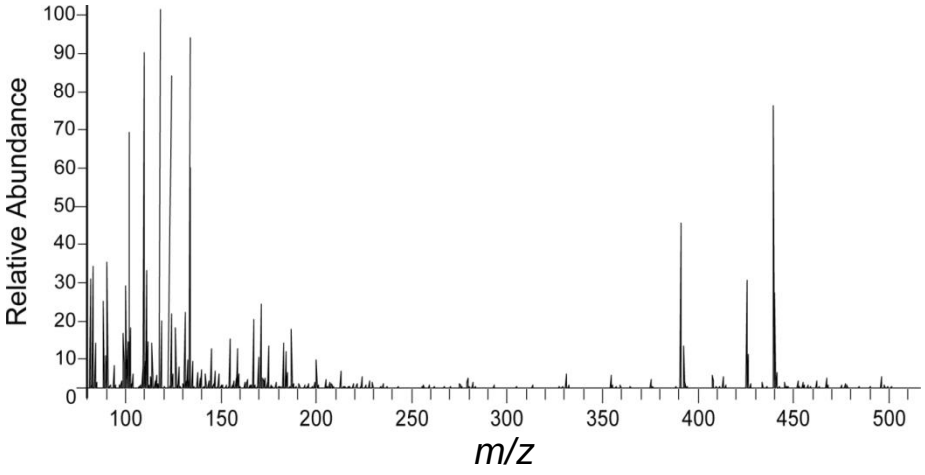

Figure 3. A mass spectrum of a matrix-coated plant sample. Each peak represents a molecule (either matrix or plant analytes). *m/z* stands for mass-to-charge ratio. The relative abundance means the height (or intensity) of the peaks relative to each other.

What is mass spectrometric imaging (MSI)?

So we have learned about the different parts of the mass spectrometer and the type of information we can learn by using a mass spectrometer. I mentioned before that my research involves a special type of mass spectrometry, called mass spectrometry imaging (MSI). This

technique not only gives me an array of mass spectra, but also gives me a picture that shows where each molecule is located within the plant. Let's go into a little more detail about MSI.

For MSI experiments, I slice my plants into very thin sections (about 16 micrometers thick) and lay them on a glass microscope slide. I coat the plant sections with matrix, and shoot it with the laser just as I did in the regular MALDI experiment discussed above. Instead of shooting my plant with the laser one time, I use software to draw a grid over my plant section and shoot the laser at every point on the grid. Instead of collecting a single mass spectrum, as we see in Figure 3, we collect a mass spectrum at every grid point. The computer software can then put the mass spectra together and show us an image similar to a heat map for each *m/z* measured by the mass spectrometer. In these heat map images, the part of the plant with the highest concentration of the particular *m/z* is shown in red and the area of the plant with the lowest concentration is shown in blue, with a range of colors in between. **Figure 4** outlines the MSI process and shows an example of an MS image.

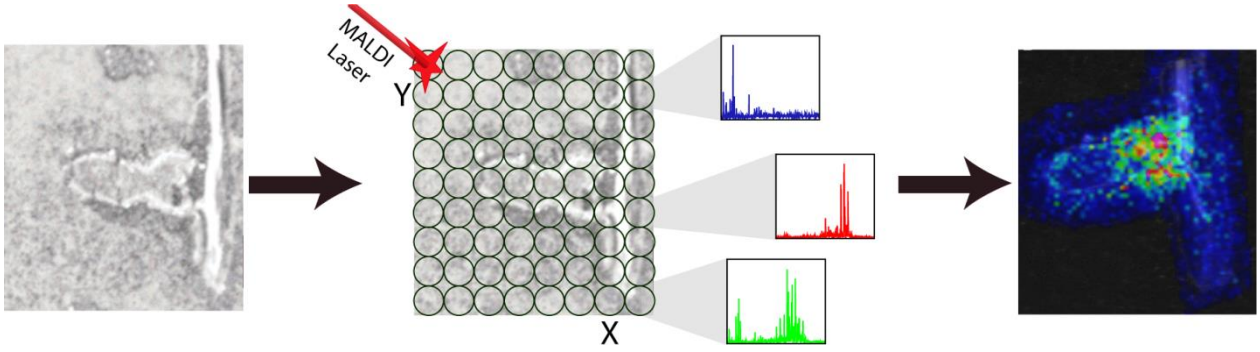

Figure 4. Outline of the MSI process. I cut the plant into a thin slice, lay it on a glass slide, and coat the slide with matrix. We use software to lay a grid pattern over the plant tissue so the laser knows every point it needs to shoot. We collect a mass spectrum at every grid point. The software compiles all the mass spectra into a heat map image for each specific *m/z* detected.

Results of my research

For my research I used MSI to look at the differences in metabolites found in normal plants (capable of fixing nitrogen) and those in mutant plants (unable to fix nitrogen). I detected and identified over 30 metabolites produced by normal plants that were absent from the non-nitrogen-fixing mutants. **Figure 5a** shows the root nodules of the normal plants (bottom right corner) compared to the three types of mutant plant I used. **Figure 5b** shows a picture of what the plants look like after I take a thin slice of the plant root, lay it on a glass microscope slide, and coat the slide with matrix. **Figure 5c** shows sample images of several of the metabolites that

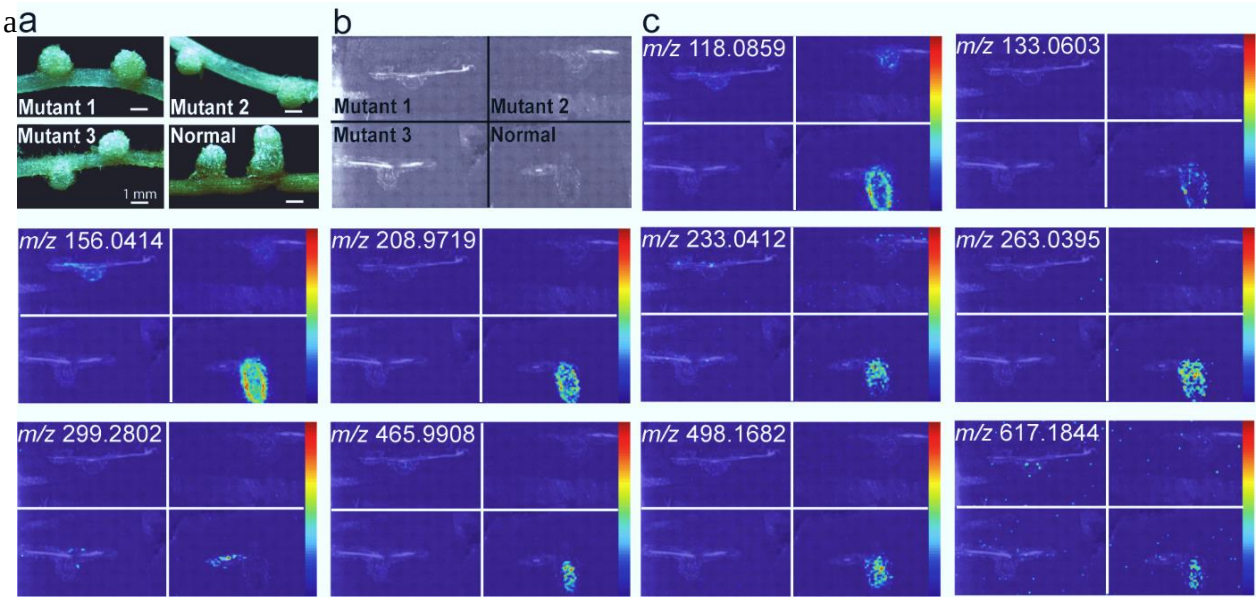

Figure 5. a) Photograph of the mutant and wild-type plant root nodules. Photo courtesy of the Jean-Michel Ané research group (Department of Agronomy, UW- Madison). b) Scanned in picture of what the plants look like after they have been sliced thin, laid on a glass microscope slide, and coated with matrix. c) Example images of ten of the metabolites that are clearly present in the wild-type plant samples but not in any of the three mutant plant samples.

Finally, I compiled a list of over 30 identified metabolites that I detected only in the normal plants, shown in **Table 1**.

Table 1. List of metabolites found only when nitrogen fixation occurs in legume root nodules

Metabolite	Measured *m/z*
Aminobutryic acid	104.0708
methyl-piperidin-iumone [M+]	114.0915
Proline	116.0706
Aminopentene-diol*	118.0863
Isoleucinol	118.1228
Asparagine*	133.0607
Glutamic Acid	148.0603
Asparagine [M+Na]*	155.0425
3-thiophen-1-yl propanoic acid	158.0397
ethyl-aminocyclopentane carboxylic acid	158.1173
Phenylalanine	166.0859
Asparagine [M+K]*	171.0165
Arginine	175.1187
Tyrosine	182.0810
methyl-alpha-galactopyranoside	195.0862
ethyl-aminocyclopentane carboxylic acid [M+K]	196.0731
Proclavaminic acid*	203.1024
methyl-alpha-galactopyranoside [M+Na]*	217.0678
Proclavaminic acid [M+Na]	225.0840
Proclavaminic acid [M+K]	241.0577
dihydroxybenzoic acid succinimido ester	252.0500
5-amino-2-(aminomethyl)-6-butoxyoxane-3,4-diol [M+Na]	257.1462
9H-fluoren-9-yl-di(propan-2-yl)phosphane	283.1618
N-(4-guanidinobutyl)-3-methyldecanamide	299.2802
SAM (S-adenosyl-L-methionine)	399.1441
2-hydroxy-5-[[2-phenyl-2-[4-(phenylcarbamoylamino)phenyl]sulfanylacetyl] amino]benzoic acid	514.1423
2-[hydroxy-[(2R)-3-hydroxy-2-[(9E,12E)-octadeca-9,12-dienoyl]oxypropoxy]phosphoryl]oxyethyl-trimethylazanium [M+]	520.3395
Oleoyl lysophosphatidylcholine	522.3552
18-[(4Z)-4-[(2-hydroxy-5-nitrophenyl)hydrazinylidene]-3-oxocyclohexa-1,5-dien-1-yl]octadecanoic acid [M+]	541.3125
3-[[[[(2R,3S,4R,5R)-5-(6-aminopurin-9-yl)-3,4-dihydroxyoxolan-2-yl]methoxy-hydroxy phosphoryl]oxy-hydroxy phosphoryl]oxy-hydroxyphosphoryl]oxypropanoic acid	580.0223
[(2R,3S,5R)-5-[4-amino-5-(4-aminobutyldisulfanyl)-2-oxopyrimidin-1-yl]-3-hydroxy oxolan-2-yl]methoxy-hydroxyphosphoryl] phosphono hydrogen phosphate [M+]	602.0052
(Z)-4-oxo-2-[(Z)-1-oxooctadec-9-enyl]-12-henicosenoic acid	603.5340
1,3-dilinolenin	613.4814
Heme	617.1844

The MS images give us a lot more information about the 30 molecules listed above that I identified only in the normal plants. The MS images show that some of these molecules are found on the inside of the nodule while others are primarily on the outside. There are even some that are only in the roots of the plant but not in the actual nodule. Biologists can use this additional information to determine how the plant might use these molecules. Biologists already figured out that some of the metabolites listed in the table above are used by the plant to transport nitrogen. What's more exciting is that biologists have no idea what some of the metabolites in the table are used for or that they had any part in the nitrogen fixation process. Now biologists can use this new information to figure out exactly how the plants use these chemicals for biological nitrogen fixation. Once they know this information, biologists can make this process more efficient, either by ensuring the plants themselves put more nitrogen back into the soil, or by genetically engineering other crops to fix their own nitrogen. This will hopefully increase crop yields and decrease the need for environmentally damaging artificial nitrogen fertilizers.

Appendix I

List of Publications and Presentations

Publications

1. **Gemperline, E.**; Horn, H.; Chevrette, M.; Mevers, E.; Clardy, J.; Li, L.; Currie, C. "Diversity of Chemical Response to Pathogen Exposure Reveals Insights into the Co-evolved Fungus-Growing Ants and *Pseudonocardia* Symbiotic System" *In Preparation*

2. **Gemperline, E.**; Horn, H.; Currie, C.; Li, L. "Novel MALDI-Mass Spectrometry Imaging Method for the Analysis of Bacteria on the Exoskeleton of Fungus-Growing Ants" *In Preparation*

3. **Gemperline, E.**; Keller, C.; Maeda, J.; Jayaraman, D.; Sussman, M.; Ané, J.; Li, L. "Examination of Endogenous Peptides in *Medicago truncatula* using Mass Spectrometry Imaging" *In Preparation*

4. **Gemperline, E.**; Keller, C.; Li, L. "Mass Spectrometry in Plant-omics" *Analytical Chemistry*. 88(7): 3422-3434 (2016) doi: 10.1021/acs.analichem.5b02938, *featured as cover article and Analytical Chemistry Podcast Interview*

5. **Gemperline, E.**; Li, L. "MALDI-MS Assisted Molecular Imaging of Metabolites in Legume Plants" *Methods in Molecular Biology* 1203: 29-40. (2015) doi:10.1007/978-1-4939-1357-2_4

6. **Gemperline, E.**; Jayaraman, D.; Maeda, J.; Ané, J.; Li, L. "Multifaceted Investigation of Metabolites During Nitrogen Fixation in the *Medicago truncatula- Sinorhizobium meliloti* Symbiosis Via High Resolution MALDI-MS Imaging and ESI-MS" *Journal of the American Society for Mass Spectrometry.* 26(1): 149-158 (2015) doi: 10.1007/s13361-014-1010-0

7. **Gemperline, E.**; Rawson, S.; Li, L. "Optimization and Comparison of Multiple MALDI Matrix Application Methods for Small Molecule Mass Spectrometric Imaging" *Analytical Chemistry*. 86(20): 10030-10035. (2014) doi:10.1021/ac5028534

8. **Gemperline, E.**; Laha, K.; Scarlett, C.; Pearce, R.; Li, L. "Measurement of NMDA Receptor Antagonist, CPP, in Mouse Plasma and Brain Tissue Following Systemic Administration Using Ion-Pair LC-MS/MS" *Analytical Methods*. 6(16): 6389-6396. (2014) doi: 10.1039/C4AY01168F

9. **Gemperline, E.**; Li, L. "MALDI-Mass Spectrometric Imaging of Endogenous Metabolites in Biological Systems" *eLS.* 2014(August): 1-9 (2014) doi: 10.1002/9780470015902.a0023207

10. **Gemperline, E.**; Li, L. "Investigation of Metabolites in *Medicago truncatula* Root Nodules with MALDI- Mass Spectrometric Imaging" *Journal of Visualized Experiments.* (85): e51434 (2014) doi:10.3791/51434

11. **Gemperline, E.**; Chen, B.; Li, L. "Challenges and Recent Advances in Mass Spectrometric Imaging of Neurotransmitters" *Bioanalysis*. 6(4): 525-540. (2014) doi: 10.4155/bio.13.341

12. **Gemperline, E.**; Ye, H.; Li, L. "A Vision for Better Health: Mass Spectrometry Imaging for Clinical Diagnostics", *Clinica Chimica Acta* , 420: 11-22 (2013) doi:10.1016/j.cca.2012.10.018

13. **Gemperline, E.**; Li, L.; Creissen, A. HTX-Imaging Technologies. Technical Note #36, "Homogeneous Spray Application of DHB on Dried Agar for MALDI Imaging of Microbial Cultures". (2015)

14. **Gemperline, E.**; Li, L.; Creissen, A. HTX-Imaging Technologies. Technical Note #34, "Dry Matrix Spray Application for MALDI Imaging of Metabolites in Root Nodule Tissue in *Medicago truncatula* Yielding Sublimation-like Results". (2014)

15. **Gemperline, E.**; Li, L.; Creissen, A. HTX-Imaging Technologies. Technical Note #28, "Optimization of DHB Matrix Spray for MALDI Imaging of Metabolites in Root Nodule Tissue of the *Medicago truncatula – Sinorhizobium meliloti* Symbiosis". (2013)

16. Lietz, C.; **Gemperline, E.**; Li, L. "Qualitative and quantitative mass spectrometry imaging of drugs, metabolites, and endogenous molecules" *Advanced Drug Delivery Reviews.* 65(8): 1074-1085. (2013) doi:10.1016/j.addr.2013.04.009

17. Ye, H.; **Gemperline, E.**; Venkateshwaran, M.; Chen, R.; Delaux, P.; Howes-Podoll, M.; Ané, J.; Li, L. "MALDI mass spectrometry-assisted molecular imaging of metabolites during nitrogen fixation in the *Medicago truncatula- Sinorhizobium meliloti* symbiosis" *The Plant Journal*. 75(1): 130-145. (2013) doi:10.1111/tpj.12191

18. Sturm, R. M.; Greer, T.; Woodards, N.; **Gemperline, E.**; Li, L. "Mass spectrometric evaluation of neuropeptidomic profiles upon heat stabilization treatment of neuroendocrine tissues in crustaceans", *Journal of Proteome Research.* 12(2): 743-752. (2013) doi:10.1021/pr300805f

Presentations

1. **Erin Gemperline**, Lingjun Li; "MALDI Mass Spectrometry Imaging in Plant-omics" 2015 Plant Proteomics Workshop, University of Wisconsin-Madison, Madison, WI; July 23rd, 2015 (oral)

2. **Erin Gemperline**, Heidi Horn, Cameron Currie, Lingjun Li; "Surface MALDI-MS Imaging for the Discovery of Natural Products from Leaf Cutter Ants" The 62nd American Society for Mass Spectrometry Annual Conference, St. Louis, MO; June 1st, 2015 (poster)

3. **Erin Gemperline**, Heidi Horn, Cameron Currie, Lingjun Li; "Surface MALDI-MS Imaging for the Discovery of Natural Products from Leaf Cutter Ants" Department of Chemistry Graduate Student/ Faculty Liaison Committee Poster Session, Madison, WI; May 11th, 2015 (poster)

4. **Erin Gemperline** and Lingjun Li; "Mass Spectrometry Imaging Applied to Biological Questions" 2015 UW-Madison Divisional Awards Ceremony and Undergraduate Research Poster Session, Madison, WI; May 1st, 2015 (poster)

5. **Erin Gemperline**, Junko Maeda, Muthusubramanian Venkateshwaran, Jean-Michel Ané, Lingjun Li; "Multifaceted Investigation of Metabolites During Nitrogen Fixation in the *Medicago truncatula–Sinorhizobium meliloti* Symbiosis via MALDI-MS Imaging and High-Resolution ESI-MS" P20 LUTS Project Symposium, Madison, WI; June 30th-July 1st, 2014 (poster)

6. **Erin Gemperline**, Junko Maeda, Muthusubramanian Venkateshwaran, Jean-Michel Ané, Lingjun Li; "Multifaceted Investigation of Metabolites During Nitrogen Fixation in the *Medicago truncatula–Sinorhizobium meliloti* Symbiosis via MALDI-MS Imaging and High-Resolution ESI-MS" The 62nd American Society for Mass Spectrometry Annual Conference, Baltimore, MD; June 16th, 2014 (poster)

7. **Erin Gemperline**, Vivian Hui Ye, Muthusubramanian Venkateshwaran, Jean-Michel Ané, Lingjun Li; "Matrix Application Method Optimization for MALDI-MS Imaging (MSI) of Metabolites During Nitrogen Fixation in the *Medicago truncatula–Sinorhizobium meliloti* Symbiosis" The 61st American Society for Mass Spectrometry Annual Conference, Minneapolis, MN; June 12th, 2013 (poster)

8. **Erin Gemperline,** Vivian Hui Ye, Maegen Howes-Podoll, Muthu Venkateshwaran, Jean-Michel Ané, Lingjun Li; "MALDI-MSI of Metabolites During Nitrogen Fixation in the *Medicago truncatula-Sinorhizobium meliloti* Symbiosis" Midwestern Universities Analytical Chemistry Conference, Madison, WI; September 28th, 2012 (poster)

Appendix II

MALDI-MS/MSI Analysis of Toxicity in Zebrafish After Exposure to Semi-fluorinated Polymer Micelles

Adapted from Appendix 1 of Dr. Sarah Decato's thesis from Dr. Sandro Mecozzi's research group. Intro, formatting, polymer solution, and zebrafish treatment was performed by SD. MSI sample prep, analysis, figure generation was performed by EG.

Introduction

The Mecozzi lab has begun toxicity and bioaccumulation studies for the novel semi-fluorinated amphiphiles described previously using a zebrafish model. The zebrafish model (ZF), *Danio rerio*, was chosen as it is an established model species used in routine chemical toxicity analysis and has a fully sequenced and well-annotated genome.[1] Preliminary results demonstrated no evidence of acute toxicity from exposure to high concentration of semi-fluorinated polymer solutions (1 mM to 10 mM). However, it was desirable to have direct evidence that the lack of toxic symptoms was indeed due to the non-toxic nature of the compounds rather than their inability to be readily internalized by the zebrafish embryo and/or zebrafish larvae. Therefore matrix-assisted laser desorption/ionization (MALDI)- mass spectrometry imaging (MSI) was attempted to confirm internalization of the semi-fluorinated polymers. The advantage of MSI is that it provides the opportunity to examine the spatial context of both small molecules and larger macromolecules in the whole organism without modification of the polymer structure (e.g. fluorescent labeling), which could affect polymer toxicity or accumulation.

MSI sample preparation and handling has been identified as the first most important and challenging aspect of the whole organism analysis.[2] The numerous steps and method options are critical to the experiment success. For example the embedding medium, matrix selection and application all greatly affect the quality of the data and ability to detect the compounds of interest. Unfortunately, the MSI literature contains little information for processing small fish or fish larvae, despite their increasing utility over more expensive, higher vertebrate models. Procedures for cryo-sectioning are extremely important for zebrafish not only for their small size, but also as they may have an air-filled swim bladder that once frozen can be crushed and

dislocate neighboring organ structures.[3,4] It was for these reasons that the following preliminary study was performed to assess whether MSI would be an appropriate technique to confirm the internalization of semi-fluorinated compounds.

Experimental

Micelle Solution Preparation

$mPEG_{1k}$-F13 polymer micelle solutions were prepared at a concentration of 0.1 mg/mL by direct dilution in 30/70 water/ACN. Subsequent concentrations were prepared as serial dilutions from this stock concentration. Aliquots (0.5 μL) of each polymer solution were then individually spotted onto the MALDI plate and mixed with (0.5 μL) matrix, CHCA (10 mg/mL in 30/70 water/ACN 0.1% FA). DHB (150 mg/mL in 50/50 water/ACN 0.1 % FA) was also used but found to be less effective.

Zebrafish Washing

Fish were exposed to 10 mM micelle solutions of $mPEG_{1k}$-F13 for 1 week and then sacrificed with Tricane mesylate (Sigma Aldrich). The “dirty fish” were extracted directly from the well with a pipette and placed into an Eppendorf tube. The “clean fish” were extracted out of the well with a pipette and put into a petri-dish with fresh egg water for 5 seconds and quickly removed and this was repeated two more times with fresh petri-dishes with fresh egg water. The fish was then put onto a Kim wipe to absorb the surface water and then put into an Eppendorf tube. The excess liquid was removed from the tube.

To mount the whole fish onto the glass microscope slide, an ImmEdge hydrophobic barrier pen (Vector Labs) was used to outline and separate the fish. An aliquot (1 μL) of the water in the fish Eppendorf tubes was also spotted onto the slide. The CHCA matrix was then applied to the glass slide with a TM-Sprayer (HTX Technologies, LLC, Carrboro, NC, USA).

Zebrafish Cryo-sectioning

Fish were sacrificed and washed according to the previously described methods. The individual fish were embedded in gelatin (100 mg/mL in double-distilled water) and gently frozen on dry ice (cryo-sectioning was also attempted in ice; however, gelatin provided much better sections). After equilibrating in the chamber for several minutes, each frozen fish was placed on its side and was then sliced into approximately 16 coronal cross-sections of 12-μm or 20-μm thickness using a cryostat at –20°C. (Under the microscope the thicker sections appear much more intact). The sections were then mounted onto a standard glass microscope slide using either thaw or cold mounting methods (cold mounting appeared to give the best results). Matrix (10 mg/mL CHCA in 30/70 water/ACN) was applied using a TM-Sprayer (HTX Technologies, LLC, Carrboro, NC, USA). CHCA was purchased from Sigma Aldrich (St. Louis, MO, USA).

MALDI-Orbitrap MS and MSI

A MALDI-Orbitrap mass spectrometer (Thermo Scientific, Waltham, MA, USA) that was equipped with an N2 laser (spot diameter of 75 μm) was used in positive ion mode for spot analysis and imaging. For micelle solutions, a mass range of *m/z* 1550-2000, 30,000 resolution, and laser energy of 8.4 μJ was used. For the washed, whole fish, a mass range of *m/z* 1550-2000, 10 micro-step, 30,000 resolution, and laser energy of 8.8 μJ was used. For cryo-slices, multiple

layers of the fish were imaged using a mass range of *m/z* 1550–2000, a mass resolution of 30,000, and a laser energy of 8.8 μJ. A mass error of ≤ 5 ppm was achieved. The tissue region to be imaged and the raster step size were controlled using the LTQ Tune software (Thermo Scientific, Waltham, MA, USA). The instrument methods were created using Xcalibur (Thermo Scientific, Waltham, MA, USA). To generate images, the spectra were collected at 75 μm intervals in both the x and y dimensions across the surface of the sample. The manual interpretation of the averaged mass spectrum was performed using ImageQuest (Thermo Scientific, Waltham, MA, USA).

Results and Discussion

In order to first confirm that the semi-fluorinated polymer could be visualized on the MALDI-Orbitrap instrument (and if so, to identify the limit of detection), the micelle solutions of $mPEG_{1k}$-F13 polymer were analyzed at varying concentrations on the MALDI-Orbitrap (see following spectra). Both DHB and CHCA matrix were used and CHCA was found to be far superior for this application. The mass detection range began at *m/z* 1550 in order to exclude the highly intense CHCA peak at *m/z* 1517. The semi-fluorinated polymers were readily visualized over the entire concentration range, from 0.1 mg/mL (0.05 mM) to 0.5 ag/mL. Although this does not indicate the detection limit for the zebrafish analysis (as there will be multiple endogenous salts, polymers, etc. to suppress the semi-fluorinated polymer signal), the initial solution spot MS parameters allowed us to proceed to the zebrafish analysis.

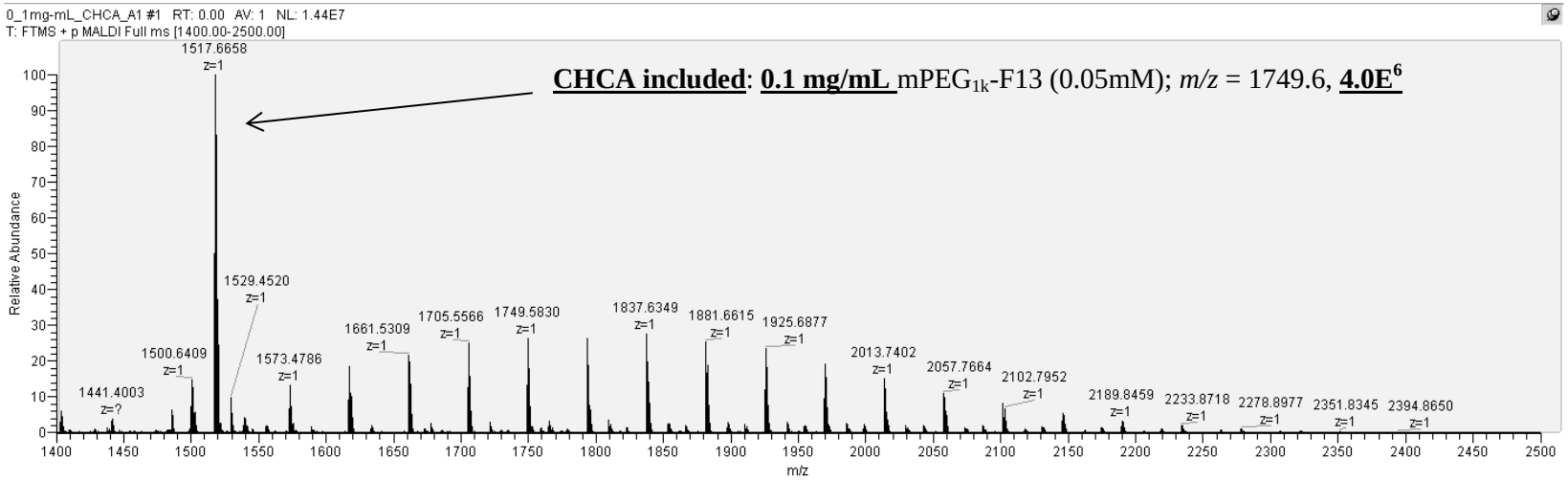
0_1mg-mL_CHCA_A1 #1 RT: 0.00 AV: 1 NL: 1.44E7
T: FTMS + p MALDI Full ms [1400.00-2500.00]
CHCA included: 0.1 mg/mL mPEG1k-F13 (0.05mM); m/z = 1749.6, 4.0E6
Relative Abundance
m/z
1517.6658 z=1
1529.4520 z=1
1500.6409 z=1
1573.4786 z=1
1661.5309 z=1
1705.5566 z=1
1749.5830 z=1
1837.6349 z=1
1881.6615 z=1
1925.6877 z=1
2013.7402 z=1
2057.7664 z=1
2102.7952 z=1
2189.8459 z=1
2233.8718 z=1
2278.8977 z=1
2351.8345 z=1
2394.8650 z=1
1441.4003 z=?

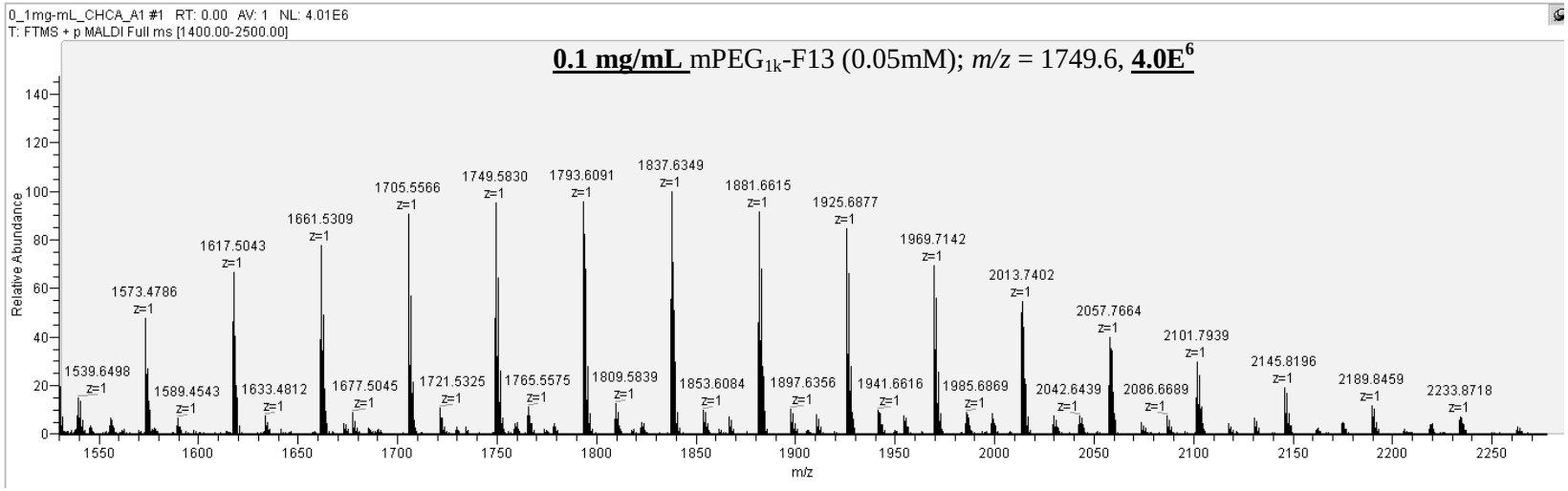
0_1mg-mL_CHCA_A1 #1 RT: 0.00 AV: 1 NL: 4.01E6
T: FTMS + p MALDI Full ms [1400.00-2500.00]
0.1 mg/mL mPEG1k-F13 (0.05mM); m/z = 1749.6, 4.0E6
Relative Abundance
m/z
1837.6349 z=1
1793.6091 z=1
1749.5830 z=1
1705.5566 z=1
1881.6615 z=1
1925.6877 z=1
1661.5309 z=1
1969.7142 z=1
1617.5043 z=1
2013.7402 z=1
1573.4786 z=1
2057.7664 z=1
2101.7939 z=1
2145.8196 z=1
2189.8459 z=1
2233.8718 z=1
1539.6498 z=1
1589.4543 z=1
1633.4812 z=1
1677.5045 z=1
1721.5325 z=1
1765.5575 z=1
1809.5839 z=1
1853.6084 z=1
1897.6356 z=1
1941.6616 z=1
1985.6869 z=1
2042.6439 z=1
2086.6689 z=1

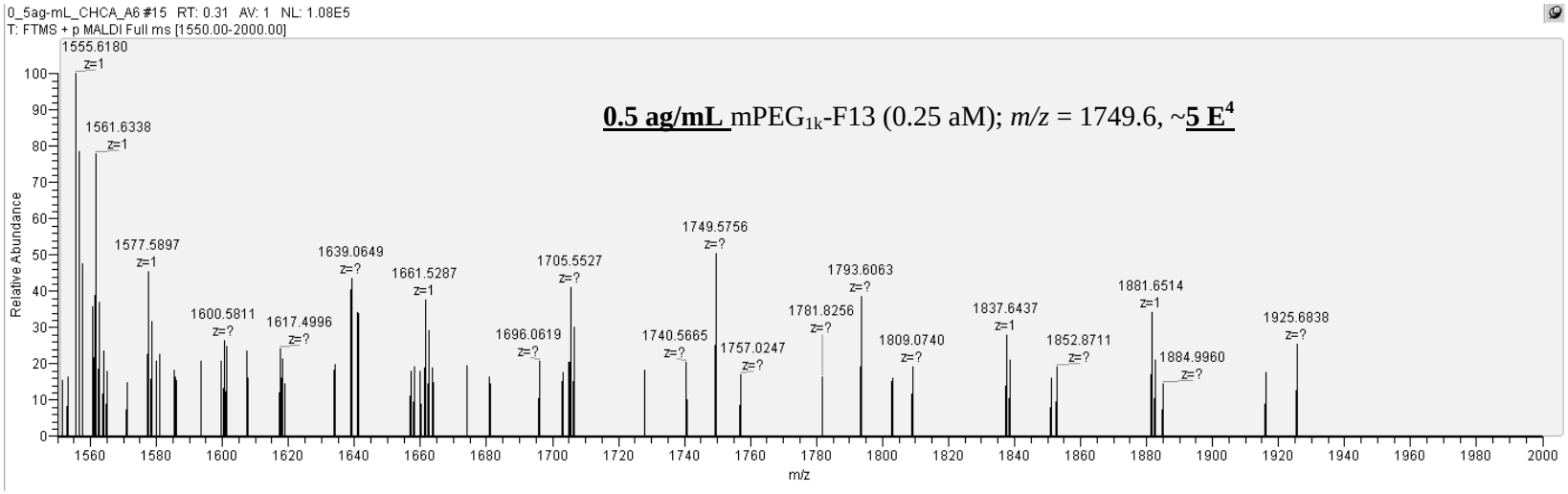
0_5ag-mL_CHCA_A6 #15 RT: 0.31 AV: 1 NL: 1.08E5
T: FTMS + p MALDI Full ms [1550.00-2000.00]
0.5 ag/mL mPEG1k-F13 (0.25 aM); m/z = 1749.6, ~5 E4
Relative Abundance
m/z
1555.6180 z=1
1561.6338 z=1
1577.5897 z=1
1600.5811 z=?
1617.4996 z=?
1639.0649 z=?
1661.5287 z=1
1696.0619 z=?
1705.5527 z=?
1740.5665 z=?
1749.5756 z=?
1757.0247 z=?
1781.8256 z=?
1793.6063 z=?
1809.0740 z=?
1837.6437 z=1
1852.8711 z=?
1881.6514 z=1
1884.9960 z=?
1925.6838 z=?

To confirm that the internalization of the polymer inside the zebrafish cryo-section, we had to ensure that residual polymer on the surface of the fish was not translocated into the slice during sectioning. Therefore a washing procedure was developed and evaluated by MSI by comparing the pre- ("dirty") and post-washing ("clean") whole fish. Three areas of the fish were analyzed including the tail, middle body, and head (see following spectra). The washing procedure was successful in removing the polymer from all three areas of the fish surface as evident by dramatic loss of polymer signal from the dirty to the clean fish. The washing procedure was performed quickly without long exposure to fresh water in order to minimize excretion of the semi-fluorinated polymer from inside the fish.

"**Clean**" $mPEG_{1k}$-F13 fish water (10 mM); *m/z* = 1749.6, **4.0E^4**

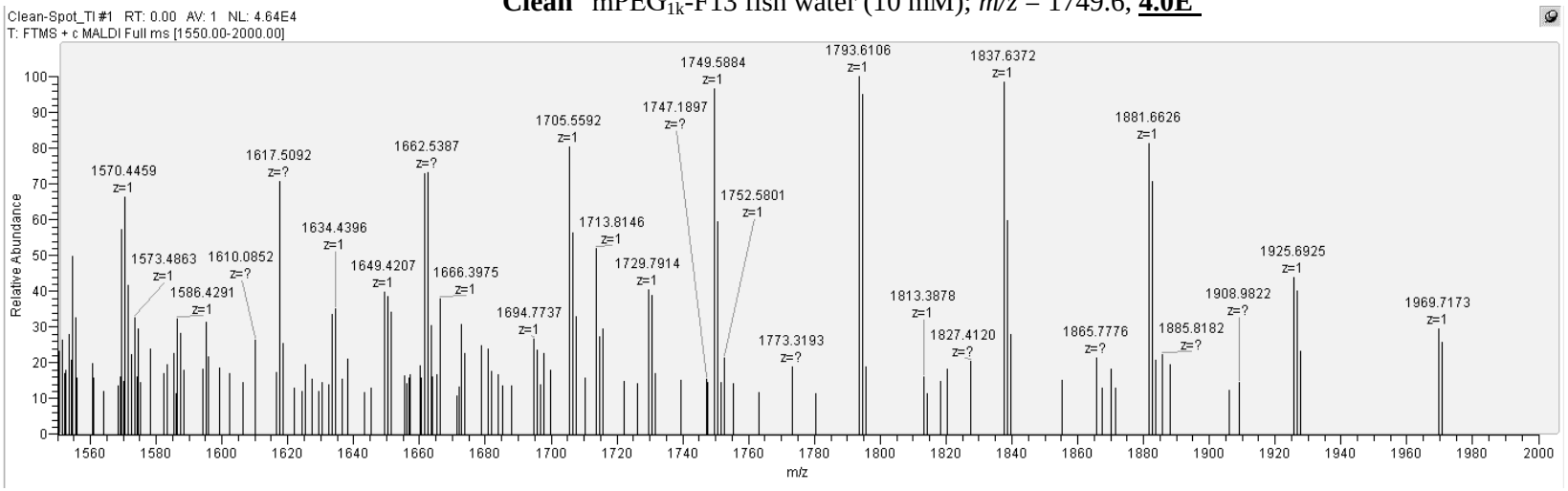

"**Dirty**" $mPEG_{1k}$-F13 fish water (10 mM); *m/z* = 1749.6, **1.0E^7**

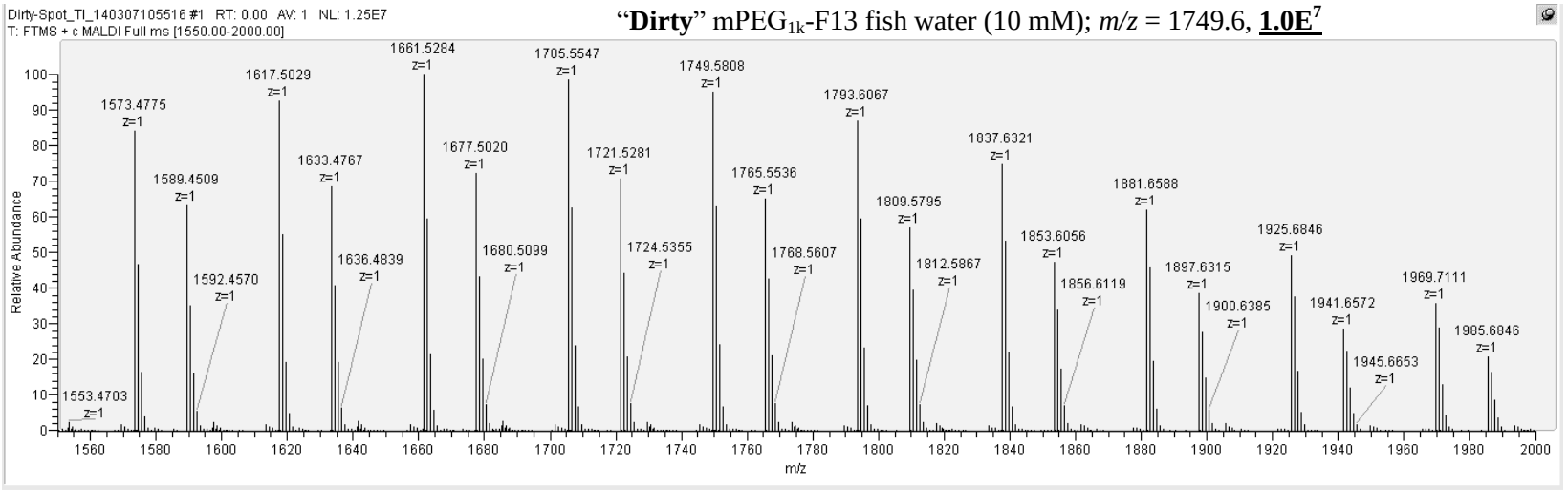

"**Clean**" mPEG$_{1k}$-F13 fish tail (10 mM)

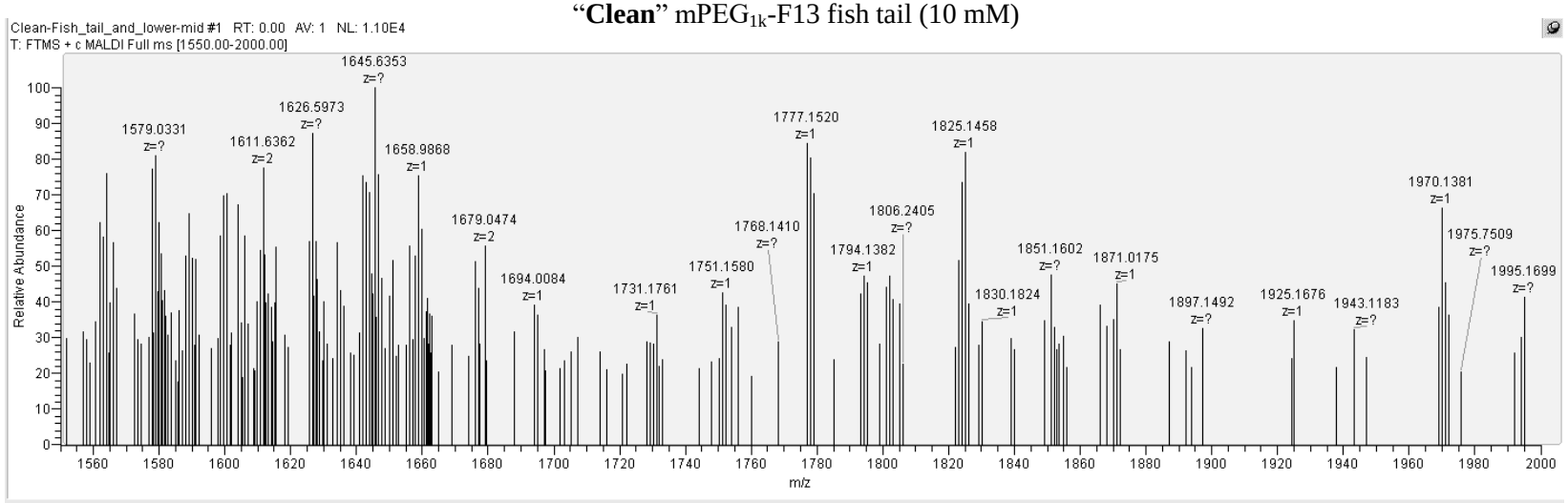

"**Dirty**" mPEG$_{1k}$-F13 fish tail (10 mM); *m/z* = 1749.6, **4.0E^4**

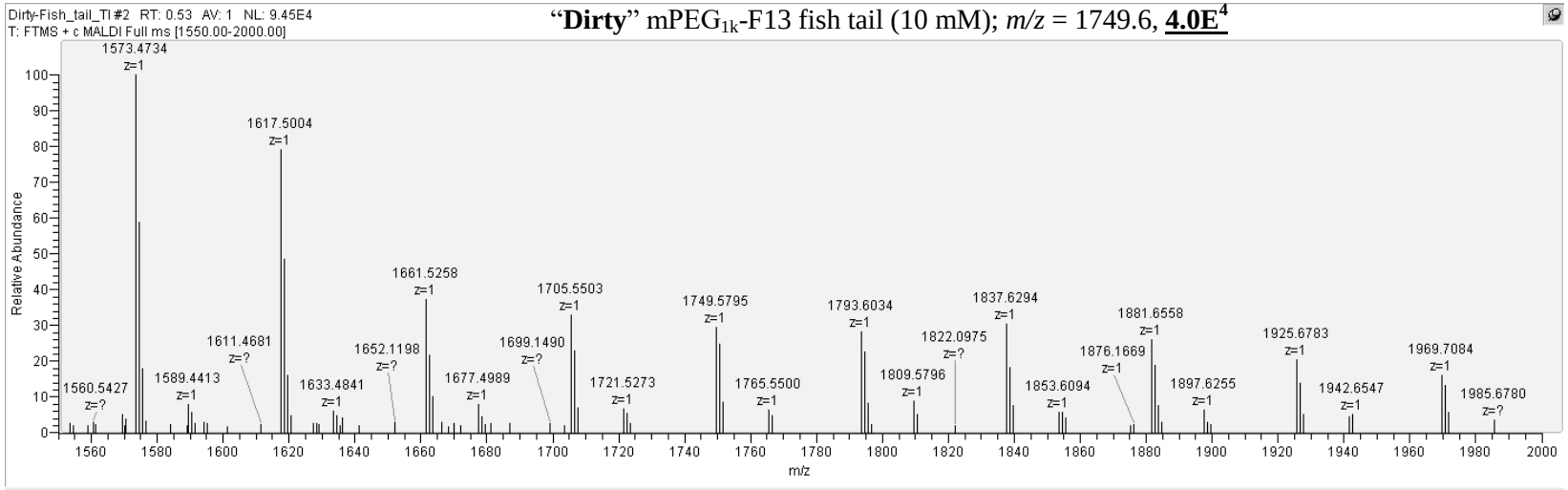

"**Clean**" $mPEG_{1k}$-F13 fish middle body (10 mM)

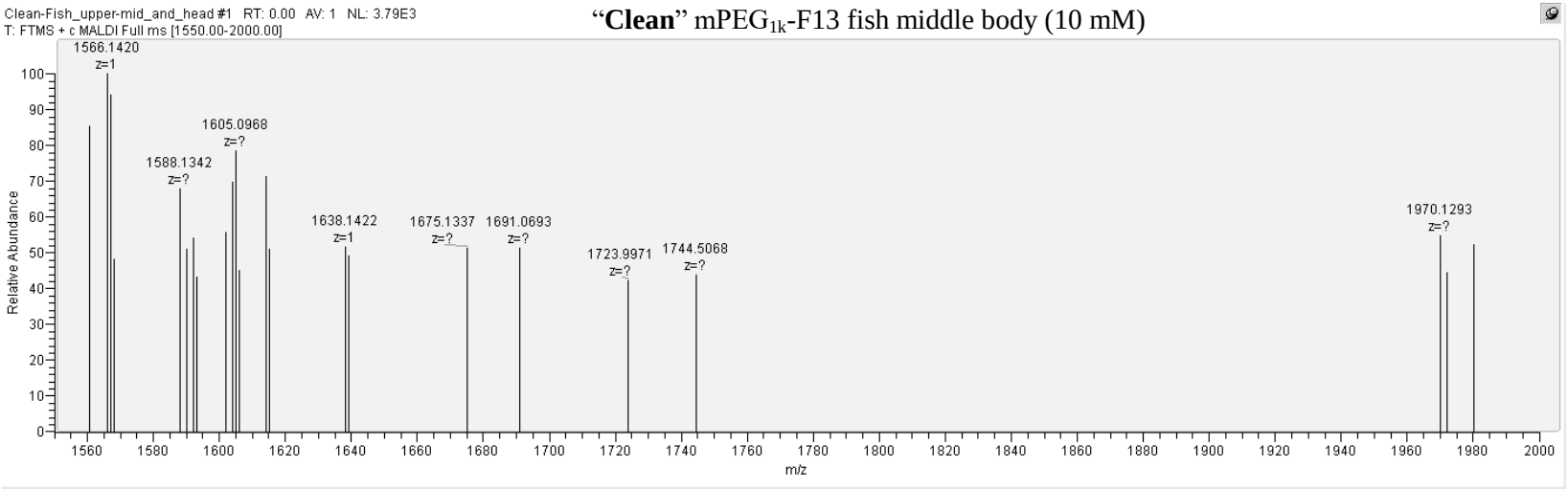

"**Dirty**" $mPEG_{1k}$-F13 fish middle body (10 mM); *m/z* = 1749.6, **<u>2.0E^4</u>**

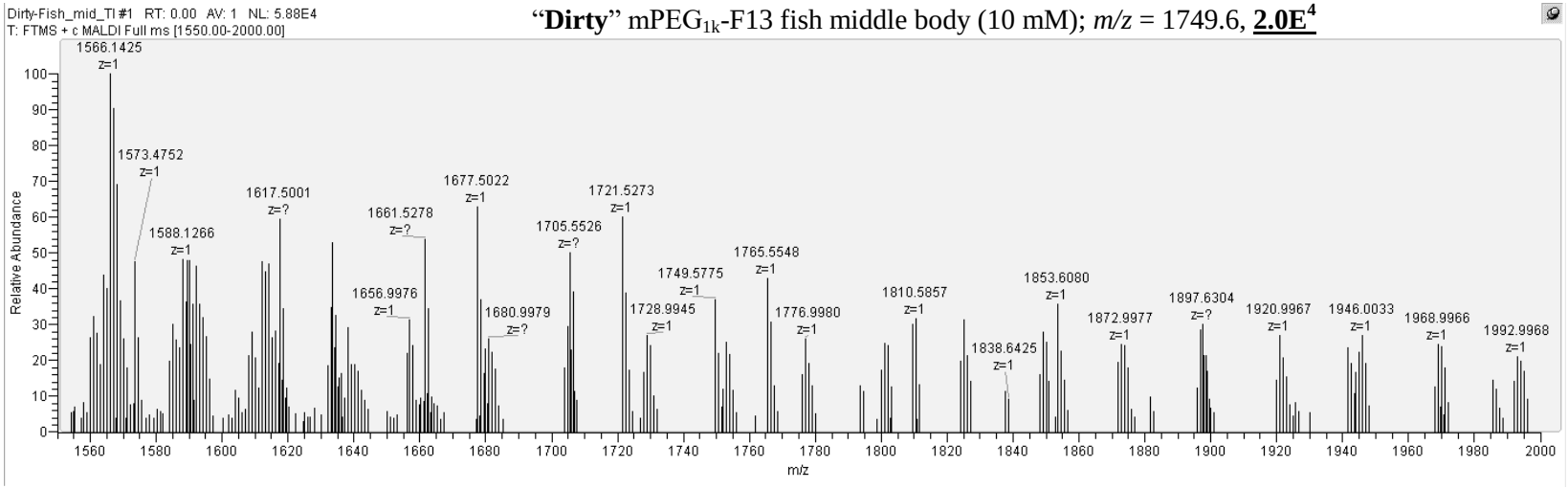

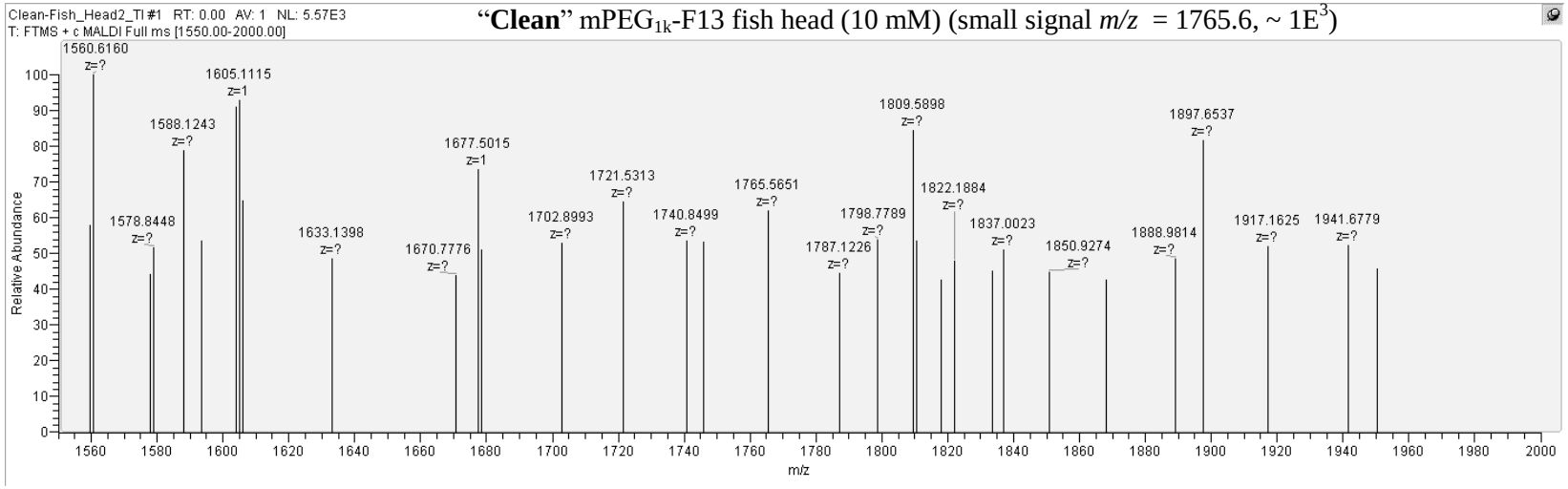
Clean-Fish_Head2_TI #1 RT: 0.00 AV: 1 NL: 5.57E3
T: FTMS + c MALDI Full ms [1550.00-2000.00]
"Clean" mPEG1k-F13 fish head (10 mM) (small signal m/z = 1765.6, ~ 1E3)
Relative Abundance
m/z
1560.6160 z=?
1605.1115 z=1
1588.1243 z=?
1677.5015 z=1
1809.5898 z=?
1897.6537 z=?
1721.5313 z=?
1765.5651 z=?
1822.1884 z=?
1578.8448 z=?
1702.8993 z=?
1740.8499 z=?
1798.7789 z=?
1837.0023 z=?
1917.1625 z=?
1941.6779 z=?
1633.1398 z=?
1670.7776 z=?
1787.1226 z=?
1850.9274 z=?
1888.9814 z=?

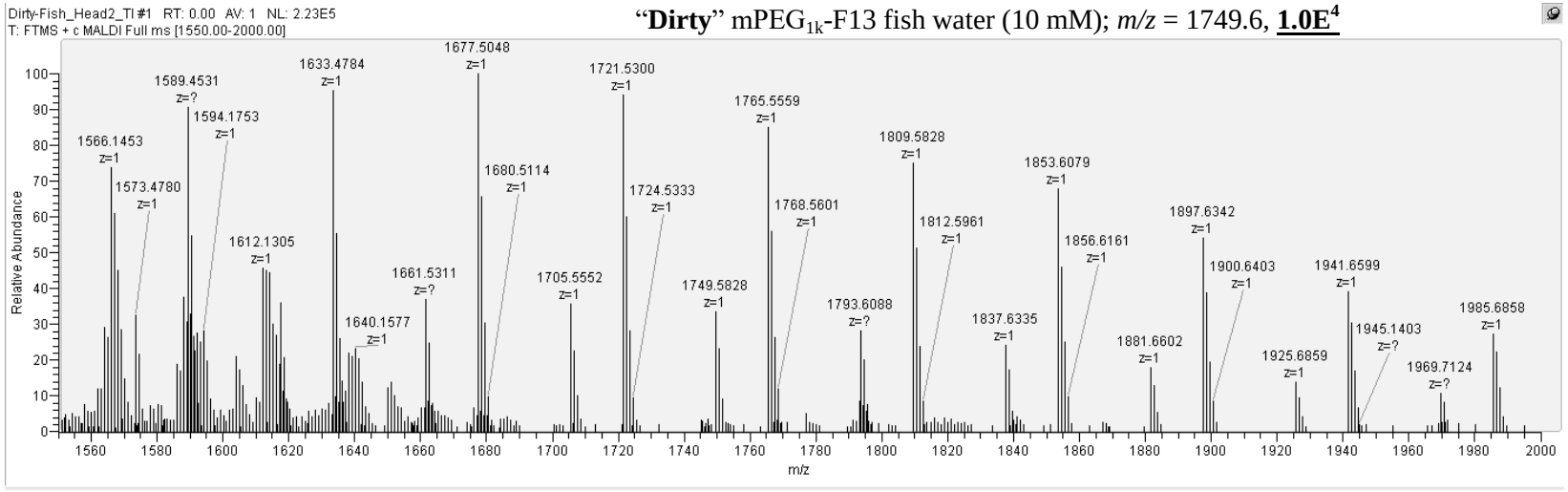
Dirty-Fish_Head2_TI #1 RT: 0.00 AV: 1 NL: 2.23E5
T: FTMS + c MALDI Full ms [1550.00-2000.00]
"Dirty" mPEG1k-F13 fish water (10 mM); m/z = 1749.6, 1.0E4
Relative Abundance
m/z
1677.5048 z=1
1633.4784 z=1
1589.4531 z=?
1721.5300 z=1
1765.5559 z=1
1809.5828 z=1
1853.6079 z=1
1594.1753 z=1
1566.1453 z=1
1680.5114 z=1
1724.5333 z=1
1768.5601 z=1
1812.5961 z=1
1897.6342 z=1
1573.4780 z=1
1612.1305 z=1
1856.6161 z=1
1900.6403 z=1
1941.6599 z=1
1661.5311 z=?
1705.5552 z=1
1749.5828 z=1
1793.6088 z=?
1837.6335 z=1
1985.6858 z=1
1640.1577 z=1
1881.6602 z=1
1945.1403 z=?
1925.6859 z=1
1969.7124 z=?

After a successful washing procedure was established the fish were then cryo-sectioned and analyzed via MSI. This preliminary imaging was done to attempt imaging with simple, routine cryo-sectioning parameters. Of the parameters attempted, the cryo-sectioned slices were the most intact when using gelatin, with cold-mounting, with 20 μm slice thickness. The slices containing the whole body were mounted onto standard glass slides and images were averaged over areas of interest (head, eye, yolk sack, tail) and over the whole body. All images showed a significant amount of large macromolecules and a polymer (especially in the eye and tail) that does not match the mass of the initial semi-fluorinated compound.

Image of $mPEG_{1k}$-F13 fish cryo-sections mounted onto glass slides

Image of zebrafish larvae (Adapted from reference)[5]

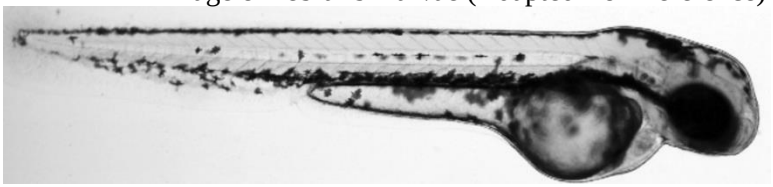

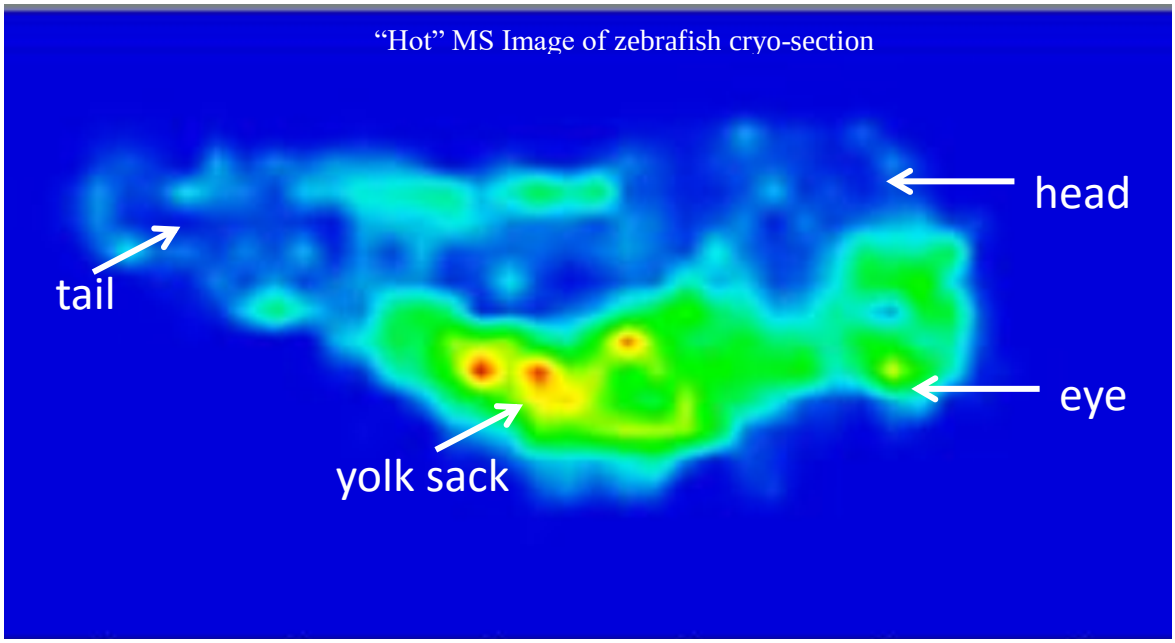
"Hot" MS Image of zebrafish cryo-section
head
tail
eye
yolk sack

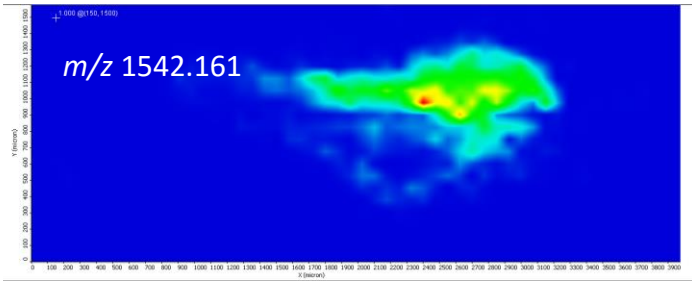
m/z 1542.161

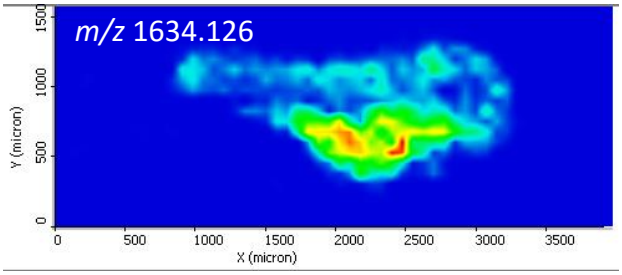
m/z 1634.126
Y (micron)
X (micron)

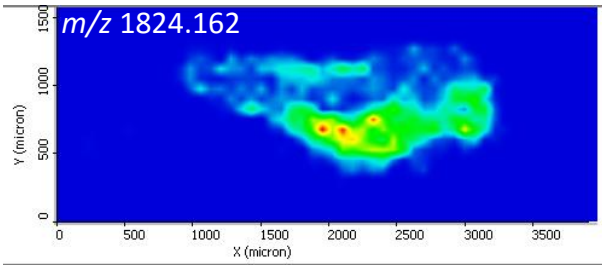
m/z 1824.162
Y (micron)
X (micron)

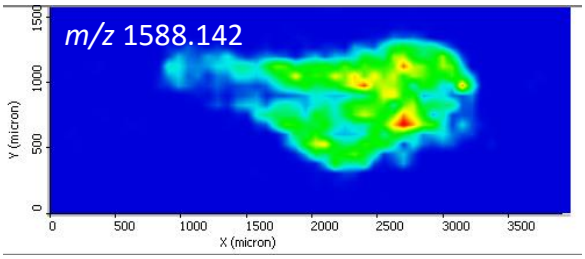
m/z 1588.142
Y (micron)
X (micron)

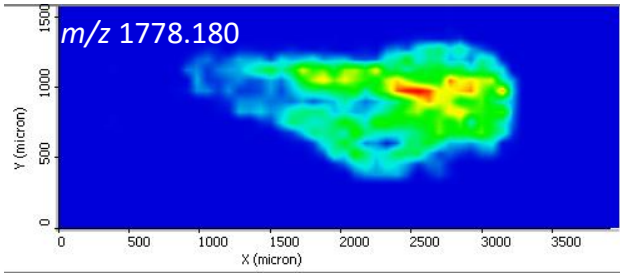
m/z 1778.180
Y (micron)
X (micron)

Average spectra of fish head (boxed region in image)

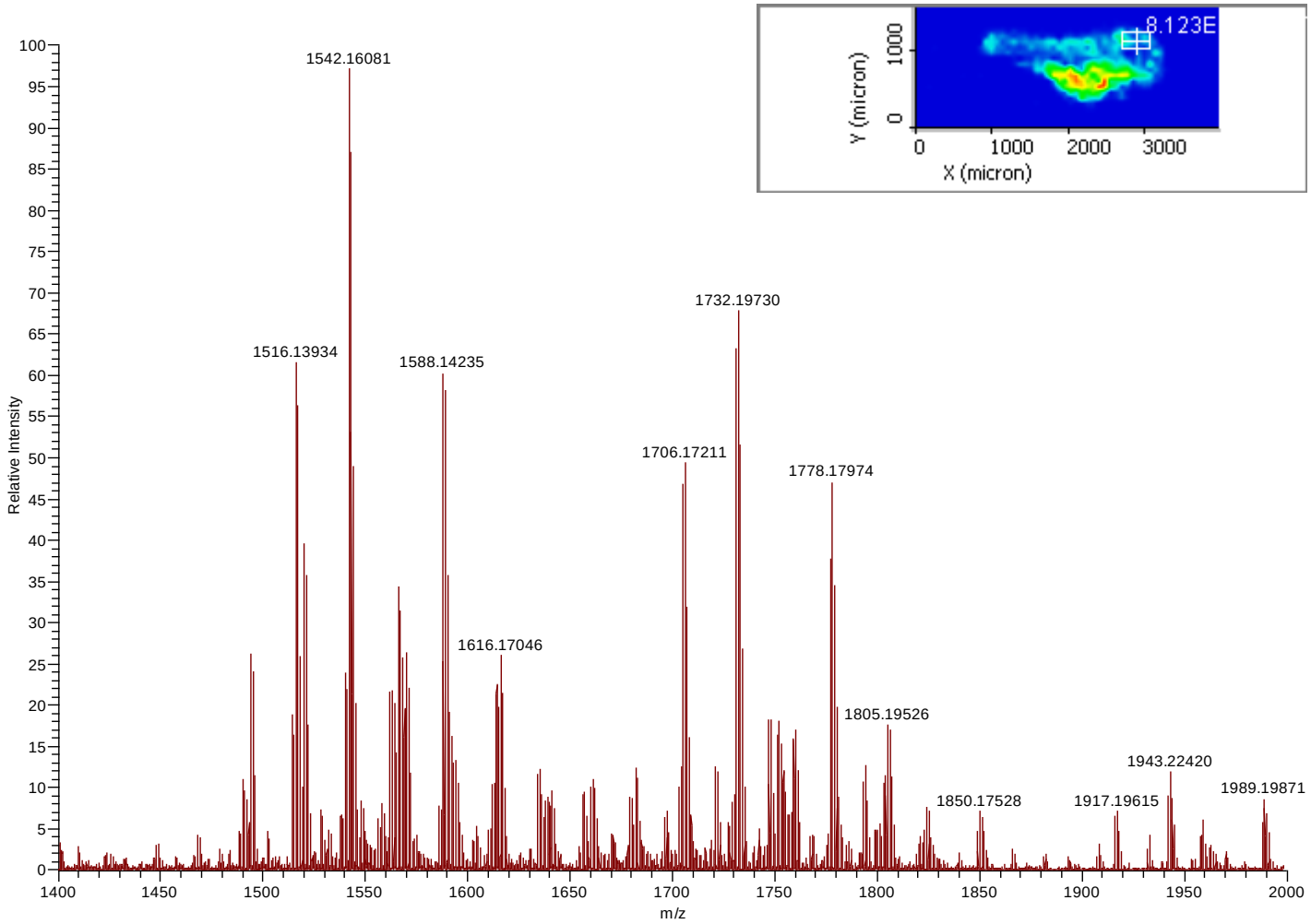

Average spectra of fish eye (boxed region in image)

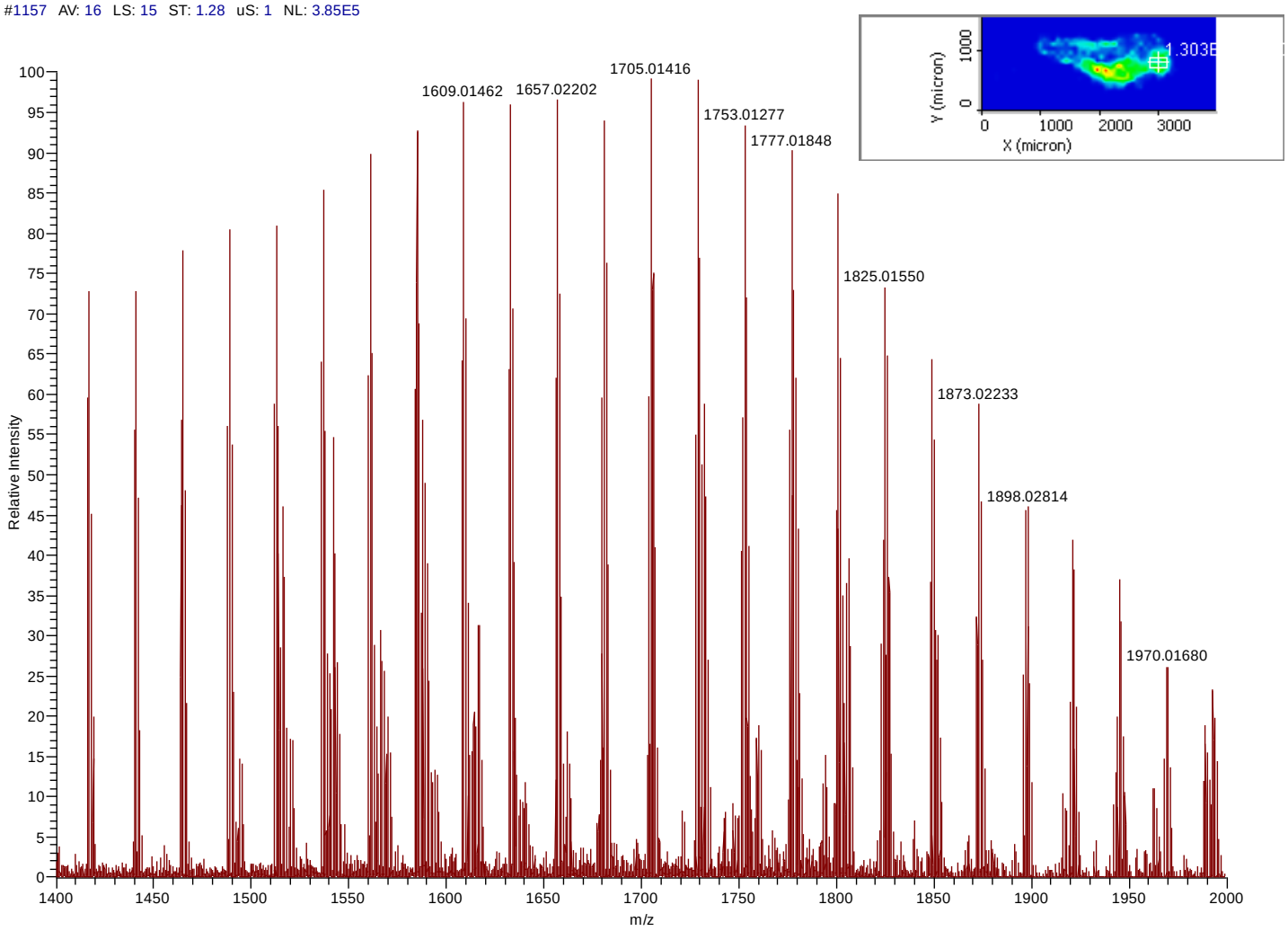

Average spectra of fish yolk sack (boxed region in image)

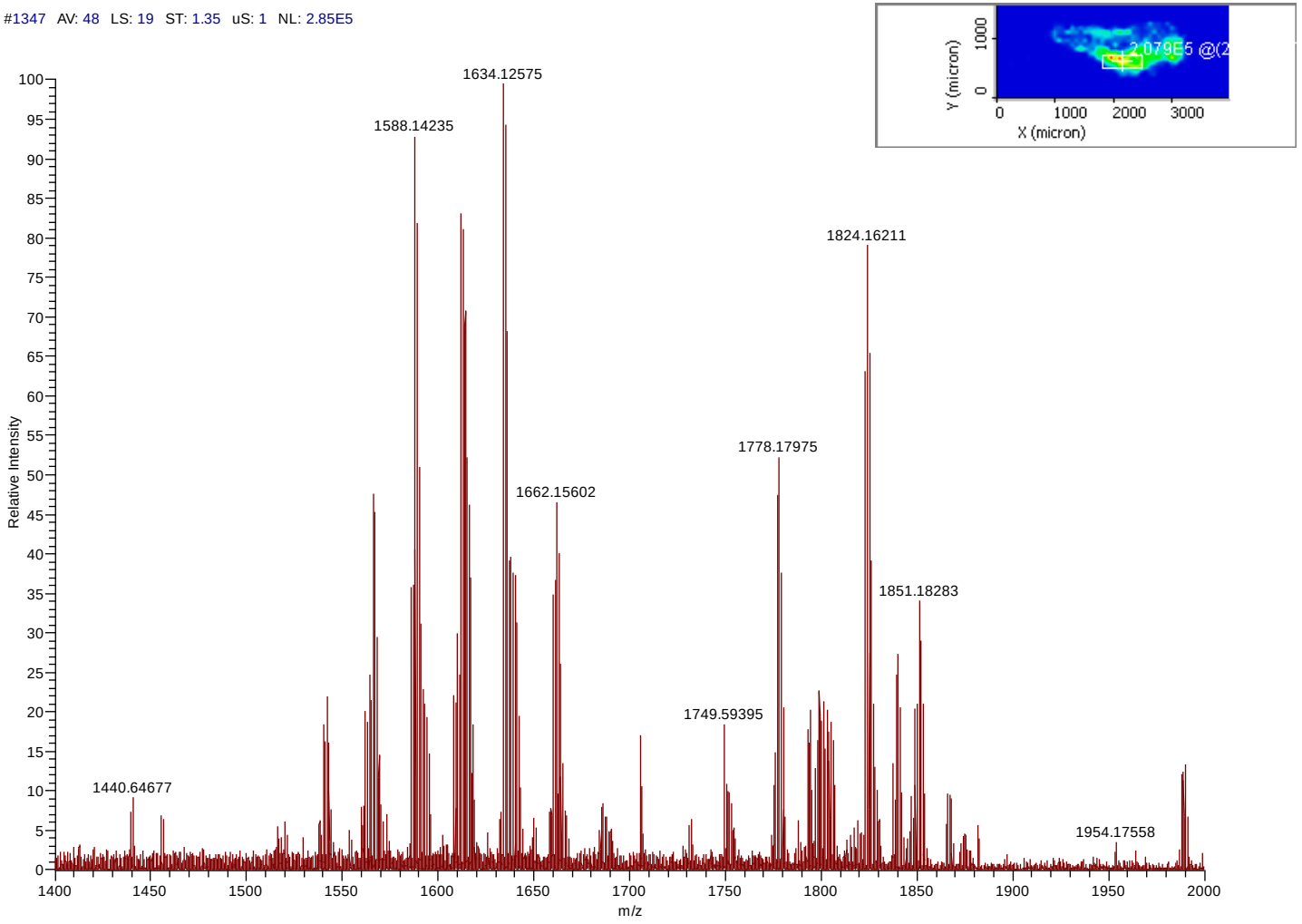

Average spectra of fish tail (boxed region in image)

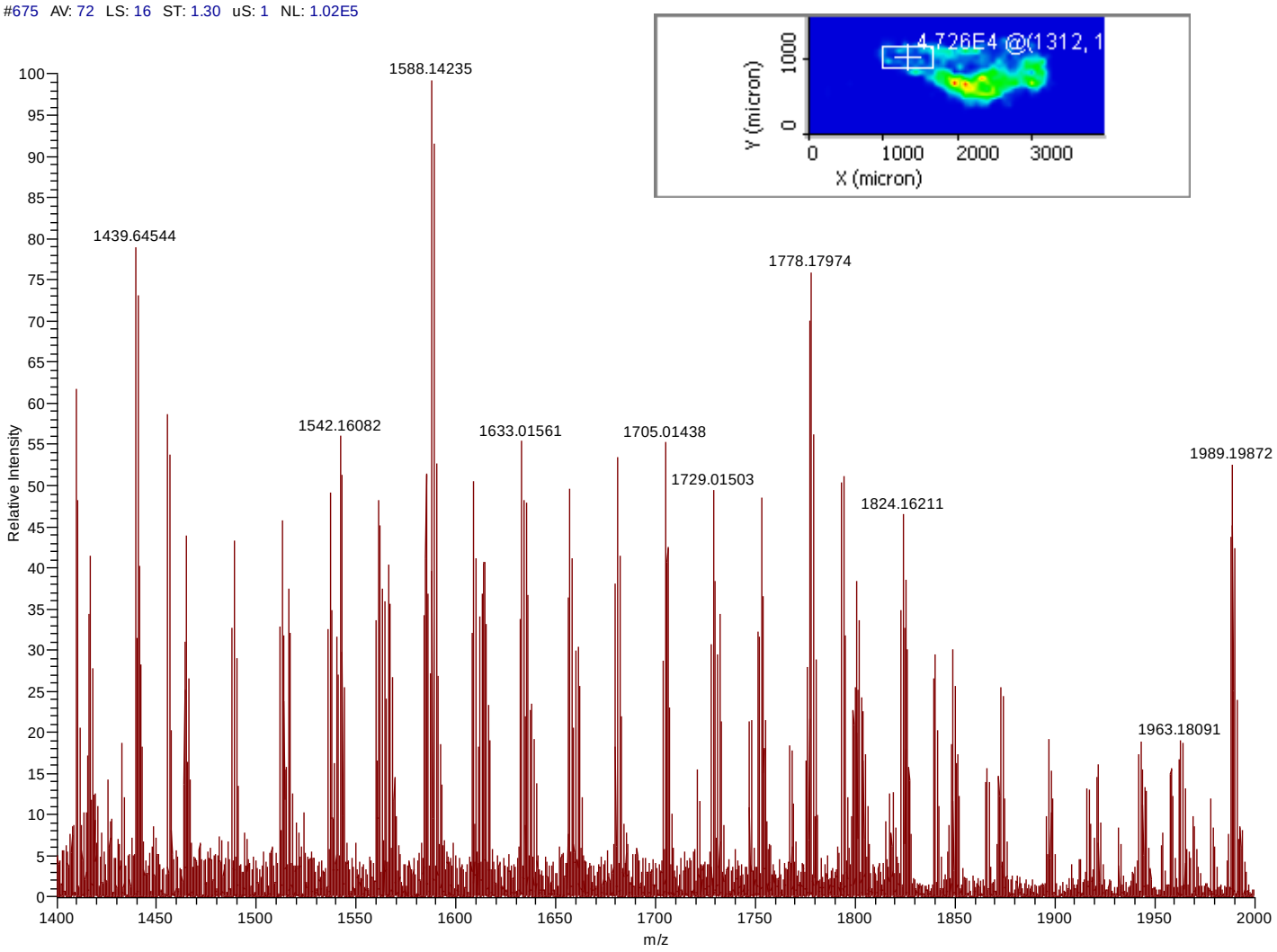

Average spectra of fish whole body (boxed region in image)

#565 AV: 660 LS: 24 ST: 1.45 uS: 1 NL: 1.93E5

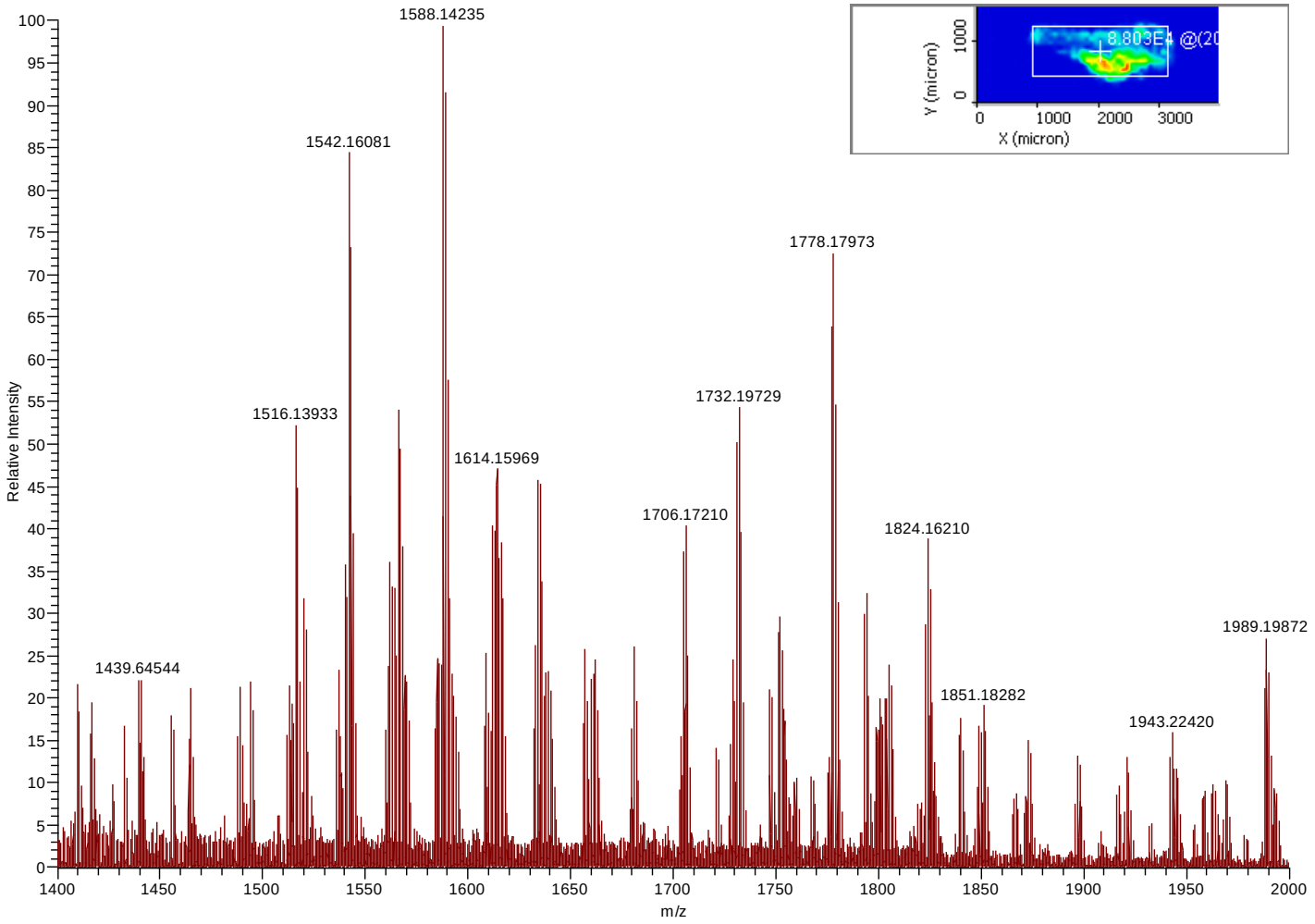

To identify the background spectra without exposure to semi-fluorinated compounds, an unexposed fish ("control") was also analyzed alongside an exposed fish (see following spectra). The very apparent similarity between the "exposed" and the "control" fish clearly show that this analysis was not successful in visualizing the polymer in the cryo-section slices.

Conclusion

There are several potential reasons for the absence of the semi-fluorinated polymer. The quick washing procedure could remove the polymer from the zebrafish body if the exchange into and out of the fish is rapid, or the polymer may be rapidly excreted during euthanasia. In order to circumnavigate these issues an alternative approach may be warranted. Due to the transparency of the zebrafish larvae it is feasible to covalently conjugate a fluorescent label to the polymer structure and visualize the internalization of the polymer via fluorescence imaging in real-time. Additionally, it is possible that the semi-fluorinated polymer didn't actually permeate to the interior of the zebrafish embryo and larvae and thus could not be detected via MALDI-MSI.

"**Exposed fish**" Average spectra of fish whole body

#1117 AV: 2736 LS: 13 ST: 1.24 uS: 1 NL: 1.43E5

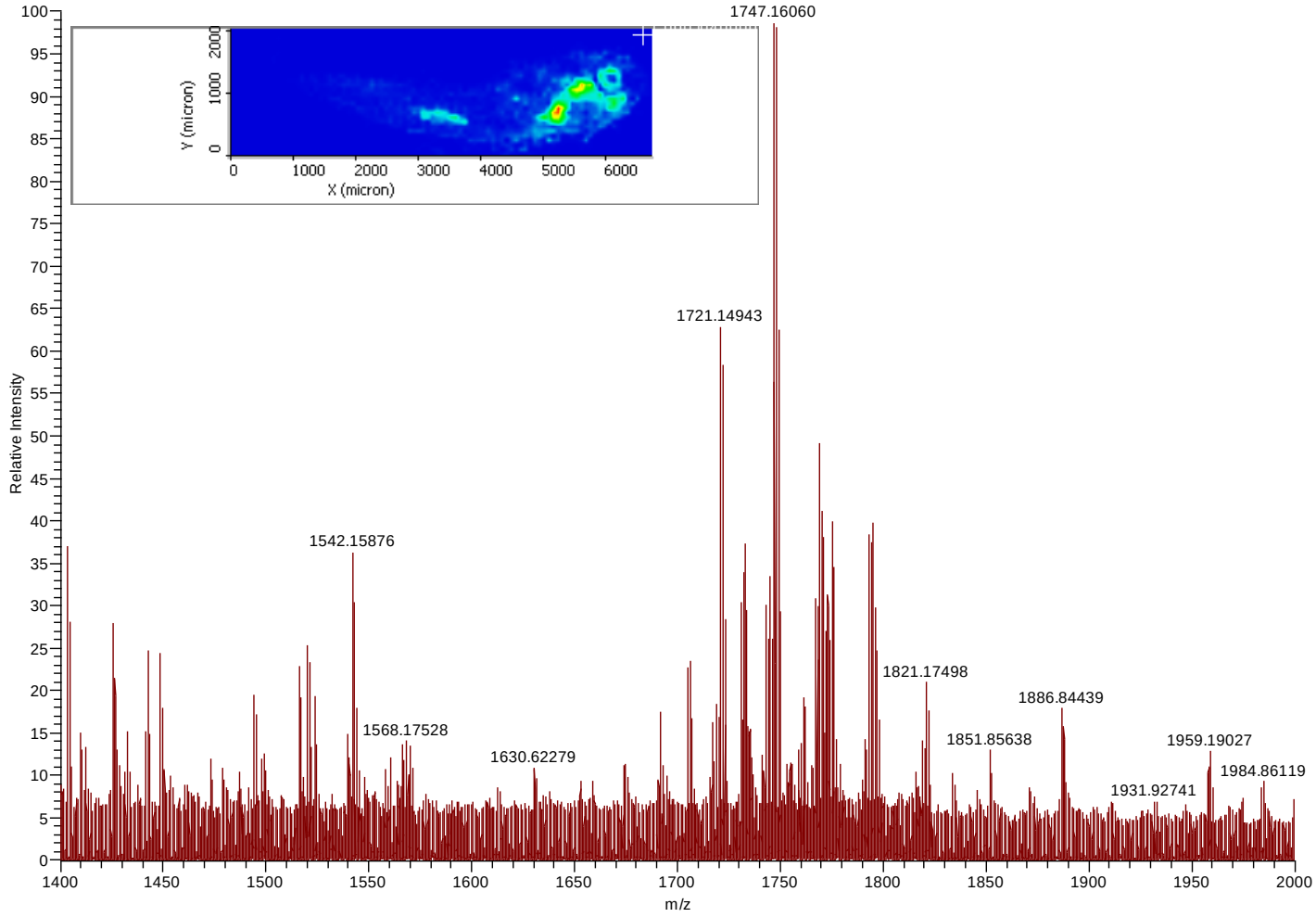

"**Unexposed (control) fish**" Average spectra of fish whole body

#357 AV: 4466 LS: 9 ST: 1.17 uS: 1 NL: 1.28E5

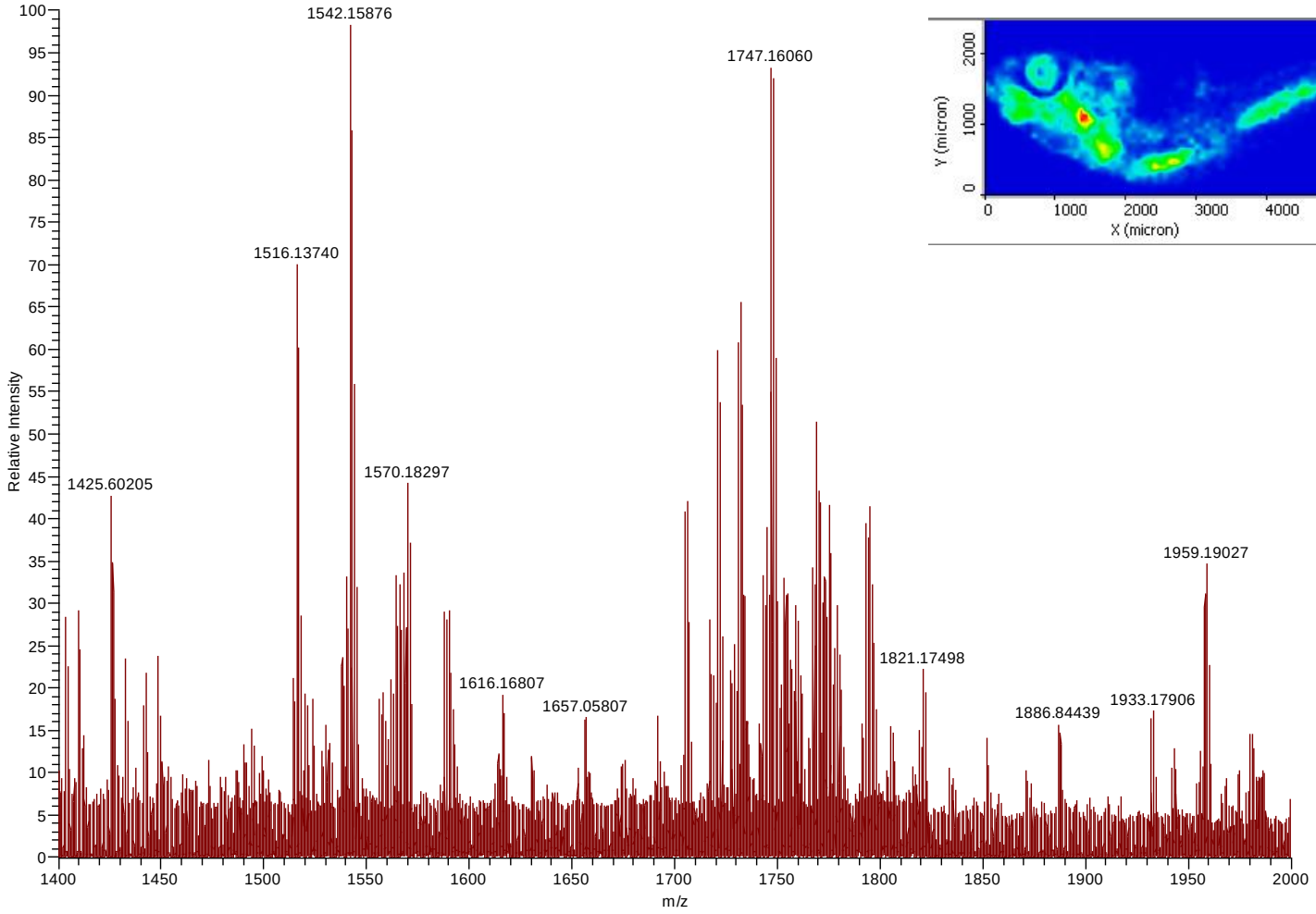

MALDI MS of the mounting glue (OCT)

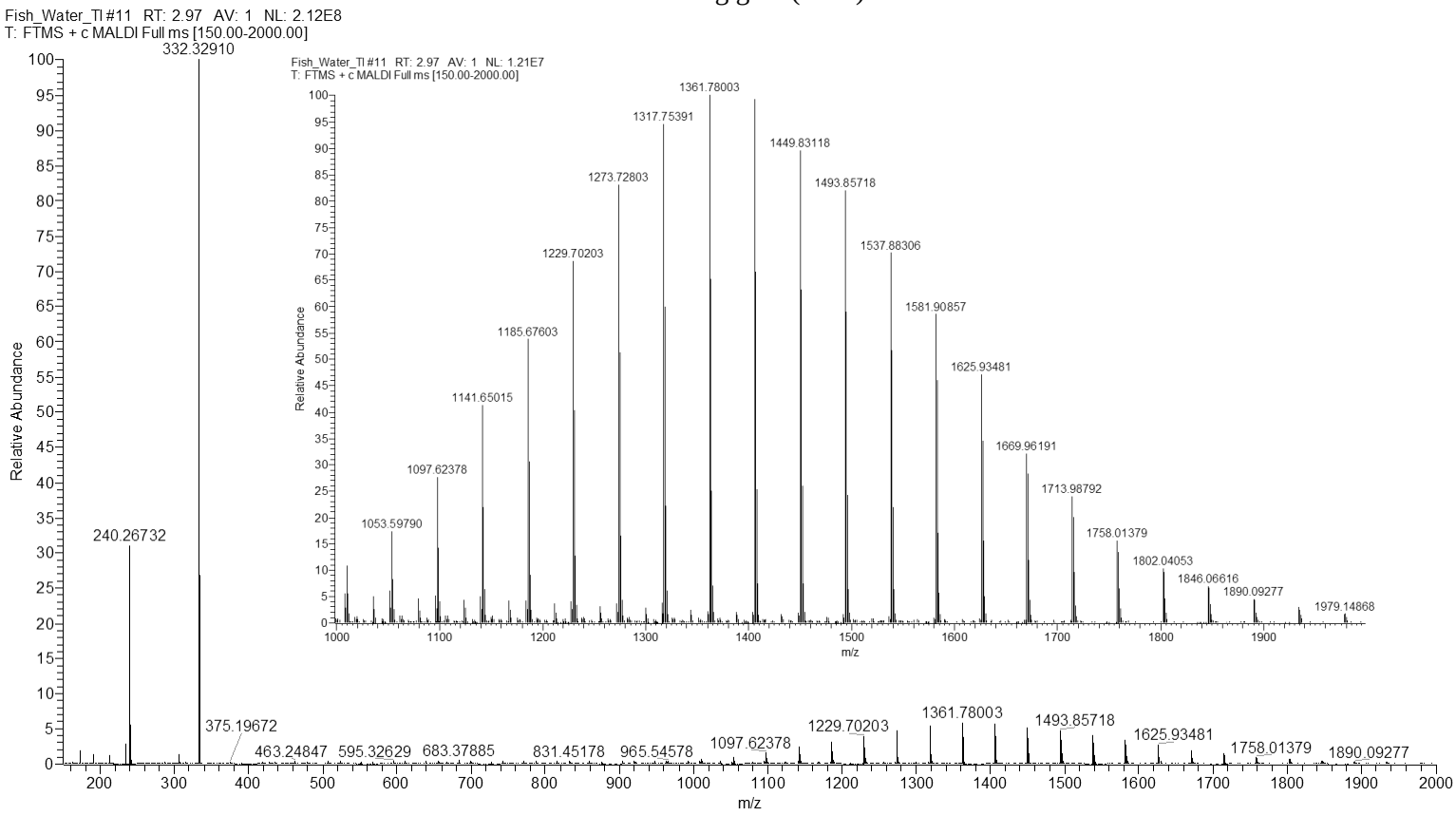

MALDI MS of the CHCA matrix

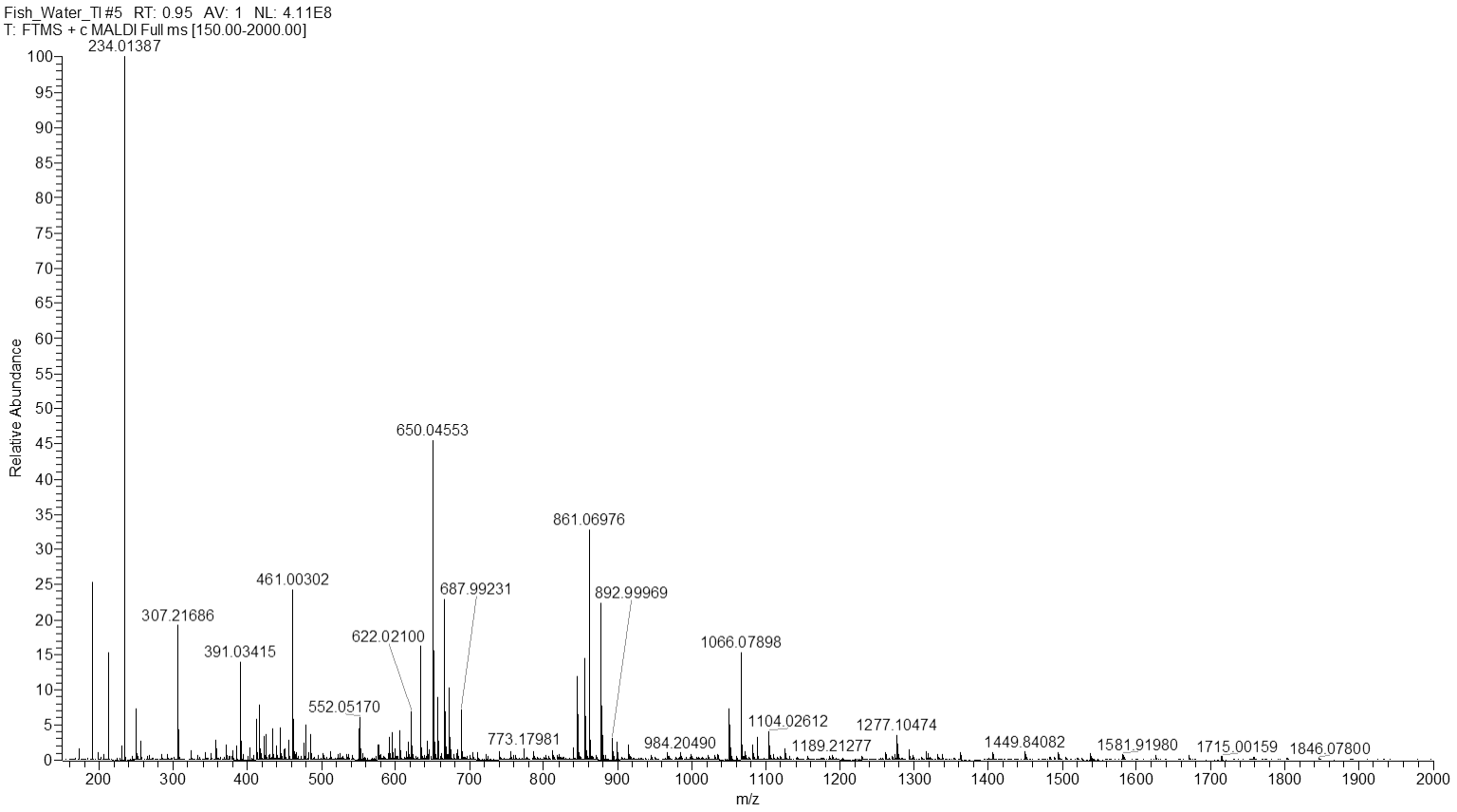

Acknowledgements

Thank you to Sarah Decato for collaborating on this project and preparing the fish and polymer samples. Thank you to Samantha Fix who helped with the zebrafish handling and polymer exposure. The MALDI-Orbitrap instrument was purchased through an NIH shared instrument grant (NCRR S10RR029531). E.G. acknowledges an NSF Graduate Research Fellowship (DGE-1256259).

References

1. Yang, L. L. ; Wang, G. Q. ; Yang, L. M. ; Huang, Z. B. ; Zhang, W. Q. ; Yu, L. Z. *Molecules* **2014**, *19* (2), 2390.

2. Goodwin, R. J. a. *J. Proteomics* **2012**, *75* (16), 4893.

3. Nelson, K. a. ; Daniels, G. J. ; Fournie, J. W. ; Hemmer, M. J. *J. Biomol. Tech.* **2013**, *24*, 119.

4. Khatib-shahidi, S. ; Andersson, M. ; Herman, J. L. ; Gillespie, T. a; Caprioli, R. M. *Anal. Chem.* **2006**, *78* (18), 6448.

5. Brooks, S. S. ; Wall, a. L. ; Golzio, C. ; Reid, D. W. ; Kondyles, a. ; Willer, J. R. ; Botti, C. ; Nicchitta, C. V. ; Katsanis, N. ; Davis, E. E. *Genetics* **2014**, *198* (2), 723.

Appendix III

MALDI-MSI of Lipids in the Electric Eel Electric Organ

Introduction

The Sussman lab performed an in-depth analysis and characterization of the electric eel, *electrophorus electricus*, a relatively new model organism. Electrocytes in the main electric organ are arranged in rows, one right after the other, from tail to head.[1]

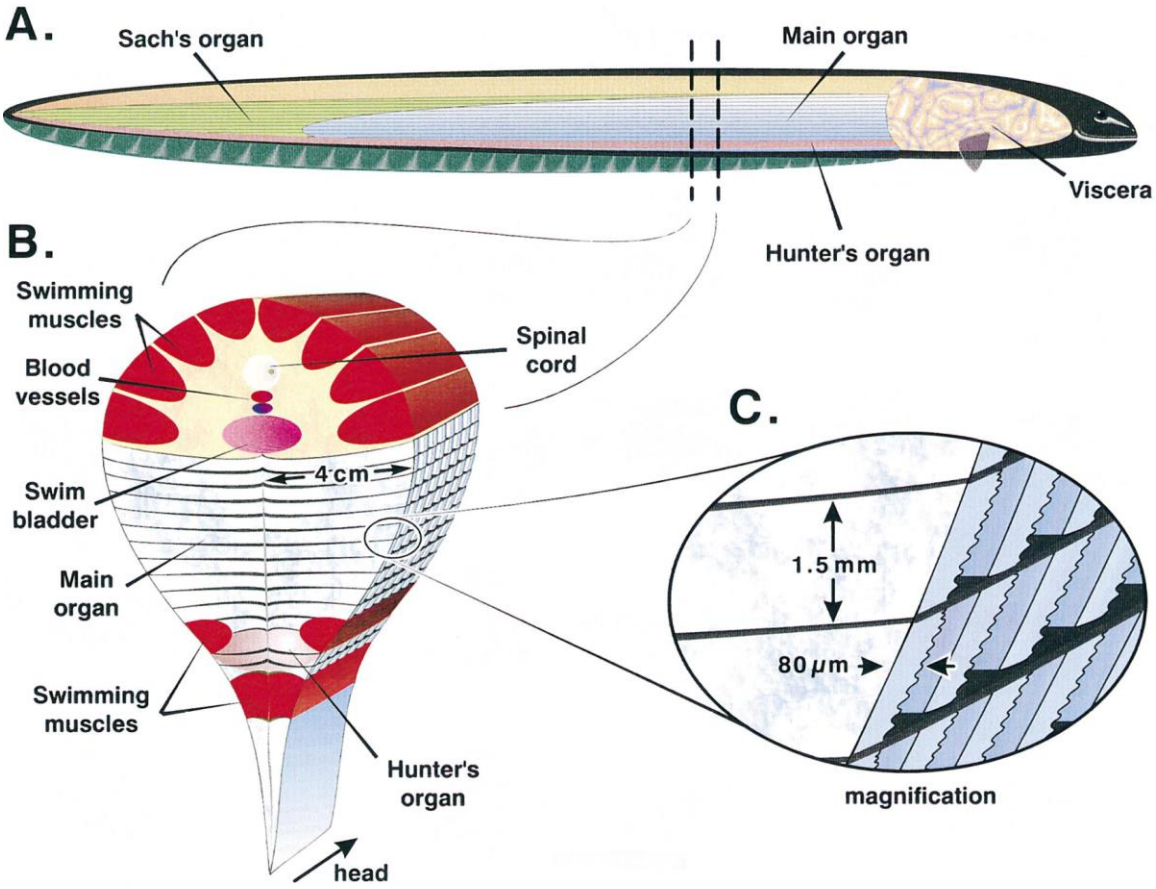

Rows of electrocytes are stacked on top of one another, and are (likely) electrically insulated from one another by some kind of septa. The make-up of the septa here is not known. Therefore matrix-assisted laser desorption/ionization (MALDI)- mass spectrometry imaging (MSI) was attempted to identify compounds that could potentially be insulating the electrocytes from each other and the rest of the animal. The advantage of MSI is that it provides the opportunity to examine the spatial context of molecules whole tissue without chemical modification or a need for prior knowledge of the analytes of interest.

Experimental

Eel Tissue Preparation

One half of an electric organ was removed from an electric eel, frozen in a 50 mL falcon tube, and stored at -80 °C. The falcon tube was removed from the -80 °C freezer and the electric organ was slowly thawed on ice until the tissue was flexible enough to lay flat. A cross section of the electric organ was removed with a razor blade, embedded in gelatin (100 mg/mL in double-distilled water), and gently frozen on dry ice.

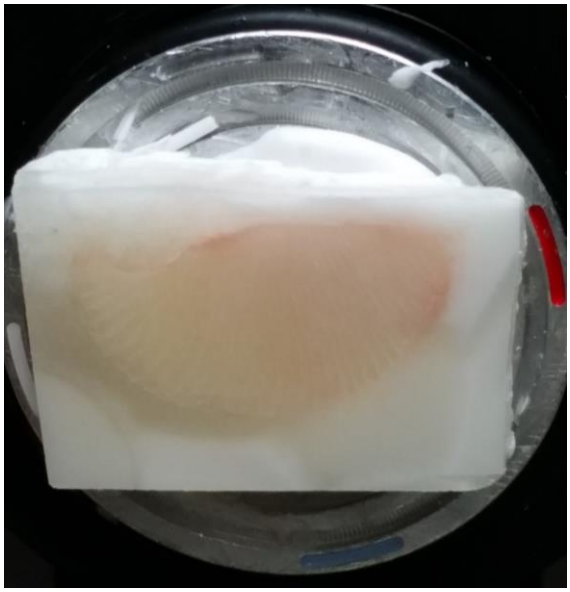

Electric organ embedded in gelatin, frozen

The remaining tissue was sealed in tin foil and stored at -80 °C. The embedded tissue was sectioned (16-μm thickness) using a cryostat at –20°C. The sections were thaw-mounted onto a standard glass microscope slide. Matrix (10 mg/mL CHCA in 50/50 water/ACN) was applied using a TM-Sprayer (HTX Technologies, LLC, Carrboro, NC, USA). CHCA was purchased from Sigma Aldrich (St. Louis, MO, USA). Additionally, parts of the electric organ were imaged using DHB and DAN, however only a complete section was imaged using CHCA.

16 μm thick section of electric organ coated with MALDI matrix, CHCA

MALDI-Orbitrap MSI and MALDI-MS/MS

A MALDI-Orbitrap mass spectrometer (Thermo Scientific, Waltham, MA, USA) that was equipped with an N2 laser (spot diameter of 75 μm) was used in positive ion mode for imaging. Imaging was performed using a mass range of *m/z* 500-1200, a mass resolution of 60,000, and a laser energy of 60 μJ. The tissue region to be imaged and the raster step size were controlled using the LTQ Tune software (Thermo Scientific, Waltham, MA, USA). The instrument methods were created using Xcalibur (Thermo Scientific, Waltham, MA, USA). To generate images, the spectra were collected at 75 μm intervals in both the x and y dimensions across the surface of the sample. The manual interpretation of the averaged mass spectrum was performed using ImageQuest (Thermo Scientific, Waltham, MA, USA). All images were normalized to the TIC.

Lipid Extraction from Electric Organ

Lipids were extracted from the electric organ tissue following the Bligh and Dyer method[2] that has been previously reported in a large-scale lipidomics study using a variety of fish/ sea animal tissue.[3] Briefly, Ten grams of animal tissue were ground in a mortar with 10 mL

of chloroform ($CHCl_3$) and 20 mL of methanol (MeOH). The ground mixture obtained was added again with 10 mL of $CHCl_3$, plus 10 mL of distilled water, and stirred. Successively, the mixture was filtered through MiraCloth and the obtained solution was allowed to stand. Finally, the solution was centrifuged for 5 min at 3000 rpm and 4 °C. The bottom layer was then collected and dried down with a RotoVap. The dried contents were resuspended in a small amount of methanol (2-4 mL) and transferred to a 2 mL Eppindorf tube. The final solution was concentrated by drying down with a SpeedVac. It is important to note that no plastic containers should be used while the solution contains chloroform. This will result in interfering polymer signal in the MS analysis.

Results and Discussion

Compounds were detected with MALDI-MSI that showed distinct localization to the electrocytes or tissue between electrocytes and could be potentially insulating the electrocytes from each other and the rest of the fish. The images are shown below:

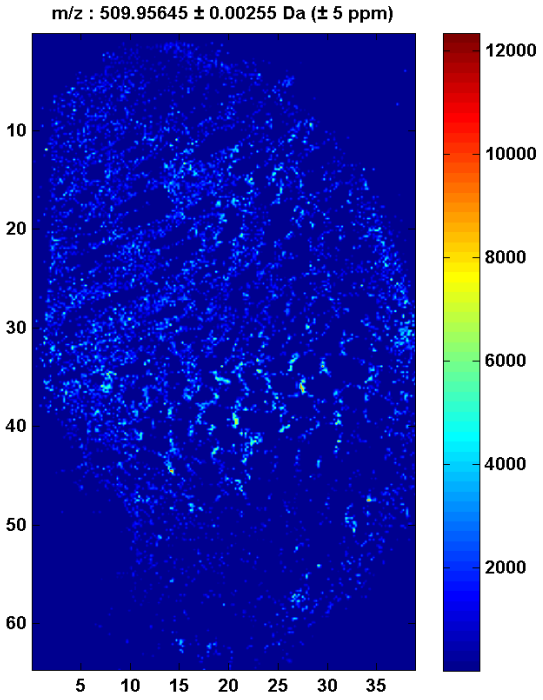
m/z : 509.95645 ± 0.00255 Da (± 5 ppm)
10
20
30
40
50
60
5
10
15
20
25
30
35
12000
10000
8000
6000
4000
2000

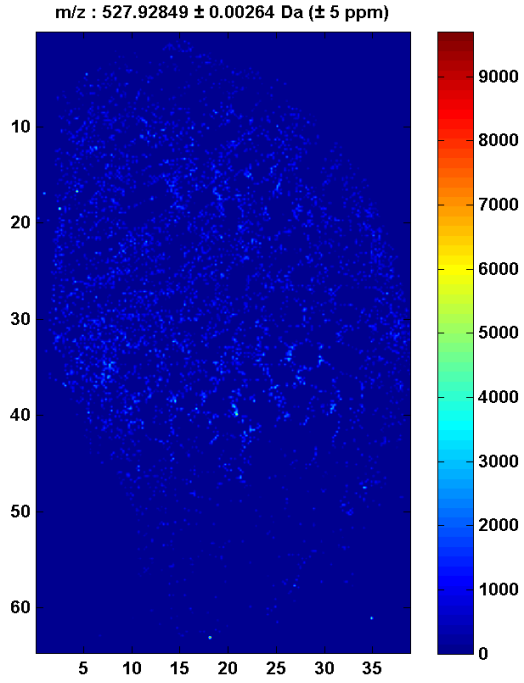
m/z : 527.92849 ± 0.00264 Da (± 5 ppm)
10
20
30
40
50
60
5
10
15
20
25
30
35
9000
8000
7000
6000
5000
4000
3000
2000
1000
0

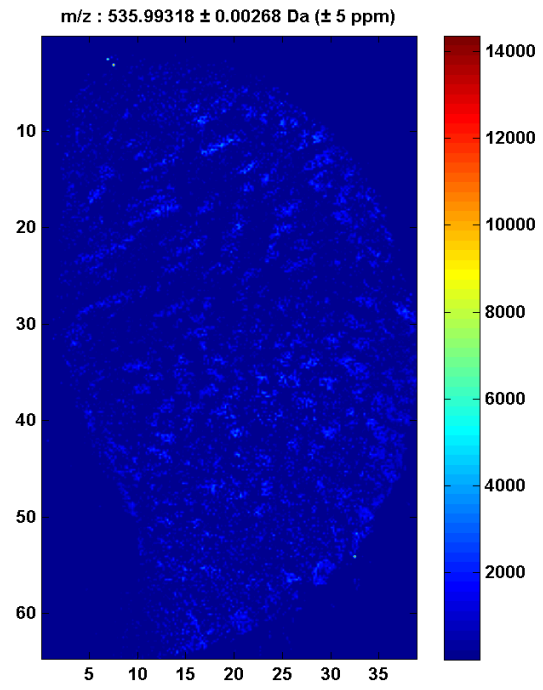
m/z : 535.99318 ± 0.00268 Da (± 5 ppm)
10
20
30
40
50
60
5
10
15
20
25
30
35
14000
12000
10000
8000
6000
4000
2000

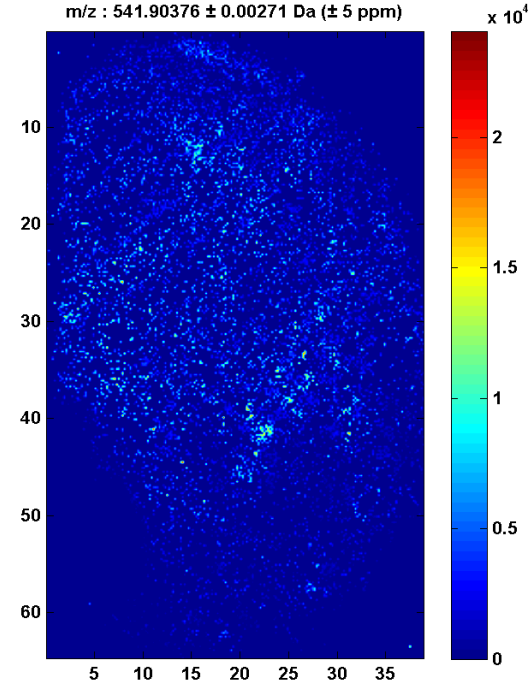
m/z : 541.90376 ± 0.00271 Da (± 5 ppm)
x 10^4
10
20
30
40
50
60
5
10
15
20
25
30
35
2
1.5
1
0.5
0

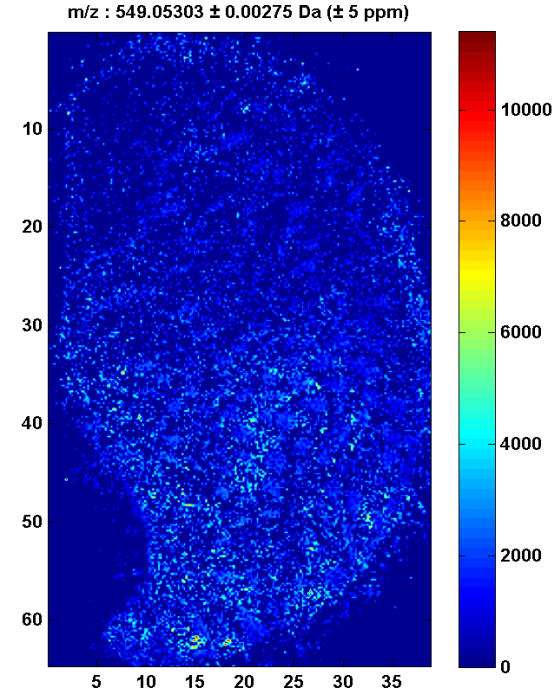
m/z : 549.05303 ± 0.00275 Da (± 5 ppm)
10
20
30
40
50
60
5
10
15
20
25
30
35
10000
8000
6000
4000
2000
0

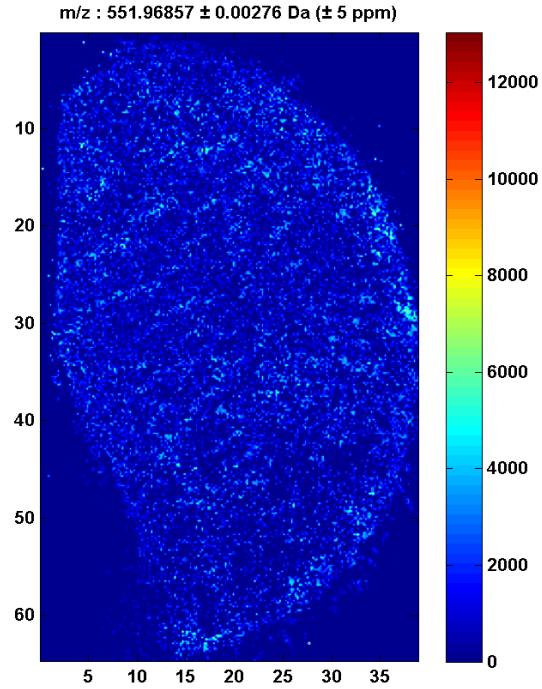
m/z : 551.96857 ± 0.00276 Da (± 5 ppm)
10
20
30
40
50
60
5
10
15
20
25
30
35
12000
10000
8000
6000
4000
2000
0

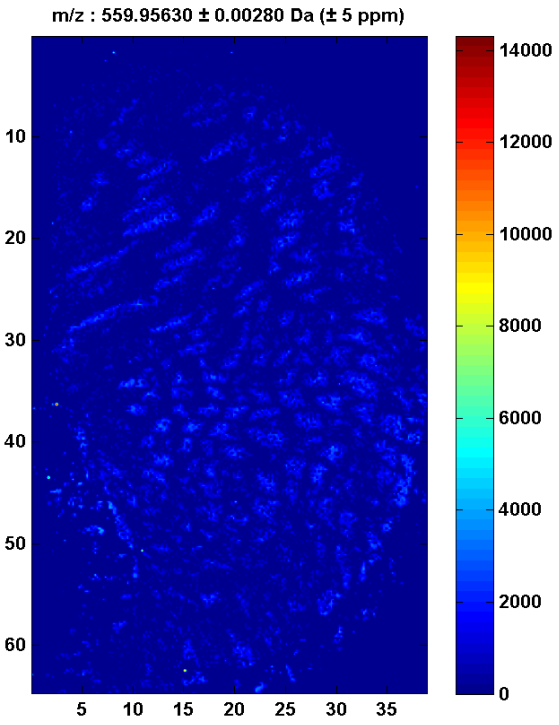
m/z : 559.95630 ± 0.00280 Da (± 5 ppm)
10
20
30
40
50
60
5
10
15
20
25
30
35
14000
12000
10000
8000
6000
4000
2000
0

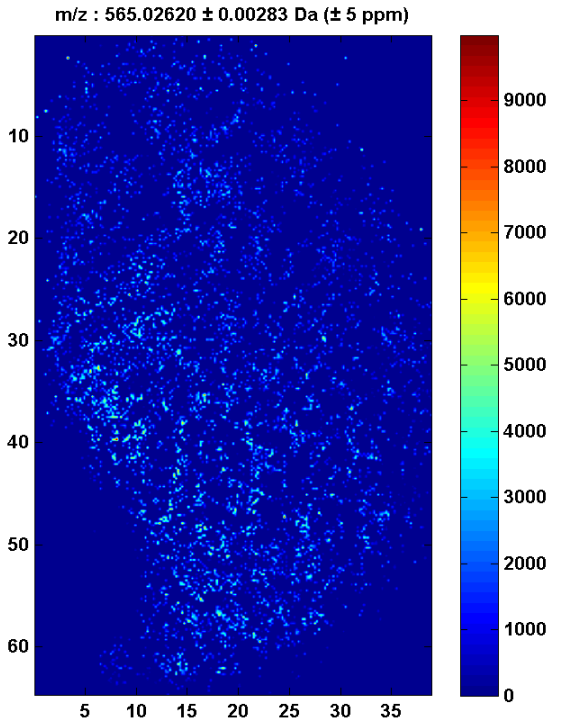
m/z : 565.02620 ± 0.00283 Da (± 5 ppm)
10
20
30
40
50
60
5
10
15
20
25
30
35
9000
8000
7000
6000
5000
4000
3000
2000
1000
0

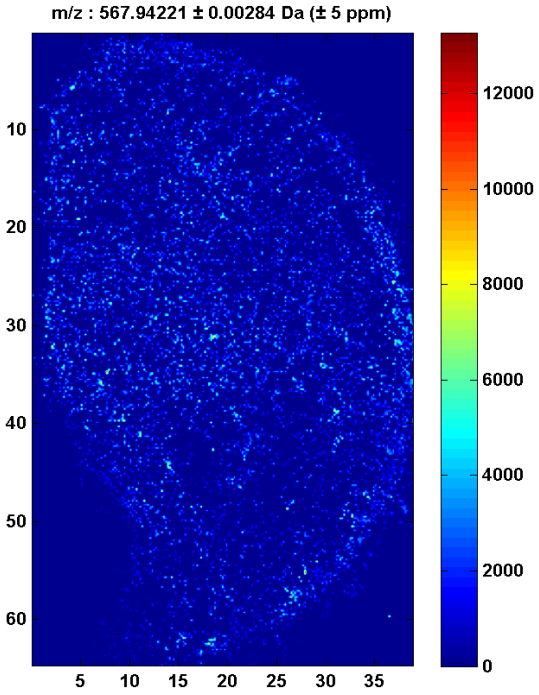
m/z : 567.94221 ± 0.00284 Da (± 5 ppm)
10
20
30
40
50
60
5
10
15
20
25
30
35
12000
10000
8000
6000
4000
2000
0

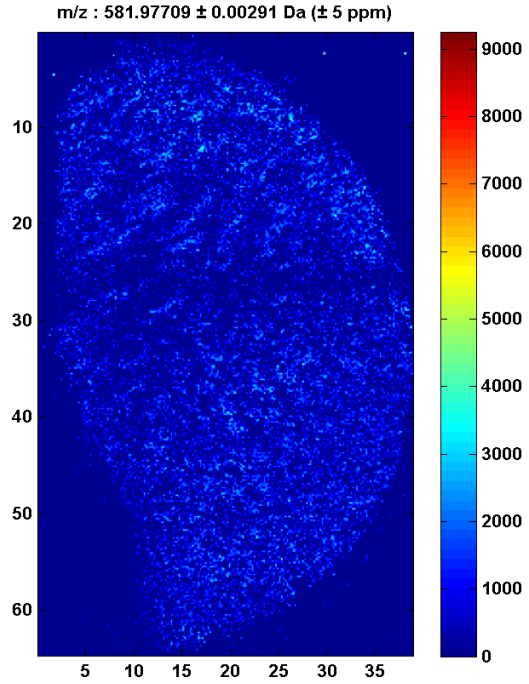
m/z : 581.97709 ± 0.00291 Da (± 5 ppm)
10
20
30
40
50
60
5
10
15
20
25
30
35
9000
8000
7000
6000
5000
4000
3000
2000
1000
0

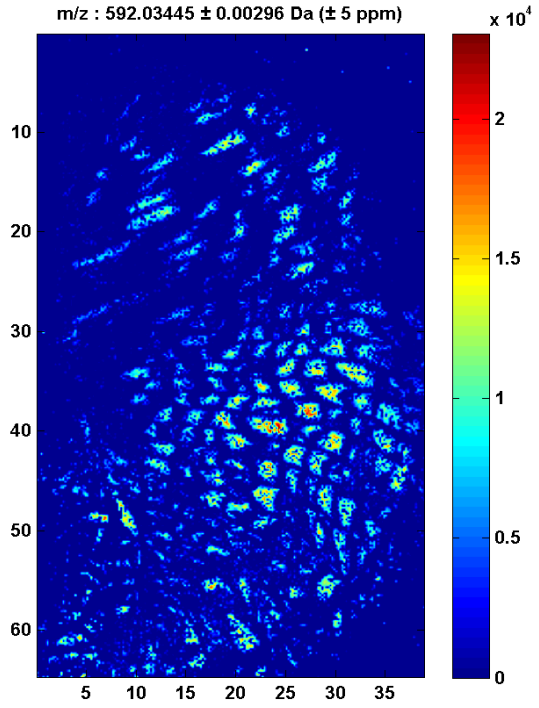
m/z : 592.03445 ± 0.00296 Da (± 5 ppm)
x 10^4
10
20
30
40
50
60
5
10
15
20
25
30
35
2
1.5
1
0.5
0
x 10^4

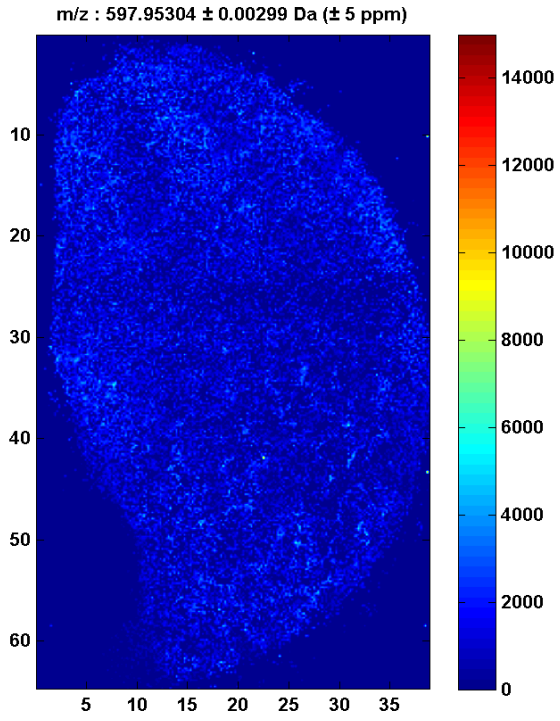
m/z : 597.95304 ± 0.00299 Da (± 5 ppm)
10
20
30
40
50
60
5
10
15
20
25
30
35
14000
12000
10000
8000
6000
4000
2000
0

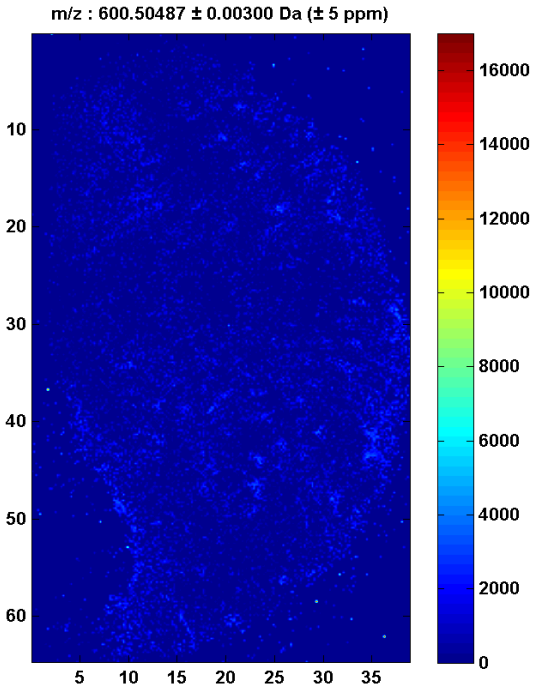
m/z : 600.50487 ± 0.00300 Da (± 5 ppm)
10
20
30
40
50
60
5
10
15
20
25
30
35
16000
14000
12000
10000
8000
6000
4000
2000
0

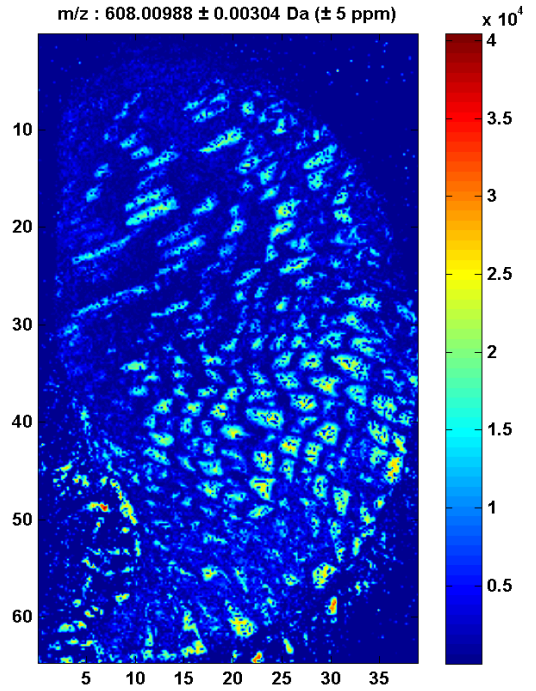
m/z : 608.00988 ± 0.00304 Da (± 5 ppm)
x 10^4
10
20
30
40
50
60
5
10
15
20
25
30
35
4
3.5
3
2.5
2
1.5
1
0.5

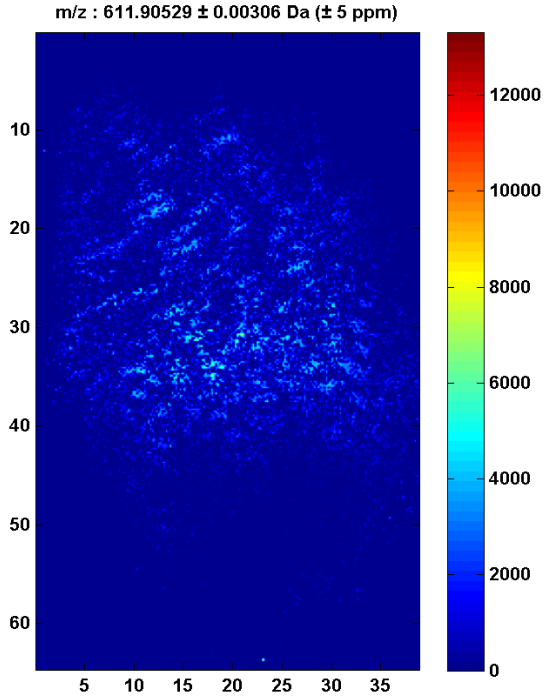
m/z : 611.90529 ± 0.00306 Da (± 5 ppm)
10
20
30
40
50
60
5
10
15
20
25
30
35
12000
10000
8000
6000
4000
2000
0

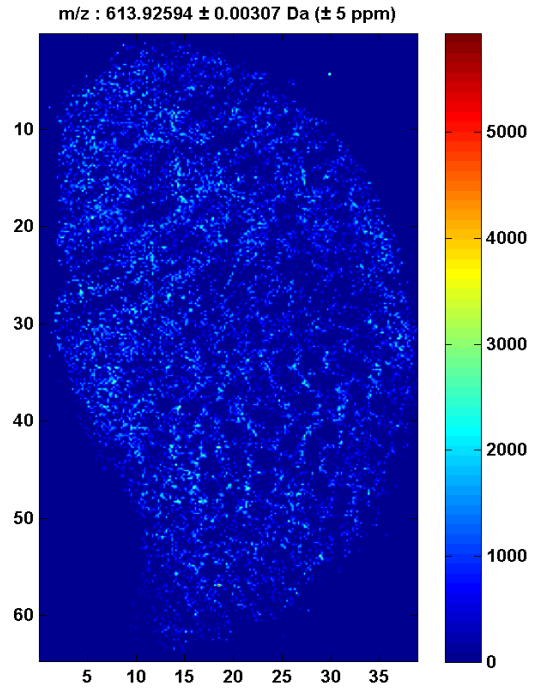
m/z : 613.92594 ± 0.00307 Da (± 5 ppm)
10
20
30
40
50
60
5
10
15
20
25
30
35
5000
4000
3000
2000
1000
0

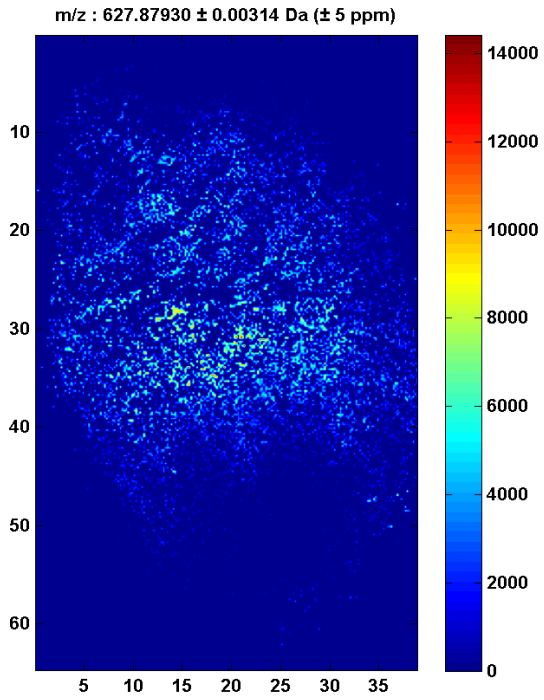
m/z : 627.87930 ± 0.00314 Da (± 5 ppm)
14000
12000
10000
8000
6000
4000
2000
0
10
20
30
40
50
60
5
10
15
20
25
30
35

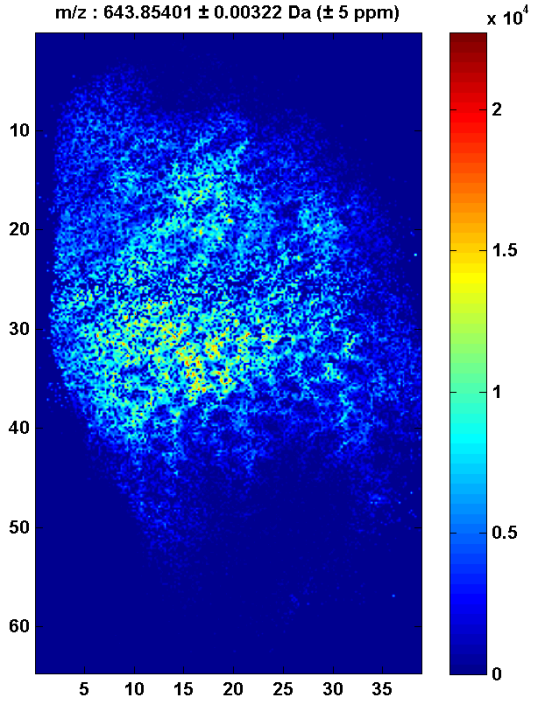
m/z : 643.85401 ± 0.00322 Da (± 5 ppm)
x 10^4
2
1.5
1
0.5
0
10
20
30
40
50
60
5
10
15
20
25
30
35

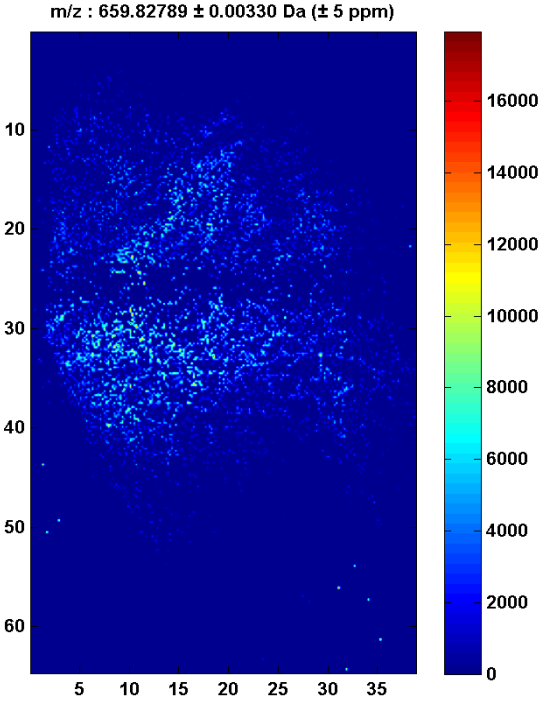
m/z : 659.82789 ± 0.00330 Da (± 5 ppm)
16000
14000
12000
10000
8000
6000
4000
2000
0
10
20
30
40
50
60
5
10
15
20
25
30
35

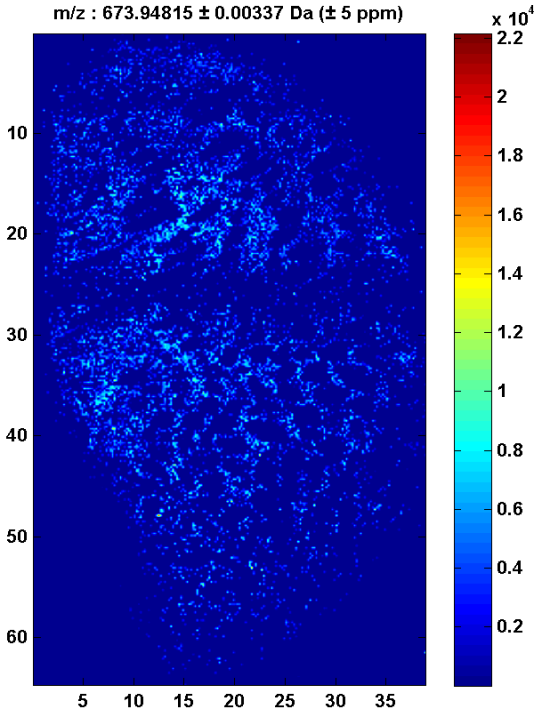
m/z : 673.94815 ± 0.00337 Da (± 5 ppm)
x 10^4
2.2
2
1.8
1.6
1.4
1.2
1
0.8
0.6
0.4
0.2
10
20
30
40
50
60
5
10
15
20
25
30
35

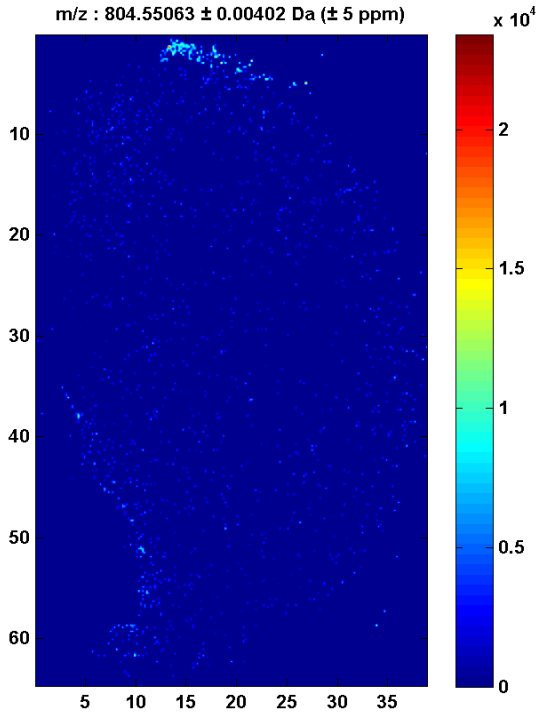
m/z : 804.55063 ± 0.00402 Da (± 5 ppm)
x 10^4
2
1.5
1
0.5
0
10
20
30
40
50
60
5
10
15
20
25
30
35

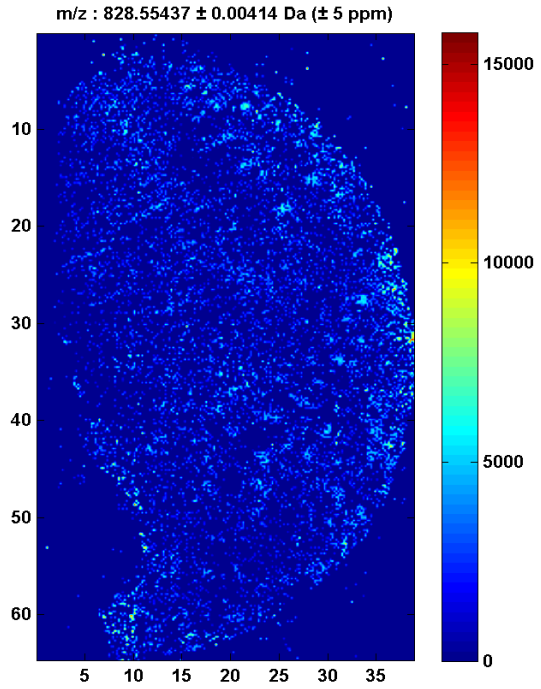
m/z : 828.55437 ± 0.00414 Da (± 5 ppm)
15000
10000
5000
0
10
20
30
40
50
60
5
10
15
20
25
30
35

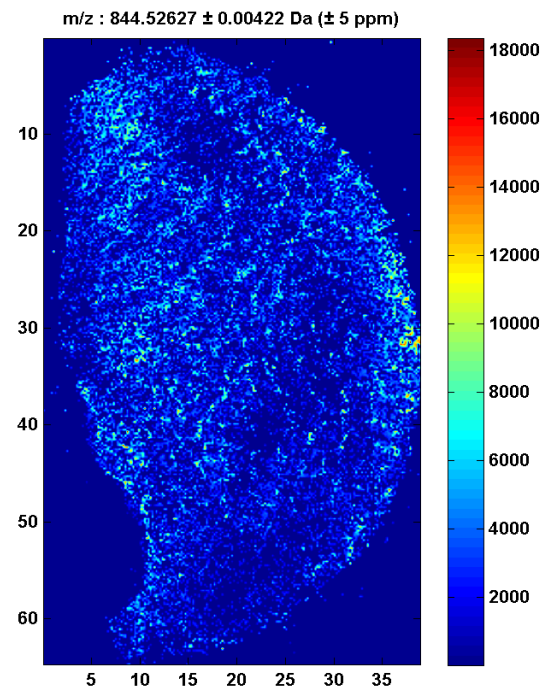
m/z : 844.52627 ± 0.00422 Da (± 5 ppm)
18000
16000
14000
12000
10000
8000
6000
4000
2000
10
20
30
40
50
60
5
10
15
20
25
30
35

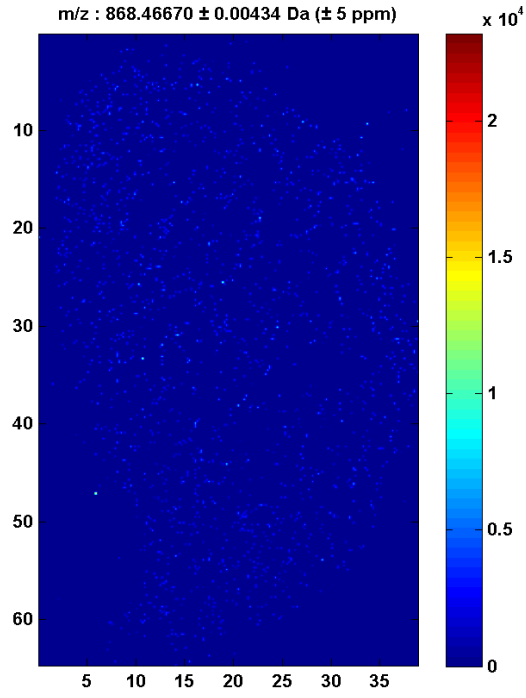
m/z : 868.46670 ± 0.00434 Da (± 5 ppm)
x 10^4
2
1.5
1
0.5
0
10
20
30
40
50
60
5
10
15
20
25
30
35

MALDI-MS/MS was performed on electric organ tissue sections and good quality MS/MS spectra were acquired for 34 of the detected compounds. The MS/MS spectra for each compound is shown below along with a table that lists the most intense peaks and the peak intensities for those peaks that were used for MS/MS database searching. The parent mass is highlighted in grey.

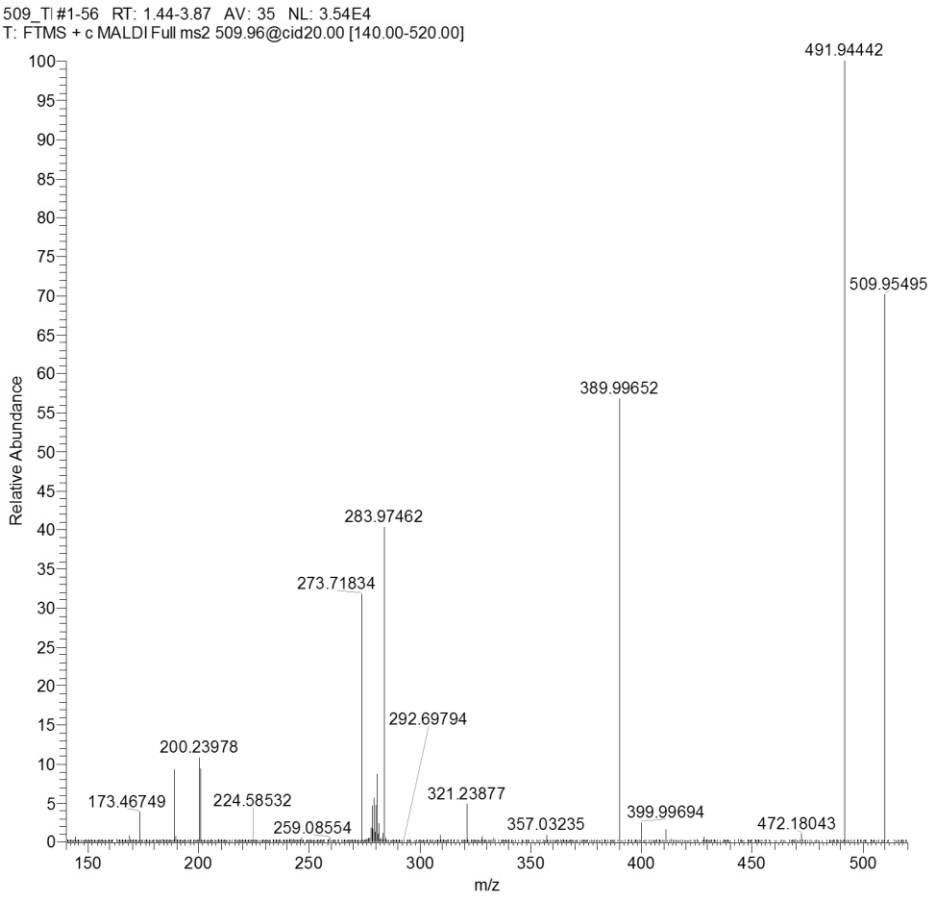

m/z	Intensity	Relative	m/z	Intensity	Relative
279.17068	1985.5	5.61	491.94442	35364.7	100
280.75821	3069.3	8.68	509.91558	2144.5	6.06
283.97462	14241.2	40.27	509.95495	24787.4	70.09
389.99652	20093.9	56.82			

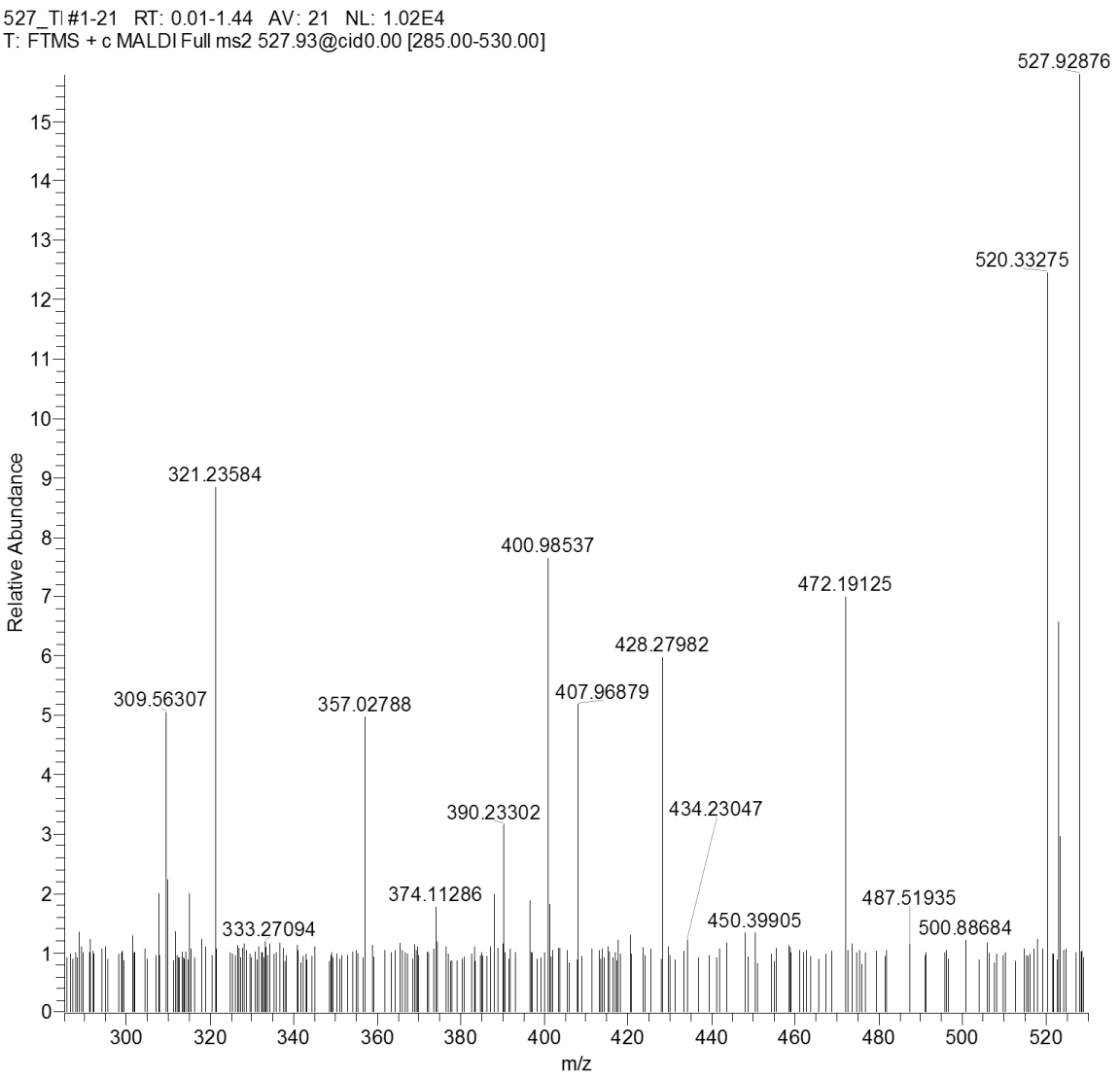

m/z	Intensity	Relative	m/z	Intensity	Relative
309.49694	439.9	4.33	472.19125	710.6	7
309.51346	385.8	3.8	520.33275	1264.4	12.45
309.56307	512.4	5.04	523.18161	667.2	6.57
357.02788	504.7	4.97	527.92876	10158.3	100
357.03960	397.1	3.91	528.00559	473.2	4.66
401.00445	652.4	6.42			
401.02492	481.6	4.74			
401.04777	356.4	3.51			
407.96879	525.6	5.17			
428.27982	604.8	5.95			

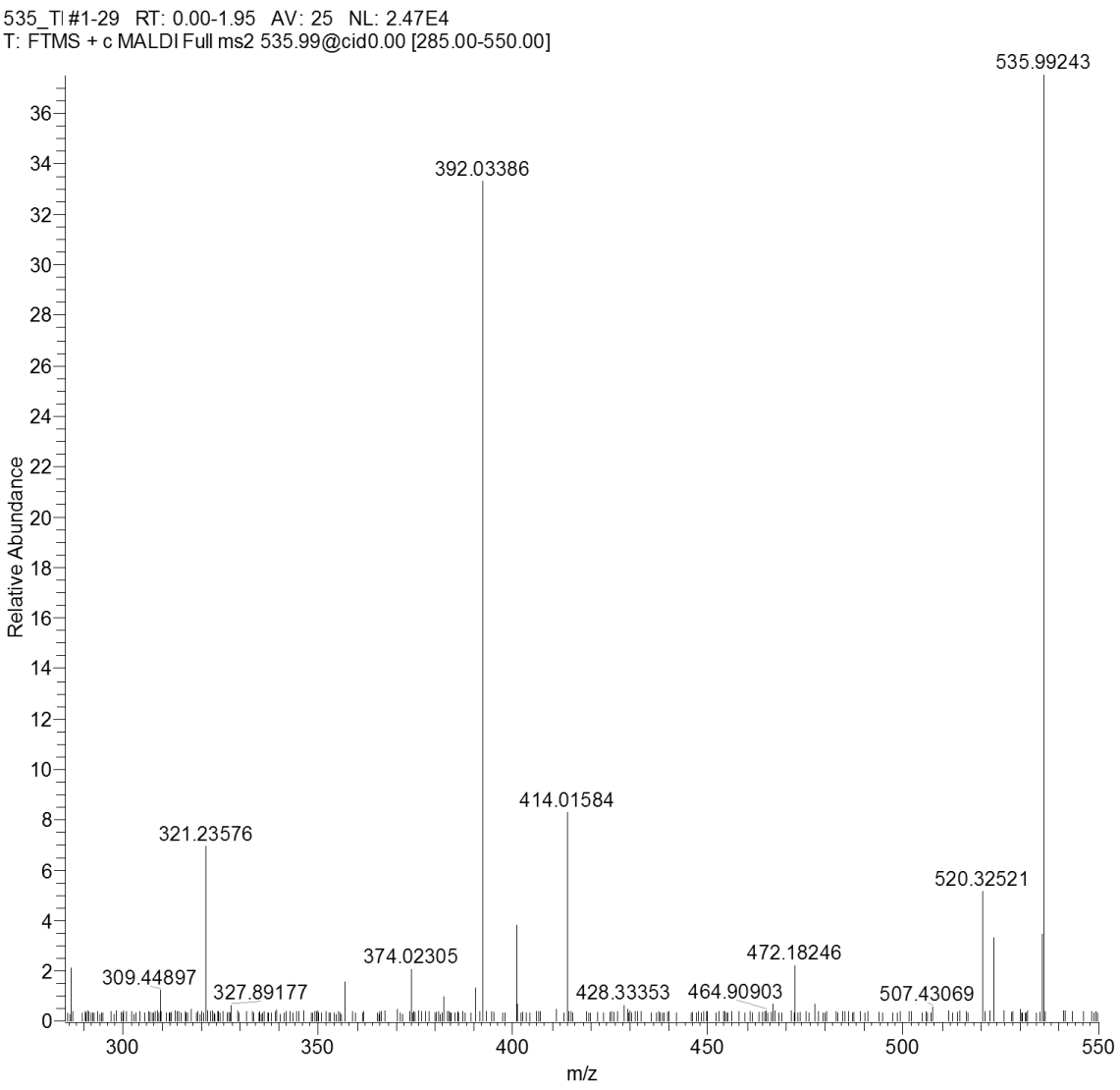

m/z	Intensity	Relative	m/z	Intensity	Relative
286.9062	526.7	2.13	523.194	351.4	1.42
357.0336	322.2	1.3	523.2118	818.9	3.31
357.0423	391.6	1.58	535.7702	848.7	3.43
374.0231	513.5	2.08	535.9924	24710.4	100
390.2412	323.7	1.31			
392.0339	8228.1	33.3			
414.0158	2043.3	8.27			
472.1825	550.7	2.23			
472.1961	464	1.88			
520.3252	1269.3	5.14			

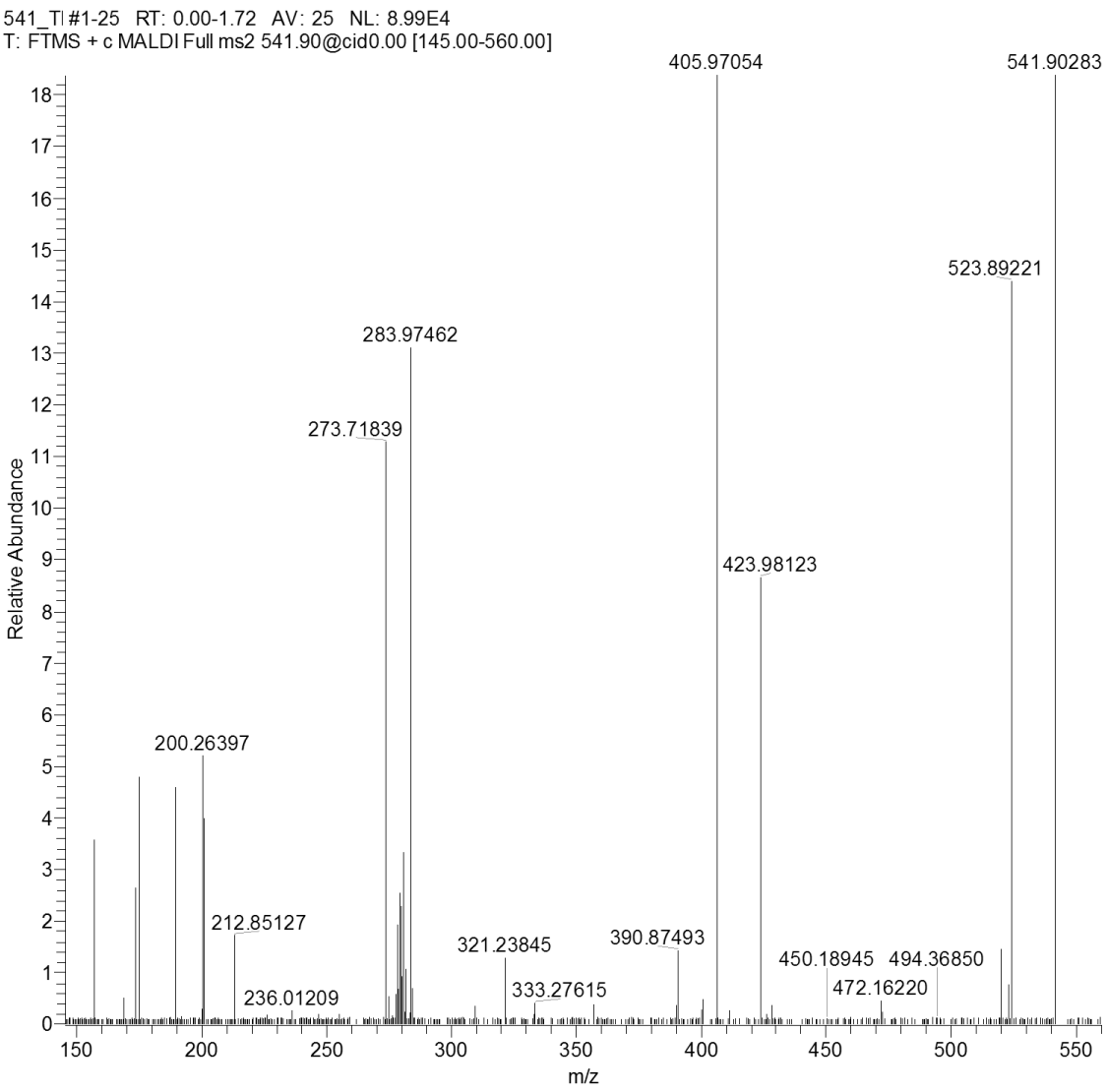

m/z	Intensity	Relative
156.88488	3193.5	3.55
174.89542	4299.3	4.78
280.75804	2986.9	3.32
283.97462	11761.3	13.09
405.97054	38771.1	43.15
423.98123	7779.5	8.66
523.89221	12919	14.38
541.90283	89858.9	100

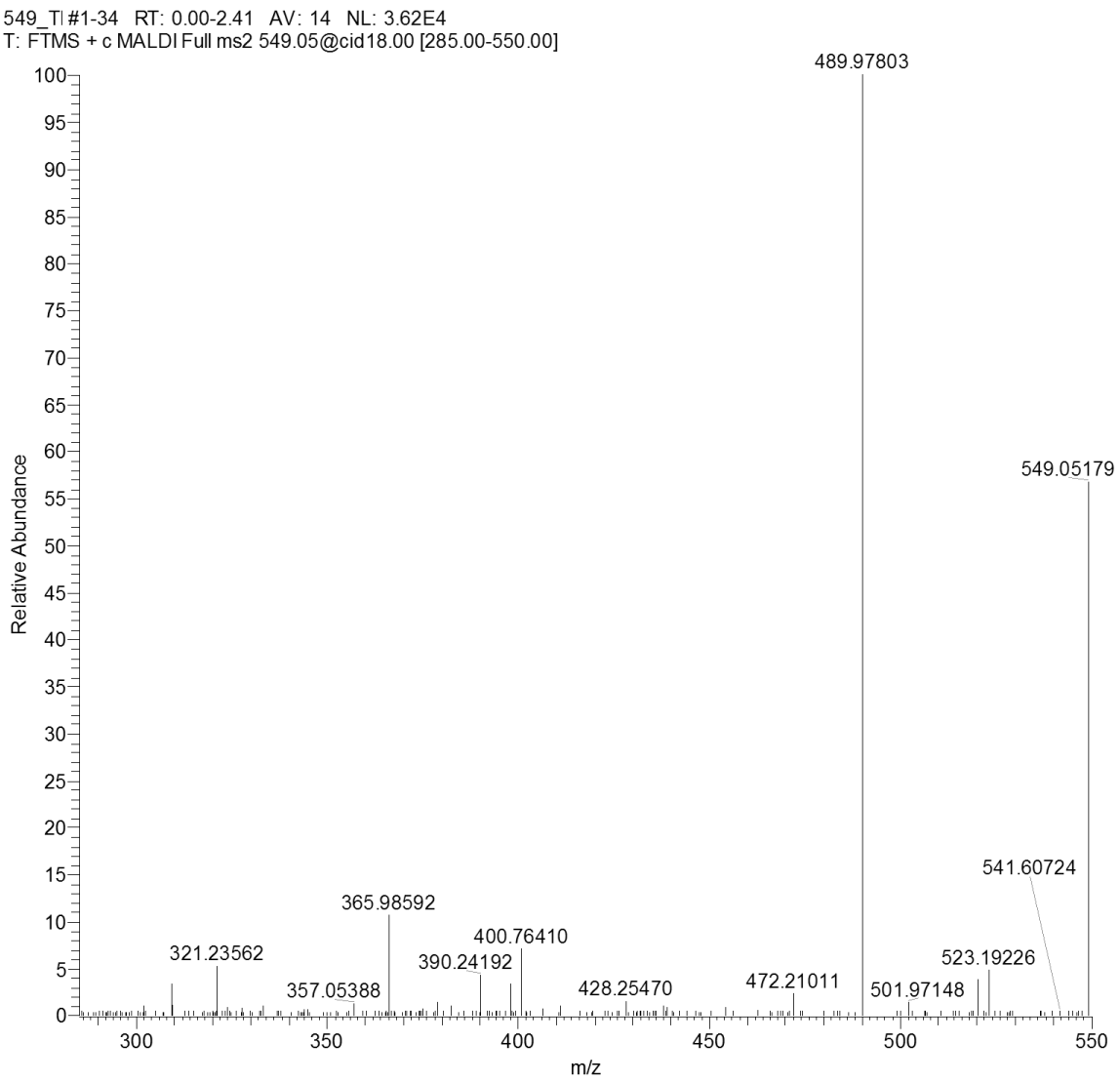

m/z	Intensity	Relative	m/z	Intensity	Relative
309.28202	1201.9	3.32	489.97803	36228.7	100
309.30074	760.8	2.1	501.97148	500.3	1.38
365.98592	3867.5	10.68	520.3451	1374.5	3.79
390.24192	1538.8	4.25	523.19226	1729.1	4.77
398.01176	1244.9	3.44	549.05179	20561.2	56.75
401.05606	640.9	1.77			
428.2547	548.6	1.51			
428.2975	540.7	1.49			
472.14456	589.3	1.63			
472.21011	832.6	2.3			

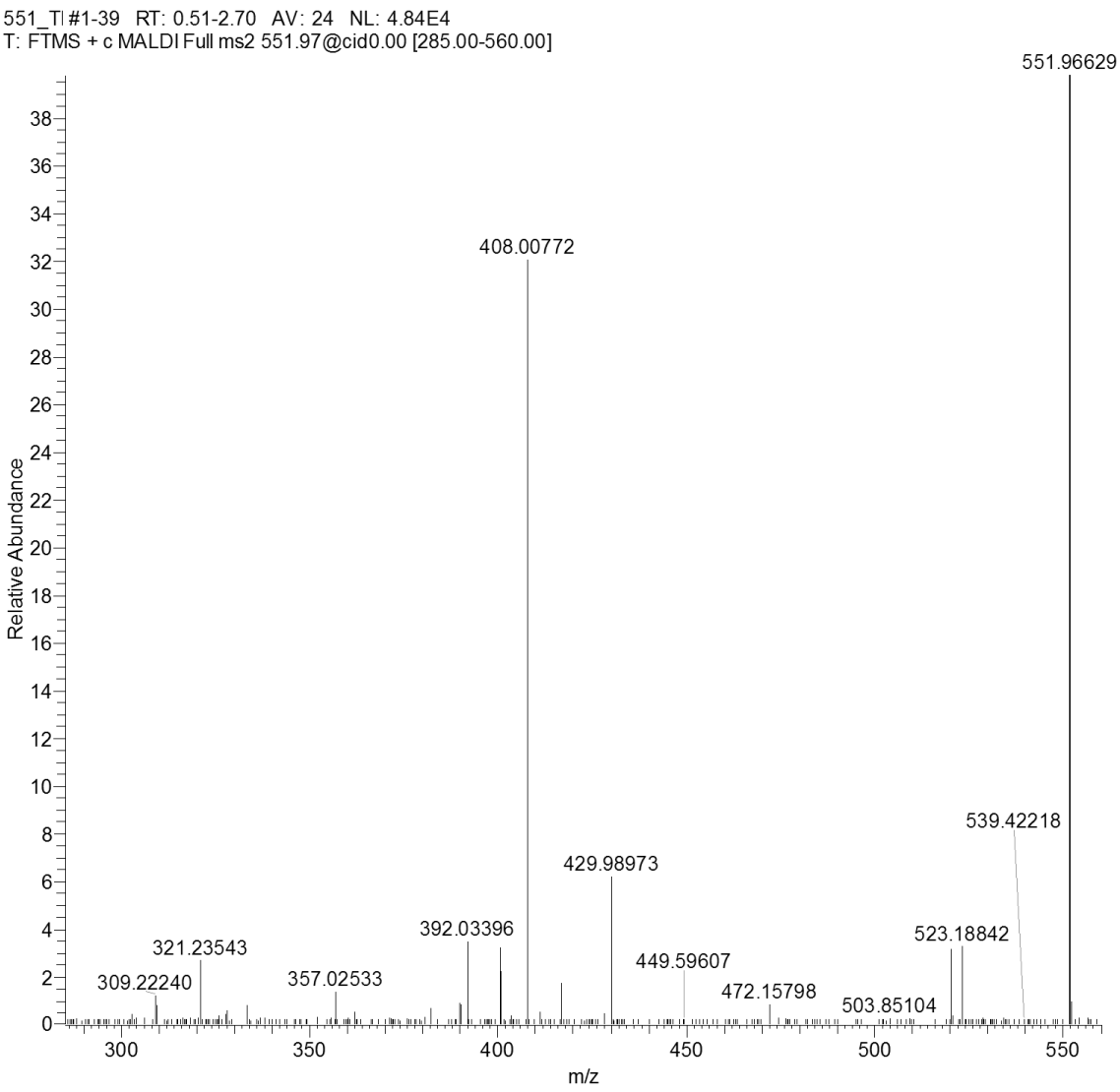

m/z	Intensity	Relative	m/z	Intensity	Relative
309.2224	583.5	1.2	551.5029	33513.5	69.19
309.2339	533.5	1.1	551.6313	743.3	1.53
357.0253	662.4	1.37	551.9663	48439.9	100
392.034	1665.8	3.44			
408.0077	15510.4	32.02			
416.9123	822.5	1.7			
429.9897	2988.5	6.17			
520.3287	1528.1	3.15			
523.1452	899.7	1.86			
523.1884	1566.3	3.23			

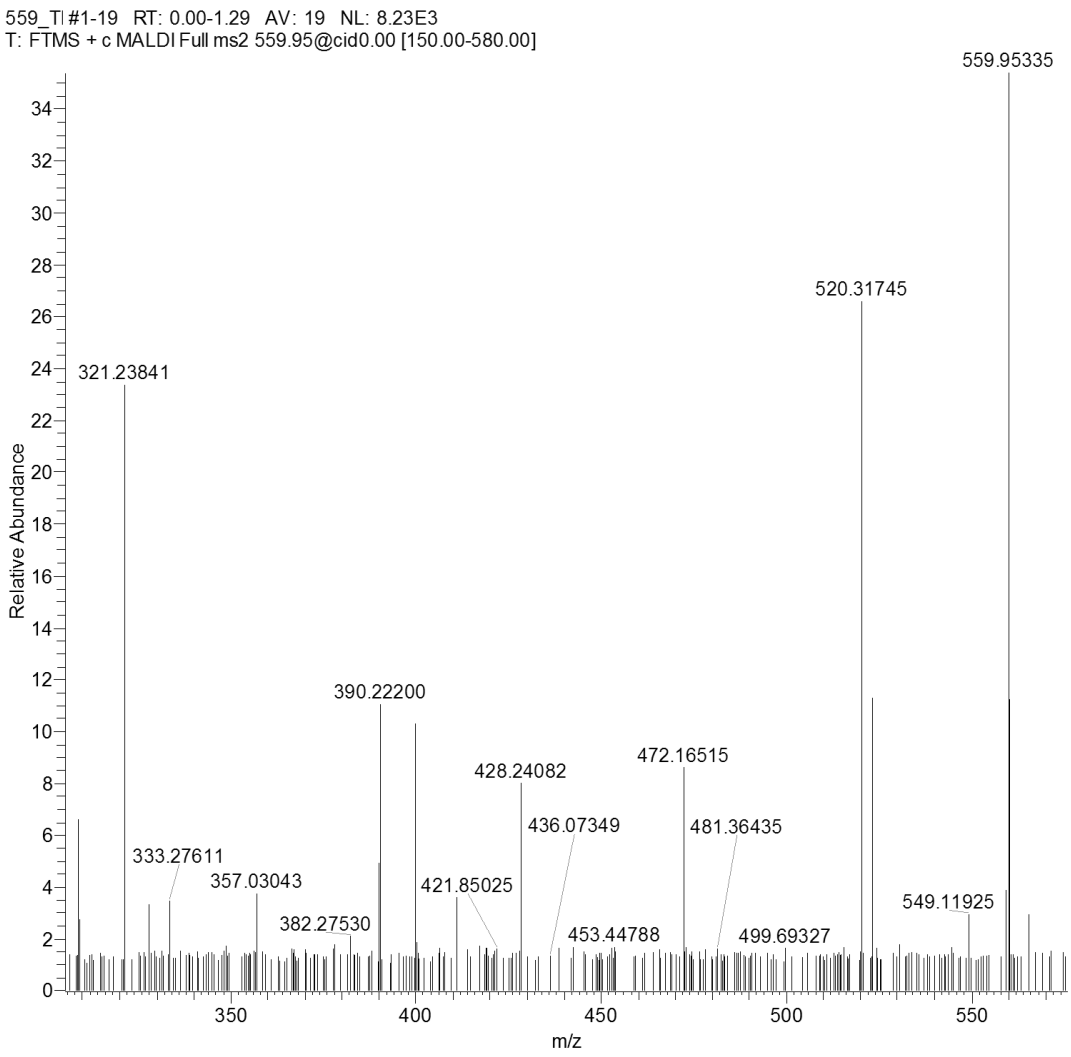

m/z	Intensity	Relative
279.1707	2635.3	19.47
279.4028	1326.6	9.8
279.9628	2187.1	16.16
280.3079	1550.3	11.45
280.7582	2867	21.18
283.9746	13534.7	100
390.222	909.1	6.72
520.3175	2189.2	16.17
523.1571	927.2	6.85
523.1755	912.6	6.74
559.9534	8233.3	60.83

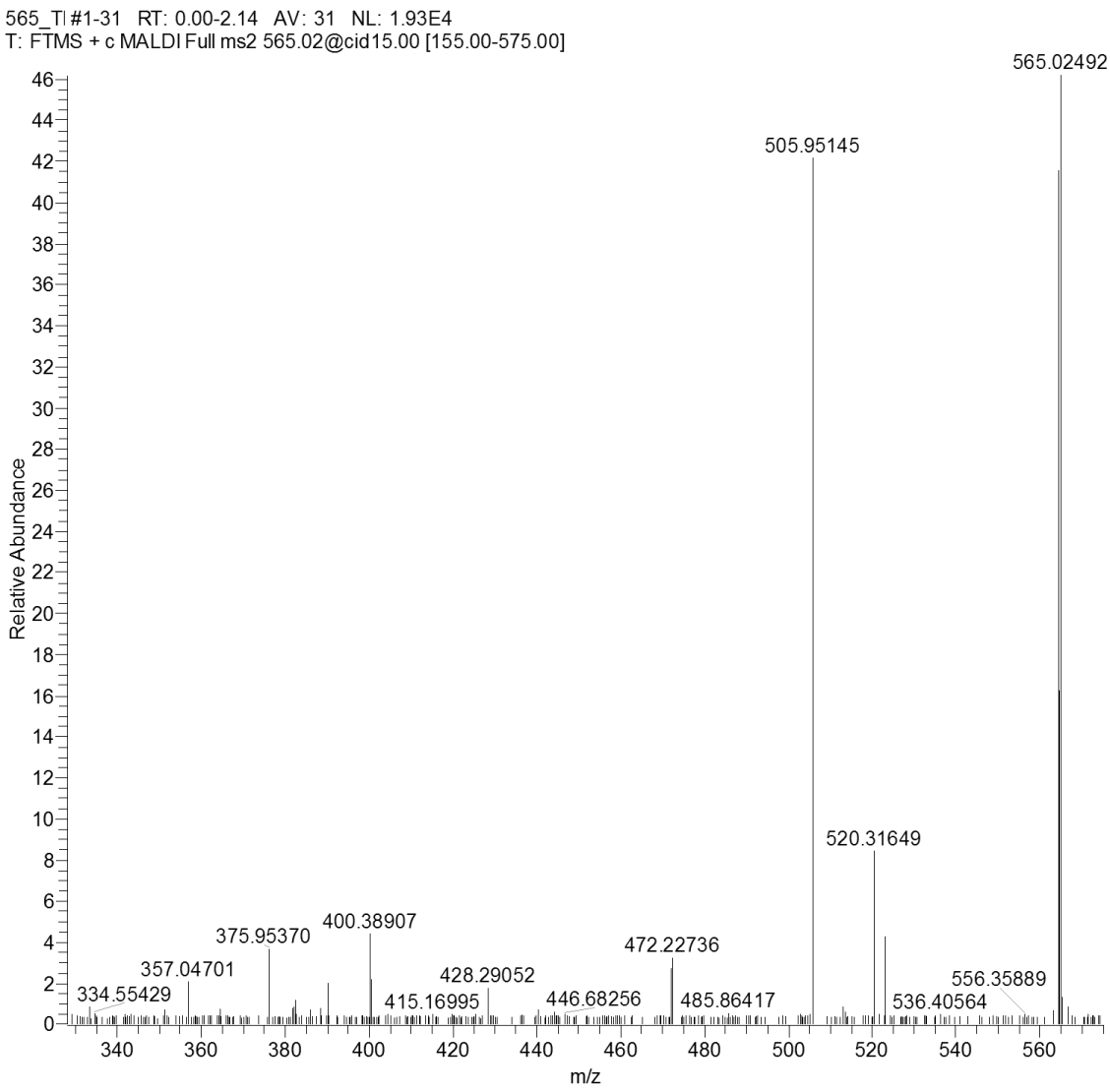

m/z	Intensity	Relative
283.9746	12809.5	66.52
505.9515	8117.8	42.15
520.3165	1616.1	8.39
564.5054	7994.3	41.51
564.5418	3127.2	16.24
564.9963	2435.6	12.65
565.0249	19257.5	100

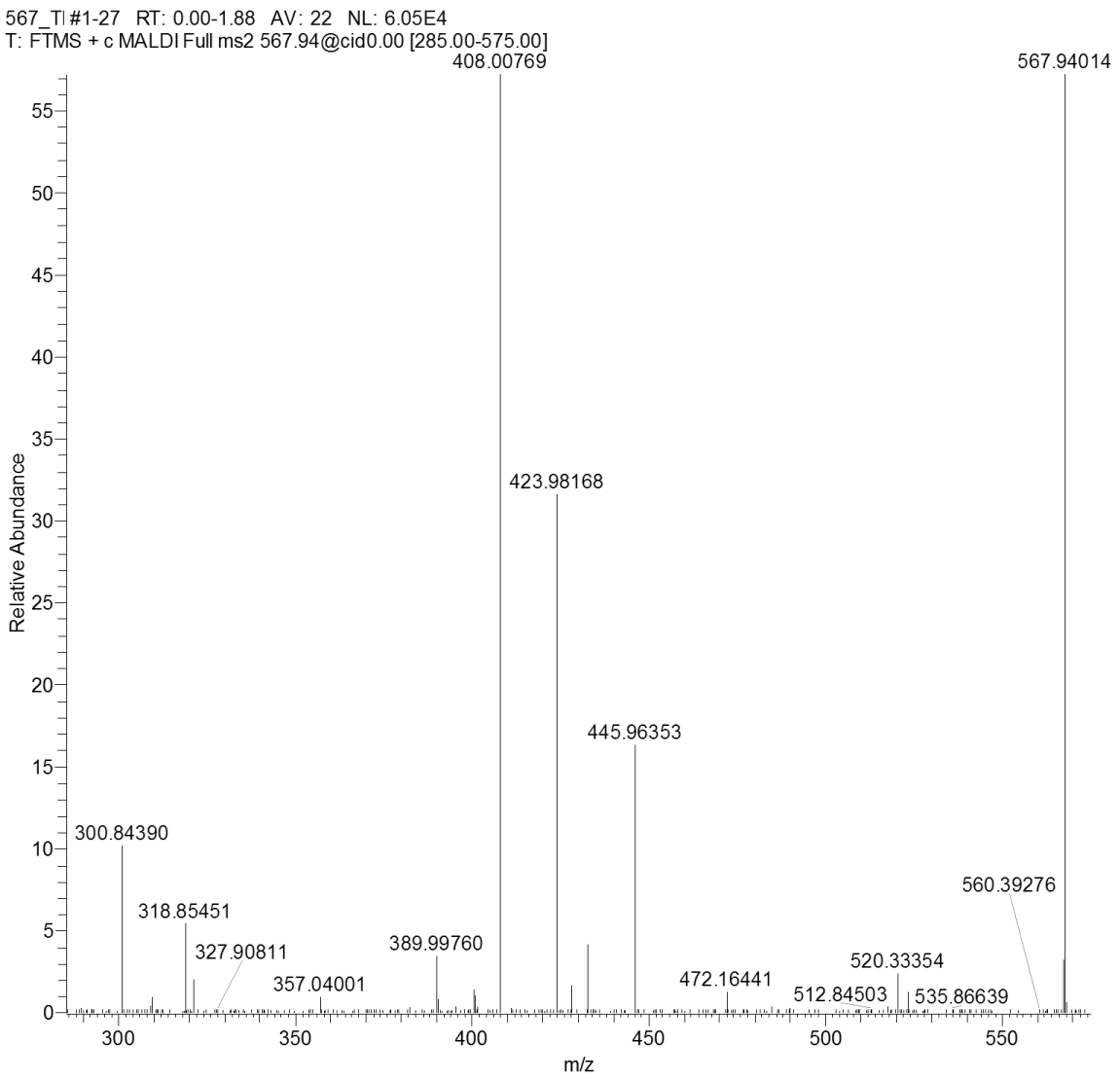

m/z	Intensity	Relative	m/z	Intensity	Relative
300.8439	6156.2	10.18	445.9635	9874.3	16.32
309.2121	562.4	0.93	472.1644	768.8	1.27
318.8545	3264.3	5.4	520.3335	1447.1	2.39
357.04	574.7	0.95	523.1921	765.9	1.27
389.9976	2092.6	3.46	567.5251	1925.3	3.18
390.2359	502.9	0.83	567.9401	60491.9	100
408.0077	34926.1	57.74			
423.9817	19131	31.63			
428.2848	995.3	1.65			
432.8859	2473.5	4.09			

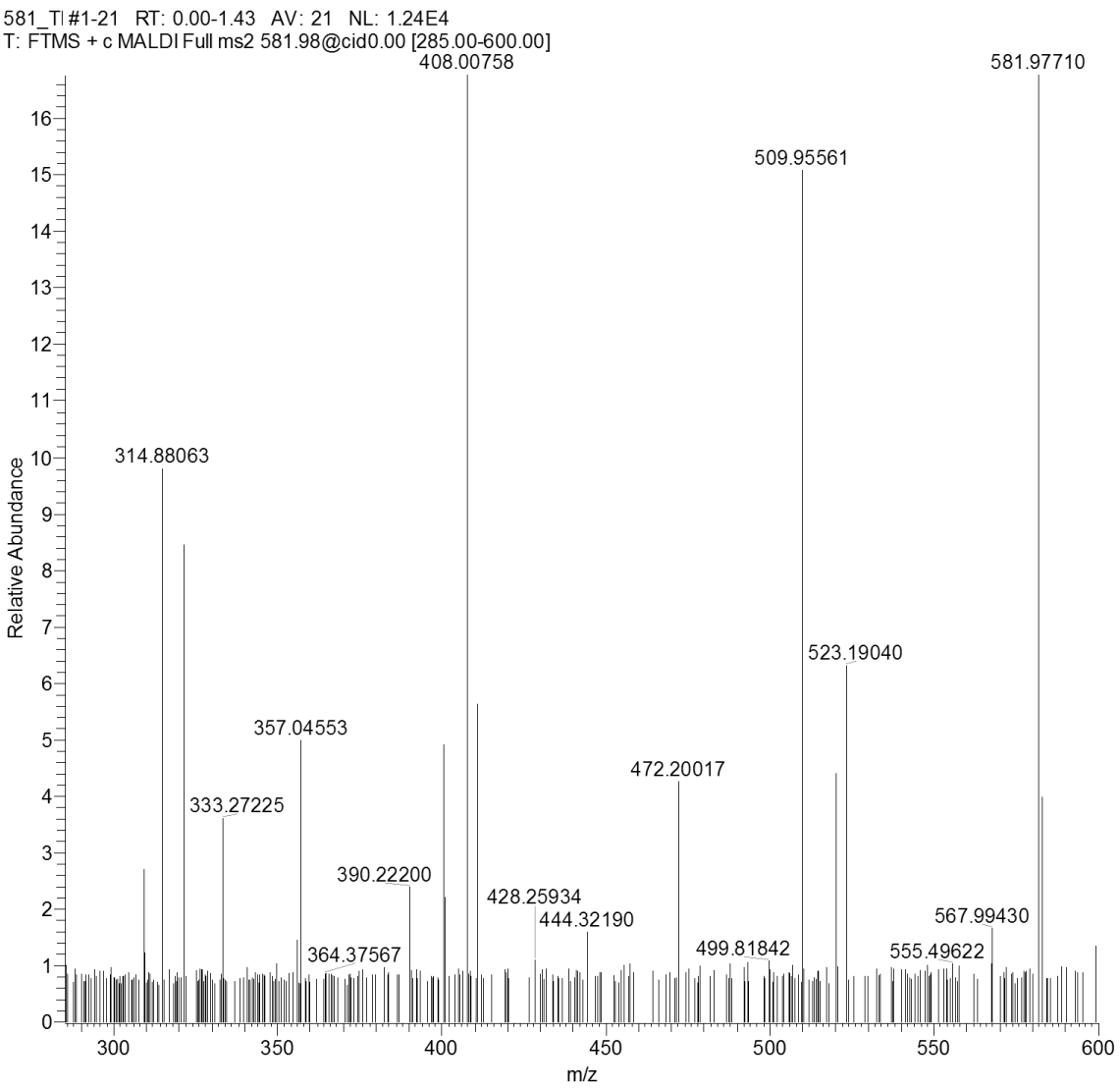

m/z	Intensity	Relative	m/z	Intensity	Relative
314.8806	1211.9	9.79	520.3279	544.8	4.4
333.2723	446.4	3.61	523.1904	780.6	6.31
357.0455	616.5	4.98	581.9771	12372.4	100
408.0076	2150.9	17.38			
411.0343	694.5	5.61			
472.1672	351.5	2.84			
472.1833	400.4	3.24			
472.2002	526.5	4.26			
472.2104	403.4	3.26			
509.9556	1864.9	15.07			

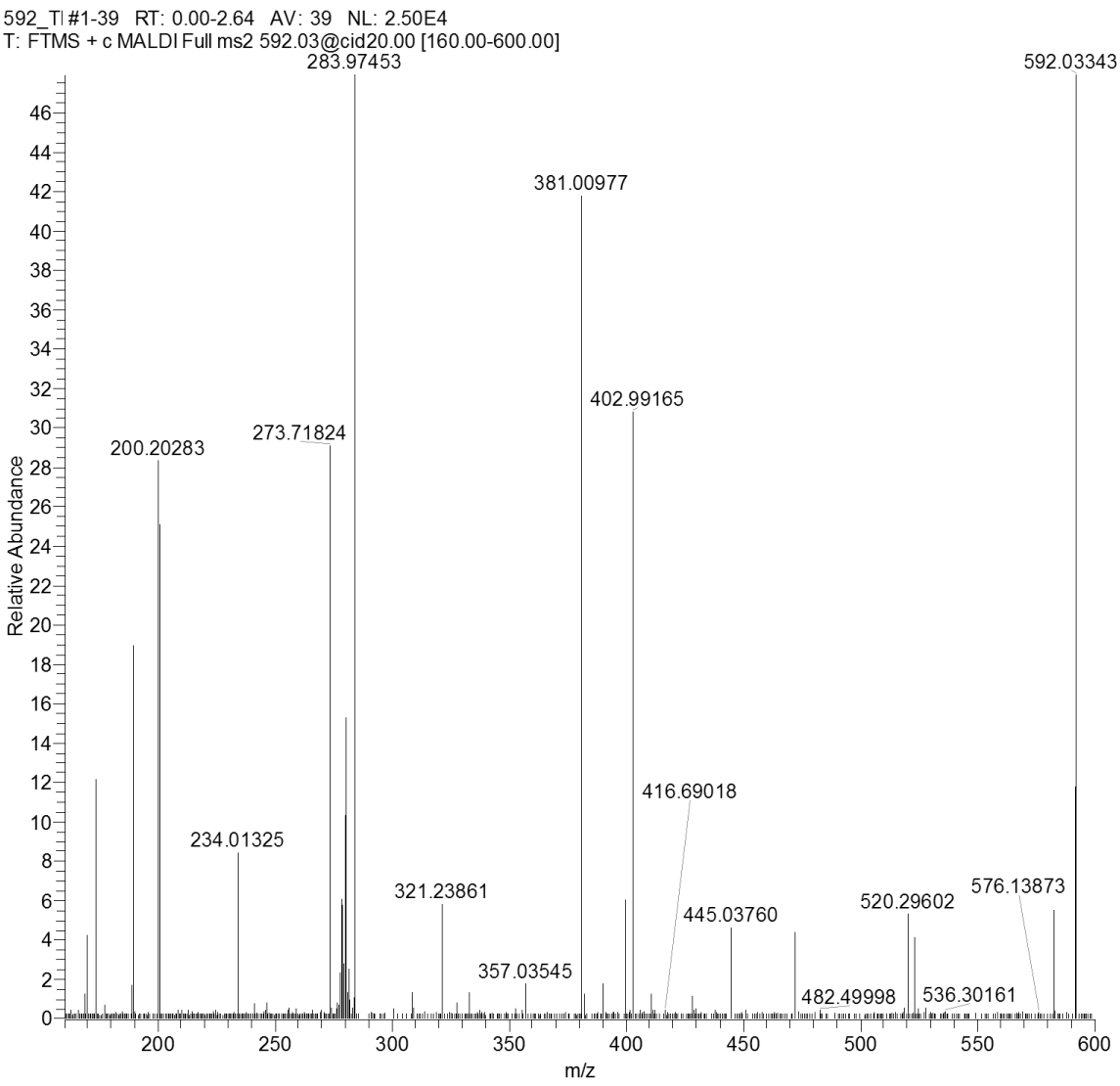

m/z	Intensity	Relative	m/z	Intensity	Relative
169.9854	1052.2	4.21	582.9311	1372.3	5.49
234.0133	2097.6	8.4	591.5335	2934.1	11.74
381.0098	10438.1	41.78	592.0334	24985.4	100
399.6294	1497.1	5.99			
402.9917	7686.7	30.76			
445.0376	1147.3	4.59			
472.1717	1081.8	4.33			
520.296	1318.6	5.28			
523.1728	1023.8	4.1			

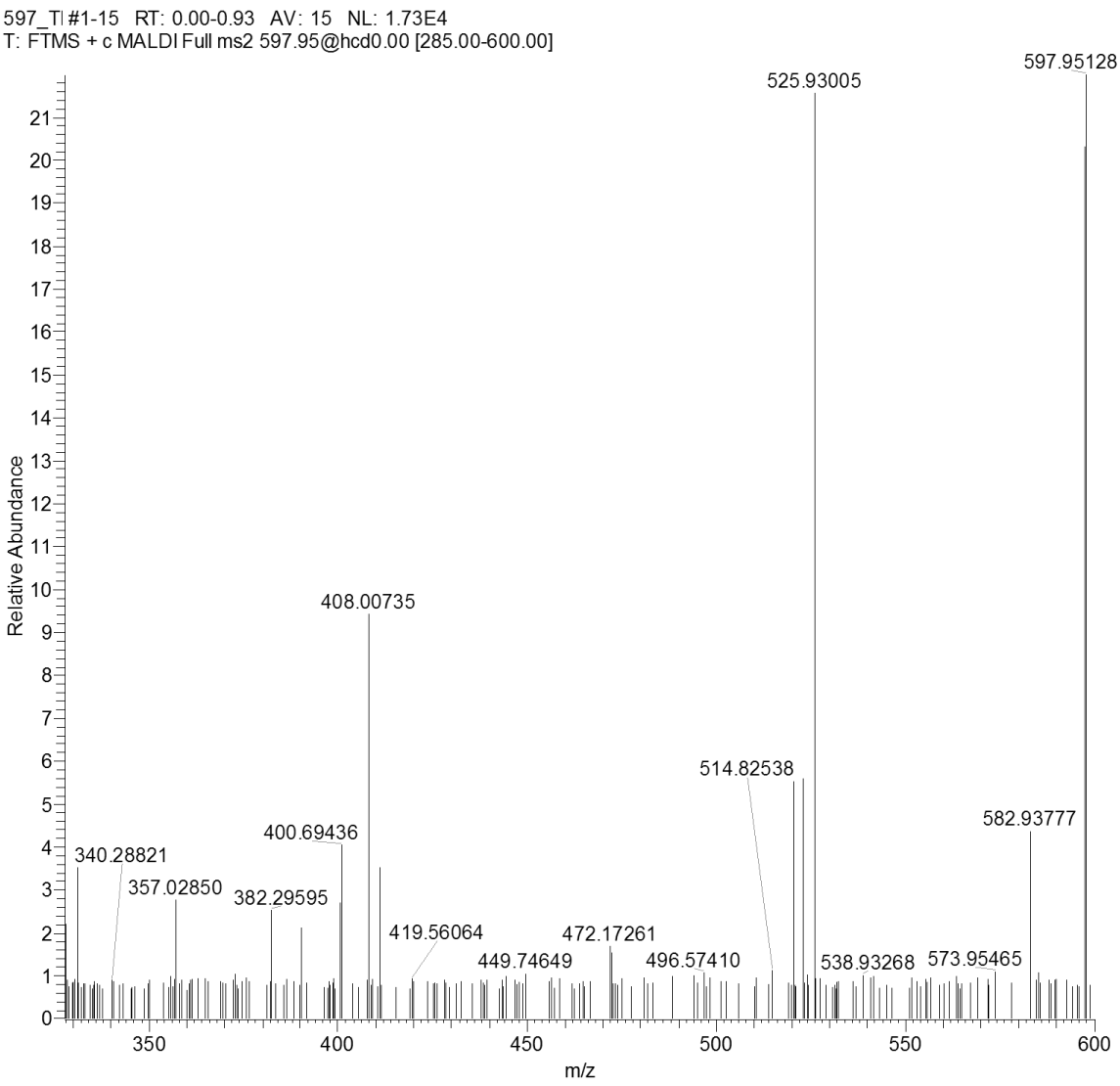

m/z	Intensity	Relative	m/z	Intensity	Relative
327.8993	380	2.2	525.9301	3726.7	21.54
330.8546	606.8	3.51	582.9378	749.9	4.34
357.0285	473.2	2.74	582.9503	566.2	3.27
382.296	436.2	2.52	597.4852	3512.2	20.3
390.2398	362.8	2.1	597.9513	17299.7	100
408.0074	1628.4	9.41			
411.0347	605	3.5			
520.3459	954.9	5.52			
523.1756	375.4	2.17			
523.2028	963.7	5.57			

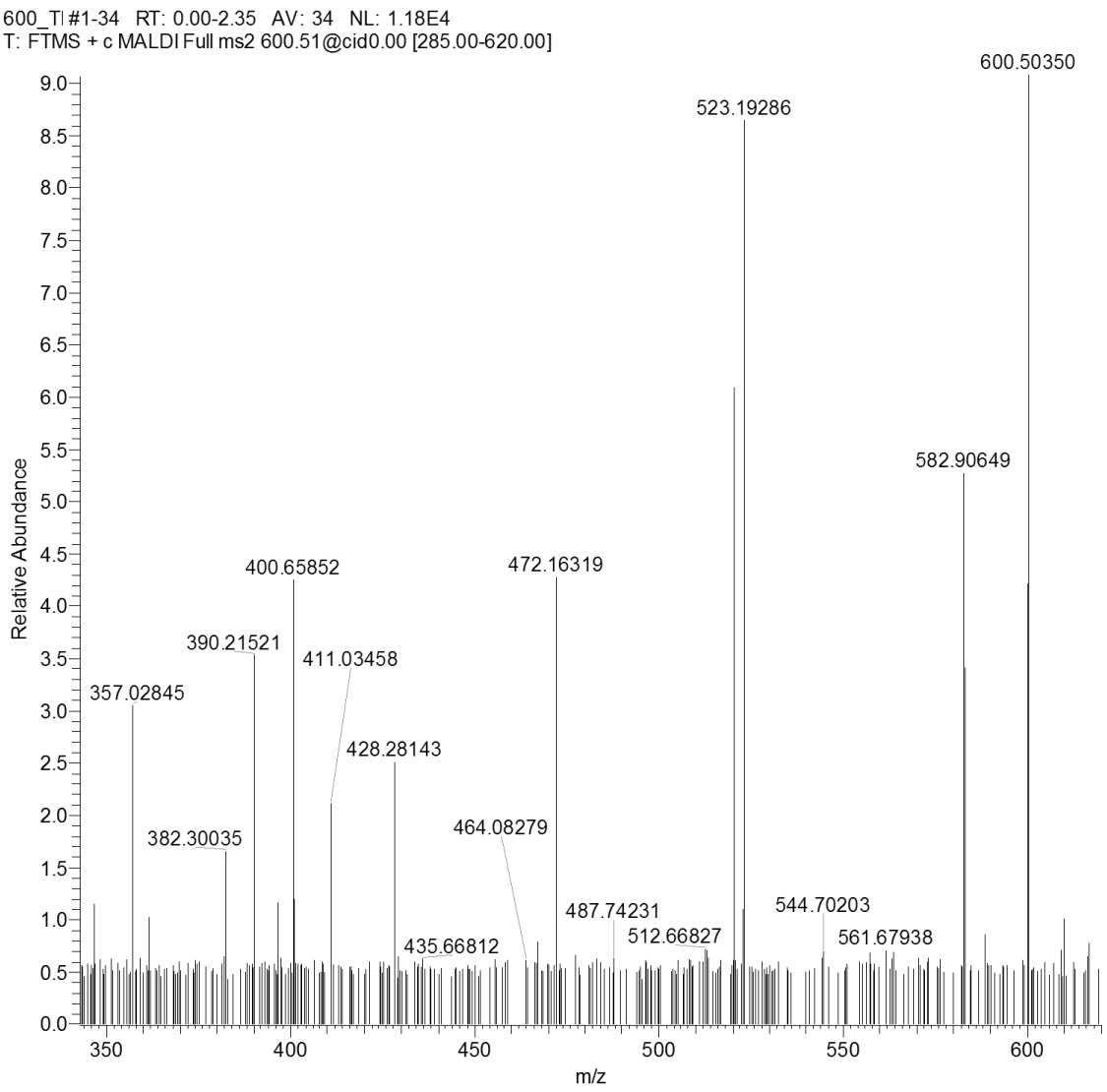

m/z	Intensity	Relative	m/z	Intensity	Relative
357.02845	360.4	3.05	582.90649	622.8	5.27
382.30035	195.6	1.66	582.93794	402.7	3.41
390.21521	416.2	3.52	600.5035	11813.9	100
411.03458	248.9	2.11			
428.28143	296	2.51			
472.16319	504.5	4.27			
520.34671	718.2	6.08			
523.15655	295.7	2.5			
523.18322	375.5	3.18			
523.19286	1020.4	8.64			

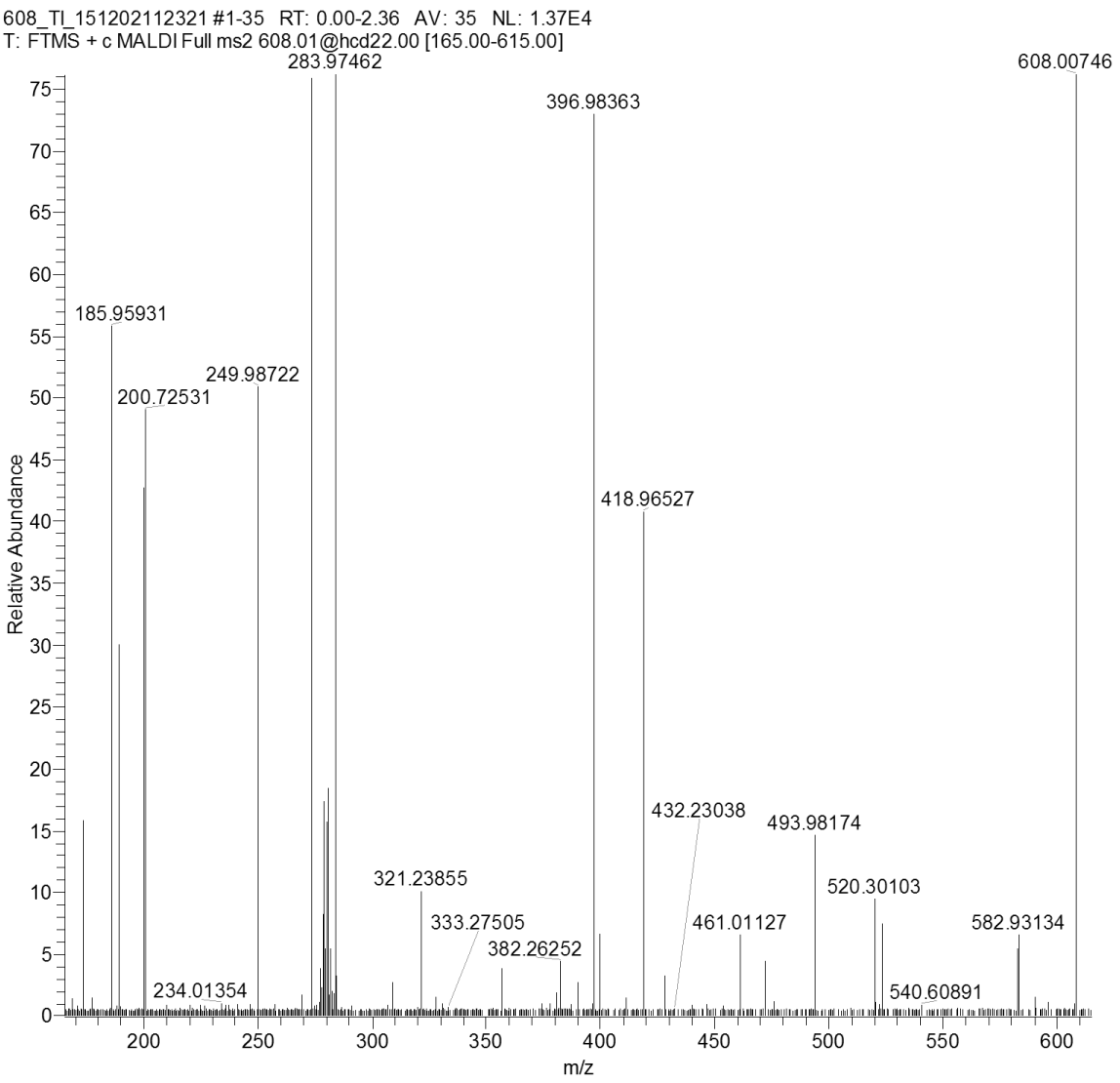

m/z	Intensity	Relative	m/z	Intensity	Relative
185.9593	7621	55.72	493.9815	7335.3	10.86
249.9871	1687.5	2.5	589.9817	1950.3	2.89
279.1705	2648.4	3.92	608.0076	67522.3	100
279.963	2106.1	3.12			
280.7583	3406.2	5.04			
283.9746	12303.3	18.22			
374.0234	1508.7	2.23			
396.9837	7216.5	10.69			
418.9655	5797.7	8.59			
475.9713	1555.9	2.3			

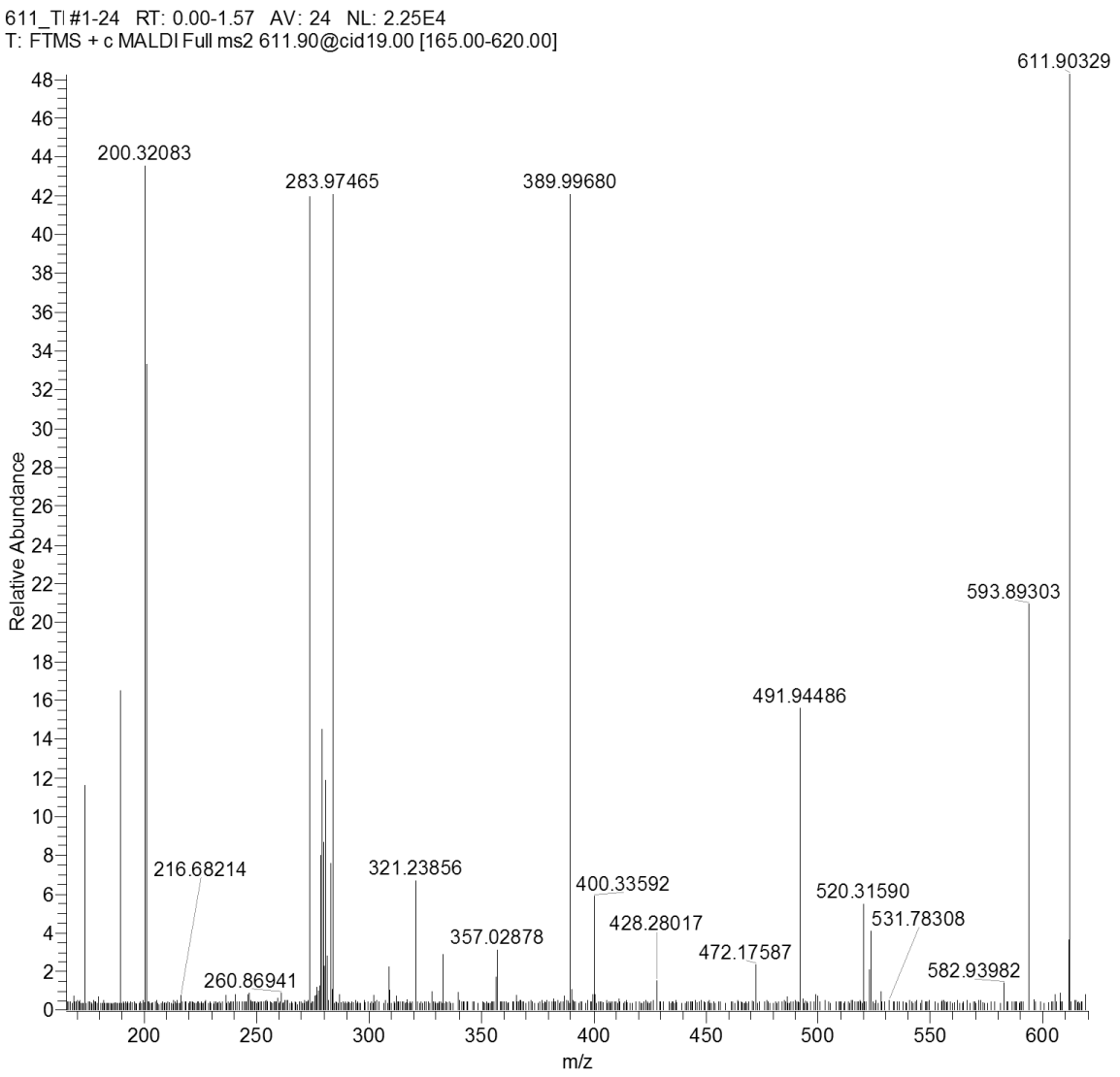

m/z	Intensity	Relative
282.85131	1710.4	7.59
283.97465	9472.6	42.05
389.9968	9465	42.01
491.94486	3496.3	15.52
520.3159	1224	5.43
523.17058	919.5	4.08
593.89303	4707	20.89
611.90329	22528.4	100

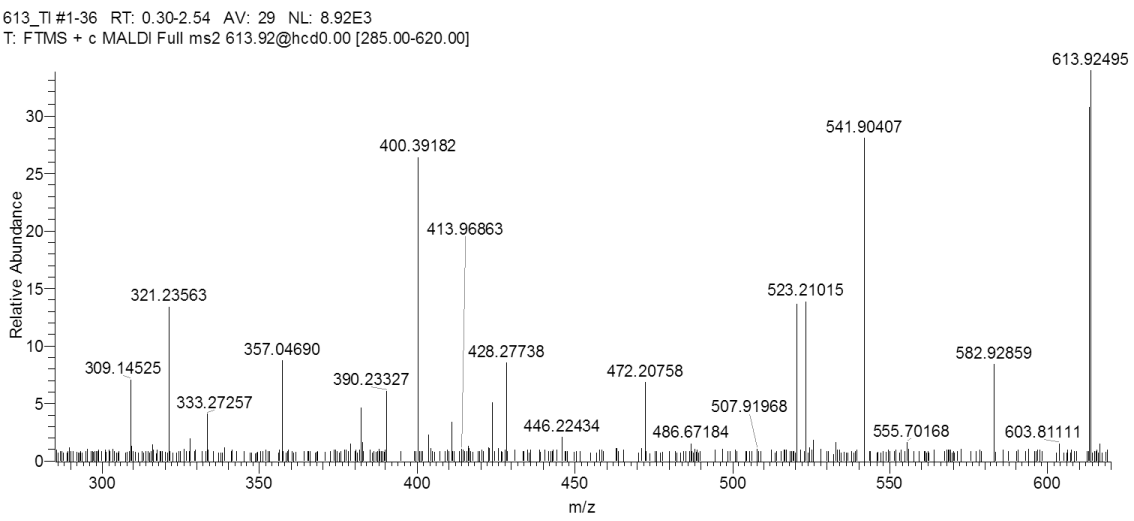

m/z	Intensity	Relative	m/z	Intensity	Relative
309.1257	511.2	5.73	472.1624	377.6	4.23
309.1453	628.1	7.04	472.2076	612.2	6.86
309.1603	425	4.76	486.6718	129.8	1.45
309.1806	373.4	4.18	520.3042	1210.8	13.57
309.2033	152.8	1.71	523.2102	1234.2	13.83
309.2903	111.1	1.25	525.5796	160.4	1.8
315.8688	122.2	1.37	532.9509	143.4	1.61
327.9261	173.9	1.95	541.9041	2495.9	27.97
333.2726	357.7	4.01	555.7017	142.5	1.6
357.0205	167.7	1.88	582.9066	177	1.98
357.0342	173.8	1.95	582.9286	742.6	8.32
357.0469	772.9	8.66	582.9571	204.7	2.29
379.0714	131.6	1.47	582.9775	273.9	3.07
382.2639	411.5	4.61	603.8111	137.5	1.54
382.5149	146.1	1.64	613.5178	2731.3	30.61
390.2333	537.9	6.03	613.5704	1480.6	16.59
390.254	253.6	2.84	613.9250	8923.9	100
403.5728	198.6	2.23			
411.0334	301.7	3.38			
416.2885	115.8	1.3			
423.8176	164.8	1.85			
423.9817	450.3	5.05			
428.2774	753.8	8.45			
446.2243	182.1	2.04			

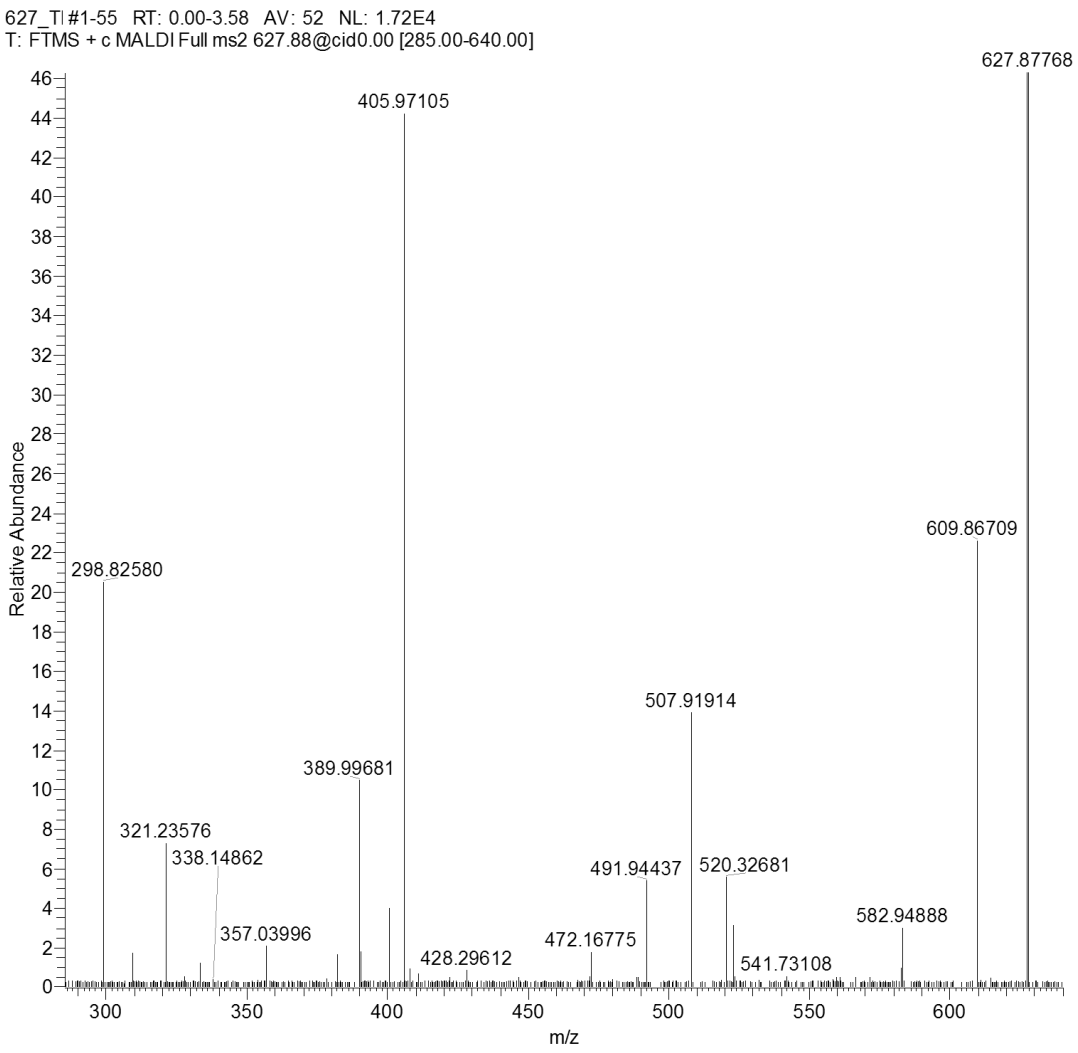

m/z	Intensity	Relative	m/z	Intensity	Relative
298.8258	3525.3	20.47	491.9444	927	5.38
309.1458	289.3	1.68	507.9191	2393.1	13.9
309.1627	277.5	1.61	520.3268	952.5	5.53
333.2727	348.4	2.02	523.1982	527.3	3.06
357.0400	348.4	2.02	523.214	279.6	1.62
382.2792	274.7	1.6	582.9275	301	1.75
389.9968	1801.5	10.46	582.9489	513.4	2.98
390.2058	282.7	1.64	609.8671	3890.6	22.59
390.2262	303.8	1.76	627.5325	17093.7	99.26
405.9711	7612.7	44.21	627.587	8991.9	52.22
472.1678	297.4	1.73	627.8777	17220.7	100

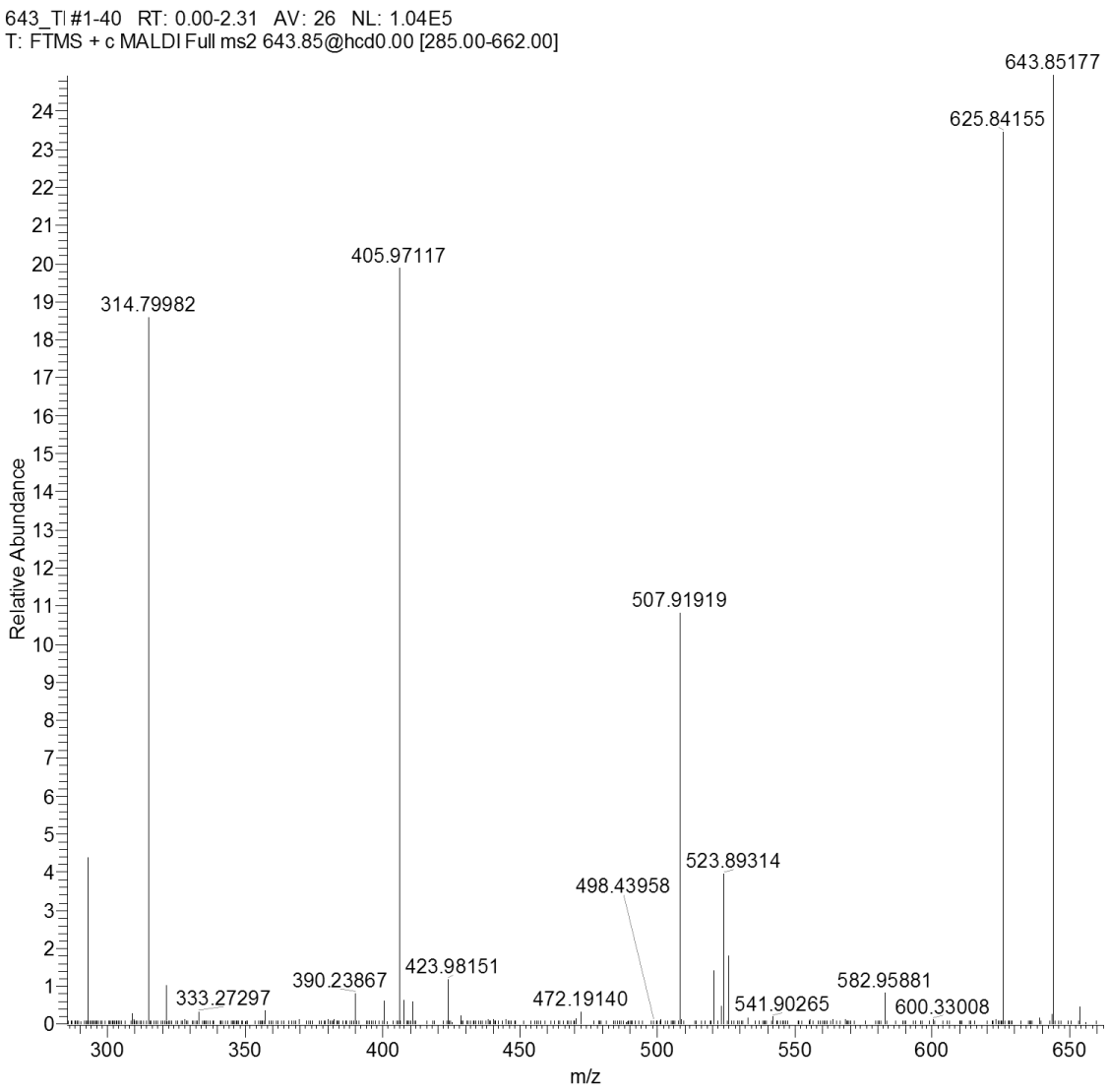

m/z	Intensity	Relative	m/z	Intensity	Relative
292.8178	4557.3	4.39	525.93	1874.5	1.81
314.7998	19279.1	18.57	582.9588	840.7	0.81
390.2387	835.8	0.8	625.8416	24360.3	23.46
405.9712	20597.8	19.84	643.8518	103827.9	100
408.0073	636.7	0.61			
411.0345	591.7	0.57			
423.9815	1214.7	1.17			
507.9192	11233.7	10.82			
520.3073	1439.9	1.39			
523.8931	4093.4	3.94			

659_Tl_a #1-28 RT: 0.00-1.72 AV: 25 NL: 4.76E4
T: FTMS + c MALDI Full ms2 659.83@hcd15.00 [285.00-662.00]

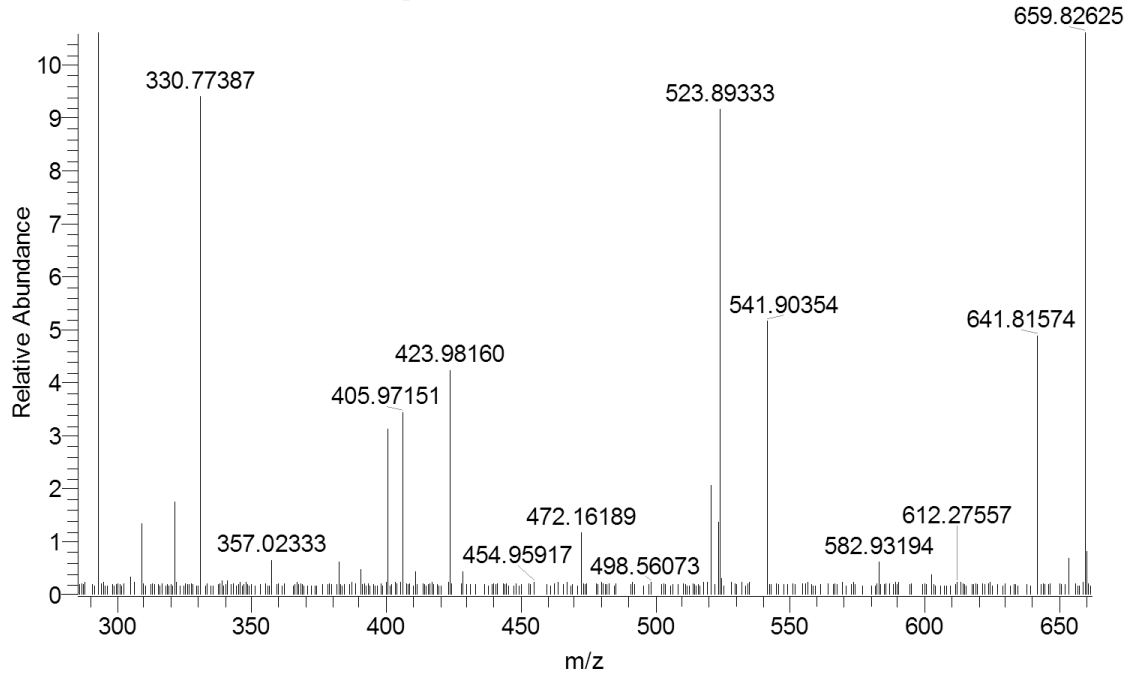

m/z	Intensity	Relative	m/z	Intensity	Relative
292.8179	8620	18.1	520.3181	971.4	2.04
309.0508	308.2	0.65	523.1687	640.4	1.34
309.0558	638.8	1.34	523.196	510.5	1.07
309.0676	200.6	0.42	523.2188	246	0.52
309.0723	474.3	1	523.8933	4362.8	9.16
330.7739	4472.6	9.39	541.9035	2452.3	5.15
357.0233	308.8	0.65	582.9319	295.3	0.62
382.2745	281.8	0.59	582.9486	214.5	0.45
390.2186	201.3	0.42	582.9759	2452.3	5.15
390.2308	228.5	0.48	641.8157	2323.3	4.88
405.9715	1635.2	3.43	653.5098	244.7	0.51
411.0337	210.1	0.44	653.5563	321	0.67
423.9816	2010.9	4.22	653.5874	229.7	0.48
428.2911	198	0.42	659.4993	1228.7	2.58
472.1619	548.5	1.15	659.8263	47618	100
472.1774	430.4	0.9			
472.1945	305.3	0.64			
472.2104	241.3	0.51			

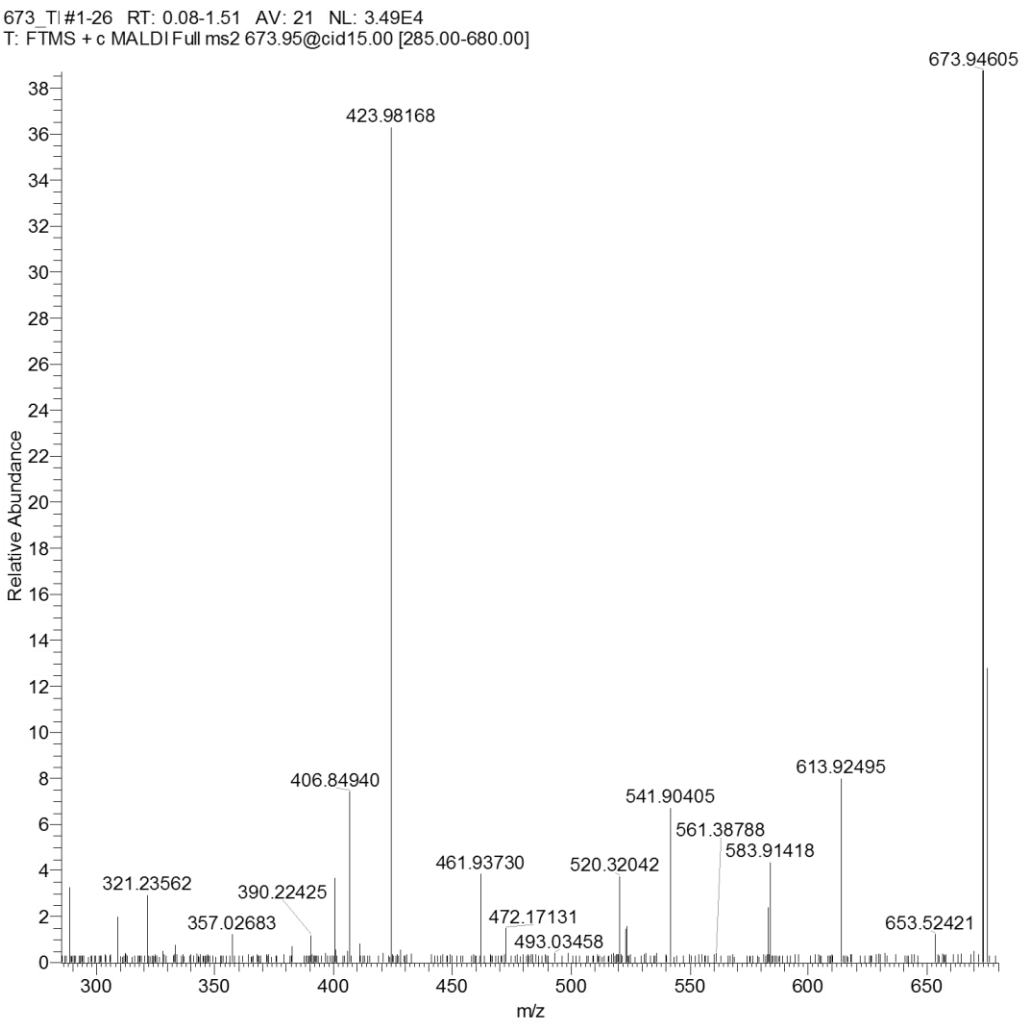

m/z	Intensity	Relative	m/z	Intensity	Relative
288.9278	1137.3	3.26	523.1848	441.2	1.26
309.1379	376	1.08	523.2062	548.6	1.57
309.1539	691.1	1.98	541.9041	2331.4	6.68
357.0268	416.9	1.19	582.9189	557.2	1.6
390.2243	394.2	1.13	582.9515	822.7	2.36
390.2328	336.7	0.96	582.9827	385.9	1.11
406.8494	2579.2	7.39	583.9142	1504.9	4.31
423.9817	12653.2	36.25	613.925	2778.3	7.96
461.9373	1332.3	3.82	653.5242	422.2	1.21
472.1713	511.3	1.46	673.5158	13882.5	39.78
520.3204	1292.9	3.7	673.9461	34901.5	100
523.1731	501.7	1.44			

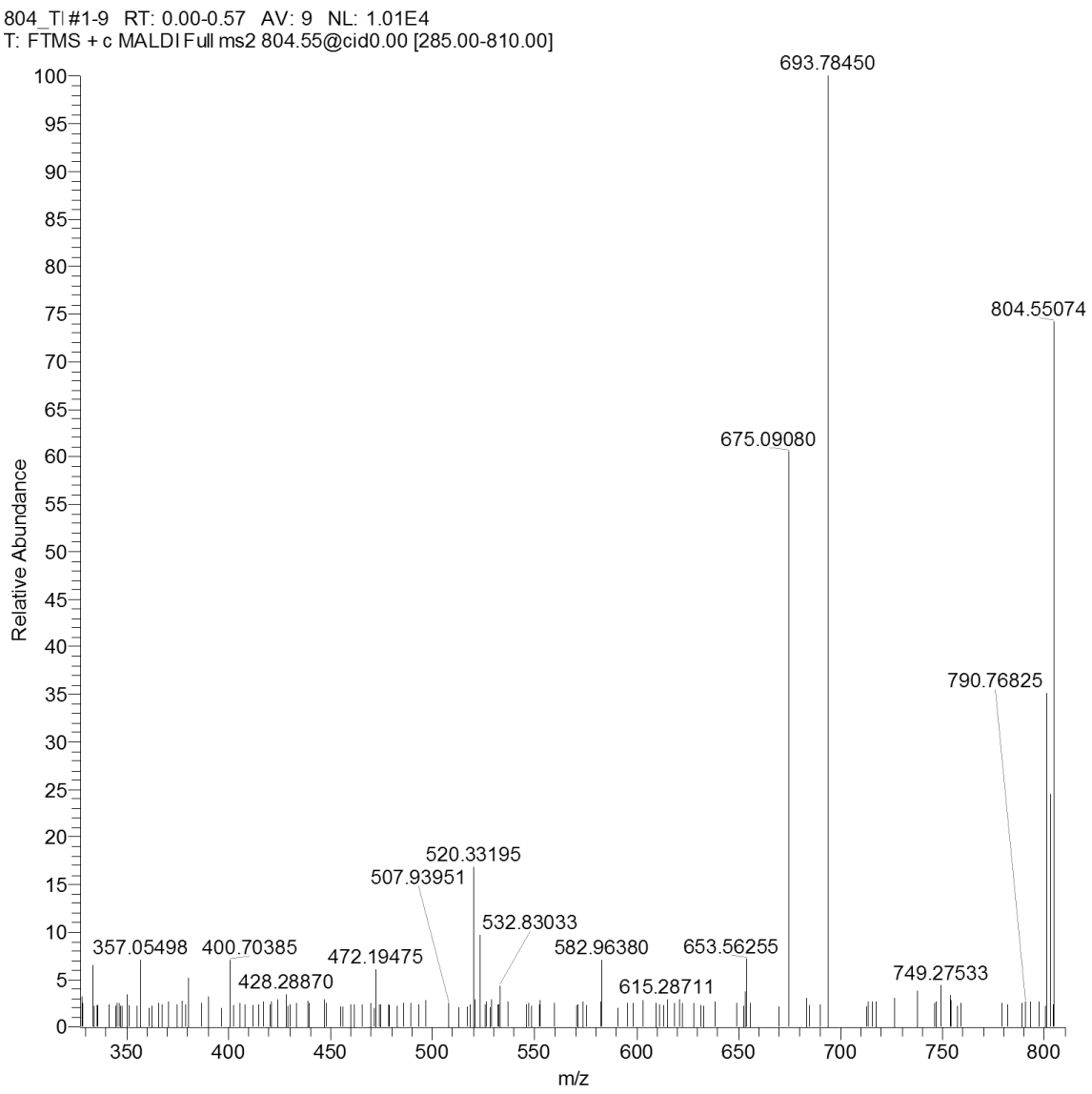

m/z	Intensity	Relative	m/z	Intensity	Relative
309.2335	860.3	8.52	653.5626	716.1	7.09
333.2717	642.2	6.36	675.0908	6109.1	60.5
357.055	706.4	7	693.7845	10097.6	100
380.2371	516.5	5.11	801.2933	3538.4	35.04
472.1948	603.8	5.98	803.0383	2474.1	24.5
520.332	1690.1	16.74	804.4673	7264.5	71.94
523.2012	974.3	9.65	804.4908	884.6	8.76
523.2164	629.8	6.24	804.5507	7486.2	74.14
582.9638	708.1	7.01			

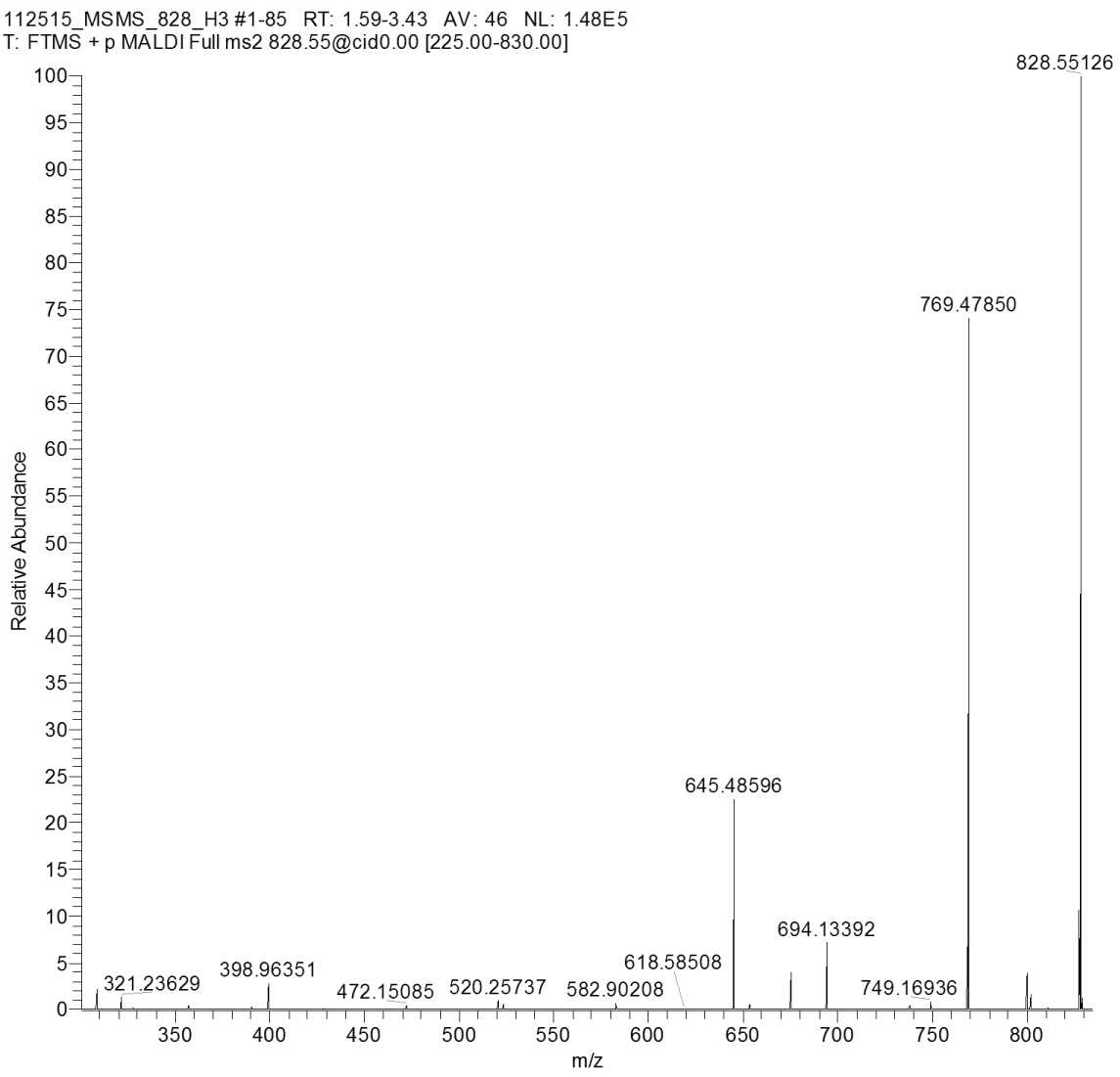

m/z	Intensity	Relative	m/z	Intensity	Relative
308.46936	5284.7	3.78	694.17181	17073.5	12.21
308.47464	5005.8	3.58	749.17102	4651.8	3.33
321.23669	5578.4	3.99	768.50378	4530.7	3.24
398.92715	7089.4	5.07	769.47839	57201.8	40.9
428.26498	3906.3	2.79	800.37823	7711.3	5.51
520.25665	4885.6	3.49	802.36053	5065.7	3.62
523.16986	4403.9	3.15	827.51099	10414.6	7.45
623.50378	15283	10.93	827.53888	6719.3	4.8
645.48566	139850.9	100	828.51715	29924.2	21.4
675.03839	4987.5	3.57	828.55505	20017.2	14.31

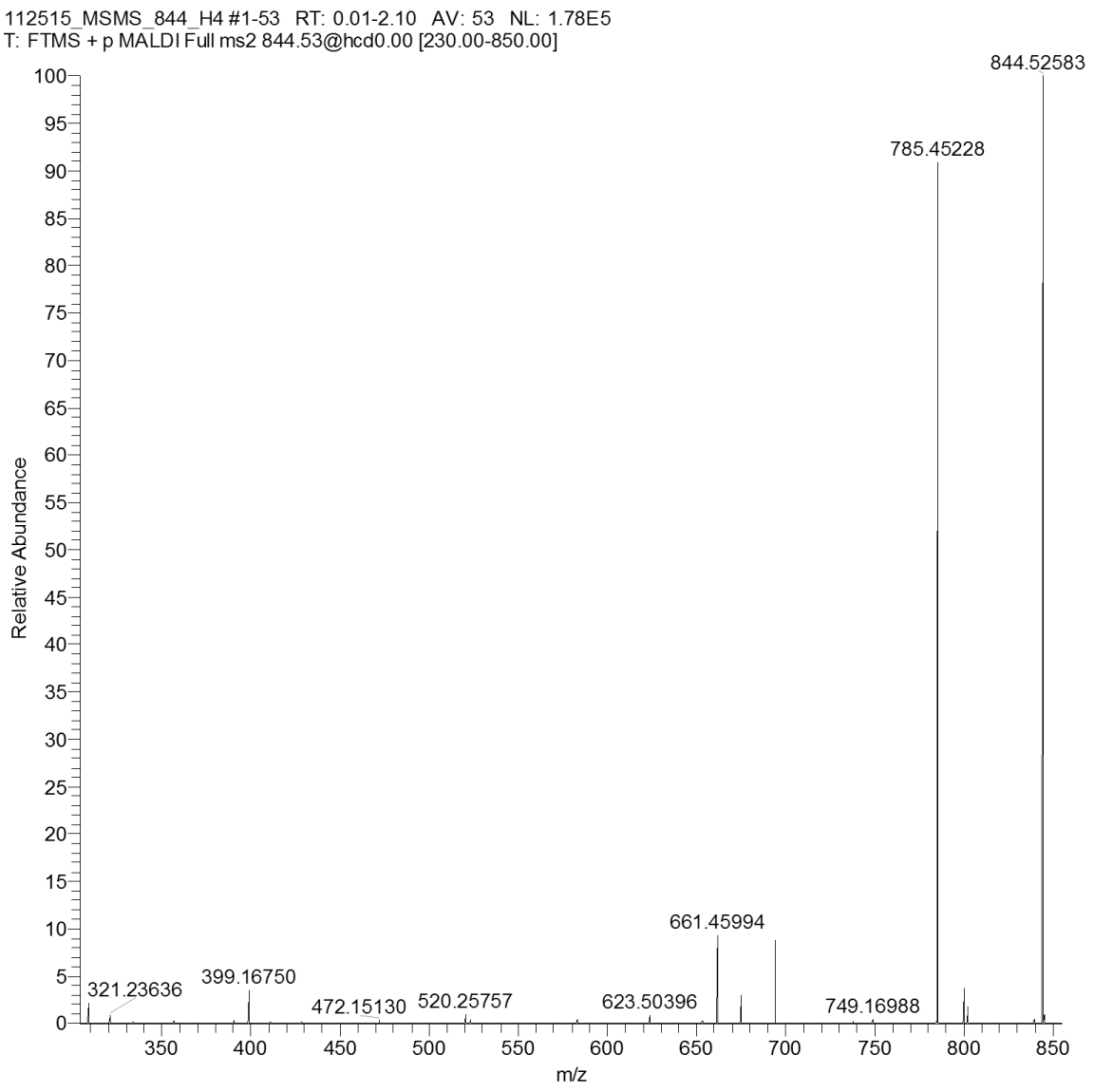

m/z	Intensity	Relative	m/z	Intensity	Relative
308.6648	4018.7	2.2	785.4523	162590.8	89.1
321.2364	1657	0.91	785.5279	985.7	0.54
399.1675	6199.6	3.4	800.2946	6692.2	3.67
520.2576	1749.1	0.96	802.198	3109.1	1.7
623.504	1574.7	0.86	843.5087	23025.5	12.62
661.4599	16713.4	9.16	843.5566	7789	4.27
675.0652	5394.6	2.96	844.4674	14016.4	7.68
694.0628	15839	8.68	844.5258	182481.1	100
749.1699	919.4	0.5			

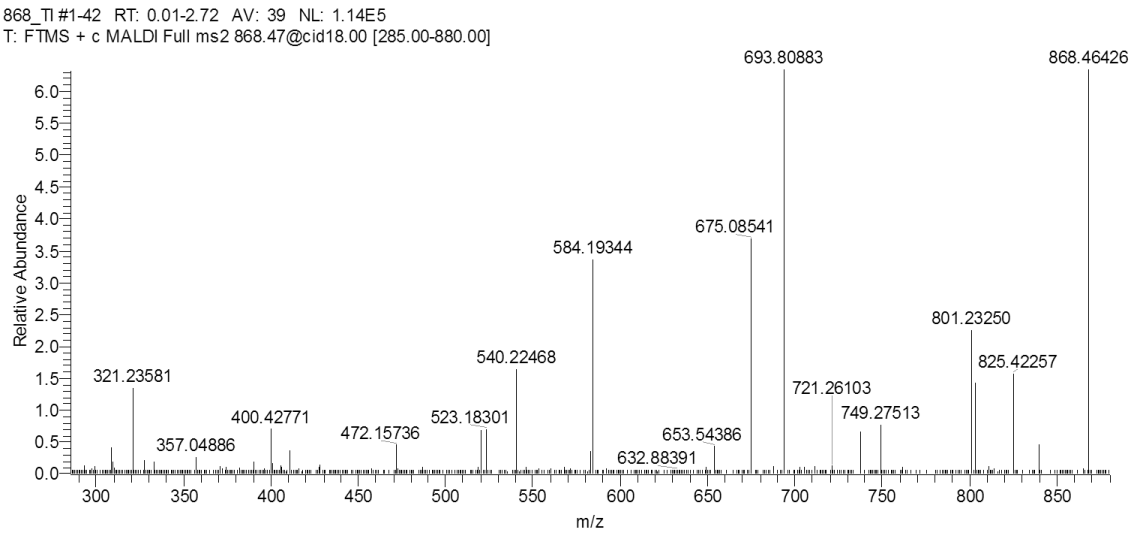

m/z	Intensity	Relative	m/z	Intensity	Relative
308.7908	666.3	4.41	520.2765	685.1	4.54
308.7989	667.4	4.42	523.1198	1005.7	6.66
308.8066	484.4	3.21	523.1647	606.9	4.02
308.8115	433.1	2.87	523.1919	345.7	2.29
308.8154	449.2	2.97	582.83	238.6	1.58
308.8299	517.3	3.43	582.8763	555.9	3.68
308.839	565.8	3.75	653.4572	495.3	3.28
308.8484	579	3.83	653.5031	397.5	2.63
333.2732	274	1.81	675.0686	4118.7	27.27
356.9892	454.7	3.01	693.9403	8175.6	54.14
357.0013	319.9	2.12	737.6731	328.3	2.17
382.2976	240.2	1.59	737.6986	469.6	3.11
390.1759	420.4	2.78	744.551	467.7	3.1
390.1862	401.3	2.66	749.1935	926.7	6.14
399.3829	1979.2	13.11	800.7281	4416.9	29.25
399.4001	1392.4	9.22	802.7185	2996.8	19.84
411.0346	304.6	2.02	839.3129	638.6	4.23
472.1305	508	3.36	867.6524	324	2.15
472.1574	301.4	2	868.4652	15101.9	100

Several *m/z* values were detected in all MALDI-MS/MS spectra and are thought to be only noise. These values include *m/z*: 89, 189, 200, 273, 283, 321, 392, and 400.

Conclusions

While we were able to detect and image many compounds and acquire quality MS/MS information, the databases online could not confidently identify any of the compounds we imaged. Accurate mass MS1 and MS/MS spectra were compared to MetFrag, ChemSpider, PubChem, METLIN, Kegg, LIPIDMaps, HMDB, and MMCD. I hypothesize that these compounds are secondary metabolites, as the MS/MS spectra do not show the characteristic fragmentation of the head group that typically indicates lipids.

The lipid extraction from electric organ tissue was used for MS/MS analysis with ESI and with MALDI. Very different classes of compounds were detected from the sample extract compared to the intact tissue sections with MALDI. Running the extract with LC-MS/MS resulted in very poor chromatography when using a C18 column. We detected strong polymer signal with LC-MS that could have been due to some sort of contamination and can be looked at further. Additionally, the chromatography needs to be completely optimized before moving forward with LC-MS analysis. HILIC chromatography may provide better separation and improved chromatography.

Acknowledgements

Thank you to Matt Huppert for aiding in the sample preparation for the MALDI-Imaging and LC-MS/MS. Thank you to Dr. Lindsay Traeger and Professor Mike Sussman for providing the electric eel tissue. The MALDI-Orbitrap instrument was purchased through an NIH shared instrument grant (NCRR S10RR029531). E.G. acknowledges an NSF Graduate Research Fellowship (DGE-1256259).

References

1. Gotter, A. L.; Kaetzel, M. A.; Dedman, J. R., Electrophorus Electricus as a Model System for the Study of Membrane Excitability. *Comparative biochemistry and physiology. Part A, Molecular & integrative physiology* **1998,** *119* (1), 225-241.

2. Bligh, E. G.; Dyer, W. J., A Rapid Method of Total Lipid Extraction and Purification. *Canadian journal of biochemistry and physiology* **1959,** *37* (8), 911-917.

3. Costa, R.; Beccaria, M.; Grasso, E.; Albergamo, A.; Oteri, M.; Dugo, P.; Fasulo, S.; Mondello, L., Sample Preparation Techniques Coupled to Advanced Chromatographic Methods for Marine Organisms Investigation. *Anal Chim Acta* **2015,** *875*, 41-53.

Appendix IV

Mass Spectrometry in Plant-omics

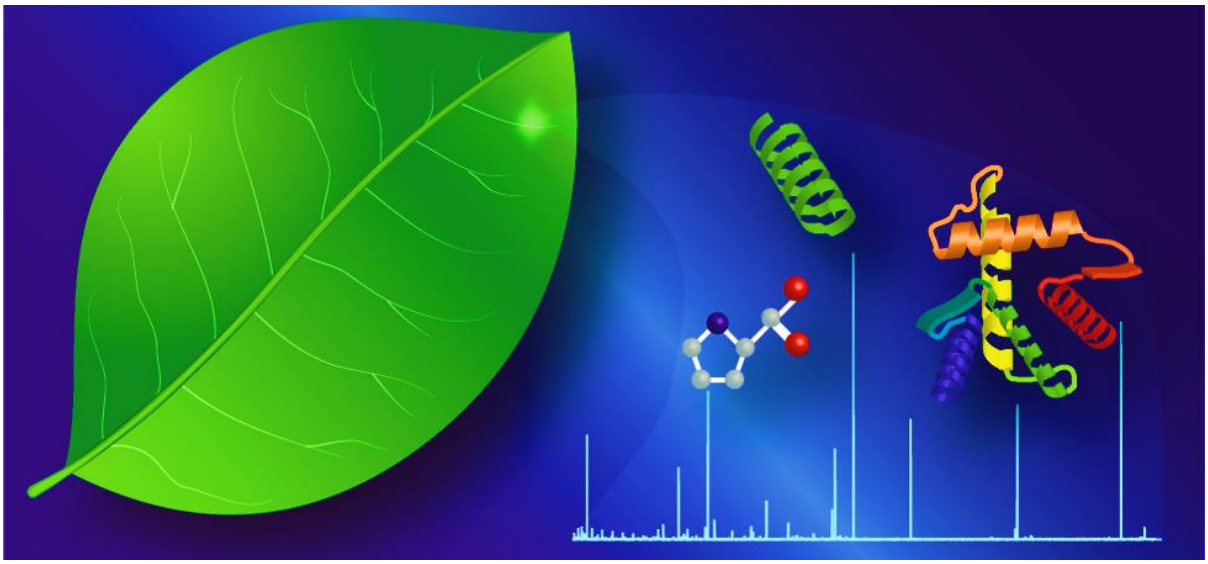

Adapted from **Gemperline, E.**; Keller, C..; Li, L. "Mass Spectrometry in Plant-omics", Analytical Chemistry, (2016) doi:10.1021/acs.acnalchem.5b02938

Abstract

Plant-omics is rapidly becoming an important field of study in the scientific community due to the urgent need to address many of the most important questions facing humanity today with regard to agriculture, medicine, biofuels, environmental decontamination, ecological sustainability, etc. High performance mass spectrometry is a dominant tool for interrogating the metabolomes, peptidomes, and proteomes of a diversity of plant species under various conditions, revealing key insights into the functions and mechanisms of plant biochemistry.

Plant-omics

Plant science is one of the oldest[1-3] areas of scientific research but is still an extremely important and rapidly developing area of study. Plant life plays an essential role in many of today's challenging issues. For example, growing robust crops with increased yield not only affects the agriculture industry, it also plays a role in environmental sustainability and contamination. Non-food crop plants are being studied and developed as biofuels for sustainable energy.[4-7] Additionally, the ability of plants to withstand attacks from pests and pathogens in their environment is being studied in the medical community in light of the rise of drug-resistant strains of infections.[8-11] Plant-derived natural products provide a potentially rich source of drug candidates and target compounds for drug discovery and development.[12-17] Research on plants is essential to finding solutions to these major issues, and the key to finding viable solutions lies in integrated, holistic studies and collaboration between scientists.

In molecular biology, the term "–ome" refers to the study of the global or total changes in an organism's DNA or genes (genome), proteins (proteome), metabolites (metabolome), etc. -Omics (genomics, proteomics, metabolomics, etc.) has come to refer generally to the study of large, comprehensive biological datasets focused on investigating changes in these -omes. Therefore, plant-omics can be described as a holistic study of any or all –omes, specifically in plants. **Figure 1** depicts the different classes of -omics and the interactions between them. Multi-omics (i.e. a combination of genomics, transcriptomics, proteomics, peptidomics, and/or

metabolomics) strategies could provide large-scale insights into complex plant systems that could otherwise be misinterpreted if only one –ome was interrogated.

Recent years have seen an explosion of new -omics technologies that have the potential to enable ground-breaking discoveries in plant sciences.[18] In the field of genomics, next generation sequencing and advances in genome analysis have helped to lay a foundation for other, downstream -omics studies. Transcriptomics, proteomics, peptidomics, and metabolomics can provide further insights into the inner workings of plant cells, cell-cell communication, and even plant-environment interactions.

Traditional biological tools for studying plant-omics include SNP genotyping for genomics, RNA-Seq and gene expression microarrays/ gene chips for transcriptomics, gel electrophoresis, ELISAs (enzyme-linked immunosorbent assay), protein microarrays and chromatography for proteomics, and chromatography and NMR (nuclear magnetic resonance) for metabolomics. These assays are still widely used in plant science research, often in combination or as a supplement to mass spectrometry analysis, especially when it comes to proteomics and metabolomics.

This Feature will focus on three –omic classes, proteomics, peptidomics, and metabolomics, which have made great advances in the plant-omics field due to the innovation of mass spectrometry. It will summarize the current state of mass spectrometry in plant-omic research,

highlighting the different mass spectrometry techniques, especially mass spectrometry imaging, discussing several examples, and providing an outlook for where the field is headed. This is not intended to serve as a comprehensive literature review but rather to provide readers with an overview of how mass spectrometry can be used to benefit plant science research.

Chromatography- Mass Spectrometry in Plant-omics

Coupling chromatography to mass spectrometry, via either liquid chromatography-mass spectrometry (LC-MS) or gas chromatography-mass spectrometry (GC-MS), is a powerful technique for analyzing proteins and peptides (LC-MS), and small molecules (both LC-MS and GC-MS) as they provide a great depth of information and offer higher sensitivity, selectivity, and greater structural determination capabilities compared to methods such as IR and Raman spectroscopy. GC-MS detects small volatile or derivatized nonvolatile molecules at lower concentrations compared to other techniques for structural characterization, such as NMR.[19] Similarly, protein gels have a limited separation capacity and detection ability often suffers from bias to a specific class or size of proteins, which decreases the number of proteins that can be identified compared to MS.[20]

Proteomics

Proteomics is used to describe the comprehensive study of the proteins present in an organism, or a particular part of the organism. Thus, proteomics provides a more comprehensive understanding of the molecular components produced and utilized by organisms to sustain various processes required for life. Traditional plant proteomic studies utilize gel electrophoresis in the workflow. However, gel electrophoresis suffers from several limitations including difficulty in analyzing highly basic or acidic proteins, bias toward more abundant proteins and limited dynamic range, making low abundance proteins hard to detect, and an inability to separate insoluble membrane proteins.[20-21] The higher sensitivity, selectivity, and structural determination capabilities of LC-MS make it an advantageous technique for a wide range of applications in plant proteomics, including descriptive proteomics of a sample, comparative proteomics using quantification techniques, post-translation modifications, and protein-protein interactions.[22]

Proteomics studies can be classified as either top-down or bottom-up. A study by Lagrain *et al.* used a top down approach to identify high molecular weight glutenin subunits (HMW-GS), which are responsible for variability in wheat quality. HMW-GS have long repetitive sequences with few cleavage sites for trypsin, making the bottom-up approach difficult due to low protein coverage, meaning isoforms and post translation modifications are difficult to distinguish. Relative average mass matching was used to identify HMW-GS along with

ω5-gliadins via LC-MS analysis. Overall, they demonstrated a useful method for the characterization of HMW-GS via top-down MS.[23] Top-down studies provide high accuracy protein structure determination, maps of post translational modifications (PTMs), and information on single amino acid polymorphisms.[24] Bottom-up analysis is more prevalent than top-down analysis for a variety of reasons, despite the usefulness of the top-down approach. Intact proteins are harder to separate than peptides as they are generally less soluble, meaning that separation of proteins prior to MS analysis is a challenge. Advances in the separation of intact proteins can improve the number of proteins identified in top down studies. For example, Tran *et al*. separated proteins with solution isoelectric focusing, gel-eluted liquid fraction entrapment electrophoresis, and nanocapillary liquid chromatography prior to MS analysis to reach a 20 fold increase in proteome coverage,[25] and Valeja *et al*. developed a 3D liquid chromatography separation involving hydrophobic interaction chromatography, ion exchange chromatography, and reversed phase chromatography to improve protein identifications with top down analysis.[26] However, these methods have yet to be applied to plant science. Also, top down approach requires more sample than bottom up method due to low ion counts for fragmentation, and a limited number of bioinformatics tools are available for data analysis.[24]

Currently, the bottom-up approach is used much more frequently than the top-down approach, and one benefit of the bottom-up approach is that it enables the identification and quantification of proteins in complex mixtures.[21] A study by Li *et al.* investigated the changes

in the proteome of *Arabidopsis thaliana* (Arabidopsis) seedlings in response to strigolactones, which are hormones that control shoot branching, as well as other aspects of growth and development. The study used iTRAQ, a common chemical label for MS^2 quantification, for relative proteome comparisons between a wild-type and a mutant version of Arabidopsis in the absence and presence of a strigolactone synthetic analog. Of the 2095 proteins identified across all samples in the wild-type, 19 were found to be reproducibly up-regulated (fold change greater than 1.25) and 18 were reproducibly down-regulated (25% or greater decrease). The up-regulated and down-regulated proteins for the mutant were nine and two respectively. This study identified proteins not previously known to be in the strigolactone pathway.[27]

The identification of post-translational modifications (PTMs) is a key area of proteomics as PTMs play a large role in the function of a protein. For example, phosphorylation sites regulate cell differentiation and signaling networks, and play a role in substrate specificity. In bottom-up proteomics, a specific PTM, such as phosphorylation, is enriched for after digestion, by affinity purification for example, and then LC-MS/MS analysis is performed to identify the peptides with that PTM.[28] Rose *et al.* used the model legume, *Medicago truncatula* (Medicago), to investigate phosphorylation changes due to Nod factors, which are necessary for Rhizobia infection and nodule development in the symbiotic relationship. The study identified 13,506 phosphosites in 7739 proteins and determined that Nod factor (NF) initiation resulted in changes in phosphorylation, but not overall protein levels. **Figure 2** shows the proteome and

phosphoproteome changes in the wild-type, nfp mutant, and dmi3 mutant plants. Changes in phosphorylation sites in wild-type plants but not in the nfp mutant were analyzed in order to determine changes in NF signal transduction. The combination of transcriptional, translational, and post-translational experiments performed resulted in a wealth of new information regarding the Nod factor signaling cascade.[29]

The depth of information provided by bottom-up proteomics studies comes at the cost of complexity in the experimental workflow and data processing. After protein extraction, the sample can undergo multiple steps, including digestion, chemical labeling, PTM enrichment, fractionation, and desalting prior to LC-MS/MS analysis depending on the scope of the study. Similarly, much effort is required after the MS acquisition in data processing. Well-annotated gene sequences are necessary in order to create predicted MS^2 theoretical fragmentation spectra for matching to experimental data. Obtaining well-annotated gene sequences is one of the more complex parts of plant proteomics data analysis as the size of plant genomes can vary tremendously. For example, sequencing studies estimate genome sizes from approximately 420 Mb for rice,[30-32] to 2300 Mb for maize,[33] to 17,000 Mb for wheat.[34] In comparison to the human genome (3000 Mb), most plant genomes are just as complex, and many of the larger plant genomes are not yet sequenced.[35] Plant genomes that are not sequenced or not well-annotated pose a challenge to a data analysis process that requires well-annotated gene sequences. Also, software to match peptides to the original protein must consider the false discovery rate and how

to assemble proteins from a list of peptide spectral matches when peptides may match more than one protein.[36]

Peptidomics

Peptidomics, the study of endogenous peptides produced by an organism, is a relatively new and underdeveloped field branching off of proteomics; therefore there is a growing need to investigate the role endogenous peptides play in an organism on a molecular level.[37-41] Known plant peptides include phytohormones (with signaling roles in both defense and non-defense processes), a wide range of defense peptides, and protease inhibitors. As signaling molecules, plant peptides play roles in cell division, development, nodulation, reproduction, and defense.[41-42] Thus, peptides affect nearly all parts of the plant and a better understanding of them could lead to improvements in crop yields and pharmaceutical products.[43]

As it stands, relatively few examples illustrate the usefulness of peptidomics analysis. Ohyama *et al.* studied the peptides excreted by Arabidopsis plants into the liquid culture growth media by LC-MS analysis. To validate their method, CLE44 over-expressor plants, which encode for a known secreted peptides, were grown. Analysis by LC-MS/MS revealed the expected secreted peptide. They then investigated an uncharacterized gene family encoding secreted peptides. Analysis of an overexpressed model gene for this family revealed a 15 amino acid peptide with PTMs.[44] Chen *et al.* investigated defense signaling peptides in tomato

plants. Endogenous peptides before and after stress induction were compared using a hypothetical peptide database created from predicted cleavage sites. Analysis revealed 14 new peptides and one known peptide that were up-regulated after wounding by more than 2 fold. One novel peptide, CAPE1, was found to have an expression pattern similar to a known peptide (systemin) and was investigated further.[45] Haruta *et al*. investigated the interaction of the peptide RALF in *Arabidopsis thaliana* using a metabolic ^{15}N labeling technique and MS analysis to determine the signaling pathway for the regulation of cell expansion. The study found that RALF interacts with the receptor FERONIA to suppress cell elongation. Furthermore, phosphoproteome analysis showed that the RALF-FERONIA interaction phosphorylated H^+-adenosine triphosphate 2, which inhibits proton transport, giving a mechanism for extracellular alkanization caused by RALF.[46] As peptidomics becomes more wide spread, studies will be able to go beyond discovery experiments to further explore the functional roles of peptides in plants.

Peptidomics employs similar workflow, and data processing steps as proteomics. Although a trypsin digest is not necessary, fractionation and other separation steps are necessary for complex samples. Also, data processing requires a tandem mass spectra database for identification of the peptides. Database searching is complicated by the fact that the cleavage sites that create the peptides are not always known, and there is no trypsin digest to create predictable cleavages and -COOH groups at the C-terminus, which complicates spectra

interpretation.[43] If all partial sequences from the protein database are compiled, the database size increases tremendously, thus increasing the database searching time, the number of false positives in the decoy database, and the score needed to confidently identify positive hits.[45] Additionally, plant peptidomics is further challenged by the low abundance of many plant peptides, which is further complicated by endogenous proteolytic degradation.[43] Careful sample preparation and data processing will help to provide high quality results that improve current knowledge on plant peptidomics.

Metabolomics

As the end products of various biochemical processes catalyzed by enzymes, metabolites provide useful molecular insight into an organism's biochemistry at a given time. With molecular weights typically under 1000 Da, metabolites are often classified as small molecule analytes. Metabolites are either primary metabolites, meaning that they are essential to a plant's growth and development, or secondary metabolites, which are diverse chemicals produced by plants that may have specific impacts on other organism. Metabolomics in plants is of particular importance as plants produce many nutrients and vitamins, and genetic engineering of plants to produce more nutrients and vitamins in the edible portions of the plant is an important area of plant metabolomics research.[47] The fact that metabolites cannot be deduced simply from genetic data, unlike transcripts and proteins, creates a challenge for the field of metabolomics. Metabolomics uses a range of analytical techniques, including MS,

NMR spectroscopy, and laser-induced fluorescence detection, of which MS is a selective and sensitive method commonly used, to characterize the metabolites present in an organism at a given time.[48]

The information learned from metabolomics studies in plants has the potential for great impact in improving plant response to stress, agricultural efficiency, and food quality.[47] For example, Oms-Oliu *et al.* studied the metabolites present in tomato fruit before, during, and after ripening. GC-MS analysis revealed major changes during the ripening process, such as an increases glucose, fructose, cell wall components, and amino acids. Additionally, metabolites like mannose and citramalic were found to strongly indicate a post-harvest state.[49] Metabolomics can also provide insights into a plant's response to stress. Zhang *et al.* used a combination of transcriptomics and metabolomics to study the effect of drought conditions on *Medicago truncatula*. Many thousands of transcripts changed in response to drought and GC-MS analysis identified changes to hundreds of metabolites. The combination of the two datasets helped to characterize the regulation of the metabolomics pathways under drought conditions.[50] An alternative ionization approach worth mentioning is leaf-spray mass spectrometry, a fairly new technique, based on paper-spray technology, where plant tissues cut in the shape of a triangle produce a spray into the inlet of the mass spectrometry from either an electrolyte present in the tissue or from an added solvent upon application of an electric field.[51] Leaf spray has been used in a number of studies for detection of a variety of metabolites.[52]

Sample preparation starts with quenching the plant tissue, which stops the metabolic processes in a cell through the use of low temperatures, such as flash-freezing with liquid nitrogen.[53] An extraction of the desired metabolites follows quenching, and separation of metabolites into subclasses prior to LC or GC-MS helps with the analysis of complex samples. A wide concentration range of metabolites in conjunction with a large number of metabolites with differing chemical properties make metabolite samples complex, and challenging to analyze.[54] Data processing of the complex datasets in metabolomics experiments can influence the quality of the results.[55] Also, the indirect relationship between metabolomics and genomics creates a challenge in confidently identifying and solving structures of metabolites. A combination of high-resolution, accurate mass matching, MS/MS fragmentation data, and retention time comparisons between pure standards or database information and experimental data are needed for identification of metabolites.[56]

Mass Spectrometry Imaging

One of the exciting new developments in mass spectrometry that is becoming more widely used for plant-omics is mass spectrometry imaging (MSI). MSI shows great promise for biological studies because it allows for molecular analysis of tissue while retaining information about the spatial distribution of the different analytes in the tissue sample.[57] The conventional

tissue extraction methods described above for proteomic, peptidomic, and metabolomic studies do not provide the spatial information that MSI can provide; however, liquid extraction is still the method of choice for large-scale studies as MSI is lower throughput and less reproducible when acquiring a large amount of samples. Several other biological techniques allow for the visualization of macromolecules in various cellular structures, such as immunolocalization or other techniques that rely on the interactions between the analyte and an external probe, and therefore require clear knowledge of the analytes of interest and specifically target larger molecules such as proteins. Mass spectrometry lends itself to discovery experiments in which a multitude of analytes, from metabolites to proteins, can be detected and studied without prior knowledge of sample contents. Herein, we discuss four different MSI techniques (MALDI, SIMS, DESI, and LAESI) and how they are being applied to plant-omics. **Table 1** summarizes the optimal analytes, mass range, and spatial resolutions of these four different MSI techniques.

Before discussing the different ionization sources used for MSI, there are a variety of different types of mass analyzers that offer distinct advantages and disadvantages when it comes to MSI experiments. Arguably the most common type of mass analyzers used for MSI are time-of-flight (TOF) and TOF/TOF analyzers in which the *m/z* is determined by the time the ions take to travel from the ionization source through the TOF tube.[58] A wide mass range of molecules (theoretically unlimited) can be detected with these types of instruments with fast analysis times and MS/MS capabilities for molecular identification, however the mass accuracy and mass

resolving power are low compared to other instrument types.

Orbitrap Fourier transform mass spectrometers are gaining popularity in MSI applications. In an Orbitrap mass spectrometer, *m/z* values are determined by measuring the axial oscillation frequency of ions moving back and forth along a spindle-like electrode, where the spinning ions generate a small current that is detected at either end of the electrode, and the mass of the ion is related to the oscillation frequency.[59] While the Orbitrap provides superior mass resolution and mass accuracy, disadvantages of the commercially available MALDI-Orbitrap compared to TOF instruments are the larger laser beam size, which limits the spatial resolution of the images to approximately 75 μm (although custom instrument modifications have produced laser beams as small as 3 μm spatial resolution), slower acquisition speed thus longer analysis time, and limited mass range (maximum of 4000 Da as higher *m/z* compounds are difficult to retain during the orbital rotation). Additionally, the commercial MALDI-LTQ Orbitrap has capabilities for CID (collision-induced dissociation) and HCD (high-energy collisional dissociation) MS/MS fragmentation, which both can be used to obtain more complete fragmentation coverage of metabolites and peptides and improved molecular identifications. Hybrid methods have been developed by the Young Jin Lee group that utilize the hybrid linear ion trap and Orbitrap portions of the MALDI- LTQ Orbitrap instrument to reduce the data acquisition time while collecting even more molecular information by interspersing ion trap scans and MS/MS scans during the longer Orbitrap scan using a spiral step plate motion.[60]

Fourier transform ion cyclotron resonance (FT-ICR) mass analyzers are also used for some MSI applications. In this type of instrument, ions are trapped in a magnetic field and excited by an electric field, thus leaving the ions rotating at their cyclotron frequency that generates a current which is detected by the mass spectrometer. FT-ICR mass analyzers can provide extremely accurate mass measurements, has MS/MS capabilities, and have a higher upper mass limit of detection compared to Orbitraps; however, like the Orbitrap, suffer from long analysis times.

Matrix-Assisted Laser Desorption/Ionization

Matrix-assisted laser desorption/ionization (MALDI)-MSI is the most popular type of MSI. A workflow comparing the sample preparation, data acquisition, and examples of raw data for LC-MS and MALDI-MSI workflows is shown in **Figure 3**. For this technique, tissues of interest are trimmed or harvested from the plant and immediately frozen before being sectioned on a cryostat into slices that are typically 10-20 μm thick.[61] Next, the tissue sections are thaw-mounted onto a stainless steel conductive plate, indium-tin-oxide (ITO)-coated conductive glass slides, or regular glass slides, depending on instrumentation.[62] The next step, MALDI matrix selection and application, is critical to the experimental workflow as the type of matrix chosen will determine the types of analytes that can be ionized and the application method will control the matrix crystal size which in turn defines the maximum image resolution.[63-64] Conventional matrices include 2,5-dihydroxybenzoic acid (DHB) and α-cyano-4-hydroxycinnamic acid (CHCA)[65] for positive mode and 9-aminoacridine (9-AA)[66] for

negative imaging mode. Less traditional matrices such as TiO_2, gold, or silver nanoparticles[67-69], 1,5-diaminonapthalene (DAN)[70], 2,3,4,5-tetrakis(3′,4′-dihydroxylphenyl)thiophene (DHPT)[71], and 1,8-bis(dimethyl-amino) naphthalene (DMAN)[72-73] are being used more frequently and are reported to improve spectral quality, crystallization and vacuum stability.[74] Spatial resolution and reproducibility of results are limited by the matrix crystal size and application consistency, among other instrumental parameters such as raster step size and laser beam diameter.[75] Matrix can be applied manually with an artist airbrush, with automated systems[76], via sublimation[77], or filtered onto tissue through a small (~20 μm) sieve or mesh.[78-79] The matrix allows for ions to be generated, which is essential for mass spectrometric analyses as the mass spectrometer can only detect charged particles.

After the matrix is applied to the sample and the analytes are co-crystallized with matrix, the sample plate is loaded into the mass spectrometer on a moveable X-Y stage. A laser is fired at the sample plate, causing the matrix to be ablated and form a gas plume in which matrix and analyte ions are formed. The moveable X-Y stage allows for the laser to raster across the sample and mass spectra to be collected at every pre-defined raster point. After completing the 2D raster, ion images for each mass in the spectrum can be shown and the software will display the relative abundance of each ion as a colored map of signal intensity across the raster area.

One advantage MALDI-MSI for biological analysis is that it can generate larger ions, such as peptides and proteins, which is one of the reasons why MALDI is the most widely-used

MSI technique.[57, 80-82] The matrix absorbs much of the incident laser energy, providing soft ionization for analytes , which allows for the ionization of larger molecules (*m/z* over 100 kDa).[83] Unfortunately, while there are advantages for the analysis in the high mass range, there are disadvantages in the low mass range. One disadvantage to using MALDI is that the matrix itself produces ions that can interfere or mask analyte ions in the small molecule mass range. This can be somewhat avoided using high resolution instrumentation or novel matrices.[67, 70-72, 84-88] There are several excellent reviews that highlight the application of MALDI-MSI (and other MSI techniques) to plant metabolomics, peptidomics, and proteomics.[89-94]

As previously stated, MALDI-MSI is the most highly used type of MS imaging, possibly due to its versatility and availability. MALDI-MSI can be used to detect a wide range of molecules from metabolites to peptides to proteins; although there are currently far more studies using MALDI-MSI for plant metabolomics. Our lab recently used MALDI-MSI to study the symbiotic relationship between the model legume, *Medicago truncatula*, and the nitrogen fixing bacteria, *Sinorhizobium meliloti*. We compared combinations of wild-type (wt) and mutant strains of plant (*dnf1*) and bacteria (*fixJ*) and identified metabolites, such as heme, various amino acids, and other organic acids that are present in functional, nitrogen-fixing nodules (wt-wt) and absent from non-functional nodules (wt-*fixJ*, *dnf1*-wt, or *dnf1*-*fixJ*).[95-96] **Figure 4** shows representative images of some of the metabolites detected in this study. The information gained from using this technique could provide valuable insight into the biological nitrogen fixation

process in legume plants by not only identifying metabolites that may be involved in this process, but by also localizing these molecules within the root nodule structures. Collaborative work between the Young Jin Lee and Basil Nikolau groups highlights MALDI-MSI for subcellular-level imaging of metabolites in maize leaves, providing insights into the known asymmetric metabolism associated with different tissue types within these leaves.[97] This proof-of-principle study of understanding molecular details and localizations at the sub-cellular level shows exciting promise for deeper interrogation of the biological mechanisms and implications. Plant peptidomics is a relatively under-explored area in mass spectrometry, and especially so in mass spectrometry imaging. One of the very few reports on plant peptide imaging focuses on imaging cyclotides in petunias. Using MALDI-MSI, Poth *et al.* were able to detect novel cyclotides (defense-related cyclic plant peptides) from petunia leaves.[98] The goal with this study would be to genetically enrich major crop species to be able to express cyclic peptides of their own, thus enhancing crop protection. While mass spectrometry analysis is the gold standard for proteomic analysis in general, there are very few reports using MALDI-MSI for plant proteomics. A previous review highlights MALDI-MSI of proteins in soybean cotyledons in a proof-of –principle figure,[92] and a known allergenic protein in peaches was shown to be localized to the skin of the peach using MSI,[99] but no further applications of MSI to plant proteomics have been reported so far.

Secondary Ion Mass Spectrometry

Secondary ion mass spectrometry (SIMS) is a long established technique and, unlike MALDI, it does not require special preparation or matrix application, although some optional methods, such as the addition of a matrix or a thin coat of metal nanoparticles, can improve the imaging results.[100-101] Remarkably, SIMS is able to reliably achieve less than 1 μm spatial resolution, making it the method of choice for subcellular investigations.

Like MALDI-MSI, in SIMS-MSI the sample is put under high vacuum. Instead of ionizing with a laser like in MALDI, the sample on the surface is bombarded with high energy primary ions which facilitate the ionization of the analytes.[102-103] The ionized analytes, or secondary ions, are sputtered from the sample surface into the mass analyzer for analysis. The highly focused ion beam in SIMS provides excellent spatial resolution (less than 1 μm); however, the primary ion source is fairly limited to molecules under 1000 Da because it is a high energy beam that easily fragments larger molecules, and for this reason, SIMS is especially popular for elemental and atomic analyses.[96, 104] SIMS-MSI of primary and secondary metabolites in pea plants and *Arabidopsis thaliana* with sub-2 μm spatial resolution has been reported by Seyer *et al*., as shown in **Figure 5**.[105] A new sample preparation method was developed for SIMS-MSI of Arabidopsis and the method was applied to confirm variations in flavonoid content in seeds from different Arabidopsis mutants. While SIMS is one of the oldest MS techniques, its application to plant-omics is lacking and could be significantly expanded in the future.

Desorption Electrospray Ionization

Although the spatial information of a sample is preserved with MSI, MSI has still been mainly viewed as an invasive process until the development of ambient ionization techniques, such as desorption electrospray ionization (DESI). DESI is a simple, ambient ionization technique that channels charged solvent droplets and ions from an electrospray source onto the surface of the sample, and the impact yields gaseous analyte ions.[106] Images can either be collected directly from the sample surface or indirectly via imprints. Like SIMS, DESI also does not require matrix to create ions and actually requires little to no sample preparation other than sectioning and mounting the sample.[107] One disadvantage DESI has compared to vacuum MS methods, SIMS and MALDI, is that it has lower spatial resolution of approximately 180–200 μm.[107]

Like the other MSI techniques mentioned above, DESI has been primarily utilized for metabolomics studies. Recently published work by Tata *et al*. used DESI-MSI to study changes in the potato plant metabolome in response to pathogen invasion.[108] Their method of imprinting the sample on tape and performing DESI-MS and DESI-MSI on the imprint allowed for simple and rapid metabolomics profiling with minimal sample preparation, and resulted in the first qualitative study of plant defense against phytopathogen invasion via ambient mass spectrometry. Hemalatha and Pradeep present a thorough analysis of molecular signatures (primarily metabolites) from a variety of plant species and tissues using DESI-MSI.[109] This

work identified metabolites with implications in varietal differences, toxic metabolite production, metabolites during plant growth cycles, plant defense, etc.

Laser Ablation Electrospray Ionization

Laser ablation electrospray ionization (LAESI) is another type of ambient ionization and utilizes the natural water content of cells and tissues as the matrix.[110] With LAESI, a laser is used to ablate molecules in the tissue which are then captured by the electrospray and generate analyte ions.[111] The Vertes group invented and developed LAESI-MSI for plant sciences. They have demonstrated the application of LAESI-MSI for live, untreated tissue analysis of metabolites on plant leaves[112] and have even demonstrated the use of LAESI for 3D MSI of metabolites in *S. lynise* and *A. squarrosa* leaf tissue as shown in **Figure 6**.[113] 3D imaging of molecular distributions can elucidate the correlation between biochemical processes and the spatial organization of a biological tissue. More recently this group has coupled LAESI-MSI with ion mobility mass spectrometry (IM-MS) of metabolites on *P. peltatum* leaves.[114] They were able to use this technique to separate structural isomers which is very important as isomers can often have extremely different biological activities. This technique can theoretically be applied to plant peptidomics and proteomics as well, but has so far only been demonstrated for the direct detection of these larger molecules on animal tissue.[115]

Data Analysis

Mass spectrometry experiments have the capacity to generate huge amounts of data. Sorting through and analyzing data is often the greatest bottleneck of MS and MSI experiments. There have been many different software tools developed for the analysis of metabolomics, peptidomics, or proteomics datasets.

Metabolomics data processing typically begins with matching obtained accurate masses to online metabolite databases such as METLIN,[116] HMDB (Human Metabolome Database),[117-118] KEGG (Kyoto Encyclopedia of Genes and Genomes),[119] PubChem,[120] MassBank,[121] MMCD (Madison Metabolomics Consortium Database),[122] LIPID MAPS,[123-124] and more. Database searching will often result in multiple potential identifications for a given mass; therefore, to further narrow down identification assignments, tandem mass spectra collected for each metabolite of interest can be compared to metabolite standards, tandem mass databases, or *in silico* fragmentation tools such as MetFrag.[125] Instrument vendors have released software packages for metabolomics analyses such as ProgenesisQI (Waters Corporation), Sieve (Thermo Scientific), ProfileAnalysis (Bruker Daltonics), to name a few, as well as open-source software tools like XCMS[126-127] and MetaboAnalyst.[128-130] These tools allow for data alignment, normalization, automatic feature selection, some statistical analysis, and even metabolite identification prediction based on MS/MS data, although confident identifications is still lacking. Software tool development for metabolomics is growing area that could still use further development as many

metabolites share common fragment masses with no consistent fragmentation rules for different functional groups (unlike peptide fragmentation) that would make accurate fragmentation prediction achievable at this time, leaving many ambiguous identifications.

Accurate mass matching can also be used to identify peptides and proteins, although the more widely-accepted approach is to match MS/MS data to sequenced genomes, using software tools like Mascot, or by de novo sequencing, with software packages like PEAKS which is also useful for endogenous peptidomics studies.[131] Several programs, such as BLAST (Basic Local Alignment Search Tool)[132] and MEME,[133] have been developed for homology searches by comparing putative peptide sequences against a database of closely related species which can provide insight into key evolutionary and functional roles of peptides.[134] In comparison to metabolomics, the more mature field of proteomics has many software tools, such as Mascot (by Matrix Science), COMPASS (Coon OMSSA Proteomic Analysis Software Suite),[135] Proteome Discoverer (by Thermo Scientific), SkyLine,[136] Morpheus,[137] etc., available that perform protein identifications based on sequencing of peptide fragment ions and protein database searching.

MSI data processing is often less straightforward and less automated than traditional extraction-based analyses. MSI data processing typically involves manually extracting ion images for each specific *m/z* in the mass spectrum and physically checking the quality of the image by making sure the analyte's spatial distribution is localized to the tissue with no contaminating ions interfering with the quality of the image. A list of *m/z* values with high quality MS images

can then be compiled for further interpretation. Vendor specific MSI analysis software (e.g., FlexImaging from Bruker Daltonics, ImageQuest from Thermo Scientific, HDImaging from Waters Corporation, and TissueView from Applied Biosystems/MDS) or open source software such as BioMap are commonly used to extract ion images for selected analytes from the collected data. Fairly recently, MSiReader, a readily available MSI data processing software, has been developed that has drastically decreased the MSI data processing time in comparison to manual data processing, allowing for higher throughput and faster overall analysis.[138] Large-scale MSI datasets can easily be tens of GB in size for a single experiment and management of these enormous data files causes significant challenges in data processing and analysis. Several key techniques have been developed to specifically address the information and analysis of large MSI datasets, such as OpenMSI[139] and memory efficient algorithms for principal component analysis.[140]

Many bioinformatics tools exist for analyzing a specific type of –omics datasets. Recently, researchers have been working toward developing plant-specific databases and software tools that can integrate multiple –omics datasets. The Sumner group reported a tandem mass spectral library of plant natural products, created using authentic standards and purified compounds.[141] The database focuses primarily on plant secondary metabolites, and contains retention time data as well as tandem mass spectra collected at six different collision energies. Other plant specific databases include the Medicago PhosphoProtein Database[142], The Plant

Proteome Database for *Arabidopsis thaliana* and maize[143], the Rice Proteome Database[144], and Promex which contains tryptic peptide mass spectra information for a dozen plant species[145]. In addition to plant specific databases for metabolomics or proteomics data, other software tools and databases have been developed to integrate multiple –omics datasets for a more comprehensive systems-biology view of the results. The Sumner group has developed MedicCyc specifically for *Medicago truncatula* metabolic pathway reconstruction with over 250 pathways of related metabolites, enzymes, and genes.[146] Similarly, AraCyc[147], MetaCyc[148], the Plant Metabolic Network (Plant Metabolic Network (PMN) on www.plantcyc.org) , and KEGG[149] are pathway tools for various other plant species.

Outlook

With regard to an integrated –omics strategy, there are obvious concerns about the complexity and dynamic range of the different classes of analytes being studied. These challenges have motivated the development of analytical workflows incorporating multi-dimensional front-end separation strategies and more advanced instrumentation offering superior separation capabilities and enhanced MS detection with faster scanning rates, better sensitivity, and higher performance. MALDI-MSI instrumentation with spatial resolution down to approximately 20 μm is readily available. Custom built instrumentation can achieve a spatial

resolution of < 3 μm and it is only a matter of time before these custom instruments become commercially available.[150-153] Improvements to ambient ionization techniques can also provide more biologically relevant information about the plant systems. Adopting these new technologies with important new capabilities, along with careful sample preparation, can provide dramatic improvements when integrated into -omic workflows.

In addition to technological advances in instrumentation, the simultaneous development, advancement, and integration of closely related –omics approaches can guide researchers to a better understanding and characterization of various biological processes and signaling mechanisms in plants. Integrated genomics and metabolomics or metabolomics and transcriptomics studies have recently been reported, and we expect more exciting studies of this nature in the future.[154-156] By integrating multiple -omics technologies it may be possible to obtain extensive molecular-level information and elucidate biological functions and underlying mechanisms. Plant-specific bioinformatics tools for integrating multi-omics strategies are beginning to emerge, but continuous development of wide-reaching, user-friendly software tools would drastically improve data analysis strategies and holistic knowledge.

A more widespread adoption of MSI as a technique for –omics studies will provide spatial information of where analytes are located within the plant. Knowing, for example, where metabolites and the proteins/enzymes that interact with them are located at different developmental stages could reveal key insights into biological processes and mechanisms within

the plant. In addition to studying plant development, MSI can also provide a way to localize differences in analytes between tissue types, disease states, genetic differences, or following genetic manipulation. It could be possible to quickly ascertain the functional potential of plants for various biotechnological applications such as bioenergy production, environmental decontamination, natural product production, and many other important applications. Collaborations between experts in various plant-omic methodologies, plant scientists, and bioinformaticians, along with ever-advancing technological innovations, impart an exciting outlook for the future of plant science.

We believe that the application of mass spectrometry technologies to plant systems-biology will greatly accelerate the progress of this field. It allows for high-throughput, large-scale analyses on the metabolomic, peptidomic, and proteomic level that can correlate with genomic information. Mass spectrometry can be used to compare the metabolic and proteomic profiles of wild-type plants to a variety of genetic mutants where knocking-out certain genes will have a known or unknown physiological response. A multi-omics profile comparison between mutants with known and unknown responses will allow researchers to infer the previously unknown function if the –omics profiles correlate well with those of known function. New software and bioinformatics tools are needed to interrogate enormous datasets generated with these high-throughput, information-rich mass spectrometry approaches. The new insights gleaned from these large-scale systems biology experiments can lead to new hypotheses and

novel findings that will ultimately advance our knowledge of fundamental plant biology and plant biotechnology.

Acknowledgements

Support for this research was provided by the University of Wisconsin–Madison (UW-Madison), Office of the Vice Chancellor for Research and Graduate Education with funding from the Wisconsin Alumni Research Foundation (WARF). E.G. acknowledges a National Science Foundation (NSF) Graduate Research Fellowship (DGE-1256259). LL acknowledges an H. I. Romnes Faculty Research Fellowship and a Vilas Distinguished Achievement Professorship with funding provided by the WARF and UW-Madison School of Pharmacy.

References

1. Taylor, T., Bacteria and Their Relations to Plant Culture. *Science* **1881,** *2* (65), 443-444.

2. Wiegand, K. M., Plant Embryo-Sacs. *Science* **1900,** *12* (296), 347.

3. Smith, E. F.; Townsend, C. O., A Plant-Tumor of Bacterial Origin. *Science* **1907,** *25* (643), 671-673.

4. Quinn, L. D.; Gordon, D. R.; Glaser, A.; Lieurance, D.; Flory, S. L., Bioenergy Feedstocks at Low Risk for Invasion in the USA: A "White List" Approach. *Bioenergy Research* **2015,** *8*, 471-481.

5. Tadege, M.; Chen, F.; Murray, J.; Wen, J.; Ratet, P.; Udvardi, M. K.; Dixon, R. A.; Mysore, K. S., Control of Vegetative to Reproductive Phase Transition Improves Biomass Yield and Simultaneously Reduces Lignin Content in Medicago Truncatula. *BioEnergy Research* **2015,** *8* (2), 857-867.

6. Kumar, S.; Kumaria, S.; Tandon, P., Efficient in Vitro Plant Regeneration Protocol from Leaf Explant of Jatropha Curcas L - a Promising Biofuel Plant. *J Plant Biochem Biot* **2010,** *19* (2), 275-277.

7. Hung, K. H.; Chiang, T. Y.; Chiu, C. T.; Hsu, T. W.; Ho, C. W., Isolation and Characterization of Microsatellite Loci from a Potential Biofuel Plant Miscanthus Sinensis (Poaceae). *Conserv Genet* **2009,** *10* (5), 1377-1380.

8. Dewick, P. M., *Medicinal Natural Products: A Biosynthetic Approach*. 3 ed.; Wiley: Chichester, 2009.

9. Russo, P.; Frustaci, A.; Del Bufalo, A.; Fini, M.; Cesario, A., Multitarget Drugs of Plants Origin Acting on Alzheimer's Disease. *Current medicinal chemistry* **2013,** *20* (13), 1686-1693.

10. Kano, S., Artemisinin-Based Combination Therapies and Their Introduction in Japan. *Kansenshogaku Zasshi* **2014,** *88* (3 Suppl 9-10), 18-25.

11. Kittakoop, P.; Mahidol, C.; Ruchirawat, S., Alkaloids as Important Scaffolds in Therapeutic Drugs for the Treatments of Cancer, Tuberculosis, and Smoking Cessation. *Curr Top Med Chem* **2014,** *14* (2), 239-252.

12. Dias, D. A.; Urban, S.; Roessner, U., A Historical Overview of Natural Products in Drug Discovery. *Metabolites* **2012,** *2* (2), 303-336.

13. Zheng, Y.; Jiang, X.; Gao, F.; Song, J.; Sun, J.; Wang, L.; Sun, X.; Lu, Z.; Zhang, H., Identification of Plant-Derived Natural Products as Potential Inhibitors of the Mycobacterium Tuberculosis Proteasome. *BMC complementary and alternative medicine* **2014,** *14*, 400.

14. Lucas, D. M.; Still, P. C.; Perez, L. B.; Grever, M. R.; Kinghorn, A. D., Potential of Plant-Derived Natural Products in the Treatment of Leukemia and Lymphoma. *Current drug targets* **2010,** *11* (7), 812-822.

15. Lee, K. H., Anticancer Drug Design Based on Plant-Derived Natural Products. *Journal of biomedical science* **1999,** *6* (4), 236-250.

16. Hung, H. Y.; Qian, K.; Morris-Natschke, S. L.; Hsu, C. S.; Lee, K. H., Recent Discovery of Plant-Derived Anti-Diabetic Natural Products. *Natural product reports* **2012,** *29* (5), 580-606.

17. Dholwani, K. K.; Saluja, A. K.; Gupta, A. R.; Shah, D. R., A Review on Plant-Derived Natural Products and Their Analogs with Anti-Tumor Activity. *Indian journal of pharmacology* **2008,** *40* (2), 49-58.

18. Ehrhardt, D. W.; Frommer, W. B., New Technologies for 21st Century Plant Science. *The Plant cell* **2012,** *24* (2), 374-394.

19. Dunn, W. B.; Bailey, N. J. C.; Johnson, H. E., Measuring the Metabolome: Current Analytical Technologies. *Analyst* **2005,** *130* (5), 606-625.

20. Roe, M. R.; Griffin, T. J., Gel-Free Mass Spectrometry-Based High Throughput Proteomics: Tools for Studying Biological Response of Proteins and Proteomes. *Proteomics* **2006,** *6* (17), 4678-4687.

21. Zhang, Y. Y.; Fonslow, B. R.; Shan, B.; Baek, M. C.; Yates, J. R., Protein Analysis by Shotgun/Bottom-up Proteomics. *Chemical Reviews* **2013,** *113* (4), 2343-2394.

22. Jorrin-Novo, J. V.; Pascual, J.; Sanchez-Lucas, R.; Romero-Rodriguez, M. C.; Rodriguez-Ortega, M. J.; Lenz, C.; Valledor, L., Fourteen Years of Plant Proteomics Reflected in Proteomics: Moving from Model Species and 2de-Based Approaches to Orphan Species and Gel-Free Platforms. *Proteomics* **2015,** *15* (5-6), 1089-1112.

23. Lagrain, B.; Brunnbauer, M.; Rombouts, I.; Koehler, P., Identification of Intact High Molecular Weight Glutenin Subunits from the Wheat Proteome Using Combined Liquid Chromatography-Electrospray Ionization Mass Spectrometry. *PLoS One* **2013,** *8* (3), e58682.

24. Armirotti, A.; Damonte, G., Achievements and Perspectives of Top-Down Proteomics. *Proteomics* **2010,** *10* (20), 3566-3576.

25. Tran, J. C.; Zamdborg, L.; Ahlf, D. R.; Lee, J. E.; Catherman, A. D.; Durbin, K. R.; Tipton, J. D.; Vellaichamy, A.; Kellie, J. F.; Li, M.; Wu, C.; Sweet, S. M.; Early, B. P.; Siuti, N.; LeDuc, R. D.; Compton, P. D.; Thomas, P. M.; Kelleher, N. L., Mapping Intact Protein Isoforms in Discovery Mode Using Top-Down Proteomics. *Nature* **2011,** *480* (7376), 254-258.

26. Valeja, S. G.; Xiu, L.; Gregorich, Z. R.; Guner, H.; Jin, S.; Ge, Y., Three Dimensional Liquid Chromatography Coupling Ion Exchange Chromatography/Hydrophobic Interaction Chromatography/Reverse Phase Chromatography for Effective Protein Separation in Top-Down Proteomics. *Anal Chem* **2015,** *87* (10), 5363-5371.

27. Li, Z.; Czarnecki, O.; Chourey, K.; Yang, J.; Tuskan, G. A.; Hurst, G. B.; Pan, C. L.; Chen, J. G., Strigolactone-Regulated Proteins Revealed by Itraq-Based Quantitative Proteomics in Arabidopsis. *Journal of Proteome Research* **2014,** *13* (3), 1359-1372.

28. Grimsrud, P. A.; Swaney, D. L.; Wenger, C. D.; Beauchene, N. A.; Coon, J. J., Phosphoproteomics for the Masses. *Acs Chemical Biology* **2010,** *5* (1), 105-119.

29. Rose, C. M.; Venkateshwaran, M.; Volkening, J. D.; Grimsrud, P. A.; Maeda, J.; Bailey, D. J.; Park, K.; Howes-Podoll, M.; den Os, D.; Yeun, L. H.; Westphall, M. S.; Sussman, M. R.; Ane, J. M.; Coon, J. J., Rapid Phosphoproteomic and Transcriptomic Changes in the Rhizobia-Legume Symbiosis. *Molecular & Cellular Proteomics* **2012,** *11* (9), 724-744.

30. Yu, J.; Hu, S. N.; Wang, J.; Wong, G. K. S.; Li, S. G.; Liu, B.; Deng, Y. J.; Dai, L.; Zhou, Y.; Zhang, X. Q.; Cao, M. L.; Liu, J.; Sun, J. D.; Tang, J. B.; Chen, Y. J.; Huang, X. B.; Lin, W.; Ye, C.; Tong, W.; Cong, L. J.; Geng, J. N.; Han, Y. J.; Li, L.; Li, W.; Hu, G. Q.; Huang, X. G.; Li, W. J.; Li, J.; Liu, Z. W.; Li, L.; Liu, J. P.; Qi, Q. H.; Liu, J. S.; Li, L.; Li, T.; Wang, X. G.; Lu, H.; Wu, T. T.; Zhu, M.; Ni, P. X.; Han, H.; Dong, W.; Ren, X. Y.; Feng, X. L.; Cui, P.; Li, X. R.; Wang, H.; Xu, X.; Zhai, W. X.; Xu, Z.; Zhang, J. S.; He, S. J.; Zhang, J. G.; Xu, J. C.; Zhang, K. L.; Zheng, X. W.; Dong, J. H.; Zeng, W. Y.; Tao, L.; Ye, J.; Tan, J.; Ren, X. D.; Chen, X. W.; He, J.; Liu, D. F.; Tian, W.; Tian, C. G.; Xia, H. G.; Bao, Q. Y.; Li, G.; Gao, H.; Cao, T.; Wang, J.; Zhao, W. M.; Li, P.; Chen, W.; Wang, X. D.; Zhang, Y.; Hu, J. F.; Wang, J.; Liu, S.; Yang, J.; Zhang, G. Y.; Xiong, Y. Q.; Li, Z. J.; Mao, L.; Zhou, C. S.; Zhu, Z.; Chen, R. S.; Hao, B. L.; Zheng, W. M.; Chen, S. Y.; Guo, W.; Li, G. J.; Liu, S. Q.; Tao, M.; Wang, J.; Zhu, L. H.; Yuan, L. P.; Yang, H. M., A Draft Sequence of the Rice Genome (Oryza Sativa L. Ssp Indica). *Science* **2002,** *296* (5565), 79-92.

31. Matsumoto, T.; Wu, J. Z.; Kanamori, H.; Katayose, Y.; Fujisawa, M.; Namiki, N.; Mizuno, H.; Yamamoto, K.; Antonio, B. A.; Baba, T.; Sakata, K.; Nagamura, Y.; Aoki, H.; Arikawa, K.; Arita, K.; Bito, T.; Chiden, Y.; Fujitsuka, N.; Fukunaka, R.; Hamada, M.; Harada, C.; Hayashi, A.; Hijishita, S.; Honda, M.; Hosokawa, S.; Ichikawa, Y.; Idonuma, A.; Iijima, M.; Ikeda, M.; Ikeno, M.; Ito, K.; Ito, S.; Ito, T.; Ito, Y.; Ito, Y.; Iwabuchi, A.; Kamiya, K.; Karasawa, W.; Kurita, K.; Katagiri, S.; Kikuta, A.; Kobayashi, H.; Kobayashi, N.; Machita, K.; Maehara, T.; Masukawa, M.; Mizubayashi, T.; Mukai, Y.; Nagasaki, H.; Nagata, Y.; Naito, S.; Nakashima, M.; Nakama, Y.; Nakamichi, Y.; Nakamura, M.; Meguro, A.; Negishi, M.; Ohta, I.; Ohta, T.; Okamoto, M.; Ono, N.; Saji, S.; Sakaguchi, M.; Sakai, K.; Shibata, M.; Shimokawa, T.; Song, J. Y.; Takazaki, Y.; Terasawa, K.; Tsugane, M.; Tsuji, K.; Ueda, S.; Waki, K.; Yamagata, H.; Yamamoto, M.; Yamamoto, S.; Yamane, H.; Yoshiki, S.; Yoshihara, R.; Yukawa, K.; Zhong, H. S.; Yano, M.; Sasaki, T.; Yuan, Q. P.; Shu, O. T.; Liu, J.; Jones, K. M.; Gansberger, K.; Moffat, K.; Hill, J.; Bera, J.; Fadrosh, D.; Jin, S. H.; Johri, S.; Kim, M.; Overton, L.; Reardon, M.; Tsitrin, T.; Vuong, H.; Weaver, B.; Ciecko, A.; Tallon, L.; Jackson, J.; Pai, G.; Van Aken, S.; Utterback, T.; Reidmuller, S.; Feldblyum, T.; Hsiao, J.; Zismann, V.; Iobst, S.; de Vazeille, A. R.; Buell, C. R.; Ying, K.; Li, Y.; Lu, T. T.; Huang, Y. C.; Zhao, Q.; Feng, Q.; Zhang, L.; Zhu, J. J.; Weng, Q. J.; Mu, J.; Lu, Y. Q.; Fan, D. L.; Liu, Y. L.; Guan, J. P.; Zhang, Y. J.; Yu, S. L.; Liu, X. H.; Zhang, Y.; Hong, G. F.; Han, B.; Choisne, N.; Demange, N.; Orjeda, G.; Samain, S.; Cattolico, L.; Pelletier, E.; Couloux, A.; Segurens, B.; Wincker, P.; D'Hont, A.; Scarpelli, C.; Weissenbach, J.; Salanoubat, M.; Quetier, F.; Yu, Y.; Kim, H. R.; Rambo, T.; Currie, J.; Collura, K.; Luo, M. Z.; Yang, T. J.; Ammiraju, J. S. S.; Engler, F.; Soderlund, C.; Wing, R. A.; Palmer, L. E.; de la Bastide, M.; Spiegel, L.; Nascimento, L.; Zutavern, T.; O'Shaughnessy, A.; Dike, S.; Dedhia, N.; Preston, R.; Balija, V.; McCombie, W. R.; Chow, T. Y.; Chen, H. H.; Chung, M. C.; Chen, C. S.; Shaw, J. F.; Wu, H. P.; Hsiao, K. J.; Chao, Y. T.; Chu, M. K.; Cheng, C. H.; Hour, A. L.; Lee, P. F.; Lin, S. J.; Lin, Y. C.; Liou, J. Y.; Liu, S. M.; Hsing, Y. I.; Raghuvanshi, S.; Mohanty, A.; Bharti, A. K.; Gaur, A.; Gupta, V.; Kumar, D.; Ravi, V.; Vij, S.; Kapur, A.; Khurana, P.; Khurana, P.; Khurana, J. P.; Tyagi, A. K.; Gaikwad, K.; Singh, A.; Dalal, V.; Srivastava, S.; Dixit, A.; Pal, A. K.; Ghazi, I. A.; Yadav, M.; Pandit, A.; Bhargava, A.; Sureshbabu, K.; Batra, K.; Sharma, T. R.; Mohapatra, T.; Singh, N. K.; Messing, J.; Nelson, A. B.; Fuks, G.; Kavchok, S.; Keizer, G.; Llaca, E. L. V.; Song, R. T.; Tanyolac, B.; Young, S.; Il, K. H.; Hahn, J. H.; Sangsakoo, G.; Vanavichit, A.; de Mattos, L. A. T.; Zimmer, P. D.; Malone, G.; Dellagostin, O.; de Oliveira, A. C.; Bevan, M.; Bancroft, I.; Minx, P.; Cordum, H.; Wilson, R.; Cheng, Z. K.; Jin, W. W.; Jiang, J. M.; Leong, S. A.; Iwama, H.; Gojobori, T.; Itoh, T.; Niimura, Y.; Fujii, Y.; Habara, T.; Sakai, H.; Sato, Y.; Wilson, G.; Kumar, K.; McCouch, S.; Juretic, N.; Hoen, D.; Wright, S.; Bruskiewich, R.; Bureau, T.; Miyao, A.; Hirochika, H.; Nishikawa, T.; Kadowaki, K.; Sugiura, M.; Project, I. R. G. S., The Map-Based Sequence of the Rice Genome. *Nature* **2005,** *436* (7052), 793-800.

32. Goff, S. A.; Ricke, D.; Lan, T. H.; Presting, G.; Wang, R.; Dunn, M.; Glazebrook, J.; Sessions, A.; Oeller, P.; Varma, H.; Hadley, D.; Hutchison, D.; Martin, C.; Katagiri, F.; Lange, B. M.; Moughamer, T.; Xia, Y.; Budworth, P.; Zhong, J.; Miguel, T.; Paszkowski, U.; Zhang, S.; Colbert, M.; Sun, W. L.; Chen, L.; Cooper, B.; Park, S.; Wood, T. C.; Mao, L.; Quail, P.; Wing, R.; Dean, R.; Yu, Y.; Zharkikh, A.; Shen, R.; Sahasrabudhe, S.; Thomas, A.; Cannings, R.; Gutin, A.; Pruss, D.; Reid, J.; Tavtigian, S.; Mitchell, J.; Eldredge, G.; Scholl, T.; Miller, R. M.; Bhatnagar, S.; Adey, N.; Rubano, T.; Tusneem, N.; Robinson, R.; Feldhaus, J.; Macalma, T.; Oliphant, A.; Briggs, S., A Draft Sequence of the Rice Genome (Oryza Sativa L. Ssp. Japonica). *Science* **2002,** *296* (5565), 92-100.

33. Schnable, P. S.; Ware, D.; Fulton, R. S.; Stein, J. C.; Wei, F.; Pasternak, S.; Liang, C.; Zhang, J.; Fulton, L.; Graves, T. A.; Minx, P.; Reily, A. D.; Courtney, L.; Kruchowski, S. S.; Tomlinson, C.; Strong, C.; Delehaunty, K.; Fronick, C.; Courtney, B.; Rock, S. M.; Belter, E.; Du, F.; Kim, K.; Abbott, R. M.; Cotton, M.; Levy, A.; Marchetto, P.; Ochoa, K.; Jackson, S. M.; Gillam, B.; Chen, W.; Yan, L.; Higginbotham, J.; Cardenas, M.; Waligorski, J.; Applebaum, E.; Phelps, L.; Falcone, J.; Kanchi, K.; Thane, T.; Scimone, A.; Thane, N.; Henke, J.; Wang, T.; Ruppert, J.; Shah, N.; Rotter, K.; Hodges, J.; Ingenthron, E.; Cordes, M.; Kohlberg, S.; Sgro, J.; Delgado, B.; Mead, K.; Chinwalla, A.; Leonard, S.; Crouse, K.; Collura, K.; Kudrna, D.; Currie, J.; He, R.; Angelova, A.; Rajasekar, S.; Mueller, T.; Lomeli, R.; Scara, G.; Ko, A.; Delaney, K.; Wissotski, M.; Lopez, G.; Campos, D.; Braidotti, M.; Ashley, E.; Golser, W.; Kim, H.; Lee, S.; Lin, J.; Dujmic, Z.; Kim, W.; Talag, J.; Zuccolo, A.; Fan, C.; Sebastian, A.; Kramer, M.; Spiegel, L.; Nascimento, L.; Zutavern, T.; Miller, B.; Ambroise, C.; Muller, S.; Spooner, W.; Narechania, A.; Ren, L.; Wei, S.; Kumari, S.; Faga, B.; Levy, M. J.; McMahan, L.; Van Buren, P.; Vaughn, M. W.; Ying, K.; Yeh, C. T.; Emrich, S. J.; Jia, Y.; Kalyanaraman, A.; Hsia, A. P.; Barbazuk, W. B.; Baucom, R. S.; Brutnell, T. P.; Carpita, N. C.; Chaparro, C.; Chia, J. M.; Deragon, J. M.; Estill, J. C.; Fu, Y.; Jeddeloh, J. A.; Han, Y.; Lee, H.; Li, P.; Lisch, D. R.; Liu, S.; Liu, Z.; Nagel, D. H.; McCann, M. C.; SanMiguel, P.; Myers, A. M.; Nettleton, D.; Nguyen, J.; Penning, B. W.; Ponnala, L.; Schneider, K. L.; Schwartz, D. C.; Sharma, A.; Soderlund, C.; Springer, N. M.; Sun, Q.; Wang, H.; Waterman, M.; Westerman, R.; Wolfgruber, T. K.; Yang, L.; Yu, Y.; Zhang, L.; Zhou, S.; Zhu, Q.; Bennetzen, J. L.; Dawe, R. K.; Jiang, J.; Jiang, N.; Presting, G. G.; Wessler, S. R.; Aluru, S.; Martienssen, R. A.; Clifton, S. W.; McCombie, W. R.; Wing, R. A.; Wilson, R. K., The B73 Maize Genome: Complexity, Diversity, and Dynamics. *Science* **2009,** *326* (5956), 1112-1115.

34. A Chromosome-Based Draft Sequence of the Hexaploid Bread Wheat (Triticum Aestivum) Genome. *Science* **2014,** *345* (6194), 1251788.

35. Hamilton, J. P.; Buell, C. R., Advances in Plant Genome Sequencing. *Plant Journal* **2012,** *70* (1), 177-190.

36. Nesvizhskii, A. I., A Survey of Computational Methods and Error Rate Estimation Procedures for Peptide and Protein Identification in Shotgun Proteomics. *Journal of Proteomics* **2010,** *73* (11), 2092-2123.

37. Clynen, E.; Baggerman, G.; Veelaert, D.; Cerstiaens, A.; Van der Horst, D.; Harthoorn, L.; Derua, R.; Waelkens, E.; De Loof, A.; Schoofs, L., Peptidomics of the Pars Intercerebralis-Corpus Cardiacum Complex of the Migratory Locust, Locusta Migratoria. *Eur J Biochem* **2001,** *268* (7), 1929-1939.

38. Verhaert, P.; Uttenweiler-Joseph, S.; de Vries, M.; Loboda, A.; Ens, W.; Standing, K. G., Matrix-Assisted Laser Desorption/Ionization Quadrupole Time-of-Flight Mass Spectrometry: An Elegant Tool for Peptidomics. *Proteomics* **2001,** *1* (1), 118-131.

39. Buchberger, A.; Yu, Q.; Li, L., Advances in Mass Spectrometric Tools for Probing Neuropeptides. *Annu Rev Anal Chem (Palo Alto Calif)* **2015**.

40. Dallas, D. C.; Guerrero, A.; Parker, E. A.; Robinson, R. C.; Gan, J. N.; German, J. B.; Barile, D.; Lebrilla, C. B., Current Peptidomics: Applications, Purification, Identification, Quantification, and Functional Analysis. *Proteomics* **2015,** *15* (5-6), 1026-1038.

41. Matsubayashi, Y.; Sakagami, Y., Peptide Hormones in Plants. In *Annual Review of Plant Biology*, Annual Reviews: Palo Alto, 2006; Vol. 57, pp 649-674.

42. Yamaguchi, Y.; Huffaker, A., Endogenous Peptide Elicitors in Higher Plants. *Current Opinion in Plant Biology* **2011,** *14* (4), 351-357.

43. Farrokhi, N.; Whitelegge, J. P.; Brusslan, J. A., Plant Peptides and Peptidomics. *Plant Biotechnology Journal* **2008,** *6* (2), 105-134.

44. Ohyama, K.; Ogawa, M.; Matsubayashi, Y., Identification of a Biologically Active, Small, Secreted Peptide in Arabidopsis by in Silico Gene Screening, Followed by Lc-Ms-Based Structure Analysis. *Plant Journal* **2008,** *55* (1), 152-160.

45. Chen, Y. L.; Lee, C. Y.; Cheng, K. T.; Chang, W. H.; Huang, R. N.; Nam, H. G.; Chen, Y. R., Quantitative Peptidomics Study Reveals That a Wound-Induced Peptide from Pr-1 Regulates Immune Signaling in Tomato. *Plant Cell* **2014,** *26* (10), 4135-4148.

46. Haruta, M.; Sabat, G.; Stecker, K.; Minkoff, B. B.; Sussman, M. R., A Peptide Hormone and Its Receptor Protein Kinase Regulate Plant Cell Expansion. *Science* **2014,** *343* (6169), 408-411.

47. Okazaki, Y.; Saito, K., Recent Advances of Metabolomics in Plant Biotechnology. *Plant Biotechnology Reports* **2012,** *6* (1), 1-15.

48. Lei, Z. T.; Huhman, D. V.; Sumner, L. W., Mass Spectrometry Strategies in Metabolomics. *Journal of Biological Chemistry* **2011,** *286* (29), 25435-25442.

49. Oms-Oliu, G.; Hertog, M.; Van de Poel, B.; Ampofo-Asiama, J.; Geeraerd, A. H.; Nicolai, B. M., Metabolic Characterization of Tomato Fruit During Preharvest Development, Ripening, and Postharvest Shelf-Life. *Postharvest Biology and Technology* **2011,** *62* (1), 7-16.

50. Zhang, J. Y.; de Carvalho, M. H. C.; Torres-Jerez, I.; Kang, Y.; Allen, S. N.; Huhman, D. V.; Tang, Y. H.; Murray, J.; Sumner, L. W.; Udvardi, M. K., Global Reprogramming of Transcription and Metabolism in Medicago Truncatula During Progressive Drought and after Rewatering. *Plant Cell and Environment* **2014,** *37* (11), 2553-2576.

51. Liu, J. J.; Wang, H.; Cooks, R. G.; Ouyang, Z., Leaf Spray: Direct Chemical Analysis of Plant Material and Living Plants by Mass Spectrometry. *Analytical Chemistry* **2011,** *83* (20), 7608-7613.

52. Klampfl, C. W.; Himmelsbach, M., Direct Ionization Methods in Mass Spectrometry: An Overview. *Analytica Chimica Acta* **2015,** *890*, 44-59.

53. Vuckovic, D., Current Trends and Challenges in Sample Preparation for Global Metabolomics Using Liquid Chromatography-Mass Spectrometry. *Analytical and Bioanalytical Chemistry* **2012,** *403* (6), 1523-1548.

54. Kueger, S.; Steinhauser, D.; Willmitzer, L.; Giavalisco, P., High-Resolution Plant Metabolomics: From Mass Spectral Features to Metabolites and from Whole-Cell Analysis to Subcellular Metabolite Distributions. *Plant Journal* **2012,** *70* (1), 39-50.

55. Katajamaa, M.; Oresic, M., Data Processing for Mass Spectrometry-Based Metabolomics. *Journal of Chromatography A* **2007,** *1158* (1-2), 318-328.

56. Creek, D. J.; Dunn, W. B.; Fiehn, O.; Griffin, J. L.; Hall, R. D.; Lei, Z. T.; Mistrik, R.; Neumann, S.; Schymanski, E. L.; Sumner, L. W.; Trengove, R.; Wolfender, J. L., Metabolite Identification: Are You Sure? And How Do Your Peers Gauge Your Confidence? *Metabolomics* **2014,** *10* (3), 350-353.

57. Balluff, B.; Schone, C.; Hofler, H.; Walch, A., Maldi Imaging Mass Spectrometry for Direct Tissue Analysis: Technological Advancements and Recent Applications. *Histochemistry and cell biology* **2011,** *136* (3), 227-244.

58. Cohen, M. Z., A Historical Overview of the Phenomenologic Movement. *Image J Nurs Sch* **1987,** *19* (1), 31-34.

59. Makarov, A., Electrostatic Axially Harmonic Orbital Trapping: A High-Performance Technique of Mass Analysis. *Anal Chem* **2000,** *72* (6), 1156-1162.

60. Perdian, D. C.; Lee, Y. J., Imaging Ms Methodology for More Chemical Information in Less Data Acquisition Time Utilizing a Hybrid Linear Ion Trap-Orbitrap Mass Spectrometer. *Anal Chem* **2010,** *82* (22), 9393-9400.

61. Crossman, L.; McHugh, N. A.; Hsieh, Y. S.; Korfmacher, W. A.; Chen, J. W., Investigation of the Profiling Depth in Matrix-Assisted Laser Desorption/Ionization Imaging Mass Spectrometry. *Rapid Commun Mass Sp* **2006,** *20* (2), 284-290.

62. Schwartz, S. A.; Reyzer, M. L.; Caprioli, R. M., Direct Tissue Analysis Using Matrix-Assisted Laser Desorption/Ionization Mass Spectrometry: Practical Aspects of Sample Preparation. *J Mass Spectrom* **2003,** *38* (7), 699-708.

63. Kaletas, B. K.; van der Wiel, I. M.; Stauber, J.; Dekker, L. J.; Guzel, C.; Kros, J. M.; Luider, T. M.; Heeren, R. M. A., Sample Preparation Issues for Tissue Imaging by Imaging Ms. *Proteomics* **2009,** *9* (10), 2622-2633.

64. Gemperline, E.; Rawson, S.; Li, L., Optimization and Comparison of Multiple Maldi Matrix Application Methods for Small Molecule Mass Spectrometric Imaging. *Analytical chemistry* **2014,** *86* (20), 10030-10035.

65. Chen, R.; Cape, S. S.; Sturm, R. M.; Li, L., Mass Spectrometric Imaging of Neuropeptides in Decapod Crustacean Neuronal Tissues. *Methods Mol Biol* **2010,** *656*, 451-463.

66. Burrell, M. M.; Earnshaw, C. J.; Clench, M. R., Imaging Matrix Assisted Laser Desorption Ionization Mass Spectrometry: A Technique to Map Plant Metabolites within Tissues at High Spatial Resolution. *J Exp Bot* **2007,** *58* (4), 757-763.

67. Shrivas, K.; Hayasaka, T.; Sugiura, Y.; Setou, M., Method for Simultaneous Imaging of Endogenous Low Molecular Weight Metabolites in Mouse Brain Using Tio2 Nanoparticles in Nanoparticle-Assisted Laser Desorption/Ionization-Imaging Mass Spectrometry. *Analytical chemistry* **2011,** *83* (19), 7283-7289.

68. Altelaar, A. F.; Klinkert, I.; Jalink, K.; de Lange, R. P.; Adan, R. A.; Heeren, R. M.; Piersma, S. R., Gold-Enhanced Biomolecular Surface Imaging of Cells and Tissue by Sims and Maldi Mass Spectrometry. *Anal Chem* **2006,** *78* (3), 734-742.

69. Hayasaka, T.; Goto-Inoue, N.; Zaima, N.; Shrivas, K.; Kashiwagi, Y.; Yamamoto, M.; Nakamoto, M.; Setou, M., Imaging Mass Spectrometry with Silver Nanoparticles Reveals the Distribution of Fatty Acids in Mouse Retinal Sections. *J Am Soc Mass Spectrom* **2010,** *21* (8), 1446-1454.

70. Thomas, A.; Charbonneau, J. L.; Fournaise, E.; Chaurand, P., Sublimation of New Matrix Candidates for High Spatial Resolution Imaging Mass Spectrometry of Lipids: Enhanced Information in Both Positive and Negative Polarities after 1,5-Diaminonapthalene Deposition. *Analytical Chemistry* **2012,** *84* (4), 2048-2054.

71. Chen, S.; Chen, L.; Wang, J.; Hou, J.; He, Q.; Liu, J.; Xiong, S.; Yang, G.; Nie, Z., 2,3,4,5-Tetrakis(3',4'-Dihydroxylphenyl)Thiophene: A New Matrix for the Selective Analysis of Low Molecular Weight Amines and Direct Determination of Creatinine in Urine by Maldi-Tof Ms. *Analytical chemistry* **2012,** *84* (23), 10291-10297.

72. Shroff, R.; Rulisek, L.; Doubsky, J.; Svatos, A., Acid-Base-Driven Matrix-Assisted Mass Spectrometry for Targeted Metabolomics. *Proceedings of the National Academy of Sciences of the United States of America* **2009,** *106* (25), 10092-10096.

73. Shroff, R.; Svatos, A., Proton Sponge: A Novel and Versatile Maldi Matrix for the Analysis of Metabolites Using Mass Spectrometry. *Analytical chemistry* **2009,** *81* (19), 7954-7959.

74. Ye, H.; Gemperline, E.; Li, L., A Vision for Better Health: Mass Spectrometry Imaging for Clinical Diagnostics. *Clinica chimica acta; international journal of clinical chemistry* **2012**.

75. Goodwin, R. J. A., Sample Preparation for Mass Spectrometry Imaging: Small Mistakes Can Lead to Big Consequences. *J Proteomics* **2012,** *75* (16), 4893-4911.

76. Baluya, D. L.; Garrett, T. J.; Yost, R. A., Automated Maldi Matrix Deposition Method with Inkjet Printing for Imaging Mass Spectrometry. *Analytical Chemistry* **2007,** *79* (17), 6862-6867.

77. Hankin, J. A.; Barkley, R. M.; Murphy, R. C., Sublimation as a Method of Matrix Application for Mass Spectrometric Imaging. *Journal of the American Society for Mass Spectrometry* **2007,** *18* (9), 1646-1652.

78. Puolitaival, S. M.; Burnum, K. E.; Cornett, D. S.; Caprioli, R. M., Solvent-Free Matrix Dry-Coating for Maldi Imaging of Phospholipids. *J Am Soc Mass Spectrom* **2008,** *19* (6), 882-886.

79. Trimpin, S.; Herath, T. N.; Inutan, E. D.; Wager-Miller, J.; Kowalski, P.; Claude, E.; Walker, J. M.; Mackie, K., Automated Solvent-Free Matrix Deposition for Tissue Imaging by Mass Spectrometry. *Analytical Chemistry* **2010,** *82* (1), 359-367.

80. Chang, W. C.; Huang, L. C. L.; Wang, Y. S.; Peng, W. P.; Chang, H. C.; Hsu, N. Y.; Yang, W. B.; Chen, C. H., Matrix-Assisted Laser Desorption/Ionization (Maldi) Mechanism Revisited. *Anal Chim Acta* **2007,** *582* (1), 1-9.

81. Karas, M.; Kruger, R., Ion Formation in Maldi: The Cluster Ionization Mechanism. *Chem Rev* **2003,** *103* (2), 427-439.

82. Knochenmuss, R., A Quantitative Model of Ultraviolet Matrix-Assisted Laser Desorption/Ionization Including Analyte Ion Generation. *Analytical Chemistry* **2003,** *75* (10), 2199-2207.

83. Tanaka, K.; Waki, H.; Ido, Y.; Akita, S.; Yoshida, Y.; Yoshida, T.; Matsuo, T., Protein and Polymer Analyses up to M/Z 100000 by Laser Ionization Time-of-Flight Mass Spectrometry. *Rapid Commun Mass Sp* **1988,** *2* (8), 151-153.

84. Ye, H.; Gemperline, E.; Li, L., A Vision for Better Health: Mass Spectrometry Imaging for Clinical Diagnostics. *Clin Chim Acta* **2013,** *420*, 11-22.

85. Fitzgerald, J. J. D.; Kunnath, P.; Walker, A. V., Matrix-Enhanced Secondary Ion Mass Spectrometry (Me-Sims) Using Room Temperature Ionic Liquid Matrices. *Analytical Chemistry* **2010,** *82* (11), 4413-4419.

86. Lemaire, R.; Tabet, J. C.; Ducoroy, P.; Hendra, J. B.; Salzet, M.; Fournier, I., Solid Ionic Matrixes for Direct Tissue Analysis and Maldi Imaging. *Analytical Chemistry* **2006,** *78* (3), 809-819.

87. Shroff, R.; Svatos, A., Proton Sponge: A Novel and Versatile Maldi Matrix for the Analysis of Metabolites Using Mass Spectrometry. *Analytical Chemistry* **2009,** *81* (19), 7954-7959.

88. Mainini, V.; Bovo, G.; Chinello, C.; Gianazza, E.; Grasso, M.; Cattoretti, G.; Magni, F., Detection of High Molecular Weight Proteins by Maldi Imaging Mass Spectrometry. *Mol Biosyst* **2013,** *9* (6), 1101-1107.

89. Lee, Y. J.; Perdian, D. C.; Song, Z. H.; Yeung, E. S.; Nikolau, B. J., Use of Mass Spectrometry for Imaging Metabolites in Plants. *Plant Journal* **2012,** *70* (1), 81–95.

90. Bjarnholt, N.; Li, B.; D'Alvise, J.; Janfelt, C., Mass Spectrometry Imaging of Plant Metabolites - Principles and Possibilities. *Natural product reports* **2014**.

91. Chatterji, B.; Pich, A., Maldi Imaging Mass Spectrometry and Analysis of Endogenous Peptides. *Expert review of proteomics* **2013,** *10* (4), 381-388.

92. Grassl, J.; Taylor, N. L.; Millar, A. H., Matrix-Assisted Laser Desorption/Ionisation Mass Spectrometry Imaging and Its Development for Plant Protein Imaging. *Plant methods* **2011,** *7* (1), 21.

93. Kaspar, S.; Peukert, M.; Svatos, A.; Matros, A.; Mock, H. P., Maldi-Imaging Mass Spectrometry - an Emerging Technique in Plant Biology. *Proteomics* **2011,** *11* (9), 1840-1850.

94. Matros, A.; Mock, H. P., Mass Spectrometry Based Imaging Techniques for Spatially Resolved Analysis of Molecules. *Front Plant Sci* **2013,** *4*, 89.

95. Gemperline, E.; Jayaraman, D.; Maeda, J.; Ane, J. M.; Li, L., Multifaceted Investigation of Metabolites During Nitrogen Fixation in Medicago Via High Resolution Maldi-Ms Imaging and Esi-Ms. *J Am Soc Mass Spectrom* **2015,** *26* (1), 149-158.

96. Ye, H.; Gemperline, E.; Venkateshwaran, M.; Chen, R.; Delaux, P. M.; Howes-Podoll, M.; Ane, J. M.; Li, L., Maldi Mass Spectrometry-Assisted Molecular Imaging of Metabolites During Nitrogen Fixation in the Medicago Truncatula-Sinorhizobium Meliloti Symbiosis. *The Plant journal : for cell and molecular biology* **2013,** *75* (1), 130-145.

97. Korte, A. R.; Yandeau-Nelson, M. D.; Nikolau, B. J.; Lee, Y. J., Subcellular-Level Resolution Maldi-Ms Imaging of Maize Leaf Metabolites by Maldi-Linear Ion Trap-Orbitrap Mass Spectrometer. *Anal Bioanal Chem* **2015,** *407* (8), 2301-2309.

98. Poth, A. G.; Mylne, J. S.; Grassl, J.; Lyons, R. E.; Millar, A. H.; Colgrave, M. L.; Craik, D. J., Cyclotides Associate with Leaf Vasculature and Are the Products of a Novel Precursor in Petunia (Solanaceae). *J Biol Chem* **2012,** *287* (32), 27033-27046.

99. Cavatorta, V.; Sforza, S.; Mastrobuoni, G.; Pieraccini, G.; Francese, S.; Moneti, G.; Dossena, A.; Pastorello, E. A.; Marchelli, R., Unambiguous Characterization and Tissue Localization of Pru P 3 Peach Allergen by Electrospray Mass Spectrometry and Maldi Imaging. *J Mass Spectrom* **2009,** *44* (6), 891-897.

100. Wu, K. J.; Odom, R. W., Matrix-Enhanced Secondary Ion Mass Spectrometry: A Method for Molecular Analysis of Solid Surfaces. *Anal Chem* **1996,** *68* (5), 873-882.

101. Kim, Y. P.; Oh, E.; Hong, M. Y.; Lee, D.; Han, M. K.; Shon, H. K.; Moon, D. W.; Kim, H. S.; Lee, T. G., Gold Nanoparticle-Enhanced Secondary Ion Mass Spectrometry Imaging of Peptides on Self-Assembled Monolayers. *Anal Chem* **2006,** *78* (6), 1913-1920.

102. Fletcher, J. S.; Lockyer, N. P.; Vickerman, J. C., Developments in Molecular Sims Depth Profiling and 3d Imaging of Biological Systems Using Polyatomic Primary Ions. *Mass spectrometry reviews* **2011,** *30* (1), 142-174.

103. Liebl, H., Sims Instrumentation and Imaging Techniques. *Scanning* **1980,** *3* (2), 79-89.

104. Sumner, L. W.; Lei, Z.; Nikolau, B. J.; Saito, K., Modern Plant Metabolomics: Advanced Natural Product Gene Discoveries, Improved Technologies, and Future Prospects. *Natural product reports* **2015,** *32* (2), 212-229.

105. Seyer, A.; Einhorn, J.; Brunelle, A.; Laprevote, O., Localization of Flavonoids in Seeds by Cluster Time-of-Flight Secondary Ion Mass Spectrometry Imaging. *Anal Chem* **2010,** *82* (6), 2326-2333.

106. Takats, Z.; Wiseman, J. M.; Gologan, B.; Cooks, R. G., Mass Spectrometry Sampling under Ambient Conditions with Desorption Electrospray Ionization. *Science* **2004,** *306* (5695), 471-473.

107. Ifa, D. R.; Wu, C. P.; Ouyang, Z.; Cooks, R. G., Desorption Electrospray Ionization and Other Ambient Ionization Methods: Current Progress and Preview. *Analyst* **2010,** *135* (4), 669-681.

108. Tata, A.; Perez, C. J.; Hamid, T. S.; Bayfield, M. A.; Ifa, D. R., Analysis of Metabolic Changes in Plant Pathosystems by Imprint Imaging Desi-Ms. *J Am Soc Mass Spectrom* **2015,** *26* (4), 641-648.

109. Hemalatha, R. G.; Pradeep, T., Understanding the Molecular Signatures in Leaves and Flowers by Desorption Electrospray Ionization Mass Spectrometry (Desi Ms) Imaging. *Journal of agricultural and food chemistry* **2013,** *61* (31), 7477-7487.

110. Nemes, P.; Vertes, A., Laser Ablation Electrospray Ionization for Atmospheric Pressure, in Vivo, and Imaging Mass Spectrometry. *Analytical Chemistry* **2007,** *79* (21), 8098-8106.

111. Chen, Z. Y.; Bogaerts, A.; Vertes, A., Phase Explosion in Atmospheric Pressure Infrared Laser Ablation from Water-Rich Targets. *Appl Phys Lett* **2006,** *89* (4).

112. Nemes, P.; Barton, A. A.; Li, Y.; Vertes, A., Ambient Molecular Imaging and Depth Profiling of Live Tissue by Infrared Laser Ablation Electrospray Ionization Mass Spectrometry. *Analytical Chemistry* **2008,** *80* (12), 4575-4582.

113. Nemes, P.; Barton, A. A.; Vertes, A., Three-Dimensional Imaging of Metabolites in Tissues under Ambient Conditions by Laser Ablation Electrospray Ionization Mass Spectrometry. *Analytical Chemistry* **2009,** *81* (16), 6668-6675.

114. Li, H.; Smith, B. K.; Mark, L.; Nemes, P.; Nazarian, J.; Vertes, A., Ambient Molecular Imaging by Laser Ablation Electrospray Ionization Mass Spectrometry with Ion Mobility Separation. *Int J Mass Spectrom* **2015,** *377*, 681-689.

115. Kiss, A.; Smith, D. F.; Reschke, B. R.; Powell, M. J.; Heeren, R. M., Top-Down Mass Spectrometry Imaging of Intact Proteins by Laser Ablation Esi Ft-Icr Ms. *Proteomics* **2014,** *14* (10), 1283-1289.

116. Smith, C. A.; O'Maille, G.; Want, E. J.; Qin, C.; Trauger, S. A.; Brandon, T. R.; Custodio, D. E.; Abagyan, R.; Siuzdak, G., Metlin: A Metabolite Mass Spectral Database. *Therapeutic drug monitoring* **2005,** *27* (6), 747-751.

117. Wishart, D. S.; Tzur, D.; Knox, C.; Eisner, R.; Guo, A. C.; Young, N.; Cheng, D.; Jewell, K.; Arndt, D.; Sawhney, S.; Fung, C.; Nikolai, L.; Lewis, M.; Coutouly, M. A.; Forsythe, I.; Tang, P.; Shrivastava, S.; Jeroncic, K.; Stothard, P.; Amegbey, G.; Block, D.; Hau, D. D.; Wagner, J.; Miniaci, J.; Clements, M.; Gebremedhin, M.; Guo, N.; Zhang, Y.; Duggan, G. E.; Macinnis, G. D.; Weljie, A. M.; Dowlatabadi, R.; Bamforth, F.; Clive, D.; Greiner, R.; Li, L.; Marrie, T.; Sykes, B. D.; Vogel, H. J.; Querengesser, L., Hmdb: The Human Metabolome Database. *Nucleic Acids Res* **2007,** *35* (Database issue), D521-526.

118. Wishart, D. S.; Jewison, T.; Guo, A. C.; Wilson, M.; Knox, C.; Liu, Y.; Djoumbou, Y.; Mandal, R.; Aziat, F.; Dong, E.; Bouatra, S.; Sinelnikov, I.; Arndt, D.; Xia, J.; Liu, P.; Yallou, F.; Bjorndahl, T.; Perez-Pineiro, R.; Eisner, R.; Allen, F.; Neveu, V.; Greiner, R.; Scalbert, A., Hmdb 3.0--the Human Metabolome Database in 2013. *Nucleic Acids Res* **2013,** *41* (Database issue), D801-807.

119. Kanehisa, M., A Database for Post-Genome Analysis. *Trends in genetics : TIG* **1997,** *13* (9), 375-376.

120. Bolton, E. E.; Wang, Y. L.; Thiessen, P. A.; Bryant, S. H., Pubchem: Integrated Platform of Small Molecules and Biological Activities. *Ann Rep Comp Chem* **2010,** *4*, 217-241.

121. Horai, H.; Arita, M.; Kanaya, S.; Nihei, Y.; Ikeda, T.; Suwa, K.; Ojima, Y.; Tanaka, K.; Tanaka, S.; Aoshima, K.; Oda, Y.; Kakazu, Y.; Kusano, M.; Tohge, T.; Matsuda, F.; Sawada, Y.; Hirai, M. Y.; Nakanishi, H.; Ikeda, K.; Akimoto, N.; Maoka, T.; Takahashi, H.; Ara, T.; Sakurai, N.; Suzuki, H.; Shibata, D.; Neumann, S.; Iida, T.; Tanaka, K.; Funatsu, K.; Matsuura, F.; Soga, T.; Taguchi, R.; Saito, K.; Nishioka, T., Massbank: A Public Repository for Sharing Mass Spectral Data for Life Sciences. *J Mass Spectrom* **2010,** *45* (7), 703-714.

122. Cui, Q.; Lewis, I. A.; Hegeman, A. D.; Anderson, M. E.; Li, J.; Schulte, C. F.; Westler, W. M.; Eghbalnia, H. R.; Sussman, M. R.; Markley, J. L., Metabolite Identification Via the Madison Metabolomics Consortium Database. *Nat Biotechnol* **2008,** *26* (2), 162-164.

123. Fahy, E.; Subramaniam, S.; Brown, H. A.; Glass, C. K.; Merrill, A. H.; Murphy, R. C.; Raetz, C. R. H.; Russell, D. W.; Seyama, Y.; Shaw, W.; Shimizu, T.; Spener, F.; van Meer, G.; VanNieuwenhze, M. S.; White, S. H.; Witztum, J. L.; Dennis, E. A., A Comprehensive Classification System for Lipids. *J Lipid Res* **2005,** *46* (5), 839-861.

124. Fahy, E.; Subramaniam, S.; Murphy, R. C.; Nishijima, M.; Raetz, C. R. H.; Shimizu, T.; Spener, F.; van Meer, G.; Wakelam, M. J. O.; Dennis, E. A., Update of the Lipid Maps Comprehensive Classification System for Lipids. *J Lipid Res* **2009,** *50,* S9-S14.

125. Wolf, S.; Schmidt, S.; Muller-Hannemann, M.; Neumann, S., In Silico Fragmentation for Computer Assisted Identification of Metabolite Mass Spectra. *Bmc Bioinformatics* **2010,** *11*.

126. Smith, C. A.; Want, E. J.; O'Maille, G.; Abagyan, R.; Siuzdak, G., Xcms: Processing Mass Spectrometry Data for Metabolite Profiling Using Nonlinear Peak Alignment, Matching, and Identification. *Anal Chem* **2006,** *78* (3), 779-787.

127. Gowda, H.; Ivanisevic, J.; Johnson, C. H.; Kurczy, M. E.; Benton, H. P.; Rinehart, D.; Nguyen, T.; Ray, J.; Kuehl, J.; Arevalo, B.; Westenskow, P. D.; Wang, J.; Arkin, A. P.; Deutschbauer, A. M.; Patti, G. J.; Siuzdak, G., Interactive Xcms Online: Simplifying Advanced Metabolomic Data Processing and Subsequent Statistical Analyses. *Anal Chem* **2014,** *86* (14), 6931-6939.

128. Xia, J. G.; Psychogios, N.; Young, N.; Wishart, D. S., Metaboanalyst: A Web Server for Metabolomic Data Analysis and Interpretation. *Nucleic Acids Res* **2009,** *37,* W652-W660.

129. Xia, J. G.; Mandal, R.; Sinelnikov, I. V.; Broadhurst, D.; Wishart, D. S., Metaboanalyst 2.0-a Comprehensive Server for Metabolomic Data Analysis. *Nucleic Acids Res* **2012,** *40* (W1), W127-W133.

130. Xia, J. G.; Sinelnikov, I. V.; Han, B.; Wishart, D. S., Metaboanalyst 3.0-Making Metabolomics More Meaningful. *Nucleic Acids Res* **2015,** *43* (W1), W251-W257.

131. Ma, B.; Zhang, K.; Hendrie, C.; Liang, C.; Li, M.; Doherty-Kirby, A.; Lajoie, G., Peaks: Powerful Software for Peptide De Novo Sequencing by Tandem Mass Spectrometry. *Rapid communications in mass spectrometry : RCM* **2003,** *17* (20), 2337-2342.

132. Altschul, S. F.; Gish, W.; Miller, W.; Myers, E. W.; Lipman, D. J., Basic Local Alignment Search Tool. *J Mol Biol* **1990,** *215* (3), 403-410.

133. Bailey, T. L.; Boden, M.; Buske, F. A.; Frith, M.; Grant, C. E.; Clementi, L.; Ren, J. Y.; Li, W. W.; Noble, W. S., Meme Suite: Tools for Motif Discovery and Searching. *Nucleic Acids Res* **2009,** *37*, W202-W208.

134. Baggerman, G.; Liu, F.; Wets, G.; Schoofs, L., Bioinformatic Analysis of Peptide Precursor Proteins. *Annals of the New York Academy of Sciences* **2005,** *1040*, 59-65.

135. Wenger, C. D.; Phanstiel, D. H.; Lee, M. V.; Bailey, D. J.; Coon, J. J., Compass: A Suite of Pre- and Post-Search Proteomics Software Tools for Omssa. *Proteomics* **2011,** *11* (6), 1064-1074.

136. MacLean, B.; Tomazela, D. M.; Shulman, N.; Chambers, M.; Finney, G. L.; Frewen, B.; Kern, R.; Tabb, D. L.; Liebler, D. C.; MacCoss, M. J., Skyline: An Open Source Document Editor for Creating and Analyzing Targeted Proteomics Experiments. *Bioinformatics* **2010,** *26* (7), 966-968.

137. Wenger, C. D.; Coon, J. J., A Proteomics Search Algorithm Specifically Designed for High-Resolution Tandem Mass Spectra. *Journal of Proteome Research* **2013,** *12* (3), 1377-1386.

138. Robichaud, G.; Garrard, K. P.; Barry, J. A.; Muddiman, D. C., Msireader: An Open-Source Interface to View and Analyze High Resolving Power Ms Imaging Files on Matlab Platform. *Journal of the American Society for Mass Spectrometry* **2013,** *24* (5), 718-721.

139. Rubel, O.; Greiner, A.; Cholia, S.; Louie, K.; Bethel, E. W.; Northen, T. R.; Bowen, B. P., Openmsi: A High-Performance Web-Based Platform for Mass Spectrometry Imaging. *Anal Chem* **2013,** *85* (21), 10354-10361.

140. Race, A. M.; Steven, R. T.; Palmer, A. D.; Styles, I. B.; Bunch, J., Memory Efficient Principal Component Analysis for the Dimensionality Reduction of Large Mass Spectrometry Imaging Data Sets. *Anal Chem* **2013,** *85* (6), 3071-3078.

141. Lei, Z.; Jing, L.; Qiu, F.; Zhang, H.; Huhman, D.; Zhou, Z.; Sumner, L. W., Construction of an Ultrahigh Pressure Liquid Chromatography-Tandem Mass Spectral Library of Plant Natural Products and Comparative Spectral Analyses. *Anal Chem* **2015**.

142. Grimsrud, P. A.; den Os, D.; Wenger, C. D.; Swaney, D. L.; Schwartz, D.; Sussman, M. R.; Ane, J. M.; Coon, J. J., Large-Scale Phosphoprotein Analysis in Medicago Truncatula Roots Provides Insight into in Vivo Kinase Activity in Legumes. *Plant Physiol* **2010,** *152* (1), 19-28.

143. Sun, Q.; Zybailov, B.; Majeran, W.; Friso, G.; Olinares, P. D. B.; van Wijk, K. J., Ppdb, the Plant Proteomics Database at Cornell. *Nucleic Acids Res* **2009,** *37*, D969-D974.

144. Komatsu, S., Rice Proteome Database: A Step toward Functional Analysis of the Rice Genome. *Plant Mol Biol* **2005,** *59* (1), 179-190.

145. Wienkoop, S.; Staudinger, C.; Hoehenwarter, W.; Weckwerth, W.; Egelhofer, V., Promex - a Mass Spectral Reference Database for Plant Proteomics. *Front Plant Sci* **2012,** *3*.

146. Urbanczyk-Wochniak, E.; Sumner, L. W., Mediccyc: A Biochemical Pathway Database for Medicago Truncatula. *Bioinformatics* **2007,** *23* (11), 1418-1423.

147. Mueller, L. A.; Zhang, P. F.; Rhee, S. Y., Aracyc: A Biochemical Pathway Database for Arabidopsis. *Plant Physiol* **2003,** *132* (2), 453-460.

148. Zhang, P. F.; Foerster, H.; Tissier, C. P.; Mueller, L.; Paley, S.; Karp, P. D.; Rhee, S. Y., Metacyc and Aracyc. Metabolic Pathway Databases for Plant Research. *Plant Physiol* **2005,** *138* (1), 27-37.

149. Kanehisa, M., Toward Pathway Engineering: A New Database of Genetic and Molecular Pathways. *Science & Technology Japan* **1996,** *59*, 34-38.

150. Spengler, B.; Hubert, M., Scanning Microprobe Matrix-Assisted Laser Desorption Ionization (Smaldi) Mass Spectrometry: Instrumentation for Sub-Micrometer Resolved Ldi and Maldi Surface Analysis. *J Am Soc Mass Spectrom* **2002,** *13* (6), 735-748.

151. Rompp, A.; Spengler, B., Mass Spectrometry Imaging with High Resolution in Mass and Space. *Histochemistry and cell biology* **2013,** *139* (6), 759-783.

152. Koestler, M.; Kirsch, D.; Hester, A.; Leisner, A.; Guenther, S.; Spengler, B., A High-Resolution Scanning Microprobe Matrix-Assisted Laser Desorption/Ionization Ion Source for Imaging Analysis on an Ion Trap/Fourier Transform Ion Cyclotron Resonance Mass Spectrometer. *Rapid Commun Mass Sp* **2008,** *22* (20), 3275-3285.

153. Boggio, K. J.; Obasuyi, E.; Sugino, K.; Nelson, S. B.; Agar, N. Y. R.; Agar, J. N., Recent Advances in Single-Cell Maldi Mass Spectrometry Imaging and Potential Clinical Impact. *Expert review of proteomics* **2011,** *8* (5), 591-604.

154. Li, L.; Hur, M.; Lee, J. Y.; Zhou, W.; Song, Z.; Ransom, N.; Demirkale, C. Y.; Nettleton, D.; Westgate, M.; Arendsee, Z.; Iyer, V.; Shanks, J.; Nikolau, B.; Wurtele, E. S., A Systems Biology Approach toward Understanding Seed Composition in Soybean. *BMC genomics* **2015,** *16 Suppl 3*, S9.

155. Kim, T.; Dreher, K.; Nilo-Poyanco, R.; Lee, I.; Fiehn, O.; Lange, B. M.; Nikolau, B. J.; Sumner, L.; Welti, R.; Wurtele, E. S.; Rhee, S. Y., Patterns of Metabolite Changes Identified from Large-Scale Gene Perturbations in Arabidopsis Using a Genome-Scale Metabolic Network. *Plant Physiol* **2015,** *167* (4), 1685-1698.

156. Quanbeck, S. M.; Brachova, L.; Campbell, A. A.; Guan, X.; Perera, A.; He, K.; Rhee, S. Y.; Bais, P.; Dickerson, J. A.; Dixon, P.; Wohlgemuth, G.; Fiehn, O.; Barkan, L.; Lange, I.; Lange, B. M.; Lee, I.; Cortes, D.; Salazar, C.; Shuman, J.; Shulaev, V.; Huhman, D. V.; Sumner, L. W.; Roth, M. R.; Welti, R.; Ilarslan, H.; Wurtele, E. S.; Nikolau, B. J., Metabolomics as a Hypothesis-Generating Functional Genomics Tool for the Annotation of Arabidopsis Thaliana Genes of "Unknown Function". *Front Plant Sci* **2012,** *3*.

Tables

Table 1. Comparison of MSI approaches detailing ionization methods, mass range, and spatial resolution, and optimal analytes.

	MALDI	**SIMS**	**DESI**	**LAESI**
Ionization Source	UV/IR laser (Soft ionization)	Ion gun (Hard ionization)	Solvent spray (Soft ionization)	Solvent spray (Soft ionization)
Mass Range (Da)	0-70,000	0-2,000 (static mode) 0-300 (dynamic mode)	0-5,000	0-66,000
Lateral Resolution (μm)	20-500	0.5-50 (static) 0.04-0.5 (dynamic)	100-1000	200-400
Molecular Classes	metabolites, lipids, peptides, proteins	elements, metabolites, lipids, small peptides	metabolites, lipids, small peptides	metabolites, lipids, peptides, proteins

Figures

Figure 1

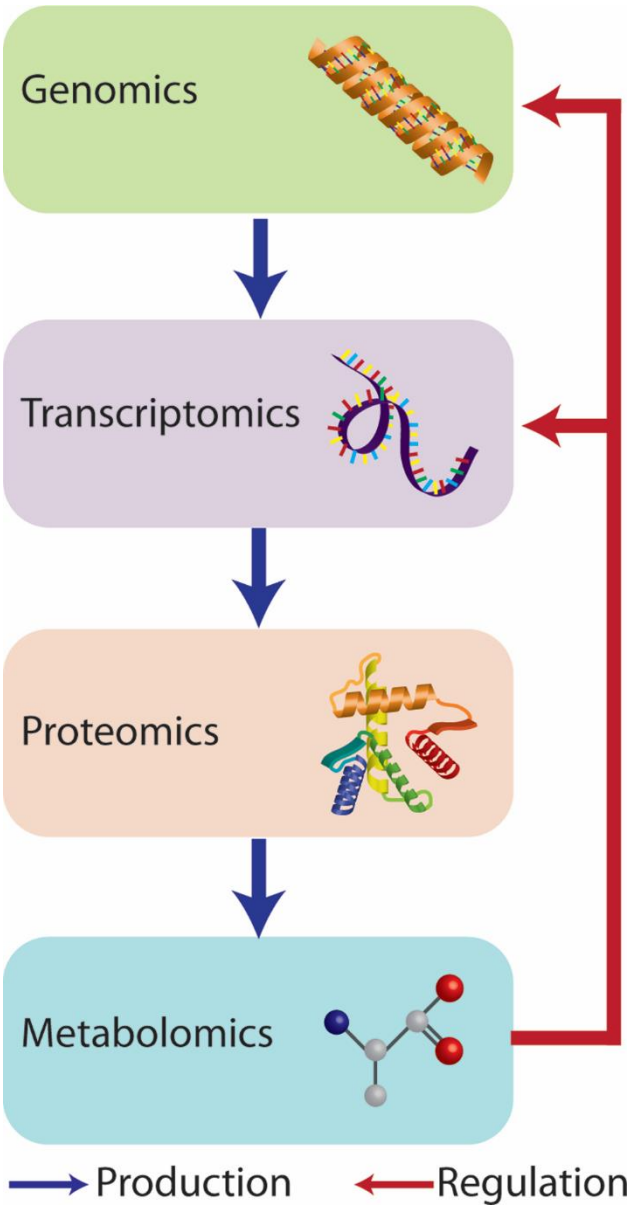

Figure 1. Interaction between genomics, transcriptomics, proteomics, and metabolomics.

Figure 2

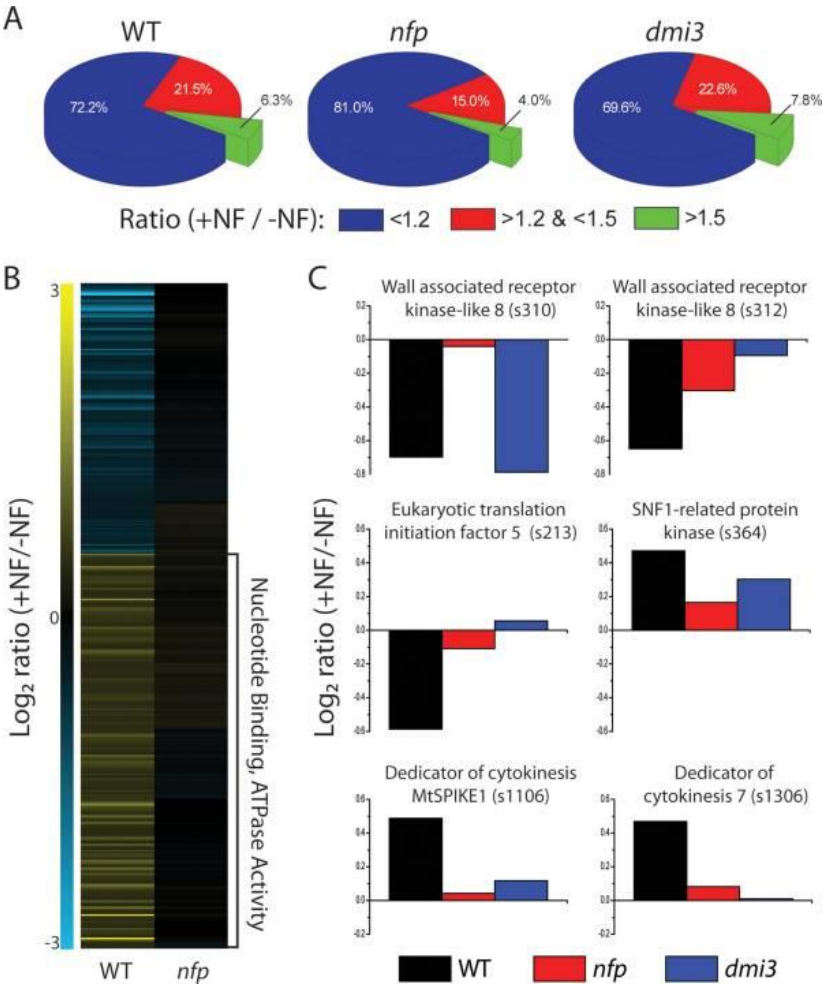

Figure 2. Global view of changes in the proteome and phosphoproteome from all the experiments combined. A) Pie charts displaying the distribution of phosphorylation changes for wild-type (WT) and *nfp* and *dmi3* mutants. Wild-type plants readily respond to NF as 6.3% of phosphoisoforms are altered more than 1.5-fold. *Nfp* displayed a lower response, 4.0%, but the presence of these changes provides evidence of a separate NF receptor sensing NF. *Dmi3* showed more NF response than wild-type plants, as the phosphorylation state of 7.8% of the phosphoisoforms was altered more than 1.5-fold. B) Heatmap of phosphoisoforms altered in wild-type and not in *nfp*. Phophoisofroms exhibiting a fold change more than 1.35 in wild-type plants and less than 1.25 in *nfp* were grouped *via* hierarchical clustering. Functional analysis revealed phosphoisoforms, which demonstrate an up-regulation in phosphorylation upon NF treatment, are enriched for the terms "nucleotide binding" and "ATPase activity". C) Representative proteins significantly altered in wild-type and not in *nfp*. Six phosphoisoforms that were significantly ($p < 0.05$, Student's *t* test, assuming equal variances) altered more than 1.35-fold in wild-type plants and less than 1.25-fold in *nfp* demonstrate the use of comparing wild-type and mutant measurements. These examples contain phosphoisoforms, which display both *nfp* dependent regulation and *dmi3* dependent regulation. Reprinted with permission from Ref. [29]. Copyright 2012 The American Society for Biochemistry and Molecular Biology, Inc.

Figure 3

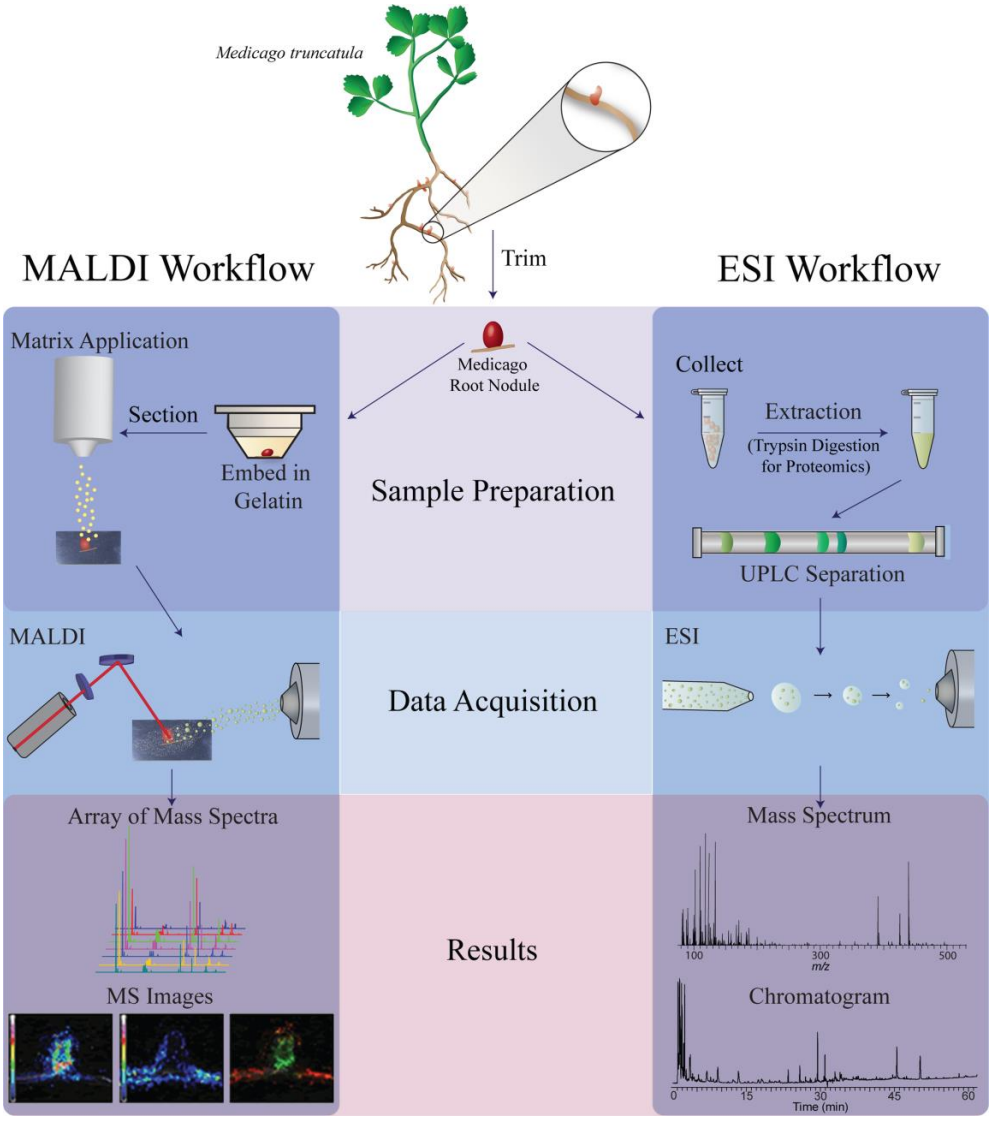

Figure 3. Comparison of MALDI-MSI (left) and LC-MS (right) Workflows.

In both types of analysis, the tissue of interest, the root nodule in this example, is trimmed from live plants and flash frozen to preserve the analytes of interest. For LC-MS, many root nodules are pooled, followed by analyte extraction and additional steps of trypsin digestion and desalting for proteomics experiments. For MALDI-MSI, a single root nodule is embedded in a stabilizing media, such as gelatin, cryo-sectioned onto a glass slide, and matrix is applied. For LC-MS, the plant extract is injected onto the UPLC column for LC separation and analyzed by the mass spectrometer yielding a mass spectrum and a chromatogram. For MALDI-MSI, the glass slide is inserted into the mass spectrometer where a mass spectrum is acquired in a raster pattern across the entire surface of the tissue resulting in a large array of mass spectra that are coordinated with spatial information. Software can then compile the array of mass spectra into heat-map-like images based on the intensity of each *m/z* at each corresponding location on the tissue.

Figure 4

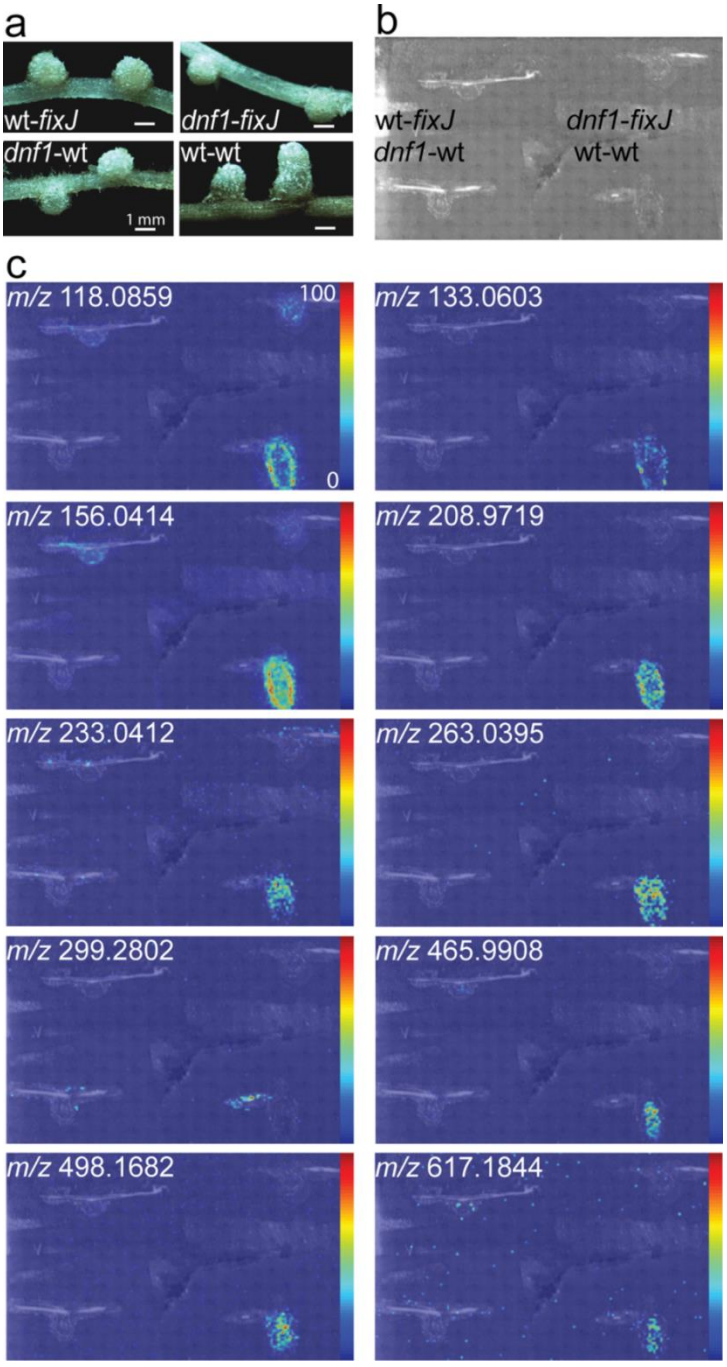

Figure 4. MALDI-MSI of metabolites in Medicago. a) A photograph of all four of the sample types that were used in this study: wild-type Medicago/ *fixJ* Rhizobia mutant (wt-*fixJ*), *dnf1* Medicago mutant/ *fixJ* Rhizobia mutant (*dnf1-fixJ*), *dnf1* Medicago mutant/ wild-type Rhizobia (*dnf1*-wt), and wild-type Medicago/ wild-type Rhizobia (wt-wt). Where wt-wt samples are capable of nitrogen fixation and samples containing either the plant or bacterial mutant (wt-*fixJ*, *dnf1*-wt, or *dnf1-fixJ*) are incapable of nitrogen fixation. b) Thaw-mounted Medicago sections on a glass slide that was covered with DHB matrix prior to MALDI-MSI. c) Representative ion images of metabolites with distinct spatial distributions that were found only in the wt-wt samples that are capable of fixing nitrogen, indicating that these metabolites may play a role in the biological nitrogen fixation process. Scale bar = 1 mm**.** Reprinted with permission from Ref. 95. Copyright 2015 Springer.

Figure 5

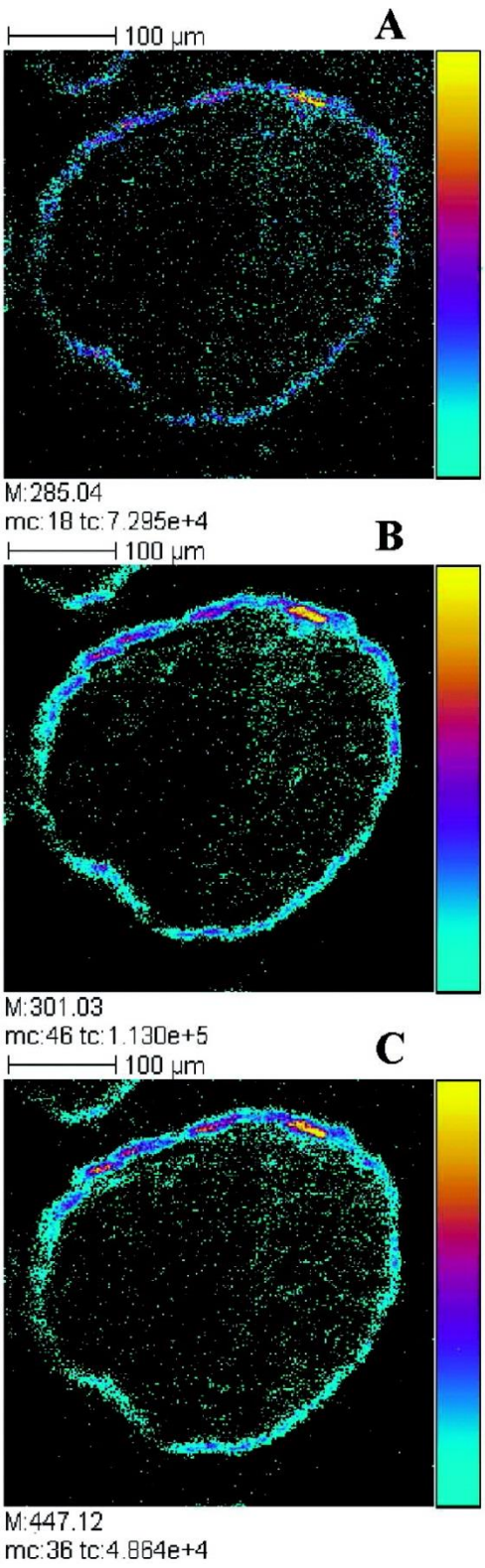

Figure 5. TOF-SIMS negative ion images of an *A. thaliana* seed section, embedded in a polyester resin: (A) *m/z* 285.04, (B) *m/z* 301.03, (C) *m/z* 447.1 (field of view 400 µm × 400 µm, 256 × 256 pixels, pixel size 1.56 µm, fluence 1.5 × 1012 ions · cm-2). Color scale bars, with amplitude in number of counts, are indicated to the right of each ion image. The amplitude of the color scale corresponds to the maximum number of counts (mc) and could be read as [0, mc]. TC is the total number of counts recorded for the specified *m/z* (sum of counts in all the pixels). The ion signals from the coat of another seed section appear in the top left of the images. Reprinted with permission from Ref. 105. Copyright 2010 American Chemical Society.

Figure 6

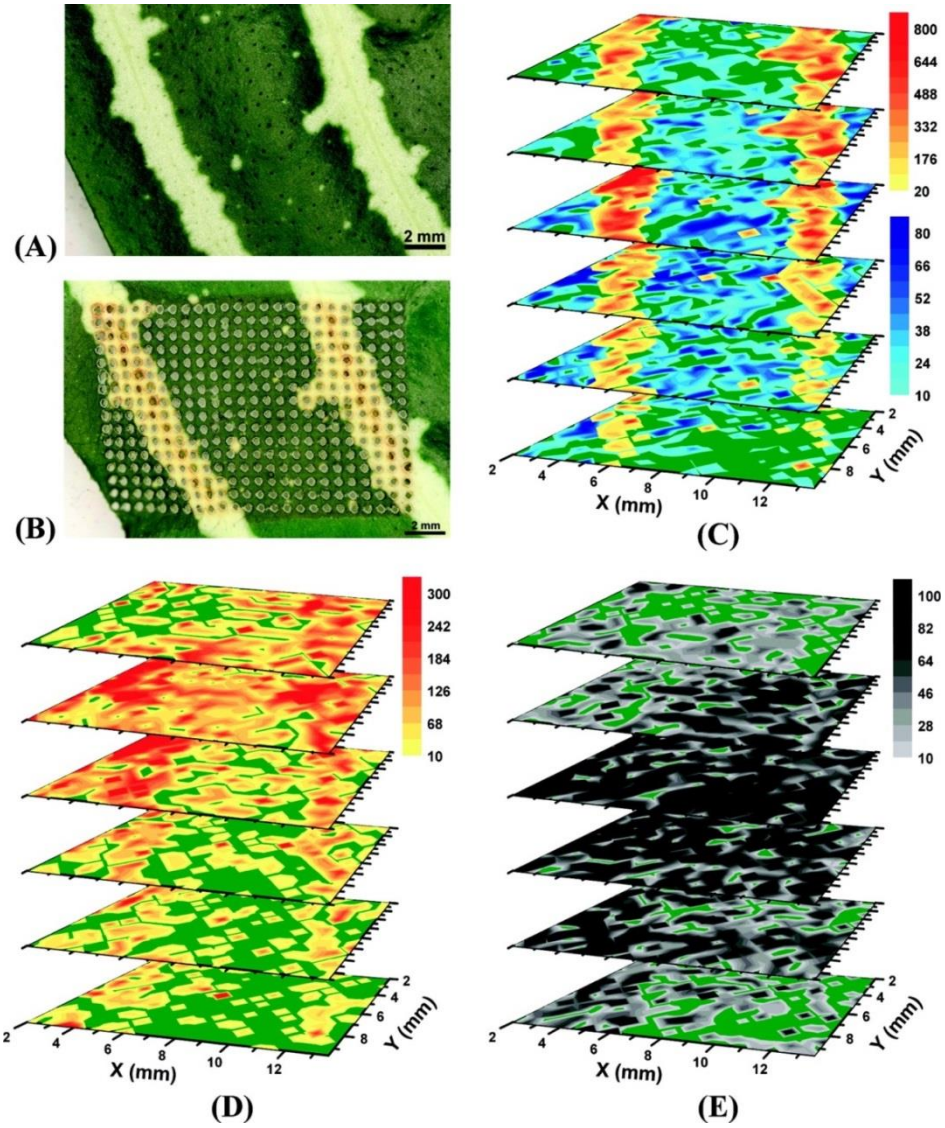

Figure 6. Metabolites in relation to tissue architecture captured by LAESI 3D imaging MS. Optical image of *A. squarrosa* leaves (A) before and (B) after analysis. (C) LAESI 3D imaging MS distribution of kaempferol/luteolin with *m/z* 287.0 (yellow/orange scale) followed the variegation pattern. Chlorophyll a with *m/z* 893.5 (blue scale) accumulated in the mesophyll layers. (D) Acacetin with *m/z* 285.0 showed higher abundance in the yellow sectors of the second and third layers with a homogeneous distribution in the others. (E) Kaempferol-(diacetyl coumarylrhamnoside) with *m/z* 663.2 accumulated in the mesophyll layers (third and fourth) with uniform lateral distributions. Reprinted with permission from Ref. 113. Copyright 2009 American Chemical Society.

Appendix V

A Vision for Better Health: Mass Spectrometry Imaging for Clinical Diagnostics

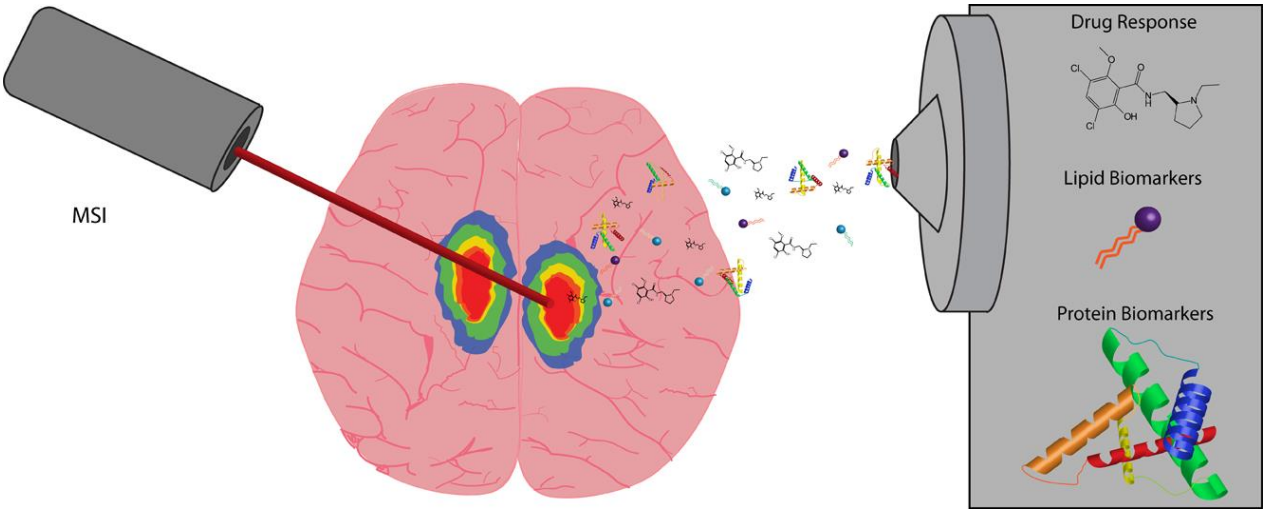

Adapted from **Gemperline, E.**; Ye, H.; Li, L. "A Vision for Better Health: Mass Spectrometry Imaging for Clinical Diagnostics", Clinica Chimica Acta, 420: 11-22 (2013) doi:10.1016/j.cca.2012.10.018

Abstract

Mass spectrometry imaging (MSI) is a powerful tool that grants the ability to investigate a broad mass range of molecules from small molecules to large proteins by creating detailed distribution maps of selected compounds. Its usefulness in biomarker discovery towards clinical applications has obtained success by correlating the molecular expression of tissues acquired from MSI with well-established histology. To date, MSI has demonstrated its versatility in clinical applications, such as biomarker diagnostics of different diseases, prognostics of disease severities and metabolic response to drug treatment, etc. These studies have provided significant insight in clinical studies over the years and current technical advances are further facilitating the improvement of this field. Although the underlying concept is simple, factors such as choice of ionization method, sample preparation, instrumentation and data analysis must be taken into account for successful applications of MSI. Herein, we briefly reviewed these key elements yet focused on the clinical applications of MSI that cannot be addressed by other means. Challenges and future perspectives in this field are also discussed to conclude that the ever-growing applications with continuous development of this powerful analytical tool will lead to a better understanding of the biology of diseases and improvements in clinical diagnostics.

1. Introduction

The integration of gel electrophoresis and liquid chromatography coupled to MS enables high throughput characterization of complex proteomes to detect disease biomarkers[1-4] or evaluate the response to the exposure of drugs or stress.[5-8] Yet spatial localization of the detected proteins and their corresponding expression changes to specific disease or treatment cannot be attained. Conventional immunohistochemical staining (IHC) allows for obtaining high resolution distribution images of targeted proteins. However, a significant limitation of this standard method is the need for labeling, which means that the target molecules must be known prior to the experiment. Alternatively, MSI has evolved as a powerful tool for the analysis of a wide range of molecules, mainly using matrix-assisted laser desorption/ionization mass spectrometry (MALDI-MS), but also using other ionization methods such as desorption electrospray ionization mass spectrometry (DESI-MS) and secondary ion mass spectrometry (SIMS). MSI has enormous advantages over conventional protein imaging techniques in that not only it is label-free, but it also enables simultaneous mapping of numerous molecules in tissue samples with great sensitivity and chemical specificity. MALDI-MSI has proven to be a valuable technology with numerous applications in localizing proteins,[9-10] examining lipid distributions[11] and mapping neuropeptides,[12-13] in both organ and cellular levels, by varying the experimental conditions. Since no prior knowledge of molecular identities is required for MSI applications, it has become a standard biomarker discovery tool to compare analyte expression pattern changes by analyzing multiplexed data sets. To date, MSI has been applied to identify biomarkers directly from tissue sections as an aid to disease diagnosis or prognosis of different disease types.[14] It has also been used to determine the response of the subjects to drugs or other therapeutic regimes, shedding light in studies of personalized medicine. Herein we review

current publications that underscore the critical role MSI, especially MALDI-MSI, plays in the study of molecular dynamics in the context of clinical research. With MSI, a better understanding of the molecular pathology of various diseases such as cancer and neurodegenerative diseases can be obtained, and this information can be used for more efficient diagnoses and improved treatments.

2. Methodology

2.1 Ionization

MALDI has shown its revolutionary power with its capability of analyzing a wide mass range of intact molecules spanning from large proteins and peptides to small metabolites and lipids with a 'soft' and efficient ionization source. Other than the wide mass range, MALDI also delivers several other unique features in comparison to other ionization techniques, such as a great tolerance for salts, producing mostly singly charged ions and low femtomole to attomole sensitivity. Moreover, its capability to acquire biomolecules' mass to charge ratio (*m/z)* and additional sequence information utilizing post source decay (PSD) or LIFT (a short form of "potential lift")[15] demonstrated its power for unraveling and understanding molecular complexity. N_2 or neodymium-doped yttrium aluminum garnet (Nd:YAG) lasers are usually employed to perform MSI experiments. The size of the laser beam and the matrix crystal combinatorially determine the spatial resolution of MALDI-MS images that can be attained. To date, a commercially available MALDI-TOF/TOF with a regular matrix sprayer is usually able to provide a spatial resolution of 30~75 μm. The resolution could be further improved down to cellular scale with the advances discussed in **2.2.2 single-cell MSI**.

SIMS is another technique that has long been established for MSI applications. In SIMS, ionization takes place by first bombarding a solid sample under a high vacuum with high energy "primary" ions.[16] Following the primary ion impact, secondary ions are sputtered from the sample surface and then be drawn into a mass analyzer, typically a TOF analyzer, for surface chemistry analysis. SIMS provides excellent spatial resolution due to its highly focused ion beam. Nevertheless, the primary ion source is fairly limited to small molecules due to its high energy that is prone to fragment large molecules in the ablation/ionization process. Recent advances in SIMS, such as metal cluster and polyatomic ion sources, provide significantly greater ion yields of ions in the *m/z* 400–3000 range with a reasonable resolution of 200 nm.[17] However, as suggested by Jones *et al.* , while SIMS can easily achieve spatially resolved images of small molecules for MSI applications, it will not likely be able to match MALDI's analytical capabilities for proteins.[17]

MALDI and SIMS-MSI both require vacuum for specimen analyses, complicating MSI procedure and limiting the applications to live biological samples. DESI, in comparison, is a simple, ambient ionization technique.[18-21] DESI channels charged solvent droplets and ions from an electrospray source onto the surface of interest.[22] The surface is impacted by the charged particles, yielding gaseous ions of the originally present biomolecules. By rastering the electrospray liquid jet across the surface of interest, DESI-MSI is accomplished. DESI's ambient nature and softness allow for the examination of various natural surfaces with no need for matrix.[23] Moreover, its clinical perspectives of miniaturization for field applications strongly poised this technique to be an innovative, portable tool since vacuum is no longer necessitated.[24] The downfall DESI has over vacuum MS methods is its spatial resolution that is generally reported to be approximately 180–200 μm.[23] Solutions have been undertaken to increase this

resolution to 12 μm by controlled desorption of analytes present in a restricted region of specimen using a minute amount of solvent between two capillaries comprising the nano-DESI probe.[20]

2.2 Sample preparation for MSI

A typical workflow of MSI generally consists of sample preparation, MSI acquisition and data analysis as simplified in **Figure 1**. These elements strongly determine the outcome of MSI experiments and are thereby elaborated in the following sections.

2.2.1 Sample preparation for tissues

2.2.1.1 Sample preparation for fresh tissues

Sample preparation in imaging experiments aims to generate reproducible and reliable MS images directly from tissue sections or cells. The structural integrity and morphology of tissues must be maintained after sample treatment without delocalization and degradation of analytes. The most common procedure after harvesting tissue is snap-freezing in powdered dry ice or liquid nitrogen, followed by storage at -80ºC until use.[25] Another method involves loosely wrapping the tissue in aluminum foil and gently placing it into liquid nitrogen, ice-cold ethanol or isopropanol bath for 30-60 seconds.[26] We recommend the latter approach since the gentler, longer freezing process avoids tissue cracking and fragmentation. Prior to long-term storage, tissue stabilization is recommended to minimize the sample aging effect. Tissue stabilization methods, such as microwave irradiation[27] and heat denaturation by Denator Stabilizer T1 (Gothenburg, Sweden), have been reported to effectively deactivate proteolytic enzymes, preventing post mortem degradation of proteins or peptides of interest.[28-29]

MSI experiments typically require 10-20 μm thick tissue sections.[30] Embedding tissues in supporting media such as gelatin[12-13] or sucrose[31] allows for easy handling and precise sectioning of tissue samples without introducing interferences to mass spectrometer, whereas polymer-containing material, such as optimal cutting temperature (OCT) compound, Tissue-tek and carboxymethylcellulose (CMC), should be avoided.[26]

Tissue sections are then transferred and attached onto a stainless steel conductive plate or indium-tin-oxide (ITO)-coated conductive glass slides[32-33] by thaw-mounting.[26] ITO-coated glass slides are more routinely used to analyze biomedical samples these days since it allows microscopic analyses of the tissue in MSI experiments with clinical diagnostic purposes.

Washing tissue sections with organic solvents is another recommended step to increase ion yields of protein/peptide signal by fixing tissues and removing ion-suppressing salts and lipids.[34] Through comparison with various solvents,[35-36] graded ethanol has become a routine procedure for MSI of clinical proteomics by enhancing protein signals effectively and reproducibly. In contrast, SIMS and DESI-MS require relatively simple sample preparation, mainly involving tissue sectioning, due to their limited applicability to low molecular weight (MW) analytes instead of peptides and proteins.

2.2.1.2 Sample preparation for FFPE tissues

Although many successes have been achieved using fresh frozen tissues for MSI, the most commonly used preservation technique for clinical tissue specimens is formaldehyde-fixed paraffin-embedding (FFPE). FFPE allows long-term storage at room temperature and is a preferred tissue preservation technique by clinical researchers. Nevertheless, the use of formalin leads to protein/peptide cross-linking and tissue embedding in paraffin wax brings severe

interferences to MS analysis.[37] The Caprioli group reported a novel technique to re-gain access to the proteins through a process of antigen retrieval by heating.[38] This process first denatures proteins, thus allowing for enzymatic digestion of these accessible proteins to non-crosslinked peptides that can be analyzed by MS. The peptides of interest are then isolated for MS/MS sequencing and searched against a database to retrieve the parent protein. With this approach, the distribution information of proteins can be obtained from FFPE tissues and correlated to the histology. This method opens up new possibilities of discovering disease biomarkers by analyzing a larger pool of samples from tissue bank, compared to available fresh frozen tissues, for statistical confidence. Unfortunately, FFPE tissues are not amenable to analyses of lipids, which are involved in various biological and disease processes, with current technologies, due to the repetitive washing of the tissues.

2.2.1.3 Laser capture microdissection

A major challenge of MSI is the lack of selectivity of the analytes during the ionization process and thus the ion suppression effect could impact the detection of low-level analytes of interest. One solution to this problem is to purify cells of interest from the entire tissue section by laser capture microdissection (LCM) prior to MSI. LCM is a technique that allows for isolation of samples down to single cell scale from thin tissue sections by irradiating a focused laser beam to the target region that is adhered to a heat-sensitive polymer film and subsequently removed upon irradiation.[39] The incorporation of LCM into MSI pipeline for spatially-resolved sampling has been demonstrated by mapping of proteins in the mouse epididymis,[32] ocular lens,[40] human breast tissue,[41] and rat kidneys.[42]

2.2.1.4 In situ tryptic digestion

Although MALDI-MSI is powerful in mapping proteins throughout tissue sections, it is significantly more difficult to identify the potential proteins of interest via MALDI-MS alone due to limited fragmentation obtainable from the singly-charged, high-mass ions produced by MALDI-MS. Therefore, the ability to digest the proteins and perform MS/MS sequencing directly on the tissue allows us to identify proteins *in situ* with high confidence without losing spatial resolution, thus facilitating the discovery of protein disease biomarkers. Groseclose *et al.* carried out *in situ* digestion by robotically spotting trypsin solution onto a coronal rat brain section in a well-defined microspotted array followed by automatic deposition of matrix.[43] Subsequent collection of MS and MS/MS spectra enables sequencing of tryptic fragments and thereby protein identification. This technique is fairly flexible in the workflow of MSI, compatible with upstream preparation like FFPE-tissue processing[44] or downstream coupling to ion mobility analysis.[45-46]

2.2.2 Single-cell MSI

While MSI offers a powerful tool for clinical diagnosis and disease prognosis evaluation, single-cell MSI presents unique merits and challenges that deserve special attention. One limiting factor of single-cell MSI is instrument sensitivity,[47] since the amount of analytes decreases as the square of the spatial resolution, as reviewed by McDonnell.[48] Induction-based fluidics (IBF) reported by Tu *et al.* alleviated this issue by using a charged capillary tip to charge the nL-sized matrix solution followed by launching the droplet onto the specimen.[49] This technique is amenable to single-cell MSI since the analyte diffusion is minimized and the resulting intensity is increased by 10-fold compared to conventional manual spotting by pipette.

An adaptable and cost-effective setup, the stretched sample method, was developed by Zimmerman *et al.* to improve the spatial resolution for single-cell scale MSI.[50] Briefly, dissected, individual cells, like neurons, were placed on a stretchable substrate, Parafilm, embedded with a monolayer of bead array Then Parafilm was manually stretched and placed on conductive ITO glass slides for further MALDI-MSI experiments.[50-51] The MS images of the cells are registered to their original locations based on the optical image taken prior to stretching.

The Sweedler group further improved the spatial resolution by reducing the incremental movement of the laser beam to smaller than the laser diameter.[52] They introduced this setup as an "oversampling" method by desorbing/ionized from a much smaller area with each incremental step after sample material is ablated away at the initial spot. Such oversampling procedures are relatively simple and do not need any additional hardware. Nevertheless, this method flaws in that the total sample has to be consumed, excluding the possibility to re-analyze the samples.

On the other hand, several custom-designed mass spectrometers permit single-cell resolution. For example, Spengler *et al.* fabricated special confocal-type objectives, which were furthered modified by Rompp and Guenther *et al.*, offering sub-micron spatial resolution.[53-55] This ion optical and laser setup was then coupled to a high-end Q-Exactive Orbitrap Fourier transform mass spectrometer (FTMS) by Schober *et al.*, delivering metabolites and lipids' MS images from Hela cells.[56] Resolution as low as 7 μm, reported by Chaurand *et al.*, was achieved by introducing a coaxial laser illumination ion source to a MALDI-TOF mass spectrometer.[33] Moreover, a proprietary Smartbeam-II MALDI laser developed by Bruker Daltonics allows beam diameters to be focused down to 10 μm and permits routine MSI analyses to be performed at the cellular level.[57]

An alternative approach to increasing single-cell spatial resolution is "microscope" MALDI-MSI by employing a setup that integrates a defocused UV laser, high-quality ion optical and a position-sensitive detector to record the position of the stigmatic projection of ions.[58-59] Luxembourg *et al.* reached a pixel size of 500 nm and a resolving power of 4 μm using this configuration.[58, 60] However, the use of this method is limited due to technical constraints like the specialized ion optics, a fast detector necessitated to achieve high magnification and computing software to reconstruct ion images.

MSI has been extensively used in differentiation between healthy and diseased tissues with the purpose of clinical prognostics and diagnostics. Its cutting-edge applications to single-cell analyses will provide detailed biochemical information at a cellular scale for mechanistic understanding and, ultimately, development of therapeutic treatments. The recent advances of single-cell MALDI-MSI and its clinical impact are presented by Boggio *et al.*[47]

2.3 Matrix application

Choosing a matrix and its application method are critical to MSI results. Other than conventional matrices such as α-cyano-4-hydroxycinnamic acid (CHCA) and 2,5-dihydroxy benzoic acid (DHB),[12-13, 26] ionic matrices made by mixing conventional matrices with organic bases are also widely used and reported to improve spectral quality, crystallization and vacuum stability.[61-62]

Matrix application is another area under continuous innovation. Several types of matrix application apparatus exist by deposited matrix either as homogeneous layers (spray coating) or discrete spots (microspotting). Pneumatic spray device such as pneumatic sprayer, airbrush, TM sprayer system from HTX imaging and thin layer chromatography sprayer, and vibrational spray

apparatus like ImagePrep Device from Bruker Daltonics are all capable of applying a uniform layer of small to medium-sized matrix droplets,[12-13, 63-64] whereas microspotters like CHIP produced by Shimadzu, deposit pL-sized droplets of matrix according to a predefined array and require multiple rounds of spotting for sufficient matrix coverage. In comparison to the wet application, solvent free methods like sublimation or dry coating yield very fine crystals amenable to high-spatial-resolution-MSI. However, it suffers from relatively low sensitivities due to the limited analyte-matrix interactions.[65] Deutskens *et al.* modified this procedure by rehydrating the sections following dry-coating and improved the detection sensitivity of proteins from rat cerebellum sections.[63]

2.4 MS Instrumentation

An ion source can be couple to most state-of-the-art mass analyzers for MSI capabilities. Time-of-flight (TOF) analyzers are most extensively used in MALDI-MSI applications. In TOF analyzers, desorbed ions are accelerated to the same kinetic energy and the *m/z* is determined by the time the ions take to travel through the TOF tube.[66] This design provides high sensitivity, a wide mass range (2~30 kDa) and fast analysis speed, thereby favored by the applications of MSI to clinical proteomics. The detection sensitivity of higher mass ions was further improved by Leinweber *et al.* who observed that the number of high MW proteins (> 20 kDa) detected from tissues by MALDI-TOF was significantly increased by doping Triton X-100 into the matrix.[67] Nevertheless, the characterization of peptides and low MW compounds necessitate the addition of another TOF tube, allowing for accurate measurement of peptides' and small molecules' masses and tandem mass fragmentation for sequence validation.[68]

The integration of ion mobility (IM) with MALDI-TOF is a breakthrough to MALDI-MS-based analyses. IM-TOF is a two-dimensional gas-phase separation technique that discriminates ions based on their *m/z* and collisional cross-section. Upon desorption/ionization from the tissue surface in MALDI source, ions travel inside an IM drift cell, which is equipped with an applied electric field and a carrier buffer gas that opposes ion motion. The ion's mass, charge, size and shape combinatorially determine its migration time inside the drift cell, consequently managing to discriminate isobaric ions according to their collisional cross-section.[69] For instance, IM-TOF has proven its usefulness in MSI of *in situ* digested proteins. Stauber *et al.* successfully separated and identified isobaric ions of Tublin and ubiquitin peptide fragments at *m/z* 1039 directly from a rat brain section based on different drift times, whereas the MS images of the two peptides would be merged without the additional separation by IM.[46] The benefit of performing IM separation prior to MS measurements is enormous and promises to find extensive applicability to MALDI-MSI-based clinical research.

Compared to the relatively low resolving power offered by a TOF/TOF mass analyzer, Fourier transform ion cyclotron resonance (FT-ICR) mass analyzers provide superior resolution and accuracy for unambiguous discrimination of analytes without sacrificing spatial resolution.[70] Moreover, it also provides unique ion trapping and storage capabilities, which are utilized by Kutz *et al.* for in-cell accumulation[71] and by Bruker Daltonics for continuous accumulation of selected ions (CASI)[72] to improve the detection sensitivity of trace-level analytes. The primary drawback of FT-ICR is the slow scan speed, which lowers the throughput for serial MSI experiments. A more powerful magnetic field could partially alleviate this problem by increasing the ion cyclotron frequency without affecting spectral quality. In addition, the Orbitrap manufactured by Thermo Fisher Scientific provides comparable resolution to an FT-

ICR. Orbitrap determines the *m/z* by measuring the axial oscillation frequency of ions back and forth along a spindle-like electrode within an electrostatic field,[73] which is proportional to the square root of the electrical-field strength, whereas the cyclotron frequency measured by FT-ICR is related to the magnetic field strength.[74] To obtain high resolving power on an FT-ICR, high-field magnets are needed, concomitantly at a high cost. Predictably, the Orbitrap is gaining more popularity in future MSI applications due to its excellent performance and relatively low cost compared with FT-ICR.

2.5 Histology-guided MSI

One of MSI's advantages is that spatial localization of analytes within a tissue is preserved in comparison to homogenization. It allows for differentiation of tissue regions based on molecular features. Therefore, MSI can be integrated with histology to directly target for diseased regions and correlate the peaks that are up-regulated/down-regulated in the specific regions with the reference information provided by histology. To date, histology-guided imaging has become the standard for applying MSI to clinical diagnostics.[47, 75-79] Hematoxylin and eosin (H&E) staining is commonly performed on clinical tissue samples. This technique allows the visualization of cells with bright field microscopy by labeling the nucleus and cytoplasm of the cells.[47] A trained pathologist can then use the H&E stained tissue to establish a diagnosis.[75] Methods of histology guided MSI have been developed that allow both the histological features and the MS image of the tissue to be observed. In such methods, the histological stain is applied to a serial section of the tissue that is to be analyzed by MSI, which dissipates the concern for mass spectrometry-friendly stains.[75-76] One downfall to this method is that it can be difficult to obtain serial sections, reproducibly, without tearing or folding the tissue on the cryostat.[77] This can cause a misalignment of the sections, causing a loss of correlation of small features. Another

method is to apply the histological stain directly to the tissue that is to be analyzed by MSI. This method requires MS-compatible stains, such as cresyl violet or methylene blue, or performing imaging first and washing off the matrix before applying the histological stain.[47, 77] The downfall of this method is that H&E staining is not compatible with MSI. Therefore the standard workflow would have to be changed in order to include non-standard histological stains and non-routine evaluation of the results.[77] The future of MSI in clinical diagnostics relies on incorporating it into the current diagnostic workflow, and must be compared and correlated with histological results.[78]

2.6 Data analysis

MSI data analysis software, such as BioMap (http://www.maldi-msi.org, available for free downloading) and proprietary programs for MSI systems (e.g., FlexImaging from Bruker Daltonics, ImageQuest from Thermo Fisher Scientific and TissueView from Applied Biosystems/MDS), are mostly employed to produce distribution maps for selected analytes. These software packages allow the user to adjust color scales, overlay ion density maps, and integrate MS images with acquired histological pictures.

Other than image processing, software that provides statistical support are also applied to MSI data analysis. For example, biomarker discovery studies usually involve comparing MSI data sets sampled from a control group with those from a treated group. Data-mining software, like ClinProTools by Bruker Daltonics, capable of performing principal component analysis (PCA) and hierarchical clustering of multiple MSI data sets to extract differentially expressed or distributed molecules, are widely used for identification of potential disease biomarker candidates.

3. Clinical Applications

Over the past decade, MSI has become a powerful tool that has been extensively applied to various clinical applications. In this section, we present current advances of this technique and its novel applications in clinical setting, including drug response measurement (**3.1**), lipid and protein biomarker discovery (**3.2**) and several other novel applications (**3.3**) as summarized in **Figure 1**.

3.1 Measuring Drug Response and Metabolites

Histology guided MSI has been extensively applied to the study of drug response and distribution.[80-83] Drexler *et al.*[80] combined quantitative whole-body autoradiography (QWBA) and imaging mass spectrometry to simulate an *in vivo* phototoxicity study of a proprietary drug candidate (Bristol-Myers Squibb Company, Princeton, NJ) within ocular tissue. QWBA reveals quantitative and tissue distribution information of radiolabeled analytes.[84] However, QWBA cannot be used to obtain information about the drug and its metabolites or degradation products. MSI is notorious for giving poor quantitative data, but can reveal information about the analyte and its products; therefore it was advantageous to combine QWBA and MSI for this study. The radio-labeled and non-labeled drug candidate, BMS-X, was dosed to two different test groups of rats. Two hours after the dose was administered, the animals were sacrificed for QWBA and MALDI-MSI experiments. The QWBA experiment showed that radio-labeled analyte(s) preferentially distributed to the back of the eye, not the cornea or lens, but revealed no information about the molecular species of the radio-labeled analyte(s). The MSI experiments detected only BMS-X, again in the back of the eye, therefore suggesting that there were no metabolites or degradation products of the drug present in the tissue. Employing complementary

technologies of MALDI-MSI and QWBA, Drexler *et al.* were able to assess the distribution of a new drug candidate and its potential metabolites which is essential for phototoxicity studies of pharmaceuticals before they can be prescribed in a clinical setting.

For pharmacokinetic and toxicity studies, the quantitative analysis of the *in vivo* distribution of a drug after it has been administered is essential. One of the major limitations to MSI is the lack of ability for successful quantification, as mentioned previously. A quantitative research method using MSI is greatly desired and could be very insightful for the pharmaceutical industry and for clinical diagnostics. Takai *et al.*[81] developed a quantitative MALDI-MSI approach to analyze the drug, raclopride (RCP), in multiple mouse organs and study drug distribution/ accumulation. RCP (*m/z* 347) is a dopamine D2 receptor-selective antagonist. RCP was initially spotted onto tissue sections and MS/MS experiments were performed in order to choose a fragment ion to monitor for the quantitation studies. The daughter ion *m/*z 129 was analyzed for the quantitation study. RCP was dosed to mice intravenously. The mice were sacrificed and whole-body sections of the mice were imaged with MALDI-MSI at different time points post-dosage:10 minutes, 30 minutes, and 60 minutes post-dosage. The average signal intensities (n=3) of RCP were calculated for each organ are each time point. For more precise quantification, Takai *et al.* used a normalization method by using the signal intensity of DHB peaks as an internal standard. The RCP signal intensities were divided by the DHB signal intensity within the specific organ of interest in order to normalize the results. Additionally, RCP was administered to mice and the concentrations of the drug in each organ studied (liver, heart, spleen, brain, and plasma) were determined by LC/MS/MS for comparison with the quantitative MSI procedure. There was a strong correlation observed between the concentrations

determined from the LC/MS/MS and the intensities calculated in the MSI method suggesting the future potential of MSI for quantitative analysis in multiple organs simultaneously.

Ambient ionization methods have gained interest and popularity for clinical MSI.[82] Wiseman *et al.* utilized desorption electrospray ionization (DESI) MS, an ambient ionization technique, to image drugs and their metabolites in histological tissue sections. Their study includes monitoring the antipsychotic drug, clozapine (*m/z* 327.1) and its dominant, N-desmethylclozapine, metabolite (*m/z* 313.1) in rat brain, lung, kidney, and testis tissue samples. By using their developed DESI-MSI method, and imaging in MS/MS mode, Wiseman *et al.* were able to detect Clozapine not only in brain tissue, but also the accumulation of the drug in lung, kidney, and testis tissue sections, which was previously unknown. The research team demonstrated the ability of DESI-MSI to detect small molecule pharmaceuticals and their metabolites simultaneously, directly from histological tissue sections. They were able to rapidly detect the drug and metabolite and display spatial distributions as well as provide relative quantitation with minimal sample preparation, giving this ambient ionization technique potential for use in the clinical setting.

There have been many reports of drug and metabolite imaging in the literature.[21, 80, 82-83, 85-93] Using multi-faceted approaches to distinguish between the drug and its metabolite provides more detailed and useful information for potential use in clinical studies. The ability to quantify active drugs simultaneously in multiple organs provides another key layer of information for toxicology studies for new potential drug candidates.

3.2 Biomarker Discovery and Validation

The discovery and validation of biomarkers, along with other laboratory and clinical evaluations, contribute to the assessment of disease severity, disease progression, and treatment response.[94] Gene expression profiling was the prominent source of biomarker discovery, but more recently, protein expression profiling has exploded in this field,[95] and lipidomics has been gaining popularity.[96]

3.2.1 Protein Biomarkers

Changes in protein levels in a tissue can correlate with disease state. These protein levels can be monitored in order to reveal, not only the type of disease, but also the severity of the disease. MSI has emerged as a powerful tool for biomarker discovery largely because of its ability to probe the proteomics of the tissue while maintaining the spatial distribution, which allows for direct comparison with histology.[75] MSI can be applied simultaneously to multiple tissues, allowing a more in depth study of the target disease and its potential biomarkers.[78]

Six common types of cancer (Barrett's cancer, breast cancer, colon cancer, hepatocellular carcinoma, gastric cancer, and thyroid carcinoma) have been probed with MALDI-MSI by Meding *et al*.[95] Patient diagnosis begins with tumor origin identification and classification and when a primary tumor cannot be identified, the sample is diagnosed as cancer of unknown primary (CUP).[95] The researchers used MALDI-MSI to establish distinct protein biomarkers for each type of known cancer. Cancer cell specific spectra were extracted and classified based on their proteomic differences with high confidence. These data were applied toward the identification of cancer from CUP samples. It is extremely important for the development of an individual patient treatment regimen that the secondary tumor (metastasis) be identified even if

the primary tumor cannot be found. Meding *et al.* introduced colon cancer liver metastases into the study in order to test the ability of MALDI-MSI to distinguish between colon cancer primary tumors, colon cancer liver metastases, and hepatocellular carcinomas (liver cancer). Their results indicated that MSI can be used to distinguish between, and classify these closely related cancer entities. This research team generated a classifier system based on MALDI-MSI methods that provides accurate tumor classification with high confidence levels. This method could become a valuable addition to the workflow for clinical tumor diagnostics.

Not only are biomarkers useful for diagnosing and classifying different types of cancer, they are also being used to distinguish between diseases with similar histological characteristics. One such example is Spitz Nevi and Spitzoid malignant melanoma which is found primarily in children.[97] Spitz Nevi is a benign skin lesion, whereas Spitzoid malignant melanoma requires surgery and chemotherapy.[98] These two diseases are very difficult to distinguish and can result in misdiagnoses when relying on histological criteria alone.[97-98] Lazova *et al.* performed a study using MALDI-MSI to compare the protein profiles of Spitz Nevi and Spitzoid malignant melanoma.[98] They have found 5 peptide peaks (*m/z* 976.49, 1060.18, 1336.72, 1410.74, and 1428.77) that were able to best discriminate between the two diseases, and a total of 12 discriminatory peaks that were used to build a classification model. Lazova *et al.* developed their model with a "training group", in which the diagnosis of Spitz Nevi or Spitzoid malignant melanoma was known, and validated it with a "test group", in which the diagnosis was unknown. The classification method for the tumor showed a sensitivity of 97% and specificity of 90%. Interestingly, the research team was able to correctly classify 28 of 31 samples based solely on the proteomic information found in the dermis and not the tumor itself. These results show great

promise for improving the diagnostic accuracy of these diseases in conjunction with standard histological evaluations.

Biomarkers can also show signs of effective treatment of a disease, not just identify the disease. Kim *et al.* utilized MSI to study drug distribution and potential biomarkers of response to therapy in prostate cancer.[99] The research team sought to study the spatial pharmacokinetics of prostate tumors treated with a novel tyrosine kinase inhibitor, AEE788. AEE788 potentially inhibits VEGFR and EGFR in nanomolar concentrations, which could enhance radiotherapy. Mice with prostate tumor xenografts were split into 4 groups: treated with AEE788, treated with radiation therapy, treated with AEE788 and radiation therapy, or untreated. The tumors were imaged for drugs or potential biomarker proteins. The drug and protein distributions were altered when the tumors were treated with irradiation. One potential biomarker was found at *m/z* 7765.4 which was present in the tumors treated with AEE788, but not when treated with radiation therapy alone. Radiation treated tumors had increased expression of multiple proteins that were not present in the AEE788 treated tumors. These could be potential biomarkers for treated vs. untreated tumors, which could provide means for evaluating efficacy of different therapeutics and optimizing individual patient treatment regimes.

3.2.2 Lipid Biomarkers

Lipidomics has recently gained popularity in clinical applications. Similarly to protein biomarker discovery, lipidomics aims to characterize lipid molecules in tissues and relate this information to disease states, among other applications.[96] Proteomics aims to characterize and quantify the cellular performers reflecting gene expression, whereas lipidomics (a subset of metabolomics) studies the molecular products of metabolism and is closest to patient phenotype,

making lipidomics an important field of study.[100] Traumatic brain injuries can have a great effect on the lipid distribution and composition of the brain. Cox *et al.* used MSI to study brain lipids after cortical impact injury.[18] For this study, rats were subjected to controlled cortical impact injury and the brains were removed at different time points of 24 hours, 3 days, and 7 days post injury. The distribution of lipid species in the brain showed large variation in the MS images, demonstrating time dependent changes in the lipid profile of the injured areas after traumatic injury. Not only do these results show lipid biomarker distributions that can reveal the extent and time post-injury, which can be used to monitor patient recovery after treatment, but also the observed changes in lipid abundances shed light on the mechanisms of injury and repair on the molecular level.

On a related note, Hanada *et al.* studied the alteration of phospholipids and prostaglandins after a spinal cord injury.[101] Alterations in lipid metabolism may play a key role in neurological disorders; therefore it is important to study these alterations to the lipid profiles during the occurrence and progression of a spinal cord injury. For this study, rats with applied spinal cord injuries were used, and the lipid distributions were studied after 12 hours, 1 day, or 1, 2, or 8 weeks post-injury. Unique distribution patterns were observed for different types of phospholipids as the tissue damage resulting from the spinal cord injury progressed. Spatiotemporal changes in phosphatidylcholines (PCs) were examined with MSI. Both temporal and irreversible alterations in distinct PC species were observed, especially in species that contained 3-docosahexaenoic acid (DHA). **Figure 2** shows the spatio-temporal images of two different DHA-containing PCs. At the impact site, an irreversible change in DHA-containing PCs was observed over time. This observation may result from an irreversible deficit of the

neurons and could lead to motor dysfunction, meaning that DHA-PC reduction could be a potential indicator of the pathology of spinal cord injuries to be used in clinical settings.

3.2.3 Small Molecule Biomarkers

Ambient ionization methods can also be used to study and identify biomarkers in cancerous tissues.[18, 102-103] Dill *et al.* used DESI-MSI to study human bladder cancer and develop a statistical method for distinguishing between cancerous and non-cancerous tissue samples in conjunction with standard histological identification methods. The researchers used a training set of samples to establish the best predictive features and a test/validation set to evaluate the performance of their statistical model on representative samples. There were 20 pairs of cancerous and adjacent normal human bladder tissue samples used in this study. DESI-MSI data show significant changes in glycerophosphoinositols, glycerophosphoserines, and fatty acids between the cancerous and normal tissue samples. A series of DESI-MSI images were used to visually characterize the distribution of particular molecular species across the set of tissue samples. These images were visually compared to optically scanned images of the H&E-stained histological sections. Their results agreed with the pathological diagnosis of cancer and normal tissue for 15 of the tissue pairs. There was excellent agreement between the H&E-stained sections and the DESI images. Interestingly, for one sample, a border of tumor was detected on the normal tissue section, demonstrating the utility of DESI-MSI for determining the margins of the tumor before surgery. Overall, these results are very encouraging for the development of a method that could be used in a clinical setting for the diagnosis of cancer.

3.3 Unique Applications for Clinical Diagnostics

Apart from drug distribution and biomarker discovery, MSI has been used for several other clinical applications.[104-107] Osteoporosis is well-known disease for which biomarkers have been extensively studied,[102, 108-114] but little attention has been devoted to bone material quality.[106] Routine clinical fracture risk assessments do not consider the quality of the bone mineral matrix. Zoehrer *et al.* used SIMS-MSI to investigate the spatial distribution and relationship of phosphorus and calcium in bone.[106] Calcium (Ca) and phosphate (P) are the main elements of the bone mineral building block, hydroxyapatite, and therefore support bone tissue mineralization. Bone material properties of the femoral head in male patients, age 65-80, with fragility fractures were compared to male, age-matched, non-fracture controls. SIMS-MSI clearly showed a greater frequency of areas on high Ca ion intensity in the tissue samples with fragility fractures, when compared to the control group. In the fragility fracture samples, a distinct, ~25 μm wide line of Ca ions was observed along the surface of the endosteum portion of the trabecular bone. In the control group, this line of Ca ions was distributed more diffusely, over a larger area of ~50 μm. Regions of high P ion intensity were observed in the control samples. The overall results show that a significant decrease in the P levels is associated with fragility fractures and the Ca/P ratio and distribution on the trabecular bone could be valuable parameters to consider during therapeutic and diagnostic trials.

Assessing the compatibility of treatments with the body is a key step necessary to ensure the safety of the patients. Biodegradable polymers are of high interest in the medical field because of their potential applications in the field of tissue engineering and as drug delivery carriers.[105] Supramolecular polymers have gained much interest as potential drug delivery carriers because of their compatibility with poorly water soluble compounds and their potential

for controlled drug release.[19, 115-121] In drug delivery systems, these polymers are designed to deliver active pharmaceutical ingredients to a localized place in the body, that needs the drug, and expose other parts of the body at a much lower dose. Klerk *et al.* has used SIMS-MSI to elucidate molecular distributions in and around such polymer. A supramolecular polymeric hydrogel (containing no drugs) was implanted into rat renal tissue and the rat kidneys were harvested 15 days after implantation. Half of the kidneys were prepared for MSI and half were used for histological comparison. The MSI images show lipids from the kidneys, the polymer capsule, and cholesterol distribution around the implantation site, as well as silicone contaminants from the surgical tools. The images show that lipids from the kidney tissue entered into the polymer capsule, as shown in **Figure 3**, demonstrating biological activity within the polymer. When the study is continued with a polymer implant that does contain active pharmaceutical ingredients, the researchers will have the opportunity to study drug release by imaging the drug distribution in the surrounding tissue at various time points. Overall, this research shows the great potential of SIMS-MSI for understanding controlled drug distribution.

Biodegradable polymers are also being applied to the field of tissue engineering, requiring extensive study of the compatibility of these materials with the body. In tissue engineering, scaffolds made of biodegradable polymers can be designed to be slowly degraded by the body as their function is taken over by newly generated tissue. During renal failure, it may be necessary for a patient to undergo hemodialysis, which requires the doctors to surgically form an arteriovenous fistulae (AVF), using vein grafts.[107] In this procedure, the patients artery and vein are sutured together with a graft connecting them, which allows for the blood to bypass the capillaries and the vein to be enlarged so that it can accommodate the volume of blood being transferred during hemodialysis [122]. These grafts are typically made, not with polymers, but with

the patient's existing veins. Although the grafts come from the patient themselves, the veins in and around the graft degrade over time due to biological changes in the tissue.[107] Previous studies have shown that graft deformation is associated with abnormal lipid metabolism in hemodialysis patients.[123-124] Tanaka *et al.* used MALDI-MSI to study the lipid profile of AVF tissues.[107] In this study, there were three types of vein samples: AVF tissues, control veins (CV), and peripheral artery occlusive disease (PAD) tissue. PAD is a disease that causes veins to deteriorate and is caused naturally, rather than through surgery like AVF. The control veins were segmental cephalic vein tissues taken from patients who underwent AVF creation, but the CV tissues were not part of the AVF. MALDI-MSI was performed on all three tissue samples, and the distributions of lysophosphatidylcholine (LPC) and phosphatidylcholine (PC) were determined. The results show that the distributions of LPC and PC differed between the three tissue types as shown in **Figure 4**. LPC was localized in the intima of the CV and PAD tissues, but distributed through the media and adventitia of the AVF tissue. The intensities of PC were much higher in the AVF and PAD tissues than it was in the CV tissue, suggesting an abnormal accumulation of these lipid molecules in both tissues. These results were compared with histological data, and both revealed complementary patterns of lipid accumulation in the AVF and PAD tissue samples. Overall, the MALDI-MSI results of this study provided the first evidence of the characteristic lipid distribution of AVF tissue on the molecular level which suggests an association between molecule-induced inflammation and tissue degeneration. This research provides valuable insight into the cause of vein degradation that can be applied to future procedures developed for hemodialysis or for the continued monitoring of patients with AVF's already in place.

4. Future Perspectives

4.1 3D MSI

One of the more exciting, recent advances in the field of clinical MSI is 3D MSI. 3D MSI grants the ability to study a broad mass range of molecular species by creating a lateral and vertical distribution map of select compounds.[125] This technique serves as a powerful discovery tool for pathologists and to the pharmaceutical industry by allowing a more complete visualization of tissue samples, which improves the ability for identification of distinct molecular signatures and drug distribution throughout the entire tissue. Advances involving imaging acquisition speed, image resolution, and data processing are always on-going in the biological sciences.[126] By adding the third dimension to the traditional 2D MSI method, there is a greater need for improvements in sample preparation, data acquisition, and data file transfer [125]. MSI generates extremely large data files; advances in computational tools will need to be made in order to improve the efficiency of data transfer and processing that will be much more time consuming when collecting a third dimension of imaging data. 3D imaging shows great promise for advancing clinical diagnostics, but there are still many areas for potential improvements before it becomes a widespread technique.

4.2 Alternative to Formalin-Fixed and Paraffin-Embedded (FFPE) Tissues

Formalin-fixation and paraffin-embedding is the standard procedure for preserving biological tissue samples for histological analysis and for long term storage at room temperature.[127] This technique preserves the cellular and morphological details of the tissue. The analysis of human tissue specimen is key to the identification of novel biomarkers that can be used to create more specific therapies and treatments. Recent progress has been made in the

analysis of FFPE tissues, but proteomic analysis from these tissues is still very difficult because formaldehyde causes protein-protein cross-linking. PreAnalytiX (Hilden, Germany) developed an alcohol-based, formalin-free tissue fixation system, PAXgene that is commercially available for research use. The PAXgene system is a two-step approach composed of the PAXgene Tissue Fixation Reagent and the PAXgene Tissue Stabilization Reagent. The fixation is carried out without the cross-linking of biomolecules, allowing the stabilization of proteins and nucleic acids while still retaining the histomorphology of the tissue. Ergin *et al.* compared MALDI-MSI capabilities on FFPE-fixed, cryopreserved, and PAXgene-fixed tissue samples.[127] The protein recovery efficiency of these three types of tissue fixation methods was compared, and the results showed that PAXgene fixation allows for high quantity of protein from mouse and human tissue samples. The protein pattern of these three tissue fixation methods was also examined, and the results showed that PAXgene and cryo-preserved tissue samples revealed similar proteomic signatures when examined by MALDI-MSI, and no protein peaks were observed from the FFPE tissue samples. Overall, these data demonstrate the potential of the PAXgene fixation system to become an integral part of protein biomarker discovery, which will facilitate advancing the clinical applications of MSI, if it becomes more widely used.

4.3 Quantitative Imaging

Quantitative imaging mass spectrometry is of great interest to the field of mass spectrometry and to the application of MSI in the clinical setting. Advances are slowly being made on the development of a reproducible, quantitative MSI method. Takai *et al.*,[81] as mentioned previously, have developed a quantitative MALDI-MSI approach to analyte the concentration of a drug in mouse tissue after specific time points. This method is based on generating a calibration curve for the drug by spiking different concentrations of the drug of

interest directly onto a tissue section and analyzing it with MSI. Their results were compared to trusted quantitation results obtained by LC/MS/MS, and had good agreement. Drexler *et al.* obtained quantitative information by combining MSI with QWBA. The downfall of this approach is that the analyte must be synthesized to contain radiolabels for QWBA, which is often time consuming and costly that are undesirable in the early stages of drug development. Several other groups combine MSI with a variety of other techniques in order to obtain quantitative data along with high spatial resolution images.[128-129] There is no universal technique for obtaining high resolution images and robust quantitative information, but progress is being made on this front, and there is potential for future improvements that would greatly impact the field of clinical diagnostics as well as many other scientific fields.

4.4 Incorporation of Ambient Ionization Techniques

MSI had been mainly viewed as an invasive process until the development of ambient ionization techniques, such as DESI. Ambient ionization techniques allow for direct analysis in real time and also remove the limitation imposed from requiring vacuum pressure conditions in traditional MSI.[125] DESI and other ambient techniques, which can be performed on untreated histological samples in the open lab environment, have the potential to promote *in situ* analysis in the clinical setting in the near future.[24] Miniature mass spectrometers have been developed that are capable of performing DESI-MSI for disease diagnostics and paper-spray ionization MS for therapeutic drug monitoring.[24] These techniques have significant potential to apply real-time diagnostic information in order, for example, to guide surgery. With the current advancements in MSI technology in the areas of miniaturization and ambient sampling, future improvements may involve configuring the instrument in the most efficient and useful way for use by doctors and surgeons in the clinic. The ability to perform *in situ* analysis and the convenience of the

portable mass spectrometers suggests the potential role of DESI-MSI and other ambient ionization techniques in guiding therapy in parallel with standard histological methods in the clinical setting.[24]

5. Conclusions

Over the past decade, MSI has obtained increasing attention from biologists and become more routinely employed to map various classes of biomolecules from biological specimen. Its novel applications to biomarker discovery in clinical settings have gained us valuable knowledge regarding disease mechanisms and related reparative processes. These studies offer significant insight in clinical studies and hold promise for our continuous search of effective treatment for diseases. Moreover, exciting technical advances are further improving this analytical tool and its clinical applications from various aspects such as sample preparation and instrumentation. We anticipate MSI for clinical applications will lead to a better understanding of the biology of diseases and improvements in clinical diagnostics.

Acknowledgements

Preparation of this manuscript was supported in part by National Science Foundation (CHE- 0957784) and National Institutes of Health through grant 1R01DK071801. L.L. acknowledges an H. I. Romnes Faculty Fellowship.

References

1. Teng, P. N.; Hood, B. L.; Sun, M.; Dhir, R.; Conrads, T. P., Differential proteomic analysis of renal cell carcinoma tissue interstitial fluid. *J Proteome Res* **2011,** *10* (3), 1333-1342.

2. Lowenthal, M. S.; Mehta, A. I.; Frogale, K.; Bandle, R. W.; Araujo, R. P.; Hood, B. L.; Veenstra, T. D.; Conrads, T. P.; Goldsmith, P.; Fishman, D.; Petricoin, E. F.; Liotta, L. A., Analysis of albumin-associated peptides and proteins from ovarian cancer patients. *Clin Chem* **2005,** *51* (10), 1933-1945.

3. Hu, S.; Arellano, M.; Boontheung, P.; Wang, J. H.; Zhou, H.; Jiang, J.; Elashoff, D.; Wei, R.; Loo, J. A.; Wong, D. T., Salivary proteomics for oral cancer biomarker discovery. *Clin Cancer Res* **2008,** *14* (19), 6246-6252.

4. Craig-Schapiro, R.; Perrin, R. J.; Roe, C. M.; Xiong, C. J.; Carter, D.; Cairns, N. J.; Mintun, M. A.; Peskind, E. R.; Li, G.; Galasko, D. R.; Clark, C. M.; Quinn, J. F.; D'Angelo, G.; Malone, J. P.; Townsend, R. R.; Morris, J. C.; Fagan, A. M.; Holtzman, D. M., YKL-40: a Novel prognostic fluid biomarker for preclinical Alzheimer's disease. *Biol Psychiat* **2010,** *68* (10), 903-912.

5. Flint, M. S.; Hood, B. L.; Sun, M.; Stewart, N. A.; Jones-Laughner, J.; Conrads, T. P., Proteomic analysis of the murine liver in response to a combined exposure to psychological stress and 7,12-Dimethylbenz(a)anthracene. *J Proteome Res* **2010,** *9* (1), 509-520.

6. Ishimura, R.; Ohsako, S.; Kawakami, T.; Sakaue, M.; Aoki, Y.; Tohyama, C., Altered protein profile and possible hypoxia in the placenta of 2,3,7,8-tetrachlorodibenzo-p-dioxin-exposed rats. *Toxicol Appl Pharm* **2002,** *185* (3), 197-206.

7. Ruepp, S. U.; Tonge, R. P.; Shaw, J.; Wallis, N.; Pognan, F., Genomics and proteomics analysis of acetaminophen toxicity in mouse liver. *Toxicol Sci* **2002,** *65* (1), 135-150.

8. Li, T. A.; Xu, S. L.; Oses-Prieto, J. A.; Putil, S.; Xu, P.; Wang, R. J.; Li, K. H.; Maltby, D. A.; An, L. H.; Burlingame, A. L.; Deng, Z. P.; Wang, Z. Y., Proteomics analysis reveals post-translational mechanisms for cold-induced metabolic changes in Arabidopsis. *Mol Plant* **2011,** *4* (2), 361-374.

9. Cazares, L. H.; Troyer, D.; Mendrinos, S.; Lance, R. A.; Nyalwidhe, J. O.; Beydoun, H. A.; Clements, M. A.; Drake, R. R.; Semmes, O. J., Imaging mass spectrometry of a specific fragment of mitogen-activated protein kinase/extracellular signal-regulated kinase kinase kinase 2 discriminates cancer from uninvolved prostate tissue. *Clin Cancer Res* **2009,** *15* (17), 5541-5551.

10. Deininger, S. O.; Ebert, M. P.; Futterer, A.; Gerhard, M.; Rocken, C., MALDI imaging combined with hierarchical clustering as a new tool for the interpretation of complex human cancers. *J Proteome Res* **2008,** *7* (12), 5230-5236.

11. Murphy, R. C.; Hankin, J. A.; Barkley, R. M., Imaging of lipid species by MALDI mass spectrometry. *J Lipid Res* **2009,** *50*, S317-S322.

12. Chen, R.; Hui, L.; Sturm, R. M.; Li, L., Three dimensional mapping of neuropeptides and lipids in crustacean brain by mass spectral imaging. *J Am Soc Mass Spectr* **2009,** *20* (6), 1068-1077.

13. DeKeyser, S. S., Kutz-Naber, K.K., Schmidt, J.J., Barrett-Wilt, G.A.and Li, L., Mass spectral imaging of neuropeptides in crustacean nervous tissue by MALDI TOF/TOF. *J Proteome Res* **2007,** *6*, 1782-1791.

14. Schwamborn, K.; Caprioli, R. M., Molecular imaging by mass spectrometry--looking beyond classical histology. *Nat Rev Cancer 10* (9), 639-646.

15. Suckau, D.; Resemann, A.; Schuerenberg, M.; Hufnagel, P.; Franzen, J.; Holle, A., A novel MALDI LIFT-TOF/TOF mass spectrometer for proteomics. *Anal Bioanal Chem* **2003,** *376* (7), 952-965.

16. Fletcher, J. S.; Lockyer, N. P.; Vickerman, J. C., Developments in molecular SIMS depth profiling and 3D imaging of biological systems using polyatomic primary ions. *Mass Spectrom Rev 30* (1), 142-174.

17. Jones, E. A.; Lockyer, N. P.; Vickerman, J. C., Mass spectral analysis and imaging of tissue by ToF-SIMS - The role of buckminsterfullerene, C-60(+), primary ions. *International Journal of Mass Spectrometry* **2007,** *260* (2-3), 146-157.

18. Dill, A. L.; Eberlin, L. S.; Costa, A. B.; Zheng, C.; Ifa, D. R.; Cheng, L. A.; Masterson, T. A.; Koch, M. O.; Vitek, O.; Cooks, R. G., Multivariate statistical identification of human bladder carcinomas using ambient ionization imaging mass spectrometry. *Chem-Eur J* **2011,** *17* (10), 2897-2902.

19. Gao, Y. H.; Yang, C. H.; Liu, X.; Ma, R. J.; Kong, D. L.; Shi, L. Q., A multifunctional nanocarrier based on nanogated mesoporous silica for enhanced tumor-specific uptake and intracellular delivery. *Macromol Biosci* **2012,** *12* (2), 251-259.

20. Laskin, J.; Heath, B. S.; Roach, P. J.; Cazares, L.; Semmes, O. J., Tissue imaging using nanospray desorption electrospray ionization mass spectrometry. *Anal Chem* **2012,** *84* (1), 141-148.

21. Vismeh, R.; Waldon, D. J.; Teffera, Y.; Zhao, Z. Y., Localization and quantification of drugs in animal tissues by use of desorption electrospray ionization mass spectrometry imaging. *Anal Chem* **2012,** *84* (12), 5439-5445.

22. Takats, Z.; Wiseman, J. M.; Gologan, B.; Cooks, R. G., Mass spectrometry sampling under ambient conditions with desorption electrospray ionization. *Science* **2004,** *306* (5695), 471-473.

23. Ifa, D. R.; Wu, C. P.; Ouyang, Z.; Cooks, R. G., Desorption electrospray ionization and other ambient ionization methods: current progress and preview. *Analyst* **2010,** *135* (4), 669-681.

24. Cooks, R. G.; Manicke, N. E.; Dill, A. L.; Ifa, D. R.; Eberlin, L. S.; Costa, A. B.; Wang, H.; Huang, G. M.; Zheng, O. Y., New ionization methods and miniature mass spectrometers for biomedicine: DESI imaging for cancer diagnostics and paper spray ionization for therapeutic drug monitoring. *Faraday Discuss* **2011,** *149*, 247-267.

25. Jehl, B.; Bauer, R.; Dorge, A.; Rick, R., The use of propane-isopentane mixtures for rapid freezing of biological specimens. *J Microsc-Oxford* **1981,** *123* (Sep), 307-309.

26. Schwartz, S. A.; Reyzer, M. L.; Caprioli, R. M., Direct tissue analysis using matrix-assisted laser desorption/ionization mass spectrometry: practical aspects of sample preparation. *J Mass Spectrom* **2003,** *38* (7), 699-708.

27. Che, F. Y.; Lim, J.; Pan, H.; Biswas, R.; Fricker, L. D., Quantitative neuropeptidomics of microwave-irradiated mouse brain and pituitary. *Mol Cell Proteomics* **2005,** *4* (9), 1391-1405.

28. Svensson, M.; Boren, M.; Skold, K.; Falth, M.; Sjogren, B.; Andersson, M.; Svenningsson, P.; Andren, P. E., Heat stabilization of the tissue proteome: a new technology for improved proteomics. *J Proteome Res* **2009,** *8* (2), 974-981.

29. Rountree, C. B.; Van Kirk, C. A.; You, H. N.; Ding, W.; Dang, H.; VanGuilder, H. D.; Freeman, W. M., Clinical application for the preservation of phosphoproteins through in-situ tissue stabilization. *Proteome Sci* **2010,** *8*.

30. Crossman, L.; McHugh, N. A.; Hsieh, Y. S.; Korfmacher, W. A.; Chen, J. W., Investigation of the profiling depth in matrix-assisted laser desorption/ionization imaging mass spectrometry. *Rapid Commun Mass Sp* **2006,** *20* (2), 284-290.

31. Verhaert, P. D. E. M.; Pinkse, M. W. H.; Strupat, K.; Conaway, M. C. P., Imaging of similar mass neuropeptides in neuronal tissue by enhanced resolution MALDI MS with an ion trap-orbitrap$^{(TM)}$ hybrid instrument. *Mass spectrometry imaging: principles and protocols* **2010,** *656*, 433-449.

32. Chaurand, P.; Fouchecourt, S.; DaGue, B. B.; Xu, B. G. J.; Reyzer, M. L.; Orgebin-Crist, M. C.; Caprioli, R. M., Profiling and imaging proteins in the mouse epididymis by imaging mass spectrometry. *Proteomics* **2003,** *3* (11), 2221-2239.

33. Chaurand, P.; Schriver, K. E.; Caprioli, R. M., Instrument design and characterization for high resolution MALDI-MS imaging of tissue sections. *J Mass Spectrom* **2007,** *42* (4), 476-489.

34. Kaletas, B. K.; van der Wiel, I. M.; Stauber, J.; Dekker, L. J.; Guzel, C.; Kros, J. M.; Luider, T. M.; Heeren, R. M. A., Sample preparation issues for tissue imaging by imaging MS. *Proteomics* **2009,** *9* (10), 2622-2633.

35. Lemaire, R.; Wisztorski, M.; Desmons, A.; Tabet, J. C.; Day, R.; Salzet, M.; Fournier, I., MALDI-MS direct tissue analysis of proteins: improving signal sensitivity using organic treatments. *Anal Chem* **2006,** *78* (20), 7145-7153.

36. Seeley, E. H.; Oppenheimer, S. R.; Mi, D.; Chaurand, P.; Caprioli, R. M., Enhancement of protein sensitivity for MALDI imaging mass spectrometry after chemical treatment of tissue sections. *J Am Soc Mass Spectr* **2008,** *19* (8), 1069-1077.

37. Scicchitano, M. S.; Dalmas, D. A.; Boyce, R. W.; Thomas, H. C.; Frazier, K. S., Protein extraction of formalin-fixed, paraffin-embedded tissue enables robust proteomic profiles by mass spectrometry. *J Histochem Cytochem* **2009,** *57* (9), 849-860.

38. Casadonte, R.; Caprioli, R. M., Proteomic analysis of formalin-fixed paraffin-embedded tissue by MALDI imaging mass spectrometry. *Nat Protoc* **2011,** *6* (11), 1695-1709.

39. EmmertBuck, M. R.; Bonner, R. F.; Smith, P. D.; Chuaqui, R. F.; Zhuang, Z. P.; Goldstein, S. R.; Weiss, R. A.; Liotta, L. A., Laser capture microdissection. *Science* **1996,** *274* (5289), 998-1001.

40. Wang, Z.; Han, J.; Schey, K. L., Spatial differences in an integral membrane proteome detected in laser capture microdissected samples. *J Proteome Res* **2008,** *7* (7), 2696-2702.

41. Xu, B. G. J.; Caprioli, R. M., Direct analysis of laser capture microdissected cells by MALDI mass spectrometry. *J Am Soc Mass Spectr* **2002,** *13* (11), 1292-1297.

42. Xu, B. J.; Shyr, Y.; Liang, X. B.; Ma, L. J.; Donnert, E. M.; Roberts, J. D.; Zhang, X. Q.; Kon, V.; Brown, N. J.; Caprioli, R. M.; Fogo, A. B., Proteomic patterns and prediction of glomerulosclerosis and its mechanisms. *J Am Soc Nephrol* **2005,** *16* (10), 2967-2975.

43. Groseclose, M. R.; Andersson, M.; Hardesty, W. M.; Caprioli, R. M., Identification of proteins directly from tissue: in situ tryptic digestions coupled with imaging mass spectrometry. *J Mass Spectrom* **2007,** *42* (2), 254-262.

44. Ronci, M.; Bonanno, E.; Colantoni, A.; Pieroni, L.; Di Ilio, C.; Spagnoli, L. G.; Federici, G.; Urbani, A., Protein unlocking procedures of formalin-fixed paraffin-embedded tissues: Application to MALDI-TOF imaging MS investigations. *Proteomics* **2008,** *8* (18), 3702-3714.

45. Djidja, M. C.; Francese, S.; Loadman, P. M.; Sutton, C. W.; Scriven, P.; Claude, E.; Snel, M. F.; Franck, J.; Salzet, M.; Clench, M. R., Detergent addition to tryptic digests and ion mobility separation prior to MS/MS improves peptide yield and protein identification for in situ proteomic investigation of frozen and formalin-fixed paraffin-embedded adenocarcinoma tissue sections. *Proteomics* **2009,** *9* (10), 2750-2763.

46. Stauber, J.; MacAleese, L.; Franck, J.; Claude, E.; Snel, M.; Kaletas, B. K.; Wiel, I. M. V. D.; Wisztorski, M.; Fournier, I.; Heeren, R. M. A., On-tissue protein identification and imaging by MALDI-ion mobility mass spectrometry. *J Am Soc Mass Spectr* **2010,** *21* (3), 338-347.

47. Boggio, K. J.; Obasuyi, E.; Sugino, K.; Nelson, S. B.; Agar, N. Y. R.; Agar, J. N., Recent advances in single-cell MALDI mass spectrometry imaging and potential clinical impact. *Expert Rev Proteomic* **2011,** *8* (5), 591-604.

48. McDonnell, L. A.; Corthals, G. L.; Willems, S. M.; van Remoortere, A.; van Zeijl, R. J. M.; Deelder, A. M., Peptide and protein imaging mass spectrometry in cancer research. *J Proteomics* **2010,** *73* (10), 1921-1944.

49. Tu, T.; Sauter, A. D.; Sauter, A. D.; Gross, M. L., Improving the signal intensity and sensitivity of MALDI mass spectrometry by using nanoliter spots deposited by induction-based fluidics. *J Am Soc Mass Spectr* **2008,** *19* (8), 1086-1090.

50. Zimmerman, T. A.; Monroe, E. B.; Sweedler, J. V., Adapting the stretched sample method from tissue profiling to imaging. *Proteomics* **2008,** *8* (18), 3809-3815.

51. Zimmerman, T. A.; Rubakhin, S. S.; Sweedler, J. V., MALDI mass spectrometry imaging of neuronal cell cultures. *J Am Soc Mass Spectr* **2011,** *22* (5), 828-836.

52. Jurchen, J. C.; Rubakhin, S. S.; Sweedler, J. V., MALDI-MS imaging of features smaller than the size of the laser beam. *J Am Soc Mass Spectr* **2005,** *16* (10), 1654-1659.

53. Koestler, M.; Kirsch, D.; Hester, A.; Leisner, A.; Guenther, S.; Spengler, B., A high-resolution scanning microprobe matrix-assisted laser desorption/ionization ion source for imaging analysis on an ion trap/Fourier transform ion cyclotron resonance mass spectrometer. *Rapid Commun Mass Sp* **2008,** *22* (20), 3275-3285.

54. Römpp, A.; Guenther, S.; Schober, Y.; Schulz, O.; Takats, Z.; Kummer, W.; Spengler, B., Histology by Mass Spectrometry: Label-Free Tissue Characterization Obtained from High-Accuracy Bioanalytical Imaging. *Angew Chem Int Edit* **2010,** *49* (22), 3834-3838.

55. Guenther, S.; Rompp, A.; Kummer, W.; Spengler, B., AP-MALDI imaging of neuropeptides in mouse pituitary gland with 5 mu m spatial resolution and high mass accuracy. *Int J Mass Spectrom* **2011,** *305* (2-3), 228-237.

56. Schober, Y.; Guenther, S.; Spengler, B.; Rompp, A., Single cell matrix-assisted laser desorption/ionization mass spectrometry imaging. *Anal Chem 84* (15), 6293-6297.

57. Schafer, R., ultrafleXtreme: redefining MALDI mass spectrometry performance. *LC GC N Am* **2009**, 14-15.

58. Luxembourg, S. L.; Mize, T. H.; McDonnell, L. A.; Heeren, R. M. A., High-spatial resolution mass spectrometric imaging of peptide and protein distributions on a surface. *Anal Chem* **2004,** *76* (18), 5339-5344.

59. Klerk, L. A.; Altelaar, A. F. M.; Froesch, M.; McDonnell, L. A.; Heeren, R. M. A., Fast and automated large-area imaging MALDI mass spectrometry in microprobe and microscope mode. *Int J Mass Spectrom* **2009,** *285* (1-2), 19-25.

60. Altelaar, A. F. M.; Taban, I. M.; McDonnell, L. A.; Verhaert, P. D. E. M.; de Lange, R. P. J.; Adan, R. A. H.; Mooi, W. J.; Heeren, R. M. A.; Piersma, S. R., High-resolution MALDI imaging mass spectrometry allows localization of peptide distributions at cellular length scales in pituitary tissue sections. *Int J Mass Spectrom* **2007,** *260* (2-3), 203-211.

61. Fitzgerald, J. J. D.; Kunnath, P.; Walker, A. V., Matrix-enhanced secondary ion mass spectrometry (ME-SIMS) using room temperature ionic liquid matrices. *Anal Chem* **2010,** *82* (11), 4413-4419.

62. Lemaire, R.; Tabet, J. C.; Ducoroy, P.; Hendra, J. B.; Salzet, M.; Fournier, I., Solid ionic matrixes for direct tissue analysis and MALDI Imaging. *Anal Chem* **2006,** *78* (3), 809-819.

63. Deutskens, F.; Yang, J. H.; Caprioli, R. M., High spatial resolution imaging mass spectrometry and classical histology on a single tissue section. *J Mass Spectrom* **2011,** *46* (6), 568-571.

64. Ye, H.; Greer, T.; Li, L., Probing neuropeptide signaling at the organ and cellular domains via imaging mass spectrometry. *J Proteomics* **2012,** *75* (16), 5014-5026.

65. Thomas, A.; Charbonneau, J. L.; Fournaise, E.; Chaurand, P., Sublimation of new matrix candidates for high spatial resolution imaging mass spectrometry of lipids: enhanced information in both positive and negative polarities after 1,5-diaminonapthalene deposition. *Anal Chem* **2012,** *84* (4), 2048-2054.

66. Cohen, M. Z., A historical overview of the phenomenologic movement. *Image J Nurs Sch* **1987,** *19* (1), 31-34.

67. Leinweber, B. D.; Tsaprailis, G.; Monks, T. J.; Lau, S. S., Improved MALDI-TOF imaging yields increased protein signals at high molecular mass. *J Am Soc Mass Spectr* **2009,** *20* (1), 89-95.

68. Vestal, M. L.; Campbell, J. M., Tandem time-of-flight mass spectrometry. *Methods Enzymol* **2005,** *402*, 79-108.

69. Kanu, A. B.; Dwivedi, P.; Tam, M.; Matz, L.; Hill, H. H., Ion mobility-mass spectrometry. *J Mass Spectrom* **2008,** *43* (1), 1-22.

70. Marshall, A. G.; Hendrickson, C. L.; Jackson, G. S., Fourier transform ion cyclotron resonance mass spectrometry: A primer. *Mass Spectrom Rev* **1998,** *17* (1), 1-35.

71. Kutz, K. K.; Schmidt, J. J.; Li, L. J., In situ tissue analysis of neuropeptides by MALDI FTMS in-cell accumulation. *Anal Chem* **2004,** *76* (19), 5630-5640.

72. Fuchser J., C. S., Becker M., High resolution molecular imaging of pharmaceuticals at theraputic levels. In *Bruker Daltonik GmbH*, 2008.

73. Makarov, A., Electrostatic axially harmonic orbital trapping: A high-performance technique of mass analysis. *Anal Chem* **2000,** *72* (6), 1156-1162.

74. Hu, Q. Z.; Noll, R. J.; Li, H. Y.; Makarov, A.; Hardman, M.; Cooks, R. G., The Orbitrap: a new mass spectrometer. *J Mass Spectrom* **2005,** *40* (4), 430-443.

75. Seeley, E. H.; Caprioli, R. M., Imaging mass spectrometry: Towards clinical diagnostics. *Proteom Clin Appl* **2008,** *2* (10-11), 1435-1443.

76. Seeley, E. H.; Caprioli, R. M., MALDI imaging mass spectrometry of human tissue: method challenges and clinical perspectives. *Trends Biotechnol* **2011,** *29* (3), 136-143.

77. Rauser, S.; Deininger, S. O.; Suckau, D.; Hofler, H.; Walch, A., Approaching MALDI molecular imaging for clinical proteomic research: current state and fields of application. *Expert Rev Proteomic* **2010,** *7* (6), 927-941.

78. Cazares, L. H.; Troyer, D. A.; Wang, B. H.; Drake, R. R.; Semmes, O. J., MALDI tissue imaging: from biomarker discovery to clinical applications. *Anal Bioanal Chem* **2011,** *401* (1), 17-27.

79. Meding, S.; Nitsche, U.; Balluff, B.; Elsner, M.; Rauser, S.; Schone, C.; Nipp, M.; Maak, M.; Feith, M.; Ebert, M. P.; Friess, H.; Langer, R.; Hofler, H.; Zitzelsberger, H.; Rosenberg, R.; Walch, A., Tumor classification of six common cancer types based on proteomic profiling by MALDI imaging. *J Proteome Res* **2012,** *11* (3), 1996-2003.

80. Drexler, D. M.; Tannehill-Gregg, S. H.; Wang, L. F.; Brock, B. J., Utility of quantitative whole-body autoradiography (QWBA) and imaging mass spectrometry (IMS) by matrix-assisted laser desorption/ionization (MALDI) in the assessment of ocular distribution of drugs. *J Pharmacol Tox Met* **2011,** *63* (2), 205-208.

81. Takai, N.; Tanaka, Y.; Inazawa, K.; Saji, H., Quantitative analysis of pharmaceutical drug distribution in multiple organs by imaging mass spectrometry. *Rapid Commun Mass Sp* **2012,** *26* (13), 1549-1556.

82. Wiseman, J. M.; Ifa, D. R.; Zhu, Y. X.; Kissinger, C. B.; Manicke, N. E.; Kissinger, P. T.; Cooks, R. G., Desorption electrospray ionization mass spectrometry: Imaging drugs and metabolites in tissues. *P Natl Acad Sci USA* **2008,** *105* (47), 18120-18125.

83. Greer, T.; Sturm, R.; Li, L. J., Mass spectrometry imaging for drugs and metabolites. *J Proteomics* **2011,** *74* (12), 2617-2631.

84. Markowitz, L.; Anis, S. I.; Linehan, S. T., QWBA - current methodologies and future advancements positioning of image. *J Labelled Compd Rad* **2010,** *53* (5-6), 330-331.

85. Cornett, D. S.; Frappier, S. L.; Caprioli, R. M., MALDI-FTICR imaging mass spectrometry of drugs and metabolites in tissue. *Anal Chem* **2008,** *80* (14), 5648-5653.

86. Leinweber, B. D.; Tsaprailis, G.; Monks, T. J.; Lau, S. S., Improved MALDI-TOF imaging yields increased protein signals at high molecular mass. *J Am Soc Mass Spectr* **2009,** *20* (1), 89-95.

87. Lorey, D. R.; Morrison, G. H.; Chandra, S., Dynamic secondary ion mass spectrometry analysis of boron from boron neutron capture therapy drugs in co-cultures: Single-cell imaging of two different cell types within the same ion microscopy field of imaging. *Anal Chem* **2001,** *73* (16), 3947-3953.

88. Prideaux, B.; Staab, D.; Stoeckli, M., Applications of MALDI-MSI to Pharmaceutical Research. *Methods Mol Biol* **2010,** *656*, 405-413.

89. Trim, P. J.; Francese, S.; Clench, M. R., Imaging mass spectrometry for the assessment of drugs and metabolites in tissue. *Bioanalysis* **2009,** *1* (2), 309-319.

90. Wittig, A.; Arlinghaus, H. F.; Kriegeskotte, C.; Moss, R. L.; Appelman, K.; Schmid, K. W.; Sauerwein, W. A. G., Laser postionization secondary neutral mass spectrometry in tissue: a powerful tool for elemental and molecular imaging in the development of targeted drugs. *Mol Cancer Ther* **2008,** *7* (7), 1763-1771.

91. Lagarrigue, M.; Lavigne, R.; Guevel, B.; Com, E.; Chaurand, P.; Pineau, C., Matrix-assisted laser desorption/ionization imaging mass spectrometry: a promising technique for reproductive research. *Biol Reprod* **2012,** *86* (3).

92. Nilsson, A.; Fehniger, T. E.; Gustavsson, L.; Andersson, M.; Kenne, K.; Marko-Varga, G.; Andren, P. E., Fine mapping the spatial distribution and concentration of unlabeled drugs within tissue micro-compartments using imaging mass spectrometry. *Plos One* **2010,** *5* (7).

93. Trim, P. J.; Henson, C. M.; Avery, J. L.; McEwen, A.; Snel, M. F.; Claude, E.; Marshall, P. S.; West, A.; Princivalle, A. P.; Clench, M. R., Matrix-Assisted Laser Desorption/Ionization-Ion Mobility Separation-Mass Spectrometry Imaging of Vinblastine in Whole Body Tissue Sections. *Anal Chem* **2008,** *80* (22), 8628-8634.

94. Young, S. P.; Piraud, M.; Goldstein, J. L.; Zhang, H. Y.; Rehder, C.; Laforet, P.; Kishnani, P. S.; Millington, D. S.; Bashir, M. R.; Bali, D. S., Assessing disease severity in Pompe disease: the roles of a urinary glucose tetrasaccharide biomarker and imaging techniques. *Am J Med Genet C* **2012,** *160C* (1), 50-58.

95. Meding, S.; Nitsche, U.; Balluff, B.; Elsner, M.; Rauser, S.; Schone, C.; Nipp, M.; Maak, M.; Feith, M.; Ebert, M. P.; Friess, H.; Langer, R.; Hofler, H.; Zitzelsberger, H.; Rosenberg, R.; Walch, A., Tumor Classification of Six Common Cancer Types Based on Proteomic Profiling by MALDI Imaging. *J Proteome Res* **2012,** *11* (3), 1996-2003.

96. Postle, A. D., Lipidomics. *Curr Opin Clin Nutr* **2012,** *15* (2), 127-133.

97. Walsh, N.; Crotty, K.; Palmer, A.; McCarthy, S., Spitz nevus versus spitzoid malignant melanoma: an evaluation of the current distinguishing histopathologic criteria. *Human pathology* **1998,** *29* (10), 1105-1112.

98. Lazova, R.; Seeley, E. H.; Keenan, M.; Gueorguieva, R.; Caprioli, R. M., Imaging mass spectrometry-a new and promising method to differentiate Spitz Nevi From Spitzoid malignant melanomas. *Am J Dermatopath* **2012,** *34* (1), 82-90.

99. Kim, D. W.; Huamani, J.; Reyzer, M. L.; Mi, D.; Caprioli, R. M.; Hallahan, D. E., Imaging mass spectrometry to map distribution of radiation enhancing vasculature targeted drug and protein biomarkers of response to therapy in prostate cancer. *Int J Radiat Oncol* **2006,** *66* (3), S554-S554.

100. Thomas, A.; Lenglet, S.; Chaurand, P.; Deglon, J.; Mangin, P.; Mach, F.; Steffens, S.; Wolfender, J. L.; Staub, C., Mass spectrometry for the evaluation of cardiovascular diseases based on proteomics and lipidomics. *Thromb Haemostasis* **2011,** *106* (1), 20-33.

101. Hanada, M.; Sugiura, Y.; Shinjo, R.; Masaki, N.; Imagama, S.; Ishiguro, N.; Matsuyama, Y.; Setou, M., Spatiotemporal alteration of phospholipids and prostaglandins in a rat model of spinal cord injury. *Anal Bioanal Chem* **2012,** *403* (7), 1873-1884.

102. Weaver, C. M.; Liebman, M., Biomarkers of bone health appropriate for evaluating functional foods designed to reduce risk of osteoporosis. *Brit J Nutr* **2002,** *88,* S225-S232.

103. Gamez-Pozo, A.; Sanchez-Navarro, I.; Calvo, E.; Agullo-Ortuno, M. T.; Lopez-Vacas, R.; Diaz, E.; Camafeita, E.; Nistal, M.; Madero, R.; Espinosa, E.; Lopez, J. A.; Vara, J. A. F.,

PTRF/Cavin-1 and MIF proteins are identified as non-small cell lung cancer biomarkers by label-free proteomics. *Plos One* **2012,** *7* (3).

104. Tanaka, H.; Zaima, N.; Yamamoto, N.; Sagara, D.; Suzuki, M.; Nishiyama, M.; Mano, Y.; Sano, M.; Hayasaka, T.; Goto-Inoue, N.; Sasaki, T.; Konno, H.; Unno, N.; Setou, M., Imaging mass spectrometry reveals unique lipid distribution in primary varicose veins. *Eur J Vasc Endovasc* **2010,** *40* (5), 657-663.

105. Klerk, L. A.; Dankers, P. Y. W.; Popa, E. R.; Bosman, A. W.; Sanders, M. E.; Reedquist, K. A.; Heeren, R. M. A., TOF-secondary ion mass spectrometry imaging of polymeric scaffolds with surrounding tissue after in vivo implantation. *Anal Chem* **2010,** *82* (11), 4337-4343.

106. Zoehrer, R.; Perilli, E.; Kuliwaba, J. S.; Shapter, J. G.; Fazzalari, N. L.; Voelcker, N. H., Human bone material characterization: integrated imaging surface investigation of male fragility fractures. *Osteoporosis Int* **2012,** *23* (4), 1297-1309.

107. Tanaka, H.; Zaima, N.; Yamamoto, N.; Suzuki, M.; Mano, Y.; Konno, H.; Unno, N.; Setou, M., Distribution of phospholipid molecular species in autogenous access grafts for hemodialysis analyzed using imaging mass spectrometry. *Anal Bioanal Chem* **2011,** *400* (7), 1873-1880.

108. Johnson, R. B.; Gilbert, J. A.; Cooper, R. C.; Parsell, D. E.; Streckfus, C. F.; Boring, J. G., Isolation of osteoporosis biomarkers from saliva. *Faseb J* **2001,** *15* (5), A716-A716.

109. Garnero, P., Biomarkers for osteoporosis management - utility in diagnosis, fracture risk prediction and therapy monitoring. *Mol Diagn Ther* **2008,** *12* (3), 157-170.

110. Bhattacharyya, S.; Siegel, E.; Jennings, S.; Khosla, S.; Suva, L. J., The discovery of new biomarkers for the diagnosis of osteoporosis: Is SELDI the answer? *J Bone Miner Res* **2005,** *20* (9), S224-S225.

111. Holland, S. A.; Bateman, K. P.; Desmarais, S.; Chauret, N.; Percival, M. D.; Seto, C., Detection of bone resorption biomarkers in an osteoporosis animal model. *Drug Metab Rev* **2003,** *35*, 164-164.

112. Liu, J. H.; Tsang, R.; Gass, M.; Kao, L.; Muse, K., Identification of women at risk for osteoporosis with bone biomarkers during early menopause. *J Bone Miner Res* **1996,** *11*, T577-T577.

113. Maddali, K. K.; Starks, C. I.; McDonough, C.; Dharmadhikari, J.; Litzenberger, B. A., Bone biomarkers significantly enhances the predictability of preclinical study outcomes and translation to first in man studies targeted towards osteoporosis. *Clin Chem* **2009,** *55* (6), A158-A158.

114. Moayyeri, A.; Hammond, C. J.; Spector, T. D., Novel metabolomic biomarkers for osteoporosis and longitudinal bone loss. *Bone* **2012,** *50*, S45-S45.

115. Chytil, P.; Etrych, T.; Kostka, L.; Ulbrich, K., Hydrolytically degradable polymer micelles for anticancer drug delivery to solid tumors. *Macromol Chem Phys* **2012,** *213* (8), 858-867.

116. Ooya, T.; Mori, H.; Terano, M.; Yui, N., Synthesis of a biodegradable polymeric supramolecular assembly for drug-delivery. *Macromol Rapid Comm* **1995,** *16* (4), 259-263.

117. Salmaso, S.; Bersani, S.; Scomparin, A.; Mastrotto, F.; Caliceti, P., Supramolecular bioconjugates for protein and small drug delivery. *Isr J Chem* **2010,** *50* (2), 160-174.

118. Nakayama, M.; Okano, T., Intelligent thermoresponsive polymeric micelles for targeted drug delivery. *J Drug Deliv Sci Tec* **2006,** *16* (1), 35-44.

119. Sant, V. P.; Smith, D.; Leroux, J. C., Novel pH-sensitive supramolecular assemblies for oral delivery of poorly water soluble drugs: preparation and characterization. *J Control Release* **2004,** *97* (2), 301-312.

120. Vergaro, V.; Scarlino, F.; Bellomo, C.; Rinaldi, R.; Vergara, D.; Maffia, M.; Baldassarre, F.; Giannelli, G.; Zhang, X. C.; Lvov, Y. M.; Leporatti, S., Drug-loaded polyelectrolyte microcapsules for sustained targeting of cancer cells. *Adv Drug Deliver Rev* **2011,** *63* (9), 847-863.

121. Gillies, E. R.; Frechet, J. M. J., Development of acid-sensitive copolymer micelles for drug delivery. *Pure Appl Chem* **2004,** *76* (7-8), 1295-1307.

122. Lin, C. H.; Mardini, S.; Lin, Y. T.; Yeh, J. T.; Wei, F. C.; Chen, H. C., Sixty-five clinical cases of free tissue transfer using long arteriovenous fistulas or vein grafts. *J Trauma* **2004,** *56* (5), 1107-1117.

123. Zhu, Y.; Lin, J. H. C.; Liao, H. L.; Verna, L.; Stemerman, M. B., Activation of ICAM-1 promoter by lysophosphatidylcholine: Possible involvement of protein tyrosine kinases. *Bba-Lipid Lipid Met* **1997,** *1345* (1), 93-98.

124. Rong, J. X.; Berman, J. W.; Taubman, M. B.; Fisher, E. A., Lysophosphatidylcholine stimulates monocyte chemoattractant protein-1 gene expression in rat aortic smooth muscle cells. *Arterioscl Throm Vas* **2002,** *22* (10), 1617-1623.

125. Ye, H.; Greer, T.; Li, L. J., From pixel to voxel: a deeper view of biological tissue by 3D mass spectral imaging. *Bioanalysis* **2011,** *3* (3), 313-332.

126. Jones, E. A.; van Zeijl, R. J. M.; Andren, P. E.; Deelder, A. M.; Wolters, L.; McDonnell, L. A., High speed data processing for imaging MS-based molecular histology using graphical processing units. *J Am Soc Mass Spectr* **2012,** *23* (4), 745-752.

127. Ergin, B.; Meding, S.; Langer, R.; Kap, M.; Viertler, C.; Schott, C.; Ferch, U.; Riegman, P.; Zatloukal, K.; Walch, A.; Becker, K. F., Proteomic analysis of PAXgene-fixed tissues. *J Proteome Res* **2010,** *9* (10), 5188-5196.

128. Hattori, K.; Kajimura, M.; Hishiki, T.; Nakanishi, T.; Kubo, A.; Nagahata, Y.; Ohmura, M.; Yachie-Kinoshita, A.; Matsuura, T.; Morikawa, T.; Nakamura, T.; Setou, M.; Suematsu, M., Paradoxical ATP elevation in ischemic penumbra revealed by quantitative imaging mass spectrometry. *Antioxid Redox Sign* **2010,** *13* (8), 1157-1167.

129. Wang, H. A. O.; Grolimund, D.; Van Loon, L. R.; Barmettler, K.; Borca, C. N.; Aeschimann, B.; Gunther, D., Quantitative chemical imaging of element diffusion into heterogeneous media using laser ablation inductively coupled plasma mass spectrometry, synchrotron micro-X-ray fluorescence, and extended X-ray absorption fine structure spectroscopy. *Anal Chem* **2011,** *83* (16), 6259-6266.

Figures

Figure 1

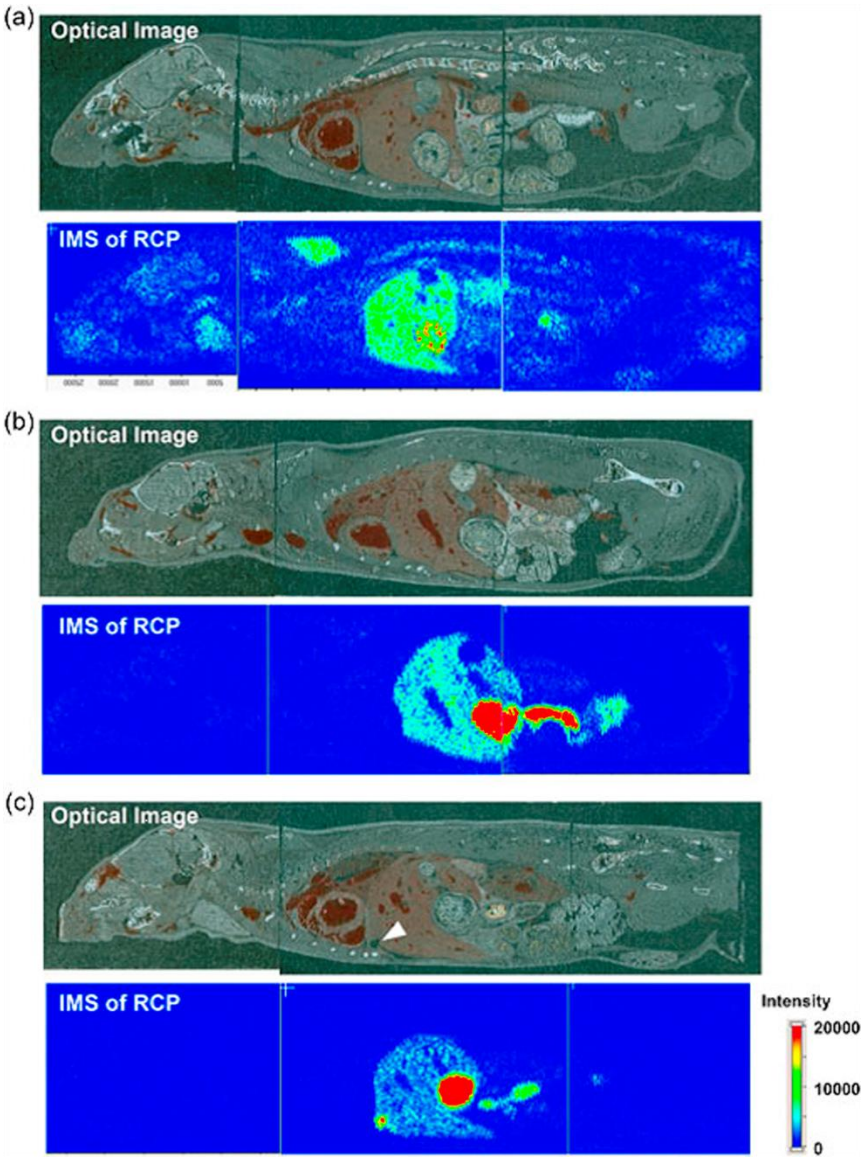

Figure 1. A schematic representation of the clinical applications of MSI. MSI spectra arising from the diseased regions are recorded, and the molecular MS images are reconstructed. The molecules like lipids or proteins that differentiate the diseased regions from the normal ones are potential biomarkers of the disease. Moreover, the metabolites that changed corresponding to drug treatment are also investigated based on this workflow. Reprinted from Ref. 81. Copyright 2012 John Wiley and Sons, Ltd.

Figure 2

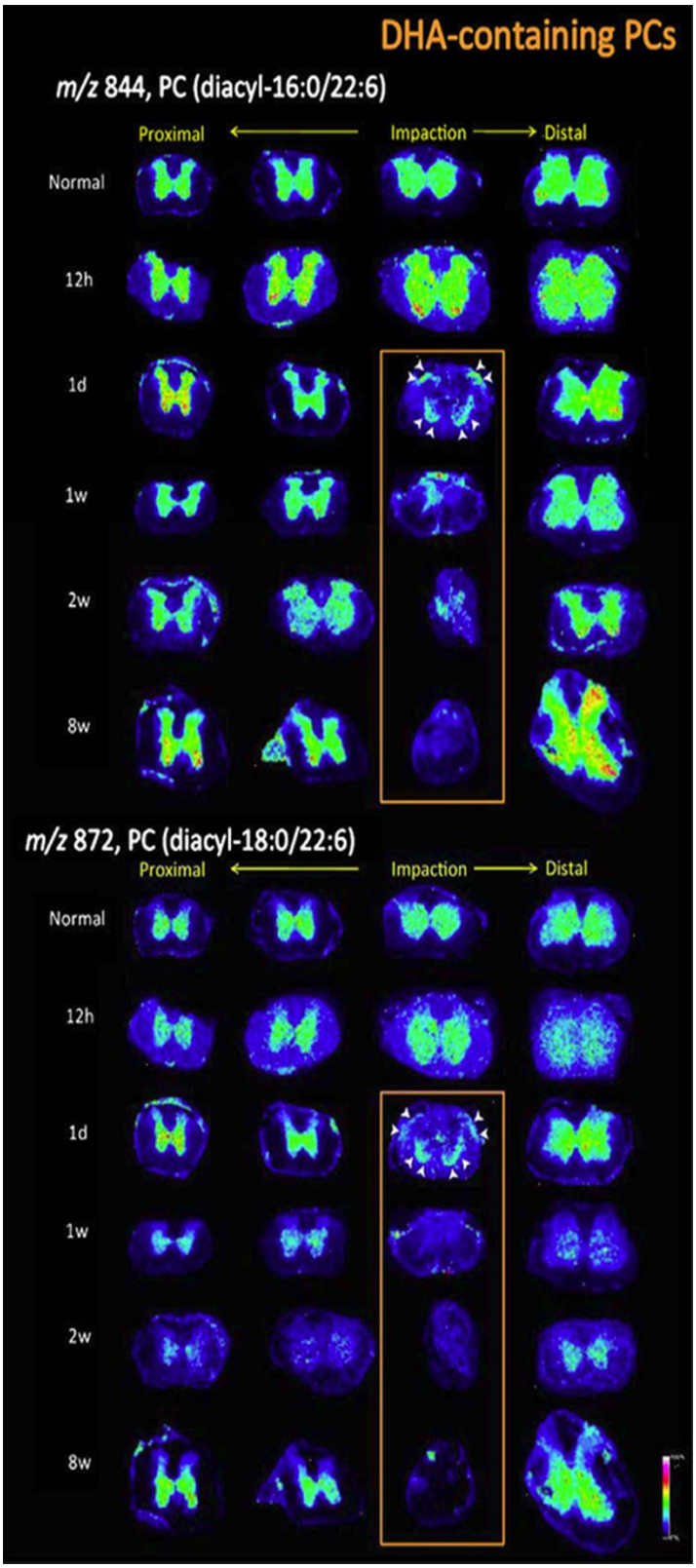

Figure 2. DHA-containing PCs exhibited impact site-specific irreversible reductions from 1 day to 8 weeks post-SCI. The MSI results for DHA-containing PCs, i.e.: PC(diacyl-16:0/22:6) and PC (diacyl-18:0/22:6), are detailed. In particular, the 24 ion images for each DHA-PC from sections of normal (sham-operated) and SCI-treated samples at five different time points are shown. The distribution of DHA-PCs was unaltered at 12 h post-SCI in comparison with the control. The primary reduction was observed around the central canal and gray commissure region to a severe extent at 1 d post-SCI, whereas the decreases at the anterior and posterior horns were moderate (arrowheads). However, at 1 week post-SCI, DHA-PCs were also lost from these tissue regions, and these reductions evolved at later time points and the DHA-PCs had almost disappeared by 8 weeks post-SCI.[101] Reprinted with permission from Hanada M, Sugiura Y, Shinjo R, *et al.* Spatiotemporal alteration of phospholipids and prostaglandins in a rat model of spinal cord injury. Anal Bioanal Chem 2012; 403:1873-1884.

Figure 3

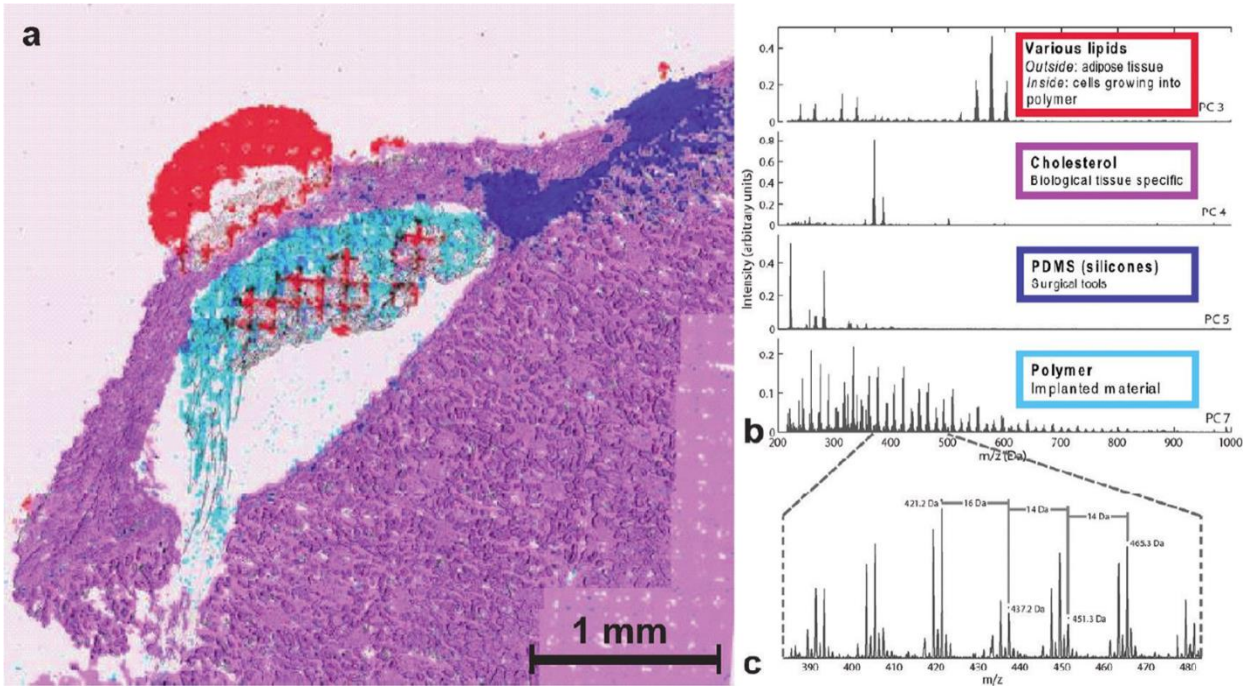

Figure 3. (a) Large area image of the hydrogel implant under the renal capsule of a rat, 15 days after implantation. Various localizations are indicated, based on PCA+VARIMAX results (see spectra in (b)) and in the overlay with an optical microscope image. The presence of lipids inside the polymer area shows cellular infiltration in the drug delivery carrier. Some smearing artifact is visible at the bottom region of the polymer. The respective spectral results are given in (b). The first and second PCs gave non-informative distributions. PC 3 shows signal for various lipids, including Diacyl glycerols (*m/z* 550-620), PC 4 shows cholesterol ($(M\text{-}OH)^+$ at *m/z* 369.4 and M^+ at *m/z* 385.4), PC 5 shows silicone contamination ($C_7H_{21}O_2Si_3^+$ at *m/z* 221.1, further identified from low-mass peaks in the corresponding region), PC 7 shows the polymer distribution, readily recognize from the *m/z* 44 spacing between the peaks, which exactly corresponds to the mass of one PEG unit. (c) Shows the PEG distribution in detail with characteristic 16 Da (K^+ and Na^+ difference or O loss) and 14 Da (CH_2 loss) intervals. The change from 0.2 to 0.3 values is due to binning down and, thus, rounding to 0.1 Da.[105] Reprinted with permission from Klerk LA, Dankers PYW, Popa ER, *et al.* TOF-secondary ion mass spectrometry imaging of polymeric scaffolds with surrounding tissue after in vivo implantation. Anal Chem 2010; 82:4337-4343. Copyright 2010 American Chemical Society

Figure 4

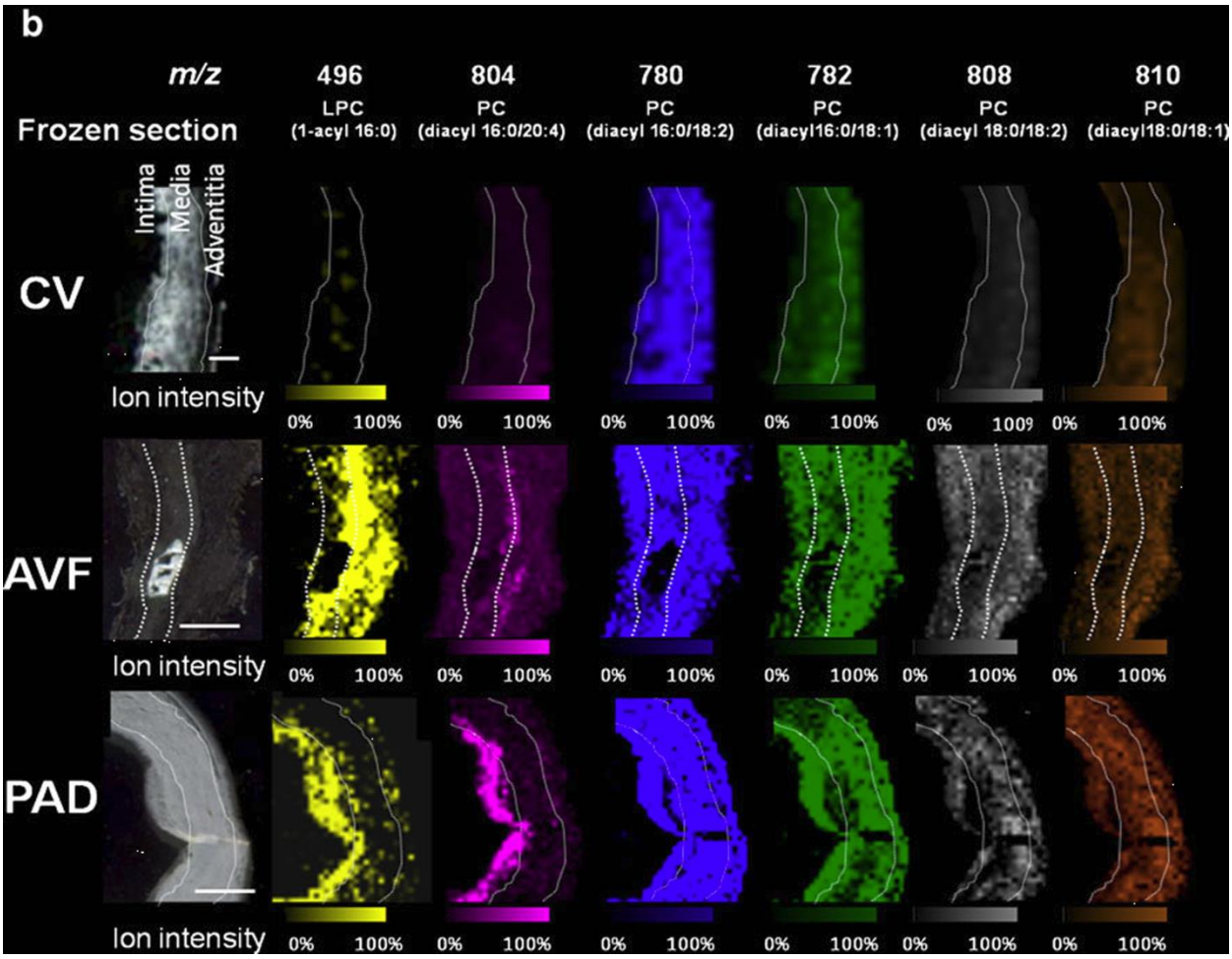

Figure 4. Imaging mass spectrometry and optical images of frozen section (8 μm) of the control vein (CV), arteriovenous fistula (AVF), and peripheral artery occlusive disease (PAD) samples Scale bar=200 μm. Ion intensity was normalized by total ion current. MSI of human AVF revealed the characteristic distribution of phospholipid molecules in the intima and media compared with that in the CV.[107] Reprinted with permission from Tanaka H, Zaima N, Yamamoto N, *et al*. Distribution of phospholipid molecular species in autogenous access grafts for hemodialysis analyzed using imaging mass spectrometry. Anal Bioanal Chem 2011; 400:1873-1880.

Appendix VI

Detailed Protocols for MALDI-MSI of Small Molecules

Adapted from **Gemperline, E.**; Li, L. "MALDI-MS Assisted Molecular Imaging of Metabolites in Legume Plants" Methods in Molecular Biology 1203: 29-40. (2015) doi:10.1007/978-1-4939-1357-2_4 and **Gemperline, E.**; Li, L. "Investigation of Metabolites in Medicago truncatula Root Nodules with MALDI- Mass Spectrometric Imaging" Journal of Visualized Experiments. (85):e51434 (2014) doi:10.3791/51434

Abstract

Most techniques used to study small molecules, such as pharmaceutical drugs or endogenous metabolites employ tissue extracts which require the homogenization of the tissue of interest that could potentially cause changes in the metabolic pathways being studied.[1] Mass spectrometric imaging (MSI) is a powerful analytical tool that provides spatial information of several compounds in a single experiment without destroying the tissue in the process. This technique has been used extensively to study proteins, peptides, and lipids, and is becoming more common for studying small molecules such as endogenous metabolites. With matrix-assisted laser desorption/ionization (MALDI)-MSI, spatial distributions of multiple metabolites can be simultaneously detected within a biological tissue section. Herein, we present a method developed specifically conducting discovery metabolomics MSI experiments on legume roots and root nodules which could reveal insights into the biological processes taking place in the plant and can also be adapted for studying metabolites in biological tissue samples. The method presented here shows a typical MSI workflow, from sample preparation to image acquisition, and focuses on the matrix application step, demonstrating several matrix application techniques that are useful for detecting small molecules. Once the MS images are generated, the analysis and identification of metabolites of interest is discussed and demonstrated. This standard workflow that can be easily modified for different tissue types, classes of biomolecules, and instrumentation.

For a video reference of this MSI procedure, see:

http://www.jove.com/video/51434/maldi-mass-spectrometric-imaging-for-investigation-metabolites

1. Introduction

The growing field of metabolomics has many important biological applications including biomarker discovery, deciphering metabolic pathways in plants and other biological systems, and toxicology profiling.[2-7] A major technical challenge when studying biological systems is to study metabolomic pathways without disrupting them.[8] MALDI-MSI allows for direct analysis of intact tissues that enables sensitive detection of analytes in single organs[9-10] and even single cells.[11-12]

Scheme 1 depicts the traditional MSI workflow. Sample preparation is a crucial step in producing reproducible and reliable mass spectral images. The quality of the images greatly depends upon factors such as tissue embedding medium, slice thickness, MALDI matrix, and matrix application technique. For imaging applications, ideal section thickness is the width of one cell (8-20 μm depending on the sample type). MALDI requires deposition of an organic, crystalline matrix compound, typically a weak acid, on the sample to assist analyte ablation and ionization.[13] Different matrices provide different signal intensities, interfering ions, and ionization efficiencies of different classes of compounds.

The matrix application technique also plays a role in the quality of mass spectral images and different techniques are appropriate for different classes of analytes. Three matrix application methods are presented in this protocol: airbrush, automatic sprayer, and sublimation. Airbrush matrix application has been widely used in MALDI imaging. The advantage of airbrush matrix application is that it is relatively fast and easy. However, the quality of the airbrush matrix application greatly depends on the skill of the user and tends to be less reproducible and cause diffusion of analytes, especially small molecules.[14] Automatic sprayer

systems have similar mechanics to airbrush matrix application, but have been developed to remove the variability seen with manual airbrush application, making the spray more reproducible. This method can sometimes be more time-consuming than traditional airbrush matrix application. Both manual airbrush and automatic sprayer systems are solvent-based matrix application methods. Sublimation is a dry matrix application technique that is becoming more and more popular for mass spectral imaging of metabolites and small molecules because it reduces analyte diffusion; however, it lacks the solvent necessary to extract and observe higher mass compounds.[15]

Confident identification of metabolites typically requires accurate mass measurements to obtain putative identifications followed by tandem mass (MS/MS) experiments for validation, with MS/MS spectra being compared to standards, literature, or theoretical spectra. In this protocol high resolution (mass error < 5 ppm), liquid chromatography (LC)-MS is coupled to MALDI-MSI to obtain both spatial information and confident identifications of endogenous metabolites, using *Medicago truncatula* roots and root nodules as the biological system. MS/MS experiments can be performed directly on the tissue with MALDI-MSI or on tissue extracts with LC-MS and used for the validation of metabolite identifications.

2. Materials

2.1 Reagents/Equipment

1. Gelatin (100 mg/mL in deionized water)
2. Cryostat
3. 25-75-0.8 mm (width-length-thickness) indium tin oxide (ITO)-coated glass slides
4. 2,5-Dihydroxybenzoic acid (DHB): 150 mg/mL in 50% methanol/0.1% formic acid v/v (airbrush) or 40 mg/mL in 50% methanol/0.1% formic acid v/v (automatic sprayer)
5. Deionized water
6. Methanol
7. Airbrush coupled with 75 mL steel container
8. TM-Sprayer system (HTX Technologies, LLC, Carrboro, NC, USA) (*see* Note 1)
9. Sublimation Apparatus
10. Scanner

2.2 Instrumentation

2.2.1 MALDI- ToF/ToF MSI

An ultrafleXtreme MALDI-TOF/TOF (Bruker Daltonics, Billerica, MA, USA) analyzer equipped with a 2 kHz, FlatTop Smartbeam-II™ Nd:YAG laser (spot diameter down to 10 µm) can be used for imaging. Acquisitions can be performed in positive or negative ion reflectron mode depending on the sample type. Instrument parameters for a Bruker MALDI-TOF/TOF can be set using FlexImaging and FlexControl software (Bruker Daltonics). To produce ion images, spectra can be generated by averaging 500 laser shots over the mass range and collected at 25-100 µm intervals in both the *x* and *y* dimensions across the surface of the sample. The mass spectra can be externally calibrated using DHB matrix peaks or external standards applied directly to the glass slide.

2.2.2 MALDI-Orbitrap MSI

A MALDI-Orbitrap LTQ (Thermo Scientific, Waltham, MA, USA) analyzer equipped with a nitrogen laser (spot diameter down to 75 µm) can be used for imaging. Acquisitions can be performed in positive or negative ion mode depending on the sample type. Instrument parameters for a Thermo MALDI-Orbitrap can be set using LTQ Tune and Xcalibur software (Thermo Scientific). To produce ion images, spectra can be collected over an assigned mass range, using 2 microscans and 2 microscans/ pixel. Spectra are collected at 75 µm intervals in both the *x* and *y* dimensions across the surface of the sample. The mass spectrometer should be externally calibrated using ProteoMass calibration mix standards (Sigma Aldrich) prior to MSI analysis.

2.2.3 High Resolution LC-MS

For confident metabolite identifications, run sample extracts with LC-MS (and targeted LC-MS/MS) using either reversed phase (RP) LC with a C18 column, or normal phase (NP) with a HILIC column depending on the analytes of interest. Use mobile phases and gradients as appropriate for the specific sample type. Perform acquisitions in positive or negative ion modes depending on the sample type.

For this specific example, the **metabolite extraction procedure was as follows**:

Approximately 50-100 root nodules with 2-3 mm of surrounding root were detached from mature *Medicago* plants and placed into a pre-chilled mortar, flash-frozen with liquid nitrogen and ground to powder. The powder was transferred to a pre-chilled 13-mL PTFE-coated centrifuge tube. The endogenous peptides were extracted with 3:1:4 methanol:chloroform:water (v/v). The solution was vortexed briefly and centrifuged for 10 min at 4 °C and 4700 rpm. The resulting aqueous supernatant was collected and dried in a SpeedVac. An additional 4 parts methanol was added to the remaining solution, followed by briefly vortexing, and centrifuging for 5 min at 4 °C and 4700 rpm. The organic layer was removed from the protein pellet and both fractions were dried in a SpeedVac. The samples were stored at -80 ^{o}C until analysis.

LC parameters were as follows:

Instrumentation: Waters Acquity UPLC, Thermo Q-Exactive mass spectrometer

Column: Phenomenex C18 column, 2.1x150mm, 1.7 µm packing material

Mobile Phase A: Water + 0.1% Formic Acid

Mobile Phase B: Acetonitrile + 0.1% Formic Acid

LC Gradients:

Aqueous Fraction Gradient

Time (min)	%A	%B
0	99	1
5	99	1
10	97	3
18	60	40
22	20	80
22.1	5	95
27	5	95
27.1	99	1
35	99	1

Organic Fraction Gradient

Time (min)	%A	%B
0	99	1
22.1	5	95
27	5	95
27.1	99	1
35	99	1

MS parameters were as follows:

Mass range: 100-1000 *m/z*

Resolution: 60,000

MS/MS parameters: HCD, NCE = 30, isolation width = 2,

3. Methods

3.1 Tissue Preparation

Sample preparation is a crucial step in producing reproducible and reliable mass spectral images. The quality of the images greatly depends upon factors such as tissue fixing methods, embedding medium, and slice thickness. Microwave irradiation and heat denaturation with the Denator Stabilizer T1 (Gothenburg, Sweden) have been reported to prevent post-mortem protein

degradation by deactivating proteolytic enzymes.[16] For imaging applications, ideal section thickness should be the width of one cell; 8-20 µm thickness is appropriate. Thicker sections tend to have better tissue integrity (i.e., less tearing or folding) but thinner sections typically result in better sensitivity.

1. Trim the root nodule from the plant, leaving 3-4 mm of root attached to the nodule (1-2 mm on each side of the nodule).
2. Immediately after dissection, submerge the tissue in a cryostat cup of gelatin (*see* **Notes 2** and **3**).
3. Use forceps to orient the tissue as desired.
4. Once the tissue is stuck to the bottom of the cup, use a syringe or pipet to cover the tissue with more gelatin (approximately 3-5 mm higher than the tissue) (*see* **Note 4**). Make sure the tissue is completely surrounded by gelatin on all sides and there are no bubbles present in the gelatin (*see* **Note 5**).
5. Flash freeze the tissue by placing the cup in a dry ice/ethanol bath until the gelatin hardens and becomes opaque (*see* **Note 6**).
6. Store tissue in -80°C freezer until use.
7. Remove frozen tissue from the -80°C freezer, cut away the plastic cryostat cup and trim excess gelatin (approximately 3-4 mm on each side of the tissue). Mount the embedded tissue to the cryostat chuck with a dime-sized amount of optimal cutting temperature (OCT) media (*see* **Note 7**). Place in cryostat box until the OCT solidifies.
8. Prior to cryostat slicing, allow the chuck and gelatin to equilibrate in the cryostat box to the appropriate temperature (approximately 15 min) (*see* **Note 8**).
9. Cryostat section slices with 8-20 µm thickness as appropriate (*see* **Note 9**).

10. Thaw mount each slice onto the ITO-coated glass slide (or MALDI plate) (*see* **Note 10** and **11**). If the tissue is too large for one glass slide (i.e., whole body slices) you may position the section on multiple slides and digitally put the images together.
11. For 3D imaging, obtain multiple slices that are evenly distributed throughout the *z*-axis of the tissue and thaw mount each section individually onto the ITO-coated glass slide(s) (*see* **Note 12**).
12. Place the ITO-coated glass slides with the tissue sections in a desiccator for at least 30 minutes before matrix application.

3.2 Matrix Application

MALDI requires deposition of an organic, crystalline compound, typically a weak acid, on the tissue of interest to assist analyte ablation and ionization [13]. Choosing a MALDI matrix and its application method is essential for quality mass spectrometric imaging experiments. Conventional matrices include CHCA (α-cyano-4-hydroxycinnamic acid) and DHB. Less traditional matrices such as DAN (1,5-diaminonapthalene), DMAN (1,8-bis(dimethylamino)napthalene), DHPT (2,3,4,5-tetra(3',4'-dihydroxylphenyl)thiophene), TiO_2 nanoparticles, ionic matrices, etc. are being used and are reported to improve spectral quality, crystallization and vacuum stability [17-21]. Different matrices provide different amounts of coverage, signal intensity, matrix interference, and ionization efficiency. It is important to choose a matrix that gives the best results for the particular analytes of interest. The matrix application technique also plays a role in the quality of mass spectral images. Three matrix application methods are presented here: airbrush, automatic sprayer, and sublimation. Airbrush matrix application has been widely used in MALDI imaging, is relatively fast and easy, but is less reproducible and sometimes causes diffusion of analytes [14]. Automatic sprayer systems, like

the TM-Sprayer, have been developed which remove the variability seen with manual airbrush application, making the spray more reproducible, but is more time-consuming. Sublimation is a dry matrix application technique that is becoming more and more popular for mass spectral imaging of metabolites and small molecules [15]. Sublimation reduces analyte diffusion, but lacks the solvent necessary to observe higher mass compounds.

3.2.1 Airbrush Application of MALDI Matrix

1. Thoroughly clean the airbrush solution container and nozzle with methanol every time before matrix application.
2. Fill the solution container with DHB matrix solution (150 mg/mL in 50% methanol/0.1% formic acid v/v) and place the airbrush approximately 35 cm from the glass slide (*see* **Note 13**).
3. Apply 10-15 coats of matrix on the surface of the slide with a spray duration of 10 s and 30 s drying time in between each coat.
4. Thoroughly clean the airbrush again with methanol when finished to avoid clogging from the matrix solution.

3.2.2 Automatic Sprayer Application of MALDI Matrix

1. Start compressed air flow to the TM-Sprayer to 10 psi.
2. Turn on the TM-Sprayer, set valve to the "Load" position.
3. Set the sprayer method with the TM-Sprayer Software (*see* **Note 14**) and turn on the solvent pump to approximately 0.250 mL/min.
4. Use a syringe to inject your matrix solution (40 mg/mL DHB in 50% methanol/0.1% formic acid v/v) into the sample loop with 20% overfill.

5. Place ITO-coated glass slide with tissue slices into the spray chamber.
6. Switch valve to “Spray” and wait 1-2 minutes for the matrix to reach the nozzle tip.
7. Start sprayer method.
8. When finished, switch valve back to “Load” keeping the pump flow on and flush the loop with 50% methanol 3 times.
9. Turn the temperature back down to 30°C. Wait for the temperature to come to at least 50°C and turn off the pump, air, and sprayer system.

3.2.3 Sublimation Application of MALDI Matrix

1. Weight out 300 mg DHB into the bottom of the sublimation chamber as shown in Figure 1a.
2. Use double-sided conductive tape to stick the glass slide to the underside of the cold finger (top portion of the sublimation chamber), with the tissue sections facing down (*see* **Note 15**) as shown in Figure 1b.
3. Clamp the top and bottom of the sublimation chamber together and connect the vacuum and water as shown in Figure 1c.
4. Place sublimation chamber in a heating mantle that is at room temperature.
5. Turn on the vacuum pump. After 15 min turn on the water. Wait an additional 5 min and turn on the heating mantle.
6. The heating mantle should reach 120°C over the course of 10 min.
7. After 10 min, turn off heat and water, close valve to vacuum (so the inside of the chamber remains under vacuum) and turn off the vacuum pump.
8. Allow the chamber to come to room temperature before releasing the vacuum pressure and removing the glass slide.

3.3 Image Acquisition

3.3.1 Image Acquisition- MALDI-ToF/ToF

1. Mark a + pattern on each corner of the slide with a WiteOut correction fluid pen. Place the glass slide into the MALDI slide adapter plate and use a scanner to scan an optical image of the slide and samples (*see* **Note 16**).
2. Set up an image acquisition file using FlexControl (Bruker Daltonics) (*see* **Note 17**).
3. Load the optical image into FlexImaging and toggle back and forth between FlexImaging and FlexControl to set the 3 "teach points" which will align the plate with the optical image (*see* **Note 18**).
4. Calibrate the instrument with the "calibration" tab in FlexControl. Common matrix peaks or external standards may be used for calibration (*see* **Note 19**).
5. Specify the areas you would like to image by tracing around the tissue slice with the "add polygon measurement region" tool. Also trace around a small spot of pure matrix for comparison (*see* **Note 20**).
6. Set the desired mass range and laser energy using FlexControl.
7. Start automatic run. The software will calculate the estimated time for completing the experiment. This can be seen at the top of the "regions" window.
8. For 3D imaging, perform acquisition as described above for all tissue sections.

3.3.2 Image Acquisition- MALDI-Orbitrap

1. Calibrate the instrument (or check the calibration) using the ProteoMass calibration kit (Sigma Aldrich).
2. Unload the spot plate, check "use imaging feature" in the Imaging tab, close LTQ Tune

3. Before inserting the imaging plate, use the scanner to take an optical image of the entire glass slide adapter (< 5 minutes to complete). Alternatively, an optical image can be scanned by the instrument after the plate is inserted (approximately 25 min per slide).
4. Re-open LTQ Tune and load the imaging plate.
5. Using the Imaging tab in LTQ tune, create a MALDI Position File for each region to be imaged. To do this, import the optical image, click "view plate" use the blue rectangle to trace around the imaging region, hit apply. Select the raster step size on the imaging tab. Always re-open the saved position file to check that the raster step size was saved properly. Always use the camera to check that the position file actually begins at the correct position on your tissue.
6. Adjust the laser energy for each sample/ matrix by moving off-tissue to a section of the slide that contains matrix and increasing or decreasing the laser energy until the desired intensity is achieved. Set the microscans to 2. Save the tune page.
7. Open the Xcalibur software and create a new instrument method. Choose "imaging" for plate motion, 2 microscans/step, browse in the correct tune page, choose normal mass (*m/z* 100-2000) or high mass (*m/z* 200-4000), and set the desired mass range. Save the instrument method.
8. Use Xcalibur to create a sample list. Assign the sample name, output folder, and imaging method. Copy and paste the entire MALDI Position File (beginning with C://) for each sample directly from LTQ Tune.
9. Begin the acquisition for one or all of the samples, setting the instrument to standby when finished.
10. For 3D imaging, perform acquisition as described above for serial tissue sections.

3.4 Image Processing

3.4.1 2D Image Generation- Bruker Software

1. Open FlexImaging software and open your imaging file. This could take several minutes depending on the processing power of your computer. The spectrum display will show the average spectrum of all collected spectra.
2. You can click on peaks on the mass spectrum with the "mass filter selection" tool to see where the analyte is distributed within the tissue section. The "color gradient" tool will let you see the intensity of the ion within that tissue section. You may also use the "show single spectrum" tool to click on a pixel on the imaging display and see the mass spectrum for that specific location on the tissue.
3. You may view the average spectra for several different regions at once by checking the "spectrum" boxes on the region window of the regions you would like to compare, right clicking on the spectrum display and selecting display type 2D stack plot.
4. Images and spectra can be saved by using the edit → copy function and pasting the image in Microsoft PowerPoint or similar programs. Figure 2 shows MSI detection of several metabolites displaying distinct distribution patterns in the root and nodule of *Medicago truncatula*, a model legume plant [7].

3.4.2 2D Image Generation- Thermo Software

1. Open ImageQuest and open the data file. An image of the overall TIC will be displayed.
2. To show an averaged spectrum for part or all of the tissue sample, use the sum feature to trace around the tissue.

3. On the left-hand side of the screen, find the “normalization” menu and select “normalize raw data”.
4. To generate an image for a peak of interest found by manually scrolling through the spectrum, select the “new data set button” on the left-hand menu. Select mass range / TIC, write in the mass of interest (to 3 decimal places), and select 5 ppm for the mass error.
5. A mass list generated from one sample can be exported and subsequently imported when the next data file is opened.
6. Images and spectra can be saved by using the edit → copy function and pasting the image in Microsoft PowerPoint or similar programs.

3.4.3 2D Image Generation- MSiReader[22]

1. Download MSiReader at the following link: http://www.msireader.com/
2. Open the data file in ImageQuest.
3. File → Export the file to .imzml
4. Open MSiReader and select .imzml for the image file type. Browse in your .imzml data file.
5. Input an *m/z* value that shows a unique distribution pattern in the tissue (find with ImageQuest).
6. Select 10 ppm for the *m/z* tolerance (this will equate to ± 5 ppm).
7. Normalize to the TIC using the drop down menu next to “normalization”.
8. You may edit the color map to your preference. “Jet” is the suggested colormap.
9. Launch the “image overlay tool” (third icon from the top, left-hand corner).
10. Load a .tiff file using the “load an image overlay” button in the top left corner.

11. Adjust the image to line up with the MS image on your tissue.
12. Create a mass list by tracing around the tissue area of interest (called the interrogation zone) with the “polygon tool”.
13. Trace around a region of pure matrix, which will be the reference zone and those peaks will be ignored.
14. Extract the peaks that are unique to the interrogation zone using the button next to the polygon tool.
15. Set the parameters in the pop-up box according to your specific interests.
16. De-select the polygon tool when the software has finished generating the mass list.
17. Automatically generate an image for each peak in a list using the fifth icon from the left.

3.4.4 3D Image Generation

1. Open the instrument vender imaging software and extract the peak of interest. Save images of serial sections as picture files (i.e. JPEG).
2. Open Image J software (http://rsbweb.nih.gov/ij/ , NIH) (*see* **Note 21**).
3. Open the consecutive series of tissue images that you saved with the vender’s software (*see* **Note 22**).
4. Align the orientation and position of each image and make slight adjustments to get the images aligned using the “translate” and “rotate” functions under “image”.
5. Under “image”, “stacks”, open “images to stack” to combine the 2D images into one stack.
6. To view the stack in 3 dimensions, open “image”, “stacks”, and click on “3D project”. Parameters such as axis of rotation, slice spacing, etc. can be adjusted by changing values in the 3D projection window.

4. Notes

1. The TM-Sprayer from HTX Technologies is a highly specialized automatic matrix sprayer. Other matrix sprayers are available; however they have different features than the TM-Sprayer and should be used according to manufacturer recommendations.
2. Gelatin is used for imbedding the tissues rather than OCT media because OCT contains a high concentration of polyethylene glycol (PEG) which produces interfering peaks in the mass spectral analysis.
3. Before placing the tissue in the cup, use a 5 mL syringe to squeeze a small amount of warm gelatin into the bottom of the cup and allow to cool slightly until it becomes sticky. This will assist in keeping the tissue stuck to the bottom of the cup and prohibit it from floating in the gelatin.
4. Keep gelatin slightly warm before pouring over tissue.
5. It is a good idea to mark the cryostat cup and sketch the orientation of the tissue in your notebook for future reference. Note which side of the tissue is facing the bottom of the cup (tissue slicing begins from the bottom of the cup).
6. Use large forceps or another apparatus to hold the cup upright. Be sure not to get ethanol into the cup; this will cause the gelatin to dissolve and not freeze completely.
7. Due to the interference caused by OCT media, OCT is used only to mount the gelatin to the chuck, but should not touch the tissue sample itself.
8. The cryostat is most commonly kept at -20°C for tissue sectioning, however setting the temperature to -25°C results in better slicing for some types of tissues.
9. For larger tissue samples such as whole body animal samples, use a section thickness of 20 µm.

10. There are two methods for thaw mounting. In the first method, warm an ITO-coated glass slide by placing the back of your hand on the back of the slide until warm. Place the ITO-coated side of the warmed slide near the cold slice and allow the slice to melt onto the slide. For the second method, use a fine paint brush to place the cold slice onto the cold slide and warm the slide and slice together with the back of your hand as mentioned previously. The latter method is trickier and can ruin the section, but also results in less analyte loss [23].
11. It is beneficial to check the integrity of the tissue sections by thaw mounting the first section onto a regular glass microscope slide and carefully examining it under a microscope before placing sections onto the more expensive ITO-coated glass slides.
12. Different organs from different biological tissues have different thicknesses, so the number of slices and the distance between slices necessary for 3D imaging varies.
13. Use the airbrush in a fume hood to avoid inhaling matrix solution. Hold the airbrush perpendicular to the glass slide, 35 cm away, and adjust the flow rate so that most of the matrix solvent evaporates before reaching the slide.
14. HTX Technologies has recommended methods that can be used as a starting point. Changing variables such as flow rate, velocity, temperature and number of passes will change the dryness of the spray, the coverage and the amount of matrix deposited. For MSI of metabolites in root nodules using 40 mg/mL DHB as the matrix, set the temperature to ~80 °C, velocity to 1250 mm/min, flow rate to 50 µL/min, and number of passes to 24. For best coverage, it is recommended to rotate the nozzle 90° and/or offset the nozzle 1.5 mm between each pass. When using other matrices be sure to use the same solvent in the syringe pump that the matrix is dissolved in. The temperature

should also be adjusted when using other matrices; slowly increase the temperature until you hear a "puffing" sound and then reduce the temperature by 5 °C for your final method.

15. If the glass slide is too large for the sublimation chamber, cut the glass slide to the appropriate size (i.e. cut in half) and apply the matrix to both halves separately. Take this into account when placing cryostat tissue slices onto the slide.
16. With EPSON Scan software, hit the "Preview" button and draw a box around the image of the slide. Hit the "Zoom" button to zoom in on the slide region. Set the resolution to 2400 dpi and scan the image. Open the image and orient the picture to match the orientation of the slide in the holder.
17. To build an acquisition file, experiment with different laser diameters, laser intensities and number of shots to optimize the signal intensity. Typically use a raster width of 50 µm; smaller raster widths give higher resolution images but takes longer time to acquire images. "LIFT" mode allows the acquisition of MS/MS spectra.
18. The WiteOut marks can be used as teach points. After setting the teach points, select the "move sample carrier" option on FlexImaging and move the plate around by clicking on different areas of the optical image to make sure that the alignment is acceptable.
19. To calibrate with matrix peaks, shoot the laser at a spot of matrix only. Use the website "http://www.chem.ualberta.ca/~liweb/links/MaClust.htm" (developed by the Liang Li group) to identify the *m/z* of theoretical matrix clusters for DHB.
20. If you are using the airbrush matrix application method, it is beneficial to image several spots of pure matrix in case there are inconsistencies with the spray coverage.

21. Several other 3D imaging software packages can also be used, such as LSM Viewer (Zeiss, Germany), Metamorph (Molecular Devices, Sunnyvale, CA, USA), and Amira (Mercury Computer Systems, Chelmsford, MA, USA). Other commercial, open-source 3D imaging software platforms include: Fiji, CellProfiler, Vaa3D, BioImageXD, Icy, and Konstanz Information Miner [24].
22. The images must be in gray scale to be processed with Image J.

Acknowledgements

This work was supported by funding from the University of Wisconsin Graduate School and the Wisconsin Alumni Research Foundation (WARF) and Romnes Faculty Research Fellowship program (to L.L.). E.G. acknowledges a National Science Foundation (NSF) Graduate Research Fellowship.

References

1. Seeley, E. H.; Schwamborn, K.; Caprioli, R. M., Imaging of Intact Tissue Sections: Moving beyond the Microscope. *J Biol Chem* **2011,** *286* (29), 25459-25466.

2. Wei, R., Metabolomics and Its Practical Value in Pharmaceutical Industry. *Curr Drug Metab* **2011,** *12* (4), 345-358.

3. Kobayashi, T.; Nishiumi, S.; Ikeda, A.; Yoshie, T.; Sakai, A.; Matsubara, A.; Izumi, Y.; Tsumura, H.; Tsuda, M.; Nishisaki, H.; Hayashi, N.; Kawano, S.; Fujiwara, Y.; Minami, H.; Takenawa, T.; Azuma, T.; Yoshida, M., A Novel Serum Metabolomics-Based Diagnostic Approach to Pancreatic Cancer. *Cancer Epidem Biomar* **2013,** *22* (4), 571-579.

4. West, P. R.; Weir, A. M.; Smith, A. M.; Donley, E. L. R.; Cezar, G. G., Predicting human developmental toxicity of pharmaceuticals using human embryonic stem cells and metabolomics. *Toxicol Appl Pharm* **2010,** *247* (1), 18-27.

5. Spegel, P.; Sharoyko, V. V.; Goehring, I.; Danielsson, A. P.; Malmgren, S.; Nagorny, C. L.; Andersson, L. E.; Koeck, T.; Sharp, G. W.; Straub, S. G.; Wollheim, C. B.; Mulder, H., Time-resolved metabolomics analysis of beta-cells implicates the pentose phosphate pathway in the control of insulin release. *The Biochemical journal* **2013,** *450* (3), 595-605.

6. Pendyala, G.; Want, E. J.; Webb, W.; Siuzdak, G.; Fox, H. S., Biomarkers for neuroAIDS: The widening scope of metabolomics. *J Neuroimmune Pharm* **2007,** *2* (1), 72-80.

7. Ye, H.; Gemperline, E.; Venkateshwaran, M.; Chen, R.; Delaux, P. M.; Howes-Podoll, M.; Ane, J. M.; Li, L., MALDI mass spectrometry-assisted molecular imaging of metabolites during nitrogen fixation in the Medicago truncatula-Sinorhizobium meliloti symbiosis. *The Plant journal : for cell and molecular biology* **2013**.

8. Prell, J.; Poole, P., Metabolic changes of rhizobia in legume nodules. *Trends in microbiology* **2006,** *14* (4), 161-168.

9. Kutz, K. K.; Schmidt, J. J.; Li, L. J., In situ tissue analysis of neuropeptides by MALDI FTMS in-cell accumulation. *Anal Chem* **2004,** *76* (19), 5630-5640.

10. Stemmler, E. A.; Cashman, C. R.; Messinger, D. I.; Gardner, N. P.; Dickinson, P. S.; Christie, A. E., High-mass-resolution direct-tissue MALDI-FTMS reveals broad conservation of three neuropeptides (APSGFLGMRamide, GYRKPPFNGSIFamide and pQDLDHVFLRFamide) across members of seven decapod crustaean infraorders. *Peptides* **2007,** *28* (11), 2104-2115.

11. Rubakhin, S. S.; Churchill, J. D.; Greenough, W. T.; Sweedler, J. V., Profiling signaling peptides in single mammalian cells using mass spectrometry. *Anal Chem* **2006,** *78* (20), 7267-7272.

12. Neupert, S.; Predel, R., Mass spectrometric analysis of single identified neurons of an insect. *Biochem Bioph Res Co* **2005,** *327* (3), 640-645.

13. Caprioli, R. M.; Farmer, T. B.; Gile, J., Molecular imaging of biological samples: localization of peptides and proteins using MALDI-TOF MS. *Anal Chem* **1997,** *69* (23), 4751-4760.

14. Baluya, D. L.; Garrett, T. J.; Yost, R. A., Automated MALDI matrix deposition method with inkjet printing for imaging mass spectrometry. *Anal Chem* **2007,** *79* (17), 6862-6867.

15. Hankin, J. A.; Barkley, R. M.; Murphy, R. C., Sublimation as a method of matrix application for mass spectrometric imaging. *Journal of the American Society for Mass Spectrometry* **2007,** *18* (9), 1646-1652.

16. Svensson, M.; Boren, M.; Skold, K.; Falth, M.; Sjogren, B.; Andersson, M.; Svenningsson, P.; Andren, P. E., Heat Stabilization of the Tissue Proteome: A New Technology for Improved Proteomics. *J Proteome Res* **2009,** *8* (2), 974-981.

17. Ye, H.; Gemperline, E.; Li, L., A vision for better health: Mass spectrometry imaging for clinical diagnostics. *Clinica chimica acta; international journal of clinical chemistry* **2012**.

18. Thomas, A.; Charbonneau, J. L.; Fournaise, E.; Chaurand, P., Sublimation of new matrix candidates for high spatial resolution imaging mass spectrometry of lipids: enhanced information in both positive and negative polarities after 1,5-diaminonapthalene deposition. *Anal Chem* **2012,** *84* (4), 2048-2054.

19. Shroff, R.; Rulisek, L.; Doubsky, J.; Svatos, A., Acid-base-driven matrix-assisted mass spectrometry for targeted metabolomics. *Proceedings of the National Academy of Sciences of the United States of America* **2009,** *106* (25), 10092-10096.

20. Chen, S.; Chen, L.; Wang, J.; Hou, J.; He, Q.; Liu, J.; Xiong, S.; Yang, G.; Nie, Z., 2,3,4,5-Tetrakis(3',4'-dihydroxylphenyl)thiophene: a new matrix for the selective analysis of low molecular weight amines and direct determination of creatinine in urine by MALDI-TOF MS. *Analytical chemistry* **2012,** *84* (23), 10291-10297.

21. Shrivas, K.; Hayasaka, T.; Sugiura, Y.; Setou, M., Method for simultaneous imaging of endogenous low molecular weight metabolites in mouse brain using TiO2 nanoparticles in nanoparticle-assisted laser desorption/ionization-imaging mass spectrometry. *Analytical chemistry* **2011,** *83* (19), 7283-7289.

22. Robichaud, G.; Garrard, K. P.; Barry, J. A.; Muddiman, D. C., MSiReader: an open-source interface to view and analyze high resolving power MS imaging files on Matlab platform. *Journal of the American Society for Mass Spectrometry* **2013,** *24* (5), 718-721.

23. Schwartz, S. A.; Reyzer, M. L.; Caprioli, R. M., Direct tissue analysis using matrix-assisted laser desorption/ionization mass spectrometry: practical aspects of sample preparation. *J Mass Spectrom* **2003,** *38* (7), 699-708.

24. Schindelin, J.; Arganda-Carreras, I.; Frise, E.; Kaynig, V.; Longair, M.; Pietzsch, T.; Preibisch, S.; Rueden, C.; Saalfeld, S.; Schmid, B.; Tinevez, J. Y.; White, D. J.; Hartenstein, V.; Eliceiri, K.; Tomancak, P.; Cardona, A., Fiji: an open-source platform for biological-image analysis. *Nat Methods* **2012,** *9* (7), 676-682.

Figures

Scheme 1

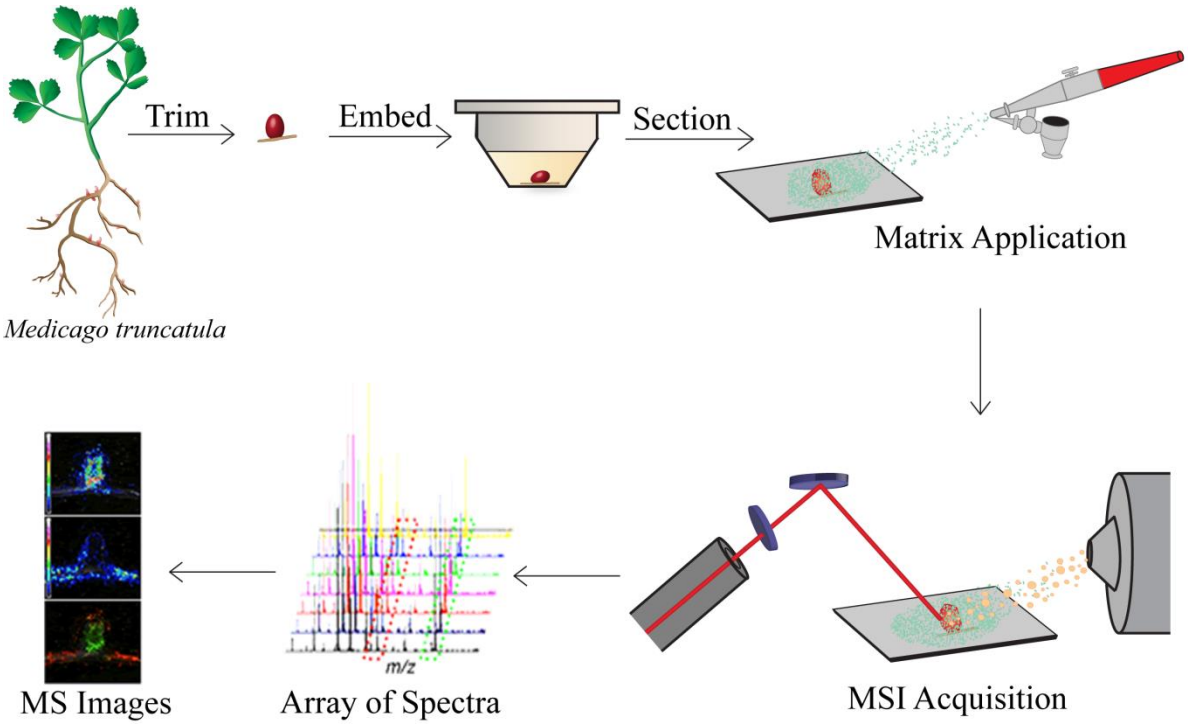

Scheme 1. General scheme of MSI technology and its application to mapping plant metabolites. Acquisition occurs by collecting mass spectra for each pixel and processing this array of spectra into representative 2D images of specific *m/z* values.

Figure 1

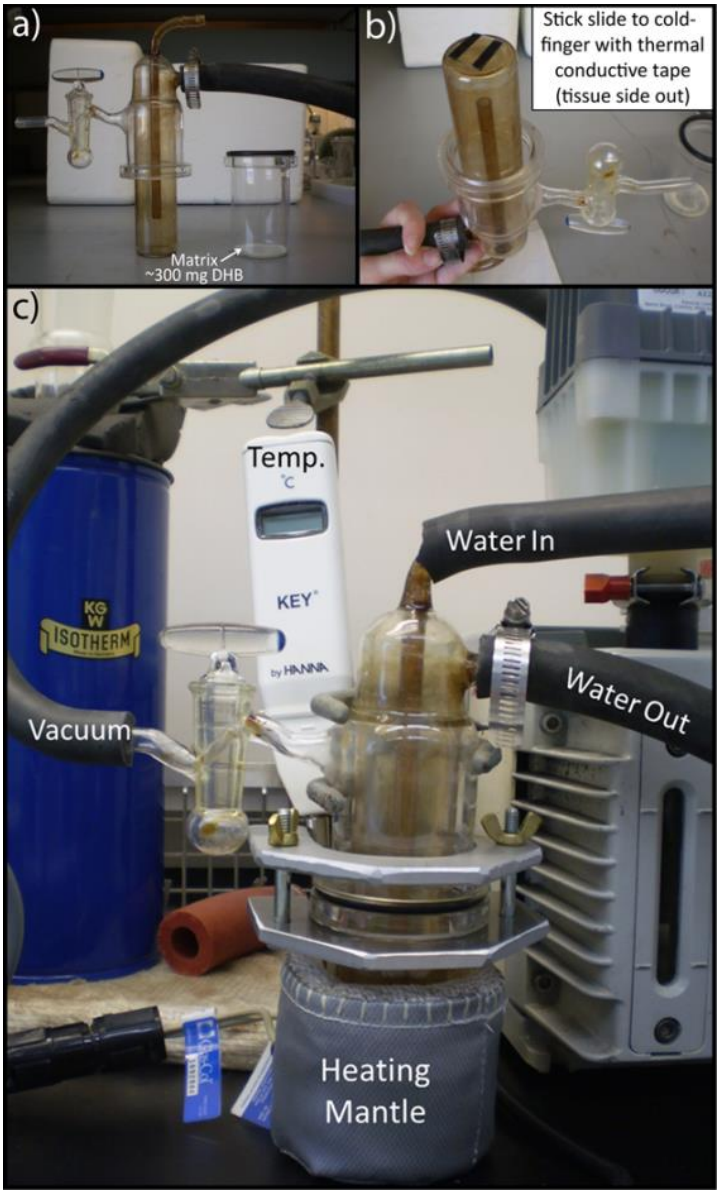

Figure 1. Labeled photograph of sublimation apparatus set up. (a) Weigh out the matrix and place it in the bottom portion of the sublimation chamber. (b) The ITO-slide with the tissue slice on it is attached to the underside of the condenser by thermal conducting tape. (c) Overall set up of the sublimation chamber connected to water, vacuum pump, and heating mantel and monitoring the temperature.

Figure 2

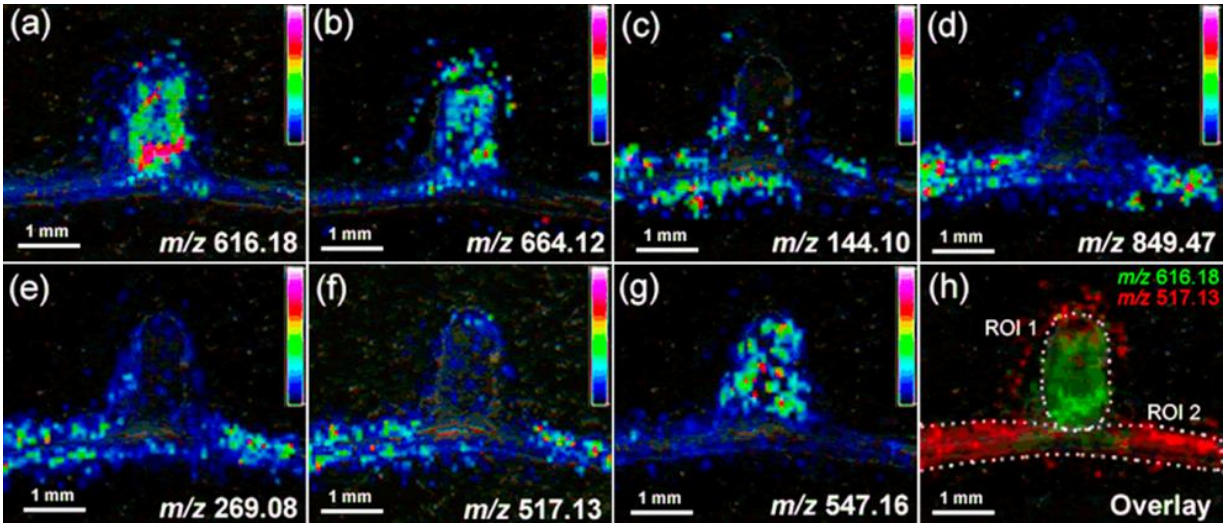

Figure 2. Representative metabolite distribution in *Medicago truncatula* root nodule section revealed by MALDI-MSI. (a) heme-moiety (*m/z* 616.15), (b) NAD (*m/z* 664.10), (c) proline betaine (*m/z* 144.10), (d) a putative sodiated lipid (*m/z* 849.47), (e) formononetin (*m/z* 269.08), (f) formononetin MalGlc (*m/z* 517.13), (g) afrormosin MalGlc (*m/z* 547.16) displaying distinct distribution patterns in roots and nodules. (h) An overlaid image of (a) and (f). Adapted from Ref. 7.